

Unification of Active Galactic Nuclei at X-rays and soft gamma-rays

Volker Beckmann

Laboratoire AstroParticule et Cosmologie (APC) - Paris,
France

Habilitation à diriger des recherches
présentée à l'Université Paris 7 - Denis Diderot

Soutenue le 10 septembre 2010 devant le jury composé de:

Pierre Binétruy	President
Peter von Ballmoos	Rapporteur
Chris Done	Rapporteur
Catherine Boisson	Rapporteur (interne)
Jérôme Rodriguez	Examineur
Etienne Parizot	Examineur

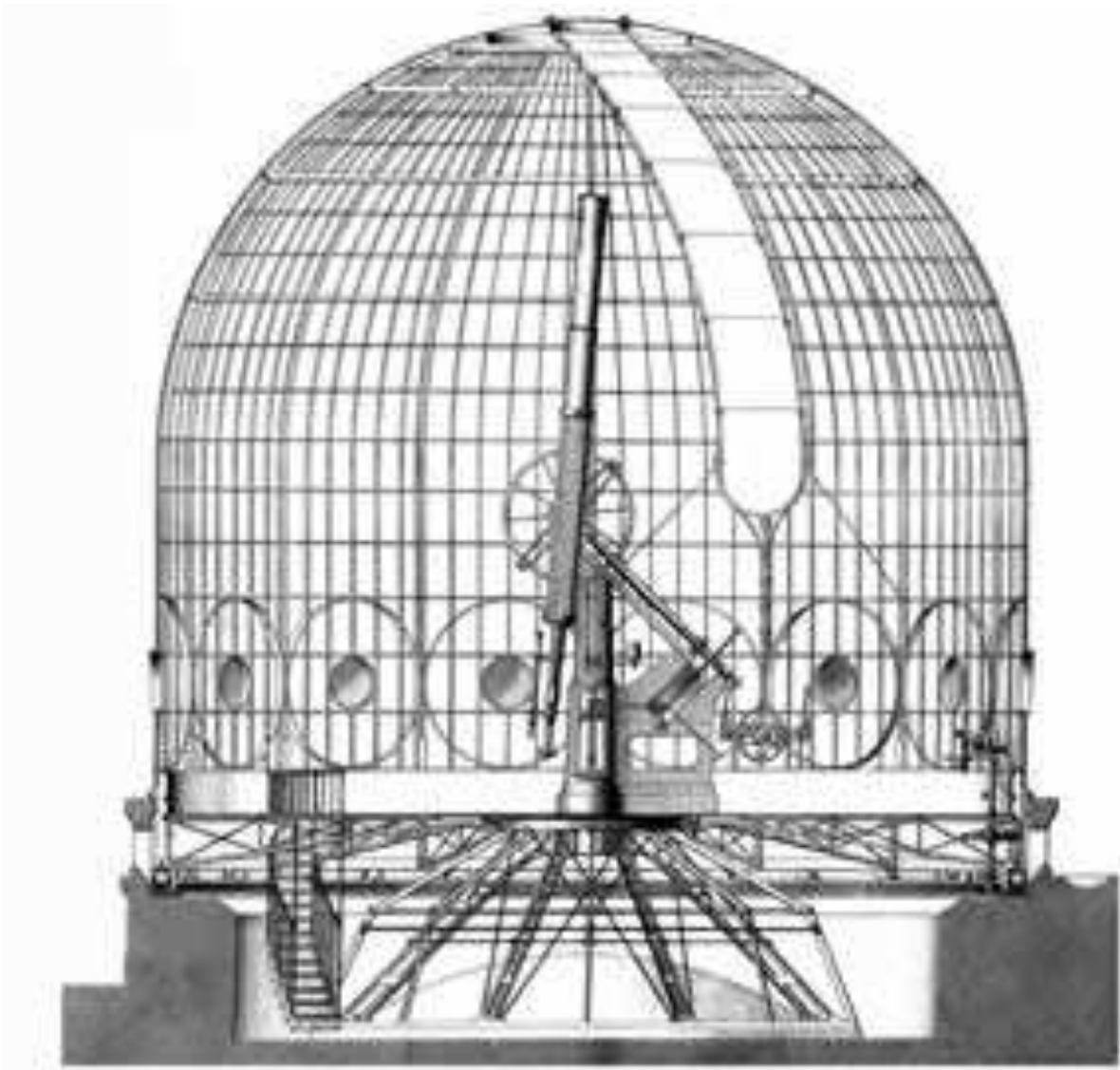


Figure 1: The 12 meter dome at the Observatoire de Paris, constructed 1845-1847 on the northern tower of the institute when François Arago was its director. Figure from Arago & Barral (1854)

Contents

1	CURRICULUM VITAE	7
1.1	Personal Information	7
1.2	Education	7
1.3	Work history	8
1.4	Experience and achievements	8
2	TEACHING AND PUBLIC OUTREACH	11
2.1	Teaching	11
2.1.1	Stellar Astrophysics	11
2.1.2	Extragalactic Astronomy and Cosmology	11
2.2	Supervision of students	12
2.2.1	Hamburg University	12
2.2.2	ISDC Data Centre for Astrophysics	12
2.2.3	François Arago Centre	12
2.3	Refereeing	13
2.4	Conference and meeting organisation	13
2.5	Public Outreach	14
2.6	Press releases	14
3	SUMMARY, RELEVANCE AND ORIGINALITY OF RESEARCH	17
4	RESEARCH	19
4.1	From <i>Welteninseln</i> to AGN	19
4.2	From optical to X-ray observations of AGN	21
4.3	The AGN phenomenon and the Unified Model	23
4.4	Verifying the unified model through evolutionary tests	28
4.4.1	Number counts	29
4.4.2	The V/V_{max} test	30
4.4.3	The luminosity function	31
4.4.4	Local luminosity function of optically selected AGN	32
4.5	Testing Unification on X-ray selected BL Lac Objects	37
4.6	Early <i>INTEGRAL</i> AGN Observations	45
4.6.1	The <i>INTEGRAL</i> Mission	45
4.6.2	The hard X-ray spectrum of AGN	50
4.6.3	The quasars MR 2251-178 and 3C 273	53
4.6.4	The Seyfert 2 NGC 4388	54

4.6.5	The Seyfert 1.5 galaxy NGC 4151	58
4.6.6	The First <i>INTEGRAL</i> AGN Catalogue	60
4.7	AGN Population Studies at Hard X-rays	62
4.7.1	The Hard X-ray 20–40 keV Luminosity Function	62
4.7.2	Hard X-ray variability of AGN	66
4.7.3	The Second <i>INTEGRAL</i> AGN Catalogue	74
4.7.4	The special case of MCG–05–23–016	78
4.8	Connection to Gamma-rays	82
4.8.1	ROSAT selected Gamma-ray Blazars	82
4.8.2	The Fermi view on hard X-ray blazars	87
4.8.3	The non-blazar population seen by Fermi	90
5	CONCLUSION & OUTLOOK	93
5.1	Conclusions	93
5.1.1	Progress concerning the unified scheme	93
5.1.2	Impact on studies of the cosmic X-ray background	94
5.1.3	Outlining the connection to the gamma-rays	94
5.2	Open questions	94
5.3	Future projects	96
5.3.1	Research	96
5.3.2	Enabling science: the François Arago Centre	98
6	LIST OF PUBLICATIONS AND CONFERENCE CONTRIBUTIONS	101
6.1	Articles in refereed international journals	101
6.2	Invited talks at international conferences	105
6.3	Refereed conference proceedings	105
6.4	Non-refereed conference proceedings	107
6.5	Other non-refereed publications	108
6.6	Communications in conferences	114
6.6.1	Talks in international conferences	114
6.6.2	Posters in international conferences	116
6.7	Seminars (only after 2005)	117
6.8	Thesis and dissertation	118
6.9	Five significant publications	118
6.9.1	The HRX-BL Lac sample - Evolution of BL Lac objects	119
6.9.2	The First <i>INTEGRAL</i> AGN Catalog	132
6.9.3	The Hard X-ray 20-40 keV AGN Luminosity Function	144
6.9.4	Hard X-ray variability of active galactic nuclei	155
6.9.5	The Second <i>INTEGRAL</i> AGN Catalogue	165
	BIBLIOGRAPHY	189
	ACKNOWLEDGMENTS	207

Chapter 1

CURRICULUM VITAE

1.1 Personal Information

Name: **Volker BECKMANN**
Citizenship: German
Date of Birth: March 7, 1968 in Hamburg (Germany)
Present Position: Chercheur au CNRS based at the APC
(UMR 7164)
Address: APC, François Arago Centre, Université Paris Diderot,
10 rue Alice Domon et Léonie Duquet,
75205 Paris Cedex 13, France
Telephone: +33 (0)157 27 60 81 Fax: +33 (0)157 27 60 71
E-mail: beckmann@apc.univ-paris7.fr

1.2 Education

- 1996/2001 PhD at University of Hamburg, Hamburger Sternwarte in Astrophysics. Title: *Evolutionary behaviour of AGN - investigations on BL Lac objects and Seyfert II galaxies*.
Referees: Prof. Dr. Dieter Reimers (Hamburger Sternwarte), and Prof. Dr. Laura Maraschi (Osservatorio Astronomico di Brera).
PhD defended on January 12, 2001. Grade: *magna cum laude*
- 1993/96 *Diplom* (Master) in Physics at the University of Hamburg.
Thesis: *X-ray spectral index of RASS-AGN*.
Referees: Prof. Dr. Sjur Refsdal and Prof. Dr. Dieter Reimers (Hamburger Sternwarte). Grade: *cum laude*
- 1989/93 *Vordiplom* (Bachelor) in Physics at the University of Hamburg

1.3 Work history

- since September 2009 Chercheur CNRS, working for the APC laboratory (Université Paris 7 - Denis Diderot). In charge of the François Arago Centre, a data and computing centre for space- and ground-based astroparticle physics.
- April 2007 - Aug. 2009 Collaborateur Scientifique of the University of Geneva, working at the ISDC Data Centre for Astrophysics. Operations coordinator and instrument specialist for the spectrograph SPI of the *INTEGRAL* mission at the ISDC. July 2007 until August 2009 also *INTEGRAL* responsible scientist.
- since April 2007 Adjunct Assistant Professor at the University of Maryland Baltimore County (UMBC).
- Oct. 2003 - March 2007 Working as a Research Associate for UMBC at NASA/Goddard Space Flight Center. Since July 2006 head of the *INTEGRAL* guest observer facility at NASA. Support of guest investigators, preparation and administration of *INTEGRAL* budget, analysis and interpretation of *INTEGRAL* data, maintaining the *INTEGRAL*/HEASARC archive.
Since August 2006 Assistant Research Professor at UMBC.
- Feb. 2001 – Sep. 2003 Working for the IAAT (University of Tübingen) at the ISDC. Developing and integrating analysis software for *INTEGRAL*, support of operations of the *INTEGRAL* satellite.
- May – July 2000 Working at the *Osservatorio Astronomico di Brera* in Milan, financed by an Italian grant (CNR).
- Apr.-Sep. 1999 Working at the *Osservatorio Astronomico di Brera*, financed by the Deutsche Akademische Austauschdienst (DAAD).
- 1996 – 2000 Scientific assistant researcher at the Hamburger Sternwarte, financed by the Deutsche Forschungsgemeinschaft (DFG).

1.4 Experience and achievements

Teaching experience

Two full courses as assistant research professor at the physics department of the the University of Maryland for physics master students. In addition, teaching (as replacement) at the University of Geneva. See Section 2.1.

Supervising experience

Supervision or co-supervision of 8 students (among which 2 PhD students). See Section 2.2.

Publications

60 publications in international refereed journals, including 17 as lead author.

22 publications in international refereed conference proceedings including 7 as lead author.

28 publications in non-refereed conference proceedings including 12 as lead author.

55 Astronomer's Telegrams including 3 as lead author.

19 GRB Circular Network (GCN) reports including 7 as lead author.

Conferences, seminars, and oral communications

25 talks in international conferences of which 3 were invited review talks.

17 poster presentations at international conferences.

ca. 30 seminars given in various institutions around the world.

Collaborations

Working in several institutes in Europe and in the U.S. I had the opportunity to get involved in many scientific collaborations. Here the most productive collaborations are the ones with colleagues at those institutes where I worked, i.e. Hamburg Observatory, ISDC Data Centre for Astrophysics, Osservatorio Astronomico di Brera, and NASA's Goddard Space Flight Center. My main collaborators over the years were and are still:

Thierry J.-L. Courvoisier (ISDC, Versoix)

Roberto Della Ceca (Osservatorio Astronomico di Brera, Milan)

Dieter Engels (Hamburger Sternwarte, Hamburg)

Neil Gehrels (NASA/GSFC, Washington D.C.)

Julien Malzac (CESR, Toulouse)

Ada Paizis (INAF/IASF-Milan)

Dieter Reimers (Hamburger Sternwarte, Hamburg)

Claudio Ricci (ISDC, Versoix)

Jérôme Rodriguez (CEA/SAP, Saclay)

Chris R. Shrader (NASA/GSFC, Washington D.C.)

Simona Soldi (CEA/SAP, Saclay)

Jack Tueller (NASA/GSFC, Washington D.C.)

Marc Türlér (ISDC, Versoix)

Anna Wolter (Osservatorio Astronomico di Brera, Milan)

Olaf Wucknitz (Argelander-Institut für Astronomie, Universität Bonn)

Professional memberships

Member of the International Astronomical Union (IAU).

Research Grants and Fellowships

year	amount	source
2008	8,000,000 CHF	4-year budget for the ISDC, for which I was responsible as being a member of the management team. Co-I
2007	2,300 \$	NASA/NHSC, P.I.
2007	9,794 \$	NASA/Chandra AO-8, P.I.
2006	57,000 \$	NASA/INTEGRAL AO-4, P.I.
2005	12,310 \$	NASA/INTEGRAL AO-3, P.I.
2004	7,686 \$	NASA/INTEGRAL AO-2, P.I.
2004	13,000 \$	NASA/RXTE Cycle 9, P.I.
2000	5,400 \$	CNR (Italy) research grant to work in Milano, P.I.
1999	7,000 \$	DAAD (Germany) fellowship to work in Milano, P.I.

Experience in space based astrophysics

Successful observation proposals for *ROSAT*, *BeppoSAX*, *XMM-Newton*, *Chandra*, *Swift*, and *INTEGRAL*, and *AGILE*. In addition, experience with the usage of data from *HST*, *RHESSI*, and *RXTE*.

Experience in ground based astrophysics

About 20 observation runs at optical and infrared telescopes, performing spectroscopy, multi-object spectroscopy, imaging, and photometry. Telescopes used include Calar Alto (CA) 3.5m, CA 2m, CA 1.2m, CA Schmidt telescope, and the Hamburg 1m Oskar-Lühning-Telescope on the northern hemisphere. On the southern hemisphere I worked at La Silla at the NTT, the 1.54m Danish telescope, and the 90cm Dutch telescope.

Chapter 2

TEACHING AND PUBLIC OUTREACH

2.1 Teaching

The University of Maryland gave me the opportunity to teach undergraduate courses. The teaching included the design of the course, development of the course structure and topics to be covered. Each course consisted of 30 lectures, weekly homework assignments including correction and evaluation of the students' work (as no teaching assistant was assigned to me), 3 exams (two midterm and one final exam) in each course, and the final grading. In addition, this included open office hours, providing advice and support to students.

Since August 2006 I am assistant professor at the University of Maryland Baltimore County, with adjunct status since April 2007.

2.1.1 Stellar Astrophysics

I taught the course *Stellar Astrophysics* at the University of Maryland Baltimore County (UMBC) as course PHYS 205 in fall 2004. The course was upgraded to PHYS 305 a year later as the prerequisites seemed to be too advanced for a second year physics major. The course included lecture twice a week with homework (also twice a week), 3 exams, and a practical project using the UMBC telescope. The course followed the text book by Carroll & Ostlie (1996). A detailed description of the course can be found on the course webpage:

<http://asd.gsfc.nasa.gov/Volker.Beckmann/edu/index.html>

2.1.2 Extragalactic Astronomy and Cosmology

In fall 2006 I taught the course *Extragalactic Astronomy and Cosmology* at UMBC (PHYS 316). The course dealt rather with the theoretical aspects of cosmology than with observational astrophysics. Main topics were the matter content of the Universe and large scale structure, dark matter and dark energy, the expanding Universe, inflation and nucleosynthesis. As for the *Stellar Astrophysics* course, I developed the curriculum of the lecture myself, including the choice of the text book (Ryden 2003). A detailed description of the course can be found on the course webpage:

<http://asd.gsfc.nasa.gov/Volker.Beckmann/physics316/index.html>

2.2 Supervision of students

2.2.1 Hamburg University

Dietmar Nagel: diploma (master) thesis student 1996/1997 at Hamburger Sternwarte. Supervision by Prof. Dr. Dieter Reimers, Dr. Norbert Bade, and myself. Dietmar Nagel died in 1997 before finishing his thesis on the search of high-redshift quasars in *ROSAT*/PSPC pointed observations.

Ralf Keil: diploma thesis student 1999/2000. Supervision by Prof. Dr. Dieter Reimers, Dr. Dieter Engels, and myself. Title of the thesis: “Narrow-line Seyfert-1-Galaxies in the ROSAT All-Sky-Survey”. Ralf is nowadays researcher at the Center of Applied Space Technology and Microgravity (ZARM) in Bremen working on ESA’s GAIA mission.

2.2.2 ISDC Data Centre for Astrophysics

Thierry Bussien: Engineering student of the École Polytechnique Fédérale de Lausanne. Thierry performed a 2.5 month *stage* at the ISDC in summer 2003 under my supervision. He worked on the available X-ray data of the blazar RX J1211.9+2242. His work was later included in the publication on this source (Beckmann et al. 2004b). Thierry finished his diplôme d’ingénieur EPF in “Sciences et Ingénierie de l’Environnement” and works as an engineer in Lausanne.

Ada Paizis: PhD student at the ISDC under supervision of Prof. Dr. Thierry J.-L. Courvoisier. During the final stage of her PhD I co-supervised her work, mainly in the writing and publication of the first *INTEGRAL* study on low mass X-ray binaries (LMXB; Paizis et al. 2003). Dr. Paizis works now as a staff researcher at the CNR in Milan (Italy).

Ines Brott: master student of Hamburg University. She did a summer-student internship at the ISDC in August 2003 under my supervision. During this month, she studied data on AGN provided by *INTEGRAL* SPI and IBIS/ISGRI. This work led later to her master thesis, which she also conducted at the ISDC in 2003/2004. Supervision of her thesis work by Prof. Dr. Thierry J.-L. Courvoisier and myself. Thesis title: “An Extragalactic Deep Field Observation with *INTEGRAL*/IBIS”. Ines nowadays conducts her PhD thesis on the modeling of stellar atmospheres at the University of Utrecht.

Sonja Hadj-Salem: Sonja performed a four week long voluntary stage at the ISDC in spring 2009 under my supervision and co-supervision by Dominique Eckert. During this time she worked on the shift operations of the *INTEGRAL* satellite and analysed IBIS/ISGRI data of the Seyfert galaxies NGC 4945, NGC 4388, and IC 4329A.

Claudio Ricci: master thesis student at the ISDC in spring/summer 2008 under supervision of Prof. Dr. Thierry J.-L. Courvoisier and myself. During the thesis Claudio analysed the *INTEGRAL* data of the radio galaxy IGR J21247+5058. Following the master, he started a PhD thesis on AGN and *INTEGRAL* at the ISDC, first under my supervision and, since I left in September 2009, under supervision of Dr. Roland Walter.

2.2.3 François Arago Centre

Olivier Do Cao: master-2 student of Université Paris 7, who conducted his master thesis work under my supervision in spring 2010. The work, entitled “Observations close to the central black hole in NGC 2110”, was aiming at the analysis of X-ray data of the Seyfert 2 galaxy NGC 2110 and the reconstruction of its spectral energy distribution. The results was presented at the 8th *INTEGRAL* workshop in Dublin in September 2010. Olivier is now doing a PhD at CEA/Saclay.

Sandra de Jong: My proposal for a PhD project entitled “Accretion processes in active galactic nuclei at high-energies” was accepted by the École Doctorale in Paris with the highest priority (*Liste A*).

Sandra started her work on this project in October 2010.

2.3 Refereeing

I am a referee for the *Astrophysical Journal*, *Astronomy & Astrophysics*, *Monthly Notices of the Royal Astronomical Society*, *Advances in Space Research*, and for *Astrophysics and Space Science*.

In addition, I have been a referee to evaluate research projects and colleagues for the South African National Science Foundation and for the Georgia National Science Foundation. From 2007 to 2009 I have been a member of the *INTEGRAL* Time Allocation Committee. I am also a member of the "Conseil scientifique du Campus Spatial" at Université Paris Diderot.

2.4 Conference and meeting organisation

Together with Jérôme Rodriguez (CEA/Saclay) I organised the 2006 "school" on high-energy astrophysics entitled "Observing the X- and Gamma-ray Sky" in Cargèse (Corsica). 22 internationally renowned experts on the field gave lectures during this two week event in April 2006 to 67 PhD students and young post-Docs. The school topics covered most of the physics relevant for X-ray astronomy, from Galactic to extragalactic objects, through their radiation processes, their temporal behaviour, and our actual understanding of these objects. The attendees had the opportunity to give short presentations about their own research or topics related to the aim of the school.

The lectures gave the attendees an overview on the history of high-energy astronomy (Jacques Paul, CEA Saclay), on fundamental physics, including an introduction to MHD (Michel Tagger, CEA Saclay), accretion (Andrew King, University of Leicester), particle acceleration (Mathew Baring, Rice University) as well as thermal and non-thermal processes (Malcolm Longair, University of Cambridge), relativistic jets (Stephane Corbel, CEA Saclay), and general relativity (Luigi Stella, INAF-Rome). X-ray and gamma-ray instrumentation was discussed (Peter von Ballmoos, CESR) and analysis concepts explained. High-energy phenomena like Gamma-ray bursts (Frederic Daigne, IAP), stellar coronae (Manuel Güdel, ETH Zürich), Galactic X-ray binaries (Tommaso Belloni, INAF-OAB), pulsars (Wim Hermsen, SRON), supernova remnants (Jacco Vink, Utrecht University), Galactic diffuse emission (Jürgen Knödlseher, CESR), X-ray sources in other galaxies (Giuseppina Fabbiano, Harvard-Smithsonian Center for Astrophysics), clusters of galaxies (Monique Arnaud, CEA Saclay), Sgr A* (Andreas Eckart, University of Cologne), and AGN (Andy Fabian, IoA Cambridge) were discussed. Presentations about current and future missions like *Suzaku* (Tadayasu Dotani, ISAS), *Fermi* (Isabelle Grenier, CEA Saclay), *Simbol-X*, *XMM-Newton*, and *Chandra* (Philippe Ferrando, CEA Saclay), *RXTE* (Jérôme Rodriguez, CEA Saclay), *INTEGRAL* (Julien Malzac, CESR), *Swift* (Volker Beckmann, NASA/GSFC), and ground based gamma-ray observations (German Hermann, University of Heidelberg) gave the students an in-depth overview on the available tools.

A detailed description of the school, including the proceedings of the lecturers, can be found under <http://asd.gsfc.nasa.gov/Volker.Beckmann/school/index.html>

2.5 Public Outreach

- 2007 – 2009 Public outreach activities for the ISDC Data Centre for Astrophysics. Close collaboration with the *Collège du Léman*.
- 2003 – 2007 Public talks in the US on popular astrophysical topics, like space based astronomy, neutron stars and black holes, etc.
- 2001 – 2003 Supporting public events at the ISDC. This included visits of school classes at the ISDC to whom we would introduce the techniques and science of *INTEGRAL*.
- 1998 – 2000 Press related work for the Hamburger Sternwarte. Here I was responsible to work with print media, radio and television. This resulted in frequent appearance of the observatory in the news, and in several features about our work on local radio stations as well as on local and nation-wide television.
- 1998 – 2000 Together with high-schools we organised practical days for school classes at the observatory. This also included lectures given in schools.
- 1996 – 1999 Organisation of public outreach work at the Hamburger Sternwarte.
This included the monthly open-telescope-nights, talks about astronomical topics to the public, and guided tours of the observatory.

2.6 Press releases

Several scientific results of my work were featured in press releases by ESA, NASA, UMBC, and the Université de Genève.

January 2009: The *INTEGRAL*/ACS detected about 200 intense flashes of gamma-ray light, lasting from 0.1 to 8 seconds in duration, from the neutron star 1E 1547.0–5408 (Baldovin et al. 2009; Savchenko et al. 2009; Mereghetti et al. 2009). The events were among the brightest ever seen in ACS since *INTEGRAL*'s launch in October 2002. We promptly reported the findings and triggered further observations. Our work is reported by ESA (“Magnetar observed during outburst thanks to rapid response of *INTEGRAL*”)

<http://sci.esa.int/science-e/www/object/index.cfm?fobjectid=44074>

and also by a special feature page at the ISDC:

<http://isdc.unige.ch/~beckmann/english/AXP.html>

November 2006: With the help of *Swift*/XRT and ground-based optical observations, the newly found hard X-ray source IGR J17497–2821 appears to be a Galactic black hole candidate (Walter et al. 2007). UMBC features my contribution to the work in a press release entitled “UMBC Astronomer Helps Discover Possible New Black Hole”:

http://www.umbc.edu/NewsEvents/releases/archives/2006/11/umbc_astronomer.html

July 2006: The “First INTEGRAL AGN catalog” reveals that the fraction of Compton thick AGN at hard X-rays is lower than expected (Beckmann et al. 2006a,c). This triggers press releases by NASA (“NASA Scientists Conduct Census of Nearby Hidden Black Holes”)

http://www.nasa.gov/vision/universe/starsgalaxies/integral_blackholes.html

by ESA (“Where are the supermassive black holes hiding?”)

http://www.esa.int/SPECIALS/Integral/SEMGM6BUQPE_0.html

and by UMBC:

http://www.umbc.edu/NewsEvents/releases//archives/2006/07/nasa_scientists.html

July 2005: We used *INTEGRAL*, *Swift*, and *RXTE* in order to identify a newly detected hard X-ray source as a highly absorbed high mass X-ray binary (HMXB; Beckmann et al. 2005a, 2006b). ESA reports about the finding (“Three satellites needed to bring out ‘shy star’”):

http://www.esa.int/esaSC/SEM5OI6DIAE_index_2.html

as well as UMBC (“Three Satellites Needed to Discover One Shy Star”):

http://www.umbc.edu/NewsEvents/releases//archives/2005/07/three_satellite.html

and the Université de Genève (“Des astronomes de l’UNIGE collaborent à la découverte d’une étoile bien mystérieuse”):

<http://www.unige.ch/presse/communiqu/04-05/0714espace.htm>

July 2004: ESA and NASA report in press releases about our work on the Seyfert 2 galaxy NGC 4388 (Beckmann et al. 2004d,c). The ESA report “ESA’s high-energy observatories spot doughnut-shaped cloud with a black-hole filling” can be found under

http://www.esa.int/esaSC/SEM962V4QWD_index_0.html

and NASA’s release “Scientists Spot Doughnut-Shaped Cloud With a Black Hole Filling” under

<http://www.nasa.gov/centers/goddard/news/topstory/2004/0720donutcloud.html>

Chapter 3

SUMMARY, RELEVANCE AND ORIGINALITY OF RESEARCH

Résumé sur l'originalité des recherches.

Through the work on X-ray and gamma-ray data of AGN I contributed significantly to the progress in the unification of AGN since I finished my PhD in 2000.

The study of the evolutionary behaviour of X-ray selected blazars (Beckmann & Wolter 2001; Beckmann et al. 2002, 2003b; Beckmann 2003) shows that their evolution is not as strongly negative as indicated by previous studies. The overall luminosity function is consistent with no evolution in the 0.1 – 2.4 keV band as seen by *ROSAT*/PSPC. There is still a difference compared to the luminosity function of FSRQ and LBL, which seem to show a positive evolution, indicating that they have been more luminous and/or numerous at cosmological distances. We indicated a scenario in order to explain this discrepancy, in which the high luminous FSRQ develop into the fainter LBL and finally into the BL Lac objects with high frequency peaks in their spectral energy distribution but overall low bolometric luminosity.

Studying the variability pattern of hard X-ray selected Seyfert galaxies, we actually found differences between type 1 and type 2 objects, in the sense that type 2 seemed to be more variable (Beckmann et al. 2007a). This breaking of the unified model is caused by the different average luminosity of the absorbed and unabsorbed sources, as discussed in Sect. 4.7.3. This can be explained by a larger inner disk radius when the AGN core is most active (the so-called receding disc model).

The work on the sample characteristics of hard X-ray detected AGN also led to the proof that the average intrinsic spectra of type 1 and type 2 objects are the same when reflection processes are taken into account (Beckmann et al. 2009d). This also explains why in the past Seyfert 2 objects were seen to have harder X-ray spectra than Seyfert 1, as the stronger reflection hump in the type 2 objects makes the spectra appear to be flatter, although the underlying continuum is the same.

Further strong evidence for the unification scheme comes from the observation of a fundamental plane which connects type 1 and type 2 objects smoothly (Beckmann et al. 2009d). In addition, in the case of the Seyfert 1.9 galaxy MCG–05–23–016 I showed that the spectral energy distribution of this source and its accretion rate is similar to that of a Galactic binary (Beckmann et al. 2008a).

Throughout the studies I have shown that the intrinsic spectral shape appears to be very stable on weeks to year time scale (Beckmann et al. 2004d, 2005b, 2007b, 2008a). This implies that the overall geometry of the AGN over these time scales did not change dramatically. The variations in intensity can then be explained in two ways: either the amount of material emitting the hard X-rays

varies, or the amount of plasma visible to the observer varied, e.g. through different orientation of the disk with respect to the observer. In an upcoming paper we will show though, that NGC 4151 indeed also shows different spectral states, similar to the low-hard versus high-soft spectra in Galactic black hole binaries (Lubiński et al. 2010). A similar result seems to emerge from our *INTEGRAL* studies on NGC 2110 (Beckmann & Do Cao 2011). For *INTEGRAL*'s AO-8 I have submitted a proposal in order to study spectral states in the Seyfert 2 galaxy NGC 2992, which seems to show a state change over the past 5 years as seen in *Swift*/BAT longterm monitoring.

The work on the luminosity function of AGN at hardest X-rays (Beckmann et al. 2006d) had a large impact on our understanding of the cosmic X-ray background. As this was the first study of its kind, it showed for the first time that indeed the fraction of highly obscured Compton thick AGN is much lower than expected before the launch of *INTEGRAL* and *Swift*. The X-ray luminosity function we revealed is indeed not consistent with the source population seen by *INTEGRAL* (Beckmann et al. 2006a, 2009d; Sazonov et al. 2007) and *Swift* (Tueller et al. 2008) being the only contributors to the cosmic hard X-ray background. Thus other sources outside the parameter space observable by these missions have to contribute significantly to the cosmic X-ray background. Our work on the luminosity function triggered several other studies on this issue. The subsequent derived luminosity functions by other groups (Sazonov et al. 2007; Tueller et al. 2008; Paltani et al. 2008) are consistent with our findings.

This also gave rise to an increased interest in the exact shape of the Cosmic X-ray background around its peak at 30 keV, triggering several attempts to a new measurement. Background studies were presented based on a Earth-occultation observation by *INTEGRAL* (Churazov et al. 2007, 2008; Türler et al. 2010) and by *Swift* (Ajello et al. 2008).

The understanding of the emission processes in AGN requires knowledge over a wide range of the spectral energy distribution (SED). In studies using *CGRO*/EGRET and *Fermi*/LAT data I derived the SED for blazars and non-blazars towards the gamma-ray range (Beckmann 2003; Beckmann et al. 2004b, 2010b). The work on the LAT data not only presented the gamma-ray detection of five gamma-ray blazars (QSO B0836+710, RX J1111.5+3452, H 1426+428, RX J1924.8–2914, and PKS 2149–306) for the first time, but also showed the potential in the combination of *INTEGRAL* and *Fermi* data. In the case of Cen A I derived the total energy output of the inverse Compton component based on the combined LAT, ISGRI, and JEM-X data, showing evidence for a spectral break at several hundred keV (Beckmann et al. 2010b).

In addition I successfully showed that gamma-ray blazars can be predicted through the study of their synchrotron branch at energies below 2 keV (Beckmann 2003 and this work).

Contributions of mine to research in fields other than AGN include the study of *INTEGRAL* detected gamma-ray bursts (e.g. Beckmann et al. 2003a, 2004a, 2008b, 2009a). Here and in collaboration with other colleagues I showed the potential of *INTEGRAL* data on GRB research. In the field of Galactic X-ray binaries I published one of the first *Swift* results on a newly discovered highly absorbed HMXB, IGR J16283-4838 (Beckmann et al. 2005a, 2006b). I also contributed significantly to analysis of many other Galactic sources, as shown in Section 4.6.1.

Chapter 4

RESEARCH

4.1 From *Welteninseln* to AGN

The main target of the research conducted by me over the recent years were active galactic nuclei (AGN) in the hard X-ray domain, thus most of my scientific attention was focused on extragalactic matters.

The dawn of extragalactic astronomy can be attributed to the year 1750, in which Thomas Wright speculated that some of the nebulae observed by then in the sky were actually not part of the Milky Way, but rather independent Milky Ways (Wright 1750). A few years later, Immanuel Kant introduced for these distant nebulae the term “*Welteninseln*”¹ (‘island universes’, Kant 1755). Although he never actually read the earlier work but only a review in the journal “*Hamburgische freie Urtheile*”, he indeed got some of the ideas he presented from Wright (Whitrow 1971). It was François Arago in 1842 who first called the attention of astronomers to Kant², whom he calls ‘the Astronomer of Königsberg,’ and declared that his name in that connection did not deserve the oblivion into which it had fallen (Arago & Barral 1854). Thus the extragalactic hypothesis spread rapidly in the scientific community, although remaining far from being commonly believed to be true. One main difficulty was the fact that some of the nebulae were actually of Galactic origin, such as planetary nebulae and globular clusters. A significant step forward was the compilation of a large catalogue of some 5,000 nebulae assembled by William Herschel in the late 18th and early 19th century (Herschel 1786, 1789, 1800a, 1802). Another advance was made by Lord Rosse, who constructed in 1845 a new 72” telescope in Ireland, managing to distinguish individual point sources in some of the nebulae, and therefore giving further support to Kant’s and Wright’s hypothesis. Spectroscopic observations by Vesto Slipher of nebulae in the early 20th century revealed that some of these show redshifted lines indicating they are moving relative to the Milky Way at velocities exceeding the escape velocity of our Galaxy (Slipher 1913).

The issue, whether some of the observed nebulae are actually extragalactic, was finally settled in

¹Kant argued about the observed nebulae: “Weit natürlicher und begreiflicher ist es, daß es nicht einzelne so große Sterne, sondern Systemata von vielen seien, deren Entfernung sie in einem so engen Raume darstellt, daß das Licht, welches von jedem derselben einzeln unmerklich ist, bei ihrer unermeßlichen Menge in einen einförmichten blassen Schimmer ausschlägt. Die Analogie mit dem Sternensystem, darin wir uns befinden, ihre Gestalt, welche gerade so ist, als sie es nach unserem Lehrbegriffe sein muß, die Schwäche des Lichts, die eine vorausgesetzte unendliche Entfernung erfordert: alles stimmt vollkommen überein, diese elliptische Figuren für eben dergleichen Weltordnungen und, so zu reden, Milchstraßen zu halten, deren Verfassung wir eben entwickelt haben; und wenn Muthmaßungen, in denen Analogie und Beobachtung vollkommen übereinstimmen, einander zu unterstützen, eben dieselbe Würdigkeit haben als förmliche Beweise, so wird man die Gewißheit dieser Systemen für ausgemacht halten müssen.”

²Arago wrote: “Kant condensait ses idées dans le moindre nombre mots possible, quand il appelait la Voie lactée le Monde des Mondes”

the 1920s. In 1920 Heber Curtis summarized a number of arguments why the Andromeda nebula M31 is a galaxy of its own, similar to the Milky Way (Curtis 1920). For example, he noticed Doppler shift in M31 due to its rotation and absorption by dust similar to what was observed in our Galaxy. Finally, a distance estimation of M31 was given with $d = 450$ kpc (Oepik 1922), about a factor of 2 lower than its actual value, but placing the Andromeda nebula clearly as an extragalactic object. Using the 100" Mt. Wilson telescope, Hubble was able to observe Cepheids in M31 and M33 and confirmed the large distance of these objects, although again underestimating their distance by a factor of ~ 3 to be about 285 kpc (Hubble 1925), and was finally able to resolve stars in M31 (Hubble 1929b). Based on his observations, he also established a system to classify galaxies, the so-called Hubble sequence (Hubble 1926), and he laid the starting point for cosmology assuming an expanding Universe (Hubble 1929a).

The first evidence that some galaxies were hosting some additional strongly emitting component in their centre was found by Carl Seyfert in the 1940s. He obtained spectra of six galaxies, showing high excitation nuclear emission lines superposed on a normal star-like spectrum (Seyfert 1943). He also noticed that some galaxies show broad emission lines, while others exhibit only narrow ones. The nature of the strong emission from the centre of some galaxies remained a mystery. A common hypothesis was the assumption that a large amount of stars would produce the observed features. Woltjer (1959) pointed out though that the observed concentration of the emission within the central 100 pc of the galaxies would require a mass of a few $10^8 M_{\odot}$. A step closer to nowadays understanding was the idea that in the centre of these galaxies resides a stellar type object of very large mass, which then would emit mainly by accretion processes of a surrounding disk of gas (Hoyle & Fowler 1963). The idea to assume in the center of an AGN a black hole instead of a hyper-massive star was put forward a year later (Salpeter 1964; Zel'Dovich & Novikov 1964).

The hypothesis that there might exist objects in the Universe whose gravity would be sufficient to trap even light was discussed first by John Mitchell³ in the late 18th century (Mitchell 1784). Independently Pierre-Simon Laplace developed the concept of "dark stars", speculating that the most massive stars would be invisible due to their strong gravity (Laplace 1796). The concept of the black hole was ignored though in later years, as light was considered to be made of massless particles with no interaction to a gravitational field. When Albert Einstein formulated the general relativity theory (Einstein 1916) the possible existence of black holes was shown to be a solution for the gravitational field of a point mass and of a spherical mass by Karl Schwarzschild (Schwarzschild 1916). Nevertheless, this solution to Einstein's theory was thought to be merely hypothetical. Only when solutions had to be found to explain phenomena like AGN and the fact that massive stars had to collapse into a black hole (Oppenheimer & Volkoff 1939), the existence of black holes was accepted by a continuously growing fraction of the scientific community.

The idea of a super-massive black hole in the centre of active galactic nuclei (Salpeter 1964; Zel'Dovich & Novikov 1964; Lynden-Bell 1969) and also in the centre of our own galaxy (Lynden-Bell & Rees 1971) was a powerful model. It explained not only the large energy output based on the release of gravitational energy through accretion phenomena, but also the small size of the emitting regions and connected to it the short variability time-scales of AGN. The field was now open to study the physics involved in the accretion phenomenon, to observe and explain AGN emission throughout the electromagnetic spectrum, and to study the distribution in space, the origin, the evolution and fate of these elusive objects.

³Mitchell wrote: "If the semi-diameter of a sphere of the same density as the Sun were to exceed that of the Sun in the proportion of 500 to 1, a body falling from an infinite height towards it would have acquired at its surface greater velocity than that of light, and consequently supposing light to be attracted by the same force in proportion to its vis inertiae, with other bodies, all light emitted from such a body would be made to return towards it by its own proper gravity."

4.2 From optical to X-ray observations of AGN

As nearly all fields in astrophysics, the study of the AGN phenomenon started out in the optical domain. Until the 19th century, observational astronomy was restricted to the wave band between 380 nm and 750 nm. Herschel (1800b) discovered that the Sun emitted heat radiation beyond the red end of the visible light, which marks the birth of infrared astronomy. Only in the 20th century other wavelengths were made accessible to astrophysical investigations. Karl Jansky detected radio emission from the sky with unknown origin, apparently coming from the Milky Way (Jansky 1933). These results were confirmed by Reber (1940), adding the discovery of M31 at ~ 15 MHz, the first detection of an extragalactic source at wavelengths other than optical.

The next spectral window opening to astrophysics was the X-ray band. The Sun was detected in X-rays by an X-ray detector on-board a V-2 rocket launched by the US Naval Research Laboratory in 1949 (Friedman et al. 1951). Although the study of the Sun in the X-rays made progress in the following years through observations of solar flares (Chubb et al. 1957), further detectable sources in the X-ray sky were not expected. Simply because of the large distance, a sun-like star or even an O-star would not be detectable by any X-ray detector one could have thought of (Giacconi & Rossi 1960). The first detection of an extra-solar object, the X-ray binary Sco X-1, and even extragalactic X-ray radiation, the cosmic X-ray background, took place in June 1962 during a 350 sec space flight by Geiger counters on-board a Aerobee rocket launched from New Mexico (Giacconi et al. 1962). Further rocket and balloon flights soon increased the number of known sources, and it was speculated that the sources of high-energy emission could be neutron stars (Oda 1964; Morton 1964), very dense stars (Hoyle et al. 1964), and supernova remnants (Heiles 1964). The first AGN detected in X-rays were observed by detectors aboard an Aerobee rocket in April 1965, which provided evidence for X-rays from Cygnus A and M 87 (Byram et al. 1966). A flight in 1969 then provided the first detection of Cen A and of 3C 273, at a significance level of 3.0σ and 3.9σ , respectively (Bowyer et al. 1970).

Rocket flights did not provide long enough exposure times in order to achieve major advances after the brightest sources had been detected. *Uhuru*, the first X-ray telescope on an orbiting satellite was then launched in December 1970 (Giacconi et al. 1971). The mission was equipped with two large area proportional counter detector systems with 840 cm^2 effective area each. It performed the first sky survey and found 339 sources in the 2–6 keV range (Forman et al. 1978). The main fraction of sources turned out to be X-ray binaries, like Cyg X-3 (Schreier et al. 1972), Her X-1 (Tananbaum et al. 1972), and Vela X-1 (Giacconi et al. 1972), confirming theoretical models that accretion onto a compact object can lead to X-ray radiation (Shklovsky 1967; Cameron 1967; van den Heuvel 1975; de Loore & de Greve 1975). *Uhuru* also provided the first detection of the Seyfert galaxies NGC 4151 and of NGC 1275 (Gursky et al. 1971), and confirmed the earlier X-ray detection of Cen A, Cygnus A, M 87, and of 3C 273. In total, 15 Seyfert galaxies were detected⁴, all of them being Seyfert 1 or Seyfert 1.5 (Tananbaum et al. 1978). The largest class of extragalactic objects were though the galaxy clusters, of which *Uhuru* detected 45 (Forman et al. 1978).

Proportional counters did not allow direct imaging of the X-ray sky though, thus the application of mirrors was the next challenge in this field. Wolter had studied the use of mirrors at grazing incidence angles as a way to focus X-rays (Wolter 1952), and the use of Wolter-type mirrors had been already proposed before the first detection of an extrasolar X-ray source (Giacconi & Rossi 1960). The first X-ray mirror in space was a 30-cm consisting of two nested mirrors flown on the SKYLAB space station in 1973. The purpose was to perform imaging observations of the sun. Instead of a detector,

⁴Mrk 335, 3C 120, MCG +08-11-011, NGC 3783, NGC 4151, NGC 5548, 3C 390.3, NGC 7469, Mrk 541, Mrk 79, IC 4329A, Mrk 509, Akn 120, VV 144, and Mrk 304.

photographic film was used, which allowed at the same time high resolution and a large field of view. In addition, the instrument was equipped with a transmission-grating spectrometer, which allowed for the first time spectroscopy in the X-ray band. The experiment was successful, revealing a highly structured and variable X-ray corona (Vaiana et al. 1973), although the analysis of the 26,000 frames on film (Walsh et al. 1974) would take years.

Several satellites hosting X-ray detectors followed, like the *Astronomische Nederlandse Satelliet* (1974–1977), which observed X-ray emission from stellar coronae (Mewe et al. 1975) and *Ariel V* (1974–1980), detecting 251 X-ray sources (McHardy et al. 1981; Warwick et al. 1981) and further establishing Seyfert 1 galaxies as X-ray sources. Based on *Ariel V* data, Elvis et al. (1978) derived the first X-ray luminosity function for Seyfert 1 galaxies and came to the conclusion that the emission originates in the very core of the galaxies and that synchrotron self-Compton radiation is the most plausible emission mechanism in the 2 – 10 keV band. The 5 years of data were also used to perform detailed analysis of the light curves of AGN, finding no evidence for a distinction in the X-ray variability of active galaxies with differing morphology or X-ray luminosity (Marshall et al. 1981). *Ariel* and *Uhuru* led also to the detection of variable absorption in NGC 4151, which was able to explain the soft X-ray flux variability in this source (Barr et al. 1977). Early on it was noticed that objects which exhibit temperatures able to emit X-ray radiation should also show a prominent line from iron fluorescence at 6.4 keV (Holt et al. 1968). First indication of the existence of this line (at a 3.3σ level) was found in data on Sco X-1 from a 150 sec rocket flight observation (Holt et al. 1969) and a few years later also in the supernova remnant Cas A (Serlemitsos et al. 1973). In AGN the iron fluorescence line was first detected in data of NASA's 8th Orbiting Solar Observatory *OSO-8* of Cen A (Mushotzky et al. 1978) and later in *Ariel V* data of NGC 5548 (Hayes et al. 1980).

In the years 1977 to 1979, the first *High Energy Astronomy Observatory (HEAO-1)* performed an X-ray all-sky survey in the 0.2 keV – 10 MeV band. This included a complete ($f_{2-10\text{keV}} > 3.1 \times 10^{-11} \text{ erg s}^{-1} \text{ cm}^{-2}$) X-ray sample at high-latitude ($|b| > 20^\circ$) containing 85 sources out of which 61 were extragalactic (Piccinotti et al. 1982). It also provided a precise measurement of the hard X-ray extragalactic background in the 3–50 keV band, revealing its peak around 30 keV (Marshall et al. 1980).

A major leap forward was the launch in 1978 of *HEAO-2*, later named *Einstein*, which first used grazing incidence mirrors on an orbiting X-ray observatory (Giacconi et al. 1979). It carried a Wolter Type I telescope and hosted four instruments for imaging and spectroscopy which could be rotated into the focal plane, achieving 2 arcsec spatial resolution (0.5 – 4.5 keV) and a spectral resolution of 20% at 6 keV. *Einstein* performed pointed observations but its high sensitivity lead to a large number of detected sources. In the field of extragalactic studies, results include the detection of X-ray jets in Cen A (Schreier et al. 1979) and M87 (Schreier et al. 1982). Prior to this mission, only 5 Seyfert 2 galaxies were known to emit X-rays, NGC 2110, NGC 5506, NGC 7582, NGC 2992, and MCG-5-23-16 (McClintock et al. 1979), but with *Einstein* data it was now possible to conduct statistical meaningful tests on the differences of type 1 and type 2 objects in the X-ray domain (e.g. Kriss et al. 1980; Lawrence & Elvis 1982). A well defined sample based on *Einstein* data is the *Einstein Observatory Extended Medium Sensitivity Survey* (EMSS; Gioia et al. 1990; Stocke et al. 1991) on a sky area of 778 deg^2 , containing 835 X-ray sources in the flux range $5 \times 10^{-14} - 10^{-11} \text{ erg cm}^{-2} \text{ s}^{-1}$, including 427 Seyfert galaxies and 36 blazars.

From now on, also population and luminosity function studies based on X-ray data gave constraining results. In addition, the main ingredients of AGN were established: a supermassive black hole in the centre of the host galaxy, which emits throughout the electromagnetic spectrum through accretion processes, absorbing material in the vicinity of the central engine affecting the soft X-ray spectrum, and an iron fluorescence line indicating reflection processes.

4.3 The AGN phenomenon and the Unified Model

The phenomenon of the Active Galactic Nuclei appears in objects of very different characteristics. Their commonality is that they all reside in the centre of galaxies (therefore the name) and that they appear to be super massive black holes (Salpeter 1964; Zel'Dovich & Novikov 1964; Lynden-Bell 1969).

The class of AGN comprises Seyfert galaxies, LINER, NELG, quasi-stellar objects (QSO), and blazars. The classification of a galaxy as an AGN is given if at least one of the following attributes is fulfilled:

- bright, point-like, and compact core
- non-thermal continuum emission
- brighter luminosities compared to normal galaxies in all wavelength regions
- broad emission lines
- polarized radiation, especially in blazars
- variability of the continuum and of the emission lines
- morphological structures like lobes (especially in the radio regime) and jets

The classification into the different groups, like Seyfert I or QSO, is based on phenomenological appearance. The following classification scheme describes the typical properties, but nevertheless there are transition objects and the classes are not well separated from each other. This fact sometimes causes confusion, when an AGN is classified differently by different authors.

- *Seyfert galaxies.* Most of the Seyfert galaxies are hosted in spiral galaxies (Sarajedini et al. 1999) and show a bright, point-like core. The optical spectrum is dominated by emission lines, which could be broadened by the velocity dispersion of the emitting gas. Broad emission lines, caused by gas velocities up to 10^4 km sec⁻¹ are thought to be emitted from the so-called broad line region (BLR). These features are the allowed low ionized lines (HI, HeI, HeII, FeII, MgII). The forbidden lines seem to originate from a different location within the AGN, the narrow line region (NLR), where velocities have to be as low as 100 . . . 1500 km sec⁻¹. The most prominent forbidden lines result from oxygen, nitrogen and neon ([OII], [OIII], [NII], [NeIII], [NeIV]).

While Seyfert I galaxies show narrow forbidden and broad allowed emission lines (Fig. 4.1), the Seyfert II galaxies emit only narrow lines. In Fig. 4.2 the optical spectrum of a Seyfert II galaxy is shown. In the type II class, the allowed lines have similar equivalent widths as the forbidden lines. This is thought to arise from a dusty torus which hides the BLR in the case of Seyfert II galaxies. While Seyfert I galaxies exhibit often strong X-ray, ultraviolet and infrared emission, the Seyfert II galaxies are less luminous in the X-rays. Transition objects between both types are classified as Seyfert 1.5 . . . Seyfert 1.9 which refers to the different intensity ratio between the broad and the narrow component. Thus the higher the type of the Seyfert, the more the BLR is supposed to be hidden by the dusty torus.

- *LINER and NELG.* The Low Ionization Nuclear Emission Line Regions (LINER) show faint core luminosities and strong emission lines originating from low ionized gas. Expected line

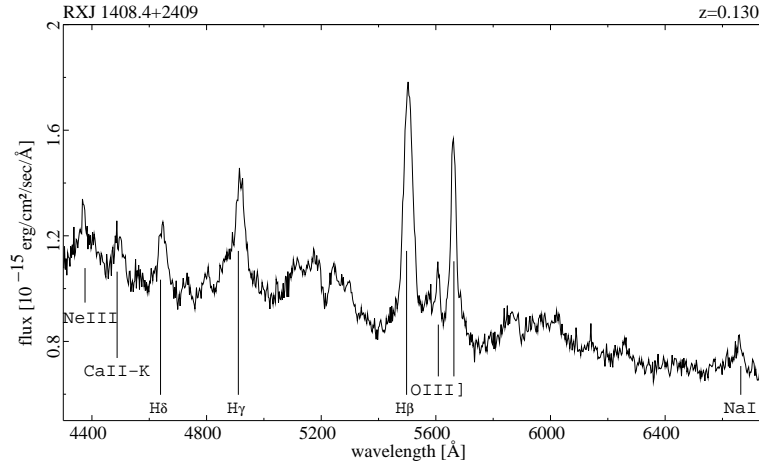


Figure 4.1: Spectrum of the X-ray bright Seyfert 1 galaxy RX J1408.4+2409. The broad line region is visible, thus the hydrogen lines are broad. Forbidden lines are comparably less prominent. Spectrum taken together with Norbert Bade in the February 1998 campaign at the Calar Alto 3.5m telescope (Bade et al. 1998; Beckmann 1999, 2000b).

widths are $200 \dots 400 \text{ km sec}^{-1}$ and their properties are very similar to the Seyfert II galaxies, but LINER do have weaker forbidden lines. The LINER seem to mark the low energy end of the AGN phenomenon. Narrow Emission Line Galaxies (NELG) show strong X-ray emission like Seyfert I galaxies, but while the H_{α} line is broad the H_{β} line is narrow at the same time. Therefore they seem to be reddened Seyfert I galaxies, where the absorption is effective only at wavelengths $\lambda \ll \lambda(H_{\alpha})$.

- *Quasars.* The classification of a quasar as a point-like, unresolvable Seyfert galaxy at cosmological distances is based on the historical phenomenological identification. Nowadays it seems that quasars are just luminous Seyfert galaxies (typically Seyfert I type). They are also hosted in galaxies though, due to the bright core and the larger distance, it is much more difficult to examine the environment of the quasars. The distinction from Seyfert I galaxies is done by a luminosity limit. Thus Seyfert galaxies with absolute magnitudes $M_B < 23^{\text{mag}}$ are called quasars (Schmidt & Green 1983). Only a small fraction of quasars shows radio emission: Most of the quasars, unlike the blazars, are radio quiet. Radio loud quasars are distinguished into the class of the radio bright Flat Spectrum Radio Quasars (FSRQ), and the Steep Radio Spectrum Quasars (SRSQ). The latter ones are dominated by radio lobes of the host galaxy, the former have a compact radio structure.
- *Radio galaxies* If the central region of a quasar is hidden but the object ejects bright radio jets and shows bright radio luminosities, the existence of an AGN core is assumed. These radio galaxies are divided into two subgroups, the low-luminosity Fanaroff-Riley class I (FR-I) galaxies, and the high luminosity FR-II objects, in which the structure is dominated by the radio lobes (Fanaroff & Riley 1974). While the radio lobes are large structures related to the host galaxy, the radio jets seem to originate directly from the central engine. The jets show polarized emission and non-thermal continua, and thus are thought to result from synchrotron emission in the core.

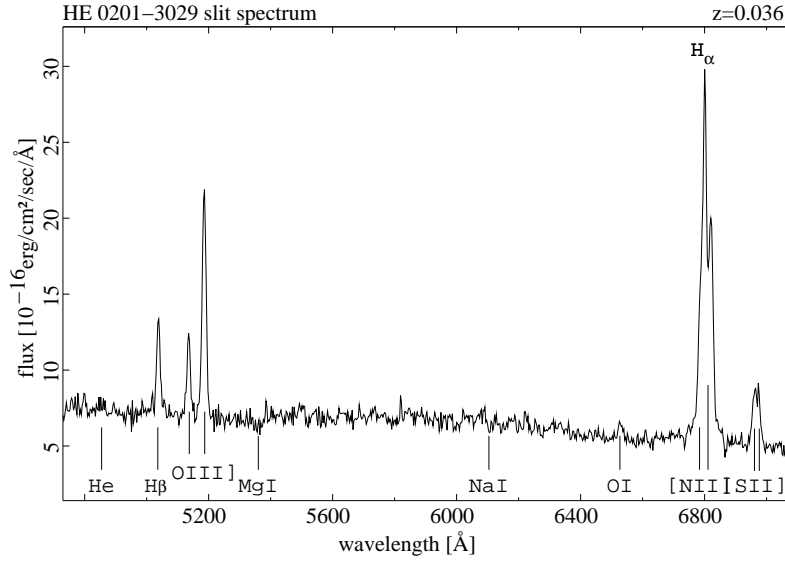


Figure 4.2: Slit spectrum of the Seyfert 2 galaxy HE 0201-3029. Note the absence of broad line components and the strong forbidden oxygen, nitrogen, and silicon lines, characteristics which are typical for type 2 objects. The spectrum was taken in December 1999 with the Danish 1.54m telescope (Beckmann 2000b).

- *Blazars*. The blazars are a special subclass of quasars. This class is dominated by high variability and is subdivided into the BL Lac objects, which are discussed extensively in Section 4.5, the Optical Violent Variables (OVV), and the Highly Polarized Quasars (HPQ). While BL Lac objects do not show prominent features in the optical spectrum, as seen in the example of RX J1211.9+2242 in Fig. 4.3, OVV and HPQ exhibit broad emission lines. Additionally, HPQ show polarization in their continua. FSRQ are also often referred to as blazars.

A fundamental question of AGN research is, whether all these different appearances of the AGN phenomenon can be explained by one model, or whether the different classes are intrinsically and physically distinct. It was pointed out early on that a Seyfert galaxy is in fact in most cases a spiral galaxy to which a faint quasar is added in the centre (Weedman 1973; Penston et al. 1974). In addition, Kristian (1973) showed that the fainter quasars indeed appear to have an extended form rather than being point-like, indicating that they reside in galaxies. Rowan-Robinson (1977) made an attempt to unify Seyfert galaxies and radio sources. While he correctly assumed that absorption by dust is important in order to explain the differences in infrared emission, he did not take into account beaming effects which are an important ingredient when trying to understand radio bright AGN. At the 1978 BL Lac conference in Pittsburgh the foundations for the beaming unification were outlined (Blandford & Rees 1978), a concept which is still believed to be true. In this picture, if the AGN appears to be a blazar, the emission is beamed along the symmetry axis of the AGN towards the observer (Fig. 4.4). In a next step, Scheuer & Readhead (1979) proposed that the radio core-dominated quasars could be unified with the radio quiet quasars, when assuming the former once beamed towards the observer, similar to what was observed in blazars. This concept turned out to have a problem though. As Orr & Browne (1982) pointed out, the core dominated and radio loud quasars showed indeed extended radio emission in MERLIN and VLA observations. Therefore, radio quiet AGN could not just be misaligned

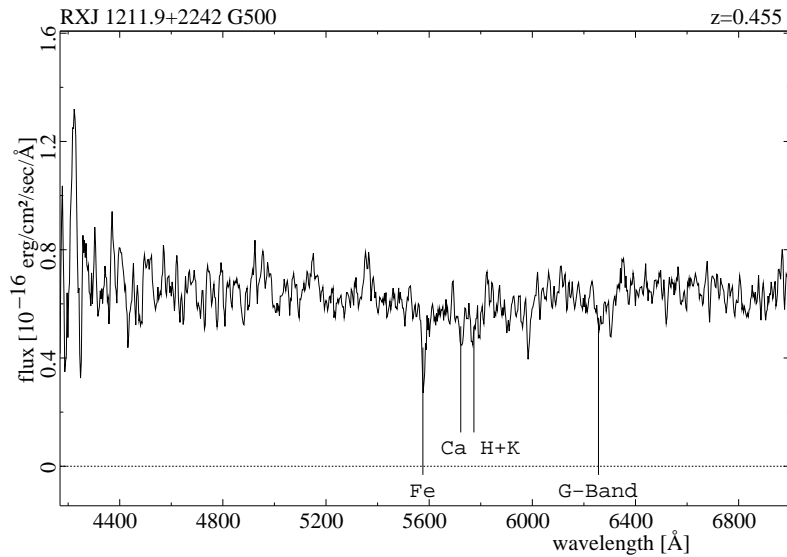


Figure 4.3: Slit spectrum of the blazar RX J1211.9+2242. Only weak absorption lines, caused by the jet emission being absorbed by the host galaxy, are detectable. The spectrum was taken in February 1998 with the Calar Alto 3.5m telescope (Beckmann et al. 2004b).

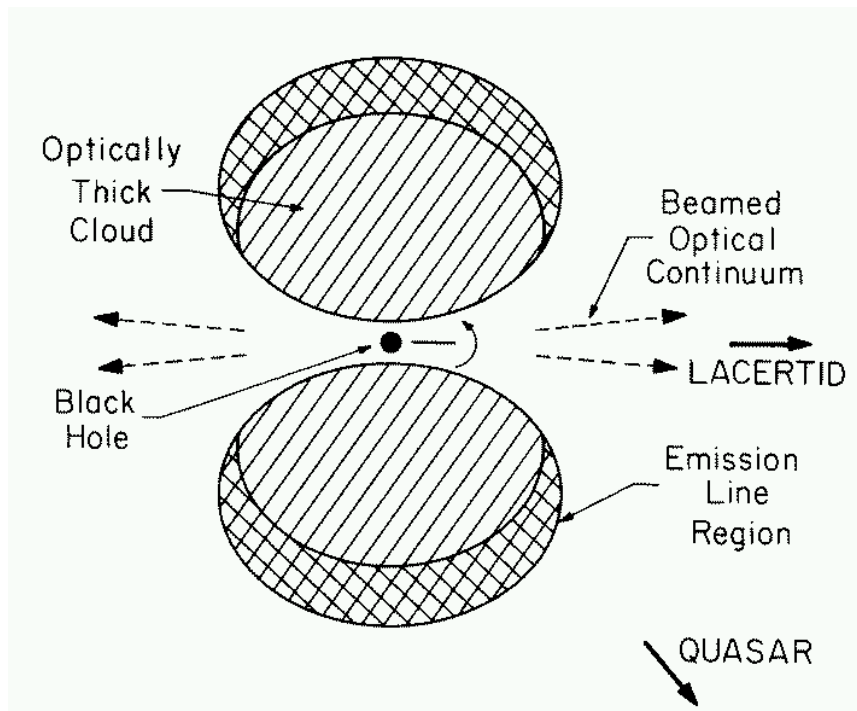


Figure 4.4: Schematic representation of a geometrical interpretation of the BL Lac phenomenon by Blandford & Rees (1978). If the optical continuum is beamed along the symmetry axis, then the emission lines may be suppressed when the source is viewed from this direction. In this figure Lacertid stands for blazar.

radio quasars. Later studies explained the differences by two effects: difference in orientation, and difference in obscuration (Barthel 1989). Here all objects which show a quasi stellar radio core and blazars would emit beamed radiation towards us, with a closer alignment to the line of sight in the case of the blazars. Radio galaxies, in this picture, emit their jet at large off-axis angle with respect to the line of sight. A still valid and rather complete overview on the problem of AGN unification was given by Antonucci (1993). In the most simplified picture, there are basically two types of AGN: radio quiet and radio louds. For each type a range of luminosities is observed, leading e.g. to the Fanaroff & Riley classes as well as to the distinction between Seyfert and quasar. All other observed differences would be explained by orientation effects. Antonucci pointed out that the existence of an optically thick torus would lead to the absence of broad emission lines in the case of Seyfert 2, as their broad line region would be hidden, compared to Seyfert 1 objects. He was also aware of the shortcomings of this simple model and that it left open the question, what the intrinsic difference between radio loud and radio quiet AGN is, and why radio loud AGN mainly reside in elliptical galaxies, while radio quiet AGN are hosted by spiral galaxies. A subsequent review by Urry & Padovani (1995) explained the unification of the sub-group of radio loud AGN. The aim was to study whether the low radio luminous FR I can be the parent population of the BL Lac objects, while FSRQ would be a subset of the FR II galaxies. Urry & Padovani (1995) pointed out the difference in evolutionary behaviour between BL Lacs and FSRQs, and considered the suggestion that FSRQ evolve into BL Lac objects, becoming weak-lined objects by virtue of increased beaming of the continuum, that is, a Lorentz factor increasing with cosmic time (decreasing with redshift; Vagnetti et al. 1991). A problem occurred though, as the luminosity functions of the two object groups could not be connected smoothly, for example because of very different radio power and line luminosity at comparable redshifts.

Recently a new approach has been tried to unify radio loud and radio quiet AGN. Garofalo et al. (2010) consider the relative spin of the central black hole with respect to the accretion disk to be the crucial factor here. Jet production, and thus radio loudness, is most effective in this model when the black hole magnetospheres conspire with their large gap regions to produce strong black hole-threading magnetic fields (Garofalo 2009). AGN would start with a black hole which has a very different, even retrograde, spin with respect to the accretion disk, leading to strong interaction with the disk and thus strong jets. As the black hole is spun up in the direction of the accretion disk, the interaction of the rotating black holes with their magnetospheres becomes less efficient and the jet weakens. Thus, the highest black hole spin might be discovered in the least active AGN (Garofalo et al. 2010). This scenario is supported by a theoretical approach of Daly (2009) determining the black hole spin that is model-independent, but assumes that spin changes only by extraction of the reducible black hole mass. This model applied to a small subset of powerful radio galaxies finds indeed that they harbor low spinning black holes.

In the larger picture, one also expects a connection of the AGN phenomenon with its host galaxy. The AGN phenomenon is thought to be closely linked to the star-formation of the surrounding region, and progenitors of AGN could be star-burst galaxies (e.g. Blain et al. 1999; Maiolino et al. 2000; Wild et al. 2007). Stevens et al. (2010) showed that there is an excess of star-forming galaxies in the fields of high-redshift quasars at $1.7 < z < 2.8$. This indicates that quasars in the early universe were indeed located in regions which were undergoing an enhanced level of major star-formation activity. They find evidence that the level of star-formation activity in individual galaxies appears to be lower around these quasars than it is around more powerful radio-loud AGN at even higher redshifts. The link between AGN and pure starburst galaxies can be the Ultra-Luminous Infrared Galaxies (ULIG). In a recent study Ruiz et al. (2010) showed that the SED of ULIGs can be modeled by a mixture of quasar and star burst galaxy contribution, but that in some cases a prominent and broad IR bump is seen, suggesting that $> 50\%$ of their emission comes from stellar formation processes. Chen et al.

(2009) find a tight correlation between the Eddington ratio of the central black hole and the mean star formation rate, strongly implying that supernova explosions play a role in the transportation of gas to galactic centers.

Also merging events appear to have an impact on the AGN activation, as has been shown e.g. in simulations by Di Matteo et al. (2005). In a recent study, Liu et al. (2010) analysed Seyfert galaxies selected from the Sloan Digital Sky Survey based on double-peaked [O III] (4959 Å and 5007 Å) emission lines in their fiber spectra. Among 43 objects, they find indeed 4 AGN double-cores which are separated by ~ 1 kpc. All these binary AGNs appear to be Seyfert 2 galaxies. And merging appears to be a common phenomenon when studying the hosts of AGNs. In a sample of 60 QSO, Letawe et al. (2010) find 60% of the host galaxies showing signs of interaction. This fraction seems to be lower when considering only hard X-ray selected AGN. Koss et al. (2010) determined the merger rate in the *Swift*/BAT selected AGN sample (Tueller et al. 2008) and found a fraction of 21% apparent merger, and a similar rate of 28% for the *INTEGRAL* AGN sample (Beckmann et al. 2009d).

Some claims have been raised of detection of “naked” AGN cores, which do not reside in a host galaxy. The most prominent case of the QSO HE 0450-2958 has recently been proven to be in fact hosted by a very compact host galaxy, involved in a violent collision with its companion (Letawe & Magain 2010). It is therefore probable that bare AGNs do not exist and that there is always a galaxy hosting the quasar core.

The unified model is facing more open questions nowadays, out of which this work wants to address the following:

- **BL Lac objects:** Where do BL Lac objects fit into the unified model of blazars?
- **Seyfert type:** Some Seyfert galaxies show a change of their type within years time scale. Does this mean that the obscuring matter disappears out of the line of sight?
- **Torus:** The absorption in AGN can change within weeks. It is likely that the absorber is therefore rather close to the central engine and should be affected by the radiation pressure. How is it that it is not driven off?
- **Evolution:** In the most simple picture, the evolution in time should not depend on the source type. If the luminosity functions are not the same, e.g. for type 1 and type 2, this has to be explained in a consistent way.
- **Intrinsic spectrum:** If the central engine is the same in all types of AGN, then the intrinsic spectrum of the unbeamed sources should look the same when absorption effects are considered.
- **Breaking unification:** Can we find parameters which break the simple unified model – and can we then explain these complications by adjusting the unified model following physical arguments?
- **Connection to GeV and TeV energies:** with the new observing facilities in the gamma-ray range, can we explain the emission at these extreme energies based on the unified model?

4.4 Verifying the unified model through evolutionary tests

The study of the evolution of AGN is a powerful test for the unified scheme. If a special class of AGN is thought to belong to a larger parent generation, then both should show the same evolution in time. If this is not the case, additional connections have to be considered in order to explain the discrepancy.

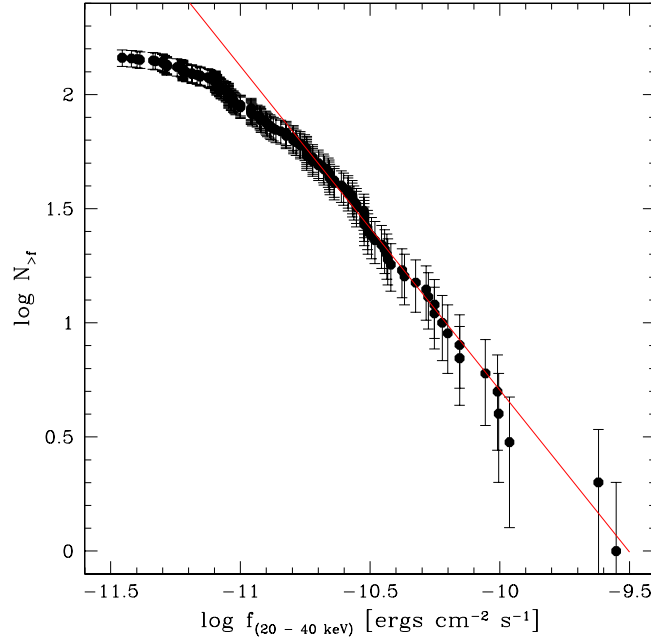


Figure 4.5: Number counts of *INTEGRAL* detected Seyfert galaxies with a detection significance $> 4\sigma$. The line indicates a fit to the objects with $f_{(20-40\text{keV})} > 1.7 \times 10^{-11} \text{ erg cm}^{-2} \text{ s}^{-1}$ and has a gradient of -1.42 ± 0.07 , consistent with the value of -1.5 expected for normal distribution in Euclidean space.

4.4.1 Number counts

The most simple study of a population within space are probably the *number counts*. Here the number of objects per flux bin is counted. Figure 4.5 shows the number counts for the second *INTEGRAL* catalogue (Beckmann et al. 2009d) as presented in Beckmann et al. (2010d). The number counts give some evidence for the distribution in space. If a complete sample is considered, i.e. all and only objects down to a given flux limit have been included, the number counts would show a gradient of $-\frac{3}{2}$ in the double logarithmic representation, if the objects are evenly distributed in Euclidean space and also all objects having normally distributed luminosities. Then one expects the number N of objects being correlated with the flux limit f_{limit} in a sense that $N \propto f_{\text{limit}}^{-3/2}$. This is just based on the fact that the number of sources increases with the radius r of a sphere in which we search by $N \propto r^3$ and that at the same time the measured flux f of an object is correlated with the distance r by $f \propto r^{-2}$. Although in the example of Fig. 4.5 one can assume that the objects are in Euclidean space (low redshifts) and have normally distributed luminosities, the number counts show a turn over toward lower fluxes around $f \simeq 1.5 \times 10^{-11} \text{ erg cm}^{-2} \text{ s}^{-1}$. This is simply because the sample starts to become incomplete at this flux level and thus not all sources which should contribute to the $N \propto f_{\text{limit}}^{-3/2}$ law are included. Therefore the number counts are often of limited use to study evolution, and rather can be used to test down to what flux level a sample is complete. Nevertheless it is an easy to use tool, able to directly compare different flux limited samples even when redshift information is missing.

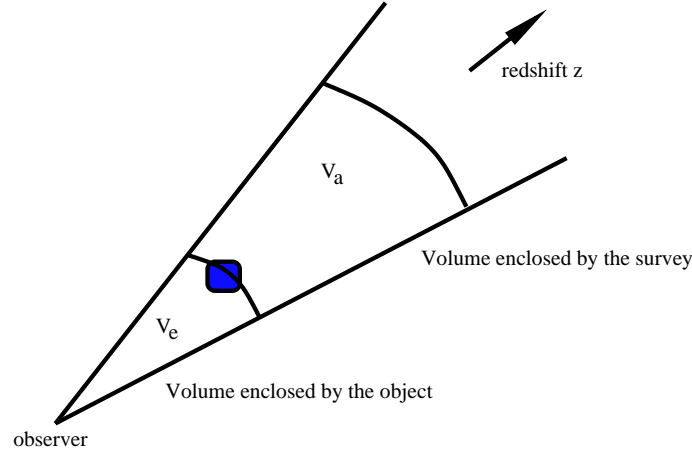


Figure 4.6: The accessible volume is computed for each object individually.

4.4.2 The V/V_{max} test

Another simple method to detect evolution in a complete sample of objects for which the redshifts are known, is the application of a V/V_{max} test (Schmidt 1968). This test is based on the ratio of the redshift of the objects in relation to the maximal allowed redshift z_{max} within the survey. If we have a sample of n objects, of which every object encloses a volume V_i and this object would have been detected (due to the survey limit) up to a volume $V_{max,i}$, than the mean

$$\left\langle \frac{V}{V_{max}} \right\rangle = \frac{1}{n} \cdot \sum_{i=1}^n \frac{V_i}{V_{max,i}} \quad (4.1)$$

will have a value in between the interval $[0..1]$. A value of $\langle \frac{V}{V_{max}} \rangle = 0.5$ would refer to an equally distributed sample in space. The area of the survey is not important for this value, because $V_i/V_{max,i} = d_p^3/d_{p,max}^3$ with d_p being the proper distance of the object redshift z and $d_{p,max}$ the value for z_{max} . This test is very sensible to the maximal detected redshift z_{max} . Therefore Avni & Bahcall (1980) improved the test by using V_e/V_a (see Figure 4.6). Here V_e stands for the volume, which is enclosed by the object, and V_a is the accessible volume, in which the object could have been found (e.g. due to a flux limit of a survey). Thus even different surveys with different flux limits in various energy bands can be combined by the V_e/V_a -test.

The error of $\langle V_e/V_a \rangle$ can be determined as follows. For an equally distributed sample the mean value $\langle m \rangle = \langle V_e/V_a \rangle$ is:

$$\langle m \rangle = \frac{\int_0^1 m \, dm}{\int_0^1 dm} = 0.5 \quad (4.2)$$

The mean square divergence of the mean value is:

$$\sigma_m^2 = \frac{\int_0^1 (m - 0.5)^2 dm}{\int_0^1 dm} = \left[\frac{1}{3}m^3 - \frac{1}{2}m^2 + \frac{1}{4}m \right]_0^1 = \frac{1}{12} \quad (4.3)$$

Therefore for n objects we get an error of:

$$\sigma_m(n) = \frac{1}{\sqrt{12n}} \quad (4.4)$$

For an arbitrary mean value $\langle m \rangle$ we get an error of:

$$\sigma_m(n) = \sqrt{\frac{1/3 - \langle m \rangle + \langle m \rangle^2}{n}} \quad (4.5)$$

4.4.3 The luminosity function

A more refined technique to study evolution of objects with redshift is the *luminosity function* (LF) analysis. To determine the cumulative LF, one has count all objects within a complete sample above a given luminosity L , and divide this number by the volume V_a which has been surveyed for these objects. For each object the maximal redshift z_{max} , where this object would have been found due to the survey limit, is computed by using the individual flux limit of the object, and the given redshift. The space density ϕ is then described by:

$$\phi(L) = \sum_{i=1}^n \frac{1}{V_{a,i}} \quad (4.6)$$

The corresponding 68% error σ on $\phi(L)$ is then determined using the formula

$$\sigma = \left(\sum_{i=1}^n V_{a,i}^{-2} \right)^{1/2} \quad (4.7)$$

which weighs each object by its contribution to the sum (see Marshall (1985) for details). An example for a cumulative luminosity function is shown in the left panel of Fig. 4.7.

Another way of presenting the distribution of luminosities within a sample is the differential luminosity function as shown in the right panel of Fig. 4.7. Here the number objects within a luminosity bin is divided by the accessible volume V_a . This presentation suffers from the fact that in most cases the binning of the sample impacts the final LF.

One problem of any luminosity function including a significant redshift range is that the spectrum of the objects is extrapolated up to high energies due to the large z_{max} values, the so-called *K-correction* (Schmidt & Green 1986). For a given spectral slope α the transformation from the observed flux $f_{observed}$ to the emitted flux f_{source} at a redshift z is given by

$$f_{source} = f_{observed} \cdot (1 + z)^{\alpha-1} \quad (4.8)$$

This means that the observed flux is lower than the emitted flux if $\alpha > 1$, because the frequency region with the lower flux is shifted into the observed wavelength region by the redshift z . This effect can be ignored in the case of hard X-ray detected non-blazar AGN, which show mainly redshifts $z < 0.1$ (Tueller et al. 2008; Beckmann et al. 2009d).

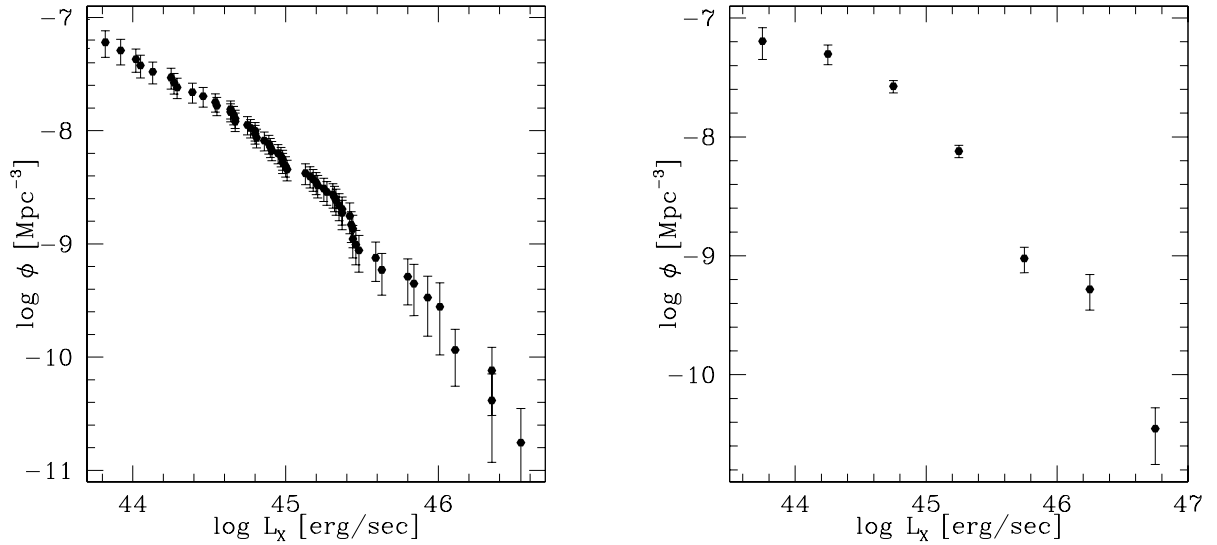


Figure 4.7: Left panel: Cumulative luminosity function of the X-ray selected BL Lac objects (Beckmann 2000b; Beckmann et al. 2003b). Right panel: Differential luminosity function of the same sample. The x-axis is binned to $\Delta L_X = 0.5$. The density refers to object density per $\Delta L_X = 1.0$.

4.4.4 Local luminosity function of optically selected AGN

As an example for the advantages and shortcomings of the luminosity function as a tool to study evolution, I would like to briefly describe the local luminosity function of optically selected Seyfert 2 galaxies (Beckmann 2000b).

In order to find and study quasars in large quantities, the Hamburger Sternwarte started a quasar survey in the optical domain in the 1980s. As in other wavelengths, also in the optical a spectrum is necessary to determine the nature of a celestial object. In the optical the search for AGN is in a way more difficult than e.g. in X-rays, where most objects seen at high Galactic latitude are indeed AGN. In the optical, only 1 out of 1000 visible galaxies appears to host an AGN. Taken to account also the many foreground stars one detects even at higher latitude, the search for AGN is one of the many scientific needle in the haystack exercises. The aim of the Hamburg Quasar Survey (HQS; Hagen et al. 1995; Engels et al. 1998; Hagen et al. 1999) was therefore, to do a spectrographic and photometric survey down to magnitude $B \approx 17 - 18$ mag by using a wide-angle Schmidt type telescope. This 1.2m telescope was equipped with a 1.7° prism in the optical path, which results in slit-less spectroscopy over a field of $5^\circ \times 5^\circ$. A twin project was conducted on the southern hemisphere using the ESO Schmidt telescope, resulting in the Hamburg/ESO Survey (HES; Reimers 1990; Reimers et al. 1996; Wisotzki et al. 1996, 2000). The surveys were restricted to Galactic latitudes $|b| > 20^\circ$ (HQS) and $|b| > 30^\circ$ (HES), as at lower latitudes too many spectra would overlap because of the high area density of foreground stars, making the spectral plates practically useless. As detector photographic plates were used, which were then scanned at Hamburger Sternwarte using a PDS 1010G micro-densitometer (Hagen et al. 1986). The photographic plates provide a non-linear dispersion with $1390 \text{ \AA}/\text{mm}$ at H_γ . Kodak IIIa-J emulsion was used, giving a wavelength coverage between the atmospheric UV-limit at $\sim 3400 \text{ \AA}$ and the cut-off of the emulsion at 5400 \AA . The low-resolution spectra give a first idea about the nature of an object between the saturation limit of the photographic plates around $B = 12 - 14$ mag and the sensitivity limit $B \sim 18.5$ mag. The plates of the HQS have been used for example to identify

the sources in the ROSAT Bright Source Catalogue. As no two photographic plates are finally equal, due to weather conditions, exposure time, quality of the emulsion and the development process, it is also not possible to apply an absolute calibration to the density spectra. Follow-up campaigns using slit spectroscopy are therefore always necessary to verify the nature of interesting objects found in the HQS or HES. Nevertheless, a highly efficient candidate search can be performed using the density spectra.

During my PhD, I studied the local luminosity function of Seyfert 2 galaxies using the density spectra of the HES for candidate selection. Although Seyfert 2 are more numerous than the Seyfert 1 galaxies, they are more difficult to find as they are on average fainter and also show lower line equivalent widths. In order to determine the local luminosity function, it is therefore necessary to achieve a complete sample on a fairly large portion of the sky. Automatic procedures were put to work in order to select candidates for the Seyfert 2 sample. As a learning sample I used 139 Seyfert 2 on the sky area covered by the HES, taken from Veron-Cetty & Veron (1998). These objects were used to define the properties of Seyfert 2 galaxies in the HES and to program an automatic filter to select Seyfert 2 candidates from the density spectra. In principle the filter was based on line and colour criteria.

The automatic search was done by two different methods: one group of candidates was selected by examining objects with detectable lines in the spectrum, and the other group by applying colour criteria. The parameters of the automatic process were optimized to include all Seyfert 2 galaxies of the learning sample within the HES database. A drawback of this procedure is doubtlessly the fact that Seyfert 2 galaxies with other properties than that of the learning sample, for example extreme color, could be rejected by the optimized selection. *spcmag* was used. This magnitude is derived from the density spectra by applying a Johnson-B filter to the objective prism data. Seyfert II candidates found by this selection procedure were then checked for counterparts in the NASA/IPAC Extragalactic Database (NED)⁵. The reduced list of candidates was then checked one by one. A major fraction of the selected candidates were obvious stars: often the automatic line detection algorithm mis-identified the absorption doublet of calcium at 3933/3968 Å as an emission line. Furthermore, when possible, the redshift of the candidates was estimated using the detected lines. Candidates which clearly showed a redshift $z \gg 0.07$ were sorted out. Using this semi-automatic procedure, in total 67 ESO fields have been worked through. Of $\sim 700,000$ overlap free density spectra, the semi-automatic procedure selected $\sim 1,700$ candidates which were all cross checked with the NED. After the final selection, 393 candidates were left over.

The remaining candidates were sorted interactively into categories of the likelihood of Seyfert II nature of the object. Using this semi-automatic procedure, in total 67 ESO fields have been worked through. Of $\sim 700,000$ overlap free density spectra, the semi-automatic procedure selected $\sim 1,700$ candidates which were all cross checked with the NED. After the final selection, 393 Seyfert 2 candidates were determined. To verify the true object type of the candidates, follow up spectroscopy was necessary. Two observation runs were done at the Danish 1.54m telescope on La Silla. The first one was in January 1999 with a total of 3 nights. Due to bad weather conditions, observations were only possible during 2 nights. Nevertheless, 58 candidates on 41 ESO fields covering $\sim 1000 \text{ deg}^2$ were observed. The second run in December 1999 was again 3 nights long, but again bad weather conditions and technical problems reduced the effective observing time to 1.5 nights. It was possible to do spectroscopy on 33 objects, including re-observations of six objects from the January campaign with insufficient signal-to-noise spectra. In total 85 objects have been observed.

The analysis finally revealed 22 Seyfert 2 galaxies with a secure identification. The spectra of 7

⁵The NED is operated by the Jet Propulsion Laboratory, California Institute of Technology, under contract with the National Aeronautics and Space Administration.

objects do not allow the distinction between Seyfert 2 and LINER/NELG. For the determination of the luminosity function it is necessary to have a complete identified sample of objects. Therefore, fields in which not all candidates had been observed, could not be considered. This reduced the number in the complete sample to 16 bona fide Seyfert 2 galaxies and 22 Seyfert 2 if we include the probable candidates. The effective survey area, which is essential when determining the volume of the complete survey, was also not easy to determine. The total area covered by a photographic plate is reduced by the fact that many spectra end up overlapping each other. These spectra cannot be used and the fraction of overlaps depends on the sensitivity of the photographic plate. The overlap rate in the fields studied here ranges from 35.6% to 84.0% with a mean value of $(55 \pm 14)\%$. This results in a total area of 994 deg^2 which is covered by the 41 spectral plates on which identification was done, but in an effective area of 449 deg^2 which is surveyed within the course of this work. Taking only into account the 27 fields which have been completely classified reduces the effective area to 307 deg^2 .

Another difficulty in deriving the optical luminosity function is the fact that in Seyfert galaxies, and especially in Seyfert 2 galaxies, the host galaxy contributes significantly to the emission (e.g. Prieto et al. 2010). In most cases of Seyfert 2, the optical wave band is dominated by the host. In the sample studied here, the AGN core is on average a factor of 13 ± 3 fainter than the host galaxy. Although host galaxy and AGN core luminosity are correlated when studying large samples, it is necessary to derive the core luminosity function when studying evolution of AGN. This is also more important for the Seyfert 2, as here the AGN core can be more or less absorbed by material which has no effect on the brightness of the host galaxy. Therefore another analysis step was necessary, in which in direct images, which were taken along with the spectra at the 1.54m telescope, a core/host separation was performed, following the procedure described by Jahnke & Wisotzki (2003).

Finally, a $\overline{V_e/V_a}$ test, already described in Section 4.4.2 on page 30, was applied in order to verify the completeness of the sample. For the Seyfert 2 objects within the completely identified fields we get $\langle V_e/V_a \rangle = 0.49 \pm 0.06$, thus the sample can be considered to be indeed complete.

Therefore, all the components to derive the local luminosity function for Seyfert 2 are at hand. In Fig. 4.8 the LF based on the complete sample of 16 objects is shown, as cumulative LF of the AGN plus host galaxy (left panel) and of the AGN core alone (right panel). The LF alone gives us an estimate of the density of Seyfert 2 in the local Universe, depending on their luminosity. In order to test the unification scheme of Seyfert 1 and Seyfert 2, one can now compare the core LF of both types. If both types are intrinsically the same, they should show, to the first order, a similar LF when considering the intrinsic absorption.

In Figure 4.9 the comparison to the Seyfert 1 LF is shown based on two studies: the HES based Seyfert 1 LF by Köhler et al. (1997), and the core LF by Cheng et al. (1985) who examined Markarian galaxies. Can we draw some conclusion based on a comparison of the LF between different types of objects? If we expect the parent population of Seyfert 1 and 2 to be the same, and if we assume that the Seyfert 2 objects are obscured, we would expect the cores of the Seyfert 2 objects to have lower absolute magnitudes. Within the luminosity function of the cores this should result in an offset in brightness. The LF of the Seyfert 2 should have a similar slope as the one for the Seyfert 1, but shifted by the extinction of the absorbing material. Based on X-ray observations one expects the column density of the absorbing material to be as high as $10^{21} \dots 10^{23} \text{ cm}^{-2}$. The expected extinction in the optical band should be high. But a large offset between the core LF of Seyfert 1 and 2 is not seen in Fig. 4.9. Even though the uncertainties are large because different techniques have been applied to derive the core magnitudes from the two classes of objects, the offset is clearly $\lesssim 1 \text{ mag}$. If we assume an average intrinsic absorption by 10^{22} cm^{-2} this leads to an extinction of $A_V \simeq 1.1 \text{ mag}$ (Predehl & Schmitt 1995). Thus, if we assume that type 1 and type 2 are intrinsically the same with similar core

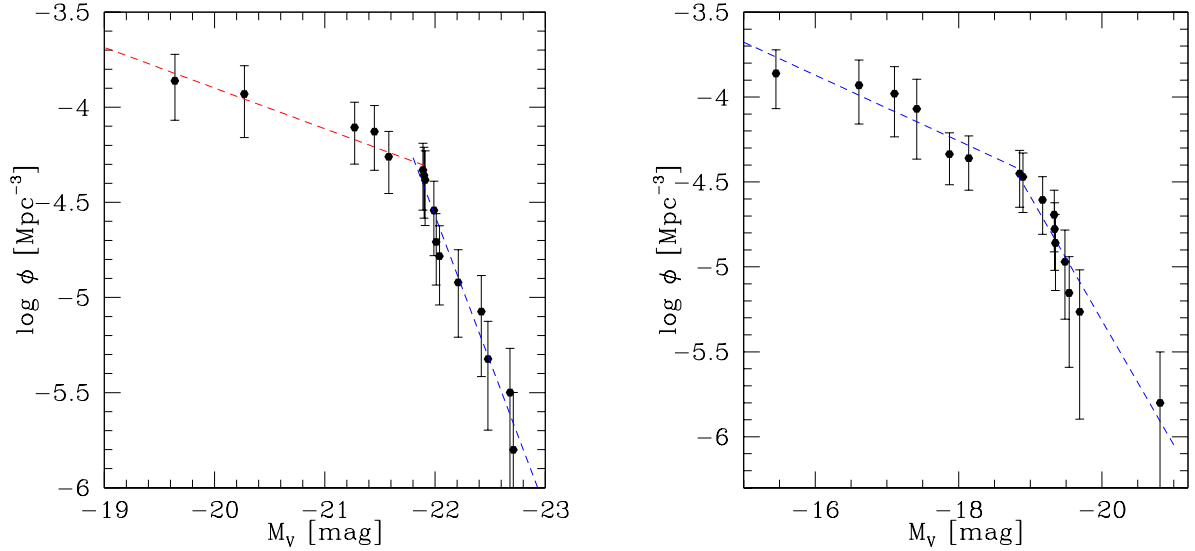


Figure 4.8: Cumulative luminosity function for the absolute magnitude of the complete sample of 16 Seyfert 2 galaxies (core + galaxy, left panel) and for the AGN cores only (right panel). The lines refer to the linear regression.

luminosity, this offset of 1.1 mag plus the offset of ~ 0.5 mag apparent in Fig. 4.9 would mean that there about 4 Seyfert 2 for each Seyfert 1 in the local Universe. If we further assume the absorbing material being organised in a torus like shape (see Fig. 4.10), we can deduce from the ratio the opening angle of this torus:

$$\frac{\text{number of Seyfert I}}{\text{number of all Seyfert galaxies}} = \frac{\text{unabsorbed area}}{4\pi} = 1 - \cos \frac{\theta}{2} \quad (4.9)$$

This would lead to an opening angle of only $\theta \simeq 80^\circ$.

This being said, the uncertainties in this comparison are too big to use this value as a solid estimate for the torus geometry. The fact that no attempt to determine the local Seyfert 2 luminosity function has been done apart from Cheng et al. (1985), Köhler (1996), and Beckmann (2000b) indicates the difficulty to overcome the many obstacles in deriving a LF for this rather faint AGN, which I summarize here:

- in the optical, AGN make only a very small fraction of the observed population ($\sim 0.1\%$ of the galaxies)
- different than Seyfert 1 galaxies, Seyfert 2 cores are faint and show lines with comparably small equivalent widths
- the host galaxy of a Seyfert 2 dominates the emission in the optical by a factor of ~ 13 , making it necessary, to do a core-host separation

In the next section it will be shown that deriving a complete sample of AGN is easier in the X-ray band, mainly because one can assume that all the emission in the X-rays comes from the AGN and because AGN are dominating the X-ray sky at high Galactic latitudes.

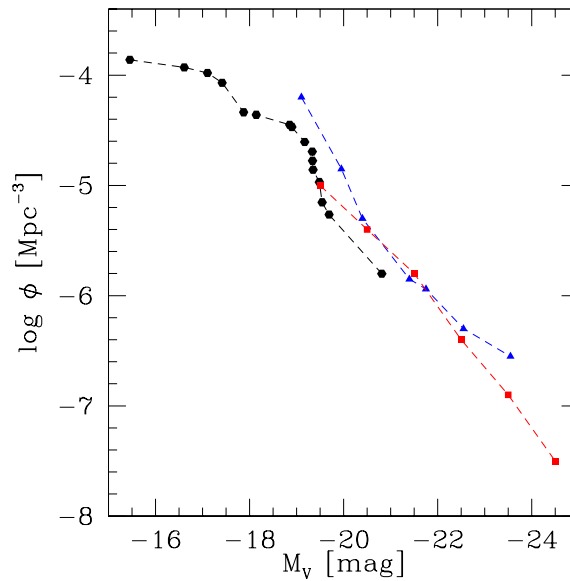


Figure 4.9: Cumulative LF for the Seyfert 2 cores of the HES selected sample (filled hexagons) in comparison to the Seyfert 1 LF from Köhler et al. (1997) (triangles) and Seyfert 1 LF based on Markarian galaxies by Cheng et al. (1985) (squares). All samples have the restriction to $z_{max} = 0.07$.

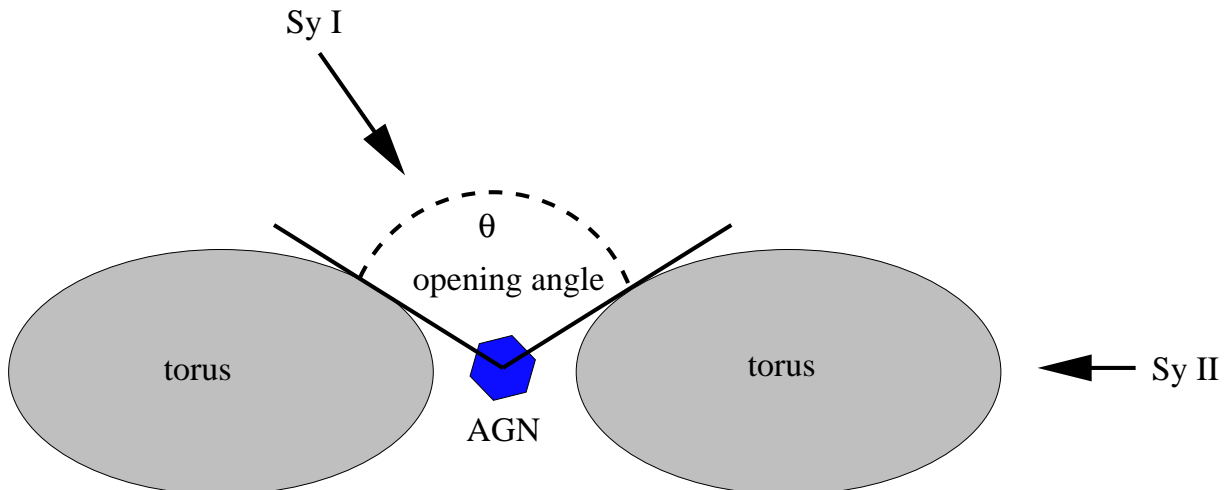


Figure 4.10: Schematic view of the simple Seyfert model with the “dusty torus”. In this model the Seyfert would appear as a Seyfert 1 object if the line of sight is not affected by the torus and as a Seyfert 2 when the line of sight toward the AGN is crossing the torus.

4.5 Testing Unification on X-ray selected BL Lac Objects

If one accepts the view that blazars are those radio loud AGN in which the observer looks into a relativistic jet which is aligned with the line of sight, there still remains the task to unify the different flavours of blazars.

Historically, there were mainly two classes of blazars. Those, which were detected due to their strong radio emission, called radio selected BL Lac objects (RBL) and those found in X-ray surveys, X-ray selected BL Lac objects (XBL). Both, XBL and RBL, seemed to have the same X-ray luminosities but the RBL showed higher radio luminosities. This led Maraschi et al. (1986) to the idea that both classes differ in the orientation with respect to the line of sight. In the case of the RBL we would see directly into the jet whereas in XBL the jet would be misaligned by several degrees. Therefore in an XBL we would see the isotropic X-ray emission of the BL Lac core, while the radiation at lower frequencies is relativistically beamed.

The model of the relativistic jet pointing towards the observer does not explain the differences between the different classes of BL Lac objects. Additional assumptions have to be made. Also the connection to the OVV's and to quasars in general is not well understood yet. On the basis of the relativistic jet model of Blandford & Rees different explanations exist. The following assumptions can also be connected to form combined models.

- *relativistic beaming*: The effect of relativistic beaming was studied by Urry & Shafer (1984). For a relativistic jet the observed luminosity, L_{obs} , is related to the emitted luminosity, L_{emi} , via

$$L_{obs} = \delta^p L_{emi} \quad (4.10)$$

with the Doppler factor δ of the jet being

$$\delta = \frac{1}{\gamma(1 - \frac{v}{c_0} \cos \theta)} \quad (4.11)$$

where v is the bulk velocity of the jet, c_0 is the speed of light, θ the angle of the jet with respect to the line of sight. γ is the Lorentz factor:

$$\gamma = \frac{1}{\sqrt{1 - \frac{v^2}{c_0^2}}} \quad (4.12)$$

This effect gives rise to a very strong, angle-dependent, amplification of the emitted radiation by a factor $\propto \delta^p$, where p depends on the spectral slope α in the observed energy region⁶: $p = 3 + \alpha$. Thus in the radio region $p \sim 3$ and we get an observed synchrotron luminosity L_{sync} of the source:

$$L_{sync} = U_{sync} \cdot 4 \cdot \pi \cdot R^2 \cdot c_0 \cdot \delta^p \quad (4.13)$$

with the energy density of the synchrotron source U_{sync} , and its size radius R . Nowadays Lorentz factors of $\gamma \sim 5$ are assumed (Lähteenmäki & Valtaoja 1999).

Since it was mainly accepted since the 1980's that the parent population of blazars are AGN it was possible to determine the degree of beaming we see in blazars. Comparing the number counts of the blazars with those of the un-beamed AGN and applying the luminosity function

⁶This is valid for monochromatic luminosities. For bolometric luminosities $p = 4 + \alpha$ because the observed bandwidth is then also changed by a factor δ

(LF) of AGN, one can predict the blazar LF. The beamed objects will have higher observed powers and will be less numerous. Urry et al. (1991) fitted the radio LF of blazars (based on the FR I radio galaxies) and derived $5 \lesssim \gamma \lesssim 30$, where γ is the Lorentz factor depending on the bulk velocity of the jet. Based on the FR I LF they argued that the opening angle of the blazar jet should be $\theta \sim 10^\circ$. This would mean that a fraction of $< 2\%$ of the FR I galaxies would be blazars because the probability to detect a source with an opening angle θ_{open} is $P(\theta \leq \theta_{open}) = 1 - \cos \theta$.

- *Viewing angle:* Stocke et al. (1985) compared the properties of XBL and RBL and found out that the XBL show less extreme behaviour than the radio selected objects. The variability and luminosity is especially lower⁷. They made the suggestion that, within the relativistic beaming hypothesis, XBL were viewed at a larger angle to the line of sight. This model was independently found and supported by Maraschi et al. (1986). They made the point that XBL and RBL showed roughly the same X-ray luminosity and therefore are essentially the same. Working on a sample of 75 blazars they suggested that the beaming cone of the XBL was much wider than the radio-optical ones. Maraschi & Rovetti (1994) developed a unified relativistic beaming model, obtaining bulk Lorentz factors of $10 < \gamma_{radio} < 20$ and an opening angle for the radio emission of $6^\circ < \theta_{open} < 9^\circ$, and $6 < \gamma_{X-ray} < 9$ with $12^\circ < \theta_{open} < 17^\circ$ for the radio emission. Urry & Padovani (1995) suggested opening angles of $\theta_X \sim 30^\circ$ for the XBL and $\theta_r \sim 10^\circ$ for the radio selected ones. Therefore, in RBL we would see a jet which is more beamed making RBL having a higher luminosity, while the isotropic X-ray emission would be the same in both types of BL Lac objects. This would make the X-ray selected BL Lac objects much more numerous than the RBL, because the ratio of number densities of the two classes will be $N_{XBL}/N_{RBL} = (1 - \cos \theta_X)/(1 - \cos \theta_r) \simeq 10$. This relation is true for an X-ray selected sample (Urry et al. 1991), but is not holding for a sample with a radio flux limit. Only 10% of the 1 Jy selected BL Lac sample (Stickel et al. 1991; Rector & Stocke 2001) are XBL.

Sambruna et al. (1996) applied the jet model to the multi-frequency spectra of the 1Jy and *EINSTEIN Medium Sensitivity Survey* (Gioia et al. 1990; Stocke et al. 1991) BL Lacs. They found out that not only viewing angle, but also systematic change of intrinsic physical parameters are required to explain the large differences in peak frequencies between HBL and LBL. They proposed that HBL have higher magnetic fields and electron energies but smaller sizes than LBL.

Also the existence of high energetic gamma-rays from HBL seem to argue against the isotropic X-ray emission prediction. In this case one would expect the gamma-ray photons to be absorbed by pair production. But in the beamed case the photon density within the jet is much lower and therefore gamma-ray photons can manage to escape the jet (Maraschi et al. 1992).

- *SSC model:* One problem in understanding the blazar SED is to find out what kind of radiation we see from the jet. The accelerated electrons (or protons) within the jet should interact with the magnetic field enclosing the jet by emitting synchrotron radiation. These photons can then be accelerated again by inverse Compton (IC) scattering on relativistic electrons. In this process the photon would be up-scattered to higher energies, while the electron is decelerated. This interaction using the synchrotron photons produced by the jet is called Synchrotron Self Compton Scattering (SSC; Maraschi et al. 1992; Ghisellini et al. 1993; Bloom & Marscher 1996).

⁷This is generally true, although there are exceptions like PKS 2155-304. This HBL showed a variations of factor ~ 4 within a few hours in the X-rays, as reported by Zhang et al. (1999)

The SSC model results in a blazar emission of synchrotron photons, and a second emission at higher energies of photons produced by IC scattering. These two branches of the SED are not independent. The ratio of the peak frequencies $\nu_{Compton}/\nu_{Synchrotr.} \propto \gamma_{peak}$, where γ_{peak} is the energy of the electrons radiating at the synchrotron peak.

- *EC model:* The External Compton Scattering (EC) model is similar to the SSC model, but it uses for the IC seed photons which are produced by the accretion disk and/or the host galaxy (Sikora et al. 1994; Dermer & Schlickeiser 1993; Blandford & Levinson 1995; Ghisellini & Madau 1996). Also this model results in two peaks in the SED, the synchrotron branch and the EC branch at higher energies. But in this scenario the ratio of peak frequencies depends on the mean frequency ν_{seed} of the seed photons and on the magnetic field strength: $\nu_{Compton}/\nu_{Synchrotr.} \propto \nu_{seed}/B$. Also a mixture of SSC and EC is possible: Sources with stronger emission lines (like OVV, FSRQ) could be dominated by the EC mechanism, at least at GeV energies. In Blazars without emission lines (BL Lacs) the SSC mechanism might dominate the entire gamma-ray region.
- *other models:* Mannheim (1993) suggested that the jet of the blazars could also be formed by protons and that the second peak in the SED could be caused by another more energetic synchrotron component. A proton dominated jet is also favoured by a recent study by Ghisellini et al. (2010) of *Fermi/LAT* detected blazars (Abdo et al. 2010b).

In 1998, Fossati et al. compiled the spectral energy distributions of well-measured blazars, as shown in Fig. 4.11. Dividing the sample into classes of bolometric luminosity, they made an important observation. Apparently, the bolometric luminosity of a blazar is inverse proportional with the peak frequency of the synchrotron or inverse Compton emission of the object (Fossati et al. 1998). In this scheme, XBL are the less luminous blazars, with their synchrotron peak located in the UV to X-ray band, which makes them easily detectable in the X-rays. The LBL are the objects with lower synchrotron peak frequency, in the optical to IR domain, making them more radio bright but slightly less X-ray bright than the XBL. Consequently, a more physical classification than XBL and RBL are the classes of high-frequency peaked objects (HBL) and low-frequency peaked objects (LBL).

Combining this information, Ghisellini et al. (1998) formulated a unification scheme for the blazar class. They argued, that the more powerful LBL have higher energy and particle density in their jets. This will lead to a more efficient cooling within the jet, which explains the lower cut-off frequency of the synchrotron branch. Applying an SSC model, this also leads to lower cut-off energies of the inverse Compton component, with a larger Compton dominance parameter compared to the HBL class. In this scheme, FSRQ represent the most powerful class of blazars, where cooling is stronger dominated by the external radiation field than in HBL and LBL. This, again, lowers the synchrotron peak frequency and inverse Compton peak frequency, and gives rise to an even higher dominance of the inverse Compton branch over the synchrotron emission. The overall scheme is shown in Fig. 4.12. This also means that in order to determine the bolometric luminosity of blazars, it is more important to know the gamma-ray emission of a LBL or FSRQ (which emit most in the inverse Compton branch) than in the case of HBLs, where it can be assumed that the inverse Compton component is as powerful as the synchrotron one.

If this simple model is true, HBL and LBL objects should show the same evolutionary behaviour, i.e. a similar $\langle V_e/V_a \rangle$ value, a similar number counts gradient, and a similar luminosity function. In order to study these aspects, the X-ray group⁸ at *Hamburger Sternwarte* used the sources detected in

⁸<http://www.hs.uni-hamburg.de/DE/For/Exg/Sur/rosat/index.html>

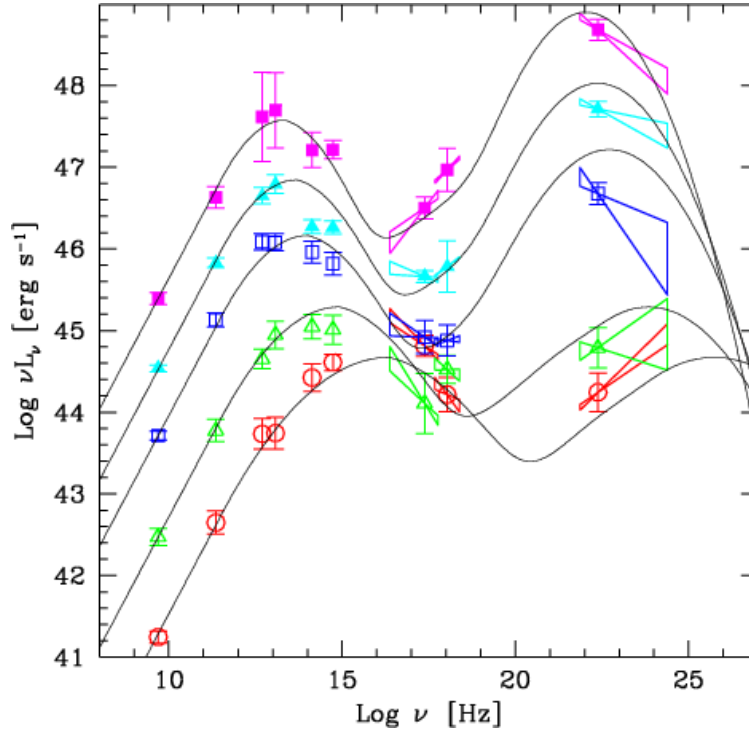


Figure 4.11: The average SED of the blazars studied by Fossati et al. (1998), including the average values of the hard X-ray spectra. The thin solid lines are the spectra constructed following the parameterization proposed in Donato et al. (2001).

the *ROSAT* All Sky Survey (RASS) Bright Source Catalogue (RASS-BSC; Voges et al. 1999). These X-ray sources were identified in Hamburg using the objective prism plates of the Hamburg Quasar Survey as described in the previous section on page 32. A flux limited subsample of the RASS-BSC, the so-called *Hamburg RASS X-ray sample* (HRX) was completely identified, including follow-up through slit-less spectroscopy in order to derive the redshifts of the AGN. This work led to the first complete sample of blazars based on the RASS, the HRX-BL sample, which we published in 1998 (Bade et al. 1998). The sample size was rather moderate, with a total of 39 BL Lac objects, with a complete flux limited sample of 35 objects down to a $f_X(0.5 - 2.0 \text{ keV}) = 8 \times 10^{-13} \text{ erg cm}^{-2} \text{ s}^{-1}$, with redshift information available for 31 of them. The simple test of the distribution of the objects in the survey volume gave $\langle V_e/V_a \rangle = 0.40 \pm 0.06$, consistent with no evolution on the 2σ level.

We then studied the dependency of evolution according to the peak frequency of the synchrotron branch. As a complete spectral energy distribution was not available in most cases, we used the relation between the optical and X-ray flux as an indicator. Ledden & Odell (1985) defined the overall spectral index between two frequencies as

$$\alpha_{1/2} = -\frac{\log(f_1/f_2)}{\log(\nu_1/\nu_2)} \quad (4.14)$$

Here f_1 and f_2 are the fluxes at two frequencies ν_1 and ν_2 . To compare this value for different objects it should be determined for the same frequencies in the source rest frame. Therefore a K-correction had to be applied (Schmidt & Green 1986). As reference frequencies we used 1.4 GHz in the radio

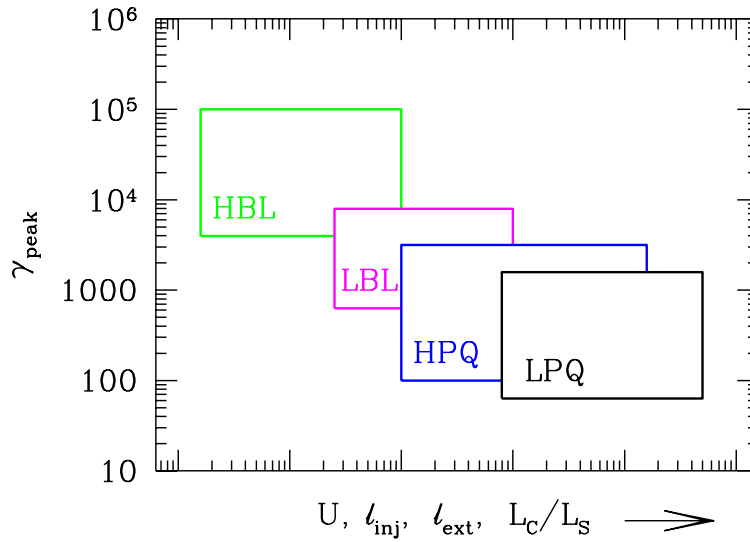


Figure 4.12: Schematic presentation of the unifying scheme for blazars proposed by Ghisellini et al. (1998). The sequence of HBL, LBL, HPQ (high-polarisation quasars), and LPQ (low-polarisation quasars) corresponds to an increase in the external radiation field l_{ext} , the total energy density U and the injected jet power l_{inj} . These in turn result in a decrease of the maximum Lorentz factor γ_{peak} , a decrease of the synchrotron/inverse Compton peak frequency, and an increase in the Compton dominance L_C/L_S .

($\lambda \approx 21$ cm), 4400 Å in the optical ($\sim B$), and 1 keV ($\lambda \approx 12.4$ Å) in the X-ray region to derive the optical-X-ray α_{OX} , the radio- X-ray α_{RX} , and the radio-optical α_{RO} spectral index. In order to study the dependency on the peak frequency, we divided the sample into 17 objects with $\alpha_{\text{OX}} < 0.91$ (X-ray dominated, i.e. HBL) and 18 with $\alpha_{\text{OX}} > 0.91$ (intermediate peaked BL Lacs, i.e. IBL). Here we found a 2σ significant difference in their evolutionary behaviour, with $\langle V_e/V_a \rangle = 0.34 \pm 0.06$ for the HBL and $\langle V_e/V_a \rangle = 0.48 \pm 0.08$ for the IBL. Considering that LBL show weak or positive evolution ($\langle V_e/V_a \rangle = 0.60 \pm 0.05$) as shown for the 1Jy sample by Stickel et al. (1991), and also FR-II radio galaxies, FSRQ, and “normal” quasars show $\langle V_e/V_a \rangle > 0.5$, there seemed to be a trend detectable: the more radio dominated LBL being more numerous and/or luminous at cosmological distances than in the neighborhood, the intermediate IBL showing no evolution, and the HBL being less numerous and/or less luminous in the past. Such a distinction is not included in the simple unified model. It has to be pointed out though that the results were significant only on a $1 - 2\sigma$ level, that the sample was rather small with still some redshift information missing, and thus the luminosity function for this sample did not give conclusive results.

Based on this work, I started a larger project in order to study the evolution of BL Lac objects (Beckmann 1999, 2000a,b, 2002b, 2003; Beckmann et al. 1999, 2003b). The main results were summarized in Beckmann et al. (2003b), and a copy of this paper can be found on page 119. The main goal was to determine the luminosity function for a sample of significantly larger size than that of Bade et al. (1998). The fraction of BL Lacs in the RASS-BSC was $\sim 10\%$. Therefore, an increase of the sample size based on optical identification alone is rather inefficient. This can be alleviated using radio information, as all BL Lacs from the core sample were detected as radio sources in the NRAO VLA Sky Survey (NVSS, Condon et al. 1998). Also all known BL Lac objects do have radio coun-

terparts down to the ~ 2.5 mJy level (Stocke et al. 1991), which is similar to the detection limit of the NVSS. We concluded therefore that for the high X-ray count-rates used we can include radio detection in the NVSS as selection criterium without loosing BL Lac objects. As X-ray input we used again the ROSAT Bright Source Catalog (RASS-BSC; Voges et al. 1999) with a count-rate limit (0.5–2.0 keV) of $hcps \geq 0.09 \text{ s}^{-1}$. We cross-correlated this catalogue with the NVSS adopting an error circle of 30'' around the X-ray position. We extended the sky area studied to 4768 deg² encompassing the area of 2837 deg² studied by Bade et al. (1998), and we applied a unique limit of $hcps \geq 0.09 \text{ s}^{-1}$.

The next task was to identify the nature of sources in the RASS-BSC and to derive redshift information for the sources lacking slit spectra with sufficient signal-to-noise. Based on the results of several optical observation runs it was then possible to increase the size of the sample to 104 BL Lac objects. In the complete sample we found 223 objects out of which 77 formed a complete sample at the $hcps \geq 0.09 \text{ s}^{-1}$, which corresponds to flux limit of $f_X(0.5 - 2.0 \text{ keV}) = 1.1 \times 10^{-12} \text{ erg cm}^{-2} \text{ sec}^{-1}$ (Beckmann 2000b). Thus, the preselection using the correlation between the X-ray RASS-BSC catalogue and the radio NVSS survey increased the efficiency of BL Lac candidate selection from 10% to 34%, without missing any BL Lac objects, as shown in Beckmann (2000b) and Beckmann et al. (2003b). This larger sample now enabled us to test again whether there is any trend in evolution seen within the class of the HBL. The result was that the trend observed in Bade et al. (1998) could not be confirmed. In our study, the trend was even reversed, with the IBLs showing a slightly more negative evolution than the HBL, although significant only on a 1σ level, with $\langle V_e/V_a \rangle = 0.40 \pm 0.06$ for the IBL and $\langle V_e/V_a \rangle = 0.45 \pm 0.05$ for the HBL. Assuming for the unknown redshifts a value between $z = 0.3$ and $z = 0.7$ makes both BL Lac classes even more consistent with no evolution.

The result of Bade et al. (1998) could have been arisen from selection effects due to the ‘‘patchy’’ search area used. A Monte-Carlo simulation done on the first HRX-BL Lac complete sample showed however, that this is not the case. By randomly selecting a subsample of 17 BL Lac objects (which is the number of objects for which Bade et al. found different types of evolution) out of the complete sample used in Beckmann et al. (2003b) there is a chance of only $< 1\%$ to find a $\langle V_e/V_a \rangle < 0.35$.

Another reason for the different results could be related to the different treatment of the radio properties. As radio detection was not a selection criterium in Bade et al., no radio flux limit was taken into account. Applying here the V_e/V_a -test to the complete sample, the accessible volume V_a was determined for $\approx 10\%$ of the objects by the radio limit. The V_e/V_a values are correspondingly increased compared to the case where only an X-ray flux limit is taken into account, resulting in a less negative evolution. There remains the fact that no BL Lac objects were found yet, with $f_R < 2$ mJy radio counterparts and the question is still open whether this is a selection effect or not. It could be that our decision to apply the radio detection as selection criterium weakened the negative evolution found in pure X-ray selected samples.

On the other hand, the fact that we did not find any evolution in the sample, is indeed in good agreement with other studies performed over the last years. Neither the REX survey (Caccianiga et al. 1999, 2002), using the NVSS in combination with the sources found in the ROSAT pointed observations, nor the Deep X-ray Radio Blazar Survey (DXRBS, Perlman et al. 1998; Padovani et al. 2007), which uses the ROSAT data base WGACAT and PMN/NVSS radio data, show a difference for the more or less X-ray dominated BL Lacs. The discrepancy in evolution compared to the FSRQ, i.e. the strongly radio dominated blazars with the synchrotron peak below the UV band, still holds. The positive evolution for FSRQ, first established by Stickel et al. (1991), was recently confirmed by Padovani et al. (2007) using the DXRBS.

The luminosity function we extracted from the sample is consistent with earlier studies based on the EMSS BL Lac sample (Wolter et al. 1994; Padovani & Giommi 1995). Only marginal differences were seen which can be due to systematic errors for the calculated luminosities in the *Einstein*/IPC

band because of differing spectral slopes, or resulting from differences in the calibration of the IPC and the *ROSAT*/PSPC detectors. The sample was large enough to divide it into a high redshift and a low redshift bin in order to examine possible differences in their LF. The dividing value was set to the median of the HRX-BL Lac sample $z_{\text{median}} = 0.272$. To derive high and low redshift LFs the accessible volume $V_{a,i}$ for the objects with $z < 0.272$ has been restricted to $z = 0.272$ whenever $z_{\text{max},i} > 0.272$. For the high redshift objects the accessible volume was computed from $z = 0.272$ up to $z_{\text{max},i}$. The resulting two cumulative luminosity functions are shown in Fig. 4.13. There seems to

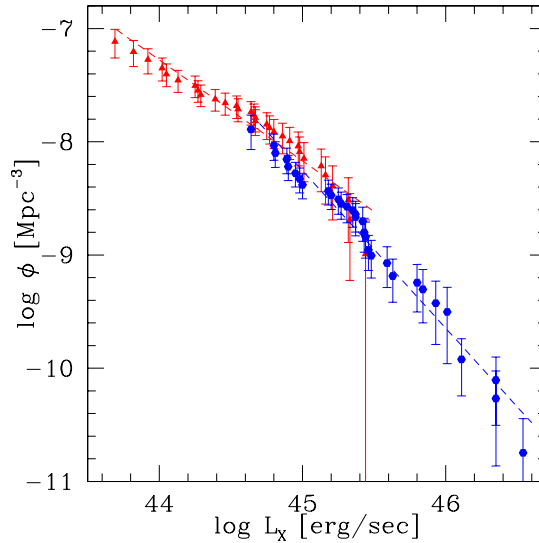


Figure 4.13: Cumulative luminosity function of the two subsamples with $z > 0.272$ (circles) and $z < 0.272$ (triangles) for X-ray selected BL Lac objects in the RASS-BSC.

be a difference between the high and low redshift LF. The slope of the low redshift objects is flatter, a linear regression results in -0.9 while for $z > 0.272$ the slope is -1.4 . But in the overlapping regime around $L_X(0.5 - 2.0 \text{ keV}) \sim 10^{45} \text{ erg s}^{-1}$ the luminosity functions show the same behaviour. The difference might originate from the circumstance that there have been more X-ray faint BL Lacs at cosmological distances than in the nearby universe, but more X-ray bright BL Lacs at small redshifts than for $z > 0.272$. This would result in the already found trend that at high redshift there have been more LBL (X-ray faint) than in the local universe, and that the number of HBL (X-ray bright) has increased.

The different evolutionary behaviour of HBLs and LBLs is a challenge for all theories to unify BL Lacs of different types and other blazars. However, the existence of transition objects and the numerous similar properties of LBLs and HBLs make it plausible that both classes belong to the same parent population (Beckmann 2002b, 2003).

As described by Böttcher & Dermer (2002) one way to unify both classes would be a transformation of LBLs into HBLs as the BL Lac objects grow older, a possibility already outlined in Vagnetti et al. (1991). In this model, BL Lac objects start as LBLs with jets of high energy densities. Strong cooling limits the electron energies leading to cutoff frequencies for the synchrotron component at optical wavelengths and for the IC component in the GeV energy range. As shown by Beckmann et al. (2002), this results in steep X-ray spectra with strong curvature. The core outshines the host galaxy leading to a low calcium break value as seen also for the HRX-BL Lac sample, as discussed

in Beckmann et al. (2003b) and shown on page 125. When by the time the source of the jet gets less powerful the energy density within the jet decreases (Tavecchio et al. 1998). The cooling efficiency decreases as well resulting in higher cutoff frequencies for HBLs. The shift of the cutoff frequencies to higher energies is therefore accompanied by decreasing bolometric luminosities, which is evident from the decrease of the luminosities in the radio, near IR and optical bands. Due to the increasing peak frequencies of the synchrotron branch more energy is released in the X-ray band and the X-ray luminosity increases quite in contrast to the luminosities at shorter frequencies (cf. page 127). The X-ray spectra are correspondingly flatter and less curved than in the LBL state (Beckmann & Wolter 2001).

To date, there seems to be little disagreement with this unification scheme for blazars. Based on this model which assumes a transition in time of the brighter FSRQ to LBLs and finally the fainter HBLs one would expect to observe a decrease in the FSRQ number density toward lower redshifts. In a recent study by Padovani et al. (2007) this was not observed though, in fact the FSRQ LF seems to evolve smoothly to $z = 0$, while Padovani et al. (2007) find no redshift dependence for the LF of BL Lac objects, contrary to Beckmann et al. (2003b). This would mean that there is no strong link between the FSRQ and BL Lac evolution.

Maraschi & Tavecchio (2003) explained the intrinsic difference between FSRQ and BL Lac objects by differences in the accretion efficiency. Assuming that blazar jets are likely powered by energy extraction from a rapidly spinning black hole (Blandford & Znajek 1977) through the magnetic field provided by the accretion disk they argued that FSRQs must have large BH masses ($10^8 - 10^9 M_{\odot}$) and high, near-Eddington accretion rates. In the case of BL Lac objects the jet luminosity would be larger than the disk luminosity. Thus a unification of FSRQs and BL Lacs can be achieved if BL Lac objects have masses similar to FSRQs but accrete at largely sub-critical rates, whereby the accretion disk radiates inefficiently. A similar unification was achieved by Ghisellini et al. (2009) suggesting that the spectral separation in BL Lacs and FSRQs can be the result from different radiative cooling suffered by the relativistic electrons in jets propagating in different ambients. The dividing line between both classes would be given by the accretion efficiency, with $\dot{M}_{\text{div}} \approx 0.01 \dot{M}_{\text{Eddington}}$.

Thus, we seem to be able to confirm that the different blazar types can be unified in a consistent way. One limiting aspect for the further study of the BL Lac luminosity function is the lack of a deeper X-ray survey on a large fraction of the sky. A deeper all-sky survey in the X-rays will be performed by eROSITA (extended ROentgen Survey with an Imaging Telescope Array; Predehl et al. 2007, 2010) which is supposed to be launched in late 2012 from the Russian Baikonur cosmodrome on board the Russian *Spectrum-Roentgen-Gamma* (SRG) satellite. A Soyuz-Fregat rocket will take the satellite into an orbit around the second Lagrange point of the Sun-Earth system, L2. eROSITA will perform a survey in the 0.1 – 10 keV band. The main science driver is to test cosmological models and to assess the origin, geometry, and dynamics of the Universe through the study of the large-scale structures. This is going to be achieved through the observation of 50,000 – 100,000 galaxy clusters. Another result of the survey will be the detection of $3 - 10 \times 10^6$ AGN up to redshift $z \approx 7 - 8$. The expected fraction of BL Lacs will be much lower than 10% as found in the HRX sample, as at a lower flux-limit the extragalactic sky is dominated even stronger by Seyfert type AGN (Cappelluti et al. 2009). But if we assume a fraction of 1% of the AGN in the eROSITA survey to be blazars, this will give us an extraordinary data set in order to establish the luminosity function for HBL and IBL out to redshift $z \approx 1$.

4.6 Early INTEGRAL AGN Observations

A main driver for my AGN research was ESA's *INTEGRAL* mission. In this section I will briefly describe the satellite and its instruments, before describing early results we achieved on AGN using *INTEGRAL* data. The main results on the unification of AGN are going to be presented in Section 4.7.

4.6.1 The INTEGRAL Mission

ESA's *INTEGRAL* space mission Winkler et al. (2003a) hosts two major hard X-ray instruments, IBIS and SPI, both coded-mask telescopes. IBIS provides imaging resolution of 12 arcmin, while SPI is optimized for spectroscopy. Both instruments operate at energies from 15 keV up to several MeV. Co-aligned with these main instruments are the two X-ray monitors JEM-X, which provide spectra and images in the 3–30 keV band, and the optical camera OMC, which provides optical photometry in the V filter. The mission includes a science data centre, considered to be the “fifth instrument” of *INTEGRAL*, being in charge of all aspects relevant to the scientific exploitation of the data.

INTEGRAL was launched on October 17, 2002 from Baikonur into a highly eccentric orbit with a perigee of 9,000 km and an apogee of 150,000 km, which avoids as much as possible the Earth's radiation belt and allows for un-interrupted observations of up to 3 days. The background at soft gamma-rays is highly variable, and at the same time, the instruments receive many more events from the background than from the astronomical sources. Therefore, a precise measurement and knowledge of the background is essential. In order to better estimate the background, *INTEGRAL* observations are mainly done in dithering mode, in which the spacecraft describes a 5×5 or hexagonal pattern on the sky, with typical separation between two pointings of 2.5° and a duration of about half an hour per pointing.

The main scientific break-throughs of the mission are as follows:

- The study of the diffuse Galactic emission, especially in the atomic lines of ^{26}Al , ^{60}Fe , ^{44}Ti , and of the 511 keV annihilation line.
- The study of the Galactic background emission and its resolution into point sources.
- The resolution of hard X-ray sources in and around the Galactic centre.
- Detection of previously unknown sources, such as the highly absorbed high-mass X-ray binaries (HMXB) and Supergiant Fast X-ray Transients (SFXT).
- Study of Galactic X-ray binaries at hardest X-rays, including black hole candidates, low-mass X-ray binaries (LMXB), and HMXB.
- AGN at hardest X-rays, study of the underlying continuum, iron line characteristics, reflection hump, and of variability patterns.
- The study of the Cosmic X-ray Background (CXB) at energies > 20 keV.
- The investigation of violent and fast transient phenomena, such as gamma-ray bursts (GRBs), soft gamma-ray repeaters (SGRs), X-rays bursts and SFXTs

An overview of the scientific results from the first 5 years of the *INTEGRAL* mission has been given in Beckmann (2008).

The imager IBIS

The IBIS telescope (Ubertini et al. 2003) is a high angular resolution gamma-ray imager, using the coded mask technique (Caroli et al. 1987). The IBIS imaging system is based on two independent solid state detector arrays optimised for low (15 – 1000 keV) and high (0.175 – 10.0 MeV) energies surrounded by an active veto system. This high efficiency shield is essential to minimise the background induced by high energy particles in the highly eccentric out of the van Allen belt orbit. A Tungsten Coded Aperture Mask⁹, 16 mm thick and ~ 1 squared meter in dimension is the imaging device. The fully-coded field of view (FCFOV) of IBIS is $9^\circ \times 9^\circ$, with a partially coded FOV extending to $19^\circ \times 19^\circ$.

The low energy detector ISGRI (Lebrun et al. 2003) is made of 128×128 multilayer CdTe detectors, providing imaging with 12 arcmin resolution above ≈ 15 keV up to about 1 MeV. ISGRI is also suited to perform spectroscopy, with an energy resolution of 9% at 100 keV. ISGRI indeed fulfilled the sensitivity expectations, i.e. it can detect a source of 1 mCrab in less than 1 Msec. The analysis of the IBIS/ISGRI data is based on a cross-correlation procedure between the recorded image on the detector plane and a decoding array derived from the mask pattern (Goldwurm et al. 2003). Apart from the studies on diffuse emission, which are mainly done through analysis of SPI data, ISGRI provides most of the data for *INTEGRAL* based research.

The high energy detector IBIS/PICsIT (Labanti et al. 2003) was designed to provide imaging and spectroscopy above 175 keV. The PICsIT design consists of an array of 4096 scintillator crystals with a photodiode readout. Unfortunately, PICsIT did not live up to the expectation to provide a wealth of information about soft gamma-ray spectra. In fact, the scientific use of its data has been fairly limited. One reason is that PICsIT needs 10 times longer exposure time to reach *CGRO/OSSE* sensitivity (Lubiński 2009). Another reason was the lack of usable analysis software. Apart from several GRBs, only 4 objects were detectable using the standard analysis software: Crab, Cyg X-1, XTE J1550-564, and Cen A. Eight more sources are detectable using an alternative analysis method (Lubiński 2009).

The spectrograph SPI

SPI (Vedrenne et al. 2003) is a high spectral resolution spectrograph, operating in the 20 keV to 8 MeV range, based on 19 Germanium detectors. The achieved energy resolution is 1.8 keV and 3.9 keV, at 198 keV and 2.7 MeV, respectively (Roques et al. 2003). SPI is also equipped with a coded mask, providing a FCFOV of 16° and an angular resolution of 2.5° . The partially coded field of view has a diameter of 35° . Source location can be as good as 10 arcmin, depending on the signal-to-noise of the object (Vedrenne et al. 2003).

In the years 2001 - 2003 I was heavily involved in the software development for SPI (Diehl et al. 2003) and also participated in the test efforts. This led to many collaborations in which I provided SPI point source analysis, e.g. as co-author on publications on Cygnus X-1 (Pottschmidt et al. 2003; Wilms et al. 2004), Cygnus X-3 (Vilhu et al. 2003; Hjalmarsdotter et al. 2004, 2008), GRS 1915+105 (Hannikainen et al. 2005), IGR J19140+0951 (Rodriguez et al. 2005), Serpens X-1 (Masetti et al. 2004), EXO 2030+175 (Camero Arranz et al. 2004, 2005, 2007), GRO J1655-40 (Shaposhnikov et al. 2007), 3C 273 (Courvoisier et al. 2003a; Chernyakova et al. 2007), Cas A (Sturmer et al. 2004), GX 9+1 (Vilhu et al. 2007), LMXBs (Paizis et al. 2003, 2004, 2006), and on the first glance of *INTEGRAL* at the Galactic plane (Winkler et al. 2003b). I also participated in the analysis of SPI data

⁹Skinner (2003): “Despite having worked with coded mask telescopes for 25 years, it is the view of the author that, if at all possible, one should avoid their use!”

on GRB (Beckmann et al. 2003a, 2004a; von Kienlin et al. 2003a,b, 2004; Mereghetti et al. 2003a,b; Malaguti et al. 2003).

Despite the effort, point source analysis using SPI data has had a smaller impact on the science output of *INTEGRAL* than IBIS/ISGRI data. There are mainly two reasons for this. First of all, given the same exposure time, IBIS/ISGRI is more sensitive below 200 keV. In the range 20–40 keV, where most source photons can be detected, ISGRI is about ten times more sensitive than SPI. The second aspect is that the angular resolution of 2.5° of SPI, compared to 0.2° in the case of ISGRI, makes it difficult or impossible to extract reliable spectra in crowded regions. The most complete analysis of point sources using SPI data has been provided by Bouchet et al. (2008). Together with colleagues at CESR, MPE, and APC, Bouchet analysed data of 173 sources in the 25–50 keV range using the *SPI iterative removal of sources* (SPIROS; Skinner & Connell 2003) method, finding 30 objects emitting a significant flux ($\gtrsim 2.5\sigma$) above 100 keV. In the energy band above 200 keV where SPI is more sensitive than ISGRI, Bouchet et al. (2008) found 20 significant sources, among them only 4 AGN: Cen A, SWIFT J1656.3–3302, NGC 4151, and NGC 4945. Thus, the contribution to the study of hard X-ray spectra of AGN by SPI is rather limited compared to IBIS/ISGRI. In parallel to the SPIROS

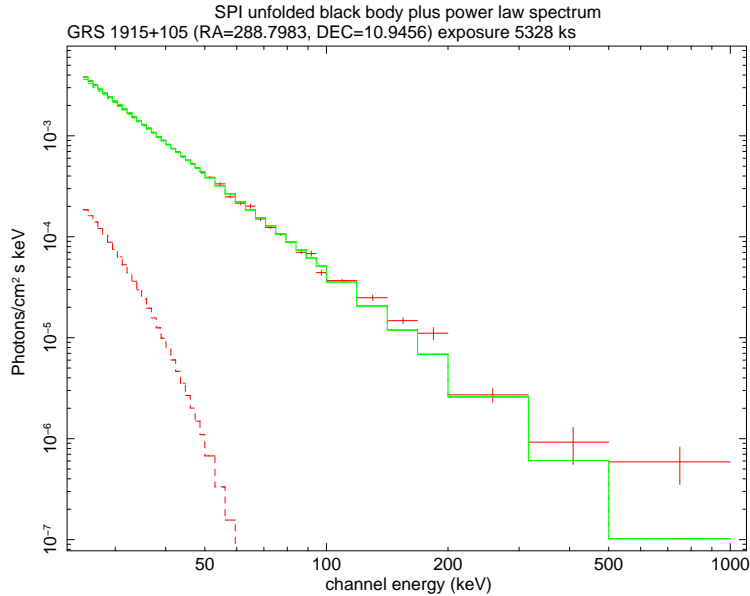


Figure 4.14: Spectrum of the micro quasar GRS 1915+105 based on 5.3 Ms of SPI data. The non-thermal contribution is modeled by a power law extending up to 1 MeV. Spectral extraction was performed using the SPIMODFIT package (Petry et al. 2009).

method to extract point source spectra from SPI data, the SPIMODFIT package has been developed at the MPE, employing a maximum-likelihood fit technique. In collaboration with Dirk Petry (MPE) I analysed the SPI data of the 20 sources detected by Bouchet et al. (2008) above 200 keV using SPIMODFIT (Petry et al. 2009). In addition, we compared the spectra with IBIS/ISGRI data, using the same data sets and the same energy binning. We found that the agreement between the SPI and ISGRI measurements is good if we normalise them on the Crab spectrum. The SPIMODFIT results also agreed well with the SPIROS based results, although we detect only eight of the twenty sources above 200 keV. I then used the SPIMODFIT technique in order to produce SPI spectra for 22 bright sources, using all available data and customized energy binning for the best possible spectral results.

The spectra are included in the *INTEGRAL* high level archive¹⁰ at the ISDC. An example is shown in Fig 4.14.

The camera of SPI is actively shielded by the hexagonal Anti Coincidence Shield (ACS) which consists of 91 BGO crystals. The ACS is used to detect bright gamma-ray bursts at hard X-rays (von Kienlin et al. 2003b). The detectors provide one summed light curve binned at 50 ms. All the 91 independent detectors have different lower energy thresholds (mainly between 50 keV and 150 keV) and an upper threshold at about 100 MeV. In addition, the ACS response varies as a function of the GRB incident angle. For these reasons the count rates cannot be easily translated into physical flux units. Nevertheless the ACS has been and is still used to study temporal structure of bright bursts, information which is especially valuable when combined with other data. I have been and am still actively involved in the analysis of ACS events, e.g. in providing ACS light curves for bright GRBs (Beckmann et al. 2008b, 2009a, 2010a) and for soft gamma-ray repeaters (SGRs; Savchenko et al. 2009, 2010; Mereghetti et al. 2009).

The X-ray monitors: JEM-X

The JEM-X monitor (Lund et al. 2003) was designed to extend the energy coverage of the *INTEGRAL* mission into the lower energetic X-ray band. JEM-X consists of two identical imaging microstrip gas chambers (JEM-X 1 & 2), each with 255 narrow anode strips and the 256 wider cathode strips, providing an energy coverage between 3 keV and 30 keV. The energy resolution (Brandt et al. 2003) is

$$\frac{\Delta E_{\text{FWHM}}}{E} = 0.4 \times \sqrt{\frac{1}{E [\text{keV}]} + \frac{1}{60}} \quad (4.15)$$

i.e. about 1.1 keV at the energy of the iron $K\alpha$ line at 6.4 keV. Both monitors are equipped with a coded mask, resulting in a FCFoV of 4.8° diameter and a resolution of 3.35 arcmin. Originally it was foreseen to operate both JEM-X detectors simultaneously. Soon after the launch it was noticed that the microstrip anodes eroded severely under the optimum setting of the detector high voltage of 900 V at the anode. During the first week of operations about one anode per day per detector was lost. Therefore the anode voltage was lowered to be about 800 V above the cathodes. In addition, only one monitor is operated at a given time, not only to spare the instruments, but also because of telemetry bandwidth constraints. Finally, the efficiency in space is somewhat reduced due to the deadtime associated with the handling of the intense particle background ($\approx 12\%$) and losses due to the on-board background rejection mechanism at lower energies (Lund et al. 2003). All this leads to a somewhat lower sensitivity of the instrument than estimated before launch. More severe though is the fact, that the field of view of JEM-X (4.8°) is much smaller than that of the main instruments IBIS ($9^\circ \times 9^\circ$) and SPI (16°). This, together with the dither pattern *INTEGRAL* performs as described above, leads to a typical effective JEM-X exposure of $\sim 25\%$ when compared to IBIS/ISGRI or SPI. In cases where the source of interest is not the target of an observation but found serendipitously in the field of view of IBIS, often no JEM-X data are available at all.

Therefore, many sources are detected by IBIS/ISGRI but not by JEM-X. In the case of the AGN for example, IBIS/ISGRI provides significant data for 148 objects, but JEM-X only for 23 of those Beckmann et al. (2009d). Thus, JEM-X data are more important and interesting for the study of bright HMXB and LMXB than for the comparably weaker extragalactic objects.

¹⁰http://www.isdc.unige.ch/heavens_webapp/heavens

The optical camera OMC

The Optical Monitoring Camera (OMC, Mas-Hesse et al. 2003) provides simultaneous measurements in the optical V-band. The telescope is a 2' refractor with a focal length of 154 mm, and a field of view of $5^\circ \times 5^\circ$ equipped with a V filter, the detector is a 1024×2048 pixel CCD, with a usable area of 1024×1024 for imaging. The large field of view combined with the moderate camera size leads to a pixel size of 18 arcsec. The instrument is mainly limited by background and reaches objects with $m_V = 18^{\text{mag}}$ at high Galactic latitudes, but only about $m_V = 15^{\text{mag}}$ in the Galactic plane. At the same time, because of telemetry constraints, it is not possible to download the data of the whole field of view during nominal operations. Therefore, only a subset of the OMC data is available, typically some dozens of windows of 11×11 pixels around pre-defined sources of interest (e.g. the target of the observation). The use of OMC data is further limited by the angular resolution, which causes source confusion in the Galactic plane in nearly all cases, the small field of view when compared to the main instruments SPI and IBIS, leading to the same effect of reduced effective exposure on the target of an observation as described in the case of JEM-X, and the fact that many of the hard X-ray sources are significantly fainter than $V \simeq 18^{\text{mag}}$. In fact, OMC is more interesting to provide optical information on the usually optically bright, hard X-ray detected AGN than on Galactic sources. Nevertheless, only for 57 out of the 199 *INTEGRAL* AGN useful OMC data are available (Beckmann et al. 2009d). This is mainly due to the fact that the IBIS/ISGRI field of view is 3.2 times larger than the OMC field of view.

The INTEGRAL Science Data Centre

The handling of *INTEGRAL* data is a complex task. The analysis of its data is more difficult compared to e.g. *XMM-Newton* or *Chandra* data for several reasons:

- Low signal-to-noise: the typical *INTEGRAL* detected source is not visible within one of the pointed observations. Long exposure times, in many cases in the Msec range, are necessary to significantly detect the sources. These data have to be added, considering also the dither pattern.
- variable background: the hard X-ray background is highly variable. Therefore several techniques have to be employed in order to get a firm grip of its level during an observation, either out of monitoring data or from the cameras themselves.
- coded mask: the coded mask technique provides the main difficulties in the *INTEGRAL* analysis. Not only does the opacity of the mask elements depend on the energy, but also the exact mask composition and geometry is not fully known. Sources and background can illuminate the detector through the mask but also through the non-masked area, despite the active shielding. It is not possible to fit the position and flux of all possible sources in the field of view simultaneously, thus assumptions have to be made, which sources to consider and where they are located in the sky.
- Calibration: The calibration depends on the orbital phase of the spacecraft, detector degradation, solar activity, temperature of the instruments, etc., leading to a highly complex system to be considered in the data analysis.

At the same time, the hard X-ray sky is highly variable, Galactic binary systems as well as gamma-ray bursts require fast reaction times so that the scientific community can best monitor and exploit these events. These considerations, among others, led to the idea to provide a dedicated science data

centre to the mission, the *INTEGRAL* Science Data Centre (ISDC; Courvoisier et al. 2003b; Beckmann 2002a). This centre is not only in charge of the scientific quick look analysis of the data, but also responsible for archiving and distribution of data. In addition, the ISDC integrates the software of the instrument teams, providing additional components if needed, and supports scientists in their efforts to analyse the complex data sets.

As part of the ISDC team I was in charge of software integration and testing for SPI (2001 – 2003 and again 2007 – 2009), and in charge of the *INTEGRAL* related operations at the ISDC (2007 – 2009).

4.6.2 The hard X-ray spectrum of AGN

In X-ray astronomy, the accretion disk surrounding a black hole is believed to produce a thermal spectrum. The lower energy photons produced from this spectrum are scattered to higher energies by relativistic electrons in a surrounding medium, e.g. a corona above the accretion disk, through inverse Compton processes (Haardt & Maraschi 1993). As the temperature of the disk and, even more important, the energy of the relativistic electrons will have a certain limit, so will the resulting inverse Compton spectrum have a high-energy cut-off. The intrinsic spectrum has a power law shape with a photon index of $\Gamma \simeq 2$ extending up to a few hundred keV. The soft photons involved in the inverse Compton scattering are believed to originate in the cool thick accretion disc with $kT < 50$ eV, while the relativistic electron gas has a temperature of about $kT \sim 100$ keV. The photons will be up-scattered from their initial energy E_i to the energy $E_f = e^y E_i$, where $y \simeq (4kT/m_e c^2) \max(\tau, \tau^2)$ is the Compton parameter, τ is the optical depth of electron gas, and T is its temperature. In the non-relativistic case with $\tau > 0.01$ this results in $y \ll 10$ and a power law which extends up to the thermal cut-off in the range $E_C \simeq kT$ to $E_C \simeq 3kT$, determined by the cut-off in the thermal distribution of the electrons (Pozdnyakov et al. 1983; Mushotzky et al. 1993).

This spectrum is undergoing reprocessing through absorption. In most cases broad emission lines due to low-ionization stages of iron are visible in the spectra, thus in these objects the absorber is commonly assumed to consist of cold ($T < 10^6$ K) optically thick material (e.g. George & Fabian 1991). This reprocessing leads to a 'hump' in the hard X-ray spectrum, first observed by *Ginga* in the Seyfert 1 galaxies NGC 7469 and IC 4329A (Piro et al. 1990). The shape and strength of the hump depends on the geometry, chemical composition, an orientation with respect to the line of sight, but has its maximum around 20 – 30 keV, where the reflection efficiency reaches its maximum. Its measurement has been difficult, as the modeled strength of this component is closely linked to the intrinsic absorption (measured at softer X-rays), spectral slope of the underlying continuum, and the high-energy cut-off, which is not well constrained in many cases. Also for this reason the location and nature of the reflector itself are a question of debate. The reflection material could reside in the outer accretion disk itself (Zdziarski et al. 1990), or at the inner edge of the absorbing gas (Ghisellini et al. 1994), or could be located in an outflowing wind (Elvis 2000).

Another signature of the reflection process is the ^{26}Fe $K\alpha_1$ fluorescence line at $E_{K\alpha} = 6.404$ keV (Bearden 1967), accompanied by the ^{26}Fe $K\alpha_2$ line at 6.391 keV. The $K\alpha$ line can be used as a probe for the reflection component (Krolik & Kallman 1987) and is observable in most Seyfert galaxies with an equivalent width of 100 – 200 eV (Matt et al. 1991). Also a $K\beta$ line at 7.06 keV is observable. The equivalent width of the iron line is a function of the strength of the reflection component, but also of the iron abundance of the reflecting material, the ionization state of the surface layers of the accretion disk, and of the geometry of the system (Mushotzky et al. 1993; Fabian et al. 2000). The iron $K\alpha$ line is not the only emission line expected in the 0.1 - 10 keV energy range, but by far the strongest, as can be seen in Fig. 4.15.

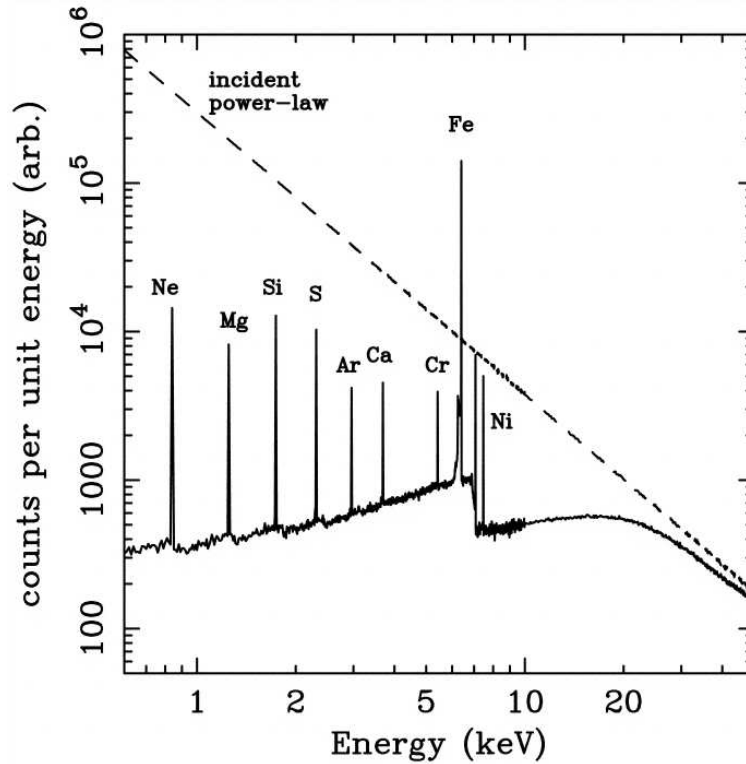


Figure 4.15: X-ray reflection from an illuminated slab. The dashed line shows the incident continuum, and solid line shows the reflected spectrum (integrated over all angles). Figure presented in Fabian et al. (2000) based on Monte Carlo simulation by Reynolds (1996).

The physics involved in this process can be modeled assuming an X-ray continuum which illuminates a slab of cold gas (Zdziarski et al. 1994). X-ray photons entering the slab can interact with the reflector in various ways. They can be Compton scattered by free or bound electrons, they can be absorbed, followed by fluorescent line emission, or absorbed followed by Auger de-excitation. The latter effect either destroys the photon, scatters it out of the slab, or reprocesses it into a fluorescent line photon which then escapes the slab (Fabian et al. 2000).

The line profile itself can be used to examine the movement and gravitational field at the location where the reflection process takes place. Intrinsicly, the fluorescence line should be a narrow line. Thus, line broadening indicates relative movement toward the observer or turbulence in the disk (Pariev & Bromley 1998). In addition, a non-symmetrical line broadening can indicate relativistic effects, in which the approaching (blue shifted) line wing is stronger through relativistic beaming than the receding (redshifted) wing. The line profile for a non-rotating Schwarzschild case (Fabian et al. 1989; Bromley et al. 1998) will look different from the case of a spinning black hole, in which Kerr metrics have to be considered (Laor 1991; Martocchia et al. 2000). The first example in which a relativistically broadened iron line was observed, was found in *ASCA* data of the Seyfert 1 galaxy MCG –6–30–15 (Tanaka et al. 1995). Subsequent work on other Seyfert 1 galaxies seemed to indicate that the feature is detectable in many cases where the signal-to-noise ratio of the X-ray spectrum is sufficient (Nandra et al. 1997; Reynolds 1997). An in-depth review on the aspect of the broad iron lines in AGN is given in Fabian et al. (2000).

It should be pointed out though, that there is an on-going debate, how much of the observed broadening can be indeed accounted for by the Kerr black hole, and how much is due to incorrect modeling of the underlying X-ray continuum. In the case of MCG-6-30-15 Miller et al. (2008, 2009) showed that indeed the spectrum can be modeled in a way which does not require a relativistically broadened iron $K\alpha$ line, but that the broad line can also be caused by several absorbers partially covering the AGN. This work was promptly disputed by Reynolds et al. (2009), claiming that the absorption-dominated model over-predicts the 6.4 keV iron line flux, a claim which was contradicted in turn by Yaqoob et al. (2010). Support for the important influence of absorption in the case of the line shape came also from recent *Suzaku* observations (Miyakawa et al. 2009). This on-going discussion about how much relativistic effects are indeed observable in the X-ray spectra of AGN gathered so far might not be settled before the arrival of higher throughput X-ray telescopes like *Astro-H* or *IXO*.

In addition to cold absorbers also warm absorbers are observed in the X-ray spectra of AGN. The first evidence of absorption due to warm material came from studies of the *Einstein* X-ray spectrum of the QSO MR 2251-178 (Halpern 1984), and from AGN spectra taken with *ROSAT* (Turner et al. 1993). Since then, highly ionized absorbers were observed in about half of the X-ray spectra of type 1 AGN, both Seyfert 1 galaxies (e.g. Reynolds 1997) and quasars (Piconcelli et al. 2005), with column densities up to $N_{\text{H}} \gtrsim 10^{23} \text{ cm}^{-2}$, and often consisting of several zones of ionized gas (e.g., Nandra et al. 1993; Pounds et al. 1994).

Another component observed in AGNs is the so-called soft X-ray excess. A soft ($E \lesssim 2 \text{ keV}$) excess over the power-law component dominant at higher energies has been found in the X-ray spectra of many Seyfert galaxies (Saxton et al. 1993). The origin of the soft excess is still an open issue. In the past the soft excess had often been associated with the high-energy tail of the thermal emission of the disc, but it has been shown recently that the temperature of the disc should be constant (0.1–0.2 keV), regardless of the mass and luminosity of the AGN (Gierliński & Done 2004). This result implies that some other mechanism is at work, as the temperature of the disc should depend on both the mass of the black hole and the accretion rate. Three competing models have been brought forward in order to explain the soft excess observed in the X-ray domain: an additional Comptonization component (e.g. Dewangan et al. 2007), ionized reflection (e.g. from the disk, see Crummy et al. 2006), or complex and/or ionized absorption (e.g. Gierliński & Done 2004; Done 2007).

To summarize, the observed AGN spectrum at X-rays consists of the primary continuum, which can be modeled by a cut-off power law, and a reflected component. The reflected spectrum shows signatures of photo-electric absorption, iron fluorescence and Compton scattering. In addition, cold and warm absorption can influence the spectrum, and an additional soft excess is observed in some cases. A model spectrum of a type 1 AGN in the X-rays showing the contribution of the various spectral features is shown in Figure 4.16.

Using *INTEGRAL* these aspects of the X-ray spectrum and its components can be studied in detail at hardest X-rays. The main advantage of investigating the average spectra of different types of AGN at energies $E > 20 \text{ keV}$ is the fact that absorption does not influence the spectrum unless the object is severely absorbed. Therefore, Seyfert 1 and Seyfert 2 objects should show the same underlying continuum when observed at hard X-rays and when the Compton reflection hump is taken into account (Ghisellini et al. 1994). Absorption becomes important at these energies only if the X-ray obscuring matter has a column density which is larger than the inverse of the Thomson cross-section ($N_{\text{H,CT}} = \sigma_{\text{T}}^{-1} \approx 1.5 \times 10^{24} \text{ cm}^{-2}$), in which case sources are called *Compton thick*. The effect on a model spectrum with photon index $\Gamma = 2$ and high-energy cut-off at $E_{\text{C}} = 300 \text{ keV}$ is shown in Fig. 4.17. It is apparent that the absorption indeed has very little influence on the flux and shape of the intrinsic source spectrum above $\gtrsim 10 \text{ keV}$. In Table 4.1 this is again demonstrated, listing the flux in three X-ray bands relative to an un-absorbed spectrum. In the energy band, the flux starts

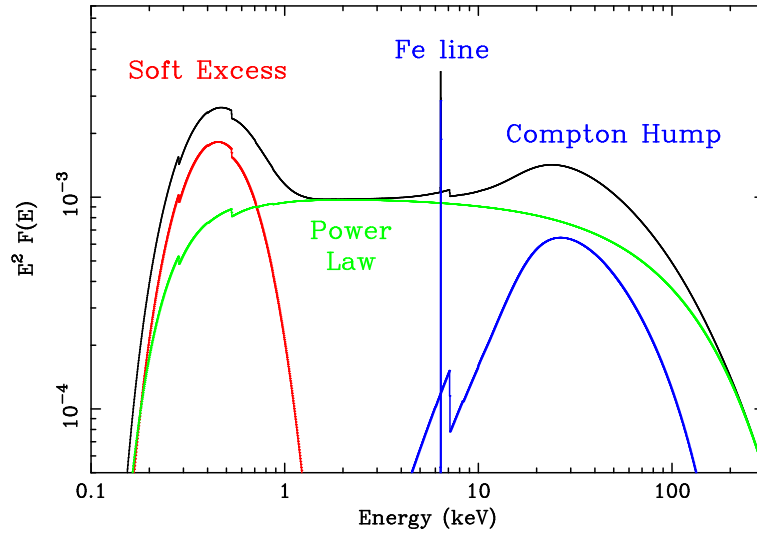


Figure 4.16: Schematic representation of a type 1 AGN spectrum in the X-rays (Fabian & Miniutti 2009).

to decrease significantly only at $N_{\text{H}} > 1.5 \times 10^{24} \text{ cm}^{-2}$, whereas in the 0.1 - 10 keV band already moderate absorption of the order of $N_{\text{H}} = 10^{20} \text{ cm}^{-2}$ suppresses 20% of the flux (therefore also Galactic absorption is important in those energy bands only, whereas can be ignored in the energy bands covered by IBIS and SPI). But this picture is too simplified though, as the spectrum at X-rays is more complex. One complication is based on the fact that all absorbed radiation will have to be re-emitted at lower energies eventually. This makes heavily obscured sources not only bright infrared emitters, but has also a direct influence on the observed X-ray spectrum. In the case of significant absorption, the entire high energy spectrum is down-scattered by Compton recoil to lower energies, where it is readily absorbed and again re-emitted at lower energies. This effect gives the hump-like shape and is shown in Fig. 4.18 (Comastri 2004). The high energy spectra of obscured AGN are therefore often much more complex than a single absorbed power law. Additional components (i.e., thermal emission from a starbursting region and/or nuclear flux scattered into the line of sight) are common in the X-ray spectra below 10 keV of several nearby Compton thick galaxies (Matt et al. 1997; Vignati et al. 1999; Beckmann et al. 2004d). The photoelectric cut-off (if any) does not provide a measure of the "true" nuclear absorption anymore, unless all these components are correctly taken into account. Nevertheless, a Compton thick absorber suppresses only a few percent of the flux in the energy bands $E > 20 \text{ keV}$ covered by *INTEGRAL* IBIS and SPI, whereas these sources are hardly detectable below 8 keV, e.g. by *Chandra* and *XMM-Newton*.

4.6.3 The quasars MR 2251-178 and 3C 273

Soon after the commissioning phase of *INTEGRAL*, during which the instruments were tested and fine tuned, the satellite set out on December 30, 2002, for the first major observational campaign on an AGN, the quasar MR 2251-178. Due to the faintness of the object ($f_{20-40 \text{ keV}} = 3 \times 10^{-11} \text{ erg cm}^{-2} \text{ s}^{-1}$, Beckmann et al. 2009d), the exposure time of only 167 ksec, and the pre-mature nature of the software at that early stage of the mission, no immediate results were derived from the data, and spectral analysis was presented later in Beckmann et al. (2006a).

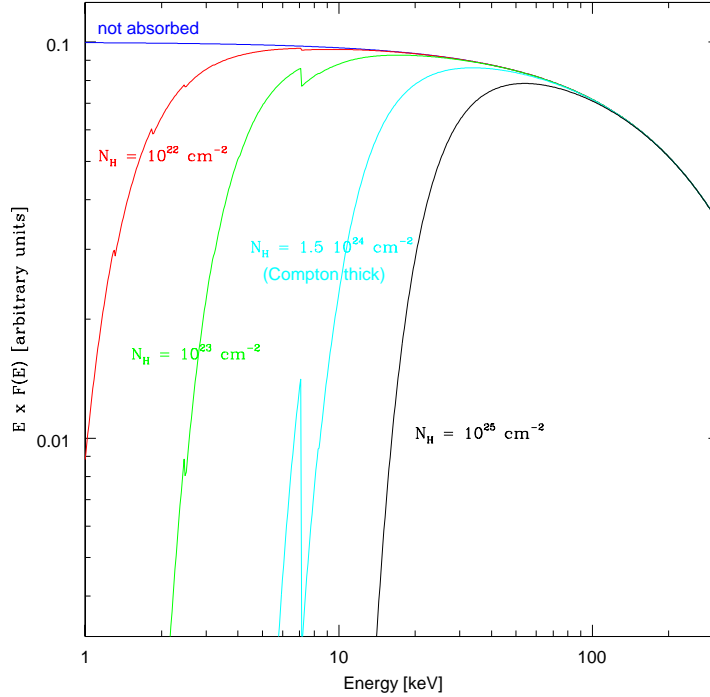


Figure 4.17: The effect of absorption on the measured X-ray spectrum of a source with photon index $\Gamma = 2$ and high-energy cut-off at $E_C = 300$ keV. Model spectra are shown for no absorption, and for hydrogen column densities of $N_H = 10^{22}$, 10^{23} , 1.5×10^{24} , and 10^{25} cm^{-2} . Effects by Compton recoil are ignored.

The next extragalactic target was the blazar 3C 273, the optically brightest AGN (Courvoisier 1998). Due to its brightness throughout the entire electromagnetic spectrum, it is one of the best studied and also among the first detected AGN in the X-ray band (Bowyer et al. 1970). Expectations were large that the observations could lead to deeper insight in the accretion processes, the disk-jet coupling, and the continuum versus iron line variability in this blazar. Unfortunately, the simultaneous *INTEGRAL*, *XMM-Newton* and *RXTE* observations starting in January 2003 caught the source in a historically low state. The combined data showed a steep, featureless spectrum which can be represented by a simple power law model with photon index $\Gamma = 1.73 \pm 0.02$. One of the main conclusions of this multi-mission effort was the insight that there was an important cross calibration effort to be performed in order to be able to confidently use multi-instrument data to model the emission of sources over several decades of energy (Courvoisier et al. 2003a). It also showed that the extensive SPI ground calibration at CEA/DAM in Bruyères-le-Châtel (Attié et al. 2003) had resulted in a good knowledge of the instrument, leading to intercalibration factors around 1.0.

4.6.4 The Seyfert 2 NGC 4388

Thanks to the large field of view of *INTEGRAL*'s main instruments, IBIS and SPI, the observations of 3C 273 and of the Virgo region revealed also other AGN, among them the bright Seyfert 2 galaxy NGC 4388. We published a paper about the first observations by *INTEGRAL* on this source (Beck-

Table 4.1: The effect of absorption on a spectrum with photon index $\Gamma = 2$. Flux in percent relative to the unabsorbed case.

$\log N_{\text{H}}$ [cm^{-2}]	$f(0.1 - 10 \text{ keV})$	$f(10 - 20 \text{ keV})$	$f(20 - 200 \text{ keV})$
0	100	100	100.0
20	81	100	100.0
21	60	100	100.0
22	38	96	100.0
23	19	96	99.8
24	3	69	98.3
CT ^{a)}	1	58	97.5
25	0	8	86.8
26	0	0	56.0

^{a)} Compton thick limit, $N_{\text{H}} = 1.5 \times 10^{24} \text{ cm}^{-2}$

mann et al. 2004d,c), which was at the same time the first publication on a Seyfert galaxy using *INTEGRAL* data. NGC 4388 ($z = 0.00842$) is a good probe to test the components at work in the X-ray band, as it is one of the brightest Seyfert 2 galaxies at hard X-rays. The energy range up to $\sim 10 \text{ keV}$ has been studied with X-ray missions like *ROSAT* (Antonelli et al. 1997), *ASCA* (Iwasawa et al. 1997), *BeppoSAX* (Risaliti 2002), *RXTE* (Sazonov & Revnivtsev 2004), and with *Chandra* (Iwasawa et al. 2003). Spectral studies of NGC 4388 of the hardest X-ray energies up to several hundreds of keV have been performed by *SIGMA* (Lebrun et al. 1992), by the *CGRO/OSSE* experiment (Johnson et al. 1994), and up to $\sim 150 \text{ keV}$ by the Phoswich Detector System (PDS) on-board *BeppoSAX* (Risaliti 2002). The two *BeppoSAX* observations in 1999 and 2000 showed a high energy spectrum with a power law of $\Gamma = 1.6$ and 1.5 , respectively. Due to the energy range covered by the PDS it was only possible to give a lower limit for a possible high energy cut-off ($E_C > 109 \text{ keV}$).

In order to increase the spectral coverage, we added to our analysis not only *INTEGRAL* data from IBIS/ISGRI, SPI, and JEM-X, but also un-published *XMM-Newton* and *RXTE* data. The hard X-ray data alone could be fit with a simple power law model which resulted for the ISGRI data in a photon index of $\Gamma = 1.70^{+0.01}_{-0.01}$ (25 – 300 keV) and a flux of $7.8 \pm 0.5 \text{ mCrab}$ in the 20 - 40 keV energy band. The SPI spectrum for was also well described by a single power law with photon index $\Gamma = 1.68^{+0.47}_{-0.35}$ (20 – 500 keV) and a flux of $9 \pm 2.6 \text{ mCrab}$ in the 20–40 keV energy band, which is consistent with the ISGRI results. The spectrum as seen by *XMM-Newton* is more complex. At energies below $\sim 2.5 \text{ keV}$ the data are well represented by a Raymond-Smith model, which describes a spectrum of radiation emitted by a hot optically thin plasma with abundances and equilibrium ionization balance appropriate to interstellar conditions (Raymond & Smith 1977). The model fit shows a low abundance (7% solar) of the emitting plasma and a temperature of about 0.80 keV, applying only Galactic absorption ($2.62 \times 10^{20} \text{ cm}^{-2}$). The so-called *mekal* model in XSPEC, developed by Mewe & Kaastra (Mewe et al. 1985; Kaastra 1992), gives the same results ($T = 0.78 \text{ keV}$, $7.4\% Z_{\odot}$). This constant soft X-ray emission is most likely not linked to the AGN. This is also supported by the fact, that this emission is extended, as has been reported from *ROSAT/HRI* measurements (Matt et al. 1994) and from *Chandra* (Iwasawa et al. 2003). The low abundance in the extended emission has been seen already in the *ASCA* observations, though with much larger uncertainties ($Z = 0.05^{+0.35}_{-0.03} Z_{\odot}$; Iwasawa et al. 1997). Iwasawa et al. (2003) argue that the extended emission at low energies is more likely to origin from photoionized plasma. Even though it is not possible, based on the *XMM-Newton* data presented here alone, to give a preference to a thermal or photoionized plasma, the latter one has the advantage of

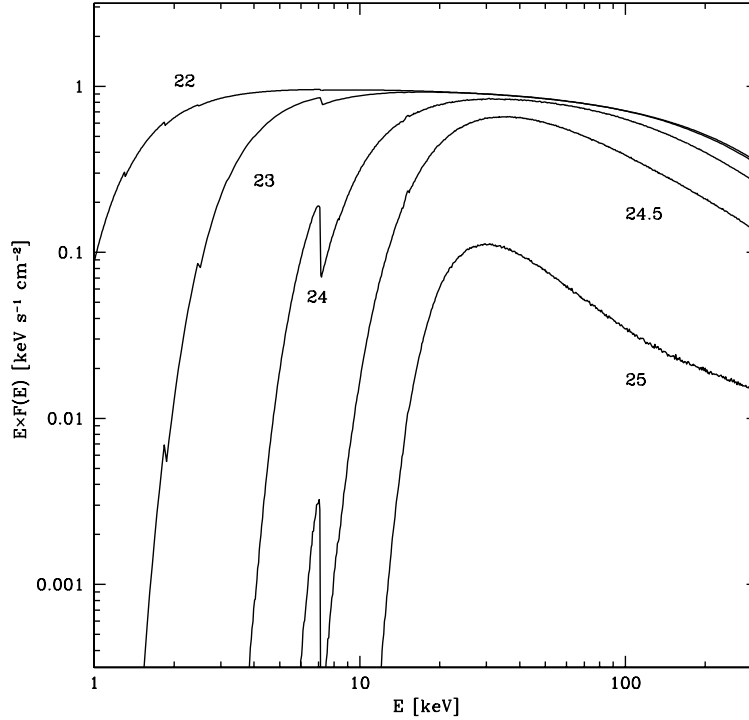


Figure 4.18: The effects of photoelectric absorption and Compton down-scattering on an X-ray spectrum with photon index $\Gamma = 2$ and exponential cut-off at $E_C = 300$ keV. Labels correspond to the logarithm of the column density. Figure from Comastri (2004).

avoiding the low abundance in the vicinity (within several kpc) of the AGN core. At harder X-rays, the *XMM-Newton* spectrum is dominated by an absorbed power law. The column density of the cold absorber is $2.7 \times 10^{23} \text{ cm}^{-2}$. The power-law index is not well constrained by the *XMM-Newton* data, so the photon index of $\Gamma = 1.7$ measured by IBIS/ISGRI and SPI, has been applied. In addition, a Gaussian line at $6.39^{+0.01}_{-0.01}$ keV is apparent in both observations, consistent with the iron $K\alpha$ line.

The *INTEGRAL* data alone did not allow us to reconstruct the complete X-ray spectrum of NGC 4388, mainly because the statistics of the ISGRI and SPI data did not constrain existing models. Comparison with former observations by *SIGMA* (Lebrun et al. 1992), OSSE Johnson et al. (1994), and *BeppoSAX/PDS* (Risaliti 2002) showed a similar spectrum at hardest X-rays as observed with *INTEGRAL*. Measurements by BATSE gave a flux of $f_{20-100 \text{ keV}} = (2.6 \pm 1.5) \times 10^{-3} \text{ ph cm}^{-2} \text{ s}^{-1}$, compared with an *INTEGRAL* value of $(2.7 \pm 0.3) \times 10^{-3} \text{ ph cm}^{-2} \text{ s}^{-1}$. This indicates that the soft gamma-ray spectrum does not vary dramatically as we found also studying the hard X-ray light curves of the source. The flux varied by a factor < 3 and the spectral shape was conserved during 13 years of various observations. The data were fit simultaneously applying the same model as for the *XMM* data alone: a Raymond-Smith model for a hot plasma with Galactic absorption, an absorbed power law, plus two Gaussian emission lines, representing the $K\alpha$ and $K\beta$ line. Figure 4.19 shows the combined spectrum of NGC 4388. The normalization factors are in the range 2.5 to 4.2 relative to the *XMM-Newton* July 2002 data, which apparently represents the lowest flux level reported so far. The power law, dominating the emission above ~ 2.5 keV, has a photon index of $\Gamma = 1.65^{+0.04}_{-0.04}$ and an absorption of $N_H = 2.73^{+0.07}_{-0.07} \times 10^{23} \text{ cm}^{-2}$.

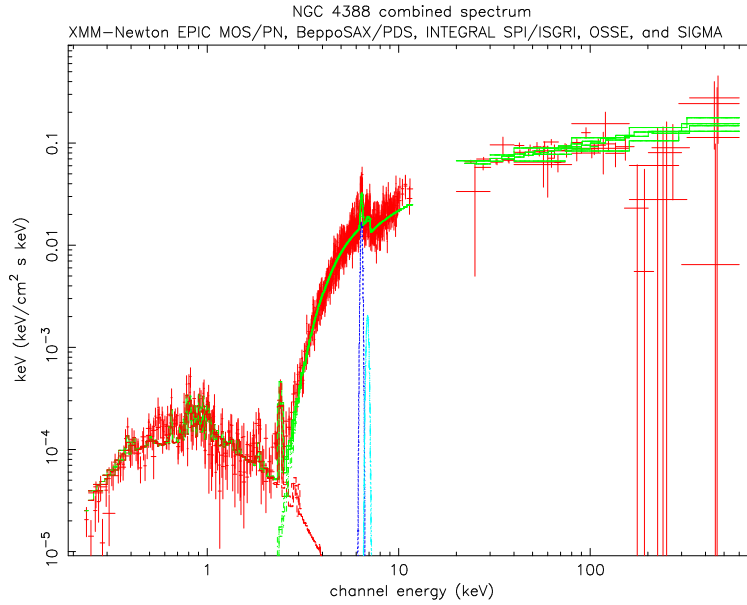


Figure 4.19: NGC 4388 combined spectrum ($E^2 f_E$ vs. E), including *XMM-Newton* EPIC MOS/PN, *BeppoSAX* PDS, *CGRO* OSSE, *SIGMA*, and *INTEGRAL* ISGRI/SPI. The high energies are dominated by the highly absorbed reflection component plus the $K\alpha$ and $K\beta$ iron fluorescence lines, while the lower energies show emission characteristic for a hot plasma with low abundance. Figure from Beckmann et al. (2004d).

Using a more complicated model with a cut-off power law plus reflection from cold material (the so-called PEXRAV model; Magdziarz & Zdziarski 1995) instead of the simple power law, did not improve the fit significantly. The data do not constrain the power law and the reflection component: Fixing the photon index to $\Gamma = 1.7$ resulted in a folding energy of $380^{+\infty}_{-200}$ keV, indicating that a cut-off is possible but could not be confirmed. Thus, no Compton reflection hump was detectable in the data. Although the iron $K\alpha$ fluorescence line indicated the presence of reflection processes, no significant decline due to Klein-Nishina processes appeared above 50 keV.

A cut-off was only detectable recently in the *INTEGRAL* data, using 870 ks of IBIS/ISGRI and 147 ks of JEM-X data (Beckmann et al. 2009d). The data showed now a hard X-ray spectrum with $\Gamma = 1.26^{+0.15}_{-0.16}$ with a cut-off energy at $E_C = 78^{+35}_{-20}$ keV. Still, the data do not allow to determine the strength of the reflection component and the cut-off simultaneously. A turn over at $E_C = 30 \pm 13$ keV with $\Gamma = 0.9 \pm 0.3$ was also reported in *Suzaku* data of NGC 4388 (Shirai et al. 2008), detecting also significant spectral variability. In addition, the *Suzaku* data allowed to fit a cut-off and reflection component simultaneously in one case, which led to a cut-off energy of $E_C = 270^{+130}_{-70}$ keV and a reflection component¹¹ of $R = 1.6^{+0.3}_{-0.4}$. Using all available data of *INTEGRAL* as of today, it is still not possible to fit the reflection component simultaneously with the exponential cut-off, although the existence of a cut-off in NGC 4388 appears to be well established now (?).

While we observed in NGC 4388 flux variations of the underlying continuum, we did not see any variability of the iron $K\alpha$ line flux (Beckmann et al. 2004d). Assuming that this line was indeed

¹¹The reflection strength R is defined as the relative amount of reflection compared to the directly viewed primary spectrum.

constant over the several years over which the observations were spread, would indicate that the distance between the reflecting material and the central engine should be at least several light years. It has to be pointed out though that the observation of a variable iron $K\alpha$ line in AGN is in general rare. This does not necessarily have to indicate a large distance of the reflector to the continuum source. In the light-bending model (Miniutti & Fabian 2004) the non-variability of the iron line in MCG-6-30-15 is explained by relativistic effects. In this model the variability is mainly caused by changes of the position of the X-ray source with respect to the black hole, and not by intrinsic variability of the disk. On the other hand, iron line variability has been seen, e.g. in the Seyfert 2 galaxy NGC 2992 (Shu et al. 2010), indicating a rather close distance between reflector and X-ray continuum source. This shows again that the question about the processes and geometry involved in the emission of the iron line as well as the importance of the relativistic effects is far from being settled.

The work on NGC 4388 showed the potential of *INTEGRAL* to test for the components observable at hard X-rays. It also showed, how important it is to combine *INTEGRAL* data with softer X-ray mission data, in order to better constrain spectral models.

4.6.5 The Seyfert 1.5 galaxy NGC 4151

The Seyfert galaxy NGC 4151 is one of the most extensively studied AGN. This is due to the fact that it is one of the brightest ($V \approx 11$ mag, bolometric luminosity $\sim 10^{44}$ erg s^{-1}) and nearest (16.5 Mpc for $H_0 = 75$ km s^{-1}) among its class. Observations throughout the electromagnetic spectrum revealed a complex and somewhat special case of a Seyfert 1.5 galaxy (see Ulrich 2000 for a general review). In the optical the host galaxy appears to be a large barred spiral with nearly face-on orientation, showing two thin spiral arms (Arp 1977). At soft X-rays NGC 4151 *Chandra* data show a complex spectrum, including line emission from a highly ionized and variable absorber, in the form of H-like and He-like Mg, Si, and S lines, as well as lower ionization gas via the presence of inner-shell absorption lines from lower-ionization species of these elements (Kraemer et al. 2005). Due to the heavy absorption, it is not possible to tightly constrain the intrinsic X-ray photon index below 10 keV. The continuum at 2 – 10 keV as studied by *ASCA* shows a flat spectrum with $\Gamma \sim 1.5$ (Weaver et al. 1994). Observations by *XMM-Newton* in the 2.5 – 12 keV energy range suggest that the spectrum can be modeled by an absorbed power-law continuum (fixed $\Gamma = 1.65$), a high energy break fixed at 100 keV, a neutral Compton reflection component with a reflection fraction of 2.0 compared to the normalization of the power law, and a narrow iron $K\alpha$ line. The fact that $R > 1$ is explained by the relative variability timescales in the direct and reflected component. The absorption of the power-law continuum was represented by a product of two absorption components (Schurch et al. 2003). The spectrum detected by *BeppoSAX* seemed to be best described by a power law with an exponential cut-off at > 100 keV and an iron fluorescence $K\alpha$ line (Piro et al. 2000; Dadina 2007). In addition to the fluorescence line also the reflection hump in the 10 – 30 keV has been reported in *Ginga/OSSE* data Zdziarski et al. (1996), in combined *ASCA* and *OSSE* data Zdziarski et al. (2002), and in *BeppoSAX* data (Schurch & Warwick 2002; Dadina 2007).

In 2004 we used the available 408 ks of *INTEGRAL* data taken in May 2003 in order to study the spectral components in NGC 4151 (Beckmann et al. 2005b). Due to the brightness of the source with $f_{20-100\text{keV}} = 5.8 \times 10^{-10}$ erg cm^{-2} s^{-1} NGC 4151 reached a 150σ and 25σ detection in *IBIS/ISGRI* and *SPI*, respectively. Thus the data allowed a more complex modeling than the cases of the earlier studies of NGC 4388 and 3C 273. Different to NGC 4388, no additional component seems to be at work in the soft X-rays in NGC 4151. The data below 10 keV can be described by an absorbed power law model with a iron $K\alpha$ line. Adding together the *INTEGRAL* JEM-X, *ISGRI*, and *SPI* data, covering the energy range from 2 to 300 keV, the simple power law continuum is not sufficient to fit the data

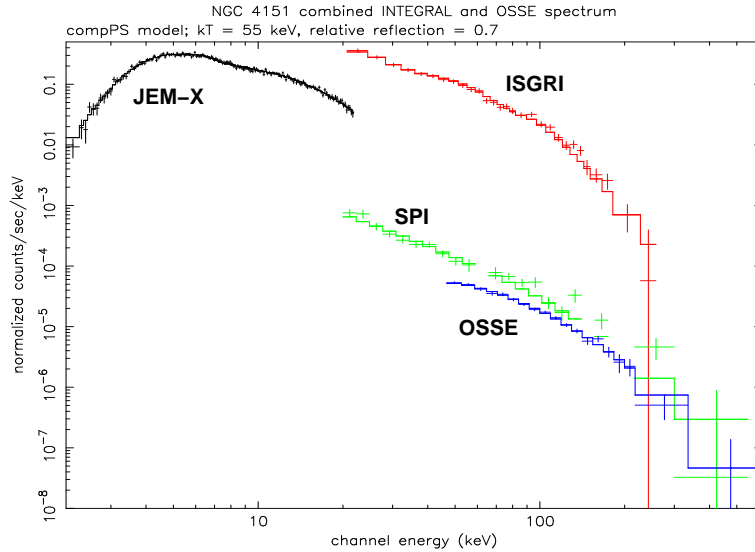


Figure 4.20: *INTEGRAL* and *CGRO/OSSE* simultaneous data fit. The OSSE data represent the average of the NGC 4151 spectra. All data are well represented by a Compton reflection model (`compPS`; Poutanen & Svensson 1996), with the individual OSSE data scaling with 0.6... 1.2 versus the *INTEGRAL*/JEM-X2 data.

though. A Compton reflection model gave a significantly better fit. We added a reflection component from cold material to the cut-off power-law (the so-called PEXRAV model; Magdziarz & Zdziarski 1995). The free parameters in the PEXRAV model are best fitted with a photon index of $\Gamma = 1.85^{+0.09}_{-0.09}$, a hydrogen column density of $N_{\text{H}} = 6.9^{+0.8}_{-0.4} \times 10^{22} \text{ cm}^{-2}$, a cut-off energy of $E_{\text{C}} = 447^{+885}_{-190} \text{ keV}$ and a relative reflection of $R = 1.0^{+0.4}_{-0.3}$. Although this model is a good representation of the data, the choice of a power law for the underlying high-energy continuum is purely phenomenological and the referee encouraged us to use a more physical approach, as included in the `compPS` model (Poutanen & Svensson 1996). This is a self-consistent model which computes Comptonization spectra using exact numerical solutions of the radiative transfer equation. The resulting spectrum is reflected from the cool medium according to the computational method of Magdziarz & Zdziarski (1995). The model fit resulted in an electron temperature of $kT_e = 94^{+4}_{-10} \text{ keV}$, an optical depth of the corona $\tau = 1.31^{+0.15}_{-0.05}$, and a relative reflection of $R = 0.72^{+0.14}_{-0.14}$, with $\chi^2_{\nu} = 0.98$ for 196 degrees of freedom.

We compared the *INTEGRAL* data directly with *CGRO/OSSE* data of NGC 4151 (Johnson et al. 1994). Figure 4.20 shows a simultaneous fit of both data sets, the average *INTEGRAL* and average *CGRO/OSSE* spectrum. When applying the `compPS` model we observe an electron temperature of $kT_e = 55^{+2}_{-1} \text{ keV}$ and a relative reflection of $R = 0.7^{+0.1}_{-0.1}$. The comparison to previous *CGRO/OSSE* measurements shows that this model is a valid representation of the high energy spectrum over decadal timescales, with the normalisation varying by a factor of 2 and the temperature of the underlying continuum varying in the range $kT_e = 50 - 100 \text{ keV}$ for the various observations. A significant variation of the spectral parameters during the *INTEGRAL* observation cannot be detected.

The results are mainly consistent with previous *BeppoSAX* observations. Three observations by *BeppoSAX*, two in 1996 and one in 1999, suggest that the strength of the reflection component is variable, with $R = 0.01$ up to $R = 0.45$ (Petrucci et al. 2001). R is normalized so that $R = 1$ in the case of an isotropic source above an infinite reflecting plane. R is often considered as an estimate of

$\Omega/2\pi$ where Ω is the solid angle subtended by the reflector as seen from the isotropic X-ray source. It has to be pointed out that a relative reflection of $R > 1$, as seen in NGC 4151 in the work of Schurch et al. (2003), represents the case when more primary X-ray radiation is emitted toward the reflector than toward the observer. This can be explained by variable emission of the central engine and a time delay between the underlying continuum and the reflected component, caused by a large distance of the reflecting material to the primary source (Malzac & Petrucci 2002). Another model which can lead to large R values is based on relativistic effects caused by a dynamic corona moving towards the reflecting disk (Malzac et al. 2001). Other explanations include a special geometry with a high intrinsic covering fraction of the cold disk material (Malzac 2001) and general relativistic light bending effects caused by a maximally rotating Kerr black hole (Miniutti & Fabian 2004).

Right now I am involved in a work on analysing all the available X-ray data on NGC 4151 together (Lubiński et al. 2010). This more extensive exercise shows indeed that there is spectral variability in this Seyfert 1.5, in the sense of a high flux state with a soft spectrum and a low flux state with a hard spectrum.

4.6.6 The First *INTEGRAL* AGN Catalogue

One of the *INTEGRAL* mission goals was to determine whether differences are detectable in the hard X-ray spectra of AGN, especially concerning the question, whether type 1 and type 2 AGN are intrinsically the same. In order to compare the two groups, a consistent analysis of all the AGN detected by *INTEGRAL* IBIS/ISGRI was necessary. A first sample of AGN detected through the Galactic plane was analysed in more detail by our group (Soldi et al. 2005). The sample was composed by five Seyfert 2 objects (MCG -05-23-16, NGC 4945, the Circinus galaxy, NGC 6300, ESO 103-G35) and the radio galaxy Centaurus A. Except for Cen A and the Circinus galaxy, which required a cut-off in the hard X-rays, the continuum emission was described by a power law with a wide range of photon indices ($\Gamma \sim 1.4-2.3$).

We then compiled the first *INTEGRAL* AGN catalog (Beckmann et al. 2006a; see also the copy of the paper on pages 132-144). We analysed all available data publicly available in March 2005, which included spacecraft revolutions 19 - 137 and 142 - 149. Data before revolution 19 are usually excluded, as the mission was still in commissioning phase and instrument settings were still adjusted. We analysed JEM-X, IBIS/ISGRI, and SPI data of all AGN known at that time. The sample included 42 extragalactic objects, of which 10 are Seyfert 1, 17 are Seyfert 2, and 9 are intermediate Seyfert 1.5. 5 blazars were included and the Coma galaxy cluster. A simple absorbed power law model fit was sufficient to represent the combined spectra in most of the cases, and only six sources required a cut-off power law model fit (i.e. NGC 4597, NGC 4593, ESO 323-077, IC 4329A, the Circinus galaxy, and NGC 5506). The sources were on average high flux and low luminosity AGN with $f_{20-100\text{keV}} > 1.5 \times 10^{-11} \text{ erg cm}^{-2} \text{ s}^{-1}$ and $\log L_X = 43.3$ in the local Universe ($\bar{z} = 0.02$).

We then tested whether the intrinsic AGN spectrum is independent of the absorption type, as expected from the unified model, by analysing averaged spectra of the Seyfert 1 and 2 types, as well as for the intermediate Seyferts and the blazars. The average Seyfert 1 spectrum was constructed using the weighted mean of 10 ISGRI spectra, the Seyfert 2 composite spectrum includes 15 sources, and 8 objects form the intermediate Seyfert 1.5 group. When computing the weighted average of the various sub classes, the Seyfert 2 objects showed flatter hard X-ray spectra ($\bar{\Gamma} = 1.95 \pm 0.01$) than the Seyfert 1.5 ($\bar{\Gamma} = 2.10 \pm 0.02$), and Seyfert 1 appeared to have the steepest spectra ($\bar{\Gamma} = 2.11 \pm 0.05$) together with the blazars ($\bar{\Gamma} = 2.07 \pm 0.10$). A similar trend was seen when dividing the Seyfert sample according to the intrinsic absorption: the 21 absorbed AGN showed a flatter hard X-ray spectrum ($\bar{\Gamma} = 1.98 \pm 0.01$) than the 13 unabsorbed sources ($\bar{\Gamma} = 2.08 \pm 0.02$). This finding that Seyfert 1

and Seyfert 2 have intrinsically different spectral slope, confirmed earlier studies by Zdziarski et al. (1995), Gondek et al. (1996), Perola et al. (2002), and Malizia et al. (2003).

What was mainly ignored in these studies was the influence of the Compton reflection hump on the slope of the hard X-ray spectrum. As the reflection hump will be stronger in objects with more absorbing material in the line of sight which can act as a reprocessor to the hard X-ray underlying continuum, stronger absorbed sources should have on average a harder spectrum when studying the spectrum up to energies of ~ 30 keV, even when the photoelectric absorption is taken into account (see Fig. 4.18). Although one was aware of this effect, the quality of the data did not allow to model the spectral slope, reflection component, cut-off, and absorption simultaneously on the average spectra. Thus, although the phenomenological observation that a simple absorbed power law model shows

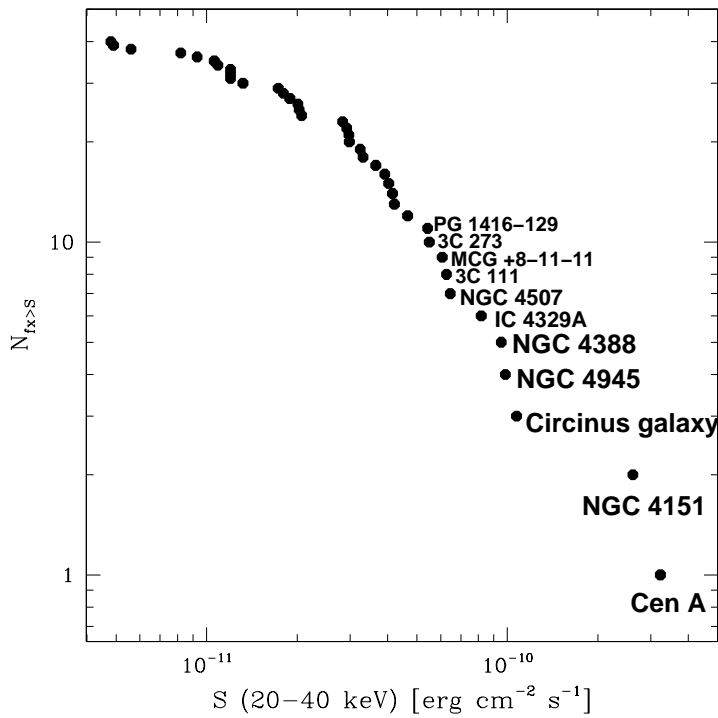


Figure 4.21: Number counts based on the first *INTEGRAL* AGN catalogue (Beckmann et al. 2006a,c). Although this sample is not a complete flux limited one, the number counts give a first impression regarding the flux distribution. Excluding the two brightest objects and objects $f_{20-40\text{keV}} < 2 \times 10^{-11} \text{ erg cm}^{-2} \text{ s}^{-1}$, the number counts relation shows a gradient of 1.4 ± 0.1 . PG 1416-129 later turned out to be a fake detection and was not included in the second AGN catalogue (Beckmann et al. 2009d).

that Seyfert 1 galaxies have steeper hard X-ray spectra than Seyfert 2 is true, this is misleading when discussing the unified scheme. The true intrinsic spectral slope of the continuum source could only be determined in larger and better sampled studies (Dadina 2008; Beckmann et al. 2009d), which then indeed showed that there is no difference between type 1 and type 2. This will be shown in Section 4.7.3.

The sample we had compiled was obviously not a complete one, in a sense that it was not flux

limited. This can be seen in Fig. 4.21. Nevertheless, we expected it to be complete at a certain significance level, above which our AGN sample should not miss any objects. In order to test where this level was, we used the $\overline{V_e/V_a}$ test, already described in Section 4.4.2 on page 30. As the sources in our sample were all at low redshift, we could assume a Euclidean space and a normal distribution. In this case, a complete sample should have $\overline{V_e/V_a} = 0.5$. We therefore computed the $\overline{V_e/V_a}$ for significance limits between 1σ and 15σ . Above the completeness limit the $\overline{V_e/V_a}$ values should be distributed around $\overline{V_e/V_{true}}$ within the statistical uncertainties. The results of the tests are shown on page 141. It appears that the sample becomes complete at a significance level around $> 6\sigma$, including 31 AGN. The average value above this significance is $\overline{V_e/V_a} = 0.505 \pm 0.022$.

This way of using the $\overline{V_e/V_a}$ test in order to determine the completeness level of a sample has been adopted by several other groups since we published the first *INTEGRAL* AGN catalogue, e.g. in Molina et al. (2009), in Malizia et al. (2009, 2010), and in Cusumano et al. (2010).

Although the first *INTEGRAL* catalogue could not add significantly to the discussion about the intrinsic hard X-ray spectrum of AGN, as it showed similar results as previous studies, it nevertheless served several purposes. First of all it showed the ability of *INTEGRAL* to have also a major impact on the studies in the extragalactic domain. The work pointed in the direction where to go, i.e. to compile for the first time a larger, complete sample of hard X-ray selected AGN, to determine its number counts and luminosity function. This led to the first hard ($E > 20$ keV) luminosity function study, described in the following section. In addition, it was apparent from this work that a much larger number of sources with high quality spectra was necessary to significantly constrain the average Seyfert spectra. This was eventually done using the second *INTEGRAL* AGN catalogue, described on page 74. The large resonance the first AGN catalogue had and has still today, which can be seen in the constantly high citation rate of Beckmann et al. (2006a), shows that there is indeed a need for spectroscopic catalogues of *INTEGRAL* detected sources, in which all sources are analysed in a consistent way. Although many astrophysicists are able to analyse *INTEGRAL* data and do single-source studies, the task of providing an analysis based on the whole *INTEGRAL* mission data set is usually a challenge not tackled.

4.7 AGN Population Studies at Hard X-rays

As described in the previous section, *INTEGRAL* had been proven to be a capable tool to study the hard X-ray emission of AGN, and to collect significantly large samples of Seyfert galaxies in order to test the unified model. This section now describes the work I did in collaboration with several colleagues concerning the open issues. In 2006 we determined the first hard X-ray luminosity function of AGN (Beckmann et al. 2006d, 2007c). Then, we performed the first hard X-ray variability study on a large and complete sample of hard X-ray selected AGN, based on data provided by *Swift*/BAT (Sect. 4.7.2). Finally we determined the intrinsic hard X-ray continuum for the different Seyfert types based on the second *INTEGRAL* AGN catalogue, which contains two hundred extragalactic objects (Sect. 4.7.3).

4.7.1 The Hard X-ray 20–40 keV Luminosity Function

The hard X-ray luminosity function (XLF) is not only interesting as a diagnostic tool in order to investigate whether the different Seyfert types show the same evolution in time and are therefore likely to be intrinsically the same. The XLF is also important to test whether the emission from AGN at hard X-rays can explain the hard cosmic X-ray background (CXB), which peaks around 30 keV (Marshall et al. 1980) and has been first detected in the early rocket flights at the dawn of X-ray

astronomy (Giacconi et al. 1962). In order to do so, one determines the XLF and uses it to compute the contribution of the source class studied to the local background.

To derive a robust luminosity function, several requirements have to be fulfilled, as already outlined in Section 4.4.3. The sample has to be complete, which means not only a flux or significance limit above which all sources are significantly detected, but also a complete identification of sources above this limit, redshift information has to be available for most of the sources, and the limit of the survey at any given point in the sky has to be known precisely. If these requirements are not fulfilled in all cases, e.g. because redshift information is missing for an AGN, these effects have to be considered in the error estimation.

In order to ensure a complete sample we followed the same strategy as in the first *INTEGRAL* AGN catalogue. We analysed the data of all AGN reported so far, and in addition we analysed deep mosaics of the extragalactic sky to find additional candidates. A total of 73 extragalactic sources was included in this study, which are listed on page 147 and 148. We then performed a $\overline{V_e/V_a}$ test (see page 148) in order to determine the significance limit of the survey, which turned out to be 5σ in IBIS/ISGRI data in the 20 – 40 keV energy band. Above this limit, in the complete sample, there were 38 AGNs. There were still 8 unidentified sources among the IBIS/ISGRI detected sources with more than 5σ detection significance. Most of those were located within the Galactic plane though, and we assumed that were mainly Galactic binary systems rather than AGN.

A more difficult task was the correct estimate of the flux limit of the survey in each point in the sky. The sensitivity of an IBIS/ISGRI mosaic image is not only determined by the total exposure time accumulated. Other effects have to be taken into account, such as the off-axis angle of a given observation, the observation mode (staring or dithering, different dither patterns), and the vicinity of bright sources, in which it is more difficult to detect sources as long as a non-perfect deconvolution of the coded mask data is done. In addition, at this stage of the mission, there were still systematics not accounted for by the analysis software.

We decided to determine the exposure time first in each point in the sky and then to use existing source detections in order to derive an exposure time versus sensitivity relation. Therefore we first determined the exposure time in 64,620 sky elements of $\sim 0.63 \text{ deg}^2$ size within our survey. In each sky bin, the exposure is the sum of each individual exposure multiplied by the fraction of the coded field of view in this particular direction. The dead time and the good time intervals (GTI) were not taken into account but the dead time is fairly constant (around 20%) and GTI gaps are very rare in IBIS/ISGRI data. On page 149 the exposure map of the survey is shown in Galactic coordinates. It is apparent that at this early stage of the mission, the focus of *INTEGRAL* was still mainly on the Galactic plane. We excluded those fields with an exposure time less than 2 ks, resulting in a total coverage of $\sim 10 \text{ sr}$. The flux limit for a given significance limit should be a function of the square root of the exposure time, if no systematic effects apply, but this assumption cannot be made here.

In order to achieve a correlation between the exposure time and the flux limit, we therefore used an empirical approach. For each object we computed what we called its 5σ equivalent flux $f_{5\sigma}$, based on its actual flux f_X and its significance s : $f_{5\sigma} = f_X * 5/s$. We found a correlation between these $f_{5\sigma}$ values and exposure times, which has a scatter of $\lesssim 0.2 \text{ dex}$ (Fig. 4.22). It can be seen that for a single source the detection limit varied quite dramatically. For example, there were apparently sources with $2.2 \times 10^{-11} \text{ erg cm}^{-2} \text{ s}^{-1}$ which reach a 5σ detection within 40 ksec, while others of the same flux reach this limit only after 140 ksec. Although this example is one of the more extreme ones in the survey, it indicates the overall difficulty in analysing coded mask instruments.

We then fitted the flux limit versus exposure time correlation with a polynomial function, shown as black curve in Fig. 4.22. The comparison with the blue dashed line in the figure, which assumes that the significance limit is a function of the square root of the exposure time, shows that indeed this

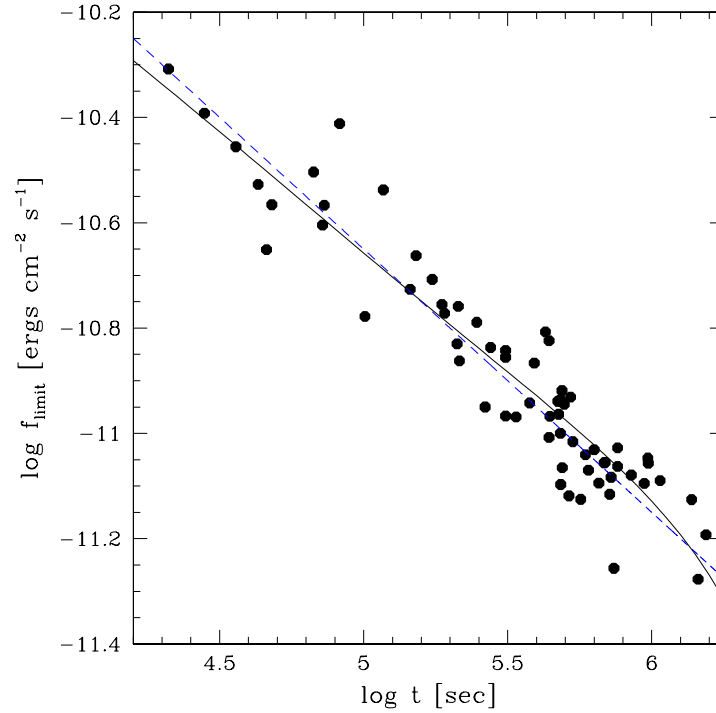


Figure 4.22: Correlation of exposure time and flux limit for a 5σ detection. The black curve shows a smooth polynomial fit for flux limit vs. logarithm of the exposure time. The blue dashed line describes a flux limit which decreases with the square root of the exposure time.

correlation can be assumed for the survey.

With a robust estimate of the flux limit as a function of exposure time we were then able to construct the number counts and luminosity function of the *INTEGRAL* detected AGN. For the analysis of the number counts, we used the complete sub-sample of 38 sources. The resulting correlation is shown on page 150. The dimmest source among this sub-sample was $f_X = 5.6 \times 10^{-12}$ ergs cm^{-2} s^{-1} , and the brightest was $f_X = 3.2 \times 10^{-10}$ ergs cm^{-2} s^{-1} . We derived a maximum likelihood (ML) probability distribution, which can be approximated by a Gaussian, with our best fit parameters of $\alpha = 1.66 \pm 0.11$. A normalization of $K = 0.44 \text{ sr}^{-1} (10^{-10} \text{ ergs cm}^{-2} \text{ s}^{-1})^\alpha$ was then obtained by performing a least-squares fit, with the slope fixed to the ML value. This calculation did not take into account possible inaccuracies associated with scatter in Fig. 4.22, and thus in the true detection limit. The slope of the number counts is consistent with the Euclidean value of $\alpha = 1.5$ on the 1.5σ level. In our later studies, using the second AGN catalogue, we confirmed that the slope is indeed slightly steeper than the Euclidean value, an effect independently seen also in the *Swift*/BAT AGN survey Tueller et al. (2008). For further discussion on this point see Sect. 4.7.3.

The complete sample of *INTEGRAL* AGNs with a detection significance $\geq 5\sigma$ also allowed us to derive the density of these objects in the local Universe as a function of their luminosity, i.e. we determined for the first time the hard X-ray luminosity function of AGN. As explained in Sect. 4.4.3, in order to derive the density of objects above a given luminosity, one has to determine for each source in a complete sample the space volume in which this source could have been found considering both the flux limit of each survey field and the flux of the object.

Because our study is based solely on low redshift objects, we were not able to constrain models

involving evolution with redshift. Nevertheless we can compare the XLF with model predictions from previous investigations. XLFs are often fit by a smoothly connected two power-law function of the form Maccacaro et al. (1991)

$$\frac{d\phi(L_X, z = 0)}{d \log L_X} = A \left[\left(\frac{L_X}{L_*} \right)^{\gamma_1} + \left(\frac{L_X}{L_*} \right)^{\gamma_2} \right]^{-1} \quad (4.16)$$

We fitted this function using a least-squares method applying the Levenberg-Marquardt algorithm (Marquardt 1963). The best fit values we obtained are $A = 0.7_{-0.5}^{+1.5} \times 10^{-5} h_{70}^3 \text{ Mpc}^{-3}$, $\gamma_1 = 0.80 \pm 0.15$, $\gamma_2 = 2.11 \pm 0.22$, and $\log L_* = 43.38 \pm 0.35$ with L_* in units of $h_{70}^{-2} \text{ ergs s}^{-1}$. The 1σ errors have been determined by applying a Monte Carlo simulation which simultaneously takes into account the flux errors on the individual sources, the error induced by deriving an average luminosity per bin, and the statistical error of the density based on the number of objects contributing to the density value. Each simulated data set included 9 luminosity values with a density value for each of them. These values were then fit by the smoothly connected two power-law function as described above. The scatter in the resulting parameters gave the error estimates as shown above.

The parameter values describing the differential luminosity function are consistent with values derived from the 2–10 keV XLF of AGNs as shown by e.g. Ueda et al. (2003), La Franca et al. (2005), and Shinozaki et al. (2006). For example the work by Ueda et al. (2003) reveals for a pure density evolution model the same values (within the error bars) for γ_1 and γ_2 , but a higher $\log L_* = 44.11 \pm 0.23$. The higher value can be easily explained by the different energy bands applied. A single power law with photon index of $\Gamma = 2$ in the range 2–40 keV would lead to $L_{(2-10 \text{ keV})}/L_{(20-40 \text{ keV})} = 2.3$, assuming no intrinsic absorption. This has, of course, no implications for the XLF at higher redshifts. The values are also consistent with the luminosity function for AGNs in the 3–20 keV band as derived by Sazonov & Revnivtsev (2004) from the *RXTE* all-sky survey.

Based on the luminosity function, the contribution of the AGNs to the total X-ray emissivity W can be estimated (Sazonov & Revnivtsev 2004). This can be done by simply multiplying the XLF by the luminosity in each bin and integrating over the range of luminosities ($10^{41} \text{ ergs s}^{-1} < L_{20-40 \text{ keV}} < 10^{45.5} \text{ ergs s}^{-1}$). This results in $W_{20-40 \text{ keV}}(> 10^{41} \text{ ergs s}^{-1}) = (2.8 \pm 0.8) \times 10^{38} \text{ ergs s}^{-1} h_{70}^3 \text{ Mpc}^{-3}$. Please note that absorption does not affect the luminosities in this energy range and therefore the values given here are intrinsic emissivities.

We then also compared the luminosity function of the absorbed ($N_{\text{H}} > 10^{22} \text{ cm}^{-2}$) and unabsorbed sources, as shown on page 151. The absorbed sources have a higher density than the unabsorbed sources at low luminosities, while this trend is inverted at high luminosities. The luminosity where both AGN types have similar densities is about $L_{(20-40 \text{ keV})} = 3 \times 10^{43} \text{ erg s}^{-1}$ which is also the turnover in the XLF using all Seyfert type AGN. In the sample we also observed the general tendency that the objects with higher absorption are on average less luminous. A comparable trend had been seen also below 10 keV, e.g. in Shinozaki et al. (2006).

The luminosity function we derived from the *INTEGRAL* 20–40 keV AGN sample appeared to be consistent with the XLF in the 2–20 keV range. As also the turnover in the XLF appeared at the same position as in the softer X-ray LF, this implies that similar source population are observed by *IBIS/ISGRI* as at lower energies. This was somewhat surprising: although the source population seen in deep *Chandra* and *XMM-Newton* fields can explain the cosmic X-ray background (CXB) at energies below 10 keV, these sources have a too steep spectrum in order to be responsible for the hump at 30 keV. For the same sources being able to explain the hump, they would require continua which have a photon index $\Gamma \ll 2$ up to the peak of the Compton hump in order to rise in the νf_ν parameter space. It was therefore expected to see with *INTEGRAL* stronger absorbed sources, which

would not contribute significantly in the energy band below 10 keV. If a larger fraction of absorbed AGNs is necessary to explain the cosmic X-ray background at ~ 30 keV as indicated by *HEAO 1 A-4* measurements (Gruber et al. 1999), the fraction of absorbed sources could be correlated with redshift. Worsley et al. (2005) examined *Chandra* and *XMM-Newton* deep fields and came to the conclusion that the missing CXB component is formed by highly obscured AGNs at redshifts $\sim 0.5 - 1.5$ with column densities of the order of $f_X = 10^{23} - 10^{24} \text{ cm}^{-2}$. Evidence for this scenario is also found in a study of *Chandra* and *Spitzer* data (Polletta et al. 2006). Combining multiwavelength data, this work estimates a surface density of 25 AGN deg^{-2} in the infrared in the 0.6 deg^2 *Chandra*/SWIRE field, and only 33% of them are detected in the X-rays down to $f_{0.3-8 \text{ keV}} = 10^{-15} \text{ ergs cm}^{-2} \text{ s}^{-1}$. The work also indicates a higher abundance of luminous and Compton-thick AGNs at higher redshifts ($z \gg 0.5$). This source population would be missed by *INTEGRAL* and *Swift*, because of the low redshifts ($\bar{z} \approx 0.02$). Further evidence for an evolution of absorption at high redshifts comes from infrared imaging surveys (Treister et al. 2009a; Fiore et al. 2009) and spectroscopic studies (Alexander et al. 2008). These works show that the fraction of obscured quasars at redshift $z = 1.5$ was around 50%, while 80% of the QSO might have been obscured toward redshift $z = 3$ (Treister et al. 2010).

Still, there was the possibility that we had missed the Compton thick AGN: 23% of the sources in our sample was lacking absorption information. In order to get an estimate for the absorption in these cases, we used soft X-ray measurements of the *ROSAT* All-Sky Survey (RASS). Assuming that the sources did not vary dramatically, and assuming a constant underlying power law between the hard X-rays and the *ROSAT* band (0.1 – 2.4 keV), we determined from the IBIS/ISGRI versus *ROSAT*/PSPC the amount of absorption necessary to explain the flux ratio. In six cases no detection was present in the RASS, with an upper limit of $f_{(0.1-2.4 \text{ keV})} \leq 10^{-13} \text{ ergs cm}^{-2} \text{ s}^{-1}$, resulting in a lower limit for the absorption $N_H > (5 - 11) \times 10^{22} \text{ cm}^{-2}$. Apparently none of these comparisons required a Compton thick absorber, therefore it appeared unlikely that a significant fraction of *INTEGRAL* AGNs will be Compton thick. This statement, that the fraction of Compton thick sources is $\ll 10\%$, is still true, also considering the second *INTEGRAL* AGN catalogue and the *Swift*/BAT AGN sample (Tueller et al. 2008).

The main result of the hard X-ray luminosity function we derived was that the AGN detectable in by *INTEGRAL* alone cannot explain the Cosmic X-ray Background, but that there had to either weaker AGN contributing significantly to the CXB, or the fraction of absorbed sources would have to have been much higher in the past than in the local universe, or that there are sources which are extremely Compton thick ($N_H > 10^{25} \text{ cm}^{-2}$) which would have been missed even by IBIS/ISGRI.

4.7.2 Hard X-ray variability of AGN

Another test for the unified model is, whether type 1 and type 2 show the same variability at hard X-rays. Different than at energies below 10 keV, there should be less influence by the absorbing material, although the reflection component could have a damping effect on the variability, especially around 30 keV where the contribution by the reflection hump to the observed spectrum is strongest.

In order to test variability for different source classes, well sampled light curves on a large number of sources are essential. *INTEGRAL* works as a true observatory, i.e. it performs pointed observations, then moves to the next target, etc., and variability time scales at hard X-rays are rather long. Thus, *INTEGRAL* data usually show only a moment in the flux history of a non-blazar AGN. A better sky coverage although at a lower sensitivity is provided by *Swift*/BAT.

The *Swift* mission

NASA's *Swift* mission (Gehrels et al. 2004) is a multiwavelength observatory for gamma-ray-burst astronomy, launched November 20, 2004 on Delta 7320 rocket. The payload combines a gamma-ray instrument (Burst Alert Telescope, 15 - 150 keV; Barthelmy et al. 2005), an X-ray telescope (XRT; Burrows et al. 2005), and a UV-optical telescope (UVOT; Roming et al. 2005). The Burst Alert Telescope (BAT) is a large field of view (~ 1.5 sr) coded mask aperture hard X-ray telescope. The BAT camera is a CdZnTe array of 0.5 m^2 with 32768 detectors, which are sensitive in the 14-195 keV energy range. Although BAT is designed to find Gamma-ray bursts which are then followed-up by the narrow field instruments of *Swift*, the almost random distribution of detected GRBs in the sky leads to an effective all-sky survey in the hard X-rays. The XRT is a focusing X-ray telescope with a 110 cm^2 effective area, 23 arcmin FOV, 18 arcsec resolution, and 0.2-10 keV energy range. The UVOT design is based on the Optical Monitor (OM) on-board ESA's *XMM-Newton* mission, with a field of view of 17×17 arcmin and an angular resolution of 2 arcsec.

The case study on NGC 2992

In an early analysis of the first 3 months of the *Swift*/BAT data, Markwardt et al. (2005) presented a catalogue of 66 high-latitude sources, out of which 44 could be identified as previously known AGN. The properties of the non-blazar AGN were very similar to that of the IBIS/ISGRI detected sources. The median redshift of the Seyfert galaxies was low ($z = 0.012$), 64% of them showed intrinsic absorption $N_H > 10^{22} \text{ cm}^{-2}$, and the more luminous sources appeared to be less absorbed. Among these AGN was the interesting case of NGC 2992. Working together with the *Swift*/BAT team, I noticed that this Seyfert 2 showed by far the largest variability in their non-blazar AGN list. At the same time, unpublished *INTEGRAL*, *BeppoSAX*, and *Swift* data were available, making this object a good candidate to study its high-energy spectrum, spectral variability, and the cross calibration between the different instruments. The results were presented in Beckmann et al. (2007b).

NGC 2992 is one of the brightest AGN in the X-ray sky. This nearby Seyfert 2 galaxy ($z = 0.0077$) has been observed by every major X-ray satellite mission. It was first detected by the *Ariel 5* Sky Survey Instrument as 2A 0943-140, an X-ray source which was later identified to be NGC 2992 with an X-ray luminosity of $L_X = 2 \times 10^{43} \text{ ergs s}^{-1}$ (Ward et al. 1978). Later observations by *HEAO*, *Einstein*, and *EXOSAT* showed that the flux varied by a factor of ~ 10 over the years. Apart from these flux variations, all these observations revealed a similar spectrum, with a photon index of $\Gamma \simeq 1.7$ and absorption of $N_H \simeq 5 \times 10^{21} \text{ cm}^{-2}$ ($N_{H,gal} = 8 \times 10^{20} \text{ cm}^{-2}$). This was also confirmed by the next generation of X-ray telescopes with higher spectral and angular resolution, like *ASCA*. Using *ASCA* data, Weaver et al. (1996) detected a delayed response of the reflection component and derived a distance of $\sim 3.2 \text{ pc}$ for the reflecting material, which they assumed to be dense, neutral gas in the central region with column densities $N_H \simeq 10^{23} - 10^{25} \text{ cm}^{-2}$. The hard X-ray tail of NGC 2992 was first measured by *BeppoSAX*/PDS and also revealed a photon index of $\Gamma \simeq 1.7$ up to an energy of $\sim 150 \text{ keV}$ with absorption by $N_H \simeq 10^{22} \text{ cm}^{-2}$ and an iron $K\alpha$ line at $E_{K\alpha} = (6.62 \pm 0.07) \text{ keV}$ (Gilli et al. 2000). Observations by *Chandra* allowed for the first time to disentangle the complex spatial structure of NGC 2992. Colbert et al. (2005) showed that the X-ray emission can be described by three components: An AGN core with a photon index of $\Gamma = 1.86$, a cold Compton reflector with a column density of $N_H \simeq 10^{22} \text{ cm}^{-2}$, and in the soft X-rays by a thermal plasma with $kT = 0.5 \text{ keV}$ and low abundance ($Z < 0.03Z_\odot$). They also showed that the spectrum in the 2 - 10 keV band can be described in first order by a simple power law with photon index $\Gamma = 0.91 \pm 0.02$ and absorption $N_H = (1.9 \pm 0.4) \times 10^{21} \text{ cm}^{-2}$, in which the flat power law accounts for the sum of the three components.

Three observations by *Suzaku* at the end of 2005 were modeled by Yaqoob et al. (2007) with a primary continuum ($\Gamma = 1.57^{+0.06}_{-0.03}$) obscured by an absorber with $N_H = 8.0^{+0.6}_{-0.5} \times 10^{21} \text{ cm}^{-2}$, plus an optically-thin thermal emission component with $kT = 0.66^{+0.09}_{-0.06} \text{ keV}$, and an Fe K emission complex containing a broad and a narrow Fe $K\alpha$ component.

Our analysis of the hard X-ray spectrum was based on 402 ks of *INTEGRAL* IBIS/ISGRI and SPI data, 15 months of *Swift*/BAT survey data, and three observations by *BeppoSAX*/PDS with a total of 79 ks exposure time. Analysing the *INTEGRAL* data altogether shows that a single power law ($\Gamma = 1.96^{+0.26}_{-0.23}$) is sufficient to fit the high energy data with $E > 20 \text{ keV}$ with an average flux of $f_{(20-100 \text{ keV})} = (6.7 \pm 0.4) \times 10^{-11} \text{ erg cm}^{-2} \text{ s}^{-1}$ ($L_X = 8.8 \times 10^{42} \text{ ergs s}^{-1}$). Similar spectral slopes were derived from *Swift*/BAT ($\Gamma = 2.04^{+0.34}_{-0.30}$, $f_{(20-100 \text{ keV})} = (4.5 \pm 0.4) \times 10^{-11} \text{ erg cm}^{-2} \text{ s}^{-1}$), and *BeppoSAX*/PDS ($\Gamma = 1.92^{+0.08}_{-0.08}$, $f_{(20-100 \text{ keV})} = (1.53 \pm 0.03) \times 10^{-10} \text{ erg cm}^{-2} \text{ s}^{-1}$).

The BAT data were also used to derive a long-term hard X-ray lightcurve. In order to do so, the data were binned in time in 28 day intervals. The lightcurve is inconsistent with a constant flux on a $> 10\sigma$ level, indicating that indeed NGC 2992 exhibits strong variability, up to a factor of 6 at time scales as short as a month. Based on the BAT data we derived hardness ratios $HR = (H - S)/(H + S)$ with count rates in the bands S (14 - 24 keV) and H (24 - 195 keV). For the period in which the BAT count rate was in a high state with a total count rate of $CR_{14-195 \text{ keV}} > 10^{-4} \text{ counts s}^{-1}$, the hardness ratio is $HR = 0.33 \pm 0.06$, and in the low state $HR = 0.24 \pm 0.07$. We therefore did not detect significant variability of the spectral shape in the *Swift*/BAT data.

In order to better constrain the low energy part of the continuum emission, we also analysed six pointed observations of *Swift*/XRT. Because the single XRT spectra showed the same shape and normalisation, we stacked the spectra together, resulting in a total exposure time of 21.5 ks. The *Swift*/XRT spectrum is well represented by an absorbed single power law with $\Gamma = 1.01^{+0.15}_{-0.14}$ and intrinsic absorption $N_H = 1.9^{+0.97}_{-0.91} \times 10^{21} \text{ cm}^{-2}$. Note that the absorption includes the Galactic hydrogen column density of $N_{H,gal} = 8 \times 10^{20} \text{ cm}^{-2}$. In addition the iron $K\alpha$ line is detectable with an equivalent width of $EW = 500 \text{ eV}$. Note that this spectrum in the 2–10 keV band represents the sum of different components as discovered by *Chandra* (Colbert et al. 2005) and is consistent with the same simple power law fit to the *Chandra* data.

Comparing the different data sets at $E > 20 \text{ keV}$ taken of NGC 2992 over the years by three different missions and four different instruments, it was apparent that although the flux level of the continuum varied, the spectral slope stayed constant within the errors of the individual measurements. We therefore performed a fit of all data simultaneously, applying intercalibration factors in order to account for different flux levels but using the same model. The resulting spectrum is shown in Figure 4.23. The overall fit shows an absorbed broken power law. The modeled absorption of $N_H = (1.6 \pm 0.9) \times 10^{21} \text{ cm}^{-2}$ is mainly dominated by the XRT spectrum, as is the spectral slope of $\Gamma_1 = 1.0 \pm 0.1$ below the turnover of $E_{break} = 16^{+2}_{-4} \text{ keV}$. Above this energy the spectrum is described by a power law of $\Gamma_2 = 1.97^{+0.07}_{-0.07}$. The fit results in a $\chi^2_\nu = 0.98$ for 103 degrees of freedom, while a simple power law fit gives an unacceptable $\chi^2_\nu = 2.1$ (107 d.o.f.).

The addition of a high-energy cut off in the spectrum does not improve the fit. On the contrary, a cut-off at an energy below $E_C = 250 \text{ keV}$ can be rejected on a 1σ level.

Thus, the hard X-ray spectrum of NGC 2992 can be described by the same simple power law model with photon index $\Gamma \simeq 2$ throughout all the different observations performed over the last thirty years. All measurements show the same power law index of $\Gamma \simeq 2$ while the intensity varies by a factor of 11, according to the long-term variability, and by a factor of 6, using the one-month time binned lightcurve of the *Swift*/BAT survey. The flat slope of $\Gamma \simeq 1$ as observed by *Swift*/XRT in the 2–10 keV range has been shown to be the superposition of three individual components (Colbert et al.

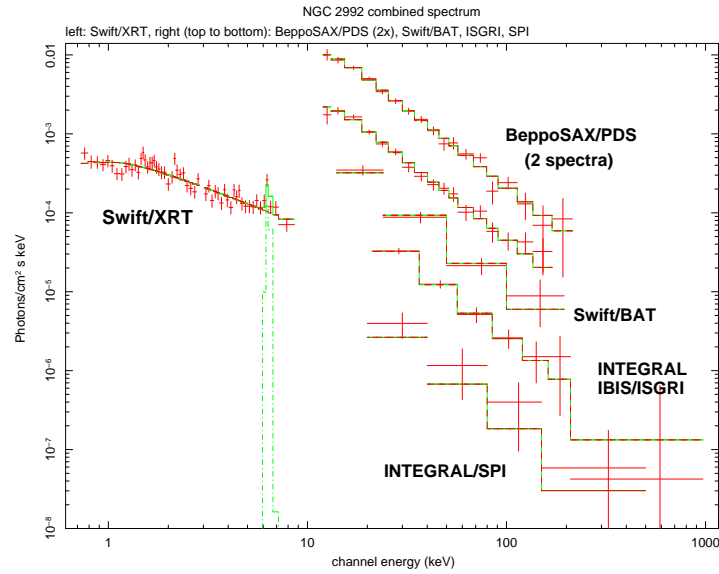


Figure 4.23: Combined spectrum of NGC 2992 based on *BeppoSAX*, *Swift* and *INTEGRAL* data in photon space. The same model has been applied to all data, plus intercalibration factors in order to account for flux variations. Note that except for the *INTEGRAL* IBIS/ISGRI and the *Swift*/XRT spectrum, all the spectra have been offset in this plot from their original position for better readability. The *BeppoSAX*/PDS spectrum from 1997 is not shown.

2005; Yaqoob et al. 2007). A monitoring campaign in the 2 – 10 keV energy range performed by the PCA on board the *Rossi X-ray Timing Explorer (RXTE)* between March 2005 and January 2006 revealed the same behaviour as seen in the > 20 keV data, i.e. that the intensity of the underlying continuum varies, whereas the spectral slope stays constant within the statistical error (Murphy et al. 2007). Also in this energy band the luminosity varied by a factor of 11, whereas the slope of the power-law fit was consistent with no variability (weighted mean $\Gamma \approx 1.7$). The timescale of those variations is of the order of days to weeks, which leads Murphy et al. (2007) to the suggestion that this variability is based on short-term flaring activity as opposed to long-term changes in accretion activity.

A similar behaviour, of a stable photon index of the unabsorbed hard X-ray spectrum under varying intensity, had been observed already in two other well-studied objects described above, NGC 4388 (Beckmann et al. 2004d) and NGC 4151 (Beckmann et al. 2005b). What kind of mechanism can produce such a constant shape of the hard X-ray emission while the intensity varies significantly? If we assume that the hard X-ray emission originates from hot plasma (e.g. a hot extended corona above the relatively cold accretion disk; see e.g. Haardt & Maraschi 1991), the temperature of this plasma has apparently been constant. The variations in intensity can then be explained in two ways: either the amount of material emitting the hard X-rays varies, or the amount of plasma visible to the observer varied. This can be caused either through absorption near the central engine of the AGN, or through different orientation of the disk with respect to the observer, or a mixture of both effects. The intrinsic absorption measured in soft X-ray does not exhibit large variations ($N_{\text{H}} = (0.2 - 1.0) \times 10^{22} \text{ cm}^{-2}$) and this absorption has no effect on the hard X-ray spectrum. In addition a variable Compton-thick absorber, which would be able to change the flux at > 20 keV significantly, would also effect the spectral slope, which is not observed. Different orientation of the accretion disk with respect to the

observer also should not have an influence on the hard X-ray emission, as the disk is thought to be Compton-thin.

Another explanation is provided by a model including hot flares produced via magnetic field reconnections (e.g. Galeev et al. 1979; Poutanen & Fabian 1999). In this flare model, sudden dissipation occurs in very localized regions above the disk in coronal loops. It has to be pointed out though, that the expected duration of those flares is rather on the scale of a day than on a monthly basis (Czerny et al. 2004). A short flare would most likely not be detectable in the *Swift*/BAT survey.

The study of NGC 2992 (Beckmann et al. 2007b) proved that *Swift*/BAT data can be used to perform hard X-ray spectral monitoring of bright AGN.

Hard X-ray variability as a function of Seyfert type

Encouraged by the variability study on NGC 2992 using *Swift*/BAT data, we performed a variability analysis using all AGN which had been detected within the first 9 months of the *Swift* mission with a detection significance of $> 10\sigma$. This work was published in Beckmann et al. (2007a) and the manuscript is included on page 155.

Flux and spectral variability has been always also a tool to determine geometry and nature of physical processes in objects, as well as to distinguish different source types. In the X-rays, already *EXOSAT* data indicated, that the AGN variability on short time scales is due to red-noise (McHardy & Czerny 1987). The corresponding power spectral density functions (PSDs) can be described by a power law with index -1 to -2. The data also showed an inverse correlation between the amplitude of variability in day-long AGN X-ray light curves and the X-ray luminosity of AGN (Barr & Mushotzky 1986), although Narrow Line Seyfert 1s apparently do not follow this correlation (Turner et al. 1999). *RXTE* allows to study AGN variability in the 2-10 keV range on long time scales. This revealed that although the variability amplitudes of AGN with different luminosities are very different on short time-scales, they are similar on long time-scales (Markowitz & Edelson 2001). *RXTE* data also showed that the PSDs of AGN show a break at long time-scales according to their black hole mass (e.g. Edelson & Nandra 1999).

Grupe et al. (2001) analysed *ROSAT* data of AGN and showed that the sources with steeper spectra exhibit stronger variability than those with a hard spectrum. As *Swift*/BAT is sensitive in the 14-195 keV energy range, it detects preferentially those *ROSAT* AGN with hard spectra, and one expects to see a lower variability in *Swift*/BAT detected AGN than measurable in average by Grupe et al. (2001). Bauer et al. (2004) showed for 136 AGN observed by *Chandra* within 2 Msec in the Chandra Deep Field South that $\sim 60\%$ show signs of variability. For the brighter sources with better photon statistics even 80 – 90% showed variability in the 0.5 – 8 keV energy range.

Lately, even quasi-periodic oscillations (QPOs) have been detected for the first time in an AGN, in the case of the Narrow Line Seyfert 1 galaxy RE J1034+396 (Gierliński et al. 2008). In their work Gierliński et al. (2008) analysed a 91 ks long *XMM-Newton* observation, and found a strong peak for a periodicity of 3730 ± 130 s, with slight changes over the observation, indicating that the feature wanders in phase, amplitude and/or frequency, as seen in QPOs of Galactic black hole binaries (Remillard & McClintock 2006). Middleton & Done (2010) pointed out that the QPO in RE J1034+396 can be identified with the 67 Hz QPO in the Galactic microquasar GRS 1915+105 if one assumes simple linear mass scaling of the QPO frequency, energy spectral components and variability power spectra from stellar to supermassive black holes accreting at the same Eddington ratio $\lambda = L_{\text{bol}}/L_{\text{Edd}}$.

The similarity of the variability in different types of AGN suggests that the underlying physical mechanism is the same. This does not apply for the blazars, for which the common model is that we look in these objects into a highly relativistic jet. Explanations for the variability in Seyfert galaxies

include a flare/spot model in which the X-ray emission is generated both in hot magnetic loops above an accretion disk and in bright spots created under the loops by strong irradiation (Czerny et al. 2004), unstable accretion disks, and variable obscuration. A still open question was the role of long term variability at energies above 20 keV. Observations of AGN had been performed by several missions like *CGRO/OSSE* and *BeppoSAX/PDS*. But long-term coverage with base lines longer than weeks was up to the launch of *Swift* only available from the data of *CGRO/BATSE*, which had no imaging capabilities.

Using the *Swift*/BAT AGN sample, we now tested whether the similarity in variability behaviour would hold also at the hard X-rays, where the influence of absorption should be small. Within the first 9 months of the mission, 243 objects had been detected with significance $> 5.5\sigma$. Out of these we used the 44 AGN with significance $> 10\sigma$: 11 Seyfert 1, 22 Seyfert 2, 5 intermediate Seyfert 1.5, one Seyfert 1.8, one Seyfert 1.9, and 5 blazars (see the table on page 158). We applied several binnings in time: 1 day, 7 days, 20 days, and 40 days. In order to test for variability, we used two methods, a maximum likelihood estimator, similar to the excess variance, and the structure function.

Any lightcurve consisting of N flux measurements x_i varies due to measurement errors σ_i . In case the object is also intrinsically variable, an additional source variance σ_Q has to be considered. The challenge of any analysis of light curves of variable sources is to disentangle them in order to estimate the intrinsic variability. A common approach is to use the 'excess variance' (Nandra et al. 1997; Vaughan et al. 2003) as such an estimator. The sample variance is given by

$$S^2 = \frac{1}{N-1} \sum_{i=1}^N (x_i - \bar{x})^2 \quad (4.17)$$

and the excess variance is given by

$$\sigma_{XS}^2 = S^2 - \overline{\sigma_i^2} \quad (4.18)$$

with $\overline{\sigma_i^2}$ being the average variance of the measurements. Almaini et al. (2000) pointed out that the excess variance represents the best variability estimator only for identical measurement errors ($\sigma_i = \text{constant}$) and otherwise a numerical approach should be used.

In this approach (see details on page 157) the maximum-likelihood estimate for σ_Q can be shown to satisfy the following, which (for a uniform prior) is mathematically identical to a least- χ^2 solution:

$$\sum_{i=1}^N \frac{(x_i - \bar{x})^2 - (\sigma_i^2 + \sigma_Q^2)}{\sigma_i^2 + \sigma_Q^2} = 0 \quad (4.19)$$

In the case of identical measurement errors ($\sigma_i = \text{constant}$) this reduces to the excess variance described in Eq. 4.18 and in this case $\sigma_Q = \sigma_{XS}$. The maximum-likelihood estimator has been successfully used also in e.g. Mateos et al. (2007) and in Chitnis et al. (2009).

Before applying the maximum-likelihood estimator further considerations had to be made. As for the early *INTEGRAL* data, we were challenged by similar problems: the analysis of the coded-mask data was not yet optimised, so that we had to assume systematic errors which were not taken into account. In order to test for this, we used the Crab as a constant source, and extracted light curves at random positions in the sky where no source had been reported. The Crab light curve was consistent to be constant when assuming 1.1% systematics. For the random positions in the sky, the (false) variability σ_Q we detected was as expected anti-correlated with the time scale we applied. We therefore subtracted the average σ_Q value of the random positions from the value derived for each source. 20 days appeared to be the best choice in order to achieve significant signal in each time bin

and to have a sufficient number of time bins. Thus, the corrected value for the variability estimator S_{Vc} was derived by subtracting the σ_Q of the random positions for 20 day time scale (3.6×10^{-5}) from the σ_Q of each source: $S_{Vc} = 100\% (\sigma_Q - 3.6 \times 10^{-5})/\bar{x}$.

An independent test for variability is to determine the structure function (SF). Structure functions are similar to auto- and cross-correlation functions and have been introduced for analysis of radio lightcurves by Simonetti et al. (1985). Applications to other data sets have been shown, e.g. by Hughes et al. (1992), de Vries et al. (2005), Favre et al. (2005), Soldi et al. (2008), and Emmanoulopoulos et al. (2010). The structure function is a useful and simple to use tool in order to find characteristic time scales for the variations in a source. We used the first-order structure function, which is defined as $D^1(\tau) = \langle [S(t) - S(t + \tau)]^2 \rangle$. Here $S(t)$ is the flux at time t , and τ is the time-lag, or variability time-scale. The function $D^1(\tau)$ can be characterized in terms of its slope: $b = d \log D^1 / d \log \tau$. For a stationary random process the structure function is related simply to the variance σ^2 of the process and its autocorrelation function $\rho(\tau)$ by $D^1(\tau) = 2\sigma^2[1 - \rho(\tau)]$. For lags longer than the longest correlation time scale, there is an upper plateau with an amplitude equal to twice the variance of the fluctuation ($2 \cdot (\sigma_Q^2 + \bar{\sigma}_i^2)$). For very short time lags, the structure function reaches a lower plateau which is at a level corresponding to the measurement noise ($2 \cdot \bar{\sigma}_i^2$). As explained in Hughes et al. (1992), the structure function, autocorrelation function, and power spectrum density function (PSD) $P(\nu)$ are related measures of the distribution of power with time scale. If the PSD follows a power law of the form $P(\nu) \propto \nu^{-a}$, then $D^1(\tau) \propto \tau^{a-1}$ (Bregman et al. 1990). For example, if $P(\nu) \propto \nu^{-1}$, then $D^1(\tau) \propto \tau^0$ (flicker noise). Flicker noise exhibits both short and long time-scale fluctuations. If $P(\nu) \propto \nu^{-2}$, then $D^1(\tau) \propto \tau^1$ (red, short, or random walk noise). This relation is however valid only in the limit $\tau_{max} \rightarrow \infty$, $\tau_{min} \rightarrow 0$. If, on the contrary, the PSD is limited to the range $[\tau_{min}, \tau_{max}]$, the relationship does not hold anymore (Paltani 1999). This is in fact the case here, as we can probe only time scales in the range of $\tau_{min} \sim 10$ days to $\tau_{max} \sim 100$ days.

In the ideal case we can learn from the structure function of the *Swift*/BAT AGN about several physical properties: whether the objects show variations, what the maximum time scale of variations is, and what the type of noise is which is causing the variations. We can determine the maximum time scale τ_{max} of variability only if a plateau is reached and, in our case, if $\tau_{max} < 9$ months. Error values on the structure function have been again determined by Monte-Carlo simulations.

Also for the SF we used the Crab as a test case. As expected, after the structure function gets out of the noisy part at time scales shorter than ~ 4 days, it stays more or less constant, as shown on page 161.

It has to be pointed out though that the structure function results can be erroneously interpreted, leading to misconceptions about the actual source properties. Emmanoulopoulos et al. (2010) performed extensive simulations, showing that the break in the SF is not always an indication for a characteristic time scale. The authors got those features even for simulated lightcurves where the underlying power spectral density was featureless. The structure function is also sensitive to data gaps, although this problem does not affect the study we performed here.

Based on the comparison of the structure function curves of the BAT AGN with those of the Crab and the random positions, we examined the curves of all objects for rising evolution in the range $\tau = 20 - 200$ days. Individual time limits l_{min} and l_{max} have been applied in order to apply a linear regression fit to the curves, taking into account the errors determined in the Monte-Carlo simulation. The l_{max} applied is not necessarily the maximum time-scale of variability τ_{max} , especially when $\tau_{max} > 100$ days. The results are reported in the last column of the Table on page 159. rr_{SF} gives the probability for a non-correlation of τ and $D^1(\tau)$. We considered objects with $\log rr_{SF} \leq -2$ as variable, i.e. objects where we find a probability of $> 99\%$ for correlation. The structure function

of the Crab lightcurve for example results in $\log rr_{SF} = -0.6$. One can see an overall agreement with the variability estimator, although in some cases there are discrepancies, e.g. for NGC 3516 and NGC 5728, which have a rising structure function, but do not give an indication of variability in the maximum likelihood approach. In total, 16 objects show a rising structure function, and 15 objects show a variability $S_{Vc} > 10\%$ in the maximum likelihood approach. A Spearman rank test of the variability estimator versus the $\log rr_{SF}$ value gives a probability of $> 98\%$ for correlation, and $> 99.5\%$ if we ignore the objects with a negative variability estimator.

We then checked the results of the variability analysis for correlations. The first check was to verify that the variability indicator is not a function of the source flux. Then, we tested for correlations of the variability with source type and absorption. From the table on page 159 one can see that none of the 11 type 1 galaxies shows significant variability, whereas of the 20 type 2 objects 50% show variability with $S_{Vc} \geq 10\%$. This effect is also apparent when comparing the variability S_{Vc} with the intrinsic absorption N_H . The correlation is shown in Fig. 2 on page 160. Blazars have been excluded. Except for NGC 2992, none of the objects with intrinsic absorption $N_H < 10^{22} \text{ cm}^{-2}$ shows significant variability according to the maximum likelihood estimator. NGC 2992 is also a special case because it is a Seyfert 2 galaxy with comparably low intrinsic absorption and the N_H varies between 0.1 and $1.0 \times 10^{22} \text{ cm}^{-2}$ (Beckmann et al. 2007a). Even when including NGC 2992 a Spearman rank test of N_H versus variability gives a correlation coefficient of $r_s = 0.31$, which corresponds to a moderate probability of correlation of 95%.

Thus, there seem to be a tendency in the sense that the stronger absorbed sources are the more variable ones. If the central engine in type 1 and type 2 objects is indeed similar, this is a surprising result. First, absorption should not play a major role in the spectrum at energies $> 15 \text{ keV}$. Most of the sources studied here show only moderate absorption with hydrogen column densities of the order of $N_H = 10^{21} - 10^{23} \text{ cm}^{-2}$. Even if absorption plays a role, the expected effect would be reverse to the observation, i.e. one would expect a damping effect of the absorption and the absorbed sources should be less variable than the unabsorbed ones. In a study of *XMM-Newton* data of AGN in the Lockman Hole by Mateos et al. (2007) it has been shown that although the fraction of variable sources is higher among type-1 than in type-2 AGN, the fraction of AGN with detected spectral variability were found to be $\sim 14 \pm 8\%$ for type-1 AGN and $34 \pm 14\%$ for type-2 AGN. This might indicate that the differences between type 1 and type 2 galaxies are indeed more complex than just different viewing angles resulting in a difference in the absorbing material along the line of sight.

A more likely explanation for the lack of variable type 1 objects in our sample could be that the correlation between absorption and variability is an indirect one, caused by two other correlations: an anti-correlation of intrinsic absorption and luminosity, and the anti-correlation of variability and luminosity. While the first dependence in the data set presented here is very weak, there is indeed a trend of lower variability for sources with higher luminosity as shown in Fig. 7 on page 162.

All the sources which show a strong variability of $S_{Vc} > 20\%$ have luminosities of $L_{(14-195 \text{ keV})} < 4 \times 10^{43} \text{ erg s}^{-1}$, and all sources with $S_{Vc} > 10\%$ have $L_{(14-195 \text{ keV})} < 2 \times 10^{44} \text{ erg s}^{-1}$. Using the results from the structure function a similar trend is seen: 13 out of 17 (i.e. 76 %) of the objects with $L_{(14-195 \text{ keV})} < 4 \times 10^{43} \text{ erg s}^{-1}$ have a significant rising part of the structure function, whereas only 3 out of 23 (13%) of the more luminous objects show this indication for variability.

The anticorrelation of X-ray variability with luminosity in AGN has been reported before for energies $< 10 \text{ keV}$ (e.g. Barr & Mushotzky 1986, Lawrence & Papadakis 1993) and has been also seen in the UV range (Paltani & Courvoisier 1994) and in the optical domain (de Vries et al. 2005), although narrow-line Seyfert 1 galaxies apparently show the opposite behaviour (e.g. Turner et al. 1999). As NGC 4051 is the only NLSy1 galaxy in our sample, we detect a continuous effect from soft to hard X-rays, which indeed indicates that the dominant underlying physical process at $\sim 5 \text{ keV}$

is the same as at ~ 20 keV. Papadakis (2004) reported that this correlation is in fact based on the connection between luminosity and the mass of the central black hole M_{BH} . This may be explained if more luminous sources are physically larger in size, so that they are actually varying more slowly. Alternatively, they may contain more independently flaring regions and so have a genuinely lower amplitude. The observed correlation might reflect the anticorrelation of variability and black hole mass. In the case of the sample presented here, such an anticorrelation is not detectable, but it has to be pointed out that estimates for M_{BH} are only available for 13 objects. In addition, the range of objects in luminosity and black hole mass might be too small in order to detect such a trend.

The luminosity might also have a direct influence on the geometry of the AGN. In the model of a receding disk, the high AGN activity pushes the disc and torus outwards through radiation pressure (Lawrence 1991; Down et al. 2010). Uttley & McHardy (2004) explained the anti-correlation of variability and M_{BH} by assuming that the X-rays are presumably produced in optically thin material close to the central black hole, at similar radii (i.e. in Schwarzschild radii, R_S) in different AGN. As $R_S = 2GM_{BH}c^{-2}$, longer time scales for the variability are expected for the more massive central engines, making the objects less variable on a monthly time scale studied here.

Thus, to summarize, we seem to observe a break down of the simple unified model here, as apart from the viewing angle, also the intrinsic luminosity plays a role in the appearance of the AGN. With the on-going *Swift* mission, there are now more than 5 years of data available to verify the behaviour we detected in Beckmann et al. (2007a). In Soldi et al. (2010b) we presented preliminary results of a study using 6 years of IBIS/ISGRI and 5 years of BAT data. The analysis confirms the trend of increasing hard X-ray variability with decreasing luminosity for the Seyfert galaxies, and the correlation between the luminosity and the black hole mass, with the more massive black holes accreting at lower Eddington ratios than the less massive ones.

4.7.3 The Second *INTEGRAL* AGN Catalogue

The first *INTEGRAL* AGN catalogue (Beckmann et al. 2006a) had shown the potential of spectroscopic sample studies using IBIS/ISGRI and JEM-X, and allowed us eventually to derive the first hard X-ray AGN luminosity function (Beckmann et al. 2006d). The sample size of only 36 Seyfert galaxies did not allow us though to put strong constraints on the Seyfert 1 / Seyfert 2 dichotomy. In order to test for differences in the intrinsic spectra, not only higher signal-to-noise spectra were required, but also a significantly larger sample.

In 2008 we therefore launched a new project to derive a spectroscopic AGN catalogue (Beckmann et al. 2009d; the manuscript can be found on page 165). This was also triggered by the significantly improved software available with OSA 7. We also changed the processing and strategy significantly compared to the first catalogue. First of all, we did not use the SPI data, as in the most relevant energy range of 20 – 100 keV the SPI data do not add significantly to the spectra. Instead we included in the second catalogue optical information based on OMC. As Seyfert galaxies usually do not show dramatic flux changes in the optical, the space-based photometry of OMC adds valuable information when reconstructing the spectral energy distribution of these sources. On the processing side, we decided to process all science windows separately and then to extract spectra from those data by summing up the single science window results for each source. In the first catalogue we had processed large observation groups containing hundreds to thousands of science windows, with the drawback that a crash of the software at any given point forced us to re-launch the processing, and the large observation groups did not allow to select subsets of the data for analysis, and thus for each source a separate analysis had to be run. The processing in single science windows also allowed us to parallelize the processing and to run it on ISDC's computing cluster. Unfortunately, there was not

sufficient data storage capacity available, thus after processing a fraction of the sky, one had to delete the single science window results in order to make space for the next sky area. For JEM-X, the parallelized approach did not lead to the best possible results, as in OSA 7 the standard spectral extraction was inferior to the extraction of spectra from the mosaic images. Thus for JEM-X we had to process the standard large observation groups.

As for the first catalogue, the list of AGN presented here is based on all *INTEGRAL* detections of AGN reported in the literature, which therefore enter into the *INTEGRAL* general reference catalogue (Ebisawa et al. 2003; Bodaghee et al. 2007). For many of the AGN, the second AGN catalogue presented spectral information for the first time based on *INTEGRAL* data, as other publications about samples of AGN often did not include spectral information (Bassani et al. 2006; Bodaghee et al. 2007; Sazonov et al. 2007; Bird et al. 2010). Different to the first AGN catalogue, the second one was based on data covering the sky more uniformly, as can be seen in the AGN distribution plot on page 167. For each extragalactic source, we analysed the IBIS/ISGRI, JEM-X, and OMC data from the early mission (revolution 26 starting on 30 December 2002) up to spacecraft revolution 530 (ending on 17 February 2007), covering more than 4 years of data. The 199 AGN reported to be found in *INTEGRAL* data are listed in Table 1 on page 168, together with their redshift, position (J2000.0), and their effective exposure time in IBIS/ISGRI and JEM-X for the data set used here. Twelve sources, which were reported in the literature but gave a detection significance $<3\sigma$ in the data presented here are listed in Table 1 and marked by an x . These objects were not considered in the following analysis. For all 187 objects with a detection significance above 3σ in the IBIS/ISGRI 18-60 keV energy band, spectral analysis was performed using an absorbed power law with N_{H} fixed to the value reported in the literature (Table 2, page 172). Only 23 detections of AGN by JEM-X reached a significance $>5\sigma$. The JEM-X spectra of the 23 AGN detected by the X-ray monitor were fit with the IBIS/ISGRI data and results reported in Table 4 on page 176. As for the ISGRI spectra alone, we also did not fit the absorption values in the case of the combined JEM-X/ISGRI spectra, because the JEM-X data starting at 3 keV did not allow a significant constraint on N_{H} .

Out of the 187 significantly detected AGN, 162 objects have been identified as Seyfert galaxies (161 with redshift information), 18 blazars (all of them with redshift), and 7 objects have been claimed to be AGN without further specification of the AGN type. Within the Seyfert group, we found 67 Seyfert 1 to 1.2 objects, 29 intermediate Seyfert 1.5, and 66 Seyfert type 1.9 and type 2. The average Seyfert 1 spectral property was constructed using the mean weighted by the errors on the photon indices of 55 ISGRI power-law fit results, the Seyfert 2 composite spectrum includes 44 sources, and 20 objects form the intermediate Seyfert 1.5 group where spectral fitting allowed constraining the spectral shape (Table 2). In addition, 11 blazars allowed spectral extraction. When computing the weighted average of the various subclasses, the 11 blazars had a hard X-ray spectrum with $\Gamma = 1.55 \pm 0.04$ when compared to the 119 Seyfert galaxies with $\Gamma = 1.93 \pm 0.01$. The Seyfert 1 ($\Gamma = 1.92 \pm 0.02$) and Seyfert 1.5 ($\Gamma = 2.02 \pm 0.03$) only show slightly steeper hard X-ray spectra than the Seyfert 2 objects ($\Gamma = 1.88 \pm 0.02$). Table 6 on page 177 gives the properties of the different Seyfert types. For 12 objects, a cut-off power law model gave a better representation of the ISGRI spectra (Table 3, page 175). The average photon index is in these cases $\langle\Gamma\rangle = 1.3 \pm 0.4$ with a cut-off energy of $\langle E_{\text{C}}\rangle = 86 \pm 25$ keV. We got a similar result when stacking the IBIS/ISGRI spectra together, as can be seen in Table 7 on page 179.

For the stacked spectrum, it was possible to constrain a model that adds a reflection component from cold material to the underlying continuum (the PEXRAV model; Magdziarz & Zdziarski 1995). This model gave a better representation of the data. The underlying continuum shows a similar gradient in the different source classes when not allowing for a high-energy cut-off in the PEXRAV model, so this fit has the same degree of freedom as the one using the cut-off power law. The differ-

ence shows up, however, in the inclination angle i and strength R of the reflection component. The value of R depends on the inclination angle i between the normal of the accretion disc and the line of sight. The smaller the inclination angle, the larger the resulting reflection component. As the data are not sufficient to fit R and i simultaneously, the inclination angle was set to $i = 30^\circ$ for Seyfert 1, $i = 45^\circ$ for Seyfert 1.5, and $i = 60^\circ$ for Seyfert 2. Using this model, Seyfert 1 and Seyfert 2 show only slightly different underlying continua and a reflection component of the same strength $R \simeq 1$ within the statistical errors. Seyfert 1.5 objects appear to have slightly steeper spectra ($\Gamma = 2.0$) and stronger reflection ($R = 3_{-1}^{+5}$). A difference between type 1 and type 2 objects is seen in the average luminosity of these subclasses. For 60 absorbed Seyfert galaxies, the average luminosity is $\langle L_{100\text{keV}} \rangle = 2.5 \times 10^{43} \text{ erg s}^{-1}$, more than a factor of 2 lower than for the 74 unabsorbed Seyfert with redshift information ($\langle L_{100\text{keV}} \rangle = 6.3 \times 10^{43} \text{ erg s}^{-1}$). The differences in luminosities are exactly the same when excluding the 5 Compton thick objects.

Considering the whole population of Seyfert galaxies we observed an increase in the fraction of unabsorbed objects compared to the first *INTEGRAL* AGN catalogue. Whereas $\frac{2}{3}$ of the Seyfert population in the first sample showed $N_{\text{H}} > 10^{22} \text{ cm}^{-2}$, there are now more unabsorbed than absorbed sources, i.e. only 44% appear to be absorbed. A similar trend has also been observed in the Swift/BAT survey (Tueller et al. 2008), where the fraction of absorbed sources is $\frac{1}{2}$.

Also in this sample we see the trend toward a decreasing fraction with luminosity in the range $L_{20-100 \text{ keV}} > 3 \times 10^{41} \text{ erg s}^{-1}$ (Fig. 7, page 180). The fraction appears low though in the lowest luminosity bin ($L_{20-100 \text{ keV}} < 3 \times 10^{41} \text{ erg s}^{-1}$), but it has to be considered that this luminosity bin contains only 3 AGN: the Seyfert 1.5 galaxies NGC 4258, NGC 4395, and NGC 5033. The fraction of Compton thick objects in the sample presented here is only 4% (5 objects out of the 135 Seyfert galaxies with measured intrinsic absorption). Although this sample is not a complete one, this indicates further that the fraction of Compton thick AGN is indeed $\ll 10\%$ as already reported in e.g. Beckmann et al. (2006a) and Bassani et al. (2006). In addition, a study based on combined *INTEGRAL* and *Swift*/BAT data puts an upper limit of $\lesssim 9\%$ on the fraction of Compton thick AGN (Treister et al. 2009b), and one can thus consider most of the Seyfert population detected by *INTEGRAL* and *Swift* to be Compton thin.

A similar low fraction of 7% Compton thick objects was found in a study by Malizia et al. (2009) of 88 Seyfert galaxies detected by *INTEGRAL*. They argue though that a large fraction of Compton thick objects is missed due to absorption above 20 keV, although this effect is not significant unless excessive absorption values ($N_{\text{H}} \gg 10^{25} \text{ cm}^{-2}$) are assumed (see Table 4.1 on page 55). In order to reach a larger fraction of Compton thick sources as claimed by Risaliti et al. (1999) in a sample selected due to their [OIII] properties, Malizia et al. (2009) then apply a cut in redshift to their sample. Below $z \leq 0.015$ they find 17 objects, and this subsample contains the 6 Compton thick objects of their whole sample. This leads to a fraction of 35% Compton thick sources and they argue that this appears to be the true ratio¹². Malizia et al. (2009) fail to explain though the fraction of 0% Compton thick objects at redshifts $z > 0.015$. It also should be pointed out that many of the high absorption column densities in Risaliti et al. (1999) are based on the non-detection of these sources at X-rays. Thus, in general, one cannot be sure whether these sources are heavily absorbed or intrinsically faint.

A recent study on infrared excess sources, which are also commonly thought to be Compton thick, showed that in fact a large fraction of these sources is not Compton thick, but more likely to be low luminosity, possibly Compton thin, AGN or dusty starbursts (Georgakakis et al. 2010). From this

¹²I do not think that this is a reasonable argument. If I own a garden, in which one tree is growing, I can draw a small square around it and determine the tree density within this square. Extrapolating to the size of my property, I might find that my garden is, in principle, a forest.

investigation it is obvious that the decomposition of the AGN and starburst contribution to the mid-IR is essential for interpreting the nature of the population of infrared excess sources, as star-formation may dominate this wavelength regime.

It appears from all recent studies on hard X-ray spectra of AGN that in fact the ratio of Compton thick sources is $\ll 10\%$. In view of recent hard X-ray surveys, Comastri et al. (2009) pointed out that only the already known Compton thick AGN have been detected by *Suzaku*, *Swift*, and *INTEGRAL* and that present observations are favouring a relatively low space density of heavily obscured sources. It might require more sensitive hard X-ray missions, like *NuSTAR*, *ASTRO-H*, and *IXO* in order to find out whether there are more Compton thick AGN at higher redshifts and to settle the question: What's the true fraction of Compton thick AGN in the Universe?

In order to test the unification scheme, we studied the dependencies with respect to two other parameters, the mass of the central black hole and, related to it, the Eddington ratio. In order to do so we also include in Table 1 on page 168 the black hole masses of the central engine and the method used to determine them, as found in the literature. Different methods can be used to estimate the mass of the central black hole M_{BH} in an AGN or a normal galaxy, most of them still carrying fairly large uncertainties. Nevertheless, considering the importance of the black hole mass in studying the properties of these objects, we decided to include a compilation of the mass estimates from the literature as the best guess that can be provided at present for each object in this catalogue. Using these masses, the Eddington luminosities of the AGN can be computed, assuming pure hydrogen, applying $L_{\text{Edd}} = 1.26 \times 10^{38} M M_{\odot}^{-1} \text{ erg s}^{-1}$. The Eddington ratio λ , i.e. the fraction of Eddington luminosity achieved by the accretion process in each AGN, is then $\lambda = L_{\text{Bol}}/L_{\text{Edd}}$. To determine the bolometric luminosity requires in principle the knowledge about the complete spectral energy distribution of the source. Here we used the 20 – 100 keV luminosities as derived from the IBIS/ISGRI data to approximate the bolometric luminosity. Assuming a canonical photon index of 2.0 for a single power law, the total X-ray luminosity is about $L_{(1-200 \text{ keV})} = 3 \times L_{(20-100 \text{ keV})}$. Assuming that the first peak of the spectral energy distribution is as strong as the X-ray luminosity, we derive $L_{\text{Bol}} = 6 \times L_{(20-100 \text{ keV})}$. This results in a Eddington ratio of $\lambda = L_{\text{Bol}}/L_{\text{Edd}} = 4.8 \times 10^{-38} L_{(20-100 \text{ keV})} \frac{M_{\odot}}{M} \text{ erg}^{-1} \text{ s}$.

The Eddington ratio can thus be computed for 71 Seyfert objects of the sample. We tested for correlations with black hole mass and Eddington ratio. There is apparently no correlation between the photon index as determined from IBIS/ISGRI data and the Eddington ratio, as can be seen in Fig. 9 on page 182. There is no significant correlation detectable, even when excluding the outliers on the top left in that figure.

As observed by Steffen et al. (2003) in *Chandra* data of AGN, it appears that the 2–8 keV luminosity function is dominated by type 1 AGN at high X-ray luminosities and by type 2 at low luminosities. The same effect is seen also in the *INTEGRAL* luminosity function (Beckmann et al. 2006d). Connected to this, we observe not only that the absorbed sources are less luminous than the unabsorbed ones, but also that absorbed sources have smaller accretion rates as seen in lower Eddington ratios (Fig. 10, page 182). In agreement with Middleton et al. (2008) results, we find that the average values of Eddington ratio for Seyfert 1 ($\langle \lambda_{\text{Sy}1} \rangle = 0.064$) are higher than those found for intermediate Seyfert type ($\langle \lambda_{\text{Sy}1.5} \rangle = 0.015$) and Seyfert 2 with $\langle \lambda_{\text{Sy}2} \rangle = 0.02$, although we do not observe the differences in the underlying spectra, as seen in their study. The same applies for the separation into unabsorbed ($\langle \lambda_{(N_{\text{H}} < 10^{22} \text{ cm}^{-2})} \rangle = 0.06$) and absorbed sources ($\langle \lambda_{(N_{\text{H}} > 10^{22} \text{ cm}^{-2})} \rangle = 0.015$). On the other hand, since we do not find a significant correlation between the hard X-ray photon index and the Eddington ratio, we cannot back up the scenario by Middleton et al. (2008) as a way to explain the different spectral hardness of type 1 and type 2 AGN.

All the correlations found within the second *INTEGRAL* AGN catalogue are given in Table 4.2. Here the correlation probability is given if larger than 90%. The correlations between Eddington ratio

Table 4.2: Correlation matrix for *INTEGRAL* AGN

	M_{BH}	Γ	L_X	Edd. ratio λ	L_V
N_H	no	no	no	no	no
M_{BH}	–	no	> 99.99%	intrinsic	> 99.99%
Γ		–	no	no	no
L_X			–	intrinsic	> 99.99%
λ				–	no

and L_X and M_{BH} are intrinsic, i.e. caused by the dependence of λ on these two parameters. We found three significant correlations in our sample between the luminosities L_X and L_V , and the mass of the central black hole M_{BH} . The three correlations lead to the assumption that these parameters, similar to L_X , L_R , and M_{BH} (Merloni et al. 2003), form a fundamental plane for AGN activity. The correlation can be expressed in the form

$$\log L_V = 0.59 \log L_X + 0.22 \log M_{BH} + 16.0; \quad (4.20)$$

i.e., $L_V \propto L_X^{0.6} M_{BH}^{0.2}$. This correlation is shown in Fig. 15 on page 185. While the fundamental plane including the radio and X-ray luminosity can be understood as a connection of the jet activity, as visible in the radio, and the accretion flow, as dominating the X-rays, the correlation found here shows a different connection. The optical luminosity is commonly thought to be dominated by the AGN accretion disc (e.g. Siemiginowska et al. 1995) and therefore by the accretion processes onto the supermassive black hole, but there is also a possible contribution by the jet (Soldi et al. 2008) and emission of the bulge, and therefore of the stars in the host galaxy contributing to it. The latter is especially important as the resolution of *INTEGRAL*'s OMC camera does not allow a deconvolution of the core and the bulge. Nevertheless it shows that there is a significant bulge- M_{BH} correlation and that accretion processes are closely linked to the mass of the central black hole. The finding that this fundamental plane holds for all Seyfert types indicates further that these AGN are indeed intrinsically the same.

The results based on the second *INTEGRAL* AGN catalogue can be interpreted within the scenario of the unified model. The whole hard X-ray detected Seyfert population fills the parameter space of spectral shape, luminosity, and accretion rate smoothly, and only an overall tendency is seen in which more massive objects are more luminous, less absorbed, and accreting at higher Eddington ratio. An explanation for why the absorbed sources have been claimed to show flatter spectra in the hard X-ray domain when fit by a simple power law can be that the slope of the continuum strongly depends on the fitted model and that Compton reflection processes play a major role here (see also Beckmann et al. 2009b). Considering these effects, it appears that the different Seyfert types are indeed intrinsically the same. This is further supported by the fact that a fundamental plane of AGN activity can be found not only between L_X , L_R , and M_{BH} (Merloni et al. 2003), which indicates a connection of accretion flow with the jet, but also between L_X and L_V , and M_{BH} , linking accretion processes to the bulge of the host galaxy and the mass of the central engine.

4.7.4 The special case of MCG–05–23–016

The fundamental plane described in the previous section might even be extended toward Galactic black holes. In a study of the bright Seyfert 1.9 galaxy MCG–05–23–016 we showed that this source

exhibits a spectral energy distribution similar to the Galactic black hole system XTE 1118+480 in the low state (Beckmann et al. 2008a).

MCG–05–23–016 presents a rather unique case. Its spectrum is, at least to the first order, nearly constant in shape and luminosity, with a possibly variable reflection component ($R = 0 \dots 1$) and high energy cut-off ($E_C = 50 \dots 120$ keV). The over all luminosity is low. Using the X-ray luminosity of $L_{2-200\text{keV}} = 10^{44}$ erg s $^{-1}$ as a proxy for the bolometric luminosity, the small black hole mass of $2 \times 10^6 M_\odot$ (Wang & Zhang 2007) leads to a large Eddington ratio of $L_{bol}/L_{Edd} \gtrsim 0.4$. As the UV/optical emission is at least of the same order as the X-ray one, it is more likely that the Eddington ratio is as high as $L_{bol}/L_{Edd} \gtrsim 0.8$. Considering the error on the mass determination, this translates in a range of $L_{bol}/L_{Edd} = 0.2 - 5$ (Beckmann et al. 2008a).

An independent way to determine the mass of a black hole is to study its temporal behaviour. Following McHardy et al. (2006), the detection of a break in the X-ray power spectral density (PSD) of an AGN would allow to estimate the black hole mass thanks to the relation $T_B = 2.1 \log(M_{BH} \times 10^{-6} M_\odot^{-1}) - 0.98 \log(L_{bol} \times 10^{-44} \text{ erg}^{-1} \text{ s}) - 2.32$. Using the data collected by *RXTE*/PCA and *XMM-Newton*/PN between 1996 and 2005, we estimated the X-ray PSD and structure function (*RXTE* data only) of MCG–05–23–016. The structure function has the advantage of working in the time domain and therefore being less sensitive to alias and windowing problems than the Fourier analysis. The PSD was calculated for each observation longer than 10 ks (on 200 seconds binned light curves), and the PSDs obtained were averaged and binned in logarithmically spaced bins (e.g. Uttley et al. 2002). The final PSD shows a flattening between $2 \times 10^{-5} - 10^{-4}$ Hz (10–50 ks), close to the minimum frequencies sampled by these data ($\sim 7 \times 10^{-6}$ Hz). Also the structure function presents the hint of a break, but rather at ~ 3.5 ks (Beckmann et al. 2009c). The lack of a longer-term monitoring prevents us from drawing a firm conclusion about the presence and the position of the break. Assuming a break in the range 0.04–0.6 days (3.5–50 ks), we achieve a black hole mass of $M_{BH} = 1.84 - 3.3 \times 10^7 M_\odot$. It has to be taken into account though that for the given bolometric luminosity the formula does not allow for black hole masses lower than $1.8 \times 10^7 M_\odot$, even when the break time approaches zero. This means that it implies an upper limit for the Eddington ratio of $L_{bol}/L_{Edd} \lesssim 0.1$ at a luminosity of $L_{bol} = 2 \times 10^{44}$ erg s $^{-1}$, which might be exceeded in the case presented here. It also means that the mass estimate of MCG–05–23–016 based on the temporal behaviour is at the lower limit of the possible values.

Figure 4.24 shows the SED of the source for the data presented in Beckmann et al. (2008a), corrected for Galactic absorption of $N_{H,Gal} = 8 \times 10^{20}$ cm $^{-2}$ in the line of sight, giving an extinction of $A_V = N_H/1.79 \times 10^{21} \text{ cm}^{-2} = 0.45$ mag (Predehl & Schmitt 1995). The extinction in the UV is higher (e.g. $A_U = 0.74$ mag), while the effect is insignificant in the near infrared with e.g. $A_K = 0.05$ mag (Schlegel et al. 1998). To the simultaneous data we added previous observations in the J, H, and Ks band from the 2MASS and VLA observations at 6 cm and 20 cm (Ulvestad & Wilson 1984) for comparison. The SED indicates that the bolometric luminosity is probably $L_{bol} > 2L_X$. Even considering the uncertainty of the mass determination, the source cannot be assumed to be a typical low-luminosity AGN, which exhibits Eddington ratios in the range 10^{-3} to 10^{-6} (Ho 1999), and the Seyfert 1.9 shows an Eddington ratio 10^8 times larger than that of Sgr A* which has a similar mass of $M = 3.3 \times 10^6 M_\odot$ (Schödel et al. 2003). If we assume that the mass is in fact $M \lesssim 5 \times 10^6 M_\odot$ then the Eddington ratio of $L_{bol}/L_{Edd} \gtrsim 0.8$ is also remarkable when compared to other Seyfert galaxies. Woo & Urry (2002) list a total of 32 Seyfert galaxies with black hole masses lower than $10^7 M_\odot$ and only 3 of them have $L_{bol}/L_{Edd} \gtrsim 1$, whereas the average of these lower mass black holes is $L_{bol}/L_{Edd} = 0.30 \pm 0.05$. In the Galactic equivalent, the hard state is usually reached at small Eddington ratios, like $L_{bol}/L_{Edd} \simeq 10^{-3}$ in the case of XTE J1118+480 (Esin et al. 2001), and 0.003 – 0.2 for

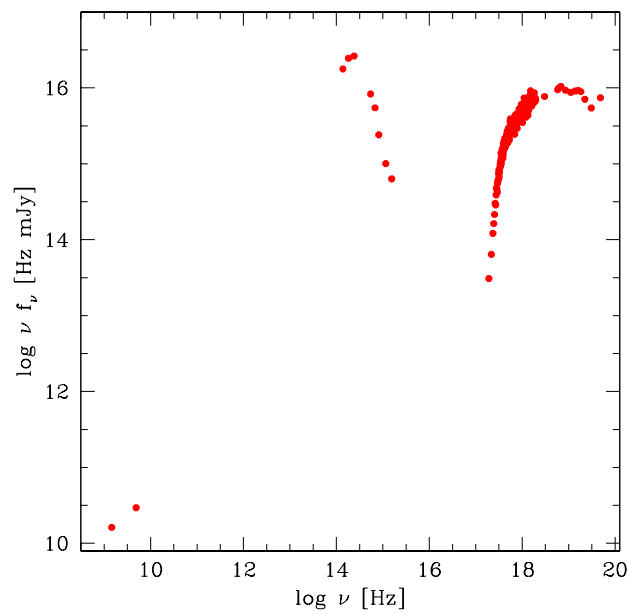


Figure 4.24: Spectral energy distribution of the combined data set of MCG-05-23-016, including *Swift*/UVOT optical and UV data as well as *Swift*/XRT soft X-ray, and *INTEGRAL* JEM-X and IBIS/ISGRI hard X-ray data. In addition, 2MASS measurements (J, H, and Ks) and radio data (6 cm and 20 cm) have been added. Data have been corrected for Galactic hydrogen column density, but not for intrinsic absorption.

XTE J1650-500 (Done & Gierliński 2006). In fact the SED of the X-ray nova XTE J1118+480 in the low state appears very similar to the one of MCG–05–23–016. In XTE J1118+480 the thermal disc component has a temperature as low as 24 eV. Considering that the temperature scales with $T \propto M^{-0.25}$, the disc emission of the Seyfert can be expected at much lower frequencies and can be hidden in the SED component peaking around $10^{14.5}$ Hz. XTE J1118+480 also shows a power law component dominating the spectrum in the 0.4 – 160 keV range with a photon index of $\Gamma = 1.8$ (McClintock et al. 2001). The overall SED in this object can be explained by an advection dominated accretion flow (ADAF) model at 2% Eddington ratio (Esin et al. 2001). Although the SED of MCG–05–23–016 appears to resemble the one of XTE 1118+480, its high Eddington ratio is unlikely to be arising from a radiative inefficient accretion as described in the ADAF. An object with higher Eddington ratio also in the hard state is GX 339-4, which reaches $L_{bol}/L_{Edd} = 0.25$ in the hard state in some cases before the state transition into the high-soft state (Zdziarski et al. 2004), consistent with MCG–05–23–016, although on average GX 339–4 reaches only an Eddington ratio of 0.015 and 0.05 during quiescence and during outburst, respectively. Considering a time scale for accretion rate changes in GX 339–4 of ~ 1000 days (Zdziarski et al. 2004), this would correspond to time scales of ~ 1 Myr in the case of MCG–05–23–016, as the variation times scale with the mass of the black hole.

Objects which are thought to exhibit extremely high Eddington ratios are the ultra-luminous X-ray sources (ULX). The true nature of these objects is still unclear though. Considering their luminosity, they are either intermediate mass black holes (IMBH) with a central mass as high as 100–100,000 M_{\odot} (e.g. Colbert & Mushotzky 1999), or alternatively they are operating at very high Eddington ratio, as large as $L_{bol}/L_{Edd} > 20$ (Soria et al. 2007; Roberts 2007). ULX also show hard spectra and low temperature disc similar to XTE J1550–564 in very high state where the disc temperature decreases (e.g. Kubota & Done 2004). A study of *Chandra* data on ULX showed that the spectra can often be fitted by a simple power-law model, without evidence for thermal accretion disc components (Berghea et al. 2008), similar to MCG–05–23–016. In some cases ULX show a disc component, e.g. the *XMM-Newton* observation of two ULX in NGC 1313 revealed soft components which are well fitted by multicolor disc blackbody models with color temperatures of $kT \simeq 150$ eV. Kajava & Poutanen (2009) studied *Chandra* and *XMM-Newton* data of several ULX, finding that some are well represented by a power law, others by a multicolor disc, and that also a soft excess is observed in some cases.

An alternative model for the accretion process onto black holes has been proposed by Courvoisier & Türler (2005), in which the accretion flows consist of different elements (clumps) which have velocities that may differ substantially. As a consequence, collisions between these clumps will appear when the clumps are close to the central object, resulting in radiation. In the case of MCG–05–23–016, this model results in low-energetic collisions, which is also indicated by the missing variability in the UV band as seen by *Swift*/UVOT, where these collisions should cause flux variations.

Low mass AGN like MCG –05–23–016 operating at high Eddington rate might be an early state in the evolution towards high-mass black holes as seen in quasars. As the highest measured redshift of a quasar to date is $z = 6.43$ (Willott et al. 2007), we can assume that these objects with black hole masses of $M > 10^8 M_{\odot}$ appear in the Universe around $z \sim 7$. If we assume the formation of the first heavy black holes with $M \sim 10^6 M_{\odot}$ at redshift $z = 10$, we indeed need high mass accretion rates. An object like MCG –05–23–016, if we consider its mass to be indeed $M \lesssim 5 \times 10^6 M_{\odot}$, with a constant Eddington ratio of $L_{bol}/L_{Edd} = 0.8$ and starting black hole mass of $M(z = 10) = 10^6 M_{\odot}$ would reach a mass of $M(z = 7) = 4 \times 10^8 M_{\odot}$. However, this would require not only the existence of a super massive black hole with $M \sim 10^6 M_{\odot}$ at redshift $z = 10$, but also a high accretion rate over a time span of 3×10^8 yrs. But even at a duty cycle of only 20% for AGN activity at $z \geq 7$, objects like MCG –05–23–016 can evolve to $10^8 M_{\odot}$, and it has to be taken into account that the duty cycle of AGN is

likely to be larger in the high-redshift Universe (Wang et al. 2008). On the other hand, it has to be considered that the environment in which the AGN grows at redshifts $z > 7$ might be significantly different than the one we observe MCG -05-23-016 at in the local Universe.

4.8 Connection to Gamma-rays

The spectra of AGN often show an unbroken continuum with a photon index around $\Gamma = 2$ in the hard X-rays. Although Seyfert galaxies are indeed supposed to have a high energy cutoff somewhere in the hard X-rays, some are also detected all the way up into the gamma-ray region. Blazars often show a rising spectrum ($\Gamma < 2$) in hard X-rays, indicating that their main energy output takes place in the gamma-rays. The main breakthrough for AGN gamma-ray astrophysics was achieved through observations by the Energetic Gamma-Ray Experiment Telescope (EGRET, Kanbach et al. 1988; Esposito et al. 1999) on board the *Compton Gamma Ray Observatory (CGRO)* which covered the energy range between 20 MeV to over 30 GeV. EGRET worked for nearly ten years before CGRO was safely de-orbited and re-entered the Earth's atmosphere in June 2000 to avoid an uncontrolled re-entry. The effective surface of the telescope was 0.15 m^2 in the 0.2–10 GeV region. The angular resolution was strongly energy dependent, with a 67 % confinement angle of 5.5° at 100 MeV, falling to 0.5° at 5 GeV on axis; bright gamma-ray sources could be localized with approximately 10 arcmin accuracy, but for faint ones the error radius could exceed 1 degree. The energy resolution of EGRET was 20 – 25 % over most of its range of sensitivity. The Third EGRET Catalogue (Hartman et al. 1999) contains 271 gamma-ray sources ($E > 100 \text{ MeV}$). Among them is only one non-blazar AGN, the radio galaxy Cen A (NGC 5128). The other AGN were blazars, i.e. BL Lac objects, flat-spectrum radio quasars, or unidentified flat-spectrum radio sources.

With the launch of NASA's *Fermi* satellite on 2008 June 11 on a Delta II Heavy, a new powerful tool to study the gamma-ray sky is now available to the scientific community. The Large Area Telescope (LAT; Atwood et al. 2009) is an imaging, wide field-of-view, high-energy telescope covering the energy range from 20 MeV to more than 300 GeV. The LAT is a pair-conversion telescope with a precision tracker and calorimeter, each consisting of a 4×4 array of 16 modules, a segmented anti-coincidence detector that covers the tracker array, and a programmable trigger and data acquisition system. The energy resolution in the most relevant energy range of 100 MeV to 1 GeV is 9% – 15% (on-axis), the 68% (1σ) containment radius is 3.5° at 100 MeV and 0.6° at 1 GeV. The field of view is 2.4 sr and the point source sensitivity within one year of operation above 100 MeV is $3 \times 10^{-9} \text{ ph cm}^{-2} \text{ s}^{-1}$. *Fermi* operates in survey mode, scanning the entire sky every 3 hours with every region viewed for ~ 30 minutes.

4.8.1 ROSAT selected Gamma-ray Blazars

Blazars are highly variable sources. Nevertheless, observations at other wavelengths can be used to predict detectability by *Fermi*/LAT.

We studied the case of the potential gamma-ray bright blazar RX J1211.9+2242 and published the results in Beckmann et al. (2004b). RX J1211.9+2242 is an optically faint ($B \approx 19.2 \text{ mag}$) but X-ray bright ($f_{2-10 \text{ keV}} = 5 \times 10^{-12} \text{ erg cm}^{-2} \text{ sec}^{-1}$) AGN, which we showed to be a BL Lac object at redshift $z = 0.455$ (Beckmann et al. 2003b). The non-simultaneous *ROSAT* and *BeppoSAX* X-ray, Calar Alto optical, and NVSS radio data suggest that the peak of the synchrotron emission of this object is at energies as high as several keV. The blazar is located within the 95% confidence radius of 53 arcmin around the un-identified EGRET source 3EG J1212+2304. Within this error circle, also

two quasars from the FIRST Bright Quasar Survey (Gregg et al. 1996) at redshift 1.722 and 1.208 are detected. Those have not been detected by the RASS and are therefore less likely to be the counterpart. In total there are only ten X-ray sources detected in this region in the *ROSAT* All-Sky Survey, and only RX J1211.9+2242 is both in the *ROSAT* Bright Source Catalog and in the NVSS radio catalog. Figure 4.25 shows a map derived from the RASS in the 0.1 – 2.4 keV energy range, centered on the position of the gamma-ray source 3EG J1212+2304. The positions of the other *ROSAT* sources are marked with “1RXS” and the positions of the two quasars and an Abell galaxy cluster inside the error circle are also indicated. Additional indication for the EGRET source being a BL Lac comes from the

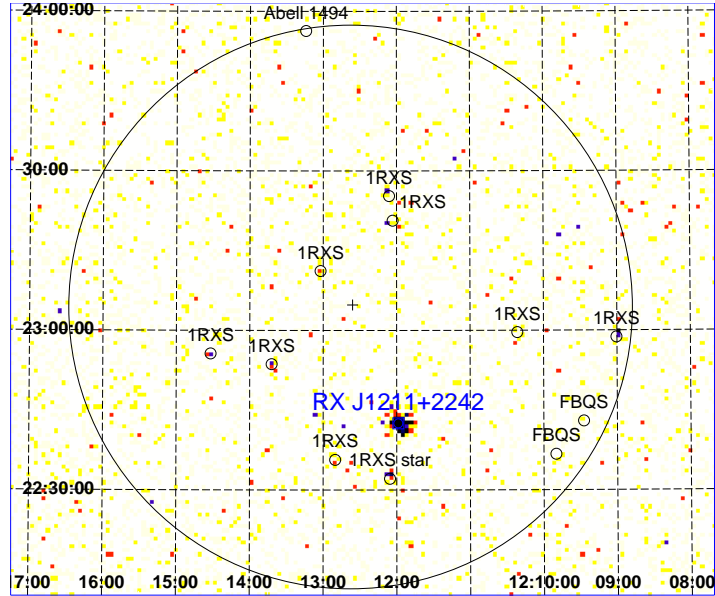


Figure 4.25: *ROSAT* All-Sky Survey map (0.1 – 2.4 keV) around the position 3EG J1212+2304. The circle marks the 53 arcmin EGRET error radius. There is only one bright X-ray source in the error circle, which is the blazar RX J1211.9+2242

variability in the gamma-rays. Its position was covered by 22 EGRET observations, in three of which it was clearly detected at different flux levels. The photon flux measurements vary from the lowest upper limit of 5.3×10^{-8} photons $\text{cm}^{-2} \text{s}^{-1}$ to a detected flux of $(50.8 \pm 16.6) \times 10^{-8}$ photons $\text{cm}^{-2} \text{s}^{-1}$. The BL Lac exhibits strong variations in the X-ray domain on long term time scales (years), though no significant variability was detected during the individual *BeppoSAX* observations. Galactic sources, such as pulsars and supernova remnants show little variability in the EGRET observations, while AGN exhibit strong flux variations (Nolan et al. 2003). This is a first indication that 3EG J1212+2304 might be an AGN. At a Galactic latitude of $b = 80^\circ$, this source is far out of the Galactic plane, making an extragalactic origin more likely, and thus supporting the blazar identification. RX J1211.9+2242 is the only plausible counterpart to this source inside the error circle. Sowards-Emmerd et al. (2003) claim that 3EG J1212+2304 is not a blazar but base this on the evidence that there is no radio flux enhancement towards the center of the (large) EGRET error circle and that there was no known blazar inside the error circle, which we have just shown is not the case.

When assuming that the EGRET source is identical with the BL Lac object, one can reconstruct its spectral energy distribution as shown in Fig. 4.26. Fitting this spectral energy distribution to a Synchrotron Self Compton model shows that physically meaningful parameters can explain the overall

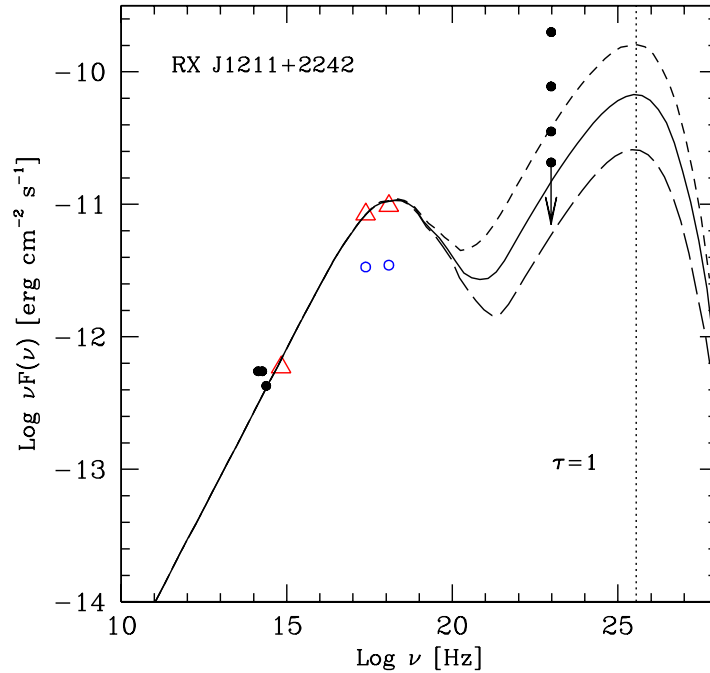


Figure 4.26: Spectral energy distribution of RX J1211.9+2242 constructed assembling the available data. The triangles mark the simultaneous optical and X-ray data (0.5–2.0 keV and 2–10 keV bands). The curves represent the SED calculated with the model described in the text, with the following parameters for all the curves: $B = 0.1$ G, $n_1 = 2$, $n_2 = 4$, $R = 5 \times 10^{15}$ cm. The three models differ for the value of $\delta = 10, 15, 20$ (short dashed, solid, long dashes, respectively), the normalization of the electron density $K = 8, 2.3, 1 \times 10^5$ part/cm³ and the break Lorentz factor $\gamma_b = 6, 4.5, 3 \times 10^5$. The frequency where absorption by infrared photons becomes important (Kneiske et al. 2004) is indicated by the dotted vertical line.

data, including the EGRET measurements. Although BL Lacs are known to exhibit a strong variability in the inverse Compton branch, it is unlikely that the *BeppoSAX* observations detect the source in an outburst phase due to an expected duty cycle $\ll 0.5$. On the other hand, most of the measurements of 3EG J1212+2304 are upper limits and the modeled IC branch falls well within the region of possible flux variations. Furthermore, no other X-ray source inside the error circle is likely to be the counterpart, and no strong radio source has been found there either. Since all the identified EGRET blazars have also been detected in the RASS, a connection between a strong *ROSAT* source and an EGRET detection is even more likely.

Assuming that the BL Lac and the gamma-ray emitter are in fact the same source, this yields a SED similar to that of Markarian 501 ($z=0.034$) in its bright state. An emitting region of $R = 5 \times 10^{15}$ cm, a magnetic field of $B = 0.1$ G, Doppler factor of $\delta = 20$ and a Lorentz factor for electrons at the break $\gamma_b = 3 \times 10^4$ reproduce the SED of RX J1211.9+2242 under the assumption that the flux during the *BeppoSAX* and optical observation was below the EGRET upper-limit of 3EG J1212+2304. The SED would reach the EGRET detections by applying $\delta = 10$ and $\gamma_b = 6 \times 10^4$. In order to match the different detections and non-detections, the IC branch flux needs to vary by a factor of ~ 50 at the peak of the emission. Again, this behaviour is similar to that observed in Markarian 501 that showed

variability in the hard X-rays (10-100 keV) by a factor of ~ 100 in different *BeppoSAX* observations coupled with a simultaneous shift of the synchrotron peak from the soft X-rays up to the soft gamma-rays. It also showed a strong variability, by a factor of ~ 100 , in the EGRET band (Tavecchio et al. 2001).

In order to verify our assumption that 3EG J1212+2304 is the counterpart of RX J1211.9+2242, we analysed gamma-ray data provided by *AGILE*. The data show no sign of the source, but the upper limit which one can derive from the data is $f_{(0.1-50 \text{ GeV})} = 2.2 \times 10^{-7} \text{ ph cm}^{-2} \text{ s}^{-1}$, fully consistent with the EGRET data. Stronger constraints can be put by using the *Fermi*/LAT data. Still, neither at the position of the EGRET source, nor at the blazar location there is any evidence for a source using the first 16 months of LAT data, as shown in Fig. 4.27. Also no source was reported at this position in

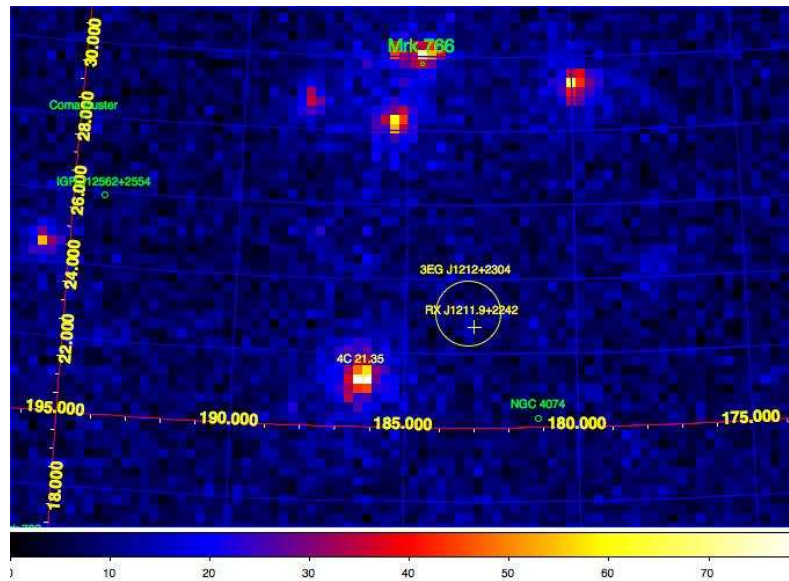


Figure 4.27: *Fermi*/LAT map based on 16 months of data around the position of the unidentified EGRET source 3EG J1212+2304. Also indicated is the position of the BL Lac RX J1211.9+2242. No source is detectable within the EGRET error circle.

the *Fermi*/LAT catalogue based on the first 11 months of observations (Abdo et al. 2010a). The upper limit after one year of observation is about $4 \times 10^{-9} \text{ ph cm}^{-2} \text{ s}^{-1}$ (for $E > 100 \text{ MeV}$). We are going to continue to analyse the LAT data, in order to search for the EGRET source. But in case it will not flare again, we will never know for sure whether RX J1211.9+2242 was indeed gamma-ray bright, as we claimed in Beckmann et al. (2004b).

Besides RX J1211.9+2242 there are seven more objects within the HRX-BL Lac complete sample which show peak frequencies above 10^{19} Hz (Beckmann 2003). These objects are also promising targets for gamma-ray emission. The spectral energy distribution for these objects indicated a peak of the synchrotron branch at energies $> 10 \text{ keV}$. Details about these objects can be found in Table 4.3. It is important to underline that the determined peak frequencies are based on non-simultaneous data. Therefore it is possible that the peak frequency, determined by a simple parabolic fit to the radio, optical, and X-ray flux, is wrong. The spectral slope in the X-rays was determined from the PSPC pointed observations in the cases of RX J0928.0+7447 and RX J1008.1+4705. For the other objects the photon index Γ results from the hardness ratios within the RASS. Although in these cases the

Table 4.3: UHBL candidates within the HRX-BL Lac complete sample

Name	z	f_R [mJy]	B [mag]	f_X^a	Γ	<i>Fermi</i> /LAT detection
RX J0710.5+5908	0.125	159	18.4	10.2	1.93	8.2σ
RX J0913.3+8133	0.639	4.9	20.7	2.3	1.65	no
RX J0928.0+7447	0.638	85.8	20.8	1.1	1.66^b	no
RX J1008.1+4705	0.343	4.7	19.9	4.4	1.93^b	no
RX J1111.5+3452	0.212	8.4	19.7	2.7	2.13	13.7σ
RX J1211.9+2242	0.455	20.2	19.6	2.6	1.96	no
RX J1237.1+3020	0.700	5.6	20.0	3.2	1.94	no
RX J1458.4+4832	0.539	3.1	20.4	2.7	1.88	no

^a *ROSAT*/PSPC flux (0.5 – 2.0 keV) in [10^{-12} erg cm $^{-2}$ sec $^{-1}$]

^b *ROSAT*/PSPC spectral slope derived from pointed observation

errors on the photon index are large, the determined slope can give a hint to the real value.

As for RX J1211.9+2242 we analysed the first 16 months of *Fermi*/LAT data in order to test for possible gamma-ray counterparts. Only 2 out of the 7 objects show a clear detection, the BL Lac objects RX J0710.5+5908 and RX J1111.5+3452 at redshift $z = 0.125$ and $z = 0.212$, respectively. RX J0710.5+5908 is also included in the first *Fermi* AGN catalogue as 1FGL J0710.6+5911, with a detection significance of 8.2σ , while RX J1111.5+3452 has not yet been reported. The source is visible in the LAT count map at energies > 100 MeV as can be seen in Fig. 4.28. Similar as for

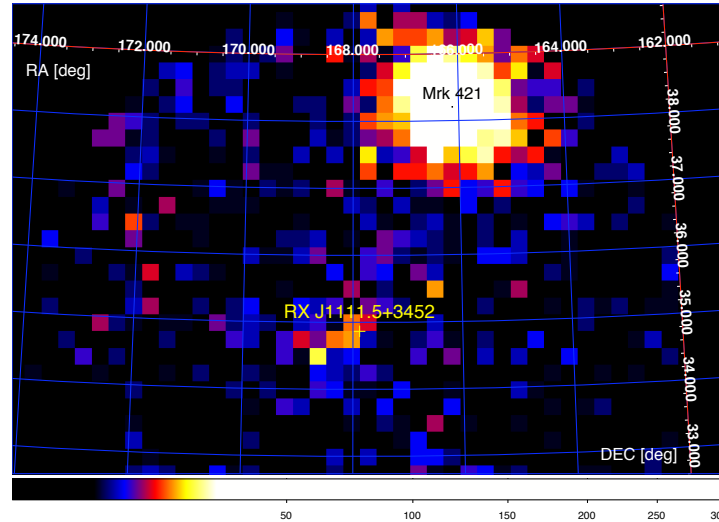


Figure 4.28: *Fermi*/LAT map showing the BL Lac RX J1111.5+3452 at energies > 100 MeV. The significance of the source is about 14σ .

coded mask instruments like IBIS and SPI, also in the case of the LAT all data and sources in the field of view have to be fit simultaneously. To fit the data, two background models were applied, one in order to take account for the contributions of the Galactic plane, and one to model the extragalactic background. In addition, the two sources in the field, Mrk 421 and RX J1111.5+3452 were fit. The likelihood analysis showed that Mrk 421 can be modeled by a simple power law with photon index

1.80 ± 0.02 . The BL Lac RX J1111.5+3542 shows a significance of 13.7σ and a spectral slope of $\Gamma = 2.6 \pm 0.1$ above 100 MeV. Although these values might be influenced by the nearby bright blazar Mrk 421, the BL Lac appears to be gamma-ray bright, as predicted from the study of the spectral energy distribution below 2.4 keV. The combined fit of the two background models and the two sources is shown in Fig. 4.29.

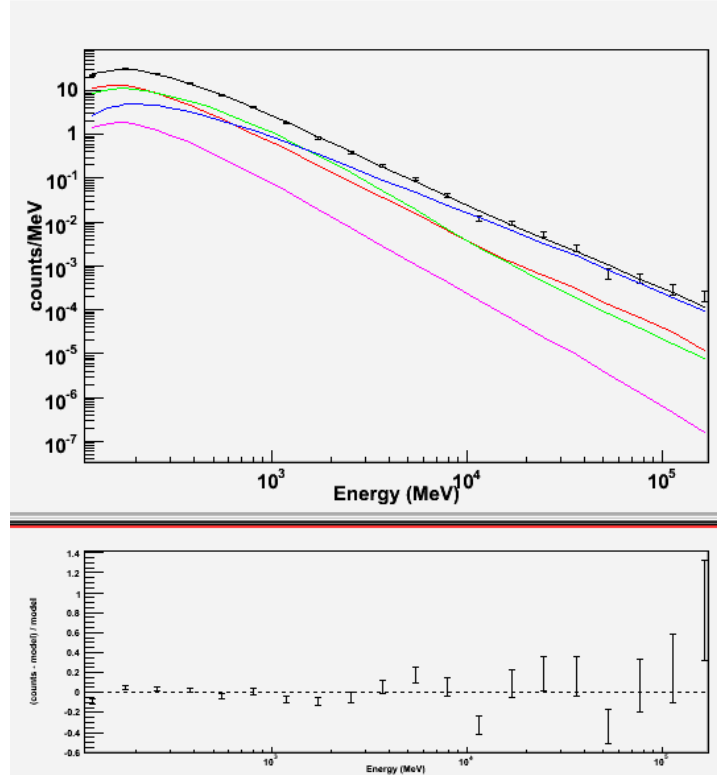


Figure 4.29: *Fermi*/LAT spectral fit for the field around the BL Lac RX J1111.5+3542. The data points based on the total flux are shown in black. The black curve shows the fit to the data, including two background models plus two sources, Mrk 421 (shown as blue curve) and the BL Lac RX J1111.5+3542 (pink curve). The lower panel shows the deviation of the model with respect to the data.

These results show that indeed non-simultaneous data can be used to predict gamma-ray detectability, although the success rate is only 25% in our case. The reason might either be that the non-detected BL Lac objects are in general faint in the LAT energy band, or that the duty cycle of these objects on years time scale is around 25%. Once several years of *Fermi*/LAT data are available, we should be able to answer this question.

4.8.2 The Fermi view on hard X-ray blazars

The identification and modeling of *Fermi*/LAT detected blazars requires a dense observation of these sources across the electromagnetic spectrum, from radio observations up to the TeV range. In the neighboring wavelengths of the LAT energy band blazars are well studied in the X-ray range up to 10 keV thanks to satellite based observations ranging from early missions like *EINSTEIN* and *EXOSAT*

towards nowadays *Chandra* and *XMM-Newton*. The TeV range is now becoming more and more accessible through state-of-the-art projects like *HESS*, *MAGIC*, *VERITAS*, and *CTA* in the not too distant future. In order to determine the energy output of blazars in the inverse Compton branch, it is necessary though to fill also the parameter space below 100 MeV. At the time being, there is no mission available or even planned to access the energy range between 1 and 100 MeV, thus, in order to constrain the SEDs of blazars and to learn as much as possible about the low-energy end of the inverse Compton emission, we have to rely on the hard X-ray band.

In order to study the SED of hard X-ray detected blazars in the gamma-ray domain, we analysed *Fermi*/LAT data of the blazars detected so far by *INTEGRAL* IBIS/ISGRI in the energy band above 20 keV (Beckmann et al. 2010b). It is worth mentioning that at the time of this work, the First *Fermi* AGN catalogue (Abdo et al. 2010a) had not yet been published.

In the second *INTEGRAL* AGN catalogue (Beckmann et al. 2009d) we listed in total 25 blazars which have been reported to be detected by IBIS/ISGRI above 20 keV, out of which 20 are detectable at $\geq 3\sigma$. The results of a single power law model fit to the data taken between January 2003 and spring 2008 are given in Table 4.4. It has to be pointed out that the *INTEGRAL* data are not simultaneous with the *Fermi* data. In cases where the IBIS/ISGRI detection significance was $< 5\sigma$, a photon index of $\Gamma = 2$ has been assumed in order to estimate the hard X-ray flux. For six of the 20 IBIS/ISGRI detected blazars, *INTEGRAL*'s X-ray monitor JEM-X gave a detection of $> 5\sigma$ in the 3 – 20 keV band: 1ES 0033+595, Mrk 421, 3C 273, H 1426+428, Mrk 501, and 3C 454.3. In addition, for six blazars V-band measurements are available, representing the average optical emission during the *INTEGRAL* observation. On average, the *INTEGRAL* IBIS/ISGRI detected blazars show the following properties. Redshift information is available for all of the sources, having an average luminosity of $\langle L_{20-100\text{keV}} \rangle = 1.3 \times 10^{46} \text{ erg s}^{-1}$, assuming isotropic emission. 15 sources allowed spectral fitting with $\langle \Gamma \rangle = 2.1$, and for 10 blazars the mass of the central black hole has been determined, giving $\langle M_{BH} \rangle = 6 \times 10^8 M_{\odot}$.

Out of the 20 blazars listed in Tab. 4.4, 15 are detectable with a significance $> 10\sigma$ in the LAT data analysed here. 11 of these LAT detected sources had already been reported in the *Fermi* LAT Bright AGN Sample (LBAS) based on the first 3 months of the mission (Abdo et al. 2009, 2010b). The four blazars which were not included in that list are QSO B0836+710, H 1426+428, RX J1924.8–2914, and PKS 2149–306, thus their gamma-ray detection was reported for the first time in Beckmann et al. (2010b).

Mrk 421 and Mrk 501 are the only two blazars commonly detected which show a falling spectrum of the spectral energy distribution (e.g. $\log \nu f_{\nu}$ versus $\log \nu$ diagram) in the X-rays, but a rising one in the gamma-rays. All other objects show a rising X-ray ($\Gamma_X < 2$) and a falling gamma-ray spectrum ($\Gamma_{\gamma} > 2$). Although the data are not simultaneous, this indicates that in Mrk 501 and Mrk 421 we detect the synchrotron branch in the hard X-rays, while the gamma-rays are dominated by the inverse Compton component. In the other cases we see in both, the X- and the gamma-rays, the inverse Compton component with the peak of this component lying in between both bands ($200\text{keV} < E_{IC\text{peak}} < 200\text{MeV}$). In these cases, the average difference between the photon indices is $\langle \Delta\Gamma \rangle = 0.9 \pm 0.3$, with the gamma-ray spectra being steeper. Obviously both, the X-ray and the gamma-ray photon index represent an average over many spectral states during which the photon index and flux can vary significantly – see for example the case of the *Fermi*/LAT time resolved spectral analysis of 3C 273 (Soldi et al. 2010a). The two objects with the very steep ($\Gamma_{\gamma} > 3$) photon index in the gamma-rays are QSO B0836+710 and PKS 2149–306, two of the fainter blazars which are not included in the LBAS. It can be expected that the ongoing *Fermi* mission will detect more of these soft gamma-ray blazars which belong to the LBL class as the survey sensitivity improves.

The work we presented in Beckmann et al. (2010b) still has the character of a feasibility study.

Table 4.4: *INTEGRAL* and *Fermi*/LAT average spectra. JEM-X and IBIS/ISGRI luminosities refer to the 3 – 20 keV and 20 – 100 keV energy band, respectively. Luminosities and fluxes are based on single power law model fits and are given in [erg s^{-1}] and [$\text{erg cm}^{-2} \text{s}^{-1}$], respectively. LAT detection significances and photon indices are based on the 0.1 – 200 GeV energy band. The radio galaxy Cen A is included for comparison. Results from Beckmann et al. (2010b).

Name	$\log L_{\text{JEM}}$	$\Gamma_{20-200\text{keV}}$	$\log L_{\text{IBIS}}$	σ_{LAT}	$f_{0.1-100\text{GeV}}$	$\log L_{\text{LAT}}$	Γ_{LAT}
1ES 0033+595	45.08	$3.6^{+0.4}_{-0.3}$	44.36	–			
IGR J03532–6829		$3.5^{+0.7}_{-0.6}$	44.63	–			
PKS 0528+134			47.51	20	6.2×10^{-11}	48.68	2.85 ± 0.06
QSO B0716+714			45.24	85	1.8×10^{-10}	46.90	2.11 ± 0.02
QSO B0836+710		$1.54^{+0.15}_{-0.09}$	47.93	15	2.2×10^{-11}	48.42	3.1 ± 0.1
Mrk 421	44.50	$2.45^{+0.03}_{-0.02}$	44.92	107	3.3×10^{-10}	45.10	1.80 ± 0.02
4C 04.42		$1.20^{+0.16}_{-0.25}$	46.83	12	2.1×10^{-11}	47.23	2.6 ± 0.1
3C 273	45.90	1.92 ± 0.03	46.09	126	3.2×10^{-10}	46.62	2.76 ± 0.02
PKS 1241–399			45.23	–			
3C 279		1.6 ± 0.2	46.40	146	4.0×10^{-10}	47.85	2.36 ± 0.01
H 1426+428	45.48		44.80	13	1.4×10^{-11}	45.01	1.65 ± 0.14
Mrk 501	44.72	2.8 ± 0.3	44.05	49	1.0×10^{-10}	44.71	1.81 ± 0.03
IGR J16562–3301		$1.32^{+0.16}_{-0.07}$	47.80	–			
PKS 1830-211		$1.49^{+0.05}_{-0.07}$	48.19	53	2.2×10^{-10}	49.38	2.69 ± 0.03
RX J1924.8–2914			45.70	17	3.6×10^{-11}	46.39	2.37 ± 0.06
1ES 1959+650		1.9 ± 0.4	44.32	33	6.1×10^{-11}	44.79	2.12 ± 0.05
PKS 2149–306		$1.3^{+0.5}_{-0.9}$	47.74	11	2.1×10^{-11}	48.48	3.1 ± 0.1
BL Lac		$1.8^{+0.4}_{-0.3}$	44.34	41	9.7×10^{-11}	45.32	2.45 ± 0.03
IGR J22517+2217		1.4 ± 0.4	48.43	–			
3C 454.3	47.49	1.58 ± 0.06	47.76	232	7.9×10^{-10}	48.65	2.48 ± 0.01
Cen A (NGC 5128)	42.54	1.84 ± 0.02	42.70	34	8.9×10^{-11}	42.09	2.88 ± 0.05

Although there are only 15 blazars commonly detected between LAT and IBIS/ISGRI, it can be expected that gamma-ray blazars exhibiting a bright outburst will be detectable by *INTEGRAL* within 100 - 200 ks. This offers the possibility to constrain the spectral energy distribution between 3 keV and several hundred keV. I am contributing to a larger group, led by Elena Pian, using *INTEGRAL* ToO observations to follow-up *Fermi* detected blazars in outburst. The proposal was successful in the recent AOs and has been resubmitted to *INTEGRAL*'s AO-8.

In the next section I will describe the example of Cen A (NGC 5128), a radio galaxy which is quasi persistent in the X-ray and gamma-ray energy ranges, showing the potential of combined *INTEGRAL* OMC, JEM-X, and IBIS/ISGRI data sets. With the on-going *Fermi* mission one will be able to detect even a larger fraction of hard X-ray blazars, especially those which show soft gamma-ray spectra such as QSO B0836+710 and PKS 2149-306.

4.8.3 The non-blazar population seen by Fermi

The gamma-ray sky revealed by *CGRO*/EGRET showed only one extragalactic source which was not a blazar, the radio galaxy Cen A (Hartman et al. 1999). With *Fermi*, this picture has changed. Apart from Cen A, at least 9 other radio galaxies have been detected with high confidence: NGC 1275, M 87, 3C 78, PKS 0625-354, NGC 6251, 3C 207, 3C 380, 3C 407, and 3C 120 (Abdo et al. 2010a). In addition, 5 narrow line radio galaxies, 4 radio-loud narrow-line Seyfert 1 (NLSy1) and 10 radio quiet NLSy1 are detectable above 100 MeV. An interesting detection is also the case of 1FGL J1305.4-4928. This source is associated with the Seyfert 2 galaxy NGC 4945, which is also a starburst galaxy and the brightest Seyfert 2 at 100 keV (Done et al. 1996). Future analysis will show whether the gamma-ray emission comes from the galaxy or from the AGN core or both (Abdo et al. 2010a).

The detection of starburst galaxies like M82 and NGC 253 by *Fermi*/LAT, *HESS*, and *VERITAS* indicates that starbursts contribute significantly to the diffuse gamma-ray and neutrino backgrounds. It also implies that relativistic bremsstrahlung and ionization losses compete with synchrotron and Inverse Compton in cooling the cosmic ray electron/positron population in starbursts, with important consequences for the physics of the FIR-radio correlation (Lacki et al. 2010).

In the case of Cen A we have shown the potential of combined *INTEGRAL* and *Fermi* observations (Beckmann et al. 2010b). Although also the data for this low-redshift ($z = 0.0018$) radio galaxy are not taken simultaneously, the source shows low variability in the X-rays and gamma-rays, especially when compared to blazars. For the case of Cen A, also *INTEGRAL*'s monitors JEM-X and OMC provide valuable data. The X-ray and gamma-ray data can be fit by a broken power law model absorbed by $N_H = 1.3 \times 10^{23} \text{ cm}^{-2}$, as shown in Fig. 4.30. The photon index in the X-rays is $\Gamma_X = 1.83 \pm 0.01$, the one in the gamma-rays $\Gamma_\gamma = 2.4 \pm 0.2$ with a break energy at $E_{\text{break}} = 135_{-27}^{+161} \text{ keV}$. Note that the combined fit flattens the result for the gamma-ray photon index, which is $\Gamma_\gamma = 2.88$ when analysing the LAT data alone. The value of the break energy has to be taken with caution, as there are no data available between 500 keV and 200 MeV, and studies of the hard X-ray data do not show a significant cut-off (Soldi et al. 2005). Nevertheless the combined modeling of the data as shown in Fig. 4.31 gives a reliable estimate for the total energy output in the X-ray to gamma-ray domain of this elusive radio galaxy, with a total unabsorbed flux between 1 keV and 10 GeV of $f = 3.3 \times 10^{-9} \text{ erg cm}^{-2} \text{ s}^{-1}$ and a luminosity of $L = 2.4 \times 10^{43} \text{ erg s}^{-1}$. In addition, the peak of the spectral energy distribution which in this model appears to be around a few hundred keV is consistent with the observations by *CGRO* OSSE, COMPTEL, and EGRET, which derived a peak energy around 500 keV for the intermediate emission state (Steinle et al. 1999). The peak flux is lower in our model, with $f_{\nu, \text{peak}} \approx 5 \times 10^{-7} \text{ Jy}$ compared to $f_{\nu, \text{peak}} \approx 8 \times 10^{-7} \text{ Jy}$ during the *CGRO* measurement.

The detection of other radio galaxies as well as of NLSy1 offers a great opportunity to use *INTE-*

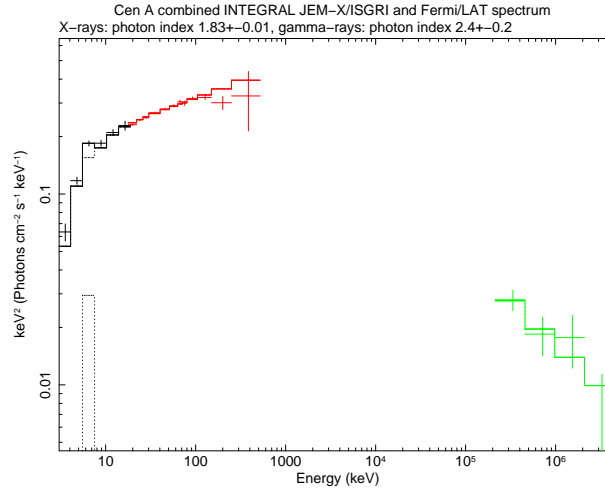


Figure 4.30: The non-simultaneous data of Cen A can be combined using a simple broken power law model.

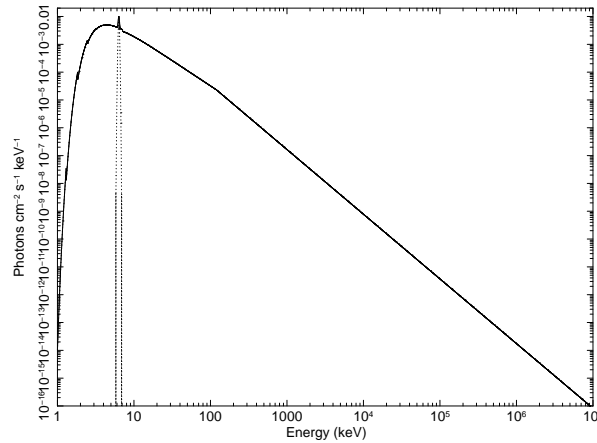


Figure 4.31: The phenomenological model sufficient to represent the X- and gamma-ray data of Cen A connects both energy ranges smoothly.

GRAL data in multiwavelength analysis of gamma-ray sources. These objects also present a challenge to the unified model, as the main question arising is: why do these sources, which are not bona fide blazars, emit in the gamma-ray and even TeV energy range? One possibility is that all these objects are misaligned blazars. But in this case, as the jet is not pointing toward the observer, strong beaming effects cannot account for the observed gamma-ray brightness. Another possibility is that we indeed do not observe the central engine in these cases, but rather the interaction of the jet, or in general material emitted from the AGN core, with the surrounding medium. In the latter case, one would expect that the variability of the gamma-ray emission is less pronounced than in the case of blazars, where the emitting region is comparably small.

Chapter 5

CONCLUSION & OUTLOOK

In this chapter I will summarise the findings from my research work over the past years concerning AGN. After that, I will outline the research projects starting from here and discuss the still open issues.

5.1 Conclusions

5.1.1 Progress concerning the unified scheme

The work concerning the unification of AGN made progress over the last years, in part also through my contributions.

The study of the evolutionary behaviour of X-ray selected blazars (Beckmann & Wolter 2001; Beckmann et al. 2002, 2003b; Beckmann 2003) shows that their evolution is not as strongly negative as indicated by previous studies. The overall luminosity function is consistent with no evolution in the 0.1 – 2.4 keV band as seen by *ROSAT*/PSPC. There is still a difference compared to the luminosity function of FSRQ and LBL, which seem to show a positive evolution, indicating that they have been more luminous and/or numerous at cosmological distances. We indicated a scenario in order to explain this discrepancy, in which the high luminous FSRQ develop into the fainter LBL and finally into the BL Lac objects with high frequency peaks in their spectral energy distribution but overall low bolometric luminosity.

Studying the variability pattern of hard X-ray selected Seyfert galaxies, we actually found differences between type 1 and type 2 objects, in the sense that type 2 seemed to be more variable (Beckmann et al. 2007a). This breaking of the unified model is caused by the different average luminosity of the absorbed and unabsorbed sources, as discussed in Sect. 4.7.3. This can be explained by a larger inner disk radius when the AGN core is most active (the so-called receding disc model).

The work on the sample characteristics of hard X-ray detected AGN also led to the proof that the average intrinsic spectra of type 1 and type 2 objects are the same when reflection processes are taken into account (Beckmann et al. 2009d). This also explains why in the past Seyfert 2 objects were seen to have harder X-ray spectra than Seyfert 1, as the stronger reflection hump in the type 2 objects makes the spectra appear to be flatter, although the underlying continuum is the same.

Further strong evidence for the unification scheme comes from the observation of a fundamental plane which connects type 1 and type 2 objects smoothly (Beckmann et al. 2009d). In addition, in the case of the Seyfert 1.9 galaxy MCG–05–23–016 I showed that the spectral energy distribution of this source and its accretion rate is similar to that of a Galactic binary (Beckmann et al. 2008a).

Throughout the studies I have shown that the intrinsic spectral shape appears to be very stable on

weeks to year time scale (Beckmann et al. 2004d, 2005b, 2007b, 2008a). This implies that the overall geometry of the AGN over these time scales did not change dramatically. The variations in intensity can then be explained in two ways: either the amount of material emitting the hard X-rays varies, or the amount of plasma visible to the observer varied, e.g. through different orientation of the disk with respect to the observer. In an upcoming paper we will show though, that NGC 4151 indeed also shows different spectral states, similar to the low-hard versus high-soft spectra in Galactic black hole binaries (Lubiński et al. 2010).

5.1.2 Impact on studies of the cosmic X-ray background

The work on the luminosity function of AGN at hardest X-rays (Beckmann et al. 2006d) had a large impact on our understanding of the cosmic X-ray background. As this was the first study of its kind, it showed for the first time that indeed the fraction of highly obscured Compton thick AGN is much lower than expected before the launch of *INTEGRAL* and *Swift*. The X-ray luminosity function we revealed is indeed not consistent with the source population seen by *INTEGRAL* (Beckmann et al. 2006a, 2009d; Sazonov et al. 2007) and *Swift* (Tueller et al. 2008) being the only contributors to the cosmic hard X-ray background. Our work on the luminosity function triggered several other studies on this issue. The subsequent derived luminosity functions by other groups (Sazonov et al. 2007; Tueller et al. 2008; Paltani et al. 2008) are consistent with our findings.

This also gave rise to an increased interest in the exact shape of the Cosmic X-ray background around its peak at 30 keV, triggering several attempts to a new measurement. Background studies were presented based on a Earth-occultation observation by *INTEGRAL* (Churazov et al. 2007, 2008; Türler et al. 2010) and by *Swift* (Ajello et al. 2008).

5.1.3 Outlining the connection to the gamma-rays

The understanding of the emission processes in AGN requires knowledge over a wide range of the spectral energy distribution (SED). In studies using *CGRO/EGRET* and *Fermi/LAT* data I derived the SED for blazars and non-blazars towards the gamma-ray range (Beckmann 2003; Beckmann et al. 2004b, 2010b). The work on the LAT data not only presented the gamma-ray detection of five gamma-ray blazars (QSO B0836+710, RX J1111.5+3452, H 1426+428, RX J1924.8–2914, PKS 2149–306) for the first time, but also showed the potential in the combination of *INTEGRAL* and *Fermi* data. In the case of Cen A I derived the total energy output of the inverse Compton component based on the combined LAT, ISGRI, and JEM-X data, showing evidence for a spectral break at several hundred keV (Beckmann et al. 2010b).

In addition I successfully showed that gamma-ray blazars can be predicted through the study of their synchrotron branch at energies below 2 keV (Beckmann 2003 and this work).

5.2 Open questions

Many issues in our understanding of the AGN phenomenon are still open. Here I outline some of them and give some outlook on how they might be tackled.

- **Unification of blazars:** The link of BL Lac objects to the more powerful FSRQ is still not well established. Is there indeed an evolution of the FSRQs toward the BL Lac as suggested e.g. in Beckmann et al. (2003b)? The *ROSAT* All Sky Survey was the most valuable tool in the recent years to provide large samples of X-ray selected BL Lac objects. But the limited

sensitivity also limited the survey studies of BL Lacs to redshifts $z \ll 0.5$. With the launch of *Spectrum-Roentgen-Gamma* (SRG) and its survey of the X-ray sky in the 0.1 – 10 keV band through eROSITA, we will have access to a deeper view into the X-ray universe. This will allow us to study the luminosity function of BL Lacs to cosmological distances of $z = 1 - 2$. A large effort by ground based telescopes will be necessary in order to derive the redshifts of the X-ray detected BL Lacs. The result will either be that we can tie together the luminosity functions of BL Lacs and FSRQ at high redshifts – or that we will have to revise our view on these enigmatic objects.

- **Intrinsic hard X-ray spectrum:** As shown in this work, only at hardest X-rays we have a clear view on the central engine of AGN, and only here we can study their intrinsic properties. *INTEGRAL*, *Swift*, and *Suzaku* reveal the properties of some dozen bright Seyfert galaxies. But in order to verify that we are not driven by selection effects in the sense that these few AGN are indeed representative for the whole population, spectral studies of fainter objects in the hard X-ray band are necessary. *Simbol-X* would have been the perfect tool in order to achieve this goal (Beckmann et al. 2009b). It has to be seen whether *NuSTAR* will be able to do a similar work in its more narrow band from 5 keV up to 80 keV. On the long term, we will need hard X-ray telescopes with higher throughput though, thus *Astro-H* and *IXO* are indeed required to tackle these questions.
- **Hard X-ray luminosity function:** *INTEGRAL* and *Swift* revealed to us the local hard X-ray luminosity function. As valuable as this is, we need to go further in order to see what happens to the source population when going to higher redshifts, back in time. A first step is to achieve an ultra-deep field using IBIS/ISGRI, aiming at an effective exposure time > 10 Ms in an extragalactic field (Beckmann et al. 2010c). This will serve as a true legacy of the *INTEGRAL* project, providing for the near future the deepest hard X-ray sky survey achievable. In order to go to redshifts of $z \approx 1$, more sensitive pencil beam surveys are required. *NuSTAR* might be able to achieve this, but also here, *Astro-H* and *IXO* will provide us with the necessary sensitivity to study cosmological distances.
- **Evolution of absorption:** As we do not see the heavily obscured AGN in the local universe, they might reside at cosmological distances. Also this hypothesis can be tackled in a first step by an *INTEGRAL* ultra deep field, and in the future through hard X-ray observations by *NuSTAR*, *Astro-H*, and *IXO*.
- **Cosmic X-ray background:** Other sources might contribute to the CXB around its peak. Ajello et al. (2009) suggested that blazar contribute significantly at hardest X-rays. A deeper survey is needed to verify this though. In addition, *INTEGRAL* can be used to better constrain the CXB emission around its peak through further Earth-occultation observations.
- **Influence of absorption on iron $K\alpha$ and the soft excess:** An ongoing discussion evolves around the question, how absorption processes influence the measurements of the spin of black holes through the relativistic iron $K\alpha$ lines in AGN. Another, related issue, is the soft X-ray excess, which appears to dominate the spectrum in a large fraction of AGN below 1 – 2 keV. In both cases, absorption might play an important role, as it can modify the underlying continuum in a way that appears similar to the effects of line broadening and of an extra emission component at soft X-rays. High resolution spectroscopy as provided through *Astro-H* will be able to settle this point.

- **Non-blazar AGN at gamma-rays and in the TeV:** The observation of AGN at gamma-rays experiences a break-through in the GeV energy range through observations by *Fermi*/LAT. The source numbers exceed already 1500 objects, among them now also more and more non-blazar AGN. A similar development, i.e. the discovery of non-beamed sources, can be seen in the TeV domain, mainly through the observations by *HESS*, *MAGIC*, and *VERITAS*. The main question in this area is, why do we detect non-blazar type sources at these high energies, where one would expect the spectrum to fall off rapidly due to limited electron temperature in the corona and due to Klein-Nishina limit which causes the total cross section to fall off with increasing energy. High spatial resolution observations of *Fermi* seem to indicate that the emission in some cases (e.g. Cen A) does not appear to originate only in the AGN core, but also on the extended features, e.g. jets and lobes, pointing toward a shock-induced origin of the gamma-ray emission. Further observational and theoretical work is necessary to clarify these aspects. The upcoming *Cherenkov Telescope Array* (CTA) will provide us with > 1000 sources in the TeV domain, thus enabling us to test the models further into the TeV range.
- **AGN variability at hard X-rays:** Little progress has been made since our study using *Swift*/BAT data of 44 AGN (Beckmann et al. 2007a). It has to be investigated whether the indications we saw for a correlation of absorption and variability strength can be verified using a better sampled data set, and what the role of luminosity is in this context.

5.3 Future projects

5.3.1 Research

My current and future research projects revolve around the open issues outlined in Sect. 5.2.

Some of the questions can still be answered by *INTEGRAL* and *Swift*. Throughout the years of *INTEGRAL* observations I was involved in pushing for extragalactic deep fields, for example in the Virgo region and in the XMM-LSS field. We will continue to try to achieve the deepest extragalactic field possible. This should give us a first indication of what the evolution of the X-ray luminosity function in redshift space looks like. It will also give us a hint whether absorption indeed becomes more or less important towards cosmological distances.

In our understanding of the intrinsic spectrum of AGN, it is important to have also single source studies of the brightest objects along side with the statistical studies we did. We will observe the remaining brightest AGN without sufficient *INTEGRAL* coverage in order to get the best hard X-ray spectral survey of Seyfert type AGN achievable today. One question we can already tackle, is the topic of spectral states in AGN. Similar to Galactic black holes, the question is whether also super-massive black holes show the low/hard versus high/soft state behaviour. This is indeed seen in the case of NGC 4151 (Lubiński et al. 2010). A similar result seems to emerge from our *INTEGRAL* studies on NGC 2110 (Beckmann & Do Cao 2011). For *INTEGRAL*'s AO-8 I have submitted a proposal in order to study spectral states in the Seyfert 2 galaxy NGC 2992, which seems to show a state change over the past 5 years as seen in *Swift*/BAT and *RXTE*/ASM long term monitoring.

With the many open issues in the hard X-ray band concerning AGN, it is important to keep pushing and working for the new hard X-ray missions to take place. The community has to continue to show their great interest and support for this kind of satellites, and *IXO* (Fig. 5.1) and *Astro-H* will be at the centre of focus here. Thus, one of my on-going projects is to stay involved in preparation and realisation of these missions.

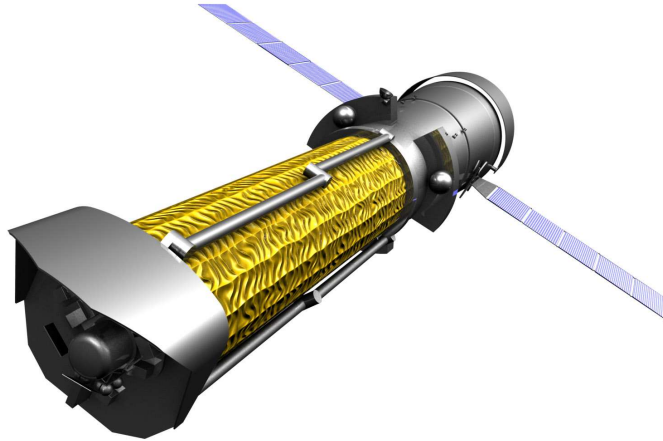


Figure 5.1: Artist's impression of the *IXO* spacecraft. It will provide an effective mirror area of 3 m^2 (at 1.25 keV) and a spectral resolution of $\Delta E \simeq 10 \text{ eV}$ and spatial resolution of 5 arcsec at the iron $K\alpha$ line.

These two missions are still several years in the future. Meanwhile, I will make use of the public data of the *NuSTAR* mission (Koglin et al. 2009), which is foreseen to be launched in August 2011. *NuSTAR* will use mirrors to observe in the hard X-ray band covering the energy range $5 - 80 \text{ keV}$ with a field of view of $13' \times 13'$, an energy resolution of 1.2 keV at 68 keV , and an angular resolution of $7.5''$ (FWHM). Figure 5.2 shows a simulated spectrum of a *NuSTAR* on-axis observation of the Seyfert 1.9 galaxy MCG-05-23-016. It is obvious that the determination of the iron $K\alpha$ line is not one of the strengths of *NuSTAR*, as it is difficult to determine the underlying continuum at this energy and due to the moderate energy resolution. Nevertheless, the coverage from $5 - 80 \text{ keV}$ will allow us to determine the strength of the Compton hump more precisely than through *INTEGRAL* IBIS/ISGRI observations. It also has to be noted that the spectrum shown in Fig. 5.2 is based on only 10 ks of observing time.

Through the deep extragalactic fields *NuSTAR* will observe, we will build the X-ray luminosity function and study also the evolution of absorption. One has to be aware though that the *NuSTAR* team is likely to proceed faster on this field than external competitors, but in any case it is important to gain experience in the field of hard X-ray spectroscopy and imaging using mirrors. And also in the case of *INTEGRAL* we were more efficient to extract the results on AGN concerning luminosity function, spectroscopic catalogue, and single source studies than the groups dedicated to this task in the first place.

In the field of the study of the spectral energy distribution of non-blazar AGN toward the gamma-rays, *Fermi*/LAT data are already available on a number of sources. I will study these sources, using the available data and, in the case of the NLSy1 detected in LAT, apply for additional hard X-ray observations by *INTEGRAL*. The data enable us to outline the complete high-energy branch in the detected objects and to tackle the questions, what is the driving emission mechanism. In order to progress on this point, I offer a PhD project within the high-energy group at the APC. The proposal for this PhD has been selected by the École Doctorale with A-priority. Once the École Doctorale has makes its decision and a qualified student is found, the successful candidate will start with this investigation in September 2010.

On the important topic of hard X-ray variability, we have already started studying a larger sample of *Swift*/BAT detected AGN (Soldi et al. 2010b). This study should lead to a publication soon, and

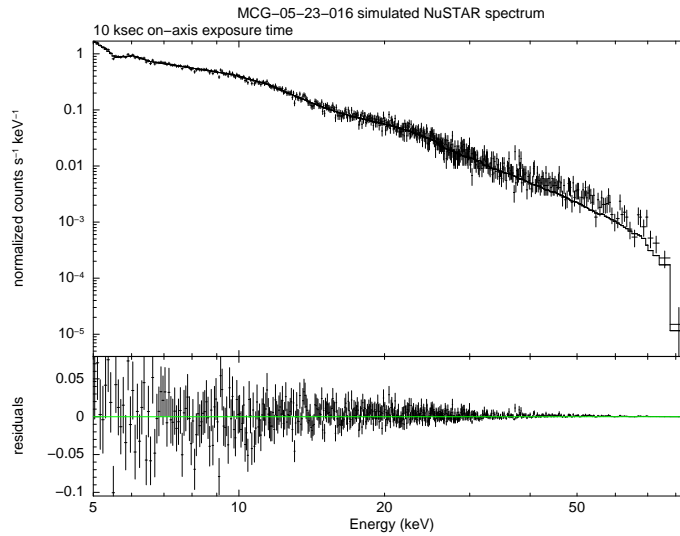


Figure 5.2: Simulated *NuSTAR* spectrum for an on-axis 10 ksec observation of MCG-05-23-016.

can then be also connected to the spectral energy distribution investigation, by answering the question: do the non-blazar AGN detected at gamma-rays show different temporal behaviour compared to the gamma-ray quiet AGN? This can be an important step forward in our understanding of the mechanism behind the high-energy emission.

5.3.2 Enabling science: the François Arago Centre

Many of the upcoming missions provide large amounts of data and/or require heavy processing. At the same time as multi-wavelength observations of celestial objects become more and more important in order to understand and pinpoint the underlying physical mechanisms, the data analysis of each of the instruments involved becomes more and more complex. Thus there is general trend of rapidly increasing data sets of increasing complexity, which are difficult to analyse and to interpret. With the CC-IN2P3 computing centre in Lyon the French scientific community has access to excellent computing and data storage facilities. In order to facilitate the access to the computing power in Lyon, to help with local processing needs and to support the community with temporary work, computing, and data storage space, the APC has initiated the foundation of a data and computing centre in the Ile de France. This initiative is strongly supported by CNRS/IN2P3, CNES, CEA/Saclay, Observatoire de Paris, Université Paris 7 Denis Diderot, and the IPGP. The centre, called the *François Arago Centre*¹ after the French Catalan mathematician, physicist, astronomer and politician François Jean Dominique Arago (1786 - 1853), is right now being installed close to the APC in 13 Rue Watt, in the 13^{eme} arrondissement of Paris. A computing farm, consisting of two Dell computer racks with 600 CPUs and 100 TByte of hard disk space is placed at the heart of the centre. My task as responsible scientist within the François Arago Centre is to ensure a smooth operation, to negotiate with the groups interested in using the centre, and to apply my knowledge and expertise in running and maintaining a scientific data, computing, and analysis centre.

The first project at the François Arago Centre will be the support of the LISA Pathfinder mission. LISA Pathfinder (formerly known as SMART-2), the second of the ESA Small Missions for Advanced Research in Technology, is a dedicated technology demonstrator for the joint ESA/NASA

¹<http://www.apc.univ-paris7.fr/FACe>

Laser Interferometer Space Antenna (LISA) mission. The technologies required for LISA are many and extremely challenging. This coupled with the fact that some flight hardware cannot be tested on ground due to the earth induced noise, led to the LISA Pathfinder (LPF) mission being implemented to test the critical LISA technologies in a flight environment. The scientific objective of the LISA Pathfinder mission consists then of the first in-flight test of gravitational wave detection metrology.

In order to analyse the incoming data from the experiment in near-real time and to be able to respond to the needs of the mission and the community involved, the François Arago Centre will be used. Its main purpose will be to provide the environment for the data exploitation during the mission, providing also meeting facilities, and a 24/7 access to data and analysis tools. This centre will function as complementary data centre to the *Science and Technology Operations Centre* (STOC) which is build up by ESA at ESAC in Villafranca. I am leading the group, which is defining the work sharing between the STOC and the François Arago Centre.

Two other projects, in which teams at the APC are already actively involved, will also be handled at the François Arago Centre starting this summer: *INTEGRAL* and *HESS*. In these two cases, the François Arago Centre will provide local computing power as well as easy access to CC-IN2P3. For the *Institut De Physique Du Globe De Paris* (IPGP) the François Arago Centre will support the Geoscope observatory, the French global network of broad band seismic stations, and will be part of its data centre. The usage of the centre by other projects is right now under discussion.

In the near future we will see plenty of extremely complex missions take shape. *CTA* will reveal to us the TeV sky in detail and in large numbers of sources, enabling us to study AGN and Galactic sources at highest energies. *Euclid* will map the geometry of the dark Universe, *Spectrum-Roentgen-Gamma*, *IXO* and *Astro-H* will open the field of X-ray astrophysics to truly cosmological distances, and finally *LISA* will show us a completely uncharted parameter space through observations of gravitational waves. Planetary and Earth-observing satellites will help us to understand the mechanisms which drive processes in the solar system and within the fragile space inhabited by humans. The François Arago Centre will be ready to take up the challenge to help the scientific community to make best use of the incoming data and to explore and understand the Universe we live in.

Même pour ceux qui ne jugent des découvertes que par leur utilité directe, l'astronomie sera toujours la science plus digne des nobles efforts et de l'application soutenue de l'intelligence de l'homme.

François Arago

Chapter 6

LIST OF PUBLICATIONS AND CONFERENCE CONTRIBUTIONS

6.1 Articles in refereed international journals

- Pian, Ubertini, Bazzano, **Beckmann**, et al. 2011, “INTEGRAL observations of the GeV blazar PKS 1502+106 and of the hard X-ray bright Seyfert galaxy Mkn 841”, *Astronomy & Astrophysics*, 526, 125
- Ricci, **Beckmann**, Audard, Courvoisier 2010, “Multi-zone warm and cold clumpy absorbers in 3 Seyfert galaxies”, *Astronomy & Astrophysics*, 518, 47
- Lubiński, Zdziarski, Walter, Paltani, **Beckmann**, et al. 2010, “Extreme flux states of NGC 4151 observed with INTEGRAL”, *MNRAS*, 408, 1851
- Savchenko, Neronov, **Beckmann**, Produit, Walter 2010, “Exceptional flaring activity of the anomalous X-ray pulsar 1E 1547.0-5408”, *Astronomy & Astrophysics*, 510, 77
- Beckmann**, Soldi, Ricci, et al. 2009, “The Second INTEGRAL AGN Catalogue”, *Astronomy & Astrophysics* 505, 417
- Petry, **Beckmann**, Halloin, Strong 2009, “Soft gamma-ray sources detected by *INTEGRAL*”, *Astronomy & Astrophysics*, 507, 549
- Ibarra, Kuulkers, Osborne, Page, Ness, Saxton, Baumgartner, **Beckmann**, et al. 2009, “Pre-nova X-ray observations of V2491 Cyg (Nova Cyg 2008b)”, *Astronomy & Astrophysics*, 497, L5
- Fiocchi, Natalucci, Chenevez, Bazzano, Tarana, Ubertini, Brandt, **Beckmann**, et al. 2009, “Renewed Activity from the X-ray Transient SAX J1810.8-2609 with INTEGRAL”, *Astrophysical Journal*, 693, 333
- Beckmann**, Courvoisier, Gehrels, et al. 2008, “The efficient low-mass Seyfert MCG–05–23–016”, *Astronomy & Astrophysics*, 492, 93
- Hjalmarsdotter, Zdziarski, Larsson, **Beckmann**, McCollough, Hannikainen, Vilhu 2008, “The nature of the hard state of Cygnus X-3”, *MNRAS*, 384, 278
- Beckmann**, Barthelmy, Courvoisier, et al. 2007, “Hard X-ray Variability of AGN”, *Astronomy &*

Astrophysics, 475, 827

- Beckmann**, Soldi, Belanger, et al. 2007, “Cygnus X-3 transition from ultrasoft to hard state”, *Astronomy & Astrophysics*, 473, 903
- Beckmann**, Tueller, Gehrels, 2007, “The 1 keV to 200 keV X-ray spectrum of NGC 2992 and NGC 3081”, *Astrophysical Journal*, 666, 122
- Bodaghee, Courvoisier, Rodriguez, **Beckmann**, et al. 2007, “A description of sources detected by INTEGRAL during the first 4 years of observations”, *Astronomy & Astrophysics*, 467, 585
- Walter, Lubinski, Paltani, Produit, Zurita, Kuulkers, **Beckmann**, et al. 2007, “IGR J17497-2821: a new X-ray Nova”, *Astronomy & Astrophysics Letters*, 461, L17
- Chernyakova, Neronov, Courvoisier, Türler, Soldi, **Beckmann**, et al. 2007, “2003 - 2005 INTEGRAL and XMM-Newton observation of 3C 273”, *Astronomy & Astrophysics*, 465, 147
- Shaposhnikov, Swank, Shrader, Rupen, **Beckmann**, Markwardt, Smith 2007, “GRO J1655–40: Early Stage of the 2005 Outburst”, *Astrophysical Journal*, 635, 434
- Beckmann**, Soldi, Shrader, Gehrels, Produit 2006, “The Hard X-ray 20-40 keV AGN Luminosity Function”, *Astrophysical Journal*, 652, 126
- Beckmann**, Shrader, Gehrels, Soldi 2006, “The First INTEGRAL AGN catalog”, *Astrophysical Journal*, 638, 642
- Paizis, Farinelli, Titarchuk, Courvoisier, Bazzano, **Beckmann**, et al. 2006, “Average hard X-ray emission from NS LMXBs: Observational evidence of different spectral states in NS LMXBs”, *Astronomy & Astrophysics*, 459, 187
- Pian, Foschini, **Beckmann**, et al. 2006, “INTEGRAL observations of the blazar 3C 454.3 in outburst”, *Astronomy & Astrophysics*, 449, L21
- Beckmann**, Shrader, Gehrels, et al. 2005, “The high energy spectrum of NGC 4151”, *Astrophysical Journal*, 634, 939
- Soldi, **Beckmann**, Bassani, et al. 2005, “INTEGRAL observations of AGN in the Galactic Plane”, *Astronomy & Astrophysics*, 444, 431
- Ebisawa, Tsujimoto, Paizis, **Beckmann**, et al. 2005, “Chandra Deep X-Ray Observation of a Typical Galactic Plane Region and Near-Infrared Identification”, *Astrophysical Journal*, 635, 214
- Beckmann**, Kennea, Markwardt, et al. 2005, “Swift, INTEGRAL, RXTE, and Spitzer reveal IGR J16283-4838”, *Astrophysical Journal*, 631, 506
- Camero Arranz, Wilson, Connell, Martinez Nunez, Blay, **Beckmann**, Reglero 2005, “INTEGRAL observations of the Be/X-ray binary EXO 2030+375 during outburst”, *Astronomy & Astrophysics*, 441, 261
- Hannikainen, Rodriguez, Vilhu, **Beckmann**, et al. 2005, “Characterizing a new class of variability in GRS 1915+105 with simultaneous INTEGRAL observations”, *Astronomy & Astrophysics*, 439, 995

- Rodriguez, Cabanac, Hannikainen, **Beckmann**, Shaw, Schultz, 2005, “Unveiling the Nature of the High Energy Source IGR J19140+0951”, *Astronomy & Astrophysics*, 432, 235
- Pian, Foschini, **Beckmann**, et al. 2005, “INTEGRAL observations of the field of the BL Lacertae object S5 0716+714”, *Astronomy & Astrophysics*, 429, 427
- Masetti, Foschini, Palazzi, **Beckmann**, et al. 2004, “Serpens X-1 observed by INTEGRAL”, *Astronomy & Astrophysics*, 423, 651
- Favre, Petrucci, **Beckmann**, Courvoisier 2004, “BeppoSAX observation of the quasar Markarian 205”, *Astronomy & Astrophysics*, 421, 91
- Beckmann**, Favre, Tavecchio, et al. 2004, “The Gamma-ray bright BL Lac object RX J1211+2242”, *Astrophysical Journal*, 608, 692
- Beckmann**, Gehrels, Favre, et al. 2004, “INTEGRAL and XMM-Newton spectral studies of NGC 4388”, *Astrophysical Journal*, 614, 641
- von Kienlin, **Beckmann**, Rau, et al., 2003, “INTEGRAL Spectrometer SPI’s GRB detection capabilities”, *Astronomy & Astrophysics* 411, L299
- Diehl, Baby, **Beckmann**, et al., 2003, “SPI-Specific Analysis Method and Software Overview”, *Astronomy & Astrophysics* 411, L117
- Vilhu, Hjalmarsdotter, Zdziarski, **Beckmann**, et al., 2003, “First INTEGRAL observations of Cygnus X-3”, *Astronomy & Astrophysics* 411, L405
- Winkler, Gehrels, Schönfelder, **Beckmann**, et al., 2003, “First results from the INTEGRAL Galactic plane scans”, *Astronomy & Astrophysics* 411, L349
- Pottschmidt, Wilms, Chernyakova, **Beckmann**, et al. 2003, “INTEGRAL-RXTE observations of Cygnus X-1”, *Astronomy & Astrophysics* 411, L383
- Mereghetti, Götz, Tiengo, **Beckmann**, et al., 2003, “INTEGRAL and XMM-Newton observations of the weak GRB 030227”, *Astrophysical Journal* 590, L73
- Della Ceca, Braitto, **Beckmann**, et al., 2003, “A Hard Medium Survey with ASCA. IV: the Radio-Loud Type 2 QSO AXJ0843+2942”, *A&A* 406, 555
- Beckmann**, Engels, Bade, Wucknitz, 2003, “The HRX-BL Lac sample - unification of HBLs and LBLs”, *Astronomy & Astrophysics*, 401, 924
- Beckmann**, Borkowski, Courvoisier, et al., 2003, “Time resolved spectroscopy of GRB030501 using INTEGRAL”, *Astronomy & Astrophysics* 411, L327
- Paizis, **Beckmann**, Courvoisier, et al., 2003, “First INTEGRAL Observations of Eight Persistent Neutron Star Low Mass X-ray Binaries”, *Astronomy & Astrophysics* 411, L363
- Courvoisier, **Beckmann**, Bourban, et al., 2003, “Simultaneous observations of the quasar 3C 273 with INTEGRAL, XMM-Newton and RXTE”, *Astronomy & Astrophysics* 411, L343
- Courvoisier, Walter, **Beckmann**, et al., 2003, “The INTEGRAL Science Data Centre”, *Astronomy & Astrophysics* 411, L53

- Malaguti, Bazzano, **Beckmann**, et al., 2003, “GRB021125: the first GRB imaged by INTEGRAL”, *Astronomy & Astrophysics* 411, L307
- Mereghetti, Götz, **Beckmann**, et al., 2003, “GRB 021219: the first Gamma-Ray Burst localized in real time with IBAS”, *Astronomy & Astrophysics* 411, L311
- von Kienlin, **Beckmann**, Covino, et al., 2003, “GRB030320: a long gamma-ray burst detected at the edge of the field of view”, *Astronomy & Astrophysics* 411, L321
- Beckmann**, Wolter, Celotti, et al., 2002, “BeppoSAX Spectral Survey of BL Lacs - new spectra and results”, *Astronomy & Astrophysics* 383, 410
- Della Ceca, Pellegrini, Bassani, **Beckmann**, et al., 2001, “Unveiling the AGN powering the “Composite” Seyfert/Star-forming galaxy NGC 7679: BeppoSAX and ASCA results”, *Astronomy & Astrophysics* 375, 781
- Beckmann**, 2000, “Absolute photometry of 49 X-ray selected BL Lac objects”, *Blazar Data*, Vol. 2, 3
- Wisotzki, Christlieb, Bade, **Beckmann**, et al., 2000, “The Hamburg/ESO survey for bright QSOs. III. A large flux-limited sample of QSOs”, *Astronomy & Astrophysics*, 358, 77
- Pursimo, Takalo, Sillanpää, **Beckmann**, et al., 2000, “Intensive Monitoring of OJ 287”, *Astronomy & Astrophysics Supplement* 146, 141
- Watson, McBreen, Smith, Hanlon, Tashiro, Foley, Metcalfe, **Beckmann**, Sanchez, Terasranta, 1999, “Simultaneous Multifrequency Observations of the BL Lac MS0205.7+3509”, *Astronomy & Astrophysics*, 345, 414
- Beckmann**, Bade, Wucknitz, 1999, “The extreme high frequency peaked BL Lac 1517+656”, *Astronomy & Astrophysics*, 352, 395
- Wu, Bade, **Beckmann**, 1999, “X-ray luminous radio-quiet high redshift QSOs in the ROSAT All-Sky Survey”, *Astronomy & Astrophysics*, 347, 63
- Sanchez-Fernandez, Castro-Tirado, Duerbeck, Mantegazza, **Beckmann**, Burwitz, Bianchini, Della Valle, Dirsch, Hook, Yan, Gimenez, 1999, “Optical observations of the black hole candidate XTE J1550-564 during the September/October 1998 outburst”, *Astronomy & Astrophysics*, 348, L9
- Bade, **Beckmann**, Douglas, et al., 1998, “On the evolutionary behavior of BL Lac objects”, *Astronomy & Astrophysics*, 334, 459
- Bade, Engels, Voges, **Beckmann**, et al., 1998, “The Hamburg/RASS Catalogue of optical identifications”, *Astronomy & Astrophysics Supplement*, 127, 145
- Reimers, Jordan, **Beckmann**, et al., 1998, “Four magnetic DB white dwarfs discovered by the Hamburg/ESO survey”, *Astronomy & Astrophysics*, 337, L13

6.2 Invited talks at international conferences

“Unification of AGN at hard X-rays”, invited review, 218th meeting of the American Astronomical Society (AAS) in Boston, USA, May 2011

“INTEGRAL – operating high-energy detectors for five years in space”, invited review, proceedings of the 10th ICATPP conference, Como, Italy, October 8-12, 2007

“INTEGRAL Studies of AGN”, invited talk at the 207th meeting of the American Astronomical Society (AAS) in Washington D.C., January 2006

6.3 Refereed conference proceedings

Beckmann & Do Cao 2011, “The elusive radio loud Seyfert 2 galaxy NGC 2110”, proc. of the 8th INTEGRAL Workshop Dublin 2010, arXiv:1102.4974

Beckmann, Jean, Lubiński, Soldi, Terrier 2011, “Extended emission and spectral break in Cen A”, proc. of the 8th INTEGRAL Workshop Dublin 2010

Soldi, **Beckmann**, Gehrels, et al. 2011, “Compton processes in the bright AGN MCG+8–11–11”, proc. of the 8th INTEGRAL Workshop Dublin 2010, arXiv:1102.4959

Fedorova, **Beckmann**, Neronov, Soldi 2011, “Spectral variability in the Seyfert 2 galaxy NGC 4388”, proc. of the 8th INTEGRAL Workshop Dublin 2010

Lebrun, Aharonian, **Beckmann**, et al. 2011, “CAPSiTT: a sensitive 100 keV - 100 MeV all-sky survey”, proc. of the 8th INTEGRAL Workshop Dublin 2010

Paltani, Lubinski, Zdziarski, Walter, **Beckmann**, et al. 2011, “INTEGRAL monitoring of NGC 4151: Evidence for a truncated disk?”, proc. of the 8th INTEGRAL Workshop Dublin 2010

Beckmann, Ricci, Soldi, et al. 2010, “Lessons learnt from INTEGRAL AGN”, proc. of the INTEGRAL Workshop Otranto 2009

Soldi, Ponti, **Beckmann**, Lubinski 2010, “AGN variability at hard X-rays”, proc. of the INTEGRAL Workshop Otranto 2009

Beckmann, Soldi, Ricci, et al. 2010, “The unified scheme seen with INTEGRAL detected AGN”, proceedings of the Bologna 2009 X-ray conference

Beckmann, Courvoisier, Gehrels, et al. 2009, “Compton reflection in AGN with Simbol-X”, American Institute of Physics Conference Series, 1126, 141

Beckmann, Soldi, Courvoisier, et al. 2009, “The efficient low-mass Seyfert MCG-05-23-016”, proc. of the 7th INTEGRAL Workshop, September 8-11, 2008, Copenhagen, Denmark

Ricci, **Beckmann**, Courvoisier, et al. 2009, “Multi-wavelength studies of the broad line radio galaxies IGR J21247+5058 and 3C 390.3”, proc. of the 7th INTEGRAL Workshop, September 8-11, 2008, Copenhagen, Denmark

Skinner, Tueller, **Beckmann**, et al. 2009, “Long term monitoring of INTEGRAL sources with Swift/BAT”, proc. of the 7th INTEGRAL Workshop, September 8-11, 2008, Copenhagen, Den-

mark

- Beckmann**, Shrader, Gehrels, Soldi, Produit 2007, “The Hard X-ray Luminosity Function of INTEGRAL Detected AGN”, proceedings of the 6th INTEGRAL Workshop, Moscow, July 2-8, 2006, ESA SP-622
- Bodaghee, Courvoisier, Rodriguez, **Beckmann**, et al. 2007, “Populations Studies of INTEGRAL Sources”, proceedings of the 6th INTEGRAL Workshop, Moscow, July 2-8, 2006, ESA SP-622
- Vilhu, Paizis, Hannikainen, Schultz, **Beckmann** 2007, “The Spreading Layer of GX 9+9”, proceedings of the 6th INTEGRAL Workshop, Moscow, July 2-8, 2006, ESA SP-622
- Paizis, Farinelli, Titarchuck, Courvoisier, Bazzano, **Beckmann**, et al. 2007, “Average hard X-ray emission from NS LMXBs”, proceedings of the conference “The Multicoloured Landscape of Compact Objects and their Explosive Origins”, Cefalu, Sicily, June 11-24, 2006
- Beckmann**, Gehrels, Favre, et al. 2004, “NGC 4388 - Spectral Studies of the first Seyfert 2 seen by INTEGRAL”, proceedings of the 5th INTEGRAL workshop, Munich 2004
- Camero Arranz, Reig, Connell, Martinez Nunez, Blay, Reglero, **Beckmann** 2004, “INTEGRAL observations of EXO 2030+375 during outburst”, proceedings of the 5th INTEGRAL workshop, Munich 2004
- Sturmer, **Beckmann**, Bykov, Lebrun, Terrier 2004, “INTEGRAL Studies of Nonthermal Emission from the Supernova Remnants Cassiopeia A, CTA 1, and MSH 11-61-A”, proceedings of the 5th INTEGRAL workshop, Munich 2004
- Hjalmarsdotter, Zdziarski, Paizis, **Beckmann**, Vilhu, 2004, “INTEGRAL observations of Cygnus X-3”, proceedings of the 5th INTEGRAL workshop, Munich 2004
- Paizis, Courvoisier, Vilhu, **Beckmann**, et al. 2004, “The INTEGRAL LMXRB Monitoring Program”, proceedings of the 5th INTEGRAL workshop, Munich 2004
- Shaw, Mowlavi, Ebisawa, **Beckmann**, et al. 2004, “Scientific performance of the ISDC Quick Look Analysis”, proceedings of the 5th INTEGRAL workshop, Munich 2004
- Piraino, Santangelo, Ferrigno, **Beckmann**, et al. 2004, “INTEGRAL monitoring of the bright neutron star low mass X-ray binaries: preliminary results on GX 17+2”, proceedings of the 5th INTEGRAL workshop, Munich 2004
- Chernyakova, Favre, Courvoisier, **Beckmann**, et al. 2004, “INTEGRAL and RXTE observations of the broad-line radio galaxy 3C 111”, proceedings of the 5th INTEGRAL workshop, Munich 2004
- Ebisawa, Paizis, Courvoisier, **Beckmann**, et al. 2004, “A Chandra Deep X-ray Exposure on the Galactic Plane and Near Infrared Identification”, proceedings of the 5th INTEGRAL workshop, Munich 2004
- Pottschmidt, Wilms, Nowak, **Beckmann**, et al. 2004, “INTEGRAL-RXTE observations of Cygnus X-1”, proceedings of the 5th INTEGRAL workshop, Munich 2004

6.4 Non-refereed conference proceedings

- Beckmann**, Ricci, Soldi 2010, “Fermi detected blazars seen by INTEGRAL”, 2009 Fermi Symposium, eConf Proceedings C091122
- Soldi, **Beckmann**, Türler 2010, “The variability of the quasar 3C 273: a radio to gamma-ray view”, 2009 Fermi Symposium, eConf Proceedings C091122
- Ricci, **Beckmann**, Audard, & Courvoisier 2010, IAU Symposium, 267, 404
- Rohlf, Courvoisier, Walter, Eyer, Beck, Türler, Produit, Paltani, **Beckmann**, Audard, Lecoer 2009, “The Evolution of ISDC Towards Future Projects”, ADASS, ASP Conf. Series 411, 279
- Beckmann** 2008, “INTEGRAL - operating high-energy detectors for five years in space”, invited review, proceedings of the 10th ICATPP conference, Como, Italy, October 8-12, 2007
- Diehl, Roques, Knödseder, Strong, **Beckmann** 2007, “INTEGRAL Science Results and Connections to Suzaku”, Progress of Theoretical Physics Supplement, 169, 299
- Wolter, **Beckmann**, Ghisellini, et al. 2007, “The hard synchrotron X-ray spectrum of the TeV BL Lac 1ES 1426+428”, proc. of “Extragalactic Jets”, Girdwood, Alaska, 21-24 May, 2007, ASP Conference Series
- Camero Arranz, Wilson, Connell, Martinez Nunez, Blay, **Beckmann**, Reglero, 2007, “INTEGRAL and RXTE observations of the Be/X-ray binary EXO 2030+375”, proc. of the “Active OB-Stars: Laboratories for Stellar & Circumstellar Physics” workshop (August 29 - September 2, 2005 Sapporo, Japan), ASP Conf. Series 361
- Beckmann**, Kennea, Markwardt, et al. 2006, “Swift, INTEGRAL, RXTE, and Spitzer reveal IGR J16283–4838”, proc. of “The X-ray Universe 2005”, San Lorenzo de El Escorial (Madrid, Spain), 26-30 September 2005, ESA-SP 604
- Beckmann**, Soldi, Shrader, Gehrels 2006, “Results from the First INTEGRAL AGN Catalogue”, proc. of “The X-ray Universe 2005”, San Lorenzo de El Escorial (Madrid, Spain), 26-30 September 2005, ESA-SP 604
- Soldi, **Beckmann**, Bassani et al. 2006, “INTEGRAL observations of six AGN in the Galactic plane”, proc. of “The X-ray Universe 2005”, San Lorenzo de El Escorial (Madrid, Spain), 26-30 September 2005, ESA-SP 604
- Wilhelm, **Beckmann**, & Vierling 2004, “Einfluss von Magnesium und anderen Kationen auf das Oberflächenpotential der Herzmuskelzelle”, symposium of the society for magnesium research, Munich 2004
- Beck, Aubord, Bartholdi, **Beckmann** et al. 2004, “Data processing at the INTEGRAL Science Data Centre”, proceedings to the 8th ADASS conference, ASP conf. series
- Moran, Hanlon, McBreen, **Beckmann** et al. 2004, “INTEGRAL Spectrometer Analysis of GRB030227 & GRB030131”, proceedings of the 2003 GRB conference in Santa Fe
- Wilms, Pottschmidt, Nowak, **Beckmann** et al. 2004, “INTEGRAL/RXTE Observations of Cygnus X-1”, proceedings to the “X-ray Timing 2003: Rossi and Beyond” meeting in Cambridge, November

2003

- Beckmann**, Borkowski, Courvoisier, et al. 2004, “Time resolved spectroscopy of GRB030501 using INTEGRAL”, in: Nuclear Physics B, 132, p. 301, proceedings of the conference “The Restless High-Energy Universe” in Amsterdam, May 2003
- von Kienlin, Rau, **Beckmann**, Deluit, 2004, “Gamma-ray Bursts Observed with the Spectrometer SPI onboard INTEGRAL”, proceedings of the 2003 GRB conference in Santa Fe
- Favre, Petrucci, **Beckmann**, Courvoisier, 2004, “BeppoSAX observations of the quasar Markarian 205”, in: Nuclear Physics B, 132, p. 173, proceedings of the conference “The Restless High-Energy Universe” in Amsterdam, May 2003
- Beckmann**, Shaw, Roques, Molkov, 2003, Possible GRB030323 localized by INTEGRAL, GRB Circular Network, 1970
- Ebisawa, **Beckmann**, Courvoisier, et al., 2003, Near Infrared Identification of the Dimmest X-ray Sources on the Galactic Plane with the ESO/NTT SOFI Camera, AN 324, 158
- Beckmann** & Wolter 2002, “New results from the Hamburg BL Lac sample”, AIP conference proceedings 599, 502, astro-ph/0007089
- Beckmann** & Celotti 2002, “BeppoSAX Spectral Survey of BL Lacs - new results”, proceedings of the ASI workshop “Blazar Astrophysics with BeppoSAX”
- Beckmann** 2002, “The INTEGRAL Science Data Centre”, proceedings of the XXII Moriond Astrophysics Meeting “The Gamma-Ray Universe”, eds. A. Goldwurm, D. Neumann, and J. Tran Thanh Van, astro-ph/0206506
- Beckmann** 2002, “Unification of Blazars”, proceedings of the XXII Moriond Astrophysics Meeting “The Gamma-Ray Universe”, eds. A. Goldwurm, D. Neumann, and J. Tran Thanh Van
- Beckmann** 2002, “Ultra High Frequency Peaked BL Lac Objects”, proceedings of the High Energy Blazar Astronomy Conference in Turku (Finland)
- Della Ceca, Braitto, **Beckmann**, Cagnoni, Maccacaro, 2000, “The ASCA HSS: Looking for Type 2 AGN”, Proceedings of the Fourth Italian Conference on AGNs, Trieste (Italy) May 15-18 2000. Mem. Soc. Astr. It., astro-ph/0007431
- Beckmann** 1999, “Evolutionary behavior of BL Lac objects”, in: Takalo L. et al. eds., “The BL Lac phenomenon”, Turku, Finland, PASPC Vol. 159, astro-ph/9810154

6.5 Other non-refereed publications

- Beckmann**, Beck, Ferrigno, et al. 2010, “GRB 100628A: INTEGRAL SPI-ACS light curve”, GRB Circular Network, 10898
- Chenevez, Kuulkers, Alfonso-Garzón, **Beckmann**, et al. 2010, “Further INTEGRAL observations of the transient X-ray burster EXO 1745–248”, ATel 2924
- Bordas, Kuulkers, Alfonso-Garzón, **Beckmann**, et al. 2010, “A hard X-ray transient in the direction

- of Terzan 5 detected by INTEGRAL”, ATel 2919
- Kuulkers, Alfonso-Garzón, **Beckmann**, et al. 2010, “INTEGRAL shows MAXI J1659–152 further declines in hard X-rays”, ATel 2890
- Vovk, Kuulkers, Alfonso-Garzón, **Beckmann**, et al. 2010, “INTEGRAL detection of the new MAXI transient MAXI J1659–152”, ATel 2875
- Türler, Ferrigno, Kuulkers, Alfonso-Garzón, **Beckmann**, et al. 2010, “INTEGRAL confirms that XTE J1728–295 = IGR J17285–2922”, ATel 2825
- Kuulkers, Chenevez, **Beckmann**, et al. 2010, “INTEGRAL sees IGR J17544–2619 active again”, ATel 2820
- Chenevez, Brandt, Sanchez-Fernandez, Kuulkers, Alfonso-Garzón, **Beckmann**, et al. 2010, “INTEGRAL/JEM-X detection of an X-ray burst from Swift J1749.4–2807”, ATel 2561
- Pavan, Chenevez, Bozzo, Kuulkers, Alfonso-Garzón, **Beckmann**, et al. 2010, “INTEGRAL and Swift detection of high energy emission from Swift J1749.4–2807”, ATel 2548
- Chenevez, Kuulkers, Alfonso-Garzón, **Beckmann**, et al. 2010, “INTEGRAL reports renewed activity from KS 1741-293”, ATel 2465
- Ferrigno, Bozzo, Martin, **Beckmann**, et al. 2010, “INTEGRAL upper limit on AGL J2206+6203”, ATel 2405
- Beckmann**, Götz, Mereghetti, et al. 2009, “GRB 090817: a long GRB localized by *INTEGRAL*”, GRB Circular Network, 9815
- Beckmann**, Götz, Mereghetti, et al. 2009, “GRB 090814B: a long GRB localized by *INTEGRAL*”, GRB Circular Network, 9795
- Beckmann**, Beck, Ferrigno, et al. 2009, “GRB 090306B: *INTEGRAL* SPI-ACS light curve”, GRB Circular Network, 8968
- Chenevez, Kuulkers, **Beckmann**, et al. 2009, “*INTEGRAL* sees transient activity in the Galactic Bulge: XTE J1751–305 and GRS 1741.9–2853 in outburst”, ATel 2235
- Bozzo, Ferrigno, Kuulkers, Falanga, Chenevez, Brandt, **Beckmann**, et al. 2009, “*Swift* follow-up of the newly discovered burster millisecond pulsar IGR J17511–3057”, ATel 2198
- Baldovin, Kuulkers, Ferrigno, Bozzo, Chenevez, Brandt, **Beckmann**, et al. 2009, “*INTEGRAL* discovered a new hard X-ray source: IGR J17511–3057”, ATel 2196
- Produit, **Beckmann**, Manousakis, et al. 2009, “*INTEGRAL* observes outburst from 1A 0535+262”, ATel 2146
- Götz, Mereghetti, Paizis, Neronov, Beckmann, Beck, Borkowski 2009, “GRB 090625B: a long GRB localized by *INTEGRAL*”, GRB Circular Network, 9572
- Bozzo, Ferrigno, Coe, den Hartog, Bird, Lubinski, Maccarone, **Beckmann**, Ubertini, Watanabe 2009, “IGR J01054–7253: a new *INTEGRAL* source discovered in the SMC”, ATel 2079

- Blanchard, **Beckmann**, Chenevez, et al. 2009, “IGR J18284–0345: a new hard X-ray transient detected by *INTEGRAL*”, ATel 1981
- Chenevez, Brandt, Kuulkers, **Beckmann**, et al. 2009, “*INTEGRAL* detects an X-ray burst from SAX J1747.0–2853 with no detectable persistent emission”, ATel 1944
- Baldovin, Savchenko, **Beckmann**, et al. 2009, “*INTEGRAL* observes continued activity from AXP 1E 1547.0–5408”, ATel 1908
- Mereghetti, Götz, von Kienlin, **Beckmann**, et al. 2009, “AXP 1E 1547.0–5408: long bursts with *INTEGRAL* SPI-ACS”, GRB Circular Network, 8841
- Savchenko, **Beckmann**, Neronov, et al. 2009, AXP 1E 1547.0–5408: *INTEGRAL* SPI-ACS confirms activity increase”, GRB Circular Network, 8837
- Götz, Mereghetti, Paizis, Ferrigno, **Beckmann**, Beck, Borkowski 2009, “GRB 090107B: a long GRB localized by *INTEGRAL*”, GRB Circular Network, 8786
- Beckmann**, Soldi, Kennea, et al. 2008, “IGR J17375–3022 detected and localised by *Swift*/XRT”, ATel 1783
- Beckmann**, Mereghetti, von Kienlin, et al. 2008, “GRB 080319A/B/C: *INTEGRAL* SPI-ACS light curves available”, GRB Circular Network, 7450
- Mereghetti, Paizis, Götz, Turler, **Beckmann**, Beck, Borkowski 2008, “GRB 081226B: a short-hard GRB detected by *INTEGRAL*”, GRB Circular Network, 8734
- Götz, Mereghetti, Paizis, Galis, **Beckmann**, Beck, Borkowski 2008, “GRB 081204: A long GRB localized by *INTEGRAL*”, GRB Circular Network, 8614
- Ricci, **Beckmann**, Carmona, Weidenspointner 2008, “Localization of the hard X-ray transient IGR J17062–6143”, ATel 1840
- Caballero-Garcia, Miller, Ferrigno, **Beckmann** 2008, “Transition of H 1743–322 to the HIMS/SIMS confirmed and preliminary spectral fit results”, ATel 1813
- Cadolle Bel, Kuulkers, Chenevez, **Beckmann**, Soldi 2008, “Further *INTEGRAL* results on SAX J1753.5–2349 and IGR J17375–3022”, ATel 1810
- Caballero-Garcia, Miller, **Beckmann**, Soldi 2008, “Decrease in flux of H 1743–322 and preliminary spectral fit results”, ATel 1798
- Soldi, **Beckmann**, Eckert, et al. 2008, “XTE J1701–407 *INTEGRAL* and *Swift* observations”, ATel 1791
- Götz, Mereghetti, Paizis, Soldi, **Beckmann**, et al. 2008, “GRB 081016: A long GRB discovered by *INTEGRAL*”, GRB Circular Network, 8377
- Ricci, Soldi, **Beckmann**, et al. 2008, “IGR J17375–3022: a new hard X-ray transient detected by *INTEGRAL*”, ATel 1781
- Ricci, Caballero-Garcia, **Beckmann**, Miller, Kuulkers 2008, “H1743–322 in stable outburst phase”, ATel 1779

- Götz, Mereghetti, Paizis, Fontani, **Beckmann**, et al. 2008, “GRB 081003B: A long GRB detected with *INTEGRAL*”, GRB Circular Network, 8317
- Mereghetti, Paizis, Götz, Fontani, **Beckmann**, et al. 2008, “GRB 081003: A long GRB detected by *INTEGRAL*”, GRB Circular Network, 8314
- Kuulkers, Brandt, Budtz-Jørgensen, Chenevez, Shaw, **Beckmann**, et al. 2008, “*INTEGRAL* spots renewed activity from H1743–322”, ATel 1739
- Mereghetti, Paizis, Götz, Ishibashi, **Beckmann**, et al. 2008, “GRB 080922: A long GRB detected by *INTEGRAL*”, GRB Circular Network, 8281
- Götz, Paizis, Mereghetti, **Beckmann**, et al. 2008, “GRB 080723B: A long GRB detected with *INTEGRAL*”, GRB Circular Network, 8002
- Manousakis, **Beckmann**, Bianchin, et al. 2008, “*INTEGRAL* hard X-ray detection of HMXB GX 304–1 and H 1417–624”, ATel 1613
- Beardmore, Page, Evans, Hoversten, Barthelmy, Burrows, Roming, Gehrels, **Beckmann**, et al. 2008, “*Swift* and *INTEGRAL* SPI-ACS Observations of GRB 080602”, GRB Circular Network Report, 145.1
- Götz, Paizis, Mereghetti, **Beckmann**, et al. 2008, “GRB 080613: A long GRB detected with *INTEGRAL*”, GRB Circular Network, 7871
- Paizis, Mereghetti, Götz, Türler, **Beckmann**, et al. 2008, “GRB 080603: A long GRB detected by *INTEGRAL*”, GRB Circular Network, 7790
- Rodriguez, Tomsick, **Beckmann**, et al. 2008, “*RXTE*/PCA and *Swift*/XRT non detection of IGR J19112+1358”, ATel 1554
- Petry, Ishibashi, **Beckmann**, von Kienlin 2008, “*INTEGRAL* observations of Mrk 421”, ATel 1507
- Carmona, **Beckmann**, Rodriguez 2008, “IGR J19112+1358: a new hard X-ray transient detected by *INTEGRAL*”, ATel 1489
- Chenevez, **Beckmann**, Kuulkers, et al. 2008, “Earlier activity from XTE J1739–302/IGR J17391–3021 detected by *INTEGRAL*”, ATel 1471
- Baldovin Saavedra, Chenevez, Kuulkers, **Beckmann**, et al. 2008, “Continuous brightening of IGR J17473–2721”, ATel 1468
- Kuulkers, Shaw, **Beckmann**, et al. 2008, “Hard X-ray activity of IGR J17473–2721”, ATel 1461
- Natalucci, **Beckmann**, Bazzano, et al. 2008, “*INTEGRAL* detection of the outburst of SAX J1750.8–2900”, ATel 1434
- Neronov, **Beckmann**, Krimm, et al. 2008, “XTE J1810–189 measurements by *INTEGRAL* and *Swift*”, ATel 1430
- Kuulkers, **Beckmann**, Shaw, et al. 2008, “*INTEGRAL* Galactic bulge monitoring observations of GRO J1750–27, H1743–322 and SLX 1746–331”, ATel 1385

- Brandt, Shaw, Hill, Kretschmar, Wijnands, Oosterbroek, Kuulkers, **Beckmann**, et al. 2008, “Further observations of GRO J1750–27 (AX J1749.1–2639) with *INTEGRAL*”, ATel 1400
- Kuulkers, Brandt, Markwardt, Remillard, Shaw, **Beckmann**, et al. 2008, “Recent activity of the Rapid Burster (MXB 1730–335)”, ATel 1398
- Canizzo, Barthelmy, Beardmore, et al. 2008, “Final *Swift* Observations of GRB 080229A”, GRB Circular Network Report, 119.2
- Mereghetti, Paizis, Götz, Manousakis, **Beckmann**, et al. 2008, “GRB 080120: a long GRB detected by *INTEGRAL*”, GRB Circular Network, 7194
- Beckmann**, Petry, Weidenspointner 2007, “*INTEGRAL* detection of two Seyfert 1 galaxies: ESO 140–43 and ESO 141–55”, ATel 1264
- Beckmann**, Ricci, Beck, et al. 2007, “GRB 070707: A long GRB detected by *INTEGRAL*”, GRB Circular Network, 6605
- Beckmann**, Ishibashi, Bottacini, Ajello, Greiner 2007, “*Swift* and *INTEGRAL* observation of 1ES 1959+650”, ATel 1317
- Bottacini, **Beckmann**, Ishibashi, Ajello, Greiner 2007, “Blazar 1ES 1959+650 shows high and hard X-ray state”, ATel 1315
- Mereghetti, **Beckmann**, Kreykenbohm, et al. 2007, “GRB 071109: A long GRB detected by *INTEGRAL*”, GRB Circular Network, 7046
- Kuulkers, Risquez Oneca, Brandt, Shaw, **Beckmann**, et al. 2007, “Recent and past activity of the supergiant fast X-ray transient IGR J17544–2619 as seen by *INTEGRAL*”, ATel 1266
- Paizis, **Beckmann**, Götz, et al. 2007, “IGR J18175–1530: a new hard X-ray transient detected by *INTEGRAL*”, ATel 1248
- Brandt, Chenevez, Kuulkers, Natalucci, Fiocchi, Tarana, Shaw, **Beckmann**, et al. 2007, “A new outburst of the recurrent neutron star transient SAX J1747.0–2853”, ATel 1228
- Galis, **Beckmann**, Chenevez, et al. 2007, “SAX J1810.8–2609 displays increasing hard X-ray activity”, ATel 1227
- Mereghetti, Paizis, Götz, Petry, **Beckmann**, et al. 2007, “GRB 070925: a long GRB detected by *INTEGRAL*”, GRB Circular Network, 6823
- Mereghetti, Paizis, Götz, **Beckmann**, et al. 2007, “GRB 070615: A long GRB detected by *INTEGRAL*”, GRB Circular Network, 6537
- Soldi, **Beckmann**, Courvoisier, Kreykenbohm 2007, “Cygnus X-3 in extreme soft state”, ATel 1081
- Galis, **Beckmann**, Bianchin, et al. 2007, “SAX J2103.5+4545 in outburst”, ATel 1063
- Türler, Balman, Bazzano, **Beckmann**, et al. 2007, “IGR J17191–2821: a new hard X-ray transient detected by *INTEGRAL*”, ATel 1021
- Türler, Balman, Bazzano, **Beckmann**, et al. 2007, “*INTEGRAL* observation of a bright X-ray outburst

of XTE J1739–302 / IGR J17391–3021”, ATel 1019

Soldi, Walter, Eckert, Balman, Bazzano, **Beckmann**, et al. 2006, “IGR J17497–2821: a new hard X-ray transient detected by *INTEGRAL*”, ATel 885

Grupe, Tueller, Markwardt, Kennea, Falcone, Mushotzky, Barthelmy, Krimm, Brandt, Schneider, Ajello, **Beckmann**, et al. 2006, “*Swift* Observations of Swift J1933.9+3258: a probable radio-quiet AGN”, ATel 859

Lichti, Paltani, Mowlavi, Ajello, von Kienlin, **Beckmann**, et al. 2006, “*INTEGRAL* observation of flaring activity of Mrk 421”, ATel 848

Lichti, Neronov, Mowlavi, Ajello, **Beckmann**, et al. 2006, “High state of Mkn 421 in the hard X-rays”, ATel 840

Tueller, Markwardt, Ajello, **Beckmann**, et al. 2006, “*Swift*/XRT Detection of the Hard X-ray Source SWIFT J1656.3–3302”, ATel 835

Rodriguez, **Beckmann**, Hannikainen, et al. 2006, “IGR J19140+0951 simultaneously observed with *INTEGRAL*, *Swift* and *RXTE*”, ATel 800

Okajima, Tueller, Markwardt, Ajello, **Beckmann**, et al. 2006, “*Swift*/BAT detection of a new X-ray source, SWIFT J1656.3–3302, in the Galactic Center region”, ATel 799

Kennea, Burrows, Nousek, Chester, Barthelmy, Gehrels, Grebenev, **Beckmann** 2005, “*Swift*-XRT detection of IGR J17098–3626”, ATel 476

Kennea, Burrows, Nousek, Chester, Roming, Barthelmy, Gehrels, **Beckmann**, Soldi 2005, “*Swift*-XRT detection of IGR J16283–4838”, ATel 459

Rodriguez, Foschini, Goldwurm, **Beckmann**, Ebisawa 2004, “Chandra observations of IGR J16316–4028”, ATel 253

Beckmann, Shaw, Roques, Molkov, 2003, “Possible GRB030323 localized by *INTEGRAL*”, GRB Circular Network, 1970

Mereghetti, Götz, Borkowski, Paizis, **Beckmann**, Türler, 2003, “Possible GRB 030320 localized by *INTEGRAL*”, GRB Circular Network, 1941

6.6 Communications in conferences

6.6.1 Talks in international conferences

- | | |
|----------------|--|
| October 2009 | INTEGRAL Workshop 2009 in Otranto. Talk: “Lessons learnt from INTEGRAL detected AGN” |
| October 2009 | CTA meeting in Zürich. Talk: “The APC data support centre and its relevance for the CTA project” |
| September 2009 | X-ray Astronomy 2009 conference in Bologna. Talk: “The Unified Scheme seen with INTEGRAL detected AGN” |
| December 2008 | Simbol-X Symposium in Paris. Talk: “Compton reflection in AGN with Simbol-X” |
| July 2008 | COSPAR conference in Montreal (Canada). Talk: “The Dichotomy of Seyfert galaxies at hardest X-rays” |
| May 2008 | “The X-ray Universe 2008”, conference in Granada, Spain. Talk: “Dichotomy of Seyfert galaxies at hardest X-rays” |
| October 2007 | General Assembly of the SSAA. Talk: “Five years of INTEGRAL - deciphering the high-energy sky” |
| October 2007 | Five Years of INTEGRAL Workshop in Chia Laguna. Talk: “Hard X-ray Variability of AGN” |
| October 2007 | 10th ICATPP Conference in Como (Italy). Invited talk: “INTEGRAL - operating high-energy detectors for five years in space” |
| April 2007 | April Meeting of the American Physical Society in Jacksonville. Talk: “Hard X-ray Emission from AGN and the Cosmic X-ray Background” |
| January 2007 | 209th meeting of the American Astronomical Society (AAS) in Seattle. Talk: “The Hard X-ray 20-40 keV AGN Luminosity Function” |
| November 2006 | Extragalactic Surveys Workshop in Cambridge (Massachusetts). Talk: “INTEGRAL 20-40 keV AGN Survey and Luminosity Function” |
| July 2006 | 6th INTEGRAL Workshop in Moscow. Talk: “The Hard X-ray Luminosity function of INTEGRAL AGN” |
| January 2006 | Invited talk at the 207th meeting of the American Astronomical Society (AAS) in Washington D.C.: “INTEGRAL Studies of AGN” |

Talks in international conferences (continued)

- September 2005 “The X-ray Universe 2005” conference in El Escorial (Spain). Talk: “The First INTEGRAL AGN catalogue”
- January 2005 ESA INTEGRAL Workshop in Noordwijk (The Netherlands). Talk: “The high energy spectrum of NGC 4151”
- July 2004 Committee on Space Research meeting in Paris (France). Talk: “INTEGRAL and XMM-Newton spectral studies of NGC 4388”
- February 2004 5th INTEGRAL Workshop in Munich (Germany). Talk: “INTEGRAL and XMM-Newton spectral studies of NGC 4388”
- June 2002 “High Energy Blazar Astronomy Conference” in Turku (Finland). Talk: “Ultra High Frequency Peaked BL Lac Objects”
- March 2002 Conference “XXII. Moriond Astrophysics Meeting” in Les Arcs (France). Talks: “The INTEGRAL Science Data Centre” and “Unification of Blazars”
- December 2001 ASI workshop at Frascati (Italy): “Blazar Astrophysics with BeppoSAX and other observatories”. Talk: “BeppoSAX Spectral Survey of BL Lacs - new results”
- March 1999 Calar Alto workshop at the MPI in Heidelberg (Germany). Talk: “Results from the Hamburg BL Lac sample”
- June 1998 Conference in Turku (Finland): “BL Lac phenomenon meeting”. Talk: “Evolutionary behavior of BL Lac objects”

6.6.2 Posters in international conferences

- September 2010 8th INTEGRAL Workshop 2010 in Dublin. Poster presentations: “Extended emission and spectral break in Cen A” and “The elusive radio loud Seyfert 2 galaxy NGC 2110”
- April 2010 IXO Science Meeting in Paris. Poster: “AGN at hardest X-rays and the perspectives for IXO”
- November 2009 Fermi Symposium in Washington D.C. Poster: “Fermi detected blazars seen by INTEGRAL”
- September 2008 7th INTEGRAL workshop in Copenhagen. Several poster presentations.
- July 2008 COSPAR conference in Montreal (Canada). Poster: “The efficient low-luminous Seyfert galaxy MCG–05–23–016”
- May 2008 “The X-ray Universe 2008”, conference in Granada, Spain. Poster: “The ISDC Data Centre for Astrophysics”
- April 2008 High Energy Astrophysics Division (HEAD) meeting in Los Angeles. Poster: “Hard X-ray Variability of AGN”
- November 2007 Workshop at the Space Telescope Science Institute, “Astrophysics 2020: Large Space Missions Beyond the Next Decade”. Poster: “ISDC - the European Data Centre for Astrophysics”
- February 2007 Herschel Open Time Key Program workshop in Noordwijk (The Netherlands). Poster: “Studying the connection between star formation and X-ray absorption with Herschel”
- October 2006 High Energy Astrophysics Division (HEAD) meeting. Poster: “The Hard X-ray 20-40 keV AGN Luminosity Function”
- January 2006 207th meeting of the American Astronomical Society (AAS) in Washington D.C.. Poster presentation: “Highly absorbed HMXBs discovered by INTEGRAL”
- September 2005 “The X-ray Universe 2005” conference in El Escorial (Spain). Talk: “The First INTEGRAL AGN catalogue”. Poster presentation: “Swift, INTEGRAL, RXTE, and Spitzer reveal IGR J16283-4838”
- July 2004 Committee on Space Research meeting in Paris (France). Poster presentations: “The Gamma-ray bright BL Lac object RX J1211+2242” and “Searching for Gamma-ray line transients with INTEGRAL/SPI”
- May 2003 BeppoSAX symposium “The Restless High-Energy Universe” in Amsterdam (The Netherlands). Poster presentation: “Time resolved spectroscopy of GRB030501 using INTEGRAL”
- September 1999 Conference in Bologna (Italy) : “X-ray Astronomy ’99 - Stellar Endpoints, AGN and the Diffuse Background”. Poster presentation: “New results from the BeppoSAX Spectral Survey of BL Lac”
- September 1997 Conference of the *Astronomische Gesellschaft* in Innsbruck (Austria). Poster presentation about “X-ray spectral index of RASS-AGN”

6.7 Seminars (only after 2005)

- March 2009 Colloquium in honor of professor Dieter Reimers at the town hall in Hamburg-Bergedorf: “The X-ray sky from ROSAT to INTEGRAL”
- February 2009 Journée Spatiale IN2P3 at the APC in Paris: “PDSDC - a data and computing centre for astroparticle space physics”
- February 2009 Simbol-X JSMG Paris: “The Swiss interest in Simbol-X”
- November 2008 APC Paris: “Lessons learnt from INTEGRAL about super-massive black holes”
- December 2007 Observatoire de Genève: “Advection Dominated Accretion Flows”
- November 2007 UMBC and NASA/GSFC: “Hard X-ray Variability of AGN”
- March 2007 Beyond Einstein Program Assessment Committee. Presentation: “The Need for a Hard X-ray Survey: EXIST”
- February 2007 INTEGRAL Science Data Centre. Presentation: “The Gamma-Ray Large Area Telescope”
- December 2006 Hamburger Sternwarte. Presentation: “The Hard X-ray 20-40 keV AGN Luminosity Function”
- December 2006 University of Louisville (Kentucky). Presentation: “Revealing the Nature of GRBs with Swift”
- April 2006 International Astrophysical School “Observing the X- and Gamma-ray Sky”. Presentation: “Revealing the Nature of GRBs with Swift”
- March 2006 INTEGRAL Science Data Centre. Two presentations: “The Hard X-ray 20-40 keV AGN Luminosity Function” and “Revealing the Nature of GRBs with Swift”
- March 2006 MPE (Garching, Germany). Presentation: “The Hard X-ray 20-40 keV AGN Luminosity Function”
- March 2006 INTEGRAL/SPI meeting (Munich, Germany). Presentations “INTEGRAL High Level Archive”, “SPIRMF”
- February 2006 Yale Center for Astronomy and Astrophysics. Presentation: “The Hard X-ray 20-40 keV AGN Luminosity Function”
- December 2006 University of Hamburg (Germany). Presentation: “Swift Gamma-Ray Burst Studies”
- August 2005 AIP (Potsdam, Germany). Presentation: “The First INTEGRAL AGN Catalog”
- January 2005 CEA/Saclay (Paris, France). Presentation: “INTEGRAL and Swift: perspectives in the Gamma-ray range”
- January 2005 Potsdam University (Germany). Presentation: “Exploring the hard X-ray domain using INTEGRAL and Swift”

6.8 Thesis and dissertation

Beckmann 2000, “Evolutionary behavior of AGN: Investigations on BL Lac objects and Seyfert II galaxies”, PhD thesis, Universität Hamburg:

<http://www.sub.uni-hamburg.de/disse/330/vbdiss.html>

Referees: Prof. Dr. Dieter Reimers (Hamburger Sternwarte), and Prof. Dr. Laura Maraschi (Osservatorio Astronomico di Brera).

Beckmann 1996, “Röntgenspektralindex von AGN”, master thesis, Universität Hamburg. Referees: Prof. Dr. Sjur Refsdal and Prof. Dr. Dieter Reimers (Hamburger Sternwarte).

6.9 Five significant publications

1. “The HRX-BL Lac sample - Evolution of BL Lac objects”, Beckmann V., Engels D., Bade N., Wucknitz O., *Astronomy and Astrophysics*, v.401, pp. 927-938 (2003)
2. “The First INTEGRAL AGN Catalog”, Beckmann V., Gehrels N., Shrader C. R., Soldi S., *The Astrophysical Journal*, Volume 638, Issue 2, pp. 642–652 (2006)
3. “The Hard X-ray 20–40 keV AGN Luminosity Function”, Beckmann V., Soldi S., Shrader, C. R., Gehrels N., Produit N., *The Astrophysical Journal*, Volume 652, Issue 1, pp. 126-135 (2006)
4. “Hard X-ray variability of active galactic nuclei”, Beckmann V., Barthelmy S. D., Courvoisier T.J.-L., Gehrels N., Soldi S., Tueller J., Wendt G., *Astronomy and Astrophysics*, Volume 475, Issue 3, pp. 827-83 (2007)
5. “The Second INTEGRAL AGN Catalogue”, Beckmann V., Soldi S., Ricci C., Alfonso-Garzón J., Courvoisier T.J.-L., Domingo A., Gehrels N., Lubiński P., Mas-Hesse J. M., Zdziarski A. A., *Astronomy and Astrophysics*, Volume 505, Issue 1, pp. 417-439 (2009)

6.9.1 The HRX-BL Lac sample - Evolution of BL Lac objects

A discussion of this work in the context of the unified model of AGN can be found in Section 4.5 on page 41. The manuscript, which is shown on the following pages, has been published as

Beckmann V., Engels D., Bade N., Wucknitz O., *Astronomy and Astrophysics*, v.401, pp. 927-938 (2003)

A&A 401, 927–938 (2003)
 DOI: 10.1051/0004-6361:20030184
 © ESO 2003

**Astronomy
&
Astrophysics**

The HRX-BL Lac sample – Evolution of BL Lac objects[★]

V. Beckmann^{1,2,3}, D. Engels¹, N. Bade¹, and O. Wucknitz⁴

¹ Hamburger Sternwarte, Gojenbergsweg 112, 21029 Hamburg, Germany

² INTEGRAL Science Data Centre, Chemin d'Écogia 16, 1290 Versoix, Switzerland

³ Institut für Astronomie und Astrophysik, Universität Tübingen, Sand 1, 72076 Tübingen, Germany

⁴ Universität Potsdam, Institut für Physik, Am Neuen Palais 10, 14469 Potsdam, Germany

Received 8 April 2002 / Accepted 12 February 2003

Abstract. The unification of X-ray and radio selected BL Lacs has been an outstanding problem in the blazar research in the past years. Recent investigations have shown that the gap between the two classes can be filled with intermediate objects and that apparently all differences can be explained by mutual shifts of the peak frequencies of the synchrotron and inverse Compton component of the emission. We study the consequences of this scheme using a new sample of X-ray selected BL Lac objects comprising 104 objects with $z < 0.9$ and a mean redshift $\bar{z} = 0.34$. 77 BL Lacs, of which the redshift could be determined for 64 (83%) objects, form a complete sample. The new data could not confirm our earlier result, drawn from a subsample, that the negative evolution vanishes below a synchrotron peak frequency $\log \nu_{\text{peak}} = 16.5$. The complete sample shows negative evolution at the 2σ level ($\langle V_c/V_d \rangle = 0.42 \pm 0.04$). We conclude that the observed properties of the HRX BL Lac sample show typical behaviour for X-ray selected BL Lacs. They support an evolutionary model, in which flat-spectrum radio quasars (FSRQ) with high energetic jets evolve towards low frequency peaked (mostly radio-selected) BL Lac objects and later on to high frequency peaked (mostly X-ray selected) BL Lacs.

Key words. BL Lacertae objects: general – X-rays: galaxies

1. Introduction

BL Lac objects are a rare type of Active Galactic Nuclei (AGN), which are observationally distinguished mainly by the absence of strong emission lines. They have strong X-ray and radio emission, and they often show strong variability and optical polarization. Their observational properties are usually explained by a particular line of sight toward the galaxy nucleus, which in BL Lacs is thought to be parallel to a jet emerging from this nucleus.

Two search strategies are commonly used to find BL Lacs. The first is a search for strong X-ray sources with a high ratio of X-ray to optical flux, yielding X-ray selected BL Lacs (XBL). The second is to search among flat spectrum radio sources to find radio selected ones (RBL). As the radio and X-ray surveys got more and more sensitive, the properties of both groups started to overlap, raising the question of how they are related. Padovani & Giommi (1995) noticed that the spectral energy distribution (quantified by $\log \nu L_\nu$) of radio and X-ray selected BL Lacs shows peaks at different frequencies, and suggested that this is the basic difference between the two classes of BL Lacs. They introduced the notation of

high-energy cutoff BL Lacs (HBLs) and *low-energy cutoff BL Lacs* (LBLs). Most, but not all, XBLs are HBLs, while the group of LBLs is preferentially selected in the radio region.

In general, BL Lacs are considered as part of a larger class of objects, the blazars, which have similar properties but show emission lines in addition, and for which this scenario applies as well. Ghisellini et al. (1998) proposed that the range of peak frequencies observed is governed primarily by the efficiency of radiative cooling, and that the other physical parameters strongly depend on it. They found an inverse correlation between the energy of the Lorentz factor of particles emitting at the peaks of the SED (γ_{peak}) and the energy density of the magnetic and radiation field of $\gamma_{\text{peak}} \propto U^{-0.6}$. This correlation was extended later on for low power (high peaked) BL Lacs by taking into account the finite time for the injection of particles in the jet (Ghisellini et al. 2002). Combined modelling of the time-dependent electron injection and the self consistent radiation transport in jets of high peaked blazars lead to the conclusion that differences in the appearance can be explained by either self-synchrotron or external Compton dominated processes (Böttcher & Chiang 2002). Other studies focussed on the importance of shock events in the blazar jets to explain variability on short timescales (e.g. Bicknell & Wagner 2002). Based on these models the most important factor in the appearance of blazars seems nowadays the energy density of the jet. Maraschi & Tavecchio (2002) showed that this energy density

Send offprint requests to: V. Beckmann,
 e-mail: Volker.Beckmann@obs.unige.ch

[★] Appendix (Tables 8 and 9, Fig. 8) is only available in electronic form at <http://www.edpsciences.org>

is related to the accretion rate in the AGN disk and proposed that all blazar types have similar black hole masses but that the low power blazars exhibit lower accretion rates.

Unlike all other AGNs, and different from RBLs also, the space density or the luminosity of XBLs showed an increase with time (e.g. Rector et al. 2000). This is called negative evolution. Bade et al. (1998) probed this property with a new ROSAT selected XBL sample and confirmed the negative evolution only for extreme XBLs, e.g. HBLs with very high energy cutoffs ($\log \nu_{\text{peak}} > 16.5$). The result for less extreme XBLs, called intermediate-energy cutoff BL Lacs (IBLs) by Bade et al., was compatible with no evolution. This difference in evolutionary behaviour indicated the presence of a smooth transition between HBLs and LBLs. However, these findings were based on only 39 BL Lacs, prompting us to increase the size of this sample considerably. The results of this effort, the HRX-BL Lac sample presented here, comprises now 77 BL Lacs and is the largest complete XBL sample so far.

Recent models tried to explain the different evolutionary behaviour of HBLs and LBLs by assuming that BL Lacs start as LBLs and evolve into HBLs as they grow older (Georganopoulos & Marscher 1998; Cavaliere & D’Elia 2002). As described by e.g. Padovani & Urry (1990) the spectral energy distributions (SED) of BL Lacs are characterized by two components, both consisting of beamed continuum emission from the plasma of the jets. The first component is synchrotron emission, peaking in the mm to far IR for LBLs. The second component is inverse Compton (IC) emission peaking at MeV energies. HBLs have SEDs peaking in the keV and in the GeV–TeV band respectively. A decrease of power of the jets during the BL Lac evolution would then be accompanied by an increase of the peak frequencies and accordingly a transformation of the LBLs into HBLs (Georganopoulos & Marscher 1998). This model is in fact valid for the whole blazar class: BL Lacs in general show lower power and beaming factors than the Flat Spectrum Radio Quasars (FSRQs), as revealed by e.g. Madau et al. (1987), Padovani (1992), Ghisellini et al. (1993). It naturally explains the different evolution, which is slightly negative for HBLs, slightly positive for LBLs, and clearly positive for the FSRQ/blazar class. This model explains the different types of BL Lac objects only by different global intrinsic power (Maraschi & Rovetti 1994), and not by a different viewing angle. Nevertheless different orientation is probably important as secondary effect necessary to explain the large scatter of observed quantities.

The HRX-BL Lac sample contributes to the discussion with a large and complete sample of X-ray selected BL Lac objects. Previous studies (e.g. Fossati et al. 1998) used a compilation of different BL Lac surveys, like the X-ray selected EMSS (Stoeckel et al. 1991; Rector et al. 2000), the radio selected 1 Jy BL Lac sample (Stickel et al. 1991; Rector & Stoeckel 2001), and a FSRQ sample derived from the 2 Jy radio sample of Wall & Peacock (1985) to investigate the overall picture of the blazar class, ranging from the FSRQs to the BL Lac objects. In contrast to this the HRX-BL Lac survey is concentrating on a blazar subclass, the HBLs and IBLs, and is homogeneous in having the same selection criteria for all objects, making it comparable with the REX-survey (Maccacaro et al. 1998;

Table 1. Boundaries of the selection area.

Boundaries (J2000.0)		Area
α	δ	[deg ²]
$7^{\text{h}} \leq \alpha < 8^{\text{h}}$	$30^{\circ} < \delta < 85^{\circ}$	426
$8^{\text{h}} \leq \alpha < 12^{\text{h}}$	$20^{\circ} < \delta < 85^{\circ}$	2248
$12^{\text{h}} \leq \alpha < 14^{\text{h}}$	$20^{\circ} < \delta < 65^{\circ}$	970
$14^{\text{h}} \leq \alpha \leq 16^{\text{h}}$	$20^{\circ} < \delta < 85^{\circ}$	1124

Caccianiga et al. 1999), the DRXBS (Perlman et al. 1998; Landt et al. 2002), and the sedentary multifrequency BL Lac sample (Giommi et al. 1999).

We will describe our selection method of BL Lac candidates in Sect. 2 and the results of the identification process using literature data and own observations in Sect. 3. The spectral energy distribution of the HRX-BL Lac sample is analyzed in Sect. 4, where we demonstrate that for the HBL class the knowledge about the X-ray and optical flux is sufficient to determine the peak frequency of the synchrotron branch. The spatial distribution of the sample is described in Sect. 5. We conclude with a discussion of the compatibility of the results from the HRX BL Lac sample with recent studies.

Throughout the article a cosmology with $H_0 = 50 \text{ km s}^{-1} \text{ Mpc}^{-1}$ and a deceleration parameter $q_0 = 0.5$, assuming a Friedmann universe with $\Lambda = 0$, has been used.

2. BL Lac candidate selection

In the beginning the HRX-BL Lac sample originated from the Hamburg-RASS Bright X-ray AGN sample (HRX), which was created by identification of the ROSAT All-Sky Survey (RASS) with the aid of objective prism plates of the Hamburg Quasar Survey (HQS; Hagen et al. 1995). The BL Lac subsample was selected on an area of 1687 deg² with a count-rate limit of $hcps \geq 0.075 \text{ s}^{-1}$ and on additional 1150 deg² with a limit of $hcps \geq 0.15 \text{ s}^{-1}$. This sample was analyzed by Bade et al. (1998) and is referred here as the HRX-BL Lac *core sample*. It consists of 39 BL Lacs, 34 of which are also part of the present sample.

The fraction of BL Lacs in the HRX was $\sim 10\%$. Therefore, an increase of the sample size based on optical identification alone is rather inefficient. This can be alleviated using radio information, as all BL Lacs from the core sample were detected as radio sources in the NRAO VLA Sky Survey (NVSS, Condon et al. 1998). Also, to the authors knowledge, all known BL Lac objects do have radio counterparts down to the $\sim 2.5 \text{ mJy}$ level, which is similar to the detection limit of the NVSS. We concluded therefore that for the high X-ray count-rates used we can include radio detection in the NVSS as selection criterium without losing BL Lac objects. As X-ray input we used the ROSAT Bright Source Catalog (RASS-BSC; Voges et al. 1999) with a count-rate limit (0.5–2.0 keV) of $hcps \geq 0.09 \text{ s}^{-1}$. We cross-correlated this catalogue with the NVSS adopting an error circle of 30'' around the X-ray position. We extended the sky area studied to 4768 deg² encompassing the area of 2837 deg² studied by

Bade et al. (1998), and we applied a unique limit of $hcps \geq 0.09 s^{-1}$. The boundaries of the area are given in Table 1.

The cross-correlation yielded 223 matches between X-ray and radio sources. The complete list of these objects is given in Table 8 (this table is only available in electronic form). The coordinates listed are the X-ray positions (J2000.0). More than 99.9% of the sources have a positioning error $\Delta \leq 25''$ (Voges et al. 1999). The column “Name” lists alternative names to the ROSAT designation, when available. Redshifts and classification are taken from the NED or SIMBAD database or were determined on the base of own follow-up observations. All objects, for which we obtained own data are marked.

The cross correlation might be incomplete for lobe-dominated radio sources, as in those cases the radio emission will consist of more than one component offset from the X-ray position. However, for none of the X-Ray BSC sources we found multiple radio sources within the search radius, and as BL Lacs are core-dominated radio sources no selection biases are expected.

3. Classification of BL Lac candidates

3.1. Results from NED and SIMBAD database queries

The 223 candidates were classified in a two-step process. First we searched for known optical counterparts in the NASA/IPAC Extragalactic Database (NED)¹ and in the SIMBAD² database. Special care was taken to avoid confusion of BL Lac objects with normal galaxies and other types of AGNs. A database entry of an object as “galaxy” without spectroscopic information was not accepted as an identification, because nearby BL Lac objects in elliptical galaxies might not have been recognized. For galaxies with redshift information and for objects with “AGN” or “QSO” identification but without additional information (e.g. redshift) the original literature was consulted before the object was dismissed as BL Lac.

In total 101 objects could be classified this way³. Of the remaining objects a few candidates were classified as stars on the objective prism plates of the HQS, and another few as obvious clusters of galaxies based on direct plates and on the fact that these sources show extended X-ray emission. For all other candidates follow-up observations were obtained.

3.2. Observations of the remaining unclassified BL Lac candidates

Spectroscopic observations to classify the remaining BL Lac candidates and to determine their redshifts were made with the 3.5 m telescope on Calar Alto equipped with the multiobject spectrograph MOSCA and with the 4.2 m WHT on La Palma equipped with ISIS (Table 2). Most of the results from the 1997

¹ The NED is operated by the Jet Propulsion Laboratory, California Institute of Technology, under contract with the National Aeronautics and Space Administration.

² The SIMBAD Astronomical Database is operated by the Centre de Données astronomiques de Strasbourg.

³ At the time of writing this paper, already 205 of the objects have a classification in the NED.

Table 2. Spectroscopic follow-up observation runs. The last column gives the number of objects observed. Some of the objects were observed several times.

Telescope & Instrument	Date	#nights	N^b
3.5 m Calar Alto (MOSCA)	March 1997	4	30
WHT / La Palma (ISIS)	April 1997	2	19
3.5 m Calar Alto (MOSCA)	Feb. 1998	6	89
3.5 m Calar Alto (MOSCA)	Feb. 1999	$\sim 1^a$	9

^a Morning and evening hours of three nights.

^b Number of objects observed in this observation run.

observation runs have already been presented in Bade et al. (1998). For the classification with MOSCA, we used the G500 grism, which covers a wavelength range 4250–8400 Å with a pixel-to-pixel resolution of 12 Å. If necessary, additional spectra were taken with the G1000 and R1000 grisms to determine redshifts. These spectra have a resolution of 6 Å and cover the ranges 4400–6600 Å and 5900–8000 Å respectively. The spectra were reduced in a standard way: bias subtraction, flat-field correction using morning and evening skyflats, and response determination of the detector using spectrophotometric standard stars. BL Lac objects by definition have no or very weak emission lines. Integration times of $\approx 1000 \dots 2000 s$ were needed to detect the weak absorption lines of the host galaxy, which is often out-shined by the non-thermal continuum of the point-like central synchrotron source. Most observations were made under non-photometric conditions.

Optical photometry in the Johnson B band has been obtained for many of the optically faint BL Lacs with the Calar Alto 1.23 m telescope (Beckmann 2000a). Especially for several of the very faint objects ($B > 20$ mag) no reliable photometry was available before. For these objects we have now optical magnitudes with an error of $\Delta B \leq 0.1$ mag. For the other objects the acquisition frames of the spectroscopic runs have been used to determine a B magnitude, or values from the literature have been taken. For the brighter objects ($B < 18$ mag) also the HQS calibrated objective prism plates have been used, which have an error of $\Delta B \leq 0.3$ mag.

3.3. Results from follow-up observations

Follow-up observations were made of 117 objects, including the unidentified candidates from the BSC/NVSS correlation and additionally a number of objects, which were considered to be promising BL Lac candidates, but did not match the selection criteria described before (e.g. too low X-ray count rate). In total we discovered 53 BL Lac objects according to the classification criteria, which are discussed in Sect. 3.4. As a considerable number of the objects was discovered independently by other groups in the meantime, we are left over with 26 new BL Lacs: 11 from the BSC/NVSS correlation and 15 from the additionally observed objects.

Table 3. Summary of identifications of objects from the BSC/NVSS correlation (cf. Table 8).

object type	total number	fraction
BL Lac	77	34.5%
Seyfert 1	65	29.1%
Seyfert 2	8	3.6%
Quasar	6	2.7%
blazar	2	0.9%
LINER	5	2.2%
Galaxy cluster	29	13.0%
Galaxies	19	8.5%
Stars	8	3.6%
SNR	2	0.9%
Unidentified	2	0.9%
Total	223	

3.3.1. The complete HRX BL Lac sample

The 11 new BL Lac objects discovered among the objects from the BSC/NVSS correlation are marked in Table 8 and their spectra are included in Fig. 8. Based on our spectra we could confirm or revise redshifts for several other BL Lac objects. Five objects from this correlation with other identifications than BL Lac and without NED or SIMBAD entry so far, are marked in Table 8 in addition.

Summarizing, the optical identification of the 223 BSC/NVSS objects leads to the following distribution of object classes within the radio/X-ray correlation (Table 3): 35% are BL Lac objects, 36% are other AGNs (QSO, Seyfert 1/2, FSRQs), 11% galaxies (including starburst galaxies and LINERs), 13% cluster of galaxies, and 4% stars (including 2 supernova remnants). Only a fraction of 1% of the 223 candidates is yet not identified.

The 77 BL Lacs from the BSC/NVSS correlation are called the *complete HRX BL Lac sample*. In comparison to the EMSS BL Lac sample, this sample probes a population of objects with lower α_{RO} and α_{OX} values and contains therefore more radio quiet and stronger X-ray dominated objects. The HRX-BL Lac sample is the largest complete sample of X-ray selected BL Lac objects. Table 4 compares the HRX BL Lac sample with four other X-ray selected BL Lac Surveys: the EMSS based sample (Rector et al. 2000), the sample by Laurent-Muehleisen et al. (1999) based on the correlation of the RASS with the Green Bank radio survey, the REX survey using the NVSS in combination with the sources found in the ROSAT pointed observations (Caccianiga et al. 1999), and the DXRBS (Perlman et al. 1998), which uses the ROSAT data base WGACAT and PMN/NVSS radio data.

3.3.2. The extended HRX BL Lac sample

Among the BL Lac candidates observed additionally we could confirm another 27 BL Lac objects, from which 15 did not appear in the literature so far. Together with the 77 BL Lacs from the complete sample they form the *extended HRX BL Lac sample* comprising 104 objects. The spectra of the 15 new BL Lacs

are presented in Fig. 8 together with the 12 new BL Lacs from the complete sample. The spectra of all other objects including those from objects not identified as BL Lacs will be accessible on the web⁴.

The properties of the 104 BL Lacs of the extended sample are presented in Table 9 (this table is only available in electronic form). The BL Lacs discovered additionally are marked by an asterisk and the new BL Lacs are labeled by “new”. This Table lists the object names, the NVSS radio coordinates (J2000.0), redshifts, ROSAT PSPC (0.5–2.0 keV) X-ray fluxes in 10^{-12} erg cm^{-2} s^{-1} , 1.4 GHz radio fluxes in mJy from the NVSS radio catalogue, B magnitudes, K magnitudes, and the calcium break index. The radio positions have an error of less than 5'' (for the faintest objects) and are therefore considerably more accurate than the X-ray positions given in Table 8.

The RASS-BSC fluxes have been computed by using the count rate and a single-power law with free fitted absorption N_{H} . The spectral slope and N_{H} are determined by the hardness ratios, a method described by Schartel (1994). The hardness ratio is defined as $HR = (H - S)/(H + S)$ with H and S being the number of counts in the hard and soft energy bands; typically two ratios are computed: $HR1$ with energy ranges $S = 0.1\text{--}0.4$ keV and $H = 0.5\text{--}2.0$ keV, and $HR2$ with $S = 0.5\text{--}0.9$ keV and $H = 1.0\text{--}2.0$ keV (Voges et al. 1999). The values for the hardness ratios range by definition from +1 for extremely hard to –1 for very soft X-ray spectra. The error estimate for the N_{H} and α_{X} values is based on the hardness ratios only, not on the photon spectrum itself. Therefore this method does not give χ^2 values, but is able to determine 68% (1σ) errors. This is done by exploring the hardness-ratio, spectral slope, and N_{H} parameter space, determining the 1σ region within it for a given set of parameter components.

The near infrared data are taken from the Two-Micron All-Sky Survey (2MASS, Skrutskie et al. 1995; Stiening et al. 1995). In Table 9 only the K -magnitude is listed, but for the analysis we also used J and H from the 2MASS.

The calcium break index (Ca-break) is defined as follows (Dressler & Shectman 1987):

$$\text{Ca-break}[\%] = 100 \cdot \frac{f_{\text{upper}} - f_{\text{lower}}}{f_{\text{upper}}} \quad (1)$$

with f_{upper} and f_{lower} being the mean fluxes measured in the $3750 \text{ \AA} < \lambda < 3950 \text{ \AA}$ and $4050 \text{ \AA} < \lambda < 4250 \text{ \AA}$ objects rest frame band respectively. The measurement of the break was possible only if the redshift was known and if the break was within the spectral range covered by the observation. Therefore break values are available for 30 of the HRX-BL Lac only. In seven cases the break value is negative. This is in most cases due to a low signal to noise of the spectra. Only for one object (1RXS J111706.3+201410) the negative calcium break index is not consistent with a value of 0% and we assume that here the underlying power law of the jet emission outshines the host galaxy, so that the measured negative “break value” is in fact based on the synchrotron component.

⁴ <http://www.hs.uni-hamburg.de/bllac.html>

Table 4. Properties of the Hamburg BL Lac samples in comparison to other recent samples.

sample	Reference	number of objects	X-ray limit	radio limit	optical limit
HRX core sample	Bade et al. (1998)	39	0.075/0.15 s ⁻¹ ^{a,g}	–	–
HRX-BL Lac	this work	77	0.09 s ⁻¹ ^{a,g}	2.5 mJy ^b	–
RGB	Laurent-Muehleisen	127	0.05 s ⁻¹ ^{a,c}	15 ... 24 mJy ^d	18.5 mag ^e
RGB complete	et al. (1999)	33	0.05 s ⁻¹ ^c	15 ... 24 mJy ^d	18.0 mag ^e
EMSS	Rector et al. (2000)	41	2 × 10 ⁻¹³ ^f	–	–
REX	Caccianiga et al. (2002)	55	4 × 10 ⁻¹³ ^g	2.5 mJy ^b	B ≤ 20.5 mag
DXRBS	Padovani (2001)	30	few × 10 ⁻¹⁴ ^c	~50 mJy	–

^a ROSAT All Sky Survey count rate limit.

^b NVSS radio flux limit at 1.4 GHz.

^c Full (0.1–2.4 keV) PSPC energy band.

^d GB catalog flux limit at 5 GHz.

^e *O* magnitude determined from POSS-I photographic plates.

^f EINSTEIN IPC (0.3–3.5 keV) flux limit in [erg cm⁻² s⁻¹].

^g Hard (0.5–2 keV) PSPC energy band.

Figure 1 shows the redshift distribution of the HRX-BL Lac extended and complete samples. The mean redshift for the *complete* and *extended* sample are $\bar{z} = 0.31$ and $\bar{z} = 0.34$, respectively. We note that in comparison to the *core sample* no new BL Lacs with $z > 0.7$ were found, which contribute to the *complete sample*.

3.4. BL Lac classification criteria

The characterizing feature of BL Lac spectra in the optical is the presence of a non-thermal continuum which is well described by a single power law. A second component is the emission of the host galaxy, which contributes absorption features in addition to continuum emission. If the BL Lac itself shows no emission lines at all, redshift determination is only possible by identifying these absorption features. The host galaxies are in majority giant elliptical galaxies (e.g. Urry et al. 2000), having strong absorption features caused by the stellar content.

Expected absorption features in the optical, which can be used for redshift determination, have already been discussed in detail by Bade et al. (1998). The most prominent feature in the spectra of elliptical galaxies is the so-called “calcium break” at 4000 Å. Its strength is given by the calcium break index, as defined before.

Most of the AGN with emission lines found in the radio/X-ray correlation are Seyfert type galaxies or LINER (see Table 3). These AGN do not show a calcium break. For the other objects the strength of the calcium break can be used to distinguish between normal elliptical galaxies and BL Lac objects. For the former, this contrast is $\geq 40\%$ with the higher flux to the red side of the break. Our criteria to classify BL Lac objects were defined by Bade et al. (1998) for the core sample and are spectroscopically similar to those applied to the Einstein Medium-Sensitivity Survey (EMSS; Stocke et al. 1991). However, we relaxed the upper limit for the strength of the calcium break index from 25% to now 40% when other properties of the object were consistent with a BL Lac classification. This follows the findings of previous studies

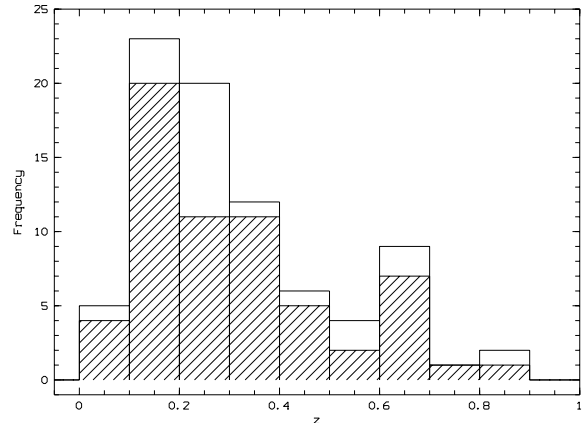


Fig. 1. Distribution of redshifts in the extended HRX-BL Lac sample. The hatched part refers to the *complete sample*.

(Marchã et al. 1996; Laurent-Muehleisen et al. 1999; Rector et al. 2000) that there exist galaxies with strengths $25\% < \text{Ca-break} < 40\%$, which fulfill all other selection criteria for BL Lac objects. Explicitly the selection criteria are now:

- no emission lines with $W_\lambda > 5 \text{ \AA}$;
- the contrast of the Ca II break from the host galaxy must be less than 40%.

With respect to the first criterium no misclassifications are expected as there were no objects found within the BSC/NVSS correlation with weak emission lines and equivalent widths of several 10 Å.

Borderline cases are more likely with respect to the calcium break index, because the transition between non-active elliptical galaxies and BL Lacs is smooth. This is clearly shown in Fig. 2, in which our measured break strength is plotted vs. the optical luminosity L_B , as derived in Sect. 4.2. Both quantities are correlated and almost evenly distributed up to Ca-break $\sim 40\%$.

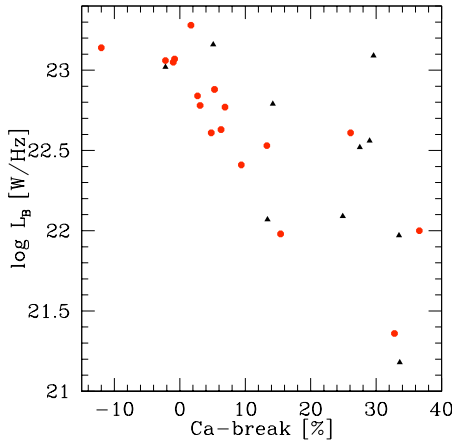


Fig. 2. Strength of the calcium break versus monochromatic luminosity L_B in the optical B -band. Circles refer to the *complete sample* while triangles mark additional objects found within the course of the work.

The observed correlation might be affected by a varying fraction of host galaxy light included in the spectra. In nearby objects the BL Lac host galaxy might not have been fully covered by the slit and therefore the calcium break strength could have been underestimated. However, as the low-redshift objects are mainly the less luminous ones, this effect cannot explain the decreasing strength of the calcium break with increasing luminosities.

This correlation is not only seen in the optical domain, but is also present if we use radio, near infrared or X-ray luminosity instead. In all wavelength regions from the optical to the X-rays the correlation between emitted luminosity and break strength is significant. Therefore we would like to stress the point that the observed correlations are not due to observational selection effects.

Misclassifications might have been occurred also due to large errors for the measured break strengths in some of our spectra with low signal to noise ratio. However for all objects except three of the HRX-BL Lac *complete sample* the break strengths are $<25\%$, making a misclassification unlikely. The three objects with a calcium break strength in the range $25\% < \text{Ca-break} < 40\%$ are 1ES 0927+500, 1RXS 114754.9+220548, and 1RXS 151040.8+333515 (cf. Table 9) and they were included in the sample, because they fulfill other BL Lac properties, for example strong polarization ($P > 6\%$) in the NVSS.

4. Spectral energy distribution

To study the spectral energy distribution (SED) of the HRX-BL Lac objects, overall spectral indices were calculated to derive general correlations within the sample. Throughout this section the *extended sample* is analyzed. Ledden and O’Dell (1985) defined the overall spectral index between two frequencies:

$$\alpha_{1/2} = -\frac{\log(f_1/f_2)}{\log(\nu_1/\nu_2)}. \quad (2)$$

Here f_1 and f_2 are the fluxes at two frequencies ν_1 and ν_2 . As reference frequencies we used 1.4 GHz in the radio ($\lambda \simeq 21$ cm), 4400 Å in the optical ($\sim B$), and 1 keV ($\lambda \simeq 12.4$ Å) in the X-ray region to derive the optical-X-ray α_{OX} , the radio-X-ray α_{RX} , and the radio-optical α_{RO} spectral index.

To compare these indices with those from the literature, shifts due to the use of different reference energies have to be taken into account. It can be shown that these shifts are small as long as the spectral shape within each band can be approximated by a single power law and the spectrum is not curved. Because the radio spectra are flat ($\alpha_{\text{R}} = 0$), the flux does not change when different reference frequencies are chosen in the radio domain. But by increasing the radio reference frequency, the α_{RX} and α_{RO} indices steepen. For example, if the reference frequency is changed from 1.4 to 5 GHz the radio-X-ray index changes by 6%: $\alpha_{\text{RX}}(5 \text{ GHz}, 1 \text{ keV}) \simeq 1.06 \times \alpha_{\text{RX}}(1.4 \text{ GHz}, 1 \text{ keV})$. If our spectral indices are compared with those using a larger X-ray reference energy, similar values for α_{OX} and α_{RX} are expected. Because of $f_\nu \propto \nu^{-\alpha}$, the expected flux at a higher energy is lower and the flux ratios increase. At the same time however, the frequency interval increases by about the same factor, if we assume $\alpha_{\text{E}} = 1$, which is a good approximation for the mean X-ray spectral energy index of BL Lac objects. The same reasoning applies for the optical region, where $\alpha_{\text{E}} \lesssim 1$, and larger changes of the relevant indices are not expected.

The HRX-BL Lac sample shows typical values for the mean overall spectral indices: $\langle \alpha_{\text{OX}} \rangle = 0.94 \pm 0.23$, $\langle \alpha_{\text{RX}} \rangle = 0.55 \pm 0.08$, $\langle \alpha_{\text{RO}} \rangle = 0.37 \pm 0.09$, if compared to Wolter et al. (1998), Laurent-Muehleisen et al. (1999), and Beckmann et al. (2002).

The region in the $\alpha_{\text{OX}} - \alpha_{\text{RO}}$ plane, which is covered by the HRX-BL Lac sample, is shown in Fig. 3. The center of the area covered by this sample is similar to that of the EMSS BL Lacs (see Padovani & Giommi 1995) though a larger range in α_{OX} and α_{RO} is covered.

4.1. Peak frequency

In order to get a more physical description of the spectral energy distribution of the BL Lac objects, we used a simple model to fit the synchrotron branch of the BL Lac. This has the advantage of describing the SED with one parameter (the peak frequency) instead of a set of three parameters (α_{OX} , α_{RO} , and α_{RX}). It has been shown by several authors that the synchrotron branch of the BL Lac SED is well approximated by a parabolic fit in the $\log \nu - \log \nu f_\nu$ plane (cf. Landau et al. 1986; Comastri et al. 1995; Sambruna et al. 1996; Fossati et al. 1998). In this way the peak position (ν_{peak}), the total luminosity and the total flux of the synchrotron emission can be derived. We chose the parameterization using fluxes $\log \nu f_\nu = a \cdot (\log \nu)^2 + b \cdot \log \nu + c$. Using luminosities instead of fluxes would change the absolute constant c only, leaving the position of the peak frequency unaffected.

If only three data points were given (one in the radio, optical, and X-ray band), the parabola was definite. When more than three data points were available (i.e. the K , H , and J near

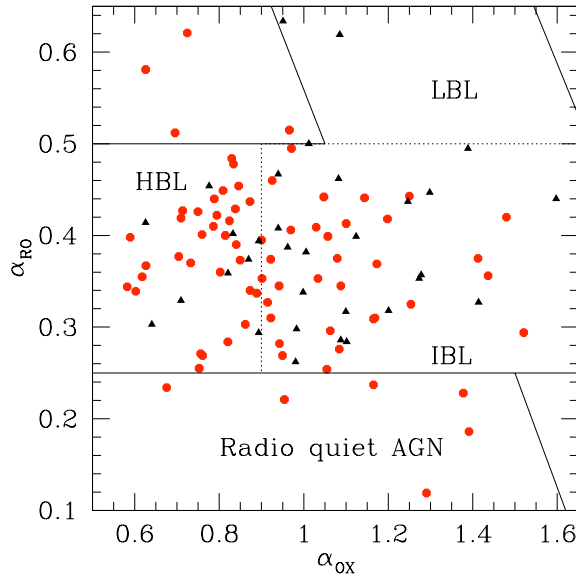


Fig. 3. The $\alpha_{\text{OX}} - \alpha_{\text{RO}}$ plane covered by the HRX-BL Lac objects. The points refer to the *complete sample*, the triangles mark additional objects found within the course of the work. Objects with $\alpha_{\text{RO}} < 0.2$ are called radio quiet.

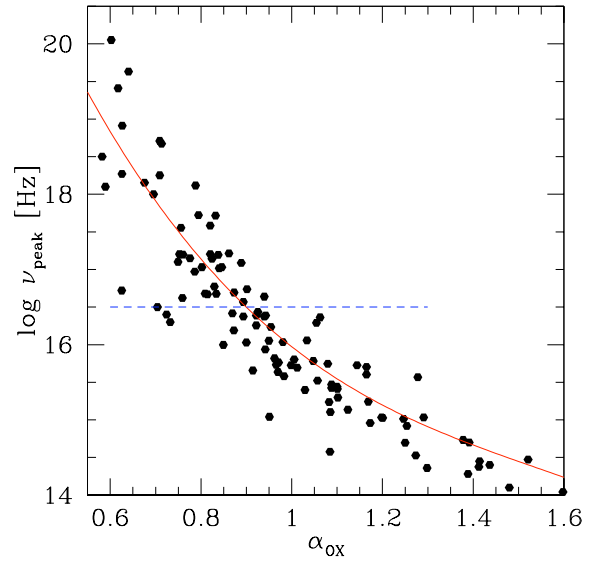


Fig. 5. Logarithm of the peak frequency vs. α_{OX} . The relation was approximated by a polynomial of third degree. The horizontal line marks the distinction between HBLs (above the line) and IBLs used in this paper.

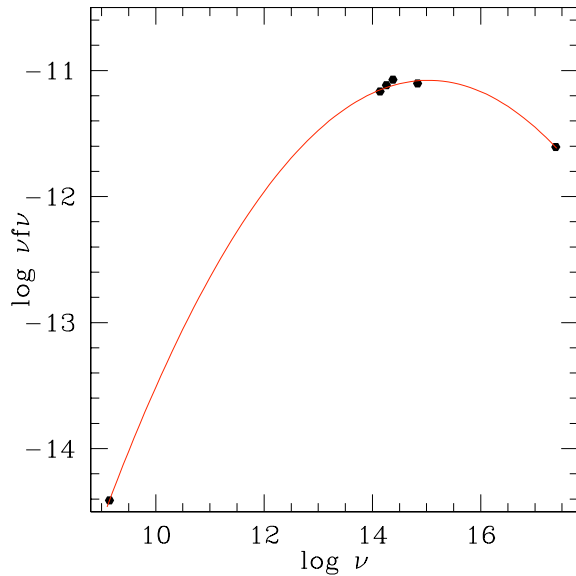


Fig. 4. Parabolic fit to the data of B2 0912+29.

infrared measurements from the 2MASS), a χ^2 minimization was used to determine best fit parameters. In principle, also the spectral slope in the X-ray band could be used to constrain the fit further. Because of the large uncertainties involved deriving these slopes from hardness ratio in the RASS, they were used mostly for consistency checks. Only in cases, where the parabolic fit resulted in peak frequencies above the highest energies observed, i.e. for objects with $\log \nu_{\text{peak}}$ above 2 keV and

steep X-ray spectra, the slopes were taken to account. An example for a parabolic fit is shown in Fig. 4. ν_{peak} is sensitive for the f_x/f_{opt} -relation, and is therefore strongly correlated with α_{OX} . This is shown in Fig. 5. The relation can be approximated by a polynomial of third degree. Using an F-test, parabolic fits of higher degree gave no improvements. Thus the peak frequency can also be determined, in the case no radio data is available by applying

$$\log \nu_{\text{peak}} = -3.0 \cdot \alpha_{\text{OX}}^3 + 13.8 \cdot \alpha_{\text{OX}}^2 - 23.3 \cdot \alpha_{\text{OX}} + 28.5 (\pm 0.51). \quad (3)$$

The standard error ($\sigma = 0.51$) is based on the deviation of the data points from the fit in Fig. 5. This result is comparable to that found by Fossati et al. (1998) when studying the dependency of α_{RO} and α_{RX} on the peak frequency.

4.2. Correlation of luminosities with the SED

A set of physical parameters which are correlated to the peak frequency are the luminosities in the different wavelength regions. To compute luminosities for all objects, the unknown redshifts were set to $z = 0.3$ which is the mean value for the HRX-BL Lac sample. While the luminosities L_R in the radio, L_K in the near infrared, and L_B in the optical region are decreasing with increasing peak frequency, the situation at X-ray energies is the other way round (as reported also by e.g. Mei et al. 2002; Beckmann 1999a).

The details about the correlation analysis are listed in Table 5, including the confidence level of the correlations.

The total luminosity L_{sync} within the synchrotron branch has been derived by integrating the spectral energy distribution between the radio and the X-ray band. This is a reasonable approximation as long as the peak frequency is below 1 keV

Table 5. Correlation of luminosity with peak frequency in the extended HRX-BL Lac sample.

region	r_{xy} Pearson coefficient	confidence level of correlation	linear regression ^a
radio (1.4 GHz)	-0.23	>97%	$\log L_R = -0.09 \cdot \log \nu_{\text{peak}} + 26.4$
near IR (<i>K</i> -band)	-0.28	>95% ^b	$\log L_K = -0.14 \cdot \log \nu_{\text{peak}} + 25.9$
optical (<i>B</i> -band)	-0.37	>99.9%	$\log L_B = -0.13 \cdot \log \nu_{\text{peak}} + 25.1$
X-ray (1 keV)	+0.51	>99.9%	$\log L_X = +0.19 \cdot \log \nu_{\text{peak}} + 17.3$
total (radio – X-ray)	-0.12		$\log L_{\text{sync}} = -0.04 \cdot \log \nu_{\text{peak}} + 22.0$

^a Luminosities in [W/Hz].

^b The lower confidence level results from the lower number of objects (52) with known *K*-band magnitudes. The other correlations are using the 104 BL Lacs of the extended sample.

($\log \nu = 17.4$), but systematically underestimates L_{sync} if the peak frequency is shifted beyond 1 keV. The relation of peak frequency with the total luminosities does not show a clear correlation.

5. Distribution in space

5.1. V_e/V_a -test

Redshifts are available for 64 (83%) of the 77 BL Lac objects which form the *complete sample*. Therefore it is possible to determine a luminosity function for the HRX-BL Lacs and to study the evolution by application of an V_e/V_a -test. The direct images of the BL Lacs without redshift determination show point-like structure, and most of them have optical spectra consistent with high redshifts ($z > 0.5$). The difficulty in determining redshifts for them indicate that these objects are highly core dominated with the host galaxy outshined by the BL Lac core. This implies that the optical luminosity of these objects should be quite high.

The V_e/V_a -test is a simple method developed by Avni & Bahcall (1980) based on the V/V_{max} test of Schmidt (1968). V_e stands for the volume, which is enclosed by the object, and V_a is the accessible volume, in which the object could have been found (e.g. due to a flux limit of a survey). Avni & Bahcall showed that different survey areas with different flux limits in various energy bands can be combined by the V_e/V_a -test. In the case of no evolution ($\langle V_e/V_a \rangle = 0.5$) is expected and following Avni & Bahcall (1980) the error $\sigma_m(n)$ for a given mean value $\langle m \rangle = \langle V_e/V_a \rangle$ based on n objects is:

$$\sigma_m(n) = \sqrt{\frac{1/3 - \langle m \rangle + \langle m \rangle^2}{n}}. \quad (4)$$

We computed the accessible volume $V_{a,i}$ for each object by applying the survey limits. In most cases this volume is determined by the X-ray flux limit, only ~10% of the objects have a smaller $V_{a,i}$ for the radio data, due to the radio flux limit of 2.5 mJy.

Applied to the *complete sample* the test yields $\langle V_e/V_a \rangle = 0.42 \pm 0.04$. This result shows that HBLs have been less numerous and/or less luminous in the past, but the significance is only 2σ . The negative evolution of X-ray selected BL Lac

objects has been reported several times before. We also performed a K-S test in order to determine the probability of uniform V_e/V_a distribution, which would mean no evolution. For the whole HRX-BL Lac sample the probability of no evolution is rather small (3.5%).

Thanks to the large number of objects with known redshifts within the HRX-BL Lac sample it is possible to examine dependencies of the evolution on other parameters, like the overall spectral indices. A division into two groups (more and less X-ray dominated objects) according to α_{OX} was already made by Bade et al. (1998) for the *core sample* and resulted in a lower $\langle V_e/V_a \rangle = 0.34 \pm 0.06$ for the HBLs ($\alpha_{\text{OX}} < 0.9$) than for the IBLs within the sample. The $\langle V_e/V_a \rangle = 0.48 \pm 0.08$ for IBLs was even consistent with no evolution. Dividing the HRX-BL Lac sample accordingly we now get for the HBLs ($\alpha_{\text{OX}} < 0.9$) $\langle V_e/V_a \rangle = 0.45 \pm 0.05$ ($N = 34$) and for the IBLs $\langle V_e/V_a \rangle = 0.40 \pm 0.06$ ($N = 30$). The difference between the two groups has practically vanished, and we are thus not able to confirm the different types of evolution for the HBLs and the IBLs. But still there are 13 objects within the HRX-BL Lac sample without known redshift, and nearly all of them are IBLs. Including them into the V_e/V_a -test by assigning them either the mean redshift of our sample ($z = 0.3$) or a high redshift ($z = 0.7$) does not change the mean V_e/V_a values significantly. The results of the different V_e/V_a -tests are shown in Table 6. Assigning even higher redshifts would increase the V_e/V_a for the IBLs, but we consider this unlikely, as the luminosities would then become exceptionally high. For example in 0716+714, PG 1246+586, or PG 1437+398 the X-ray luminosities would exceed values of $L_X = 10^{46}$ erg s⁻¹ in the 0.5–2.0 keV range.

We conclude therefore that the HRX sample shows no difference in evolution for HBLs and IBLs. The results presented here are in good agreement with recent other investigations on the evolutionary behaviour of BL Lac objects, as shown in Table 6. Except the sedentary survey (Giommi et al. 1999) none of the studies could confirm the highly significant negative evolution found e.g. by Bade et al. (1998) for the HRX-BL Lac *core sample* or by Wolter et al. (1994) for the EMSS BL Lacs. The best sample to be compared with should be the REX survey, which also uses the combination of RASS and NVSS data, although going to lower X-ray flux limits while using only the

Table 6. Results from the V_e/V_a -tests for the HRX-BL Lac *complete sample*.

selection	unknown z set to	N^a	$\langle V_e/V_a \rangle$	$K - S^b$ [%]
all (known z)	–	64	0.42 ± 0.04	3.5
all	0.3	77	0.44 ± 0.03	5.3
all	0.7	77	0.46 ± 0.03	5.3
HBLs (known z)	–	34	0.45 ± 0.05	24.0
all HBLs	0.3	36	0.48 ± 0.05	46.1
all HBLs	0.7	36	0.48 ± 0.05	46.1
IBLs (known z)	–	30	0.40 ± 0.06	14.0
all IBLs	0.3	41	0.41 ± 0.05	10.7
all IBLs	0.7	41	0.43 ± 0.05	10.7

^a Number of objects used for this test.

^b $K - S$ test probability that the V_e/V_a values have a uniform distribution in the $[0..1]$ interval (probability for no evolution).

Table 7. Results from the V_e/V_a -tests for comparable investigations.

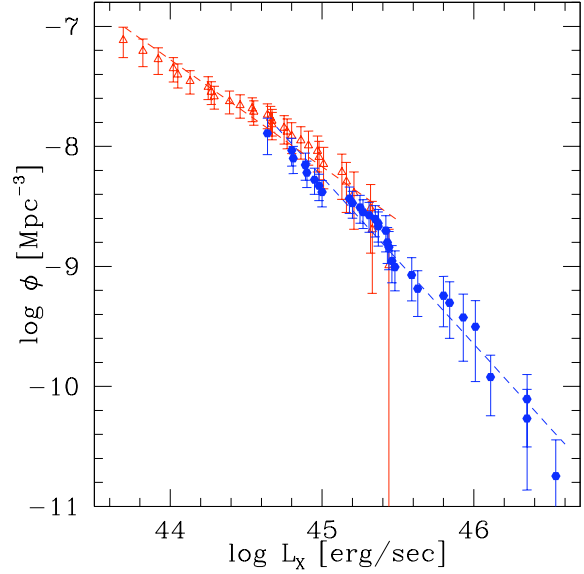
survey	selection	unknown z	N^a	$\langle V_e/V_a \rangle$
REX	total	0.27	55	0.48 ± 0.04
REX	HBL	0.27	22	0.49 ± 0.06
sedentary	total	0.25	155	0.42 ± 0.02
DXRBS	all BL Lacs	0.40	30	0.57 ± 0.05
DXRBS	HBL	0.40	11	0.65 ± 0.09
DXRBS	LBL	0.40	19	0.52 ± 0.07

^a Number of objects used for this test.

are of the PSPC pointed observation. The REX has also a mean redshift of $z = 0.3$ and the $\langle V_e/V_a \rangle$ are within one sigma when compared to the HRX-BL Lac sample.

5.2. X-ray luminosity functions

For the V_e/V_a -test the knowledge of the redshifts is of minor importance. However, the luminosity function which defines the space density at a given object luminosity can only be derived when having a complete sample with known distances. Based on this function we wish to estimate the fraction of AGN which appear to be BL Lac objects. To determine the cumulative luminosity function (CLF), one has to count all objects within a *complete sample* above a given luminosity, and divide this number by the volume V_a which has been surveyed for these objects. We follow here the procedure described by Marshall (1985) to derive the space density and the corresponding errors. The survey area of the HRX-BL Lac *complete sample* is 4768 deg^2 (Table 1). Because the fraction of objects without known redshift is 17% the effective area which is used to compute the luminosity function is decreased by this fraction to 3959 deg^2 . This implies that the redshift distribution of the missing objects is the same as for the rest. As discussed before, this assumption might be incorrect, as we expect many of them having rather high redshifts. The effect of different

**Fig. 6.** Cumulative luminosity function of the two subsamples with $z > 0.272$ (circles) and $z < 0.272$ (open triangles).

evolution for high and low redshift objects, described in the next paragraph, would be even stronger in this case.

The *complete sample* is large enough to divide it into a high redshift and a low redshift bin in order to examine possible differences in their CLF. The dividing value was set to the median of the HRX-BL Lac sample $z_{\text{median}} = 0.272$. To derive high and low redshift CLFs the accessible volume $V_{a,i}$ for the objects with $z < 0.272$ has been restricted to $z = 0.272$ whenever $z_{\text{max},i} > 0.272$. For the high redshift objects the accessible volume was computed from $z = 0.272$ up to $z_{\text{max},i}$. The resulting two cumulative luminosity functions are shown in Fig. 6.

There seem to be differences between the high and low redshift CLF. The slope of the low redshift CLF is flatter. A linear regression gives a slope of -0.9 while for $z > 0.272$ the slope is -1.4 . But in the overlapping regime at $L_x(0.5-2.0 \text{ keV}) \sim 10^{45}$ the luminosity functions show similar slopes.

The left panel of Fig. 7 shows the comparison of the HRX-BL Lac *complete sample* X-ray luminosity function with the results from the EMSS BL Lac sample (Wolter et al. 1994; Padovani & Giommi 1995). The expected luminosities of the HRX-BL Lacs within the EINSTEIN IPC energy band (0.3–3.5 keV) were calculated assuming a spectral slope of $\alpha_X = 1.0$. Space densities are given as number of objects per Gpc^3 and X-ray luminosity bin following Padovani & Giommi (1995). The data from the EMSS are consistent with those from the HRX-BL Lac *complete sample* within the 1σ error bars. The marginal differences can be due to systematic errors for the calculated luminosities in the IPC band because of differing spectral slopes, or resulting from differences in the calibration of the IPC and the PSPC detectors.

In the right panel of Fig. 7 we compare the differential luminosity function of the *complete sample* with the corresponding function for AGNs at $z < 0.5$. The AGN X-ray luminosity

function was taken from the ROSAC sample (“A ROSAT based Search for AGN-Clusters”, Tesch 2000). This AGN sample was constructed similarly as the HRX-BL Lac sample and both samples match closely in brightnesses and redshifts. The ROSAC-AGN sample contains 182 RASS-AGNs with $z < 0.5$ identified in an area of 363 deg^2 in the constellation of Ursa Major. The AGN X-ray luminosities have been corrected for the different X-ray band (0.1–2.4 keV instead 0.5–2.0 keV) using the same spectral slopes used for the ROSAC sample.

We find that the space density of BL Lacs in the luminosity range $44 < \log L_X < 46$ is about 10% of the space density of AGNs. In case that all AGNs have jets and would be classified as BL Lacs when looking into their jet, an jet opening angle of $\sim 50^\circ$ would follow. But as the jet emission is expected to be beamed, the BL Lacs appear to be brighter than they are. Following Urry & Shaefer (1984) the observed luminosity is $L_{\text{obs}} = \delta^p L_{\text{emi}}$ with L_{emi} being the emitted luminosity, and

$$\delta = \frac{1}{\gamma(1 - \frac{v}{c_0} \cos \theta)} \quad (5)$$

where γ is the Lorentz factor of the jet emission. p depends on the spectral slope and the jet flow model. For the simple case of a moving blob and continuous reacceleration (Lind & Blandford 1985) which applies e.g. for the model of a wide X-ray jet (Celotti et al. 1993) the exponent is $p = 3 + \alpha$, where $\alpha \simeq 1$ is the spectral index. For a conical jet this exponent is $p = 2 + \alpha$ (Urry & Shaefer 1984). Assuming an jet opening angle of $\theta \sim 30^\circ$ (Urry & Padovani 1995) and a Lorentz factor $\gamma \sim 5$ the amplification factor is $\delta^p \simeq 50$ (for the conical jet) and $\delta^p \simeq 200$ (for the wide X-ray jet). Correcting the luminosities accordingly yields a fraction of $\leq 0.1\%$ BL Lacs among all AGNs. A smaller opening angle and/or larger Lorentz factor would lead to an even lower BL Lac fraction among the AGN.

6. Discussion

The large number of objects included in the HRX-BL Lac sample enabled us to study in detail a number of BL Lac properties in different wavelength regions. In the following, we will discuss these properties with special emphasis on their compatibility with the most recent models trying to unify the HBL and LBL objects.

6.1. Strength of the calcium break and luminosities

We observed a clear anti-correlation between calcium break strength and the luminosity in the radio, near infrared, optical, and X-rays bands. We explain this with a wide range of luminosities for the non-thermal source, while the host galaxies seem to have approximately constant luminosity. The higher the luminosity of the central source, the more does the core outshine the hosting galaxy, leading to decreasing break strength with increasing luminosity.

The identification of several HRX-BL Lac with $25\% < \text{Ca-break} < 40\%$ and the smooth extension of the correlation between break strength and luminosities into this range, supports previous findings that BL Lacs can have

Ca-break $> 25\%$ (Marchã et al. 1996; Laurent-Muehleisen et al. 1999; Rector et al. 2000; Landt et al. 2002) in contrast to earlier suggestions (Stocke et al. 1989).

Landt et al. (2002) studied in detail the dependency of the calcium break strength on the luminosity of the blazars inside the DXRBS sample (Padovani 2001). They found the same correlation as described here for the HRX-BL Lac sample and show that the calcium break values decrease with increasing jet power, and therefore with increasing luminosity. Based on this they conclude that the break value of BL Lac objects could be an indicator of the orientation. Nevertheless different luminosities of the core component (i.e. of the jet) will also play a major role in the effect, and it seems to be difficult to disentangle the influence from different orientation and from different jet luminosity. Thus though we find for the HRX-BL Lac sample the same correlation as described by Landt et al. (2002) we conclude here only that the break strength is an indicator of different apparent luminosity, either based on different orientation, or on different jet power, or on mixture of both effects.

6.2. HBL/LBL: Evolutionary dichotomy?

Most of the results for the HRX-BL Lac *core sample* (Bade et al. 1998) could be confirmed by the *complete sample* presented here. The most significant discrepancy are the different results of the V_e/V_a test. We found negative evolution using the *complete sample*, but we did not find differences in evolution, if we divide the sample by α_{OX} (or peak frequency).

The results of Bade et al. (1998) could have been arisen from selection effects due to the “patchy” search area used. A Monte-Carlo simulation done on the HRX-BL Lac *complete sample* shows however, that this is not the case. By randomly selecting a subsample of 17 BL Lac objects (which is the number of objects for which Bade et al. found different types of evolution) out of the HBLs of the *complete sample* there is a chance of $< 1\%$ only to find a $\langle V_e/V_a \rangle < 0.35$.

Another reason for the different results could be related to the different treatment of the radio properties. As radio detection was not a selection criterium in Bade et al., no radio flux limit was taken into account. Applying here the V_e/V_a -test to the *complete sample* (cf. Sect. 5), the accessible volume V_a was determined for $\approx 10\%$ of the objects by the radio limit. The V_e/V_a values are correspondingly increased compared to the case where only X-ray flux limit is taken into account, resulting in a less negative evolution. There remains the fact that no BL Lac objects were found yet, with $f_R < 2 \text{ mJy}$ radio counterparts and the question is still open whether this is a selection effect or not. It could be that our decision to apply the radio detection as selection criterium weakens the negative evolution found in pure X-ray selected samples.

The result, that the evolution of BL Lac objects of the HBL and IBL type is consistent with no evolution is in good agreement with other recent studies. Neither REX or DXRBS, nor the HRX-BL Lac sample show a difference for the more or less X-ray dominated BL Lacs. On the contrary it seems that the evolution of the IBL might even be slightly more positive than that of the HBL class. This picture clearly differs from

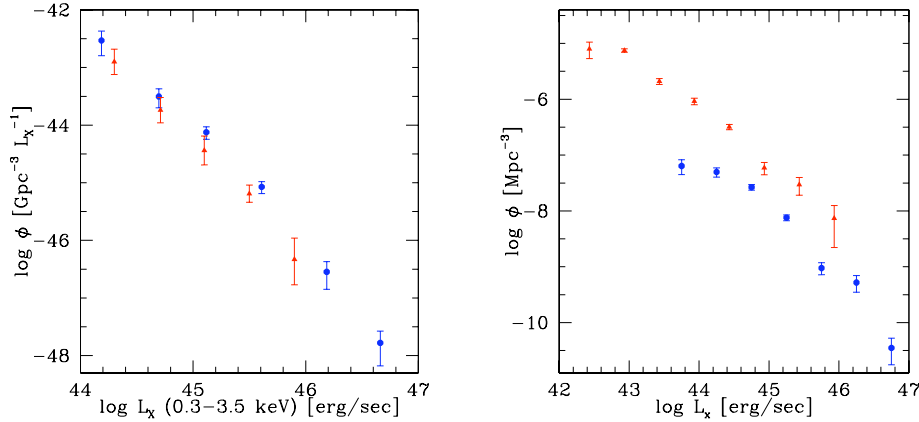


Fig. 7. Left panel: The differential X-ray luminosity function of the HRX-BL Lac *complete sample* (circles) in comparison to EMSS BL Lacs (triangles; Padovani & Giommi 1995). The X-ray data of the HRX-BL Lac objects have been extrapolated to the EINSTEIN IPC energy band assuming a spectral slope of $\alpha_X = 1$. Right panel: Comparison of the X-ray luminosity function of RASS selected AGNs from the ROSAC sample (triangles; Tesch 2000) with HRX-BL Lacs (circles). The density of BL Lacs is ~ 10 times lower than for all AGNs.

the EMSS BL Lac result of $\langle V_e/V_a \rangle = 0.36 \pm 0.05$, while the sendentary survey, presented by Giommi et al. (1999) seems not be complete enough up to now to draw a firm conclusion. Caccianiga et al. (2002) argue, that the REX might miss the negative evolution of the HBL is not visible simply because the sample is not deep enough, and this argumentation then would also apply for the HRX-BL Lac sample, which X-ray flux limit is about two times higher than that of the REX BL Lacs. Their simulation result in the conclusion that even a completion of the REX survey might not lead to a highly significant negative evolution (2σ for the simulated sample).

Finally, the evolution found in the course of this work is in good agreement with that of FR-I galaxies ($\langle V_e/V_a \rangle = 0.40 \pm 0.06$) within the 3CR sample (Laing et al. 1984). This supports the assumption that the FR-I galaxies build the parent population of BL Lac objects (see e.g. Padovani & Urry 1990).

In contrast to HBLs, the LBLs show weak or positive evolution ($\langle V_e/V_a \rangle = 0.61 \pm 0.05$) as shown for the 1 Jy sample by Rector & Stocke (2001). Following the sequence of blazars, also FSRQs exhibit significant positive evolution ($\langle V_e/V_a \rangle = 0.58 \pm 0.03$ for the 119 FSRQs in the DXRBS sample; Padovani 2001). Also FR-II radio galaxies and “normal” quasars seem to be more numerous and/or luminous at cosmological distances than in the neighborhood, leaving the question for the reasons of the HBL/LBL evolutionary dichotomy of relevance also in future.

6.3. A unifying model for LBL and HBL

The different evolutionary behaviour of HBLs and LBLs is a challenge for all theories to unify both BL Lac types into one class. However, the existence of transition objects and the numerous similar properties of LBLs and HBLs make it plausible that both classes belong to the same parent population.

As described by Böttcher & Dermer (2002) one way to unify both classes would be a transformation of LBLs into

HBLs as the BL Lac objects grow older. In this model, BL Lac objects start as LBLs with jets of high energy densities. Strong cooling limits the electron energies leading to cutoff frequencies for the synchrotron component at optical wavelengths and for the IC component in the GeV energy range. As shown by Beckmann et al. (2002), this results in steep X-ray spectra with strong curvature. The core outshines the host galaxy leading to a low calcium break value (Landt et al. 2002) as seen also for the HRX-BL Lac sample (cf. Fig. 2).

When by the time the source of the jet gets less powerful the energy density within the jet decreases (Tavecchio et al. 1998). The cooling efficiency decreases as well resulting in higher cutoff frequencies for HBLs. The shift of the cutoff frequencies to higher energies is therefore accompanied by decreasing bolometric luminosities, which is evident from the decrease of the luminosities in the radio, near IR and optical bands. Due to the increasing peak frequencies of the synchrotron branch more energy is released in the X-ray band and the X-ray luminosity increases quite in contrast to the luminosities at shorter frequencies (cf. Table 5). The X-ray spectra are correspondingly flatter and less curved than in the LBL state (Beckmann & Wolter 2001).

Objects which do not fit into this scenario are doubtlessly the extremely luminous HBLs, like 1ES 1517+656 (Beckmann et al. 1999b). The scenario presented here assumes the HBLs to be on average less luminous than the LBLs. Apart from the exceptionally high X-ray luminosity, this object also shows an optical luminosity typical for a Flat Spectrum Radio Quasar (FSRQ). Padovani (2001) argues that those high state BL Lacs with high peak frequency might belong to the high energy peaked FSRQ class (HFSRQ), flat-spectrum radio quasars with synchrotron peak in the UV/X-ray band. In this case 1ES 1517+656 should show strong emission lines, e.g. strong H_α and H_β which would be located in the near infrared for this high-redshift BL Lac ($z = 0.7$) and would have been missed by previous observations.

The HRX-BL Lac sample could be the basis to study the extreme end of the HBL population, the ultra high frequency peaked BL Lac objects (UHBL). Sambruna et al. (1996) argued that objects with cutoff frequencies higher than 10^{18} Hz would be detected only in hard X-ray surveys but should be faint at lower frequencies, which would make their discovery difficult.

Nevertheless HBLs have already been detected at TeV energies, as e.g. 1ES 1426+428 (Aharonian et al. 2002; Horan et al. 2002) and 1ES 1959+650 (Horns & Konopelko 2002). Recently Costamante & Ghisellini (2002) showed that it is possible to select candidates for TeV BL Lacs on the basis of the knowledge of the SED, i.e. strong X-ray flux and a sufficiently strong radio-through-optical flux, which results in high peak frequencies of the synchrotron branch.

Also 13 HBLs within the HRX-BL Lac sample show peak frequencies $\nu_{\text{peak}} > 10^{18}$ Hz from the parabolic fit to the synchrotron branch and three objects even $\nu_{\text{peak}} > 10^{19}$ Hz. 1RXS J121158.1+224236 might even be a UHBL with a peak frequency of the synchrotron branch at $\nu_{\text{peak}} \approx 10^{22}$ Hz. To confirm the high peak frequencies, for this extreme source, observations with the BeppoSAX satellite have been performed and results will be presented in a forthcoming paper. Investigations in the gamma region (~ 1 MeV) are needed to decide whether these energies are dominated by the synchrotron emission or if already the inverse Compton branch is rising. The SPI spectrograph on-board the INTEGRAL mission (see e.g. Winkler & Hermsen 2000), which has been successfully launched in October 2002, will allow to do spectroscopy in this energy region (20 keV–8 MeV).

Acknowledgements. We would like to thank the anonymous referee for the valuable suggestions which helped us to improve the paper. This research has made use of the NASA/IPAC Extragalactic Database (NED) which is operated by the Jet Propulsion Laboratory, California Institute of Technology under contract with the National Aeronautics and Space Administration. We acknowledge support by the Deutsche Forschungsgemeinschaft through grants Re 353/39-1 and En 176/23-1.

References

- Aharonian, F., Akhperjanian, A., Barrio, J., et al. 2002, *A&A*, 384, L23
- Avni, Y., & Bahcall, J. N. 1980, *ApJ*, 235, 694
- Bade, N., Beckmann, V., Douglas, N. G., et al. 1998, *A&A*, 334, 459
- Beckmann, V. 1999a, in *PASPC 159*, ed. L. O. Takalo, & A. Silanpää
- Beckmann, V., Bade, N., & Wucknitz, O. 1999b, *A&A*, 352, 395
- Beckmann, V. 2000a, *BLAZAR Data*, 2, 3
- Beckmann, V. 2000b, Ph.D. Thesis, Hamburg University, <http://www.sub.uni-hamburg.de/disse/330/vbdi ss.html>
- Beckmann, V., & Wolter, A. 2001, *AIP Conf. Proc.*, 599, 502 [astro-ph/0007089]
- Beckmann, V., Wolter, A., Celotti, A., et al. 2002, *A&A*, 383, 410
- Bicknell, G. V., & Wagner, S. J. 2002, *PASA*, 19, 129
- Böttcher, M., & Dermer, C. D. 2002, *ApJ*, 564, 86
- Böttcher, M., & Chiang, J. 2002, *ApJ*, 581, 127
- Caccianiga, A., Maccacaro, M., Wolter, A., et al. 1999, *ApJ*, 513, 51
- Caccianiga, A., Maccacaro, M., Wolter, A., et al. 2002, *ApJ*, 566, 181
- Cavaliere, A., & D'Elia, V. 2002, *ApJ*, 571, 226
- Celotti, A., Maraschi, L., Ghisellini, G., et al. 1993, *ApJ*, 416, 118
- Comastri, A., Molendi, S., & Ghisellini, G. 1995, *MNRAS*, 277, 297
- Condon, J. J., Cotton, W. D., Greisen, E. W., et al. 1998, *AJ*, 115, 1693
- Costamante, L., & Ghisellini, G. 2002, *A&A*, 384, 56
- Dressler, A., & Shectman, S. 1987, *AJ*, 94, 899
- Fossati, G., Maraschi, L., Celotti, A., et al. 1998, *MNRAS*, 299, 433
- Georganopoulos, M., & Marscher, A. P. 1998, *ApJ*, 506, 621
- Ghisellini, G., Padovani, P., Celotti, A., & Maraschi, L. 1993, *ApJ*, 407, 65
- Ghisellini, G., Celotti, A., Fossati, G., et al. 1998, *MNRAS*, 301, 451
- Giommi, P., Menna, M. T., & Padovani, P. 1999, *MNRAS*, 310, 465
- Ghisellini, G., Celotti, A., & Costamante, L. 2002, *A&A*, 386, 833
- Hagen, H.-J., Groote, D., Engels, D., & Reimers, D. 1995, *A&AS*, 111, 195
- Horan, D., Badran, H. M., Bond, I. H., et al. 2002, *ApJ*, 571, 753
- Horns, D., & Konopelko, K. 2002, *ATel*, 96, 1
- Landau, R., Golisch, B., Jones, T. J., et al. 1986, *ApJ*, 308, 78
- Landt, H., Padovani, P., Perlman, E. S., et al. 2001, *MNRAS*, 323, 757
- Landt, H., Padovani, P., & Giommi, P. 2002, *MNRAS*, 336, 945
- Laurent-Muehleisen, S. A., Kollgaard, R. I., Feigelson, I. D., et al. 1999, *ApJ*, 525, 127
- Ledden, J. E., & O'Dell, S. L. 1985, *ApJ*, 298, 630
- Lind, K. R., & Blandford, R. D. 1985, *ApJ*, 295, 358
- Maccacaro, M., Caccianiga, A., Della Ceca, R., et al. 1998, *Astron. Nachr.*, 319, 15
- Madau, P., Ghisellini, G., & Persic, M. 1987, *MNRAS*, 224, 257
- Maraschi, L., & Rovetti, F. 1994, *ApJ*, 436, 79
- Maraschi, L., & Tavecchio, F. 2002, *ApJ*, in press [astro-ph/0205252]
- Marchã, M. J. M., Browne, I. W. A., Impey, C. D., & Smith, P. S. 1996, *MNRAS*, 281, 425
- Marshall, H. L. 1985, *AJ*, 299, 109
- Mei, D. C., Zhang, L., & Jiang, Z. J. 2002, *A&A*, 391, 917
- Padovani, P., & Urry, C. M. 1990, *ApJ*, 356, 75
- Padovani, P. 1992, *MNRAS*, 257, 404
- Padovani, P., & Giommi, P. 1995, *ApJ*, 444, 567
- Padovani, P. 2001, *Blazar Demographics and Physics*, *ASP Conf. Ser.*, 227, 163
- Padovani, P., & Urry, C. M. 2001, *Blazar Demographics and Physics*, *ASP Conf. Ser.*, 227
- Perlman, E. S., Padovani, P., Giommi, P., et al. 1998, *AJ*, 115, 1253
- Rector, T. A., Stocke, J. T., Perlman, E. S., et al. 2000, *AJ*, 120, 1626
- Rector, T. A., & Stocke, J. T. 2001, *AJ*, 122, 565
- Sambruna, R. M., Maraschi, L., & Urry, C. M. 1996, *ApJ*, 463, 444
- Schartel, N. 1994, Ph.D. Thesis, MPE Garching
- Schmidt, M. 1968, *ApJ*, 151, 393
- Skrutskie, M. F., Beichmann, C., & Capps, R. 1995, *Am. Astron. Soc. Meet.*, 187, 75.07
- Stiening, R., Skrutskie, M. F., & Capps, R. 1995, *Am. Astron. Soc. Meet.*, 187, 75.08
- Stickel, M., Fried, J. W., & Kühr, H. 1991, *ApJ*, 374, 431
- Stocke, J. T., Morris, S. L., Gioia, I. M., et al. 1989, in *BL Lac Objects*, ed. L. Maraschi, T. Maccacaro, & M.-H. Ulrich (Berlin: Springer), 242
- Stocke, J. T., Morris, S. L., Gioia, I. M., et al. 1991, *ApJS*, 76, 813
- Tavecchio, F., Maraschi, L., & Ghisellini, G. 1998, *ApJ*, 509, 608
- Tesch, F. 2000, Ph.D. Thesis, Hamburg University, <http://www.sub.uni-hamburg.de/disse/284/Disse.pdf>
- Urry, C. M., & Shaefer, R. A. 1984, *ApJ*, 280, 569
- Urry, C. M., & Padovani, P. 1995, *PASP*, 107, 803
- Urry, C. M., Scarpa, R., O'Dowd, M., et al. 2000, *ApJ*, 532, 816
- Voges, W., Aschenbach, B., Boller, Th., et al. 1999, *A&AS*, 349, 389
- Wall, J. V., & Peacock, J. A. 1985, *MNRAS*, 216, 173
- Winkler, C., & Hermsen, W. 2000, *AIP Conf. Proc.*, 510, 676
- Wolter, A., Caccianiga, A., Della Ceca, R., & Maccacaro, T. 1994, *ApJ*, 433, 29
- Wolter, A., Comastri, A., Ghisellini, G., et al. 1998, *A&A*, 335, 899

6.9.2 The First INTEGRAL AGN Catalog

A discussion of this work in the context of the unified model of AGN can be found in Section 4.6.6 on page 60. The manuscript, which is shown on the following pages, has been published as

Beckmann V., Gehrels N., Shrader C. R., & Soldi S., *The Astrophysical Journal*, Volume 638, Issue 2, pp. 642–652 (2006)

THE FIRST *INTEGRAL* AGN CATALOGV. BECKMANN,¹ N. GEHRELS, AND C. R. SHRADER²Exploration of the Universe Division, NASA Goddard Space Flight Center, Code 661, Greenbelt, MD 20771;
beckmann@milkyway.gsfc.nasa.gov

AND

S. SOLDI³*INTEGRAL* Science Data Centre, Chemin d'Écogia 16, 1290 Versoix, Switzerland

Received 2005 July 8; accepted 2005 October 18

ABSTRACT

We present the first *INTEGRAL* AGN catalog, based on observations performed from launch of the mission in 2002 October until 2004 January. The catalog includes 42 AGNs, of which 10 are Seyfert 1, 17 are Seyfert 2, and 9 are intermediate Seyfert 1.5. The fraction of blazars is rather small, with five detected objects, and only one galaxy cluster and no starburst galaxies have been detected so far. A complete subset consists of 32 AGNs with a significance limit of 7σ in the *INTEGRAL* ISGRI 20–40 keV data. Although the sample is not flux limited, the distribution of sources shows a ratio of obscured to unobscured AGNs of 1.5–2.0, consistent with luminosity-dependent unified models for AGNs. Only four Compton-thick AGNs are found in the sample. Based on the *INTEGRAL* data presented here, the Seyfert 2 spectra are slightly harder ($\Gamma = 1.95 \pm 0.01$) than Seyfert 1.5 ($\Gamma = 2.10 \pm 0.02$) and Seyfert 1 ($\Gamma = 2.11 \pm 0.05$).

Subject headings: catalogs — galaxies: active — galaxies: Seyfert — gamma rays: observations — X-rays: galaxies

Online material: color figures

1. INTRODUCTION

The X-ray sky as seen by X-ray satellites over the past 40 years shows a substantially different picture than, for example, the optical band. While the visual night sky is dominated by main-sequence stars, Galactic binary systems and supernova remnants form the brightest objects in the X-rays. Common to both regimes is the dominance of active galactic nuclei (AGNs) toward lower fluxes. In the X-ray range itself, one observes a slightly different population of AGNs at soft and at hard X-rays. Below 5 keV the X-ray sky is dominated by AGNs of the Seyfert 1 type; above 5 keV the absorbed Seyfert 2 objects appear to become more numerous. These type 2 AGNs are also the main contributors to the cosmic X-ray background (XRB) above 5 keV (Setti & Woltjer 1989; Comastri et al. 1995, 2001; Gilli et al. 2001), although only $\sim 50\%$ of the XRB above 8 keV can be resolved (Worsley et al. 2005). In addition to the rather persistent Seyfert galaxies, blazars are detectable in the hard X-rays. Because of the fact that we look into a highly relativistic jet in the case of those sources, the blazars exhibit strong variability on all timescales and are especially variable in the X-ray and high-energy gamma-ray domain. For an overview of the various extragalactic X-ray surveys, see Brandt & Hasinger (2005); for early *International Gamma-Ray Astrophysics Laboratory* (*INTEGRAL*) results, see Krivonos et al. (2005).

The hard X-ray energy range is not currently accessible to X-ray telescopes using grazing incidence mirror systems. Instead, detectors without spatial resolution, such as the Phoswich

Detection System (PDS; Frontera et al. 1997) on *BeppoSAX* (Boella et al. 1997) and the Oriented Scintillation Spectrometer Experiment (OSSE; Johnson et al. 1993) on the *Compton Gamma Ray Observatory* (*CGRO*; Gehrels et al. 1993), have been applied. A synopsis of these previous results is as follows. The 2–10 keV Seyfert 1 continua are approximated by a $\Gamma \simeq 1.9$ power-law form (Zdziarski et al. 1995). A flattening above ~ 10 keV has been noted and is commonly attributed to Compton reflection (George & Fabian 1991). There is a great deal of additional detail in this spectral domain—“warm” absorption, multiple-velocity component outflows, and relativistic line broadening—that is beyond the scope of this paper. The Seyfert 2 objects are more poorly categorized here; the general belief is that they are intrinsically equivalent to the Seyfert 1 objects, but viewed through much larger absorption columns (see, e.g., Véron-Cetty & Véron [2000] for a recent review).

Above 20 keV the empirical picture is less clear. The ~ 20 –200 keV continuum shape of both Seyfert types is consistent with a thermal Comptonization spectral form, although in all but a few cases the data are not sufficiently constraining to rule out a pure power-law form. Nonetheless, the nonthermal scenarios with pure power-law continua extending to approximately mega-electron volt energies reported in the pre-*CGRO* era are no longer widely believed and are likely a result of background systematics. However, a detailed picture of the Comptonizing plasma—its spatial, dynamical, and thermodynamic structure—is not known. We hope that among the critical determinations that *INTEGRAL* or future hard X-ray instruments will provide are the plasma temperature and optical depth (or Compton y -parameter) for a large sample of objects.

The other major class of gamma-ray-emitting AGNs, the blazars (flat-spectrum radio quasars [FSRQs] and BL Lac objects), are even more poorly constrained in the *INTEGRAL* spectral domain. The detection of ~ 70 of these objects with the

¹ Also with the Department of Physics, Joint Center for Astrophysics, University of Maryland, Baltimore County, Baltimore, MD 21250.

² Also with Universities Space Research Association, 10211 Wincopin Circle, Columbia, MD 21044.

³ Also with Observatoire de Genève, 51 Chemin des Maillettes, 1290 Sauverny, Switzerland.

Energetic Gamma-Ray Experiment Telescope (EGRET) on *CGRO* in the 1990s has established the presence of $\Gamma \sim 10$ relativistic plasma at small angles to the observer's line of sight. The so-called TeV blazars are similar objects, but with the peak power shifted to even greater energies, probably due to an even smaller viewing angle (see, e.g., Fossati et al. [1998], and for earlier *INTEGRAL* results, Pian et al. [2005]). The most common interpretation of the broadband continuum emission is the synchrotron self-Compton (SSC) model, although the external Compton (EC) models are still also plausible. Broadband temporal coverage can in principle discriminate between these possibilities, although each of these components can separately contribute to the hard X-ray band under extreme circumstances. The *INTEGRAL* band-pass covers a critical region that can in principle establish the amplitude and shape of the high-end synchrotron component or the low-end SSC component.

Critical to each of these issues is the need to obtain improved continuum measurements over the hard X-ray to soft gamma-ray range for as large a sample of objects as possible. *INTEGRAL* (Winkler et al. 2003), since its launch in 2002 October, offers an unprecedented >20 keV collecting area and state-of-the-art detector electronics and background rejection capabilities. Thus, it offers hope of substantial gains in our knowledge of the AGN phenomenon. We were thus motivated at this juncture, some 3 years into the mission, to formulate and present the collective look at the data so far obtained and assess the potential for progress in the *INTEGRAL* era.

As the satellite spent most of its observing time up to now concentrating on the Galactic plane, some low-latitude AGNs have been detected. Observations at higher Galactic latitude have also led to studies of individual sources: 3C 273 (Courvoisier et al. 2003b), NGC 4388 (Beckmann et al. 2004), GRS 1734–292 (Sazonov et al. 2004), the S5 0716+714 field (Pian et al. 2005), PKS 1830–211 (De Rosa et al. 2005), NGC 4151 (Beckmann et al. 2005), six AGNs near the Galactic plane (Soldi et al. 2005), and an early study of all extragalactic sources seen through the Galactic plane (Bassani et al. 2004). Two of the new sources discovered by *INTEGRAL*, IGR J18027–1455 and IGR J21247+5058, have also been shown to be AGNs (Masetti et al. 2004).

With the ongoing observation of the sky by *INTEGRAL*, a sufficient amount of data is now accessible to compile the first *INTEGRAL* catalog of AGNs. In this paper we present an analysis of recent observations performed by the *INTEGRAL* satellite instruments IBIS/ISGRI, SPI, and JEM-X, and compare the results with previous studies.

2. OBSERVATIONS

Observations in the X-ray to soft gamma-ray domain have been performed by the instruments on board the *INTEGRAL* satellite (Winkler et al. 2003). This mission offers the unique possibility to perform simultaneous observations over the 2–8000 keV energy region. This is achieved by the X-ray monitor (2–30 keV) JEM-X (Lund et al. 2003), the soft gamma-ray imager (20–1000 keV) ISGRI (Lebrun et al. 2003), and the spectrograph SPI (Vedrenne et al. 2003), which operates in the 20–8000 keV region. Each of these instruments employs the coded-aperture technique (Caroli et al. 1987). In addition to these data an optical monitor (OMC; Mas-Hesse et al. 2003) provides photometric measurements in the *V* band.

2.1. INTEGRAL Data

Data used for the analysis presented here were all in the public domain by the end of 2005 March. This includes data from orbit

revolutions 19–137 and 142–149. Data before revolution 19 have been excluded, as the instrument settings changed frequently and therefore the data from this period are not suitable to be included in a homogeneous survey. So far, most of the *INTEGRAL* observing time has been spent on the Galactic plane, with some deep exposures at high Galactic latitude, for example, in the Virgo and the Centaurus regions.

Our sample objects have been selected in three ways. The first criterion was a detection in the ISGRI data in a single pointed observation. The duration of one pointing of the spacecraft is usually 2–3 ks long. The standard analysis of the data is performed at the *INTEGRAL* Science Data Centre (ISDC; Courvoisier et al. 2003a). These results are publicly available.⁴ Within one pointing, the detection threshold for a source in the center of the field of view of ISGRI is about 20 mcrab. A second-level search was done using combined data sets of individual observations and contained within separate revolutions, which are about 3 days long. In cases where an observation lasted longer than a revolution, the data set was split by revolution. The results from this analysis are publicly available through the HEASARC archive.⁵ Clearly, the sensitivity of this second method depends strongly on the duration of the analyzed observation. The sensitivity also depends on the dither pattern of the observation and on the position of the source within the field of view. In addition to those two ways of combining the list of AGNs seen by *INTEGRAL*, we added all AGNs that have so far been reported as *INTEGRAL* detections in the literature. This combined list of objects is presented in Table 1. In order to get meaningful results for each of the sources in this AGN sample, it was necessary to perform an individual analysis for each one. We used the data for which the spacecraft was pointed within a 10° radius about each AGN for ISGRI and SPI, and within 5° for JEM-X. The exposure times listed in Table 1 refer to the effective ISGRI values. These values are approximately the same for the spectrograph SPI, but for the JEM-X monitor it has to be taken into account that they cover a much smaller sky area. Thus, in the case of dithering observation, the source is not always in the field of view of the monitors, and the exposure times are correspondingly shorter.

The analysis was performed using the Offline Science Analysis (OSA) software version 5.0 distributed by the ISDC (Courvoisier et al. 2003a). This version shows substantial improvement compared to the previous OSA 4.2 version, except for the JEM-X spectral extraction, for which we used the 2005 March 15 version of the OSA. The significances listed in Table 1 have been derived by using the OSA software for ISGRI (20–40 keV), SPI (20–40 keV), and JEM-X (2–20 keV). In cases where there were no publicly available data covering the source position, we put “n/a” in the significance column. In those cases where no JEM-X or SPI detection was achieved, an ellipsis has been inserted. For comparison, we list the photon flux measured by *CGRO* OSSE in the 15–150 keV energy band, as reported by Johnson et al. (1997) for Seyfert galaxies and by McNaron-Brown et al. (1995) for blazars. Apart from gamma-ray bursts, no extragalactic source detections by IBIS/PICsIT have been reported.

The analysis of the *INTEGRAL* IBIS data is based on a cross-correlation procedure between the recorded image on the detector plane and a decoding array derived from the mask pattern (Goldwurm et al. 2003). The ISGRI spectra have been extracted from the count rate and variance mosaic images at the position of the source, which in all cases corresponds to the brightest pixel

⁴ See <http://isdc.unige.ch/index.cgi?Data+sources>.

⁵ See http://heasarc.gsfc.nasa.gov/docs/integral/inthp_archive.html.

TABLE 1
INTEGRAL AGN CATALOG

Name	Type	z	R.A. (J2000.0)	Decl. (J2000.0)	Exposure ^a (ks)	Target	ISGRI (σ)	SPI (σ)	JEM-X (σ)	OSSE ^b
NGC 788.....	Sy 1/2	0.0136	02 01 06	-06 46 56	311	...	10.1
NGC 1068.....	Sy 2	0.003793	02 42 41	-00 00 48	311	...	4.4
NGC 1275.....	Sy 2	0.017559	03 19 48	+41 30 42	264	...	19.1	...	78	1.8 \pm 0.5
3C 111.....	Sy 1	0.048500	04 18 21	+38 01 36	67	...	9.5	0.1	...	2.7 \pm 0.5
MCG +8-11-11.....	Sy 1.5	0.020484	05 54 54	+46 26 22	21	...	5.5	3.7 \pm 0.3
Mrk 3.....	Sy 2	0.013509	06 15 36	+74 02 15	472	...	13.3	2.9	...	1.8 \pm 0.4
Mrk 6.....	Sy 1.5	0.018813	06 52 12	+74 25 37	482	...	8.8	1.1
NGC 4051.....	Sy 1.5	0.002336	12 03 10	+44 31 53	443	...	8.8	3.0
NGC 4151.....	Sy 1.5	0.003320	12 10 33	+39 24 21	483	X	163.3	27.2	2089	24.5 \pm 0.4
NGC 4253.....	Sy 1.5	0.012929	12 18 27	+29 48 46	715	...	4.3	3.1
NGC 4388.....	Sy 2	0.008419	12 25 47	+12 39 44	215	X	37.9	4.0	19	9.1 \pm 0.4
NGC 4395.....	Sy 1.8	0.001064	12 25 49	+33 32 48	739	...	10.0
NGC 4507.....	Sy 2	0.011801	12 35 37	-39 54 33	152	...	15.8	3.6	n/a	5.2 \pm 0.6
NGC 4593.....	Sy 1	0.009000	12 39 39	-05 20 39	723	...	20.9	3.8	3	<2.9
Coma cluster.....	GClstr	0.023100	12 59 48	+27 58 48	516	X	6.6	1.4	8.9	...
NGC 4945.....	Sy 2	0.001878	13 05 27	-49 28 06	276	X	33.4	6.7	...	10.9 \pm 0.7
ESO 323-G077.....	Sy 2	0.015014	13 06 26	-40 24 53	761	...	9.9	1.3
NGC 5033.....	Sy 1.9	0.002919	13 13 28	+36 35 38	377	...	2.9	1.2
Cen A.....	Sy 2	0.001830	13 25 28	-43 01 09	532	X	166.1	24.8	1479	42.5 \pm 0.4
MCG -06-30-015.....	Sy 1	0.007749	13 35 54	-34 17 43	567	X	2.9	2.2	9	4.1 \pm 0.6
4U 1344-60.....	?	0.043	13 47 25	-60 38 36	603	...	40.9	5.9
IC 4329A.....	Sy 1.2	0.016054	13 49 19	-30 18 36	440	X	43.5	6.2	1	7.5 \pm 0.4
Circinus galaxy.....	Sy 2	0.001448	14 13 10	-65 20 21	589	...	79.5	8.6	2	...
NGC 5506.....	Sy 1.9	0.006181	14 13 15	-03 12 27	101	X	19.6	n/a	39	5.0 \pm 0.6
PG 1416-129.....	Sy 1	0.129280	14 19 04	-13 10 44	117	...	12.0	1.1	n/a	...
IC 4518.....	Sy 2	0.015728	14 57 43	-43 07 54	338	...	4.8	0.5
NGC 6221.....	Sy 1/2	0.004977	16 52 46	-59 13 07	523	...	7.6	7.0
NGC 6300.....	Sy 2	0.003699	17 17 00	-62 49 14	173	...	9.8	...	3	...
GRS 1734-292.....	Sy 1	0.021400	17 37 24	-29 10 48	3332	...	43.8	16.9	15.2	...
IGR J18027-1455.....	Sy 1	0.035000	18 02 47	-14 54 55	942	...	12.1	5.8	14	...
ESO 103-G35.....	Sy 2	0.013286	18 38 20	-65 25 39	36	...	12.2	1.5
1H 1934-063.....	Sy 1	0.010587	19 37 33	-06 13 05	684	...	6.6	4.4
NGC 6814.....	Sy 1.5	0.005214	19 42 41	-10 19 25	488	...	13.9	1.7	...	2.8 \pm 0.5
Cygnus A.....	Sy 2	0.056075	19 59 28	+40 44 02	1376	...	7.3	2.5
Mrk 509.....	Sy 1	0.034397	20 44 10	-10 43 25	73	X	10.1	2.6	6	3.6 \pm 0.6
IGR J21247+5058.....	Radio gal.?	0.020	21 24 39	+50 58 26	213	...	30.8	5.2
MR 2251-178.....	Sy 1	0.063980	22 54 06	17 34 55	489	X	35.9	1.9
MCG -02-58-022.....	Sy 1.5	0.046860	23 04 44	-08 41 09	489	...	5.9	1.6	...	3.3 \pm 0.8
S5 0716+714.....	BL Lac	0.3 ^c	07 21 53	+71 20 36	482	X	0.7
S5 0836+710.....	FSRQ	2.172	08 41 24	+70 53 42	391	...	8.5	0.6
3C 273.....	Blazar	0.15834	12 29 07	+02 03 09	655	X	35.6	6.0	32	10.6 \pm 0.3
3C 279.....	Blazar	0.53620	12 56 11	+05 47 22	497	X	6.8	...	3	3.3 \pm 0.5
PKS 1830-211.....	Blazar	2.507	18 33 40	-21 03 40	1069	...	16.1	1.4

Note.—Units of right ascension are hours, minutes, and seconds, and units of declination are degrees, arcminutes, and arcseconds.

^a ISGRI exposure time.

^b Flux in 50–150 keV, in units of 10^{-4} photons $\text{cm}^{-2} \text{s}^{-1}$.

^c Tentative redshift.

in the 20–40 keV band. The SPI analysis was done using the specific analysis software (Diehl et al. 2003), including version 9.2 of the reconstruction software SPIROS (Skinner & Connell 2003), which is based on the “iterative removal of sources” technique (IROS; Hammersley et al. 1992): a simple image of the field of view is made using a mapping technique that is optimized for finding a source, assuming that the data can be explained by only that source plus background. The mapping gives the approximate location and intensity of the source, which are then improved by maximizing a measure of the goodness of fit. The residuals of the fit are used as the input for a further image reconstruction and source search (Skinner & Connell 2003). The fitting process is easier when an input catalog is provided. In this work, we use the source positions found with ISGRI as an

input catalog for the SPI analysis, as the sensitivity of ISGRI is higher than that of SPI below 200 keV.

With respect to the calibration uncertainty, the IBIS instrument team stated that the systematic error is of the order of 1.5% (IBIS Team 2005, private communication). Nevertheless, this value corresponds to on-axis observations within a short period of time with no disturbing influence, such as enhanced background activity. A combined fit of Crab spectra taken in revolutions 43, 44, 120, 170, and 239, i.e., over a 1.5 yr span of the mission, shows a larger uncertainty in the flux. The scale of diversity, assuming that the Crab is a source with constant flux, gives some hint as to what the scale of discrepancies is in count rates observed in various conditions, i.e., with different dithering patterns or instrumental settings. Clearly, the absolute calibration

TABLE 2
OSSE-DETECTED AGN NOT SEEN BY *INTEGRAL*

Name	Type	Exposure ^a (ks)
3C 120	Sy 1	3
3C 390.3	Sy 1	...
3C 454.3	Blazar	2
CTA 102	Blazar	6
ESO 141-G55	Sy 1	23
H 1517+656	BL Lac	2
III Zw 2	Sy 1/2	79
Mrk 279	Sy 1.5	13
Mrk 841	Sy 1.5	...
M82	Starburst	84
NGC 253	Starburst	...
NGC 2110	Sy 2	...
NGC 3227	Sy 1.5	...
NGC 3783	Sy 1	...
NGC 526A	Sy 1.5	...
NGC 5548	Sy 1.5	...
NGC 7172	Sy 2	...
NGC 7213	Sy 1.5	...
NGC 7314	Sy 1.9	489
NGC 7469	Sy 1.2	2
NGC 7582	Sy 2	...
PKS 0528+134	Blazar	1040
PKS 2155-304	BL Lac	...
QSO 1028+313	Sy 1.5	...

^a ISGRI exposure time.

cannot be more precise than the observed variations. Hence, it seems that for the 22–120 keV band we may conclude that the joint 1 σ uncertainty of the spectral extraction method and the calibration files is about 5%. It may happen that for other sources and in some special circumstances we may encounter a larger discrepancy, especially for faint sources, but a systematic error of 5% should be a valid approximation. In most cases the fit to the data from the three instruments used in this work did not show any improvement when adding variable cross calibration. This is mainly due to the fact that most spectra have low signal-to-noise ratios (S/Ns), and adding a further parameter to the fit procedure worsens the fit result, according to an F -test.

The spectral shape calibration was also tested on *INTEGRAL* Crab observations. With the so-called canonical model for the Crab showing a single power law with photon index $\Gamma = 2.1$ (Toor & Seward 1974), the values retrieved from *INTEGRAL* are $\Gamma = 2.1$ (JEM-X) and $\Gamma = 2.2$ (SPI and ISGRI; Kirsch et al. 2005). It should be kept in mind, however, that the Crab is significantly brighter than the sources discussed here, and systematic effects might depend on source brightness. All the extracted images and source results are available in electronic form.⁶

2.2. CGRO Data

CGRO OSSE covered the energy range 50–10,000 keV (Johnson et al. 1993). It therefore preferentially detected AGNs with hard and bright X-ray spectra, which we also expect to be detectable by *INTEGRAL*. So far, several of the AGNs detected by OSSE have not been seen by *INTEGRAL*. We list those sources and the *INTEGRAL* ISGRI exposure time on the particular AGN in Table 2.⁷

⁶ See http://heasarc.gsfc.nasa.gov/docs/integral/inthp_archive.html.

⁷ See footnote 6.

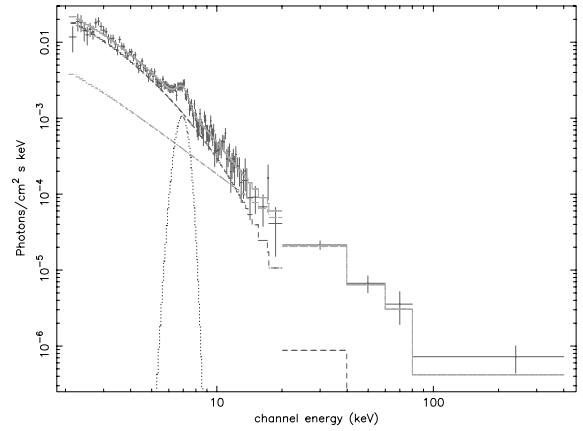


Fig. 1.—*INTEGRAL* spectrum of NGC 1275. [See the electronic edition of the Journal for a color version of this figure.]

3. X-RAY TO GAMMA-RAY SPECTRA

3.1. Time-averaged Spectral Analysis

The overall spectra extracted from the *INTEGRAL* JEM-X, ISGRI, and SPI data for 10 AGNs are shown in Figures 1–10 (see § 4 for details). A single power-law fit with absorption from material in the line of sight has been applied to the *INTEGRAL* spectra of all sources, and the results are presented in Table 3 and in Figure 11. The errors on the photon indices are 90% confidence errors. The intrinsic absorption was determined by subtracting the Galactic hydrogen column density from the total absorption as measured in the soft X-rays. In the cases where the *INTEGRAL* JEM-X data were not available or did not restrict the absorption column density sufficiently, values from the literature have been used to fix this component in the spectral fit (Table 3). No systematic error has been added to the data. The spectral fitting was done using version 11.3.2 of XSPEC (Arnaud 1996). In most cases a single power law gave an acceptable fit to the data, which also is based on the fact that the S/Ns of many of the

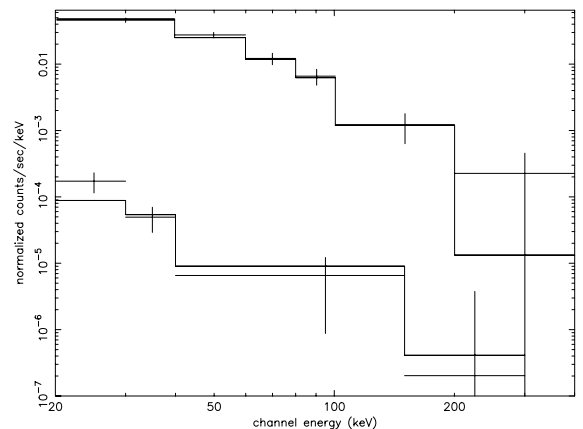
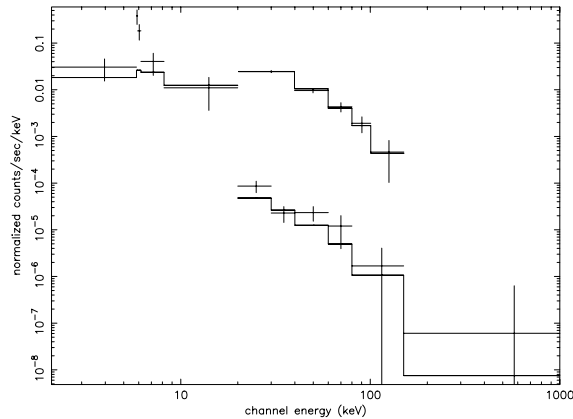


Fig. 2.—*INTEGRAL* count spectrum of NGC 4507. No JEM-X data are available for this source. We note that when SPI spectral data are presented here and elsewhere, the detector counts have really been effective area-corrected by the image reconstruction algorithm (Skinner & Connell 2003). Thus, the SPI spectra are really in photons $\text{cm}^{-2} \text{s}^{-1} \text{keV}^{-1}$.

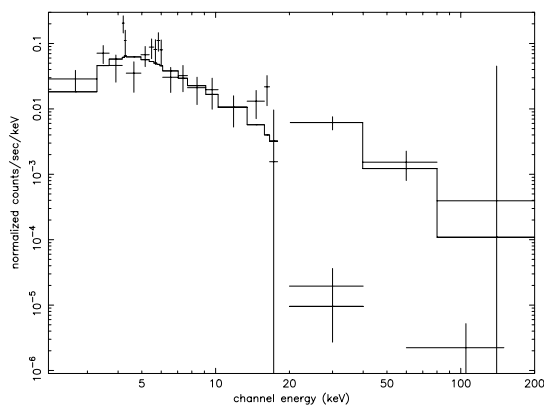
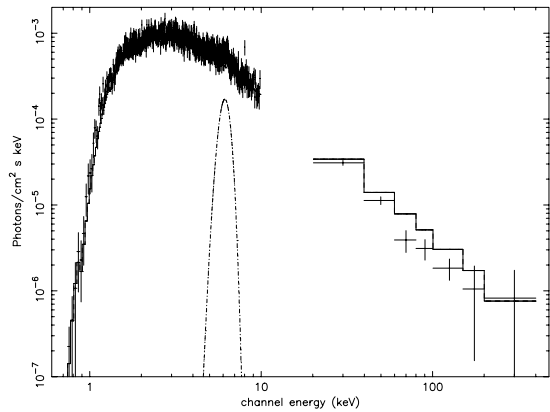
FIG. 3.—*INTEGRAL* count spectrum of NGC 4593.

spectral data are rather low. In six cases a cutoff power-law fit led to better fit results. We report those results in Table 4.

3.2. Averaged Spectra of AGN Subtypes

In order to investigate the spectra of AGN subtypes, we have derived averaged spectra of the Seyfert 1 and 2 types, as well as for the intermediate Seyferts and the blazars, and according to the intrinsic absorption. The average Seyfert 1 spectrum was constructed using the weighted mean of 10 ISGRI spectra, the Seyfert 2 composite spectrum includes 15 sources, and 8 objects form the intermediate Seyfert 1.5 group. The two brightest sources, Cen A and NGC 4151, have been excluded from the analysis, as their high S/N would dominate the averaged spectra. The averaged spectra have been constructed by computing the weighted mean of all fit results on the individual sources, as shown in Table 3. In order to do so, all spectra were fit by an absorbed single power-law model. When computing the weighted average of the various subclasses, the Seyfert 2 objects show flatter hard X-ray spectra ($\Gamma = 1.95 \pm 0.01$) than the Seyfert 1.5 ($\Gamma = 2.10 \pm 0.02$), and Seyfert 1 appear to have the steepest spectra ($\Gamma = 2.11 \pm 0.05$) together with the blazars ($\Gamma = 2.07 \pm 0.10$).

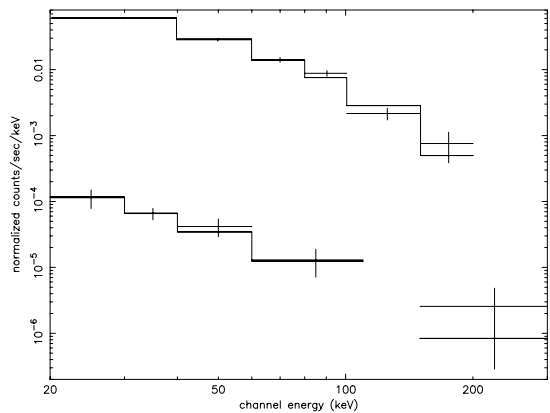
The classification according to the Seyfert type of the objects is based on optical observations. An approach to classify sources

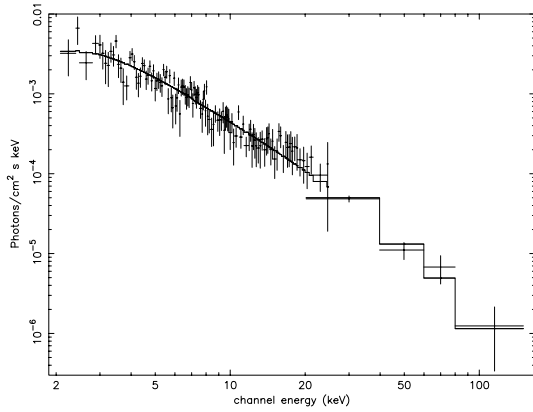
FIG. 4.—*INTEGRAL* count spectrum of MCG -06-30-015 with JEM-X (2–18 keV), ISGRI (20–200 keV; upper spectrum), and SPI (lower two points).FIG. 5.—Combined *XMM-Newton* EPIC pn and *INTEGRAL* ISGRI photon spectrum of 4U 1344–60. The SPI spectrum is not shown, for better readability. The iron $K\alpha$ line indicates a redshift of about $z = 0.043$. [See the electronic edition of the *Journal* for a color version of this figure.]

due to their properties in the X-rays can be done by separating the sources with high intrinsic absorption ($N_{\text{H}} > 10^{22} \text{ cm}^{-2}$) from those objects that do not show significant absorption in the soft X-rays. It has to be pointed out that not all objects that show high intrinsic absorption in the X-rays are classified as Seyfert 2 galaxies in the optical, and the same applies for the other AGN subtypes. Nevertheless, a similar trend in the spectral slopes can be seen: the 21 absorbed AGNs show a flatter hard X-ray spectrum ($\Gamma = 1.98 \pm 0.01$) than the 13 unabsorbed sources ($\Gamma = 2.08 \pm 0.02$). The blazars have again been excluded from these samples.

4. NOTES ON INDIVIDUAL SOURCES

Spectra are presented in this paper for *INTEGRAL* sources that are not yet published and for which at least two instruments yield a detection of $>3\sigma$. Spectral fits did not require any cross-calibration correction between the instruments, except for GRS 1734–292 and for the two brightest sources, Cen A and NGC 4151. In cases where the spectra of different instruments overlap, the spectral plots have been performed in count space; otherwise, they are performed in photon space.

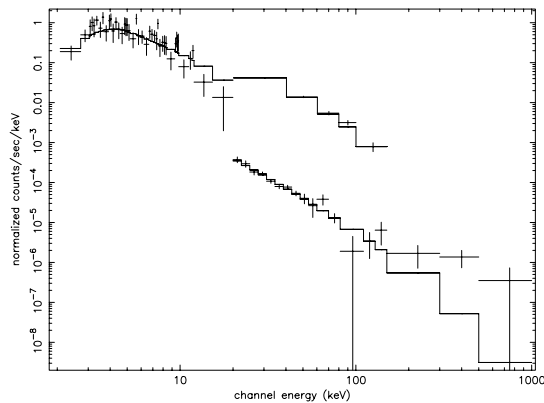
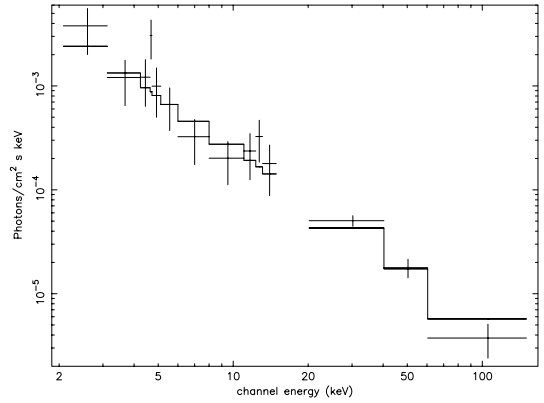
FIG. 6.—*INTEGRAL* ISGRI and SPI count spectrum of IC 4329A.

FIG. 7.—*INTEGRAL* spectrum of NGC 5506.

NGC 1275.—A Seyfert 2 galaxy at $z = 0.018$, detected in the ISGRI and JEM-X data (Fig. 1). The spectrum represents the blend of the Perseus cluster with the spectrum of the AGN. The measured spectrum in the 2–400 keV energy range is fitted by a slightly absorbed ($N_{\text{H}} = 6.7^{+8.1}_{-6.7} \times 10^{21} \text{ cm}^{-2}$) bremsstrahlung model ($kT = 3.4^{+0.4}_{-0.4}$) plus a power law with a photon index fixed to the measurement from the ISGRI data ($\Gamma = 2.12$). In addition, a Gaussian line with $E = 6.9^{+0.2}_{-0.2}$ keV and an equivalent width of $\text{EW} = 670$ eV has been applied to achieve a reasonable fit result ($\chi^2_{\nu} = 0.98$). We see no evidence of flattening of the continuum above ~ 10 keV, which is often attributed to Compton reflection, nor can we quantitatively identify a spectral break.

NGC 4507.—Detected by ISGRI and SPI (Seyfert 2, $z = 0.012$; Fig. 2). The combined data are best represented by a power law ($\Gamma = 1.0^{+1.7}_{-0.8}$) with a high-energy cutoff ($E_{\text{cut}} = 55^{+123}_{-11}$ keV). This is consistent with results from *Ginga* and OSSE, which showed $\Gamma = 1.3 \pm 0.2$ and $E_{\text{cut}} = 73^{+48}_{-24}$ keV (Bassani et al. 1995).

NGC 4593.—A Seyfert 1 galaxy in the Virgo region at $z = 0.009$ that shows a cutoff power law with $\Gamma = 1.0^{+0.6}_{-0.6}$ and $E_{\text{cut}} = 35^{+49}_{-12}$ keV and is detected up to 150 keV (Fig. 3), with a flux of $f_{20-100 \text{ keV}} = 6.8 \times 10^{-11} \text{ ergs cm}^{-2} \text{ s}^{-1}$ ($\chi^2_{\nu} = 1.00$). This is significantly different from the spectrum measured by *BeppoSAX*,

FIG. 8.—*INTEGRAL* count spectrum of GRS 1734–292.FIG. 9.—*INTEGRAL* spectrum of Mrk 509. No SPI data are available for this source.

$\Gamma = 1.94^{+0.06}_{-0.05}$ and $E_{\text{cut}} \gg 222$ keV (Guainazzi et al. 1999), but with a similar flux ($f_{20-100 \text{ keV}} = 7 \times 10^{-11} \text{ ergs cm}^{-2} \text{ s}^{-1}$).

Cen A.—This Seyfert 2 ($z = 0.0018$) is one of the brightest objects in the sample. The statistics allow us in this case to determine the intercalibration factors between JEM-X, ISGRI, and SPI ($1.0 : 0.92^{+0.04}_{-0.04} : 1.10^{+0.06}_{-0.06}$). An absorbed power-law plus a Gaussian line gives the best fit to the data with $N_{\text{H}} = 14.6^{+1.4}_{-1.4} \times 10^{22} \text{ cm}^{-2}$, $\Gamma = 1.96^{+0.02}_{-0.02}$, and an equivalent width of the iron $K\alpha$ line of $\text{EW} = 108$ eV. Adding an exponential cutoff does not improve the fit ($E_C = 870^{+3810}_{-410}$ keV). The results are consistent with results published on a subset of *INTEGRAL* data and with *BeppoSAX* data (Soldi et al. 2005).

MCG –06-30-015.—This Seyfert 1 galaxy ($z = 0.0077$) was detected by all three instruments (Fig. 4). The spectrum is well represented ($\chi^2_{\nu} = 1.19$) by a power law with $\Gamma = 2.8^{+0.4}_{-0.3}$ and weak evidence for absorption of $N_{\text{H}} = 5.9^{+8.6}_{-5.5} \times 10^{22} \text{ cm}^{-2}$ ($\chi^2_{\nu} = 1.11$).

4U1344–60.—A bright ($f_{20-100 \text{ keV}} = 5.7 \times 10^{-11} \text{ ergs cm}^{-2} \text{ s}^{-1}$) X-ray source, which has been unidentified until Michel et al. (2004) reported the identification of it as a low-redshift AGN, but no further information was provided. In order to clarify the

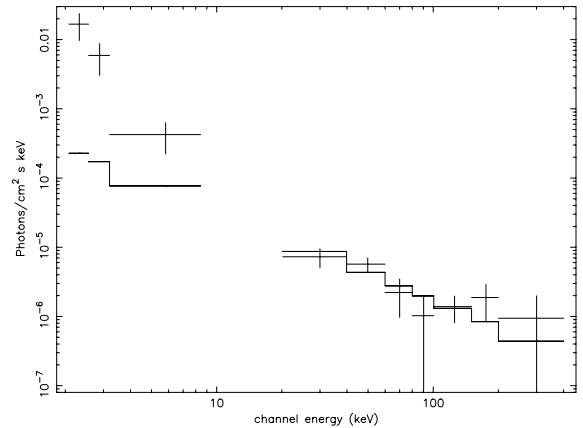
FIG. 10.—*INTEGRAL* spectrum of the blazar 3C 279. The source is not detectable in the SPI data.

TABLE 3
INTEGRAL AGN FIT RESULTS

Name	ISGRI (f_{20-40} keV) (10^{-11} ergs cm^{-2} s^{-1})	ISGRI (f_{40-100} keV) (10^{-11} ergs cm^{-2} s^{-1})	JEM-X (f_{2-10} keV) (10^{-11} ergs cm^{-2} s^{-1})	$\log L_X^a$ (20–100 keV) (ergs s^{-1})	N_{H} (10^{22} cm^{-2})	Γ	References
NGC 788.....	2.98 ± 0.24	5.06 ± 0.41	...	43.52	<0.02	1.69 ^{+0.31} _{-0.27}	1
NGC 1068.....	0.93 ± 0.27	1.66 ± 0.48	...	41.92	>150	1.71 ^{+0.82} _{-0.80}	2
NGC 1275.....	1.89 ± 0.21	2.29 ± 0.25	4.34 ± 0.03	43.47	3.75	2.12 ^{+0.60} _{-0.43}	3
3C 111.....	6.27 ± 0.57	8.10 ± 0.74	...	44.90	0.634	2.03 ^{+0.45} _{-0.37}	1
MCG +8-11-11.....	6.07 ± 0.97	5.80 ± 0.92	...	44.06	<0.02	2.41 ^{+1.24} _{-0.70}	4
Mrk 3.....	3.65 ± 0.39	4.62 ± 0.64	...	43.53	110	2.05 ^{+0.27} _{-0.23}	4
Mrk 6.....	2.01 ± 0.20	2.68 ± 0.26	...	43.57	10	2.01 ^{+0.42} _{-0.35}	4
NGC 4051.....	1.80 ± 0.20	1.48 ± 0.17	...	41.60	<0.01	2.62 ^{+0.81} _{-0.53}	4
NGC 4151.....	26.13 ± 0.16	31.97 ± 0.20	20.89 ± 0.01	43.15	4.9	2.10 ± 0.02	5
NGC 4253.....	0.93 ± 0.22	1.38 ± 0.32	...	42.93	0.8	1.85 ^{+0.78} _{-0.60}	4
NGC 4388.....	9.54 ± 0.25	13.08 ± 0.35	4.63 ± 0.25	43.55	27	1.92 ^{+0.09} _{-0.09}	6
NGC 4395.....	0.56 ± 0.22	1.20 ± 0.47	...	40.64	0.15	1.31 ^{+0.85} _{-0.71}	1
NGC 4507.....	6.46 ± 0.36	9.11 ± 0.50	...	43.68	29	1.92 ^{+0.35} _{-0.31}	4
NGC 4593.....	3.31 ± 0.16	3.39 ± 0.16	2.90 ± 0.89	43.08	0.02	1.02 ^{+0.63} _{-0.59}	4
Coma cluster.....	1.09 ± 0.12	1.00 ± 0.15	8.82 ± 1.27	43.40	<0.01	2.65 ^{+0.18} _{-0.18}	3
NGC 4945.....	9.85 ± 0.23	15.78 ± 0.37	...	42.30	400	1.93 ^{+0.09} _{-0.08}	4
ESO 323-G077.....	1.20 ± 0.19	2.03 ± 0.33	...	43.21	55	1.72 ^{+0.51} _{-0.33}	7
NGC 5033.....	1.06 ± 0.24	0.84 ± 0.19	...	41.55	2.9	2.7 ^{+7.3} _{-1.1}	4
Cen A.....	32.28 ± 0.17	43.79 ± 0.23	29.58 ± 0.02	42.75	12.5	1.94 ^{+0.02} _{-0.02}	3
MCG –06-30-015....	2.98 ± 0.19	3.50 ± 0.22	4.46 ± 0.51	42.93	17.7	2.04 ^{+0.10} _{-0.11}	4
4U 1344–60.....	2.83 ± 0.15	3.73 ± 0.20	...	44.36	2.19	1.65 ^{+0.02} _{-0.03}	4
IC 4329A.....	8.19 ± 0.17	10.71 ± 0.23	0.98 ± 1.21	44.04	0.42	2.01 ^{+0.09} _{-0.08}	4
Circinus galaxy.....	10.73 ± 0.18	9.39 ± 0.15	1.29 ± 0.73	41.97	360	2.74 ^{+0.09} _{-0.09}	4
NGC 5506.....	4.21 ± 0.33	3.69 ± 0.30	8.87 ± 0.23	42.83	3.4	2.15 ^{+0.09} _{-0.08}	4
PG 1416–129.....	5.43 ± 0.64	8.62 ± 1.01	...	45.78	0.09	1.77 ^{+0.51} _{-0.41}	1
IC 4518.....	0.49 ± 0.32	1.04 ± 0.68	...	42.92	?	1.48 ^{+3.47} _{-1.57}	8
NGC 6221.....	1.32 ± 0.20	1.77 ± 0.27	...	42.39	1	1.82 ^{+0.35} _{-0.33}	8
NGC 6300.....	3.91 ± 0.37	3.72 ± 0.35	4.66 ± 1.69	42.36	22	2.42 ^{+0.54} _{-0.41}	9
GRS 1734–292.....	4.03 ± 0.09	3.13 ± 0.07	68.4 ± 4.5	43.88	3.7	2.67 ^{+0.12} _{-0.11}	3
IGR J18027–1455....	2.03 ± 0.16	1.66 ± 0.13	4.38 ± 0.31	44.03	19.0	2.60 ^{+0.56} _{-0.42}	3
ESO 103-G35.....	2.97 ± 0.66	5.27 ± 1.17	...	43.51	13–16	1.64 ^{+0.47} _{-0.70}	1
1H 1934–063.....	0.48 ± 0.25	0.83 ± 0.44	...	42.51	?	2.92 ^{+0.81} _{-0.63}	1
NGC 6814.....	2.92 ± 0.23	2.64 ± 0.21	...	42.52	<0.05	2.48 ^{+0.49} _{-0.36}	1
Cygnus A.....	3.24 ± 0.14	3.55 ± 0.15	...	44.71	20	2.24 ^{+0.17} _{-0.19}	10
Mrk 509.....	4.66 ± 0.47	4.96 ± 0.50	4.56 ± 0.78	44.42	<0.01	1.73 ^{+0.15} _{-0.16}	4
IGR J21247+5058....	4.15 ± 0.27	6.85 ± 0.45	...	44.00	?	1.73 ^{+0.24} _{-0.22}	4
MR 2251–178.....	1.20 ± 0.17	1.27 ± 0.18	...	44.40	0.02–0.19	2.31 ^{+1.21} _{-0.68}	1
MCG –02-58-022....	1.20 ± 0.28	1.75 ± 0.41	...	44.18	<0.01–0.08	1.71 ^{+0.89} _{-0.63}	1
S5 0716+714.....	0.14 ± 0.11	0.71 ± 0.59	...	45.21 ^c	<0.01	...	1
S5 0836+710.....	1.73 ± 0.28	3.02 ± 0.50	...	47.87	0.11	1.65 ^{+0.46} _{-0.39}	1
3C 273.....	5.50 ± 0.15	6.29 ± 0.17	9.21 ± 0.29	45.92	0.5	2.17 ^{+0.12} _{-0.12}	3
3C 279.....	0.82 ± 0.24	1.79 ± 0.52	6.05 ± 2.36	46.37	0.02–0.13	1.3 ^{+0.7} _{-0.28}	1
PKS 1830–211.....	2.07 ± 0.14	2.82 ± 0.19	...	48.09	<0.01–0.7	1.96 ^{+0.27} _{-0.24}	1

^a For $H_0 = 70$ and $\Lambda_0 = 0.73$

^b Tentative redshift.

REFERENCES.—(1) Tarturus database; (2) Matt et al. 1997; (3) This work; (4) Lutz et al. 2004; (5) Beckmann et al. 2005; (6) Beckmann et al. 2004; (7) Sazonov & Revnivtsev 2004; (8) Levenson et al. 2001; (9) Matsumoto et al. 2004; (10) Young et al. 2002.

nature of this object, we analyzed 31 ks of *XMM-Newton* data of the Cen B field, taken in 2001 August. Although 4U 1344–60 appears to be near to the rim of the EPIC camera, a spectrum can be extracted from EPIC pn data, which show an iron line at $6.13_{-0.09}^{+0.08}$ keV, with a flux of $f_{\text{K}\alpha} = 1.8_{-0.3}^{+0.2} \times 10^{-4}$ photons cm^{-2} s^{-1} and an equivalent width of 410 eV. If we consider this line to be the iron $\text{K}\alpha$ fluorescence line at 6.4 keV, the redshift of 4U 1344–60 is $z = 0.043_{-0.014}^{+0.016}$. The simultaneous fit with the *INTEGRAL* ISGRI and SPI data shows that the spectrum is well represented by an absorbed power-law plus Gaussian line with $N_{\text{H}} = 2.64_{-0.07}^{+0.07} \times 10^{22}$ cm^{-2} and $\Gamma = 1.65_{-0.03}^{+0.02}$ ($\chi^2_{\nu} = 1.06$ for 711 degrees of freedom [dof]; Fig. 5).

IC 4329A.—This source (Seyfert 1.2; $z = 0.016$) is well represented by a power law ($\Gamma = 1.5_{-0.4}^{+0.4}$) with exponential cut-

off ($E_C = 104_{-48}^{+344}$ keV; see Fig. 6). The results are consistent on a 2–3 σ level with the spectrum measured by *BeppoSAX* ($\Gamma = 1.90 \pm 0.05$, $E_C \simeq 300$ keV; Perola et al. 2002).

NGC 5506.—The JEM-X and ISGRI spectrum of this Seyfert 1.9 ($z = 0.006$) shows an absorbed ($N_{\text{H}} = 2.7_{-2.3}^{+2.4} \times 10^{22}$ cm^{-2}) high-energy cutoff spectrum with $\Gamma = 1.81_{-0.25}^{+0.25}$ and $E_{\text{cut}} = 57_{-27}^{+139}$ keV ($\chi^2_{\nu} = 1.07$; Fig. 7). No SPI data are available for this source, because SPI was undergoing an annealing cycle during the observations of NGC 5506. The results are consistent with *BeppoSAX* measurements (Bianchi et al. 2003), although the iron $\text{K}\alpha$ line and the reflection component are not detectable in the *INTEGRAL* data.

IC 4518 (VV 780).—This Seyfert 2 galaxy ($z = 0.016$) was reported to be detectable in a 700 ks observation in 2004 January

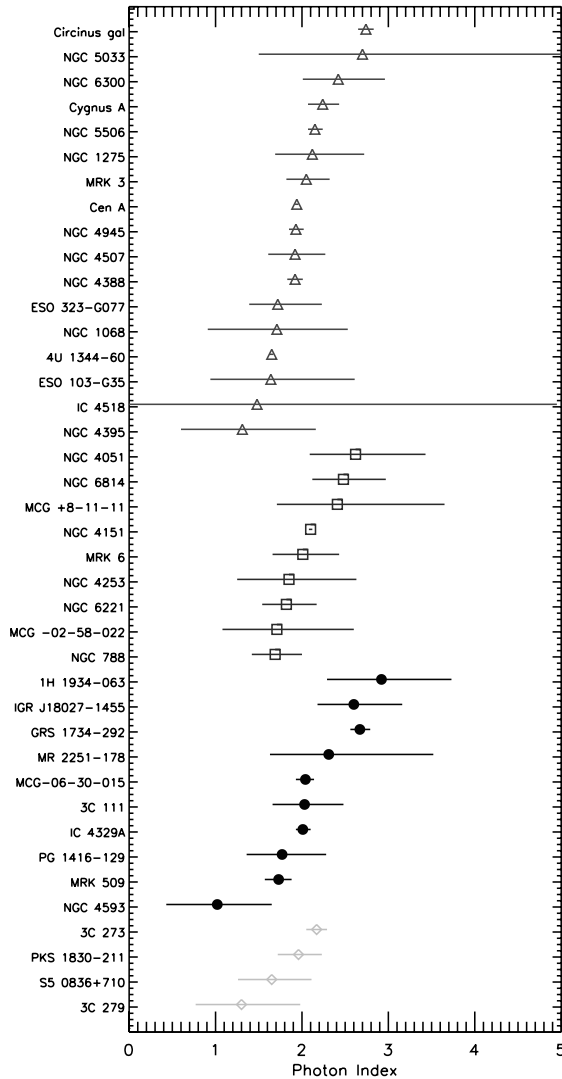


FIG. 11.—Photon index of a single power-law fit to the *INTEGRAL* data of our sample, ordered in four categories. *Top to bottom*: Seyfert 2, Seyfert 1.5, Seyfert 1, and blazars. [See the electronic edition of the *Journal* for a color version of this figure.]

TABLE 4
CUTOFF POWER-LAW FITS

Source	Γ (Power Law)	E_C (keV)
NGC 4507.....	$1.0^{+1.7}_{-0.8}$	55^{+123}_{-11}
NGC 4593.....	$1.02^{+0.63}_{-0.59}$	35^{+49}_{-12}
ESO 323-G077.....	$1.48^{+0.65}_{-1.18}$	181^{+319}_{-131}
IC 4329A.....	$1.51^{+0.39}_{-0.40}$	104^{+344}_{-48}
Circinus galaxy.....	$2.23^{+0.48}_{-0.55}$	$87^{+\infty}_{-46}$
NGC 5506.....	$1.81^{+0.25}_{-0.28}$	57^{+139}_{-27}

on SN 1006 (Kalemci et al. 2005). The source was detected with 8.7σ in the 20–40 keV band with a photon index of $\Gamma = 2.2 \pm 0.4$ and a flux of $f_{20-40 \text{ keV}} = 6.8 \times 10^{-12} \text{ ergs cm}^{-2} \text{ s}^{-1}$. Note that in Tables 1 and 3 we refer to our measurements, which are consistent with the values derived by Kalemci et al. (2005).

GRS 1734–292 (AX J1737.4–2907).—This Seyfert 1 galaxy ($z = 0.021$) is located near to the Galactic center ($l = 358^\circ 9$, $b = 1^\circ 4$). Because this region is monitored regularly by *INTEGRAL*, 3.3 Ms of observations are available in the public data. Although an ISGRI spectrum of this source has been published already (Sazonov et al. 2004), we discuss this object in more detail, because Sazonov et al. included neither the JEM-X nor the SPI data in their study. The fact that the source is located in a crowded region makes the analysis more difficult, especially for SPI data with its ~ 2.5 spatial resolution. Figure 8 shows the combined JEM-X2, ISGRI, and SPI spectrum. The data are represented by a simple power law with $\Gamma = 2.63^{+0.09}_{-0.09}$ and, in this case, intercalibration factors had to be applied to achieve an acceptable fit result ($\chi^2_\nu = 1.09$; 161 dof). Adding a cutoff or an absorption component to the model does not improve the fit. The average flux is $f_{20-40 \text{ keV}} = 9 \times 10^{-11} \text{ ergs cm}^{-2} \text{ s}^{-1}$. This source is of additional interest, as it lies within the error circle for the EGRET source 3EG J1736–2908 (Sazonov et al. 2004). If this is a real association, it would be the only known case of a “gamma-ray-loud” Seyfert 1.

Mrk 509.—This source (Seyfert 1; $z = 0.034$) was not detected by SPI and yielded only low S/N spectra with JEM-X and ISGRI (Fig. 9). No absorption component was necessary to fit the combined spectrum. A pure single power law ($\Gamma = 1.66^{+0.15}_{-0.16}$) resulted in $\chi^2_\nu = 0.99$, consistent with measurements by *XMM-Newton* ($\Gamma = 1.75$; Pounds et al. 2001) and with *BeppoSAX* ($\Gamma = 1.58^{+0.09}_{-0.08}$), although the latter data showed, in addition, a cutoff at $E_C = 67^{+30}_{-20} \text{ keV}$ (Perola et al. 2002).

S5 0716+714.—Results on *INTEGRAL* observations of this BL Lac object in 2004 April, performed in ToO mode when the source was in a high optical state, have been published by Pian et al. (2005). Using the OSA reduction version 4.0, they achieved a marginal detection of 4.5σ in the 30–60 keV band. Using the data presented here and the current version of the software, the source is not detectable because the strong variability of the source resulted in a low average flux.

3C 279.—This blazar ($z = 0.5362$) led to a weak detection with JEM-X and to none with SPI. The spectrum (model shown in Fig. 10) is dominated by the ISGRI statistics and is well represented by a single power law with photon index $\Gamma = 1.3^{+0.7}_{-0.5}$ ($\chi^2_\nu = 0.98$), consistent with *BeppoSAX* ($\Gamma = 1.66 \pm 0.05$; Ballo et al. 2002) and *CGRO OSSE* observations ($\Gamma = 2.1^{+0.4}_{-0.4}$; McNaron-Brown et al. 1995). The JEM-X data show an excess in the 2–7 keV energy band. This excess might be caused by the transition from the synchrotron to the inverse Compton branch in this energy range, which would lead to a convex spectrum.

Several sources may have been marginally suspected in the *INTEGRAL* data. They either were targets of dedicated observations or were detected in some single science windows. We performed the same analysis as for the other sources presented here, but found only spurious source candidates that result from image reconstruction problems such as ghosts and mask patterns. Among those sources are Mrk 231, ESO 33-2, PKS 0637–75, MCG –05-23-16, QSO 1028+313, NGC 4736, NGC 4418, 3C 353, and QSO 1730–130.⁸

⁸ See http://heasarc.gsfc.nasa.gov/docs/integral/inthp_archive.html.

5. DISTRIBUTION IN SPACE AND SAMPLE COMPLETENESS

In order to explore the space distribution of hard X-ray-selected objects, one generally needs to consider a statistically complete flux-limited sample. However, this is difficult to achieve with a data set comprised of various lines of sight and widely differing exposures. In addition, the telescope effective area can be highly position dependent within the coded aperture field of view. Thus, we opt to leave the compilation of a $\log N$ - $\log S$ distribution and perhaps a hard X-ray AGN luminosity distribution to a future paper.

Alternatively, the V_e/V_a test is a simple method developed by Avni & Bahcall (1980) based on the V/V_{\max} test of Schmidt (1968). V_e stands for the volume, which is enclosed by the object, and V_a is the accessible volume, in which the object could have been found (e.g., due to a flux limit of a survey). Avni & Bahcall showed that different survey areas with different flux limits in various energy bands can be combined by the V_e/V_a test. In the case of no evolution, $\langle V_e/V_a \rangle = 0.5$ is expected, and the error $\sigma_m(n)$ for a given mean value $\langle m \rangle = \langle V_e/V_a \rangle$ based on n objects is

$$\sigma_m(n) = \sqrt{\frac{1/3 - \langle m \rangle + \langle m \rangle^2}{n}}. \quad (1)$$

This evolutionary test is applicable only to samples with a well-defined flux limit down to which all objects have been found. It can therefore also be used to test the completeness of a sample. We performed a series of V_e/V_a tests to the *INTEGRAL* AGN sample, assuming completeness limits in the range of 1σ up to 15σ ISGRI 20–40 keV significance, adding 5% systematic error to the flux uncertainty as described in § 2.1. For a significance limit below the true completeness limit of the sample, one expects the V_e/V_a tests to derive a value $\langle V_e/V_a \rangle < \langle V_e/V_a \rangle_{\text{true}}$, where $\langle V_e/V_a \rangle_{\text{true}}$ is the true test result for a complete sample. Above the completeness limit the $\langle V_e/V_a \rangle$ values should be distributed around $\langle V_e/V_a \rangle_{\text{true}}$ within the statistical uncertainties. The results of the tests are shown in Figure 12. It appears that the

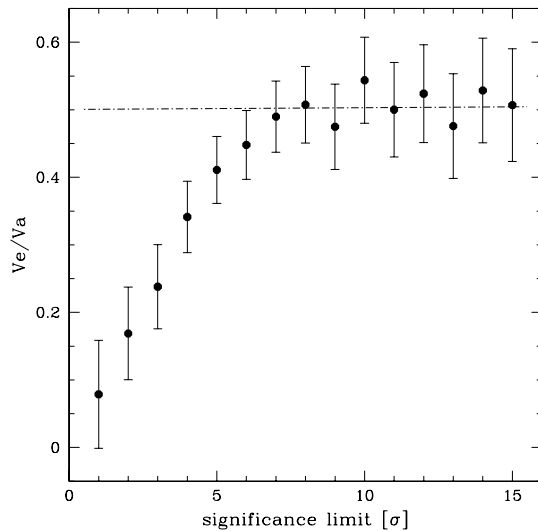


FIG. 12.—Result of the V_e/V_a test, assuming different completeness limits in ISGRI significance. The dot-dashed line shows the average $\langle V_e/V_a \rangle$ value for the objects with significance $\geq 7\sigma$.

TABLE 5
AVERAGE SPECTRA

Source Type	Γ^a
Unabsorbed Sy.....	2.08 ± 0.02
Absorbed Sy	1.98 ± 0.01
Seyfert 1.....	2.11 ± 0.05
Seyfert 1.5.....	2.10 ± 0.02
Seyfert 2.....	1.95 ± 0.01
Blazar.....	2.07 ± 0.10

^a Weighted mean of the individual source results.

sample becomes complete at a significance level around $>6\sigma$, including 31 AGNs. The average value above this significance is $\langle V_e/V_a \rangle = 0.505 \pm 0.022$. This value is consistent with the expected value of 0.5, which reflects no evolution and an even distribution in the local universe. If we do not apply the 5% systematic error to the data, the average value is lower ($\langle V_e/V_a \rangle = 0.428 \pm 0.018$), indicating that a systematic error is indeed apparent in the ISGRI data.

6. DISCUSSION

The typical *INTEGRAL* spectrum can be described by a simple power-law model with average photon indices ranging from $\Gamma = 2.0$ for obscured AGNs to $\Gamma = 2.1$ for unabsorbed sources (Table 5). The simple model does not give reasonable results in cases of high S/N, where an appropriate fit requires additional features such as a cutoff and a reflection component (Soldi et al. 2005; Beckmann et al. 2005). The results presented here show slightly steeper spectra than previous investigations of AGNs in comparable energy ranges. The same trend is seen in the comparison of Crab observations, where the *INTEGRAL* ISGRI spectra also appear to be slightly steeper than in previous observations (Kirsch et al. 2005) and comparable to *Rossi X-Ray Timing Explorer (RXTE)* and *INTEGRAL* ISGRI spectra of Cen A (Rothschild et al. 2006).

Zdziarski et al. (1995) did a study of Seyfert galaxies observed by *Ginga* and *CGRO OSSE* with a similar redshift distribution ($\bar{z} = 0.022$) as the Seyferts detected by *INTEGRAL* ($\bar{z} = 0.020$). The same trend in spectral slope from $\Gamma = 1.92^{+0.03}_{-0.03}$ for radio-quiet Seyfert 1 galaxies down to $\Gamma = 1.67^{+0.31}_{-0.49}$ for Seyfert 2 galaxies was detectable in the sample, and a potential cutoff appeared at energies $E_C > 250$ keV. The average of all Seyfert spectra ($\Gamma = 1.9$) appears to be similar to the one in our sample ($\Gamma = 1.96 \pm 0.01$).

Gondek et al. (1996) confirmed that Seyfert 1 galaxies show a continuum with photon index $\Gamma = 1.9^{+0.1}_{-0.1}$, with high-energy cutoff $E_C > 500$ keV and moderate reflection component ($R = 0.76^{+0.15}_{-0.15}$), based on *European X-Ray Observatory Satellite (EXOSAT)*, *Ginga*, *High Energy Astronomical Observatory (HEAO 1)*, and *CGRO OSSE* data. More recent studies by Perola et al. (2002) on *BeppoSAX* data of nine Seyfert 1 galaxies confirmed this picture. Malizia et al. (2003) used the *BeppoSAX* data (3–200 keV) of 14 Seyfert 1 and 17 Seyfert 2 galaxies to study average spectral properties. Also, this work finds Seyfert 1 galaxies to be softer ($\Gamma \sim 1.9$) than Seyfert 2 galaxies ($\Gamma \sim 1.75$), which also show stronger absorption. Both types show iron lines with an equivalent width of 120 eV and a Compton reflection component of $R \sim 0.6$ –1, but the energy cutoff of the type 1 objects appears to be at higher energies (200 keV compared to $E_C \sim 130$ keV for the Seyfert 2 galaxies).

Deluit & Courvoisier (2003) used for their analysis only the *BeppoSAX* PDS spectra of 14 Seyfert 1, 9 Seyfert 1.5, and 22

Seyfert 2 galaxies. Their study led to a somewhat different result. Contrary to other studies, Seyfert 2 objects showed a steeper spectrum ($\Gamma = 2.00^{+0.05}_{-0.05}$) than Seyfert 1 objects ($\Gamma = 1.89^{+0.28}_{-0.46}$), but with the large error on the results, the difference is not significant. A cutoff does not seem to be required by the *BeppoSAX* data. A marginally significant cutoff was detected in the Seyfert 1 spectra with $E_C = 221^{+\infty}_{-158}$ keV. The average spectra showed moderate reflection for Seyfert 1/2 objects ($R = 0.48$ and 0.39 , respectively), while the Seyfert 1.5 objects appeared to have $R = 2.33$ (Deluit & Courvoisier 2003). It has to be kept in mind that the results in this study were based on *BeppoSAX* PDS spectra alone, without taking into account the valuable information from the lower energy LECS/MECS data, which could have significantly constrained the shape of the underlying continuum.

The *INTEGRAL* AGN sample confirms the previously found trend with harder spectra for the obscured objects. This can be roughly understood by the argument that in order to overcome a substantial absorption, obscured objects have to have hard X-ray spectra to be detectable. Comparing the ratio X of obscured ($N_H > 10^{22}$ cm $^{-2}$) to unobscured AGNs, we find in the *INTEGRAL* data that $X = 1.7 \pm 0.4$. Excluding the targets of observations leads to $X = 1.6 \pm 0.5$. The ratios change slightly when taking into account only those objects that belong to the complete sample with an ISGRI significance of 7σ or higher (Table 1). This subsample includes 32 AGNs, with 18 obscured and 10 unobscured objects (absorption information is missing for the remaining four objects). Using only the complete sample changes the ratio to $X = 1.8 \pm 0.5$ and 1.9 ± 0.6 (targets excluded), respectively. Splitting this result into objects near the Galactic plane ($|b| < 20^\circ$) and off the plane shows for all objects a ratio of $X = 3.3 \pm 1.1$ and 1.1 ± 0.5 , respectively. This trend shows that the harder spectra of those objects, where the absorption in the line of sight through the Galaxy is low compared to the intrinsic absorption, are more likely to shine through the Galactic plane.

One would expect a higher ratio in order to explain the unresolved X-ray background in this energy range (e.g., Worsley et al. 2005). But it has to be taken into account that our sample only represents the high-flux and low-luminosity sources ($\langle \log L_X \rangle = 43.3$) in the local universe ($\langle z \rangle = 0.020$). Gilli et al. (1999) showed that the ratio between type 2 and all quasi-stellar objects (QSOS) should be at most 2 in the local universe. The *BeppoSAX* HELLAS survey showed that the fraction of unobscured AGNs increases with the flux of the objects (Comastri et al. 2001). Evidence that the fraction of obscured AGNs depends on the redshift was found by Ueda et al. (2003) when studying the hard X-ray luminosity function. They found that the density evolution of AGNs depends on the luminosity that will lead to an increase of the type 2 fraction with redshift. In a recent study La Franca et al. (2005) found that both effects combined (the fraction of absorbed AGNs decreases with the intrinsic X-ray luminosity and increases with the redshift) can be explained by a luminosity-dependent density evolution model. They also showed that the luminosity function of AGNs like those presented here peaks at $z \sim 0.7$, while a high-luminosity AGN peaks at $z \sim 2$. Consistent with our study, La Franca et al. also found a ratio of $X = 2.1$ at $L_X = 10^{42.5}$ ergs s $^{-1}$ in the 2–10 keV energy band. Unified models predict, depending on the applied model, a ratio of $X = 1.5$ – 2.0 for high-flux, low-redshift AGNs (Treister & Urry 2005), while a recent study of *Chandra* data showed that $X = 8.5 \pm 6.3$ for low-redshift, low-luminosity AGNs (Barger et al. 2005), indicating a larger dominance of obscured objects. So far, these investigations have been focused on the X-rays below 10 keV, and *INTEGRAL* can add substantial information

to the nature of bright AGNs in the local universe. Considering the expected composition of the hard X-ray background, it is remarkable that our sample includes only four Compton-thick AGNs. If Compton-thick AGNs are dominant in the hard X-rays, they would have to be fainter than the objects detected by *INTEGRAL* so far.

The energy range 15–200 keV is now also accessible through the BAT instrument on board *Swift* (Gehrels et al. 2004). A study by Markwardt et al. (2005) of observations of the extragalactic sky indicated a ratio of $X = 2$ between obscured and unobscured AGNs, fully consistent with the results from the *INTEGRAL* AGN sample. Although the *Swift* BAT survey covers different areas of the sky, the energy band is similar to the *INTEGRAL* ISGRI range, and the type of AGNs detectable should be the same. The sample presented here is still too small to constrain the ratio of obscured to unobscured sources, but it might indicate that the unified model predicts this value of $X \simeq 2$ correctly, differing from earlier claims (Treister & Urry 2005; La Franca et al. 2005).

7. CONCLUSIONS

The AGN sample derived from the *INTEGRAL* public data archive comprises 42 low-luminosity and low-redshift ($\langle \log L_X \rangle = 43.3$ and $\langle z \rangle = 0.020 \pm 0.004$, excluding the blazars) objects, including five blazars in the hard X-ray domain. Only one galaxy cluster is detected, but no starburst galaxy has yet been detected. The results from the JEM-X2, ISGRI, and SPI data show that within the statistical limitations of the data the high-energy continua of AGNs can be described by a simple power law with photon index $\Gamma = 2.11 \pm 0.05$ (Seyfert 1), $\Gamma = 2.10 \pm 0.02$ (Seyfert 1.5), and $\Gamma = 1.95 \pm 0.01$ (Seyfert 2). A similar trend is seen when dividing the Seyfert galaxies according to their intrinsic absorption into unabsorbed ($N_H < 10^{22}$ cm $^{-2}$; $\Gamma = 2.08 \pm 0.02$) and absorbed ($\Gamma = 1.98 \pm 0.01$) sources. Blazars naturally show strongly variable spectra, but the average spectral slope is of the same order ($\Gamma = 2.07 \pm 0.10$). It has to be taken into account that the simple model does not represent the data as soon as a sufficient S/N is apparent, such as in the Circinus galaxy and Cen A (Soldi et al. 2005; Rothschild et al. 2006) or NGC 4151 (Beckmann et al. 2005). But the average spectra indicate that a cutoff in most cases, if apparent, appears at energies $E_C \gg 200$ keV.

The AGN sample presented here is complete down to a significance limit of $\sim 7\sigma$. This results in a complete sample of 32 AGNs. Within this complete sample, the ratio between obscured and unobscured AGNs is $X = 1.8 \pm 0.5$, consistent with the unified model for AGNs and with recent results from the *Swift* BAT survey. Only four Compton-thick AGNs are found in the whole sample, and only three are found in the complete sample.

Sazonov et al. (2005) reported five additional AGNs in recent observations, not detectable in the data presented here. In addition, one AGN seen by OSSE, the blazar 3C 454.3 (McNaron-Brown et al. 1995), has recently been detected by *INTEGRAL* during an outburst (Foschini et al. 2005). With the ongoing observations of the *INTEGRAL* and *Swift* missions, the number of detectable AGNs will increase further, especially with a number of already performed and scheduled observations far off the Galactic plane. This will enable us to solve the mystery of the hard X-ray background above 10 keV in the near future.

We would like to thank the anonymous referee for comments that helped to improve the paper. This research has made use of the NASA/IPAC Extragalactic Database (NED), which is

operated by the Jet Propulsion Laboratory; of data obtained from the High Energy Astrophysics Science Archive Research Center (HEASARC), provided by the NASA Goddard Space Flight Center; and of the SIMBAD Astronomical Database, which is operated by the Centre de Données astronomiques de

Strasbourg. This research has made use of the Tartarus (ver. 3.1) database, created by Paul O'Neill and Kirpal Nandra at Imperial College London, and Jane Turner at NASA/GSFC. Tartarus is supported by funding from PPARC, and NASA grants NAG5-7385 and NAG5-7067.

REFERENCES

- Arnaud, K. A. 1996, in ASP Conf. Ser. 101, *Astronomical Data Analysis Software and Systems V*, ed. G. H. Jacoby & J. Barnes (San Francisco: ASP), 17
- Avni, Y., & Bahcall, J. N. 1980, *ApJ*, 235, 694
- Ballo, L., et al. 2002, *ApJ*, 567, 50
- Barger, A. J., Cowie, L. L., Mushotzky, R. F., Yang, Y., Wang, W.-H., Steffen, A. T., & Capa, P. 2005, *AJ*, 129, 578
- Bassani, L., Malagutti, G., Jourdain, E., Roques, J. P., & Johnson, W. N. 1995, *ApJ*, 444, L73
- Bassani, L., et al. 2004, in Proc. 5th *INTEGRAL* Workshop (ESA SP-552; Noordwijk: ESA), 139
- Beckmann, V., Gehrels, N., Favre, P., Walter, R., Courvoisier, T. J.-L., Petrucci, P.-O., & Malzac, J. 2004, *ApJ*, 614, 641
- Beckmann, V., et al. 2005, *ApJ*, 634, 939
- Bianchi, S., Balestra, I., Matt, G., Guainazzi, M., & Perola, G. C. 2003, *A&A*, 402, 141
- Boella, G., Butler, R. C., Perola, G. C., Piro, L., Scarsi, L., & Bleeker, J. A. M. 1997, *A&AS*, 122, 299
- Brandt, W. N., & Hasinger, G. 2005, *ARA&A*, 43, 827
- Caroli, E., Stephen, J. B., Di Cocco, G., Natalucci, L., & Spizzichino, A. 1987, *Space Sci. Rev.*, 45, 349
- Comastri, A., Fiore, F., Vignali, C., Matt, G., Perola, G. C., & La Franca, F. 2001, *MNRAS*, 327, 781
- Comastri, A., Setti, G., Zamorani, G., & Hasinger, G. 1995, *A&A*, 296, 1
- Courvoisier, T. J.-L., et al. 2003a, *A&A*, 411, L53
- . 2003b, *A&A*, 411, L343
- Deluit, S., & Courvoisier, T. J.-L. 2003, *A&A*, 399, 77
- De Rosa, A., et al. 2005, *A&A*, 438, 121
- Diehl, R., et al. 2003, *A&A*, 411, L117
- Foschini, L., et al. 2005, *ATel*, 497
- Fossati, G., Maraschi, L., Celotti, A., Comastri, A., & Ghisellini, G. 1998, *MNRAS*, 299, 433
- Frontera, F., Costa, E., & Dal Fiume, D. 1997, *A&AS*, 122, 357
- Gehrels, N., Chipman, E., & Kniffen, D. A. 1993, *A&AS*, 97, 5
- Gehrels, N., et al. 2004, *ApJ*, 611, 1005
- George, I. M., & Fabian, A. C. 1991, *MNRAS*, 249, 352
- Gilli, R., Risaliti, G., & Salvati, M. 1999, *A&A*, 347, 424
- Gilli, R., Salvati, M., & Hasinger, G. 2001, *A&A*, 366, 407
- Goldwurm, A., et al. 2003, *A&A*, 411, L223
- Gondek, D., et al. 1996, *MNRAS*, 282, 646
- Guainazzi, M., et al. 1999, *A&A*, 346, 407
- Hammersley, A. P., Ponman, T. J., & Skinner, G. K. 1992, *Nucl. Instrum. Methods Phys. Res. A*, 311, 585
- Johnson, W. N., Zdziarski, A. A., Madejski, G. M., Paciesas, W. S., Steinle, H., & Lin, Y.-C. 1997, in *The Fourth Compton Symposium*, ed. C. D. Dermer, M. S. Strickman, & J. D. Kurfess (Woodbury: AIP), 283
- Johnson, W. N., et al. 1993, *ApJS*, 86, 693
- Kalemci, E., Boggs, S. E., & Lund, N. 2005, *ATel*, 410
- Kirsch, M. G., et al. 2005, *Proc. SPIE*, 5898, 224
- Krivonos, R., Vikhlinin, A., Churazov, E., Lutovinov, A., Molkov, S., & Sunyaev, R. 2005, *ApJ*, 625, 89
- La Franca, F., et al. 2005, *ApJ*, 635, 864
- Lebrun, F., et al. 2003, *A&A*, 411, L141
- Levenson, N. A., Weaver, K. A., & Heckman, T. M. 2001, *ApJS*, 133, 269
- Lund, N., et al. 2003, *A&A*, 411, L231
- Lutz, D., Maiolino, R., Spoon, H. W. W., & Moorwood, A. F. M. 2004, *A&A*, 418, 465
- Malizia, A., Bassani, L., Stephen, J. B., Di Cocco, G., Fiore, F., & Dean, A. J. 2003, *ApJ*, 589, L17
- Markwardt, C. B., Tueller, J., Skinner, G. K., Gehrels, N., Barthelmy, S. D., & Mushotzky, R. F. 2005, *ApJ*, 633, L77
- Masetti, N., Palazzi, E., Bassani, L., Malizia, A., & Stephen, J. B. 2004, *A&A*, 426, L41
- Mas-Hesse, J. M., et al. 2003, *A&A*, 411, L261
- Matsumoto, C., Nava, A., Maddox, L. A., Leighly, K. M., Grupe, D., Awaki, H., & Ueno, S. 2004, *ApJ*, 617, 930
- Matt, G., et al. 1997, *A&A*, 325, L13
- McNaron-Brown, K., et al. 1995, *ApJ*, 451, 575
- Michel, L., Herent, O., Motch, C., Pye, J., & Watson, M. G. 2004, in ASP Conf. Ser. 314, *Astronomical Data Analysis Software and Systems XIII*, ed. F. Ochsenbein, M. G. Allen, & D. Egret (San Francisco: ASP), 570
- Perola, G. C., et al. 2002, *A&A*, 389, 802
- Pian, E., et al. 2005, *A&A*, 429, 427
- Pounds, K., Reeves, J., O'Brien, P., Page, K., Turner, M., & Nayakshin, S. 2001, *ApJ*, 559, 181
- Rothschild, R. E., et al. 2006, *ApJ*, in press (astro-ph/0512451)
- Sazonov, S. Y., Churazov, E., Revnivtsev, M. G., Vikhlinin, A., & Sunyaev, R. 2005, *A&A*, 444, L37
- Sazonov, S. Y., & Revnivtsev, M. G. 2004, *A&A*, 423, 469
- Sazonov, S. Y., Revnivtsev, M. G., Lutovinov, A. A., Sunyaev, R. A., & Grebenev, S. A. 2004, *A&A*, 421, L21
- Schmidt, M. 1968, *ApJ*, 151, 393
- Setti, G., & Woltjer, L. 1989, *A&A*, 224, L21
- Skinner, G., & Connell, P. 2003, *A&A*, 411, L123
- Soldi, S., et al. 2005, *A&A*, 444, 431
- Toor, A., & Seward, F. D. 1974, *AJ*, 79, 995
- Treister, E., & Urry, C. M. 2005, *ApJ*, 630, 115
- Ueda, Y., Akiyama, M., Ohta, K., & Miyaji, T. 2003, *ApJ*, 598, 886
- Vedrenne, G., et al. 2003, *A&A*, 411, L63
- Véron-Cetty, M. P., & Véron, P. 2000, *A&A Rev.*, 10, 81
- Winkler, C., et al. 2003, *A&A*, 411, L1
- Worsley, M. A., et al. 2005, *MNRAS*, 357, 1281
- Young, A. J., Wilson, A. S., Terashima, Y., Arnaud, K. A., & Smith, D. A. 2002, *ApJ*, 564, 176
- Zdziarski, A. A., Johnson, W. N., Done, C., Smith, D., & McNaron-Brown, K. 1995, *ApJ*, 438, L63

6.9.3 The Hard X-ray 20-40 keV AGN Luminosity Function

A discussion of this work in the context of the unified model of AGN can be found in Section 4.7.1 on page 62. The manuscript, which is shown on the following pages, has been published as

Beckmann V., Soldi S., Shrader, C. R., Gehrels N., & Prodit N., *The Astrophysical Journal*, Volume 652, Issue 1, pp. 126-135 (2006)

THE HARD X-RAY 20–40 keV AGN LUMINOSITY FUNCTION

V. BECKMANN,¹ S. SOLDI,^{2,3} C. R. SHRADER,^{4,5} N. GEHRELS,⁴ AND N. PRODIT²

Received 2006 March 1; accepted 2006 June 28

ABSTRACT

We have compiled a complete extragalactic sample based on $\sim 25,000 \text{ deg}^2$ to a limiting flux of $3 \times 10^{-11} \text{ ergs cm}^{-2} \text{ s}^{-1}$ ($\sim 7000 \text{ deg}^2$ to a flux limit of $10^{-11} \text{ ergs cm}^{-2} \text{ s}^{-1}$) in the 20–40 keV band with *INTEGRAL*. We have constructed a detailed exposure map to compensate for effects of nonuniform exposure. The flux-number relation is best described by a power law with a slope of $\alpha = 1.66 \pm 0.11$. The integration of the cumulative flux per unit area leads to $f_{20-40 \text{ keV}} = 2.6 \times 10^{-10} \text{ ergs cm}^{-2} \text{ s}^{-1} \text{ sr}^{-1}$, which is about 1% of the known 20–40 keV X-ray background. We present the first luminosity function of AGNs in the 20–40 keV energy range, based on 38 extragalactic objects detected by the imager IBIS-ISGRI on board *INTEGRAL*. The luminosity function shows a smoothly connected double-power-law form with an index of $\gamma_1 = 0.8$ below and $\gamma_2 = 2.1$ above the turnover luminosity of $L_* = 2.4 \times 10^{43} \text{ ergs s}^{-1}$. The emissivity of all *INTEGRAL* AGNs per unit volume is $W_{20-40 \text{ keV}} (> 10^{41} \text{ ergs s}^{-1}) = 2.8 \times 10^{38} \text{ ergs s}^{-1} h_{70}^3 \text{ Mpc}^{-3}$. These results are consistent with those derived in the 2–20 keV energy band and do not show a significant contribution by Compton-thick objects. Because the sample used in this study is truly local ($\bar{z} = 0.022$), only limited conclusions can be drawn for the evolution of AGNs in this energy band.

Subject headings: galaxies: active — galaxies: Seyfert — gamma rays: observations — surveys — X-rays: galaxies

Online material: color figures

1. INTRODUCTION

The Galactic X-ray sky is dominated by accreting binary systems, while the extragalactic sky shows mainly active galactic nuclei (AGNs) and clusters of galaxies. Studying the population of sources in X-ray bands has been a challenge ever since the first observations by rocketborne X-ray detectors (Giacconi et al. 1962). At soft X-rays (0.1–2.4 keV), deep exposures by *ROSAT* have revealed an extragalactic population of mainly broad-line AGNs, such as type 1 Seyfert and quasars (Hasinger et al. 1998; Schmidt et al. 1998). In the 2–10 keV range, surveys have been carried out with the *Advanced Satellite for Cosmology and Astrophysics (ASCA)*; e.g., Ueda et al. 2001), *XMM-Newton* (e.g., Hasinger 2004), and *Chandra* (e.g., Brandt et al. 2001) and have shown that the dominant extragalactic sources are more strongly absorbed than those within the *ROSAT* energy band. For a summary on the deep X-ray surveys below 10 keV see Brandt & Hasinger (2005). At higher energies the data become more scarce. Between a few keV and $\sim 1 \text{ MeV}$, no all-sky survey using imaging instruments has been performed to date. The *Ross X-Ray Timing Explorer (RXTE)* sky survey in the 3–20 keV energy band revealed about 100 AGNs, showing an even higher fraction of absorbed ($N_{\text{H}} > 10^{22} \text{ cm}^{-2}$) sources of about 60% (Sazonov & Revnivtsev 2004).

The *International Gamma-Ray Astrophysics Laboratory (INTEGRAL)*; Winkler et al. 2003) offers an unprecedented $> 20 \text{ keV}$ collecting area and state-of-the-art detector electron-

ics and background-rejection capabilities. Notably, the imager IBIS, with an operating range from 20 to 1000 keV and a fully coded field of view of $10^\circ \times 10^\circ$, now enables us to study a large portion of the sky. A first catalog of AGNs showed a similar fraction of absorbed objects to the *RXTE* survey (Beckmann et al. 2006a). The Burst Alert Telescope (BAT) of the *Swift* mission (Gehrels et al. 2004) operates in the 15–200 keV band and uses a detector similar to IBIS-ISGRI, but provides a field of view about twice the size. The BAT data of the first 3 months of the mission provided a high Galactic latitude survey, including 44 AGNs (Markwardt et al. 2005). Within this sample a weak anticorrelation of luminosity versus intrinsic absorption was found, as previously found in the 2–10 keV band (Ueda et al. 2003; La Franca et al. 2005), revealing that most of the objects with luminosities $L_{\text{X}} > 3 \times 10^{43} \text{ ergs s}^{-1}$ show no intrinsic absorption. Markwardt et al. (2005) also pointed out that this luminosity corresponds to the break in the luminosity function.

Related to the compilation of AGN surveys in the hard X-rays is the question of which sources form the cosmic X-ray background (CXB). While the CXB below 20 keV has been the focus of many studies, the most reliable measurements in the 10–500 keV range have been provided by the *High Energy Astronomical Observatory (HEAO-1)*, launched in 1977 (Marshall et al. 1980). The most precise measurements provided by the UCSD/MIT Hard X-Ray and Gamma-Ray instrument (*HEAO-1 A-4*) show that the CXB peaks at an energy of about 30 keV (Marshall et al. 1980; Gruber et al. 1999). The isotropic nature of the X-ray background points to an extragalactic origin, and as the brightest persistent sources are AGNs, it was suggested early on that those objects are the main source of the CXB (e.g., Setti & Woltjer 1989). In the soft X-rays this concept has been proven to be correct through the observations of the *ROSAT* deep X-ray surveys, which showed that 90% of the 0.5–2.0 keV CXB can be resolved into AGNs (Schmidt et al. 1998). At higher energies (2–10 keV), *ASCA* and *Chandra* surveys measured the hard X-ray luminosity function (XLF) of AGNs and its cosmological evolution. These studies show that in this energy range the CXB can be explained

¹ NASA Goddard Space Flight Center, Astrophysics Science Division, Code 661, Greenbelt, MD 20771; and Joint Center for Astrophysics, Department of Physics, University of Maryland, Baltimore County, Baltimore, MD 21250; beckmann@milkyway.gsfc.nasa.gov.

² *INTEGRAL* Science Data Centre, Chemin d'Écogia 16, 1290 Versoix, Switzerland.

³ Observatoire de Genève, 51 Chemin des Maillettes, 1290 Sauverny, Switzerland.

⁴ NASA Goddard Space Flight Center, Astrophysics Science Division, Code 661, Greenbelt, MD 20771.

⁵ Universities Space Research Association, 10211 Wincopin Circle, Columbia, MD 21044.

by AGNs, but with a higher fraction of absorbed ($N_{\text{H}} > 10^{22} \text{ cm}^{-2}$) objects than in the soft X-rays (e.g., Ueda et al. 2003). A study based on the *RXTE* survey by Sazonov & Revnivtsev (2004) derived the local hard X-ray luminosity function of AGNs in the 3–20 keV band. They showed that the summed emissivity of AGNs in this energy range is smaller than the total X-ray volume emissivity in the local universe, and suggested that a comparable X-ray flux may be produced by lower luminosity AGNs, nonactive galaxies, and clusters of galaxies together. Using the *HEAO-1 A-2* AGNs, Shinozaki et al. (2006), however, obtained a local AGN emissivity that is about twice as large as the value of Sazonov & Revnivtsev (2004) but consistent with the estimates by Miyaji et al. (1994), which were based on the cross-correlation of the *HEAO-1 A-2* map with *Infrared Astronomical Satellite* (*IRAS*) galaxies.

With the ongoing observations of the sky by *INTEGRAL*, a sufficient amount of data is now available to derive the AGN hard X-ray luminosity function. In this paper we present an analysis of recent observations performed by the *INTEGRAL* satellite and compare the results with previous studies. In § 2 we describe the AGN sample, and in § 3 the methods to derive the number-flux distribution of *INTEGRAL* AGNs are presented, together with the analysis of their distribution. Section 4 shows the local luminosity function of AGNs, as derived from our data, followed by a discussion of the results in § 5. Throughout this work we applied a cosmology with $H_0 = 70 \text{ km s}^{-1} \text{ Mpc}^{-1}$ ($h_{70} = 1$), $k = 0$ (flat universe), $\Omega_{\text{matter}} = 0.3$, and $\Lambda_0 = 0.7$, although a $\Lambda_0 = 0$ and $q_0 = 0.5$ cosmology does not change the results significantly because of the low redshifts in our sample.

2. THE *INTEGRAL* AGN SAMPLE

Observations in the X-ray to soft gamma-ray domain have been performed by the soft gamma-ray imager (20–1000 keV) ISGRI (Lebrun et al. 2003) on board the *INTEGRAL* satellite (Winkler et al. 2003).

The data used here are taken from orbit revolutions 19–137 and revolutions 142–149. The list of sources was derived from the analysis as described in Beckmann et al. (2006a). The analysis was performed using the Off-line Science Analysis (OSA) software version 5.0 distributed by the *INTEGRAL* Science Data Centre (ISDC; Courvoisier et al. 2003a). Additional observations performed later led to further source detections within the survey area. We extracted spectra at those positions from the data following the same procedure. It is understood that most of those objects did not result in a significant detection $\geq 3 \sigma$ in the data set used here, but it ensures completeness of the sample at a significance limit of 5σ (see § 3).

The list of 73 sources is shown in Table 1. Twenty-two of the sources have Galactic latitudes $-10^\circ < b < +10^\circ$ (14, if we only consider the sources with significance $\geq 5 \sigma$). In addition to the sample presented here, eight new *INTEGRAL* sources with no identification have been detected in our survey with a significance of $\geq 5 \sigma$. These unidentified sources, most of them in the Galactic plane, are not included in this work. The significances listed have been derived from the intensity maps produced by the OSA software. Differently than Beckmann et al. (2006a) we did not use the significances as determined for the whole ISGRI energy range by the extraction software, but determined the significances based on the count rate and count-rate error for ISGRI in the 20–40 keV energy band only, as this is the relevant energy range for this work. Fluxes are determined by integrating the best-fit spectral model over the 20–40 keV bandpass. The uncertainty in the absolute flux calibration is about 5%. The luminosities listed are the luminosities in this energy band, based on

the measured (absorbed) flux. The absorption listed is the intrinsic absorption in units of 10^{22} cm^{-2} , as measured in soft X-rays below 10 keV by various missions, as referenced. We also include the most important reference for the *INTEGRAL* data of the particular source in the last column of Table 1. The extracted images and source results are available in electronic form.⁶

In order to provide a complete list of AGNs detected by *INTEGRAL*, we also included those sources that are not covered by the data used for our study. Those sources are marked in Table 1 and are not used in our analysis.

3. NUMBER-FLUX DISTRIBUTION OF *INTEGRAL* AGNs

3.1. Completeness of the Sample

In order to compute the AGN number-flux relation, it is necessary to have a complete and unbiased sample. Toward this end, one must understand the characteristics of the survey, such as the sky coverage and completeness for each subset of the total sample. Because of the inhomogeneous nature of the survey exposure map, we applied a significance limit rather than a flux limit to define a complete sample. The task is to find a significance limit that ensures that all objects above a given flux limit have been included. To test for completeness, the V_e/V_a statistic has been applied, where V_e stands for the volume that is enclosed by the object, and V_a is the accessible volume in which the object could have been found (Avni & Bahcall 1980).

In the case of no evolution $\langle V_e/V_a \rangle = 0.5$ is expected. This evolutionary test is applicable only to samples complete to a well-defined significance limit. It can therefore also be used to test the completeness of a sample. We performed a series of V_e/V_a tests on the *INTEGRAL* AGN sample, assuming completeness limits in the range of 0.5σ up to 16σ ISGRI 20–40 keV significance. For a significance limit below the true completeness limit of the sample one expects the V_e/V_a tests to derive a value $\langle V_e/V_a \rangle < \langle V_e/V_a \rangle_{\text{true}}$, where $\langle V_e/V_a \rangle_{\text{true}}$ is the true test result for a complete sample. Above the completeness limit the $\langle V_e/V_a \rangle$ values should be distributed around $\langle V_e/V_a \rangle_{\text{true}}$ within the statistical uncertainties.

The results of the tests are shown in Figure 1. It appears that the sample becomes complete at a significance cutoff of approximately 5σ , which includes 38 AGNs. The average value is $\langle V_e/V_a \rangle = 0.43 \pm 0.05$. This is consistent with the expected value of 0.5 at the 1.5σ level, suggesting no evolution and a uniform distribution in the local universe. It is unlikely that cosmological effects have an influence on the result, as the average redshift in the sample is $\bar{z} = 0.022$, with a maximum redshift of $z = 0.13$. A positive cosmological evolution would result in a slightly higher value than 0.5. We would like to remind the reader that we use the $\langle V_e/V_a \rangle$ test not to determine any cosmological effects, but to see at what significance level it returns a stable value.

3.2. Deriving the Area Corrected Number-Flux Distribution

A correct representation of the number-flux distribution (i.e., $\log N_{>S}$ vs. $\log S$; see Beckmann et al. 2006b) for the sample presented here must account for the different exposure times comprising our survey, and the resulting sensitivity variations. We determine here the number density, and thus the number of AGNs above a given flux has to be counted and divided by the sky area in which they are detectable throughout the survey. We therefore first determined the exposure time in 64,620 sky elements of $\sim 0.63 \text{ deg}^2$ size within our survey. In each sky bin, the

⁶ See http://heasarc.gsfc.nasa.gov/docs/integral/inthp_archive.html.

TABLE 1
INTEGRAL AGN CATALOG

Name	Type	z	R.A. (J2000.0)	Decl. (J2000.0)	Exposure ^a (ks)	ISGRI (σ)	f_x^b	$\log L_{20-40 \text{ keV}}$ (ergs s ⁻¹)	$N_{\text{H}}^{\text{c,d}}$	References
IES 0033+595	BL Lac	0.086	00 35 53	+59 50 05	1449	3.5	0.37	43.83	0.36 (1)	2
NGC 788	Sy 1/2	0.0136	02 01 06	-06 48 56	311	10.7	2.98	43.09	<0.02 (3)	4
IGR J02097+5222	Sy 1	0.0492	02 09 46	+52 22 48	26	4.9	3.8	44.34	?	5
NGC 1068	Sy 2	0.003793	02 42 41	-00 00 48	311	4.3	0.93	41.47	>150 (6)	4
QSO B0241+62	Sy 1	0.044557	02 44 58	+62 28 07	43	3.4	2.02	43.97	1.5 (7)	8
NGC 1142	Sy 2	0.028847	02 55 12	-00 11 01	311	5.5	1.58	43.48	?	9
NGC 1275	Sy 2	0.017559	03 19 48	+41 30 42	264	8.4	1.89	43.12	3.75 (4)	4
3C 111	Sy 1	0.048500	04 18 21	+38 01 36	67	10.0	6.27	44.54	0.63 (3)	4
UGC 3142	Sy 1	0.021655	04 43 47	+28 58 19	247	16.8	5.46	43.76	?	2
LEDA 168563	Sy 1	0.0290	04 52 05	+49 32 45	28	2.8	2.27	43.64	?	2
MCG +8-11-11	Sy 1.5	0.020484	05 54 54	+46 26 22	21	6.2	6.07	43.76	<0.02 (7)	4
Mrk 3	Sy 2	0.013509	06 15 36	+71 02 15	472	15.9	3.65	43.17	110 (7)	4
Mrk 6	Sy 1.5	0.018813	06 52 12	+74 25 37	482	8.7	2.01	43.21	10 (7)	4
S5 0716+714	BL Lac	0.3 ^e	07 21 53	+71 20 36	482	0.7	0.14	44.41 ^e	<0.01 (3)	10
ESO 209-12	Sy 1.5	0.040495	08 01 58	-49 46 36	1543	6.7	0.86	43.52	?	8
FRL 1146	Sy 1	0.031789	08 38 31	-35 59 35	849	3.6	0.60	43.15	?	8
S5 0836+710	FSRQ	2.172	08 41 24	+70 53 42	391	6.4	1.73	47.79	0.11 (3)	10
MCG-05-23-16	Sy1.9	0.008486	09 47 40	-30 56 56	2	2.3	11.20	43.25	1.6 (11)	11
IGR J10404-4625	Sy 2	0.0237	10 40 22	-46 25 26	46	1.5	0.67	42.93	?	12
NGC 3783	Sy 1	0.00973	11 39 02	-37 44 19	18 ^f	5.6	6.2	43.11	<0.4 (3)	13
IGR J12026-5349	AGN	0.028	12 02 48	-53 50 08	191	5.5	1.86	43.52	2.2 (14)	14
NGC 4051	Sy 1.5	0.002336	12 03 10	+44 31 53	443	8.4	1.80	41.34	<0.01 (7)	4
NGC 4151	Sy 1.5	0.003320	12 10 33	+39 24 21	483	163.3	26.13	42.80	6.9 (15)	15
NGC 4253	Sy 1.5	0.012929	12 18 27	+29 48 46	715	6.1	0.93	42.54	0.8 (7)	4
4C +04.42	BL Lac	0.965	12 22 23	+04 13 16	690	4.5	0.80	46.58	?	8
NGC 4388	Sy 2	0.008419	12 25 47	+12 39 44	215	34.8	9.54	43.18	27 (16)	16
NGC 4395	Sy 1.8	0.001064	12 25 49	+33 32 48	739	5.1	0.56	40.14	0.15 (3)	4
3C 273	Blazar	0.15834	12 29 07	+03 03 09	655	34.2	5.50	45.58	0.5 (4)	17
NGC 4507	Sy 2	0.011801	12 35 37	-39 54 33	152	14.9	6.46	43.30	29 (7)	4
IGR J12391-1612	Sy 2	0.036	12 39 06	-16 10 47	83	1.4	3.46	44.02	1.9 (14)	14
NGC 4593	Sy 1	0.009000	12 39 39	-05 20 39	723	20.1	3.31	42.78	0.02 (7)	4
IGR J12415-5750	Sy 2	0.024	12 41 24	-57 50 24	440	1.1	0.33	42.64	?	18
3C 279	Blazar	0.53620	12 56 11	-05 47 22	497	3.6	0.82	45.97	≤ 0.13 (3)	4
Coma Cluster	GClstr	0.023100	12 59 48	+27 58 48	516	7.2	1.09	43.11	<0.01 (4)	4
NGC 4945	Sy 2	0.001878	13 05 27	-49 28 06	276	33.8	9.85	41.88	400 (7)	11
ESO 323-G077	Sy 2	0.015014	13 06 26	-40 24 53	761	6.9	1.20	42.78	55 (19)	19
IGR J13091+1137	AGN	0.0251	13 09 06	+11 38 03	48	2.0	1.06	43.18	90 (14)	18
NGC 5033	Sy 1.9	0.002919	13 13 28	+36 35 38	377	4.6	1.06	41.30	2.9 (7)	4
Cen A	Sy 2	0.001830	13 25 28	-43 01 09	532	167.4	32.28	42.38	12.5 (4)	11
MCG-06-30-015	Sy 1	0.007749	13 35 54	-34 17 43	567	4.9	0.73	41.99	7.7 (7)	4
4U 1344-60	Sy 1.5	0.012	13 47 25	-60 38 36	603	16.6	2.83	43.02	5 (20)	4
IC 4329A	Sy 1.2	0.016054	13 49 19	-30 18 36	440	41.7	8.19	43.68	0.42 (7)	4
Circinus galaxy	Sy 2	0.001448	14 13 10	-65 20 21	589	58.9	10.73	41.69	360 (7)	11
NGC 5506	Sy 1.9	0.006181	14 13 15	-03 12 27	101	12.6	4.21	42.55	3.4 (7)	4
NGC 5548	Sy 1.5	0.017175	14 18 00	+25 08 12	211 ^f	2.4	0.71	42.67	0.51 (7)	4
PG 1416-129	Sy 1	0.129280	14 19 04	-13 10 44	117	8.3	4.86	45.33	0.09 (4)	4
ESO 511-G030	Sy 1	0.022389	14 19 22	-26 38 41	145	5.1	1.93	43.34	<0.05 (19)	19
IC 4518	Sy 2	0.015728	14 57 43	-43 07 54	338	2.3	0.49	42.44	?	4
IGR J16119-6036	Sy 1	0.016	16 11 54	-60 36 00	475	1.2	0.25	42.16	?	2
IGR J16482-3036	Sy 1	0.0313	16 48 17	-30 35 08	973	4.2	0.73	43.22	?	12
NGC 6221	Sy 1/2	0.004977	16 52 46	-59 13 07	523	5.6	1.32	41.86	1 (21)	4
Oph Cluster	GClstr	0.028	17 12 26	-23 22 33	1763	30.8	4.10	43.90	?	22
NGC 6300	Sy 2	0.003699	17 17 00	-62 49 14	173	10.0	3.91	42.07	22 (23)	11
GRS 1734-292	Sy 1	0.021400	17 37 24	-29 10 48	3332	45.9	4.03	43.62	3.7 (4)	24
2E 1739.1-1210	Sy 1	0.037	17 41 54	-12 11 52	631	5.5	1.03	43.51	?	8
IGR J18027-1455	Sy 1	0.035000	18 02 47	-14 54 55	942	12.6	2.03	43.76	19.0 (4)	25
PKS 1830-211	Blazar	2.507	18 33 40	-21 03 40	1069	12.7	2.07	48.02	≤ 0.7 (3)	26
ESO 103-G35	Sy 2	0.013286	18 38 20	-65 25 39	36	4.2	2.97	43.07	19 (27)	11
3C 390.3	Sy 1	0.0561	18 42 09	+79 46 17	490 ^f	9.5	2.0	44.16	<0.1 (28)	13
2E 1853.7+1534	Sy 1	0.084	18 56 00	+15 38 13	761	9.3	1.74	44.48	?	12
1H 1934-063	Sy 1	0.010587	19 37 33	-06 13 05	684	2.7	0.48	42.08	?	4
NGC 6814	Sy 1.5	0.005214	19 42 41	-10 19 25	488	12.1	2.92	42.24	<0.05 (3)	4
IGR J19473+4452	Sy 2	0.0539	19 47 19	+44 49 42	969	5.9	1.05	43.86	11 (14)	14
Cygnus A	Sy 2	0.056075	19 59 28	+40 44 02	1376	21.6	3.24	44.39	20 (29)	4
MCG +04-48-002	Sy 2	0.014206	20 28 35	+25 44 00	187	3.1	1.10	42.70	?	2

HARD X-RAY 20–40 keV AGN LUMINOSITY FUNCTION

TABLE 1—Continued

Name	Type	z	R.A. (J2000.0)	Decl. (J2000.0)	Exposure ^a (ks)	ISGRI (σ)	f_X^b	$\log L_{20-40 \text{ keV}}$ (ergs s ⁻¹)	$N_H^{c,d}$	References
4C +74.26	AGN	0.104	20 42 37	+75 08 02	72 ^f	1.9	0.93	42.35	0.21 (3)	13
Mrk 509	Sy 1	0.034397	20 44 10	-10 43 25	73	8.6	4.66	44.11	<0.01 (3)	4
CJF B2116+818	Sy 1	0.086	21 14 01	+82 04 48	192 ^f	4.8	1.8	44.51	<0.1 (1)	13
IGR J21247+5058	AGN	0.020	21 24 39	+50 58 26	213	11.9	4.15	43.57	?	25
NGC 7172	Sy 2	0.00868	22 02 02	-31 52 11	401 ^f	15.1	3.3	47.74	9.0 (27)	13
3C 454.3	Blazar	0.859	22 53 58	+16 08 54	92 ^f	2.8	3.1	46.56	?	30
MR 2251-178	Sy 1	0.063980	22 54 06	-17 34 55	489	7.0	1.20	44.07	≤ 0.19 (3)	4
MCG -02-58-022	Sy 1.5	0.046860	23 04 44	-08 41 09	489	3.9	1.20	43.79	≤ 0.08 (3)	4

^a IBIS-ISGRI exposure time.

^b Flux $f_{(20-40 \text{ keV})}$ in 10^{-11} ergs cm⁻² s⁻¹.

^c Intrinsic absorption in 10^{22} cm⁻².

^d References for N_H values appear in parentheses.

^e Tentative redshift.

^f Not covered by survey presented here.

REFERENCES.—(1) Donato et al. 2005; (2) Bassani et al. 2006; (3) Tartarus database; (4) Beckmann et al. 2006a; (5) Kuiper et al. 2005; (6) Matt et al. 1997; (7) Lutz et al. 2004; (8) Bird et al. 2006; (9) Virani et al. 2005; (10) Pian et al. 2005; (11) Soldi et al. 2005; (12) Masetti et al. 2006; (13) this work; (14) Sazonov et al. 2005; (15) Beckmann et al. 2005; (16) Beckmann et al. 2004; (17) Courvoisier et al. 2003b; (18) Revnivtsev et al. 2006; (19) Sazonov & Revnivtsev 2004; (20) Piconcelli et al. 2006; (21) Levenson et al. 2001; (22) Revnivtsev et al. 2004; (23) Matsumoto et al. 2004; (24) Sazonov et al. 2004; (25) Masetti et al. 2004; (26) De Rosa et al. 2005; (27) Akylas et al. 2001; (28) Gliozzi et al. 2003; (29) Young et al. 2002; (30) Pian et al. 2006.

exposure is the sum of each individual exposure multiplied by the fraction of the coded field of view in this particular direction. The dead time and the good time intervals (GTI) are not taken into account, but the dead time is fairly constant (around 20%) and GTI gaps are very rare in IBIS-ISGRI data. Figure 2 shows the exposure map in Galactic coordinates for this survey. We excluded those fields with an exposure time less than 2 ks, resulting in 47,868 sky elements with a total coverage of 9.89 sr. The flux limit for a given significance limit should be a function of the square root of the exposure time if no systematic effects apply, but this assumption cannot be made here. The nature of coded-mask imaging leads to accumulated systematic effects at longer exposure times. In order to achieve a correlation between the exposure time and the flux limit, we therefore used an empirical approach. For each object we computed what we will call its 5σ

equivalent flux $f_{5\sigma}$, based on its actual flux f_X and its significance s : $f_{5\sigma} = f_X \times 5/s$. We found a correlation between these $f_{5\sigma}$ values and exposure times, which has a scatter of $\lesssim 0.2$ dex (Fig. 3). The correlation was then fitted by a smooth polynomial of the third degree. This function was then used to estimate the limiting flux of each individual survey field. It must be noted that the individual limits are not important, only the distribution of those flux limits. The total area in the survey for a given flux limit is shown in Figure 4.

Based on the flux limits for all survey fields, we are now able to construct the number-flux distribution for the *INTEGRAL* AGNs, determining for each source flux the total area in which the source is detectable with a 5σ detection significance in the 20–40 keV energy band. The resulting correlation is shown in Figure 5.

3.3. The Slope of the Number-Flux Distribution

We applied a maximum-likelihood (ML) algorithm to our empirical number-flux distribution to obtain a power-law approximation of the form $N(>S) = KS^{-\alpha}$. We note that we are fitting the “integrated” $N(>S)$ function, as distinct from the “differential” number-flux function. The latter entails binning the data; thus, some loss of information is incurred. The advantage of fitting the differential distribution is that a simple least-squares procedure may be employed. However, given the modest size of our sample, the expected loss of accuracy was considered unacceptable.

Our approach was based on the formalism derived by Murdoch et al. (1973), also following the implementation of Piccinotti et al. (1982). The latter involved modification of the basic ML incorporated to facilitate handling of individual source flux-measurement errors. The ML method also involves the application of a Kolmogorov-Smirnov (K-S) test as part of the procedure to optimize the fit, as detailed in Murdoch et al. (1973); we note that the K-S test as applied in this context is not a measure of the overall goodness of fit). Once the slope is determined, a χ^2 minimization is used to determine the amplitude K .

For this analysis, we used the complete subsample of 38 sources for which the statistical significance of our flux determinations was at a level of 5σ or greater. The dimmest source among this subsample was $f_X = 5.6 \times 10^{-12}$ ergs cm⁻² s⁻¹, and the brightest was $f_X = 3.2 \times 10^{-10}$ ergs cm⁻² s⁻¹. We derived an ML probability

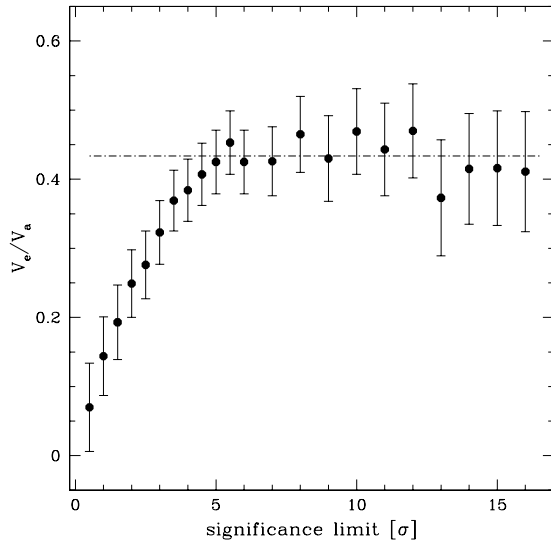


FIG. 1.—Result of the V_e/V_a test, assuming different completeness limits in ISGRI significance. The dot-dashed line shows the average $\langle V_e/V_a \rangle$ value for the objects with significance $\geq 5\sigma$.

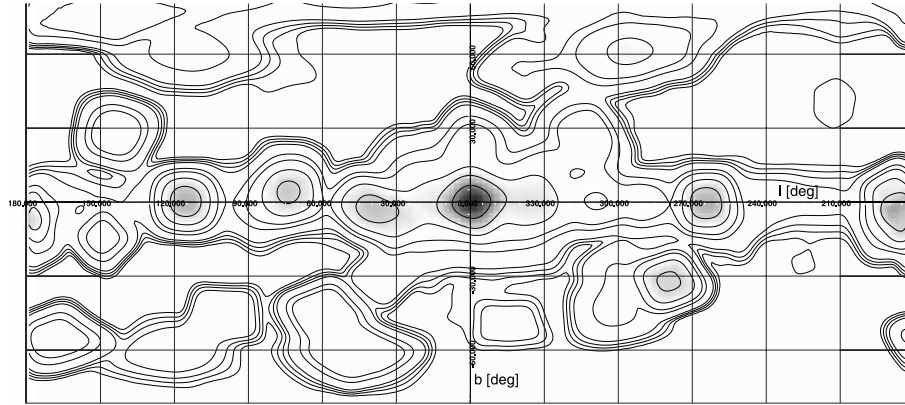


FIG. 2.—Exposure map representing the data used in our analysis in Galactic coordinates. Contours indicate 2, 5, 10, 20, 100, 200, and 500 ks, and 1 and 2 Ms exposure time. *INTEGRAL* spent most of the observing time on and near the Galactic plane, with a strong focus on the Galactic center and on areas including bright hard X-ray sources, such as the Cygnus region, Vela, GRS 1915+105, and the Crab. Fields at high Galactic latitude include Coma, Virgo, and the region around NGC 4151.

distribution, which can be approximated by a Gaussian, with our best-fit parameters of $\alpha = 1.66 \pm 0.11$. A normalization of $K = 0.44 \text{ sr}^{-1} (10^{-10} \text{ ergs cm}^{-2} \text{ s}^{-1})^\alpha$ was then obtained by performing a least-squares fit, with the slope fixed to the ML value. This calculation did not take into account possible inaccuracies associated with scatter in Figure 3, and thus in the true detection limit. The true exposure time is also affected by small variations in dead-time effects known to occur in the ISGRI detector. A conservative upper limit on the exposure time uncertainty is $<2\%$.

This leads to uncertainty in the final $\log N$ – $\log S$ primarily manifest in the normalization, but it should not affect the slope significantly. Furthermore, the uncertainty in the detection limit will mainly affect the low-flux end of the $\log N$ – $\log S$ distribution. The high-flux end is less sensitive to scatter, since it is based on a larger sky area (Fig. 4). To make a more quantitative assessment, we have recomputed the ML $\log N$ – $\log S$ calculation for scenarios in which the exposure time–flux limit curve shifted in

amplitude and pivoted about the 700 ks point, where we have the highest density of measurements. For those scenarios, we found that the inferred $\log N$ – $\log S$ slope varied by less than about 5%, which is contained within the range of our quoted 1σ uncertainty. The amplitude varied by as much as 7% in the extreme case, but by only a few percent for the pivoted cases. Thus, we conclude that the maximum uncertainty resulting from possible systematics in our effective area correction is bounded by about 5% in slope and 7% in amplitude.

4. THE LOCAL LUMINOSITY FUNCTION OF AGNs AT 20–40 keV

The complete sample of *INTEGRAL* AGNs with a detection significance $\geq 5\sigma$ also allows us to derive the density of these objects in the local universe as a function of their luminosity. In order to derive the density of objects above a given luminosity,

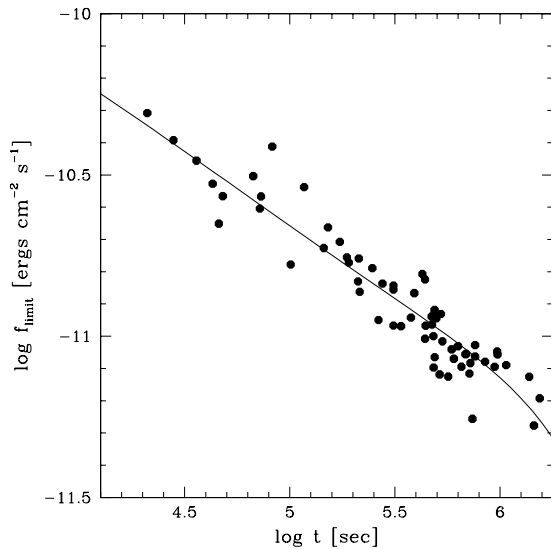


FIG. 3.—Correlation of exposure time and flux limit (5σ ; 20–40 keV) for the AGNs in this study (see § 3.3). The curve shows a smooth polynomial fit for flux limit vs. logarithm of the exposure time.

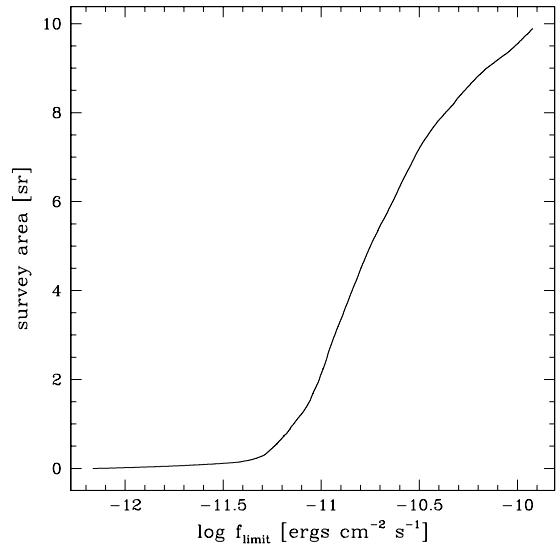


FIG. 4.—Total survey area with respect to the 5σ flux limit in the 20–40 keV. The curve is based on all 47,868 sky elements of the survey with an exposure of at least 2 ks. For a flux limit of $f_X \geq 3 \times 10^{-11} \text{ ergs cm}^{-2} \text{ s}^{-1}$ the survey covers 76% of the sky, and for $f_X \geq 10^{-11} \text{ ergs cm}^{-2} \text{ s}^{-1}$, 17%.

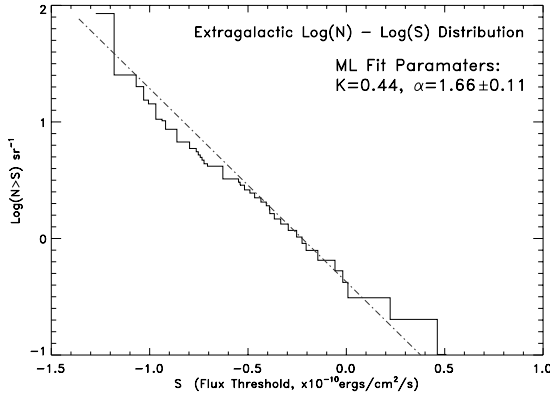


FIG. 5.—Number-flux distribution per steradian of *INTEGRAL* AGNs with a detection significance $>5\sigma$. Blazars have been excluded. The maximum likelihood slope, as described in § 3.3, is 1.66 ± 0.11 .

one has to determine for each source in a complete sample the space volume in which this source could have been found, considering both the flux limit of each survey field and the flux of the object. We have again used the correlation between exposure time and flux limit, as discussed in the previous section, in order to assign a 5σ flux limit to each survey field. Then the maximum redshift z_{\max} at which an object with luminosity L_X would have been detectable in each sky element was used to compute the total accessible volume

$$V_a = \sum_{i=1}^N \frac{\Omega_i}{4\pi} V_i [z_{\max,i}(L_X)], \quad (1)$$

with N being the number of sky elements in which the object would have been detectable, Ω_i the solid angle covered by sky element i , and V_i the enclosed volume based on the maximum redshift at which the object could have been detected in this sky element. Figure 6 shows the cumulative luminosity function for 38 *INTEGRAL*-detected ($\geq 5\sigma$) AGNs in the 20–40 keV energy band. Here the density ϕ describes the number of objects per Mpc^3 above a given luminosity L : $\phi = \sum_{i=1}^K V_{a,i}^{-1}$ with K being the number of objects with luminosities $>L_X$. Blazars have been excluded because their emission is not isotropic. The redshifts in the sample range from $z = 0.001$ to $z = 0.129$, with an average redshift of $\bar{z} = 0.022$. Thus, the luminosity function is truly a local one. Figure 7 shows the luminosity function in differential form. In this presentation the data points are independent of each other. In case one of the luminosity bins should suffer from incompleteness compared to the other bins, this would result in a break or dip in the differential luminosity function. The errors are based on the number of objects contributing to each value. The differential XLF also shows, like the cumulative one, a turnover around $L_X = (5-10) \times 10^{43} \text{ ergs s}^{-1}$.

Because our study is based solely on low-redshift objects, we are not able to constrain models involving evolution with redshift. Nevertheless, we can compare the XLF presented here with model predictions from previous investigations. XLFs are often fit by a smoothly connected double-power-law function of the form (Maccacaro et al. 1991)

$$\frac{d\phi(L_X, z=0)}{d \log L_X} = A \left[\left(\frac{L_X}{L_*} \right)^{\gamma_1} + \left(\frac{L_X}{L_*} \right)^{\gamma_2} \right]^{-1}. \quad (2)$$

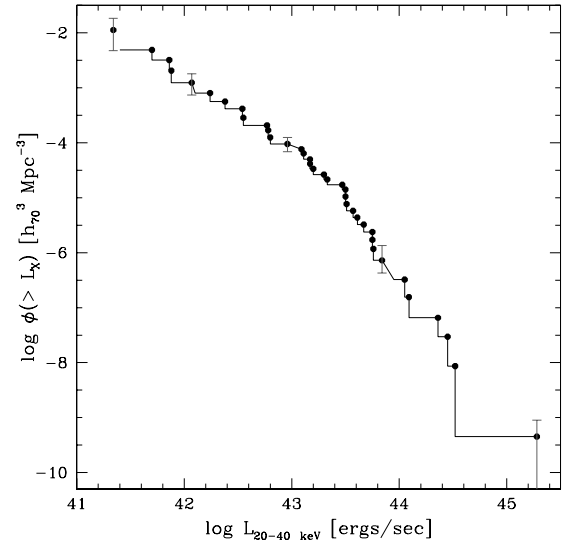


FIG. 6.—Cumulative luminosity function of *INTEGRAL* AGNs with a detection significance $>5\sigma$. Blazars have been excluded. The density ϕ describes the number of objects per Mpc^3 above a given luminosity L_X . As an example, some error bars indicating the Poissonian error are shown. Note that the errors are not independent of each other. [See the electronic edition of the Journal for a color version of this figure.]

We fit this function using a least-squares method applying the Levenberg-Marquardt algorithm (Marquardt 1963). The best-fit values we obtained are $A = 0.7^{+1.5}_{-0.5} \times 10^{-5} h_{70}^3 \text{ Mpc}^{-3}$, $\gamma_1 = 0.80 \pm 0.15$, $\gamma_2 = 2.11 \pm 0.22$, and $\log L_* = 43.38 \pm 0.35$, with L_* in units of $h_{70}^2 \text{ ergs s}^{-1}$. The 1σ errors have been determined by applying a Monte Carlo simulation, which simultaneously takes into account the flux errors on the individual sources, the error induced by deriving an average luminosity per bin, and the

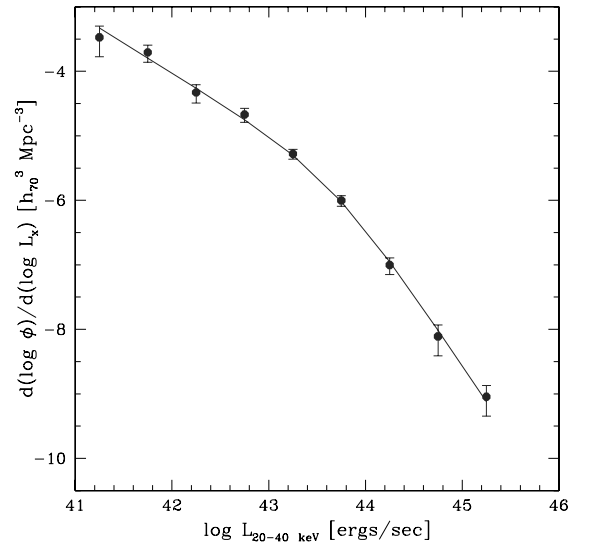


FIG. 7.—Differential luminosity function of AGNs with $\Delta \log L_X = 0.5$ binning. The line shows a fit to a smoothly connected double-power-law function with a turnover luminosity at $L_* = 2.4 \times 10^{43} \text{ ergs s}^{-1}$. [See the electronic edition of the Journal for a color version of this figure.]

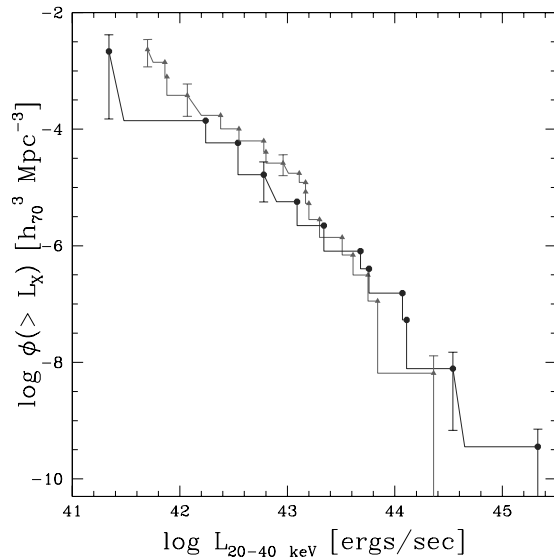


FIG. 8.—Cumulative AGN luminosity function for 19 absorbed ($N_{\text{H}} \geq 10^{22} \text{ cm}^{-2}$; triangles) and 12 unabsorbed sources (octagons). As an example, some error bars indicating the Poissonian error are shown. [See the electronic edition of the Journal for a color version of this figure.]

statistical error of the density based on the number of objects contributing to the density value. Each simulated data set included nine luminosity values with a density value for each of them. These values were then fit by the smoothly connected double-power-law function, as described above. The scatter in the resulting parameters gave the error estimates shown above.

The parameter values describing the differential luminosity function are consistent with values derived from the 2–10 keV XLF of AGNs, as shown by, e.g., Ueda et al. (2003), La Franca et al. (2005), and Shinozaki et al. (2006). For example, the work by Ueda et al. (2003) reveals for a pure density evolution model the same values (within the error bars) for γ_1 and γ_2 , but a higher $\log L_* = 44.11 \pm 0.23$. The higher value can easily be explained by the different energy bands applied. A single power law with a photon index of $\Gamma = 2$ in the range 2–40 keV would lead to $L_{(2-10 \text{ keV})}/L_{(20-40 \text{ keV})} = 2.3$, assuming no intrinsic absorption. This has, of course, no implications for the XLF at higher redshifts. The values are also consistent with the luminosity function for AGNs in the 3–20 keV band, as derived by Sazonov & Revnivtsev (2004) from the *RXTE* all-sky survey.

Information about intrinsic absorption is available for 32 of the 38 objects (89%) from soft X-ray observations. This enables us to derive the luminosity function for absorbed ($N_{\text{H}} \geq 10^{22} \text{ cm}^{-2}$) and unabsorbed sources, as shown in Figure 8. The absorbed sources have a higher density than the unabsorbed sources at low luminosities, while this trend is inverted at high luminosities. The luminosity where both AGN types have similar densities is about $L_{(20-40 \text{ keV})} = 3 \times 10^{43} \text{ ergs s}^{-1}$. This tendency is also evident when comparing the fraction of absorbed AGNs with the luminosity in the three luminosity bins depicted in Figure 9. The luminosity bins have been chosen so that an equal number of objects are contained in each bin. The position of the data point along the luminosity axis indicates the average luminosity in this bin, while the error bars in luminosity indicate the range of luminosities covered. A comparable trend has also been

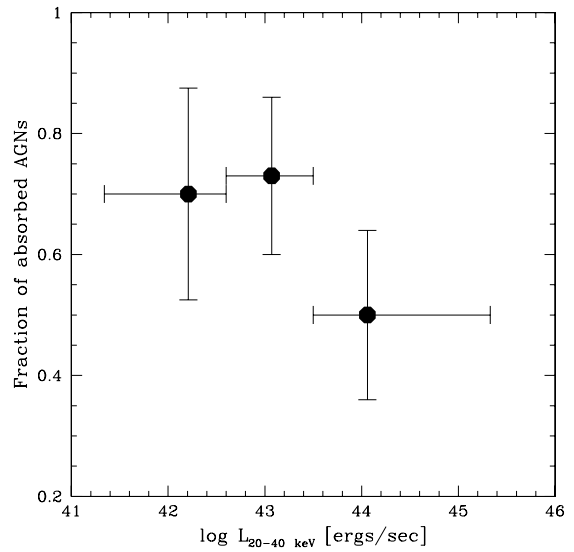


FIG. 9.—Fraction of absorbed AGNs ($N_{\text{H}} \geq 10^{22} \text{ cm}^{-2}$) vs. luminosity. The position of the data point along the luminosity axis indicates the average luminosity in this bin, while the error bars in luminosity indicate the range of luminosities covered.

seen below 10 keV. In a recent study of *HEAO-1* data of 49 AGNs, Shinozaki et al. (2006) showed that the XLF for absorbed AGNs drops more rapidly ($\gamma_2 = 3.34^{+0.90}_{-0.65}$) at higher luminosities than that of unabsorbed AGNs ($\gamma_2 = 2.34^{+0.24}_{-0.22}$).

Based on the luminosity function, the contribution of the AGNs to the total X-ray emissivity W can be estimated (Sazonov & Revnivtsev 2004). This can be done by simply multiplying the XLF by the luminosity in each bin and integrating over the range of luminosities ($10^{41} \text{ ergs s}^{-1} < L_{20-40 \text{ keV}} < 10^{45.5} \text{ ergs s}^{-1}$). This results in $W_{20-40 \text{ keV}}(>10^{41} \text{ ergs s}^{-1}) = (2.8 \pm 0.8) \times 10^{38} \text{ ergs s}^{-1} h_70^3 \text{ Mpc}^{-3}$. Please note that absorption does not affect the luminosities in this energy range and that therefore the values given here are intrinsic emissivities.

5. DISCUSSION

A simple power-law model fitted to the number-flux distribution (Fig. 5) has a slope of $\alpha = 1.66 \pm 0.11$. Even though the difference from the Euclidian value is not statistically significant at the 1.5 σ level, a deviation from this value could have two reasons. The difference might indicate that the area density at the low-flux end of the distribution has been slightly overcorrected. One has to keep in mind that only a few sources derived from a small area of the sky are constraining the low-flux end. Another reason for the difference could be that the distribution of AGNs in the very local universe is not isotropic, caused, e.g., by the local group and other clustering of galaxies. Krivonos et al. (2005) studied the extragalactic source counts as observed by *INTEGRAL* in the 20–50 keV energy band in the Coma region. Based on 12 source detections, they determine a surface density of $(1.4 \pm 0.5) \times 10^{-2} \text{ deg}^{-2}$ above a threshold of $10^{-11} \text{ ergs cm}^{-2} \text{ s}^{-1}$ in the 20–50 keV energy band, while we get a consistent value of $(1.2 \pm 0.2) \times 10^{-2} \text{ deg}^{-2}$. Comparing the total flux of all the objects in the AGN sample ($f_{20-40 \text{ keV}} = 2.6 \times 10^{-10} \text{ ergs cm}^{-2} \text{ s}^{-1} \text{ sr}^{-1}$) with the flux of the X-ray background, as presented by Gruber et al. (1999), shows that the *INTEGRAL* AGNs account

only for about 1% of the expected value. This is expected when taking into account the high flux limit of our sample; La Franca et al. (2005) have shown that objects with $f_{2-10 \text{ keV}} > 10^{-11} \text{ ergs cm}^{-2} \text{ s}^{-1}$ contribute less than 1% to the CXB in the 2–10 keV energy range. This flux limit extrapolates to the faintest flux in our sample of $f_{20-40 \text{ keV}} = 5.6 \times 10^{-12} \text{ ergs cm}^{-2} \text{ s}^{-1}$ for a $\Gamma = 1.9$ power-law spectrum.

We compared the unabsorbed emissivity per unit volume of our objects $W_{20-40 \text{ keV}} (> 10^{41} \text{ ergs s}^{-1}) = 2.8 \times 10^{38} \text{ ergs s}^{-1} h_{70}^3 \text{ Mpc}^{-3}$ with that observed by *RXTE* in the 3–20 keV band. Assuming an average power law of $\Gamma = 2$, the extrapolated value is $W_{3-20 \text{ keV}} (> 10^{41} \text{ ergs s}^{-1}) = (7.7 \pm 2.2) \times 10^{38} \text{ ergs s}^{-1} h_{70}^3 \text{ Mpc}^{-3}$, which is a factor of 2 larger than the value measured by *RXTE* (Sazonov & Revnivtsev 2004), but consistent within the 1σ error. If we apply the conversion to the 2–10 keV energy band, we derive the intrinsic emissivity $W_{2-10 \text{ keV}} = (6.4 \pm 1.8) \times 10^{38} \text{ ergs s}^{-1} \text{ Mpc}^{-3}$, consistent with the value derived from the *HEAO-1* measurements [$W = (5.9 \pm 1.2) \times 10^{38} \text{ ergs s}^{-1} \text{ Mpc}^{-3}$; Shinozaki et al. 2006]. This showed that the local X-ray volume emissivity in the 2–10 keV band is consistent with the emissivity from AGNs alone. It has to be pointed out that the value derived from our sample and the one based on *HEAO-1* data are higher than the one based on the *RXTE* All-Sky Survey [$W = (2.7 \pm 0.7) \times 10^{38} \text{ ergs s}^{-1} \text{ Mpc}^{-3}$; Sazonov & Revnivtsev 2004].

The luminosity function derived from the *INTEGRAL* 20–40 keV AGN sample appears to be consistent with the XLF in the 2–20 keV range. A turnover in the XLF at $\simeq 2.4 \times 10^{43} \text{ ergs s}^{-1}$ is observed (Fig. 7). In addition, below this luminosity the fraction of absorbed AGNs starts to exceed that of unabsorbed ones, although the effect is significant only on a 1σ level (Fig. 8). Both effects have also been seen in the 2–10 keV (Ueda et al. 2003; La Franca et al. 2005; Shinozaki et al. 2006) and in the 3–20 keV band (Sazonov & Revnivtsev 2004). This implies that we do detect a similar source population as at lower energies.

If a larger fraction of absorbed AGNs is necessary to explain the cosmic X-ray background at $\sim 30 \text{ keV}$, as indicated by *HEAO-1* A-4 measurements (Gruber et al. 1999), the fraction of absorbed sources could be correlated with redshift. It has, for example, been proposed that there is an evolution of the population leading to a higher fraction of absorbed sources at higher redshifts. It should be noted, however, that this effect is not clearly detectable in the 2–10 keV range. The fraction of absorbed sources seems to depend on luminosity (Ueda et al. 2003; Treister & Urry 2005), as is also seen in the 20–40 keV band (Fig. 9). However, some studies come to the conclusion that there is no evolution of intrinsic N_{H} (Ueda et al. 2003; Treister & Urry 2005), while others find the fraction of absorbed sources increasing with redshift (La Franca et al. 2005). La Franca et al. also find that a combination of effects (the fraction of absorbed AGNs decreases with the intrinsic X-ray luminosity and increases with the redshift) can be explained by a luminosity-dependent density evolution model. They further show that the luminosity function of AGNs with low luminosities, such as those presented here, peaks at $z \sim 0.7$, while high-luminosity AGNs peak at $z \sim 2$. Unified models also predict, depending on the applied model, a fraction of absorbed AGNs of 0.6–0.7 compared to the total population for high-flux low-redshift objects (Treister & Urry 2005). Worsley et al. (2005) examined *Chandra* and *XMM-Newton* deep fields and came to the conclusion that the missing CXB component is formed by highly obscured AGNs at redshifts ~ 0.5 – 1.5 , with column densities of the order of $f_{\text{X}} = 10^{23}$ – 10^{24} cm^{-2} . Evidence for this scenario is also found in a

study of *Chandra* and *Spitzer* data (Polletta et al. 2006). Combining multiwavelength data, this work estimates a surface density of 25 AGNs deg^{-2} in the infrared in the 0.6 deg^2 *Chandra* SWIRE field, and only 33% of them are detected in the X-rays down to $f_{0.3-8 \text{ keV}} = 10^{-15} \text{ ergs cm}^{-2} \text{ s}^{-1}$. The work also indicates a higher abundance of luminous and Compton-thick AGNs at higher redshifts ($z \gg 0.5$). This source population would be missed by the study presented here, because of the low redshifts ($\bar{z} = 0.022$) of the *INTEGRAL* AGNs.

Several studies (Ueda et al. 2003; Treister & Urry 2005) propose that the absorbed AGNs needed to explain the CXB should be Compton thick, and therefore would have been missed at 2–10 keV. This argument does not hold for the *INTEGRAL* observations, where the impact of absorption is much less severe than at lower energies. The effect on the measured flux of a source with photon index $\Gamma = 2$ for Compton-thick absorption ($N_{\text{H}} = 10^{24} \text{ cm}^{-2}$) is only a 5% decrease in flux (40% for $N_{\text{H}} = 10^{25} \text{ cm}^{-2}$). It is, therefore, unlikely that many Compton-thick objects have been missed by the *INTEGRAL* studies performed to date. One possibility would be that they are among the newly discovered sources found by *INTEGRAL*. The fraction of unidentified objects among the *INTEGRAL* discovered sources is approximately 50%. Eight such sources without cross identification have a significance above 5σ in the data set discussed here. Thus, if they are ultimately identified as AGNs, they would have to be considered in this study. It should be pointed out, though, that most of the sources discovered by *INTEGRAL* are located close to the Galactic plane and are more likely to belong to the Galaxy: the Second IBIS-ISGRI Soft Gamma-Ray Survey Catalog (Bird et al. 2006) lists 55 new sources detected by *INTEGRAL*, of which 93% are located within $-10^\circ < b < +10^\circ$. Among these 55 sources, 3 are listed as extragalactic sources, 18 are of Galactic origin, and 29 have not been identified yet.

In addition, those objects that have been classified as AGNs based on soft X-ray and/or optical follow-up studies are no more likely to be Compton-thick objects than the overall AGN population studied here. Only four AGNs (NGC 1068, NGC 4945, Mrk 3, Circinus galaxy) detected by *INTEGRAL* have been proven to be Compton-thick objects so far, and none of them showed absorption of $N_{\text{H}} > 5 \times 10^{24} \text{ cm}^{-2}$. In order to clarify this point, observations at soft X-rays of those objects without information about intrinsic absorption are required for all *INTEGRAL*-detected AGNs (Table 1). At present, 23% of the *INTEGRAL* AGNs are missing absorption information. A first indication of what the absorption in these sources might be can be derived from comparison of the *INTEGRAL* fluxes with *ROSAT* All-Sky Survey (RASS) Faint Source Catalogue data (Voges et al. 2000). In order to do so, we assumed a simple power law with photon index $\Gamma = 2.0$ between the *ROSAT* 0.1–2.4 keV band and the *INTEGRAL* 20–40 keV range and fit the absorption. In the six cases where no detection was achieved in the RASS, an upper limit of $f_{(0.1-2.4 \text{ keV})} \leq 10^{-13} \text{ ergs cm}^{-2} \text{ s}^{-1}$ has been assumed, resulting in a lower limit for the absorption $N_{\text{H}} > (5-11) \times 10^{22} \text{ cm}^{-2}$. In Figure 10 we show the distribution of intrinsic absorption. It has to be pointed out that the estimated values can only give an idea about the distribution of intrinsic absorption and should not be taken literally, as the spectral slope between the measurements is unknown and the observations are not simultaneous. Nevertheless, apparently none of the RASS detections and nondetections requires an intrinsic absorption of $N_{\text{H}} > 2 \times 10^{23} \text{ cm}^{-2}$. Therefore, it appears unlikely that a significant fraction of *INTEGRAL* AGNs will show an intrinsic absorption $N_{\text{H}} > 10^{24} \text{ cm}^{-2}$. However, if we assume that the RASS nondetections

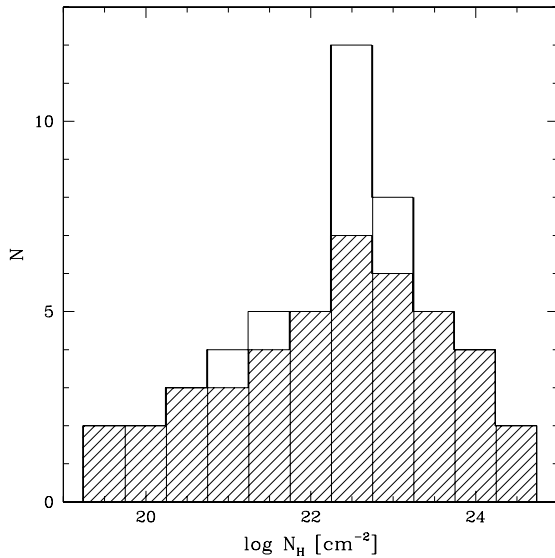


FIG. 10.—Distribution of intrinsic absorption for all *INTEGRAL* AGNs (blazars excluded), as measured in the soft X-rays. The shaded area shows the reliable measurements; the other values are based on comparison of RASS and *INTEGRAL* data. Lower limits on absorption have been excluded.

are all Compton-thick AGNs, the fraction of this class of sources rises from 6% to 16% when considering all 63 nonblazar AGNs seen by *INTEGRAL*, and from 8% to 13% for the complete sample with 38 objects. This is in good agreement with the fraction of 11% of Compton-thick AGNs, as seen in the *Swift* BAT survey (Markwardt et al. 2005). The picture is less clear when referring to the optical classification. Here the *INTEGRAL* survey finds 12 Seyfert 1 (33%), 14 Seyfert 2, and 10 intermediate Seyfert 1.5 galaxies in the complete sample, while the *Swift* BAT survey contains only 20% type 1 Seyfert galaxies. It should be pointed out, though, that the classification based on intrinsic absorption gives a more objective criterion in order to define AGN subclasses than the optical classification with its many subtypes. The finding of the BAT survey, that virtually all sources with $\log L_X < 43.5$ are absorbed, cannot be confirmed by our study, in which we detect a fraction of 33% of sources with $N_H < 10^{22} \text{ cm}^{-2}$ among the sources below this luminosity. This is also reflected in the observation that although the absorbed sources become more dominant below this luminosity, the trend is not overwhelmingly strong (Fig. 8).

Most investigations to date have been focused on the X-rays below 20 keV, and *INTEGRAL* can add substantial information to the nature of bright AGNs in the local universe. Considering the expected composition of the hard X-ray background, it does not currently appear that the population detected by *INTEGRAL* can explain the peak at 30 keV, as Compton-thick AGNs are apparently less abundant than expected (Treister & Urry 2005). However, this picture might change if we assume that all *INTEGRAL* AGNs lacking soft X-ray data and without counterparts in the RASS are Compton thick. In addition, the sample presented here might be still too small to constrain the fraction of obscured sources, and the missing Compton-thick AGNs could be detectable when studying sources with $f_{(20-40 \text{ keV})} < 10^{-11} \text{ ergs cm}^{-2} \text{ s}^{-1}$.

6. CONCLUSIONS

The extragalactic sample derived from the *INTEGRAL* public data archive comprises 63 low-redshift Seyfert galaxies ($\langle z \rangle = 0.022 \pm 0.003$) and 8 blazars in the hard X-ray domain. Two galaxy clusters are also detected, but no starburst galaxy has been as yet. This *INTEGRAL* AGN sample is thus the largest one presented so far. Thirty-eight of the Seyfert galaxies form a complete sample with significance limit of 5σ .

The number-flux distribution is approximated by a power law with a slope of $\alpha = 1.66 \pm 0.11$. Because of the high flux limit of our sample, the objects account in total for less than 1% of the 20–40 keV cosmic X-ray background. The emissivity of all AGNs per unit volume $W_{20-40 \text{ keV}} (> 10^{41} \text{ ergs s}^{-1}) = 2.8 \times 10^{38} \text{ ergs s}^{-1} h_0^3 \text{ Mpc}^{-3}$ appears to be consistent with the background estimates in the 2–10 keV energy band, based on the cross-correlation of the *HEAO-1* A-2 map with *IRAS* galaxies (Miyaji et al. 1994).

The luminosity function in the 20–40 keV energy range is consistent with that measured in the 2–20 keV band. Below the turnover luminosity of $L_* = 2.4 \times 10^{43} \text{ ergs s}^{-1}$ the absorbed AGNs become dominant over the unabsorbed ones. The fraction of Compton-thick AGNs with known intrinsic absorption is found to be small (8%) in our AGN sample. For the sources without reliable absorption information we derived an estimate from the comparison with *ROSAT* All-Sky Survey data and find that the data do not require additional Compton-thick objects within the sample presented here. It has to be pointed out, though, that the sources without RASS counterparts could be Compton thick, which would increase the ratio of this source type to 13% in the complete sample. Evolution of the source population can play a major role in the sense that the fraction of absorbed sources among AGNs might be correlated with redshift, as proposed, for example, by Worsley et al. (2005).

Over the lifetime of the *INTEGRAL* mission, we expect to detect on the order of 200 AGNs. Combining these data with the studies based on *Swift* BAT, operating in a similar energy band to IBIS-ISGR1, will further constrain the hard X-ray luminosity function of AGNs, but we will still be limited to the relatively high-flux end of the distribution. Because of this, *INTEGRAL* and *Swift* BAT will most likely not be able to test evolutionary scenarios of AGNs, and thus will be inadequate to explain the cosmic X-ray background at $E > 20 \text{ keV}$. Future missions with larger collecting areas and/or focusing optics will be required to answer the question of what dominates the universe in the hard X-rays.

V. B. would like to thank Olaf Wucknitz for providing software to handle the $\Lambda_0 > 0$ cosmology. This research has made use of the NASA/IPAC Extragalactic Database (NED), which is operated by the Jet Propulsion Laboratory; and of data obtained from the High Energy Astrophysics Science Archive Research Center (HEASARC), provided by NASA's Goddard Space Flight Center; and of the SIMBAD Astronomical Database, which is operated by the Centre de Données astronomiques de Strasbourg. This research has also made use of the Tartarus (Version 3.1) database, created by Paul O'Neill and Kirpal Nandra at Imperial College London, and Jane Turner at NASA/GSFC. Tartarus is supported by funding from PPARC, and NASA grants NAG5-7385 and NAG5-7067.

REFERENCES

- Akylas, A., Georgantopoulos, I., & Comastri, A. 2001, *MNRAS*, 324, 521
 Avni, Y., & Bahcall, J. N. 1980, *ApJ*, 235, 694
 Bassani, L., et al. 2006, *ApJ*, 636, L65
 Beckmann, V., Gehrels, N., Favre, P., Walter, R., Courvoisier, T. J.-L., Petrucci, P.-O., & Malzac, J. 2004, *ApJ*, 614, 641
 Beckmann, V., Gehrels, N., Shrader, C. R., & Soldi, S. 2006a, *ApJ*, 638, 642
 Beckmann, V., Soldi, S., Shrader, C. R., & Gehrels, N. 2006b, in *Proc. the X-ray Universe (ESA SP-604; Noordwijk: ESA)*, in press (astro-ph/0510833)
 Beckmann, V., et al. 2005, *ApJ*, 634, 939
 Bird, A., et al. 2006, *ApJ*, 636, 765
 Brandt, W. N., & Hasinger, G. 2005, *ARA&A*, 43, 827
 Brandt, W. N., et al. 2001, *AJ*, 122, 2810
 Courvoisier, T. J.-L., et al. 2003a, *A&A*, 411, L53
 ———. 2003b, *A&A*, 411, L343
 De Rosa, A., et al. 2005, *A&A*, 438, 121
 Donato, D., Sambruna, R. M., & Gliozzi, M. 2005, *A&A*, 433, 1163
 Gehrels, N., et al. 2004, *ApJ*, 611, 1005
 Giacconi, R., Gursky, H., Paolini, R., & Rossi, B. 1962, *Phys. Rev. Lett.*, 9, 439
 Gliozzi, M., Sambruna, R., & Eracleous, M. 2003, *ApJ*, 584, 176
 Gruber, D. E., Matteson, J. L., Peterson, L. E., & Jung, G. V. 1999, *ApJ*, 520, 124
 Hasinger, G. 2004, *Nucl. Phys. B*, 132, 86
 Hasinger, G., Burg, R., Giacconi, R., Schmidt, M., Trümper, J., & Zamorani, G. 1998, *A&A*, 329, 482
 Krivonos, R., Vikhlinin, A., Churazov, E., Lutovinov, A., Molkov, S., & Sunyaev, R. 2005, *ApJ*, 625, 89
 Kuiper, L., Hermsen, W., in 't Zand, J., & den Hartog, P. R. 2005, *Astron. Tel.* 662, 1
 La Franca, F., et al. 2005, *ApJ*, 635, 864
 Lebrun, F., et al. 2003, *A&A*, 411, L141
 Levenson, N. A., Weaver, K. A., & Heckman, T. M. 2001, *ApJS*, 133, 269
 Lutz, D., Maiolino, R., Spoon, H. W. W., & Moorwood, A. F. M. 2004, *A&A*, 418, 465
 Maccacaro, T., della Ceca, R., Gioia, I. M., Morris, S. L., Stocke, J. T., & Wolter, A. 1991, *ApJ*, 374, 117
 Markwardt, C. B., Tueller, J., Skinner, G. K., Gehrels, N., Barthelmy, S. D., & Mushotzky, R. F. 2005, *ApJ*, 633, L77
 Marquardt, D. 1963, *SIAM J. Appl. Math.*, 11, 431
 Marshall, F. E., et al. 1980, *ApJ*, 235, 4
 Masetti, N., Palazzi, E., Bassani, L., Malizia, A., & Stephen, J. B. 2004, *A&A*, 426, L41
 Masetti, N., et al. 2006, *A&A*, 449, 1139
 Matsumoto, C., Nava, A., Maddox, L. A., Leighly, K. M., Grupe, D., Awaki, H., & Ueno, S. 2004, *ApJ*, 617, 930
 Matt, G., et al. 1997, *A&A*, 325, L13
 Miyaji, T., Lahav, O., Jahoda, K., & Boldt, E. 1994, *ApJ*, 434, 424
 Murdoch, H. S., Crawford, D. F., & Jauncey, D. L. 1973, *ApJ*, 183, 1
 Pian, E., et al. 2005, *A&A*, 429, 427
 ———. 2006, *A&A*, 449, L21
 Piccinotti, G., Mushotzky, R. F., Boldt, E. A., Holt, S. S., Marshall, F. E., Serlemitsos, P. J., & Shafer, R. A. 1982, *ApJ*, 253, 485
 Picconcelli, E., et al. 2006, *A&A*, 453, 839
 Polletta, M., et al. 2006, *ApJ*, 642, 673
 Revnivtsev, M. G., Lutovinov, A. A., Suleimanov, B. F., Molkov, S. V., & Sunyaev, R. A. 2004, *Astron. Lett.*, 30, 772
 Revnivtsev, M. G., Sazonov, S. Yu., Molkov, S. V., Lutovinov, A. A., Churazov, E. M., & Sunyaev, R. A. 2006, *Astron. Lett.*, 32, 145
 Sazonov, S. Y., Churazov, E., Revnivtsev, M. G., Vikhlinin, A., & Sunyaev, R. 2005, *A&A*, 444, L37
 Sazonov, S. Y., & Revnivtsev, M. G. 2004, *A&A*, 423, 469
 Sazonov, S. Y., Revnivtsev, M. G., Lutovinov, A. A., Sunyaev, R. A., & Grebenev, S. A. 2004, *A&A*, 421, L21
 Schmidt, M., et al. 1998, *A&A*, 329, 495
 Setti, G., & Woltjer, L. 1989, *A&A*, 224, L21
 Shinozaki, K., Miyaji, T., Ishisaki, Y., Ueda, Y., & Ogasaka, Y. 2006, *AJ*, 131, 2843
 Soldi, S., et al. 2005, *A&A*, 444, 431
 Treister, E., & Urry, C. M. 2005, *ApJ*, 630, 115
 Ueda, Y., Akiyama, M., Ohta, K., & Miyaji, T. 2003, *ApJ*, 598, 886
 Ueda, Y., Ishisaki, Y., Takahashi, T., Makishima, K., & Ohashi, T. 2001, *ApJS*, 133, 1
 Virani, S. N., et al. 2005, *BAAS*, 207, 2007
 Voges, W., et al. 2000, *IAU Circ.*, 7432, 3
 Winkler, C., et al. 2003, *A&A*, 411, L1
 Worsley, M. A., et al. 2005, *MNRAS*, 357, 1281
 Young, A. J., Wilson, A. S., Terashima, Y., Arnaud, K. A., & Smith, D. A. 2002, *ApJ*, 564, 176

6.9.4 Hard X-ray variability of active galactic nuclei

A discussion of this work in the context of the unified model of AGN can be found in Section 4.7.2 on page 66. The manuscript, which is shown on the following pages, has been published as

Beckmann V., Barthelmy S. D., Courvoisier T.J.-L., Gehrels N., Soldi S., Tueller J., & Wendt G., *Astronomy and Astrophysics*, Volume 475, Issue 3, pp. 827-83 (2007)

Hard X-ray variability of active galactic nuclei

V. Beckmann^{1,2,3}, S. D. Barthelmy⁴, T. J.-L. Courvoisier^{1,2}, N. Gehrels⁴, S. Soldi^{1,2}, J. Tueller⁴, and G. Wendt¹

¹ INTEGRAL Science Data Centre, Chemin d'Écogia 16, 1290 Versoix, Switzerland
 e-mail: Volker.Beckmann@obs.unige.ch

² Observatoire Astronomique de l'Université de Genève, Chemin des Maillettes 51, 1290 Sauverny, Switzerland

³ CSST, University of Maryland Baltimore County, 1000 Hilltop Circle, Baltimore, MD 21250, USA

⁴ Astrophysics Science Division, NASA Goddard Space Flight Center, Code 661, MD 20771, USA

Received 26 July 2007 / Accepted 12 September 2007

ABSTRACT

Aims. Active Galactic Nuclei are known to be variable throughout the electromagnetic spectrum. An energy domain poorly studied in this respect is the hard X-ray range above 20 keV.

Methods. The first 9 months of the Swift/BAT all-sky survey are used to study the 14–195 keV variability of the 44 brightest AGN. The sources have been selected due to their detection significance of $>10\sigma$. We tested the variability using a maximum likelihood estimator and by analysing the structure function.

Results. Probing different time scales, it appears that the absorbed AGN are more variable than the unabsorbed ones. The same applies for the comparison of Seyfert 2 and Seyfert 1 objects. As expected the blazars show stronger variability. 15% of the non-blazar AGN show variability of $>20\%$ compared to the average flux on time scales of 20 days, and 30% show at least 10% flux variation. All the non-blazar AGN which show strong variability are low-luminosity objects with $L_{(14-195 \text{ keV})} < 10^{44} \text{ erg s}^{-1}$.

Conclusions. Concerning the variability pattern, there is a tendency of unabsorbed or type 1 galaxies being less variable than the absorbed or type 2 objects at hardest X-rays. A more solid anti-correlation is found between variability and luminosity, which has been previously observed in soft X-rays, in the UV, and in the optical domain.

Key words. galaxies: active – galaxies: Seyfert – X-rays: galaxies – surveys

1. Introduction

Active Galactic Nuclei (AGN) are the most prominent persistent X-ray sources in the extragalactic sky. X-ray observations provide a powerful tool in order to investigate the physical conditions in the central engine of AGN. The emission in this energy band is thought to originate close to the supermassive black hole, providing insights into the geometry and the state of the matter. The flux and spectral variability of the sources in the hard X-rays reflect the size and physical state of the regions involved in the emission processes (see Uttley & McHardy 2004, for a brief review).

Data of *EXOSAT* showed early on that the variability of AGN in the 0.1–10 keV range on short time scales appears to be red-noise in nature (McHardy & Czerny 1987). The corresponding power spectral density functions (PSDs) can be described by a power law with index -1 to -2 . The data also showed an inverse correlation between the amplitude of variability in day-long AGN X-ray light curves and the X-ray luminosity of AGN (Barr & Mushotzky 1986), although Narrow Line Seyfert 1s apparently do not follow this correlation (Turner et al. 1999). *RXTE/PCA* allows us to study AGN variability in the 2–20 keV range on long time scales. This revealed that although the variability amplitudes of AGN with different luminosities are very different on short time-scales, they are similar on long time-scales (Markowitz & Edelson 2001) of about a month. *RXTE* data also showed that the PSDs of AGN show a break at long time-scales according to their black hole mass (e.g. Edelson & Nandra 1999).

Grupe et al. (2001) analysed *ROSAT* (0.1–2.4 keV) data of AGN and showed that the sources with steeper spectra exhibit stronger variability than those with a hard spectrum. Bauer et al. (2004) showed for 136 AGN observed by *Chandra* within 2 Ms in the *Chandra* Deep Field South that $\sim 60\%$ show signs of variability. For the brighter sources with better photon statistics even 80–90% showed variability in the 0.5–8 keV energy range.

The similarity of the variability in different types of AGN suggests that the underlying physical mechanism is the same. This does not apply for the blazars, for which the common model is that we look into a highly relativistic jet. Explanations for the variability in Seyfert galaxies include a flare/spot model in which the X-ray emission is generated both in hot magnetic loops above an accretion disk and in bright spots created under the loops by strong irradiation (Czerny et al. 2004), unstable accretion disks (King 2004), and variable obscuration (e.g. Risaliti et al. 2002). A still open question is the role of long term variability at energies above 20 keV. Observations of AGN have been performed by several missions like *CGRO/OSSE* and *BeppoSAX/PDS*. But long-term coverage with base lines longer than weeks is up to now only available from the data of *CGRO/BATSE*, which had no imaging capabilities.

As the Burst Alert Telescope (BAT, Barthelmy et al. 2005) on-board *Swift* (Gehrels et al. 2004) is sensitive in the 14–195 keV energy range, it preferentially detects those *ROSAT* AGN with hard spectra, and one expects to see a lower variability in *Swift*/BAT detected AGN than measurable in average e.g. by Grupe et al. (2001) for the *ROSAT* data.

In this paper we use the data of the first 9 months of the *Swift*/BAT all-sky survey to study variability of the 40 brightest AGN. Data analysis is described in Sect. 2. Two methods are applied to determine the intrinsic variability. Firstly, a maximum likelihood estimator (Almaini et al. 2000) to determine the strength of variability is used. This approach is similar to determining the “excess variance” (Nandra et al. 1997) but allows for individual measurement errors. Secondly, we apply the structure function (Simonetti et al. 1985) in order to find significant variability. The results are discussed in Sect. 3 and conclusions are presented in Sect. 4.

2. Data analysis

2.1. *Swift*/BAT detected AGN

The Burst Alert Telescope (BAT, Barthelmy et al. 2005) is a large field of view (~ 1.5 sr) coded mask aperture hard X-ray telescope. The BAT camera is a CdZnTe array of 0.5 m^2 with 32 768 detectors, which are sensitive in the 14–195 keV energy range. Although BAT is designed to find Gamma-ray bursts which are then followed-up by the narrow field instruments of *Swift*, the almost random distribution of detected GRBs in the sky leads to an effective all-sky survey in the hard X-rays. The effective exposure during the first 9 months varies over the sky from 600 to 2500 ks. As shown by Markwardt et al. (2005), who also explain the survey analysis, one expects no false detection of sources above a significance threshold of 5.5σ .

Within the first 9 months, 243 sources were detected with a significance higher than 5.5σ . Among those sources, 103 are either known AGN or have been shown to be AGN through follow-up observations of new detections. A detailed analysis of the AGN population seen by *Swift*/BAT will be given by Tueller et al. (2007). In order to study variability, we restricted our analysis to objects which show an overall significance of $>10\sigma$, resulting in 44 sources. The list of objects, sorted by their name, is given in Table 1, together with the average 14–195 keV count rate and the variability estimator as described in the next section. Among the objects are 11 Seyfert 1, 22 Seyfert 2, 5 Seyfert 1.5, one Seyfert 1.8, one Seyfert 1.9, and 4 blazars. The five blazars are 3C 454.3, 4C +71.07, 3C 273, and Markarian 421. In addition IGR J21247+5058 is detected, which has been identified as a radio galaxy (Masetti et al. 2004), but which might also host a blazar core (Ricci et al. 2007). The ten brightest sources are (according to their significance in descending order): Cen A, NGC 4151, NGC 4388, 3C 273, IC 4329A, NGC 2110, NGC 5506, MCG –05–23–016, NGC 4945, and NGC 4507. For all 44 objects information about intrinsic absorption is available from soft X-ray observations. Among the Seyfert galaxies we see 15 objects with $N_{\text{H}} > 10^{23} \text{ cm}^{-2}$, and 4 with $N_{\text{H}} < 10^{21} \text{ cm}^{-2}$. Examples for *Swift*/BAT lightcurves can be found in Beckmann et al. (2007) for the case of NGC 2992 and NGC 3081.

2.2. Maximum likelihood estimator of variability

Any lightcurve consisting of N flux measurements x_i varies due to measurement errors σ_i . In case the object is also intrinsically variable, an additional source variance σ_Q has to be considered. The challenge of any analysis of light curves of variable sources is to disentangle them in order to estimate the intrinsic variability. A common approach is to use the “excess variance”

(Nandra et al. 1997; Vaughan et al. 2003) as such an estimator. The sample variance is given by

$$S^2 = \frac{1}{N-1} \sum_{i=1}^N (x_i - \bar{x})^2 \quad (1)$$

and the excess variance is given by

$$\sigma_{\text{XS}}^2 = S^2 - \overline{\sigma_i^2} \quad (2)$$

with $\overline{\sigma_i^2}$ being the average variance of the measurements. Almaini et al. (2000) point out that the excess variance represents the best variability estimator only for identical measurement errors ($\sigma_i = \text{constant}$) and otherwise a numerical approach should be used. Such an approach to estimate the strength of variability has been described by Almaini et al. and has lately been used e.g. for analysing *XMM-Newton* data of AGN in the Lockman Hole (Mateos et al. 2007). Assuming Gaussian statistics, for a light curve with a mean \bar{x} , measured errors σ_i and an intrinsic σ_Q , the probability density for obtaining N data values x_i is given by

$$p(x_i|\sigma_i, \sigma_Q) = \prod_i \frac{\exp(-0.5(x_i - \bar{x})^2/(\sigma_i^2 + \sigma_Q^2))}{(2\pi)^{1/2}(\sigma_i^2 + \sigma_Q^2)^{1/2}}. \quad (3)$$

This is simply a product of N Gaussian functions representing the probability distribution for each bin.

We may turn this around using Bayes’ theorem to obtain the probability distribution for σ_Q given our measurements:

$$p(\sigma_Q|x_i, \sigma_i) = p(x_i|\sigma_i, \sigma_Q) \frac{p(\sigma_Q)}{p(x_i)} \propto L(\sigma_Q|x_i, \sigma_i) \quad (4)$$

where $L(\sigma_Q|x_i, \sigma_i)$ is the likelihood function for the parameter σ_Q given the data. This general form for the likelihood function can be calculated if one assumes a Bayesian prior distribution for σ_Q and x_i . In the simplest case of a uniform prior one obtains

$$L(\sigma_Q|x_i, \sigma_i) \propto p(x_i|\sigma_i, \sigma_Q) = \prod_i \frac{\exp(-0.5(x_i - \bar{x})^2/(\sigma_i^2 + \sigma_Q^2))}{(2\pi)^{1/2}(\sigma_i^2 + \sigma_Q^2)^{1/2}}. \quad (5)$$

The parameter of interest is the value of σ_Q , which gives an estimate for the intrinsic variation we have to add in order to obtain the given distribution of measurements.

By differentiating, the maximum-likelihood estimate for σ_Q can be shown to satisfy the following, which (for a uniform prior) is mathematically identical to a least- χ^2 solution:

$$\sum_{i=1}^N \frac{(x_i - \bar{x})^2 - (\sigma_i^2 + \sigma_Q^2)}{(\sigma_i^2 + \sigma_Q^2)^2} = 0. \quad (6)$$

In the case of identical measurement errors ($\sigma_i = \text{constant}$) this reduces to the excess variance described in Eq. (2) and in this case $\sigma_Q = \sigma_{\text{XS}}$. We applied this method to the lightcurves with different time binning (1 day, 7 days, 20 days, 40 days). σ_Q is the intrinsic variability in each time bin, and it is larger for shorter time binning. As expected, the statistical error σ_i is also larger for shorter time bins. But the ratio between intrinsic variability and statistical error σ_Q/σ_i is smaller for shorter time bins. In order to learn something about the strength of variability, we used $S_{\text{V}} = 100\% \cdot \sigma_Q/\bar{x}$, where \bar{x} is the average count rate of the source. As a control object we use the Crab. This constant

Table 1. Results on variability estimator following Almaini et al. (2000). \bar{x} : *Swift*/BAT (14–195 keV) average count rate; σ_Q : intrinsic variability for 1 day binned lightcurve; S_V : variability estimator $S_V = 100\% \cdot \sigma_Q/x$.

source name	x [10^{-4} cps]	σ_Q (1 day) [10^{-4} cps]	S_V (1 day)	S_V (7 day)	S_V (20 day)	S_V (40 day)
3C 111	2.24 ± 0.08	1.17	52.2	12.4	14.7	9.6
3C 120	2.34 ± 0.08	0.89	37.9	36.2	12.8	12.1
3C 273	5.05 ± 0.06	1.51	31.1	25.2	23.9	22.1
3C 382	1.59 ± 0.07	1.09	68.7	33.5	15.7	–
3C 390.3	1.76 ± 0.07	0.92	52.4	36.0	18.9	7.4
3C 454.3	3.44 ± 0.07	2.28	66.8	57.2	52.3	38.2
4C +71.07	1.22 ± 0.07	0.82	67.5	48.4	29.6	24.3
Cen A	13.57 ± 0.07	2.26	16.7	12.6	12.1	7.4
Cyg A	2.12 ± 0.06	0.96	45.3	23.3	18.9	10.6
ESO 103–035	2.03 ± 0.09	1.38	68.6	42.4	18.1	3.8
ESO 297–018	0.97 ± 0.07	1.08	112.2	64.1	39.3	27.9
ESO 506–027	2.31 ± 0.07	1.46	63.7	35.6	27.7	22.0
EXO 055620–3820.2	1.04 ± 0.06	1.02	101.2	63.6	16.2	21.6
GRS 1734–292	2.33 ± 0.11	1.29	54.7	37.8	14.9	13.0
IC 4329A	5.62 ± 0.07	1.03	18.3	13.1	7.4	6.8
IGR J21247+5058	2.64 ± 0.06	1.06	40.9	27.4	24.7	20.0
MCG+08–11–011	2.01 ± 0.09	1.20	59.1	37.6	26.0	–
MCG–05–23–016	3.95 ± 0.08	1.20	30.4	21.8	15.1	8.2
MR 2251–178	2.19 ± 0.10	1.49	68.1	27.7	13.6	11.8
Mrk 3	1.92 ± 0.07	0.83	43.1	25.4	19.5	14.2
Mrk 348	1.79 ± 0.07	1.11	62.9	30.8	32.7	22.9
Mrk 421	1.33 ± 0.06	3.14	235.3	217.1	181.6	178.8
NGC 1142	1.59 ± 0.07	0.79	50.4	34.4	18.3	18.5
NGC 1275	2.05 ± 0.08	1.24	60.1	29.4	24.6	17.7
NGC 1365	1.33 ± 0.06	0.88	66.0	36.4	31.5	24.8
NGC 2110	4.64 ± 0.07	1.67	36.0	31.7	33.3	32.3
NGC 2992	1.19 ± 0.08	1.34	111.3	73.8	76.0	51.9
NGC 3081	1.67 ± 0.08	1.25	73.1	46.5	44.4	23.1
NGC 3227	2.44 ± 0.06	0.78	32.2	28.3	20.0	21.8
NGC 3281	1.54 ± 0.08	0.95	64.4	36.6	26.8	23.7
NGC 3516	1.98 ± 0.06	0.93	47.2	18.8	10.6	7.7
NGC 3783	3.27 ± 0.07	1.05	32.1	16.0	9.0	7.2
NGC 4051	0.81 ± 0.06	0.81	99.4	48.3	16.0	29.0
NGC 4151	7.13 ± 0.06	2.87	40.3	35.8	33.3	30.3
NGC 4388	4.73 ± 0.06	1.56	33.0	24.4	18.9	18.4
NGC 4507	3.51 ± 0.07	1.10	31.2	13.0	13.3	12.3
NGC 4593	1.60 ± 0.07	1.04	64.1	33.8	22.2	15.4
NGC 4945	3.66 ± 0.07	1.65	45.2	33.9	30.5	22.7
NGC 5506	4.28 ± 0.07	1.03	24.1	12.5	9.2	6.6
NGC 5728	1.67 ± 0.08	1.16	68.4	20.5	17.0	14.7
NGC 7172	2.65 ± 0.10	1.44	53.8	48.3	25.2	21.9
NGC 7582	1.19 ± 0.08	0.99	80.8	61.9	50.4	38.7
QSO B0241+622	1.41 ± 0.07	0.95	66.8	39.8	28.4	16.2
XSS J05054–2348	1.07 ± 0.06	0.99	93.8	55.8	34.1	34.2
Crab	453.8 ± 0.10	11.6	2.56	1.72	1.27	1.07

source shows an intrinsic variability of $S_V = 2.6\%$ (1 day binning) down to $S_V = 1.1\%$ (40 day binning). This value might be assumed to be the systematic error in the *Swift*/BAT data. In addition, we used lightcurves extracted at random positions in the sky. Here the S_V value does not give a meaningful result (as the average flux is close to zero). But the fact that $\sigma_Q > 0$ for a random position indicates that a σ_Q as large as the one for a random position cannot be attributed to intrinsic variability, but might instead be caused by instrumental effects or due to the image deconvolution process. The uncorrected results are reported in Table 1. The variability estimator S_V is given in percentage [%]. Note that the variability estimator σ_Q usually decreases with the length of the time bins, as does the statistical error of the measurements. The average fluxes are listed in detector counts per second. As the Crab shows a count rate

of 0.045 s^{-1} , a count rate of 10^{-4} s^{-1} corresponds to a flux of $f_{14-195 \text{ keV}} \simeq 6 \times 10^{-11} \text{ erg cm}^{-2} \text{ s}^{-1}$ for a Crab-like ($\Gamma = 2.08$) spectrum.

The sources extracted at random positions show a $\sigma_Q = 3.6 \times 10^{-5}$ on the 20 day time scale ($\sigma_Q = 9.2 \times 10^{-5}$, 5.4×10^{-5} , 2.2×10^{-5} , for 1, 7 and 40 day binning, respectively). Thus, in order to get corrected for systematic errors, we subtracted 3.6×10^{-5} from the σ_Q of each source in the 20 day measurement and determined the S_{Vc} based on this value: $S_{Vc} = 100\%(\sigma_Q - 3.6 \times 10^{-5})/x$. The errors on the variability estimator have been determined by Monte-Carlo simulations. The flux and error distribution of each source have been used. Under the assumption that the source fluxes and errors are following a Gaussian distribution, for each source 1000 lightcurves have

Table 2. Results on variability estimator – corrected values and structure function. *type*: optical classification; \bar{x} : *Swift*/BAT (14–195 keV) average count rate; N_{H} : intrinsic absorption; L_{X} : luminosity (14–195 keV) assuming a Crab-like spectrum ($\Gamma \approx 2.1$); σ_Q : intrinsic variability for 20 day binned lightcurve; S_{vc} : corrected intrinsic variability; rr_{SF} : probability for non-correlation from structure function analysis

source name	type	\bar{x} [10^{-4} cps]	$\log N_{\text{H}}$ [cm^{-2}]	$\log L_{\text{X}}$ [erg s^{-1}]	σ_Q (20 day) [10^{-4} cps]	S_{vc} (20 day) [%]	$\log rr_{\text{SF}}$
Mrk 421	blazar	1.33	19.0 ¹	44.21	2.44	142 ± 38	-10.8
3C 454.3	blazar	3.44	20.8 ²	47.65	1.81	42 ± 12	-3.9
3C 273	blazar	5.05	20.5 ³	46.26	1.16	15 ± 5	-2.8
4C +71.07	blazar	1.22	21.0 ³	48.10	0.36	0 ± 10	0.0
IGR J21247+5058	rad. gal.	2.60	21.8 ⁴	44.15	0.65	11 ± 6	-1.1
QSO B0241+622	Sy1	1.41	22.2 ⁵	44.58	0.40	3 ± 9	-0.3
IC 4329A	Sy1	5.62	21.7 ³	44.29	0.42	1 ± 2	-3.5
NGC 4593	Sy1	1.60	20.3 ⁵	43.24	0.36	0 ± 7	-3.1
GRS 1734–292	Sy1	2.33	22.6 ⁶	44.16	0.36	0 ± 5	-0.7
3C 111	Sy1	2.24	22.0 ³	44.86	0.33	-1 ± 7	-1.2
3C 390.3	Sy1	1.76	21.0 ³	44.88	0.33	-2 ± 6	-0.2
3C 120	Sy1	2.34	21.2 ³	44.54	0.29	-3 ± 10	-1.8
NGC 3783	Sy1	3.27	22.5 ⁵	43.62	0.26	-3 ± 4	-3.6
MR 2251-178	Sy1	2.19	20.8 ³	45.09	0.29	-3 ± 7	-0.1
3C 382	Sy1	1.59	21.1 ³	44.86	0.25	-7 ± 6	-0.8
EXO 055620–3820.2	Sy1	1.04	22.2 ³	44.21	0.16	-19 ± 9	-0.1
NGC 4151	Sy1.5	7.13	22.8 ⁶	43.02	2.38	27 ± 7	-7.6
MCG+08–11–011	Sy1.5	2.01	20.3 ⁵	44.06	0.54	9 ± 8	-0.1
NGC 3227	Sy1.5	2.44	22.8 ⁷	42.69	0.49	5 ± 9	-4.2
NGC 3516	Sy1.5	1.98	21.2 ³	43.32	0.21	-8 ± 7	-4.3
NGC 4051	Sy1.5	0.81	20.5 ³	41.77	0.13	-28 ± 9	-1.3
NGC 1365	Sy1.8	1.33	23.6 ⁵	42.72	0.42	5 ± 12	-0.8
NGC 5506	Sy1.9	4.28	22.5 ⁵	43.34	0.39	-4 ± 3	-6.1
MCG–05–23–016	Sy1.9	3.94	22.2 ⁸	43.58	0.60	6 ± 4	-2.2
NGC 2992	Sy2	1.19	20.9 ⁹	42.98	0.91	45 ± 19	-6.6
NGC 2110	Sy2	4.64	22.6 ³	43.58	1.52	25 ± 7	-2.9
NGC 3081	Sy2	1.67	23.8 ¹⁰	43.15	0.75	23 ± 11	-6.2
NGC 7582	Sy2	1.19	23.0 ³	42.64	0.63	23 ± 21	-2.2
NGC 4945	Sy2	3.66	24.6 ⁵	42.24	1.11	21 ± 7	-2.8
Mrk 348	Sy2	1.79	23.3 ¹¹	43.74	0.58	12 ± 10	-1.9
NGC 7172	Sy2	2.65	23.9 ³	43.43	0.68	12 ± 9	-0.3
ESO 506–027	Sy2	2.31	23.8 ¹²	44.29	0.63	12 ± 7	-3.9
NGC 4388	Sy2	4.73	23.4 ¹³	43.65	0.89	11 ± 4	-1.5
Cen A	Sy2	13.57	23.1 ¹⁴	42.78	1.65	10 ± 2	-2.8
NGC 1275	Sy2	2.05	22.6 ¹⁴	43.93	0.51	7 ± 7	-1.1
NGC 4507	Sy2	3.51	23.5 ⁵	43.82	0.48	3 ± 5	-0.9
Cyg A	Sy2	2.12	23.3 ¹⁵	44.96	0.40	2 ± 5	-1.5
NGC 3281	Sy2	1.54	24.3 ¹⁶	43.37	0.38	1 ± 8	-0.3
Mrk 3	Sy2	1.92	24.0 ⁵	43.67	0.38	1 ± 6	-0.1
XSS J05054–2348	Sy2	1.07	22.7 ¹²	44.25	0.36	0 ± 10	-1.1
ESO 103–035	Sy2	2.03	23.2 ³	43.68	0.36	0 ± 8	-1.7
ESO 297–018	Sy2	0.97	23.7 ¹²	43.92	0.36	0 ± 12	-2.4
NGC 1142	Sy2	1.59	23.5 ¹²	44.25	0.29	-4 ± 10	-0.6
NGC 5728	Sy2	1.67	23.5 ¹⁷	43.29	0.29	-4 ± 8	-5.3

References. (1) Fossati et al. (2000); (2) Lawson & Turner (1997); (3) Tartarus database; (4) Ricci et al. (2007); (5) Lutz et al. (2004); (6) Beckmann et al. (2005); (7) Godoin et al. (2003); (8) Soldi et al. (2005), (9) Beckmann et al. (2007); (10) Bassani et al. (1999); (11) Akylas et al. (2006); (12) from *Swift*/XRT analysis; (13) Beckmann et al. (2004); (14) Beckmann et al. (2006); (15) Young et al. (2002); (16) Vignali & Comastri (2002); (17) Mushotzky (private communication).

been simulated. Each of these lightcurves contains the same number of data points as the original lightcurve. The data have then been fitted by the same procedure and the error has been determined based on the 1σ standard deviation of the σ_Q values derived. The results are shown in Table 2. The sources have been sorted by source type and then in descending variability.

It has to be taken into account that the source type in Table 2 is based on optical observations only. The radio properties are not taken into account. 3C 111, 3C 120, 3C 382, and 3C 390.3 are not standard Seyfert 1 galaxies but broad-line radio

galaxies, and Cen A and Cyg A are narrow-line radio galaxies. In the case of IGR J21247+5058 the nature of the optical galaxy is not clear yet. In all of these cases, the prominent jet of the radio galaxy might contribute to the hard X-ray emission. In addition the optical classification is often but not always correlated with the absorption measured in soft X-rays: Most, but not all, Seyfert 2 galaxies show strong absorption ($N_{\text{H}} > 10^{22} \text{ cm}^{-2}$), whereas most, but not all, Seyfert 1 galaxies exhibit small hydrogen column densities ($N_{\text{H}} < 10^{22} \text{ cm}^{-2}$), as noted e.g. by Cappi et al. (2006).

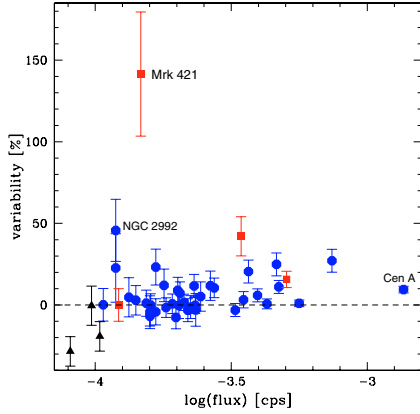


Fig. 1. Variability estimator S_{ν_c} as a function of *Swift*/BAT 14–195 keV count rate. A count rate of 10^{-4} s^{-1} corresponds to a flux of about $f_{14-195 \text{ keV}} \approx 6 \times 10^{-11} \text{ erg cm}^{-2} \text{ s}^{-1}$. Blazars have been marked with squares and the three objects with the lowest count rates ($< 1.05 \times 10^{-4} \text{ s}^{-1}$) are marked with triangles.

Obviously, the fainter the source is, the more difficult it is to get a good measurement for the variability. Thus, one might suspect that there is a correlation between source flux and variability S_{ν_c} . Figure 1 shows the variability estimator S_{ν_c} as a function of flux (14–195 keV in counts per second). There is no correlation between flux and variability, although all the sources for which no variability was detectable are of low flux. A Spearman rank test (Spearman 1904) gives a correlation coefficient as low as $r_s = 0.2$, rejecting the hypothesis that flux and variability are correlated. The estimation of variability becomes more uncertain for objects with very low fluxes. We therefore mark the three sources with the lowest flux in the figures and do not consider them when studying correlations between parameters. From Table 2 it is already apparent that none of the 11 type 1 galaxies shows significant variability, whereas of the 20 type 2 objects 50% show variability with $S_{\nu_c} \geq 10\%$. This effect is also apparent when comparing the variability S_{ν_c} with the intrinsic absorption N_{H} as measured in soft X-rays (e.g. by *Swift*/XRT or *XMM-Newton*). The correlation is shown in Fig. 2. Blazars have been excluded. Except for NGC 2992, none of the objects with intrinsic absorption $N_{\text{H}} < 10^{22} \text{ cm}^{-2}$ shows significant variability according to the maximum likelihood estimator. NGC 2992 is also a special case because it is a Seyfert 2 galaxy with comparably low intrinsic absorption and the N_{H} varies between 0.1 and $1.0 \times 10^{22} \text{ cm}^{-2}$ (Beckmann et al. 2007). Even when including NGC 2992 a Spearman rank test of N_{H} versus variability gives a correlation coefficient of $r_s = 0.31$, which corresponds to a moderate probability of correlation of 95%.

2.3. Structure function

As an independent test for variability, we determined the structure function of the objects. Structure functions are similar to auto- and cross-correlation functions and have been introduced for analysis of radio lightcurves by Simonetti et al. (1985). Applications to other data sets have been shown, e.g. by Hughes et al. (1992), Paltani (1999), de Vries (2005), and Favre et al. (2005). The structure function is a useful and simple to use tool in order to find characteristic time scales for the variations in a source. We use the first-order structure function, which

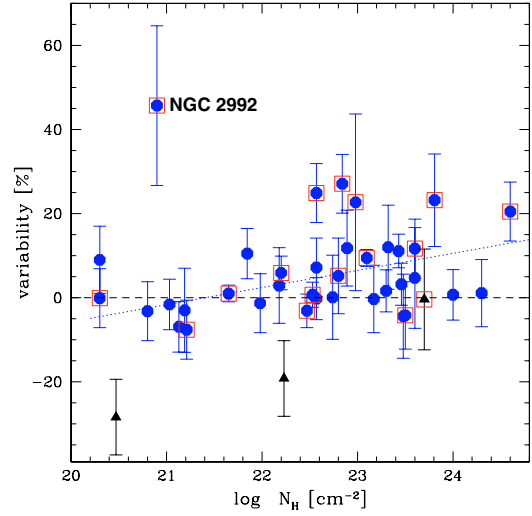


Fig. 2. Variability estimator S_{ν_c} as a function of intrinsic absorption N_{H} . Blazars have been excluded and the three objects with the lowest count rates ($< 1.05 \times 10^{-4} \text{ s}^{-1}$) are marked with triangles. Objects enclosed by a square show a rising part of the structure function with a correlation probability of $rr_{\text{SF}} \leq 0.01$ (see Sect. 2.3 for details). The object with the highest S_{ν_c} is NGC 2992. The dotted line indicates the linear regression to the data points, excluding NGC 2992 and the three low-flux objects.

is defined as $D^1(\tau) = \langle [S(t) - S(t + \tau)]^2 \rangle$. Here $S(t)$ is the flux at time t , and τ is the time-lag, or variability time-scale. The function $D^1(\tau)$ can be characterized in terms of its slope: $b = d \log D^1 / d \log \tau$. For a stationary random process the structure function is related simply to the variance σ^2 of the process and its autocorrelation function $\rho(\tau)$ by $D^1(\tau) = 2\sigma^2[1 - \rho(\tau)]$. For lags longer than the longest correlation time scale, there is an upper plateau with an amplitude equal to twice the variance of the fluctuation ($2 \cdot (\sigma_0^2 + \sigma_i^2)$). For very short time lags, the structure function reaches a lower plateau which is at a level corresponding to the measurement noise ($2 \cdot \sigma_i^2$). As explained in Hughes et al. (1992), the structure function, autocorrelation function, and power spectrum density function (PSD) $P(\nu)$ are related measures of the distribution of power with time scale. If the PSD follows a power law of the form $P(\nu) \propto \nu^{-a}$, then $D^1(\tau) \propto \tau^{a-1}$ (Bregman et al. 1990). For example, if $P(\nu) \propto \nu^{-1}$, then $D^1(\tau) \propto \tau^0$ (flicker noise). Flicker noise exhibits both short and long time-scale fluctuations. If $P(\nu) \propto \nu^{-2}$, then $D^1(\tau) \propto \tau^1$ (short or random walk noise). This relation is however valid only in the limit $\tau_{\text{max}} \rightarrow \infty$, $\tau_{\text{min}} \rightarrow 0$. If, on the contrary, the PSD is limited to the range $[\tau_{\text{min}}, \tau_{\text{max}}]$, the relationship does not hold anymore (Paltani 1999). This is in fact the case here, as we can probe only time scales in the range of $\tau_{\text{min}} \sim 10$ days to $\tau_{\text{max}} \sim 100$ days. In the ideal case we can learn from the structure function of the *Swift*/BAT AGN about several physical properties: whether the objects show variations, what the maximum time scale of variations is, and what the type of noise is which is causing the variations. We can determine the maximum time scale τ_{max} of variability only if a plateau is reached and, in our case, if $\tau_{\text{max}} < 9$ months.

Error values on the structure function have been again determined by Monte-Carlo simulation. The flux and error distribution of each source has been used. Under the assumption that the source fluxes and errors are following a Gaussian distribution,

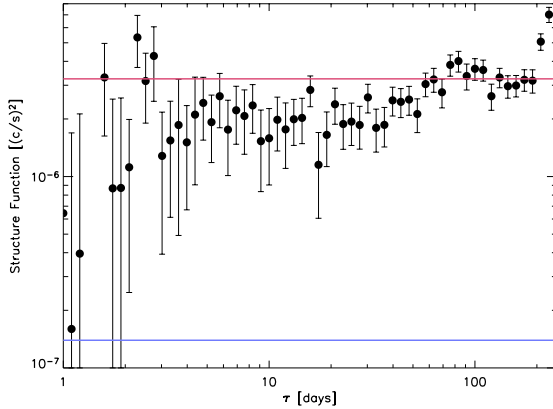


Fig. 3. Structure function for *Swift*/BAT data of the Crab (one day binning). The upper line indicates an amplitude equal to twice the variance of the fluctuation, the lower line corresponds to the level of the average measurement noise ($2 \cdot \overline{\sigma_i^2}$).

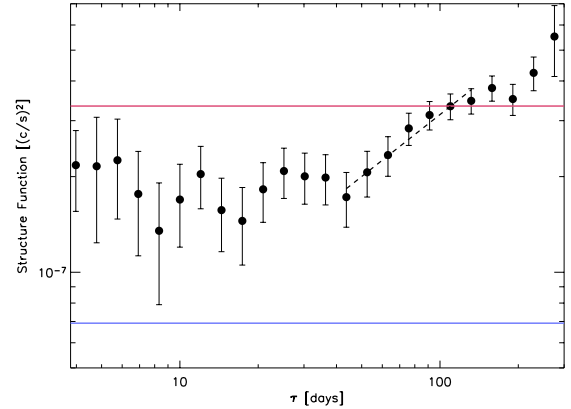


Fig. 4. Structure function for *Swift*/BAT data of the Seyfert 1.5 galaxy NGC 4151 (one day binning). The upper and lower lines indicate $2(\sigma_Q^2 + \overline{\sigma_i^2})$ and $2\overline{\sigma_i^2}$, respectively. The dashed line indicates the linear regression applied to the data, resulting in $D^1(\tau) \propto \tau^{0.65}$.

for each source 1000 lightcurves with 1 day binning have been simulated. These lightcurves have then been used to extract the structure function. The scatter in each point $D^1(\tau)$ is then considered when fitting a straight line to the data applying linear regression.

To test the quality of the BAT data lightcurves for determining the structure function we show in Fig. 3 the one obtained for the Crab as an example for a constant source. As expected, after the structure function gets out of the noisy part at time scales shorter than ~ 4 days, it stays more or less constant. Thus, no variability is detected in the Crab up to time scales of the duration of the survey. Figure 4 shows the structure function for the BAT data of NGC 4151. This source has a lower flux than the Crab, thus the noisy part of the structure function extends up to $\tau \approx 20$ –40 days. At longer time scales, the function is rising. It is not clear though whether it levels out after 150 days, which would mean there is no variability on time scales longer than 150 days. But the source is variable on timescales ranging from 3 weeks to (at least) 5 months. For comparison we checked the *CGRO*/BATSE Earth-occultation archive¹ which contains light curves for 4 sources of our sample, i.e. 3C 273, Cen A, NGC 4151, and NGC 1275. Figure 5 shows the 20–70 keV structure function of NGC 4151 based on *CGRO*/BATSE data. The sampling here is worse at the time scales probed by the *Swift*/BAT survey, but reaches out to time scales up to $\tau \approx 8$ years. One can see that the turnover does not appear within the probed time scale, consistent with the results we derived from the BAT data. Also for the other 3 objects the results from BATSE and BAT are consistent, showing variability for Cen A and 3C 273 over all the sampled time scales, and no variability for NGC 1275. We also checked the lightcurves for random positions in the sky. One example is shown in Fig. 6.

Based on the comparison of the structure function curves of the BAT AGN with those of the Crab and the random positions, we examined the curves of all objects of the sample presented here for rising evolution in the range $\tau = 20$ –200 days. Individual time limits l_{\min} and l_{\max} have been applied in order to apply a linear regression fit to the curves, taking into account the errors determined in the Monte-Carlo simulation. Therefore this method inherits a subjective element which obviously

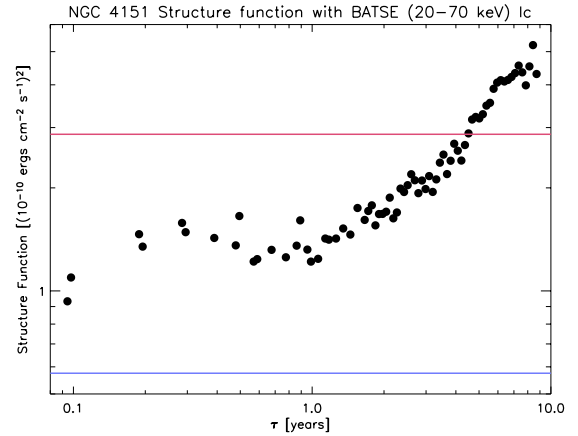


Fig. 5. Structure function for *CGRO*/BATSE data (20–70 keV) of NGC 4151. The upper and lower lines indicate $2(\sigma_Q^2 + \overline{\sigma_i^2})$ and $2\overline{\sigma_i^2}$, respectively.

limits the usefulness of the output. On the other hand, a fixed l_{\min} and l_{\max} does not take into account the difference in significance between the sources. The l_{\max} applied is not necessarily the maximum time-scale of variability τ_{\max} , especially when $\tau_{\max} > 100$ days. The last column of Table 2 reports the results. rr_{SF} gives the probability for a non-correlation of τ and $D^1(\tau)$. We consider here objects with $\log rr_{\text{SF}} \leq -2$ as variable, i.e. objects where we find a probability of $> 99\%$ for correlation. The structure function of the Crab lightcurve for example results in $\log rr_{\text{SF}} = -0.6$. One can see an overall agreement with the variability estimator, although in some cases there are discrepancies, e.g. for NGC 3516 and NGC 5728, which have a rising structure function, but do not give an indication of variability in the maximum likelihood approach. In total, 16 objects show a rising structure function, and 15 objects show a variability $S_{\text{vc}} > 10\%$ in the maximum likelihood approach. 10 objects show a rising structure function and $S_{\text{vc}} > 10\%$. A Spearman rank test of the variability estimator versus the $\log rr_{\text{SF}}$ value gives a probability of $> 98\%$ for correlation, and $> 99.5\%$ if we ignore the objects with a negative variability estimator. Some caution has to

¹ <http://f64.nsstc.nasa.gov/batse/occultation/>

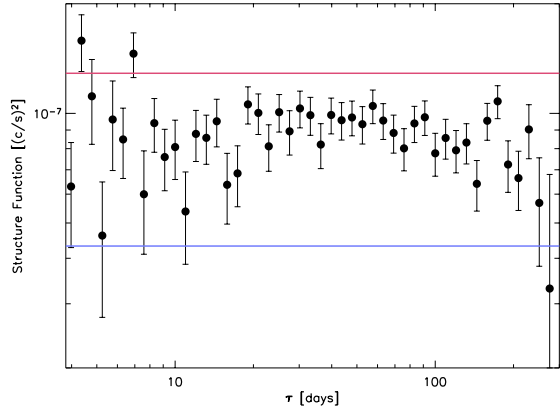


Fig. 6. Structure function for *Swift*/BAT data of a random position in the sky (XXX J0044.1+5019). The upper and lower lines indicate $2\sigma_Q^2 + \sigma_i^2$ and $2\sigma_i^2$, respectively.

be applied when comparing those two values: while the variability estimator measures the strength of the variability, the $\log rr_{SF}$ indicates the probability that there is indeed significant variation. A bright source can have a small but very significant variability. The fact that the variability estimator is based on 20-day binned lightcurves, while the structure functions are extracted from 1-day binned data should not affect the results strongly: because of the moderate sampling of the light curves, the structure function analysis cannot probe variability below ~ 20 days in most cases.

Concerning a dependence of variability on intrinsic absorption, the structure function method confirms the tendency seen in variability estimator. As shown in Fig. 2, 25% of the objects with $N_H < 10^{22} \text{ cm}^{-2}$ and 46% of the objects with $N_H > 10^{22} \text{ cm}^{-2}$ show a rising structure function. Again, this should be taken as a tendency, not as a strong correlation.

3. Discussion

Studying the correlation between absorption and variability, there is a tendency that the stronger absorbed sources are the more variable ones (Fig. 2). If the central engine in type 1 and type 2 objects is indeed similar, this is a surprising result. First, absorption should not play a major role in the spectrum at energies $> 15 \text{ keV}$ unless the absorption is $N_H \gg 10^{23} \text{ cm}^{-2}$. But most of the sources studied here show only moderate absorption with hydrogen column densities of the order of $N_H = 10^{21} - 10^{23} \text{ cm}^{-2}$. Even if absorption plays a role, the expected effect would be reverse to the observation, i.e. one would expect a damping effect of the absorption and the absorbed sources should be less variable than the unabsorbed ones. In a recent study of *XMM-Newton* data of AGN in the Lockman Hole by Mateos et al. (2007) it has been shown that although the fraction of variable sources is higher among type-1 than in type-2 AGN, the fraction of AGN with detected spectral variability were found to be $\sim 14 \pm 8\%$ for type-1 AGN and $34 \pm 14\%$ for type-2 AGN. This might indicate that the differences between type 1 and type 2 galaxies are indeed more complex than just different viewing angles resulting in a difference in the absorbing material along the line of sight. In this context, alternative and modified accretion models might be considered, such as matter accretion via clumps of matter and interaction between

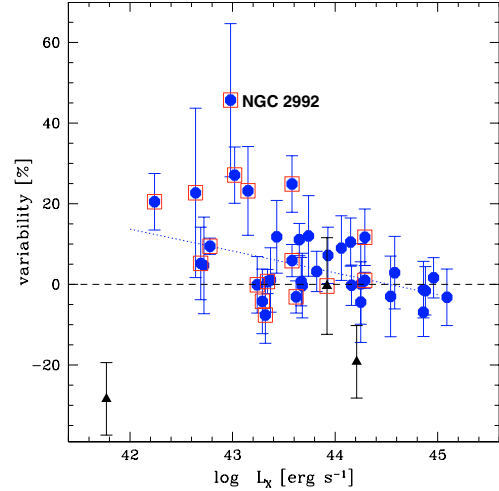


Fig. 7. Variability estimator S_{Vc} as a function of X-ray luminosity in the 14–195 keV band. The three objects with the lowest count rates ($< 1.05 \times 10^{-4} \text{ s}^{-1}$) are marked with triangles. The blazars are located outside the area covered in this plot. The dotted line indicates the linear regression to the data points.

these clumps (Courvoisier & Türler 2005) or star collisions in a cluster of stars orbiting around the central massive black hole (Torricelli-Ciamponi et al. 2000).

Another explanation for the lack of variable type 1 objects in our sample could be that the correlation between absorption and variability is an indirect one, caused by two other correlations: an anti-correlation of intrinsic absorption and luminosity, and the anti-correlation of variability and luminosity. While the first dependence in the data set presented here is very weak, there is indeed a trend of lower variability for sources with higher luminosity (Fig. 7). A Spearman rank test of luminosity versus variability estimator results in a correlation coefficient of $r_s = -0.47$, which corresponds to a correlation probability of $> 99\%$. All the sources which show a $S_{Vc} > 20\%$ have luminosities of $L_{(14-195 \text{ keV})} < 4 \times 10^{43} \text{ erg s}^{-1}$, and all sources with $S_{Vc} > 10\%$ have $L_{(14-195 \text{ keV})} < 2 \times 10^{44} \text{ erg s}^{-1}$. Using the results from the structure function a similar trend is seen: 76% of the objects with $L_{(14-195 \text{ keV})} < 4 \times 10^{43} \text{ erg s}^{-1}$ have a significant rising part of the structure function, whereas only 13% of the more luminous objects show this indication for variability.

The results based on the structure function have to be interpreted with caution due to the relatively small number of significant data points. Nevertheless it appears that the maximum time length τ_{\max} for variability is significantly longer than in the optical and UV region. Collier & Peterson (2001) studied 4 of the objects presented here and found a τ_{\max} significantly smaller in all cases for the optical and UV. The same applies for the AGN variability study performed by Favre et al. (2005) using UV data, including 7 of the objects studied here. On the contrary, de Vries et al. (2005) do not find a turn-over in optical lightcurves up to $\tau_{\max} \sim 40 \text{ yr}$.

The average gradient β of the rising part of the structure functions (assuming $D^1(\tau) \propto \tau^\beta$) with $rr_{SF} < 0.01$ is $\bar{\beta} = 0.4 \pm 0.1$ and ranging for the individual sources from $\beta = 0.2$ (3C 454.3, NGC 5506, and 3C 273) to $\beta = 1.0$ (ESO 506-027), consistent with measurements of the power spectrum of 11 AGN in the X-rays by *EXOSAT*, which resulted in $\bar{\beta} = 0.55 \pm 0.09$

(Lawrence & Papadakis 1993). The average value is closer to the slope expected from disk instability models ($\beta = 0.8\text{--}1.0$, Mineshige et al. 1994), rather than to the slope of the starburst model ($\beta = 1.4\text{--}1.8$, Arétxaga et al. 1997). This result should not be overemphasized as de Vries et al. (2004) pointed out that the measurement noise does have a direct effect on the slope of the structure function. The larger the noise, the shallower the slope.

Compared to softer X-rays, the Seyfert galaxies appear to exhibit less variability than e.g. at 2–10 keV. This indicates that there is an overall tendency for an anticorrelation of variability with energy. This has been reported for some of the objects studied here e.g. for 3C 390.3 and 3C 120 (Gliozzi et al. 2002) which show no significant variation here, and also for NGC 3227 (Uttley & McHardy 2005). In the latter article the case of NGC 5506 is also described in which this trend is reversed in the soft X-rays. This object does not show significant variability applying the maximum likelihood estimator, but shows indeed a rising structure function with $\tau_{\text{max}} \geq 200$ days.

The fraction of variable objects in our study is about 30% among the Seyfert type AGN according to both methods, the variability estimator and the structure function. This is a lower fraction than detected at softer X-rays. For example among the AGN in the *Chandra* Deep Field South 60% of the objects show variability (Bauer et al. 2004), and *XMM-Newton* data of the Lockman Hole reveal a 50% fraction (Mateos et al. 2007). Part of the lower variability detected in the *Swift*/BAT AGN sample might be due to the lower statistics apparent in the lightcurves when compared to the soft X-ray data. Bauer et al. (2004) pointed out that the fraction of variable sources is indeed a function of source brightness and rises up to 80–90% for better photon statistics and also Mateos et al. find >80% of the AGN variable for the best quality light curves. Within our sample we are not able to confirm this trend, which might be due to the small size of the sample.

An anticorrelation of X-ray variability with luminosity in AGN has been reported before for energies <10 keV (e.g. Barr & Mushotzky 1986; Lawrence & Papadakis 1993) and has been also seen in the UV range (Paltani & Courvoisier 1994) and in the optical domain (de Vries et al. 2005), although narrow-line Seyfert 1 galaxies apparently show the opposite behaviour (e.g. Turner et al. 1999). As only one of the objects (NGC 4051) discussed here is a NLSy1 galaxy, we detect a continuous effect from soft to hard X-rays, which indeed indicates that the dominant underlying physical process at ~ 5 keV is the same as at ~ 20 keV. In a more recent study, Papadakis (2004) reported that this correlation is in fact based on the connection between luminosity and the mass of the central black hole M_{BH} . This may be explained if more luminous sources are physically larger in size, so that they are actually varying more slowly. Alternatively, they may contain more independently flaring regions and so have a genuinely lower amplitude. The observed correlation might reflect the anticorrelation of variability and black hole mass. In the case of the sample presented here, such an anticorrelation is not detectable, but it has to be pointed out that estimates for M_{BH} are only available for 13 objects. In addition, the range of objects in luminosity and black hole mass might be too small in order to detect such a trend. Uttley & McHardy (2004) explained the anticorrelation of variability and M_{BH} by assuming that the X-rays are presumably produced in optically thin material close to the central black hole, at similar radii (i.e. in Schwarzschild radii, R_S) in different AGN. As $R_S = 2GM_{\text{BH}}c^{-2}$, longer time scales for the variability are expected for the more massive central engines, making the objects less variable on a monthly time scale studied here.

4. Conclusions

We presented the variability analysis of the brightest AGN seen by *Swift*/BAT, using two ways of analysis: a maximum-likelihood variability estimator and the structure function. Both methods show that $\sim 30\%$ of the Seyfert type AGN exhibit significant variability on the time scale of 20–150 days. The analysis indicates that the type 1 galaxies are less variable than the type 2 type ones, and that unabsorbed sources are less variable than absorbed ones. With higher significance we detect an anti-correlation of luminosity and variability. No object with luminosity $L_X > 5 \times 10^{43} \text{ erg s}^{-1}$ shows strong variability. The anti-correlation might either be caused by intrinsic differences between the central engine in Seyfert 1 and Seyfert 2 galaxies, or it might be connected to the same anti-correlation seen already at softer X-rays, in the UV and in the optical band. Further investigations on this subject are necessary in order to clarify whether one can treat the AGN as an upscale version of Galactic black hole systems (e.g. Vaughan et al. 2005).

The data presented here do not allow a final conclusion on this point. The correlations are still too weak and for too many objects it is not possible to determine the strength of the intrinsic variability. Similar studies at softer X-rays seem to indicate that with increasing statistics we will be able to detect significant variability in a larger fraction of objects. The study presented here will be repeated as soon as significantly more *Swift*/BAT data are available for analysis. As this study was based on 9 months of data, a ten times larger data set will be available in 2012. Eventually, the data will allow more sophisticated analysis, such as the construction of power density spectra. In addition the same analysis can be applied to *INTEGRAL* (Winkler et al. 2003) IBIS/ISGRI data. Although *INTEGRAL* does not achieve a sky coverage as homogeneous as *Swift*/BAT, it allows a more detailed analysis of some AGN in specific regions, e.g. along the Galactic plane.

The combination of results from both missions, *Swift* and *INTEGRAL*, should allow us to verify whether indeed Seyfert 2 galaxies are more variable at hard X-rays than the unabsorbed Seyfert 1, and whether this points to intrinsic differences in the two AGN types.

Acknowledgements. We thank the anonymous referee who gave valuable advice which helped us to improve the paper. This research has made use of the NASA/IPAC Extragalactic Database (NED) which is operated by the Jet Propulsion Laboratory and of data obtained from the High Energy Astrophysics Science Archive Research Center (HEASARC), provided by NASA's Goddard Space Flight Center. This research has also made use of the Tartarus (Version 3.1) database, created by Paul O'Neill and Kirpal Nandra at Imperial College London, and Jane Turner at NASA/GSFC. Tartarus is supported by funding from PPARC, and NASA grants NAG5-7385 and NAG5-7067.

References

- Aeylas, A., Georgantopoulos, I., Georgakakis, A., Kitsionas, S., & Hatziminaoglou, E. 2006, *A&A*, 459, 693
- Almaini, O., Lawrence, A., Shanks, T., et al. 2000, *MNRAS*, 315, 325
- Arétxaga, I., Cid Fernandes, R., & Terlevich, R. J. 1997, *MNRAS*, 286, 271
- Barr, P., & Mushotzky, R. F. 1986, *Nature*, 320, 421
- Barthelmy, S. D., Barbier, L. M., Cummings, J. R., et al. 2005, *SSRv*, 120, 143
- Bassani, L., Dadina, M., Maiolino, R., et al. 1999, *ApJS*, 121, 473
- Bauer, F. E., Vignali, C., Alexander, D. M., et al. 2004, *AdSpR*, 34, 2555
- Beckmann, V., Gehrels, N., Favre, P., et al. 2004, *ApJ*, 614, 641
- Beckmann, V., Shrader, C. R., & Gehrels, N. 2005, *ApJ*, 634, 939
- Beckmann, V., Gehrels, N., Shrader, C. R., & Soldi, S. 2006, *ApJ*, 638, 642
- Beckmann, V., Gehrels, N., & Tueller, J. 2007, *ApJ*, 666, 122
- Bregman, J. N., Glassgold, A. E., Huggins, P. J., et al. 1990, *ApJ*, 352, 574
- Cappi, M., Panessa, F., Bassani, L., et al. 2006, *A&A*, 446, 459
- Collier, S., & Peterson, B. M. 2001, *ApJ*, 555, 775
- Courvoisier, T. J.-L., & Türler, M. 2005, *A&A*, 444, 417

- Czerny, B., Rózańska, A., Dovciak, M., Karas, V., & Dumont, A.-M. 2004, *A&A*, 420, 1
- de Vries, W. H., Becker, R. H., White, R. L., & Loomis, C. 2005, *AJ*, 129, 615
- Edelson, R., & Nandra, K. 1999, *ApJ*, 514, 96
- Favre, P., Courvoisier, T. J.-L., & Paltani, S. 2005, *A&A*, 443, 451
- Fossati, G., Celotti, A., Chiaberge, M., et al. 2000, *ApJ*, 541, 166
- Gehrels, N., Chincarini, G., & Giommi, P. 2004, *ApJ*, 611, 1005
- Gliozzi, M., Sambruna, R., & Eracleous, M. 2003, *ApJ*, 584, 176
- Gondoin, P., Orr, A., Lumb, D., & Siddiqui, H. 2003, *A&A*, 397, 883
- Grupe, D., Thomas, H. C., & Beuermann, K. 2001, *A&A*, 367, 470
- Hughes, P. A., Aller, H. D., & Aller, M. F. 1992, *ApJ*, 396, 469
- King, A. R. 2004, *MNRAS*, 348, 111
- Lawrence, A., & Papadakis, I. E. 1993, *ApJ*, 414, L85
- Lawson, A. J., & Turner, M. J. L. 1997, *MNRAS*, 288, 920
- Lutz, D., Maiolino, R., Spoon, H. W. W., & Moorwood, A. F. M. 2004, *A&A*, 418, 465
- Markowitz, A., & Edelson, R. 2001, *ApJ*, 547, 684
- Markwardt, C. B., Tueller, J., Skinner, G. K., et al. 2005, *ApJ*, 633, L77
- Masetti, N., Palazzi, E., Bassani, L., Malizia, A., & Stephen, J. B. 2004, *A&A*, 426, L41
- Mateos, S., Barcons, X., Carrera, F. J., et al. 2007, *A&A*, 473, 105
- McHardy, I. M., & Czerny, B. 1987, *Nature*, 325, 696
- Mineshige, S., Takeuchi, M., & Nishimori, H. 1994, *ApJ*, 435, L125
- Nandra, K., George, I. M., Mushotzky, R. F., Turner, T. J., & Yaqoob, T. 1997, *ApJ*, 476, 70
- Paltani, S. 1999, *PASPC*, 159, 293
- Paltani, S., & Courvoisier, T. J.-L. 1994, *A&A*, 291, 74
- Papadakis, I. E. 2004, *MNRAS*, 348, 207
- Ricci, C., Beckmann, V., Courvoisier, T. J.-L., et al. 2007, in prep.
- Risaliti, G., Elvis, M., & Nicastro, F. 2002, *ApJ*, 571, 234
- Simonetti, J. H., Cordes, J. M., & Heeschen, D. S. 1985, *ApJ*, 296, 46
- Soldi, S., Beckmann, V., Bassani, L., et al. 2005, *A&A*, 444, 431
- Spearman, C. 1904, *Am. J. Psychol.*, 15, 72
- Torricelli-Ciamponi, G., Foellmi, C., Courvoisier, T. J.-L., & Paltani, S. 2000, *A&A*, 358, 57
- Tueller, J., Mushotzky, R. F., Barthelmy, S. D., et al. 2007, *ApJ* submitted
- Turner, T. J., George, I. M., Nandra, K., & Turcan, D. 1999, *ApJ*, 524, 667
- Uttley, P., & McHardy, I. M. 2004, *PTHPS*, 155, 170
- Uttley, P., & McHardy, I. M. 2005, *MNRAS*, 363, 586
- Vaughan, S., Edelson, R., Warwick, R. S., & Uttley, P. 2003, *MNRAS*, 345, 1271
- Vaughan, S., Fabian, A. C., & Iwasawa, K. 2005, *Ap&SS*, 300, 119
- Vignali, C., & Comastri, A. 2002, *A&A*, 381, 834
- Winkler, C., Courvoisier, T. J.-L., Di Cocco, G., et al. 2003, *A&A*, 411, L1
- Young, A. J., Wilson, A. S., Terashima, Y., Arnaud, K. A., & Smith, D. A. 2002, *ApJ*, 564, 176

6.9.5 The Second INTEGRAL AGN Catalogue

A discussion of this work in the context of the unified model of AGN can be found in Section 4.7.3 on page 74. The manuscript, which is shown on the following pages, has been published as

Beckmann V., Soldi S., Ricci C., Alfonso-Garzón J., Courvoisier T. J.-L., Domingo A., Gehrels N., Lubiński P., Mas-Hesse J. M., & Zdziarski A. A., *Astronomy and Astrophysics*, Volume 505, Issue 1, pp. 417-439 (2009)

A&A 505, 417–439 (2009)
 DOI: 10.1051/0004-6361/200912111
 © ESO 2009

**Astronomy
&
Astrophysics**

The second INTEGRAL AGN catalogue[★]

V. Beckmann^{1,2,3}, S. Soldi⁴, C. Ricci^{1,2}, J. Alfonso-Garzón⁵, T. J.-L. Courvoisier^{1,2}, A. Domingo⁵, N. Gehrels⁶,
 P. Lubiński^{7,1}, J. M. Mas-Hesse⁵, and A. A. Zdziarski⁷

¹ ISDC Data Centre for Astrophysics, Chemin d'Écogia 16, 1290 Versoix, Switzerland

e-mail: beckmann@apc.univ-paris7.fr

² Observatoire Astronomique de l'Université de Genève, Chemin des Maillettes 51, 1290 Sauverny, Switzerland

³ APC Laboratory, Université Paris Diderot, 10 rue A. Domon et L. Duquet, 75205 Paris Cedex 13, France

⁴ Laboratoire AIM – CNRS – CEA/DSM – Université Paris Diderot (UMR 7158), CEA Saclay, DSM/IRFU/Sap, 91191 Gif-sur-Yvette, France

⁵ Centro de Astrobiología LAEX (CSIC-INTA), POB 78, 28691 Villanueva de la Cañada, Madrid, Spain

⁶ Astrophysics Science Division, NASA Goddard Space Flight Center, Code 661, MD 20771, USA

⁷ Centrum Astronomiczne im. M. Kopernika, Bartycka 18, 00-716 Warszawa, Poland

Received 19 March 2009 / Accepted 30 June 2009

ABSTRACT

Aims. The INTEGRAL mission provides a large data set for studying the hard X-ray properties of AGN and allows testing of the unified scheme for AGN.

Methods. We present analysis of INTEGRAL IBIS/ISGRI, JEM-X, and OMC data for 199 AGN supposedly detected by INTEGRAL above 20 keV.

Results. The data analysed here allow significant spectral extraction on 148 objects and an optical variability study of 57 AGN. The slopes of the hard X-ray spectra of Seyfert 1 and Seyfert 2 galaxies are found to be consistent within the uncertainties, whereas higher cut-off energies and lower luminosities we measured for the more absorbed/type 2 AGN. The intermediate Seyfert 1.5 objects exhibit hard X-ray spectra consistent with those of Seyfert 1. When applying a Compton reflection model, the underlying continua appear the same in Seyfert 1 and 2 with $\Gamma \approx 2$, and the reflection strength is about $R \approx 1$, when assuming different inclination angles. A significant correlation is found between the hard X-ray and optical luminosity and the mass of the central black hole in the sense that the more luminous objects appear to be more massive. There is also a general trend toward the absorbed sources and type 2 AGN having lower Eddington ratios. The black hole mass appears to form a fundamental plane together with the optical and X-ray luminosity of the form $L_V \propto L_X^{0.6} M_{\text{BH}}^{0.2}$, similar to what is found between L_R , L_X , and M_{BH} .

Conclusions. The transition from the type 1 to type 2 AGN appears to be smooth. The type 2 AGN are less luminous and have less accreting super massive black holes. The unified model for Seyfert galaxies seems to hold, showing in hard X-rays that the central engine is the same in Seyfert 1 and 2, but seen under different inclination angles and absorption. The fundamental plane links the accretion mechanism with the bulge of the host galaxy and with the mass of the central engine in the same way in all types of Seyfert galaxies.

Key words. galaxies: active – galaxies: Seyfert – X-rays: galaxies – surveys – catalogs

1. Introduction

The extragalactic X-ray sky is dominated by active galactic nuclei (AGN), which are commonly assumed to host an accreting supermassive black hole in the centres of galaxies. X-ray spectroscopy has been vital in the study of the AGN phenomenon, because it probes the condition of matter in the vicinity of the black hole. One model for the X-ray emission is that of a hot corona lingering on top of the inner accretion disc of the black hole and emitting inverse Compton radiation from disc photons that have been upscattered by energetic electrons. Another model assumes a disc with a hot inner advection-dominated accretion flow (ADAF; e.g. Abramowicz et al. 1996). An alternative model for the accretion process onto black holes is that of clumpy accretion flows (e.g. Guilbert & Rees 1988). Courvoisier & Türler (2005) assume that the different elements (clumps) of the

accretion flow have velocities that may differ substantially. As a consequence, collisions between these clumps will appear when the clumps are close to the central object, resulting in radiation.

Because optical spectroscopy distinguishes between two main types of low-luminosity AGN, the broad-line Seyfert 1 and narrow-line Seyfert 2 objects, a similar distinction is apparent between unabsorbed sources with on-average softer X-ray spectra and the flatter spectra of absorbed sources. This has been noticed by Zdziarski et al. (1995), based on *Ginga* and *CGRO/OSSE* data and later confirmed e.g. by Gondek et al. (1996) using combined *EXOSAT*, *Ginga*, *HEAO-1*, and *CGRO/OSSE* spectra, and by Beckmann et al. (2006) using *INTEGRAL* IBIS/ISGRI data of AGN above 20 keV. A study of *BeppoSAX* PDS spectra of 45 Seyfert galaxies has come to a similar conclusion, although the spectra of Seyfert 2 appeared steeper when considering a possible cut-off in the spectra of Seyfert 1 galaxies (Deluit & Courvoisier 2003). X-ray data already show that most, but not all, AGN unabsorbed in the X-rays are Seyfert 1 type, and most, but not all, AGN that are absorbed belong to the Seyfert 2 group (e.g. Awaki et al. 1991).

* All tables of this paper are also available in electronic form at the CDS via anonymous ftp to cdsarc.u-strasbg.fr (130.79.128.5) or via <http://cdsweb.u-strasbg.fr/cgi-bin/qcat?J/A+A/505/417>

Thus a longstanding discussion has been, whether these two groups indeed represent physically different types of objects, or whether they can be unified under the assumption that they are intrinsically the same but seen from a different viewing angle with respect to absorbing material in the vicinity of the central engine (e.g. Antonucci 1993), and that the difference in X-ray spectral slope can be explained solely by the absorption and reflection components. This *unified model* naturally explains the different Seyfert types in a way that the broad-line region is either visible (Seyfert 1) or hidden (Seyfert 2) possibly by the same material in the line of sight as is responsible for the absorption detectable at soft X-rays (e.g. Lawrence & Elvis 1982). On the other hand, the model has some problems explaining other aspects of AGN, for example, that some Seyfert galaxies change their type from 1 to 2 and back, but also the observation that Seyfert 2 objects exhibit flatter hard X-ray spectra than Seyfert 1 even in the energy range >20 keV, where absorption should not play a major role unless $N_{\text{H}} \gg 10^{24}$ cm $^{-2}$. Also, the existence of Seyfert 2 galaxies that show no absorption in the soft X-rays, like NGC 3147 and NGC 4698 (Pappa et al. 2001) cannot be explained by the unified model.

Lately, two hard X-ray missions have provided surveys at >20 keV with enough sky coverage to be suitable for population studies of AGN. One is the NASA-led *Swift* mission (Gehrels et al. 2004) launched in 2004, the other one the ESA-led *INTEGRAL* satellite (Winkler et al. 2004), launched in October 2002. Due to its observation strategy of following-up gamma-ray bursts, *Swift*/BAT (Barthelmy et al. 2005) provides a more homogeneous sky coverage in the 15–195 keV energy range, while the hard X-ray imager IBIS/ISGRI on-board *INTEGRAL* is more sensitive and extends up to several hundred keV with better spectral resolution. *INTEGRAL* provides broad-band coverage through the additional X-ray monitor JEM-X in the 3–30 keV range (Lund et al. 2003) and provides photometry with the optical camera OMC in the V-band (Mas-Hesse et al. 2003).

The AGN surveys provided by *Swift*/BAT (Tueller et al. 2008) and *INTEGRAL* IBIS/ISGRI (Beckmann et al. 2006b; Bassani et al. 2007) have already led to the discovery that the fraction of absorbed and Compton thick sources is less than expected from cosmic X-ray background synthesis models (e.g. Treister & Urry 2005; Gilli et al. 2007). With the ongoing *INTEGRAL* mission, it is now possible to compile a large sample of AGN for spectroscopic and correlation studies and to probe the unified model for AGN. The data analysis is described in Sect. 2, the average properties of the AGN in the sample in Sect. 3, the discussion of the properties in the view of unified models in Sect. 4, and we end with the conclusions in Sect. 5. Notes on individual sources can be found in the Appendix (Sect. A).

2. Data analysis

The list of AGN presented here is based on all *INTEGRAL* detections of AGN reported in the literature, therefore enter into the *INTEGRAL* general reference catalogue¹ (Ebisawa et al. 2003; Bodaghee et al. 2007). It has to be pointed out that for many sources, we present the first *INTEGRAL* spectral analysis, because Bodaghee et al. (2007), Sazonov et al. (2007), and Bassani et al. (2006) did not include spectral analysis, and Beckmann et al. (2006) discussed a sample of 38 AGN based only on

¹ For the latest version of the catalogue see <http://isdc.unige.ch/index.cgi?Data-catalogs>

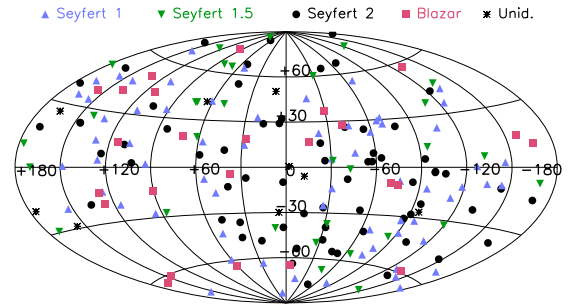


Fig. 1. *INTEGRAL*-detected AGN during the first 5 years of the mission. As unidentified we mark those sources where the AGN type has not been determined yet.

1.3 years of *INTEGRAL* data. With the *INTEGRAL* mission continuing smoothly, most of the sky has been observed in the first 5 years of operations, leading to a rather uniform sky distribution of detected AGN, as shown in Fig. 1. For each extragalactic source, we analysed the IBIS/ISGRI, JEM-X, and OMC data from the early mission (revolution 26 starting on 30 December 2002) up to spacecraft revolution 530 (ending on 17 February 2007), covering more than 4 years of data. To include only high-quality data, the selection considers ISGRI data taken at an off-axis angle smaller than 10° and includes only those observations that lasted for at least 500 s. Analysis software used in this work is version 7 of the Offline Standard Analysis Software (OSA) provided by the ISDC Data Centre for Astrophysics (Courvoisier et al. 2003). For each source, imaging analysis was performed to determine the significant sources in the field around the AGN. Taking their fluxes into account is important when analysing data from coded-mask instruments, because all sources in the field add to the background of the source of interest. Then standard spectral extraction was used, considering all significant sources in the field.

For the X-ray monitor JEM-X, a similar selection of data was performed, using a maximum off-axis angle of 3° due to the smaller field of view compared to IBIS. The much lower effective exposure time when compared to IBIS/ISGRI (Table 1) results in only 23 detections of AGN by JEM-X with a significance $>5\sigma$. For JEM-X, spectra were extracted from the mosaic images, since this procedure is more reliable for faint sources than the standard spectral extraction in OSA 7.

Naturally, some sources reported in the literature do not show up significantly in the data analysed here, because they were observed after February 2007, or they are, like the blazar class, highly variable and therefore do not give a significant detection in the combined data set. The 199 AGN reported to be found in *INTEGRAL* data are listed in Table 1, together with their redshift, position (J2000.0), and their effective exposure time in IBIS/ISGRI and JEM-X for the data set used here. Twelve sources, which were reported in the literature but gave a detection significance $<3\sigma$ in the data presented here are listed in Table 1 and marked by an x. These objects are not considered in the following analysis. All errors given in this paper are at the 1σ level.

2.1. Black hole masses

We also include in Table 1 the black hole masses of the central engine and the method used to determine them, as found in the literature. Different methods can be used to estimate the mass of

Table 1. INTEGRAL AGN catalogue. The column *Method* indicates the method used to determine the black hole mass, see Sect. 2.1 for details.

Name	Type	z	RA [deg]	Dec [deg]	ISGRI [ks]	JEM-X [ks]	$\log M_{\text{BH}}$ [M_{\odot}]	Method
IGR J00040+7020 ^x	Sy2	0.096	1.00638	70.32125	1947.3	20.9		
IGR J00254+6822	Sy2	0.012	6.38092	68.36147	2534.6	178.9		
IGR J00335+6126	Sy1	0.105	8.3265	61.46178	3338.7	356.5	8.5 ± 0.5^a	LL/CL
IES 0033+59.5	BLLac	0.086	8.96929	59.83461	3338.7	356.4		
Mrk 348	Sy2	0.0151	12.19642	31.95697	150.7	21.1	7.2 ± 0.7^b	SO
NGC 418 ^x	AGN	0.0190	17.64842	-30.22128	38.5	-		
NGC 526A	Sy1.5	0.0191	20.97583	-35.06528	73.7	-	8.1 ± 0.7^c	S
ESO 297-18	Sy2	0.0252	24.65492	-40.01131	59.5	-	9.7 ± 0.5^n	KM
IGR J01528-0326	Sy2	0.0167	28.20375	-3.44749	837.1	79.6		
NGC 788	Sy2	0.0136	30.27687	-6.81553	926.6	117.9	7.5 ± 0.7^b	SO
Mrk 590	Sy1.2	0.0264	33.63984	-0.76669	936.0	266.6	$7.14^{+0.1}_{-0.09}^d$	R
IGR J02097+5222	Sy1	0.0492	32.40700	52.44543	698.4	2.0		
SWIFT J0216.3+5128	Sy2	0.0288	34.11292	51.42375	481.9	2.0		
Mrk 1040	Sy1.5	0.0167	37.06079	31.31094	42.8	-	7.6 ± 0.3^e	S
IGR J02343+3229	Sy2	0.0162	38.57500	32.48333	70.5	-		
NGC 985	Sy1	0.0431	38.65738	-8.78761	808.1	48.3	8.9 ± 0.5^n	KM
NGC 1052	Sy2	0.0050	40.27000	-8.25578	707.0	31.1	8.2 ± 0.3^e	S
RBS 345	Sy1	0.0690	40.56667	5.53000	443.2	-		
NGC 1068	Sy2	0.0288	40.67012	-0.01344	914.4	44.8	7.2 ± 0.1^e	M
QSO B0241+62	Sy1	0.0446	41.24042	62.46847	711.9	35.2		
IGR J02466-4222	AGN	0.0695	41.65375	-42.36600	191.4	21.9		
IGR J02501+5440	Sy2	0.015	42.67417	54.70419	773.8	13.5		
MCG-02-08-014	Sy2	0.0168	43.09750	-8.51042	528.1	4.7		
NGC 1142	Sy2	0.0288	43.80133	-0.18381	634.1	-	9.4 ± 0.5^n	KM
QSO B0309+411	Sy1	0.136	48.25817	41.33366	488.4	303.1		
IGR J03184-0014 ^x	QSO	-	49.60000	-0.22889	-	-		
NGC 1275	Sy2	0.0176	49.95067	41.51170	506.8	282.0	8.5 ± 0.7^e	S
IH 0323+342	Sy1	0.0629	51.17150	34.17941	431.6	0.9		
IGR J03334+3718	Sy1.5	0.0547	53.32833	37.30305	463.4	5.6		
NGC 1365	Sy1.5	0.0055	53.40208	-36.13806	143.3	3.0	7.7 ± 0.3^f	S
IGR J03532-6829	BLLac	0.0870	58.30833	-68.48306	740.8	9.4		
3C 111	Sy1	0.0485	64.58867	38.02661	160.1	-	9.6 ± 0.8^c	B
3C 120	Sy1	0.0330	68.29623	5.35434	365.9	79.3	7.7 ± 0.2^g	R
UGC 3142	Sy1	0.0217	70.94537	28.97194	449.6	39.9		
LEDA 168563	Sy1	0.0290	73.01958	49.54583	112.5	-		
ESO 33-2	Sy2	0.0181	73.99834	-75.54056	1110.4	-		
4U 0517-17	Sy1.5	0.0179	77.68958	16.49861	1145.4	19.8		
Ark 120	Sy1	0.0327	79.04784	-0.15017	571.9	63.1	$8.18^{+0.05}_{-0.06}^g$	R
IGR J05270-6631 ^x	QSO	0.978	81.56021	-66.5125	631.7	323.4	8.4 ± 0.5^a	LL/CL
PKS 0528+134 ^x	blazar	2.060	82.73507	13.53199	917.6	157.3		
NGC 2110	Sy2	0.0078	88.04742	-7.45622	20.5	-	8.3 ± 0.3^e	S
MCG+08-11-011	Sy1.5	0.0205	88.72338	46.43934	50.8	-	8.1 ± 0.6^c	SO
IRAS 05589+2828	Sy1	0.0330	90.54042	28.47139	1689.9	29.0		
SWIFT J0601.9-8636	Sy2	0.0064	91.41292	-86.63111	177.8	31.9	7.9 ± 0.5^n	KM
IGR J06117-6625	Sy1.5	0.230	92.95208	-66.40847	1122.2	97.2		
Mrk 3	Sy2	0.0135	93.90129	71.03748	814.9	55.4	8.7 ± 0.3^e	S
IGR J06239-6052	Sy2	0.0405	95.94004	-60.97927	598.0	-		
IGR J06292+4858 ^x	BLLac	0.097	97.300	48.97389	-	-		
PKS 0637-752	Sy1	0.651	98.94379	-75.27133	1066.6	22.7	9.4 ± 0.5^e	CL
Mrk 6	Sy1.5	0.0188	103.0513	74.42689	819.4	109.7	8.2 ± 0.5^n	KM
QSO B0716+714	BLLac	0.3	110.4727	71.34343	863.8	162.8		
LEDA 96373	Sy2	0.0294	111.6096	-35.90583	180.9	5.6		
IGR J07437-5137	Sy2	0.025	115.9208	-51.61694	947.3	-		
IGR J07565-4139	Sy2	0.021	119.0817	-41.62836	1703.0	50.6		
IGR J07597-3842	Sy1	0.040	119.9242	-38.73223	1288.1	31.8	8.3 ± 0.5^p	LL
ESO 209-12	Sy1.5	0.0405	120.4900	-49.77833	2288.6	117.7		
PG 0804+761	Sy1	0.10	122.7444	76.04514	694.9	44.9	$8.84^{+0.05}_{-0.06}^g$	R
Fairall 1146	Sy1.5	0.0316	129.6279	-35.99306	1689.9	26.2		
QSO B0836+710	BLLac	2.1720	130.3515	70.89506	754.4	29.7		
IGR J09026-4812 ^m	Sy1	0.039	135.6555	-48.22608	3773.3	470.1		
SWIFT J0917.2-6221	Sy1	0.0573	139.0392	-62.32486	669.0	16.1		
IGR J09253+6929	Sy1	0.039	141.321	69.488	324.1	-	7.6 ± 0.5^a	LL/CL
Mrk 110	NLS1	0.0353	141.3036	52.28625	54.2	-	$7.42^{+0.09}_{-0.1}^g$	R
IGR J09446-2636	Sy1.5	0.1425	146.1500	-26.60000	157.1	-		
NGC 2992	Sy1	0.0077	146.4252	-14.32639	383.3	66.7	7.7 ± 0.3^e	S

Table 1. continued.

Name	Type	z	RA [deg]	Dec [deg]	ISGRI [ks]	JEM-X [ks]	$\log M_{\text{BH}}$ [M_{\odot}]	Method
MCG-05-23-016	Sy2	0.0085	146.9173	-30.94886	130.2	-	6.3 ± 0.5^c	SO
IGR J09523-6231	Sy1.5	0.252	148.0854	-62.54333	1059.1	111.1	-	-
NGC 3081	Sy2	0.0080	149.8731	-22.82628	255.3	-	7.4 ± 0.3^b	S
SWIFT J1009.3-4250	Sy2	0.033	152.4512	-42.81222	437.4	-	-	-
IGR J10147-6354	Sy1.2	0.202	153.6750	-63.89194	1182.9	104.6	8.6 ± 0.5^a	LL/CL
NGC 3227	Sy1.5	0.0039	155.8776	19.86492	142.0	-	$7.3^{+0.2^h}_{-0.1}$	K
NGC 3281	Sy2	0.0107	157.9669	-34.85369	211.3	41.9	8.0 ± 0.5^a	KM
SWIFT J1038.8-4942	Sy1.5	0.060	159.6875	-49.78194	908.6	10.2	-	-
IGR J10404-4625	Sy2	0.0237	160.0928	-46.42353	673.6	-	-	-
Mrk 421	BLLac	0.0300	166.1138	38.20883	826.1	482.4	8.3 ± 0.3^e	S
IGR J11366-6002	Sy2	0.014	174.1754	-60.05217	2196.0	315.7	-	-
NGC 3783	Sy1	0.0097	174.7574	-37.73853	22.9	-	$7.47^{+0.07^g}_{-0.09}$	R
IGR J12026-5349	Sy2	0.028	180.6985	-53.83547	1535.9	116.6	-	-
NGC 4051	Sy1.5	0.0023	180.7901	44.53144	793.2	-	6.3 ± 0.2^g	R
NGC 4138	Sy1.5	0.0030	182.3745	43.68500	798.4	31.4	6.8 ± 0.5^a	KM
NGC 4151	Sy1.5	0.0033	182.6364	39.40545	820.3	548.3	$7.5^{+0.1^h}_{-0.6}$	K
NGC 4180	AGN	0.0070	183.2627	7.03881	1016.8	72.1	-	-
Was 49	Sy2	0.0610	183.5742	29.52872	931.4	-	-	-
Mrk 766	Sy1.5	0.0129	184.6110	29.81267	994.6	-	6.5 ± 0.3^i	S
NGC 4258	Sy1.5	0.0015	184.7397	47.30397	816.2	4.6	7.59 ± 0.01^i	M
4C 04.42	BLLac	0.9650	185.5940	4.22106	1277.5	232.6	-	-
Mrk 50	Sy1	0.0234	185.8506	2.67911	1320.8	264.8	-	-
NGC 4388	Sy2	0.0084	186.4455	12.66203	869.2	146.8	7.2 ± 0.6^b	SO
NGC 4395	Sy1.5	0.0011	186.4539	33.54661	1103.5	-	$4.7^{+0.3^i}_{-0.7}$	V
3C 273	QSO	0.1583	187.2779	2.05239	2004.6	299.2	$9.81^{+0.1^k}_{-0.07}$	R
NGC 4507	Sy2	0.0118	188.9023	-39.90925	389.3	-	7.6 ± 0.6^c	SO
SWIFT J1238.9-2720	Sy2	0.0250	189.7271	-27.30778	71.3	-	8.6 ± 0.5^a	KM
IGR J12391-1612	Sy2	0.0367	189.7762	-16.17975	618.7	39.4	8.9 ± 0.5^a	KM
NGC 4593	Sy1	0.0090	189.9143	-5.34425	1466.5	213.5	$6.99^{+0.08^h}_{-0.1}$	R
IGR J12415-5750	Sy1.5	0.0242	190.3575	-57.83417	1653.1	101.6	8.0 ± 0.5^a	LL/CL
PKS 1241-399	QSO	0.1910	191.1223	-40.21289	551.3	-	-	-
ESO 323-32	Sy1	0.0160	193.3348	-41.63717	744.4	23.9	-	-
3C 279	BLLac	0.5362	194.0465	-5.78931	1144.1	185.0	8.4 ± 0.5^e	CL
IGR J13000+2529 ^x	AGN	-	195.0000	25.48333	937.1	241.0	-	-
Mrk 783	Sy1.5	0.0672	195.7452	16.40763	728.2	11.2	-	-
IGR J13038+5348	Sy1	0.0302	195.9975	53.79172	366.3	16.5	7.5 ± 0.5^a	KM
NGC 4945	Sy2	0.0019	196.3587	-49.47083	1100.0	141.8	6.2 ± 0.3^l	M
IGR J13057+2036	AGN	-	196.4273	20.58103	853.1	12.0	-	-
ESO 323-77	Sy1	0.0150	196.6108	-40.41389	920.1	65.3	7.4 ± 0.6^c	LL
IGR J13091+1137	Sy2	0.025	197.2733	11.63414	391.1	8.2	8.6 ± 0.5^a	KM
IGR J13109-5552	Sy1	0.104	197.6795	-55.86991	1506.6	26.6	-	-
NGC 5033	Sy1.5	0.0029	198.3650	36.59358	743.2	6.2	-	-
IGR J13149+4422	Sy2	0.0366	198.8155	44.40750	421.4	56.8	-	-
Cen A	Sy2	0.0018	201.3651	-43.01911	1268.0	149.5	8.0 ± 0.6^c	K
ESO 383-18	Sy2	0.0124	203.3596	-34.01631	756.8	191.6	-	-
MCG-06-30-015	Sy1.2	0.0077	203.9741	-34.29558	767.2	213.0	$6.7^{+0.1^i}_{-0.2}$	S
NGC 5252	Sy2	0.0230	204.5667	4.54236	58.9	-	$9.03^{+0.4^l}_{-0.02}$	K
Mrk 268	Sy2	0.0399	205.2964	30.37811	728.7	-	-	-
4U 1344-60	Sy1.5	0.0129	206.8833	-60.61000	1537.7	231.2	-	-
IC 4329A	Sy1	0.0161	207.3304	-30.30956	381.9	52.6	$\sim 7^g$	R
Circinus Galaxy	Sy2	0.0014	213.2871	-65.34084	2272.1	201.3	$6.04^{+0.07^l}_{-0.09}$	M
NGC 5506	Sy1.9	0.0062	213.3120	-3.20750	102.9	88.5	6.7 ± 0.7^b	SO
IGR J14175-4641	Sy2	0.076	214.2664	-46.69419	1268.8	21.4	-	-
NGC 5548	Sy1.5	0.0172	214.4985	25.13706	200.9	42.4	7.82 ± 0.02^h	R
RHS 39	Sy1	0.0222	214.8425	-26.64472	454.4	8.1	8.7 ± 0.5^a	KM
H 1426+428	BLLac	0.1291	217.1358	42.67472	499.5	224.7	9.1 ± 0.7^e	SB
IGR J14471-6414	Sy1	0.053	221.6158	-64.27319	1797.1	171.8	-	-
IGR J14471-6319	Sy2	0.038	221.8120	-63.28868	1842.9	230.3	-	-
IGR J14492-5535	AGN	-	222.3038	-55.60578	1886.0	142.4	-	-
IGR J14515-5542	Sy2	0.018	222.8880	-55.67733	1869.2	144.0	-	-
IGR J14552-5133	NLS1	0.016	223.8223	-51.57102	2007.3	7.9	6.3 ± 0.5^p	LL
IGR J14561-3738	Sy2	0.024	224.0342	-37.64803	2185.9	340.8	-	-

Table 1. continued.

Name	Type	z	RA [deg]	Dec [deg]	ISGRI [ks]	JEM-X [ks]	$\log M_{\text{BH}}$ [M_{\odot}]	Method
IGR J14579-4308	Sy2	0.016	224.4296	-43.13000	2012.9	333.4		
Mrk 841	Sy1.5	0.0364	226.0050	10.43782	131.3	6.7	8.5 ± 0.7^c	R
ESO 328-36	Sy1	0.0237	228.6958	-40.35861	2200.9	384.8		
IGR J15161-3827	Sy2	0.0365	229.0375	-38.44806	2181.2	372.1		
NGC 5995	Sy2	0.0252	237.1040	-13.75778	1129.2	28.6		
IGR J15539-6142	Sy2	0.015	238.3967	-61.68206	1754.0	101.0		
IGR J16024-6107	Sy2	0.0114	240.4517	-61.14822	1792.4	84.3		
IGR J16056-6110	Sy1.5	0.052	241.4643	-61.19525	1727.2	64.4		
IGR J16119-6036	Sy1	0.016	242.9642	-60.63194	1789.6	60.9		
IGR J16185-5928	NLS1	0.035	244.6518	-59.45482	2066.0	44.6	7.4 ± 0.5^p	LL
IGR J16351-5806	Sy2	0.009	248.8071	-58.08047	2230.3	39.3		
IGR J16385-2057	NLS1	0.0269	249.6250	-20.94389	1505.9	80.4		
IGR J16426+6536	NLS1	0.323	250.7670	65.54747	56.0	-	7.0 ± 0.5^c	LL/CL
IGR J16482-3036	Sy1	0.0313	252.0623	-30.58502	2450.9	53.7		
ESO 138-1	Sy2	0.0091	252.8333	-59.23389	1509.2	21.4		
NGC 6221	Sy2	0.0050	253.1942	-59.21639	1481.0	21.4		
NGC 6240	Sy2	0.0245	253.2457	2.40047	300.5	67.7		
Mrk 501	BLLac	0.0337	253.4676	39.76017	476.3	70.6	9.2 ± 0.3^e	S
IGR J16558-5203	Sy1	0.054	254.0234	-52.06135	3065.7	249.6	7.9 ± 0.5^p	LL
IGR J16562-3301	BLLac	-	254.0701	-33.03680	3669.2	111.4		
NGC 6300	Sy2	0.0037	259.2467	-62.81972	237.9	8.9	5.5 ± 0.4^c	X
IGR J17204-3554	AGN	-	260.1042	-35.90000	6318.5	292.3		
QSO B1730-130 ^x	QSO	0.9020	263.2613	-13.08042	1080.1	33.1		
GRS 1734-292	Sy1	0.0214	264.3681	-29.13403	9122.1	665.7	8.9 ± 0.7^q	SO
IGR J17418-1212	Sy1	0.0372	265.4625	-12.19611	1300.1	45.5		
IGR J17488-3253	Sy1	0.020	267.2297	-32.91449	6159.4	410.4		
IGR J17513-2011	Sy2	0.047	267.8068	-20.20405	6220.1	268.7	6.0 ± 0.5^p	LL
IGR J18027-1455	Sy1	0.0034	270.6974	-14.91522	2463.8	173.0		
IGR J18244-5622	Sy2	0.0169	276.0812	-56.36909	103.3	4.4		
IGR J18249-3243	Sy1	0.355	276.2361	-32.71661	5126.8	208.7		
IGR J18259-0706	Sy1?	-	276.48958	-7.17264	2009.5	226.1		
PKS 1830-211	BLLac	2.5070	278.4162	-21.06106	2775.4	111.2		
3C 382	Sy1	0.0579	278.7641	32.69635	15.2	0.7	9.2 ± 0.5^n	KM
ESO 103-35	Sy2	0.0133	279.5846	-65.42805	28.5	-	7.1 ± 0.6^c	X
3C 390.3	Sy1	0.0561	280.5374	79.77142	448.0	33.2	$8.46^{+0.09g}_{-0.1}$	R
ESO 140-43 ^x	Sy1	0.0141	281.2917	-62.35583	378.0	27.7		
IGR J18559+1535	Sy1	0.084	284.0000	15.63694	2594.9	24.7		
ESO 141-55 ^x	Sy1	0.0366	290.3092	-58.67083	378.0	79.9	7.1 ± 0.6^c	SO
IRXS J192450.8-29143	BLLac	0.3520	291.2127	-29.24170	955.7	28.6		
1H 1934-063	Sy1	0.0106	294.3879	-6.21806	654.2	2.1	7.9 ± 0.6^c	SO
IGR J19405-3016	Sy1	0.052	295.0631	-30.26347	930.3	22.3		
NGC 6814	Sy1.5	0.0052	295.6683	-10.32333	438.5	7.4	7.1 ± 0.2^h	CL
IGR J19473+4452	Sy2	0.0539	296.8307	44.82845	1194.3	1.0		
3C 403	Sy2	0.0590	298.0617	2.50778	490.2	-		
QSO B1957+405	Sy2	0.0561	299.8682	40.73386	2258.1	69.5	9.4 ± 0.1^l	K
IES 1959+650 ^x	BLLac	0.048	299.9994	65.14851	11.2	-	8.1 ± 0.3^e	S
ESO 399-20	NLS1	0.0250	301.7383	-34.54833	857.2	24.7		
IGR J20187+4041	Sy2	0.0144 ^r	304.6606	40.68344	2851.0	442.7		
IGR J20286+2544	Sy2	0.013	307.1462	25.73361	840.2	4.1		
4C 74.26 ^x	QSO	0.1040	310.6549	75.13403	77.1	-	9.6 ± 0.5^e	CL
Mrk 509	Sy1.2	0.0344	311.0406	-10.72348	71.7	57.3	$8.16^{+0.03g}_{-0.04}$	R
S5 2116+81	Sy1	0.086	318.5021	82.07975	176.5	-	8.8 ± 0.5^n	KM
IGR J21178+5139	AGN	-	319.4468	51.64823	1261.9	171.3		
IGR J21247+5058	Sy1	0.020	321.1640	50.97329	1392.7	174.7		
IGR J21272+4241 ^x	Sy1.5	0.316	321.7917	42.69194	836.3	189.8		
IGR J21277+5656	Sy1	0.0144	321.9373	56.94436	984.5	166.6		
RX J2135.9+4728	Sy1	0.0252	323.9766	47.47453	1213.4	136.3		
PKS 2149-306	FSRQ	2.345	327.9813	-30.46492	258.6	47.1		
NGC 7172	Sy2	0.0086	330.5071	-31.87167	346.5	68.8	7.7 ± 0.6^c	SO
BL Lac	BLLac	0.0686	330.6804	42.27778	738.1	-	8.2 ± 0.7^e	SB
IGR J22292+6647	Sy1 ^p	0.113 ^p	337.3062	66.78106	1678.9	9.3		
NGC 7314	Sy1	0.0048	338.9419	-26.05047	546.8	1.7	6.0 ± 0.5^c	S
Mrk 915	Sy1	0.0241	339.1938	-12.54517	609.0	12.8		
IGR J22517+2217	BLLac	3.668	342.9280	22.29900	251.3	5.8		
3C 454.3	BLLac	0.8590	343.4906	16.14822	207.1	36.3	9.2 ± 0.7^e	CL

Table 1. continued.

Name	Type	z	RA [deg]	Dec [deg]	ISGRI [ks]	JEM-X [ks]	$\log M_{\text{BH}}$ [M_{\odot}]	Method
IH 2251-179	Sy1	0.0640	343.5245	-17.58203	579.2	314.6	$< 6.9^e$	W
NGC 7469	Sy1	0.0163	345.8156	8.87386	139.2	–	7.09 ± 0.05^g	R
MCG-02-58-022	Sy1.5	0.0469	346.1812	-8.68572	624.5	28.2	7.1 ± 0.6^e	SO
NGC 7603 ^x	Sy1.5	0.0295	349.7359	0.24347	104.5	–	8.1 ± 0.3^e	S
IGR J23206+6431	Sy1	0.0732	350.15	64.52	3888.2	349.8	–	–
IGR J23308+7120	Sy2	0.037	352.6552	71.37911	1965.1	–	–	–
IGR J23524+5842	Sy2	0.164	358.0917	58.75908	4076.7	361.1	–	–

^{*} Beckmann et al. (2007b); ^a Masetti et al. (2009); ^b Bian & Gu (2007); ^c Middleton et al. (2008); ^d Kaspi et al. (2000); ^e Woo & Urry (2002); ^f Merloni et al. (2003); ^g Peterson et al. (2004); ^h Hicks & Malkan (2008); ⁱ Uttley & McHardy (2005); ^k Paltani & Türler (2005); ^l Graham (2008); ^m Zurita-Heras et al. (2009); ⁿ Winter et al. (2009); ^o Butler et al. (2009); ^p Masetti et al. (2006); ^q see Appendix A; ^r Goncalves et al. (2009); ^x not detected in the data set presented here.

the central black hole M_{BH} in an AGN or a normal galaxy, most of them still carrying fairly large uncertainties. Nevertheless, considering the importance of the black hole mass in studying the properties of these objects, we decided to include a compilation of the mass estimates from the literature as the best guess that can be provided at present for each object in this catalogue.

We have included masses estimated from gas and/or stellar kinematics in the nuclear region of the galaxy, in the presence (method “M”, see e.g. Greenhill 1997) or not (“K”, Hicks & Malkan 2008) of a water maser, from assuming virialized motions of the broad line region (BLR) clouds, either using the reverberation-mapping technique (“R”, Kaspi et al. 2000) or estimating the size of the BLR from the emission line luminosity (of the $H\beta$ line usually; “LL”, Wu et al. 2004) or from the optical continuum luminosity (usually measured at 5100 Å; “CL”, Kaspi et al. 2000). Other methods are based on the empirical relation between the black hole mass and the stellar velocity dispersion σ_s , using either direct measurements of the latter (“S”, Ferrarese & Merritt 2000) or indirect estimates of σ_s from the width of the [O III] line (“SO”, Greene & Ho 2005) or from the morphological parameters of the bulge (“SB”, O’Dowd et al. 2002). Some estimates use the bulge luminosity (“B”, Wandel 2002), the K -band stellar magnitude (assuming that it is dominated by the bulge; “KM”, Novak et al. 2006), the X-ray variability time scales (“X”, Gierliński et al. 2008), or the properties of outflowing warm absorber clouds (“W”, Morales & Fabian 2002). Whenever the uncertainty on the estimate of the black hole mass is not available in the reference paper, we assumed a conservative one following the typical uncertainties of the method used for the mass measurement.

The most reliable methods are those involving direct measurements of gas and stellar kinematics, with average uncertainties in the range 0.15–0.3 dex, reaching 0.1 dex or less when water maser emission is detected (see Vestergaard 2004, for more details). Also the reverberation mapping technique provides black hole masses with accuracy around 0.15–0.3 dex, which drops to values of 0.4–0.5 dex and even to 1 dex when the radius of the BLR is estimated from the emission line or the continuum luminosity. Masses estimated from the stellar velocity dispersion can have uncertainties around 0.3 dex when σ_s is directly measured, while indirect measurements of σ_s result in much less precise estimates (≥ 0.7 dex). Larger uncertainties are provided by the other methods mentioned above, 0.5–0.6 dex for method “B”, 0.5–1 dex for “X” (Awaki et al. 2005), 0.5 dex for “KM” (Winter et al. 2009), and only upper limits can be derived with the method based on outflowing warm absorber clouds.

2.2. X-ray spectral fitting

For all 187 objects with a detection significance above 3σ in the IBIS/ISGRI 18–60 keV energy band, spectral analysis was performed using an absorbed power law with N_{H} fixed to the value reported in the literature (Table 2) and adopting XSPEC version 11.3.2 (Arnaud 1996). When the significance was below 5σ , the photon index was fixed to $\Gamma = 2$. The N_{H} value used for the fitting is the intrinsic absorption plus the Galactic hydrogen column density, whereas in Table 2 only the intrinsic absorption is reported. In cases where no absorption information was found, *Swift/XRT* and *XMM-Newton* data were analysed to determine the level of absorption. For those objects detected only at a low significance level (i.e. between 3 and 5σ), the photon index was fixed to $\Gamma = 2.0$ in order to extract a flux value. Table 2 gives the fit results to the IBIS/ISGRI data. Fluxes are model fluxes according to the best-fit result. In the cases where a cut-off power law model gave a significantly better fit to the ISGRI data we set the Γ column to “C”. For these 12 objects, the fluxes reported are based on the best-fit model reported in Table 3. These 12 sources and all sources that gave a high IBIS/ISGRI detection significance of $>30\sigma$ are also discussed in more detail in Appendix A.

The JEM-X spectra of the 23 AGN detected by the X-ray monitor were fit with the IBIS/ISGRI data and results reported in Table 4. As for the ISGRI spectra alone, we also did not fit the absorption values in the case of the combined JEM-X/ISGRI spectra, because the JEM-X data starting at 3 keV did not allow a significant constraint on N_{H} in most cases. In cases where the flux of the source varied significantly, so no combined fit could be performed resulting in $\chi^2_{\nu} < 2$, only simultaneous data were used (e.g. in the case of NGC 4388). For two AGN, NGC 1275 and IGR J17488–3253, a more complex model than an absorbed cut-off power law was required to represent the combined JEM-X and IBIS/ISGRI data (see Appendix A).

2.3. Optical data

Optical data in the V band are provided by the optical monitoring camera (OMC). Data were extracted from the OMC Archive² getting one photometric point per shot. The photometric apertures were centred on the source position, as listed in version 5 of the OMC Input Catalogue (Domingo et al. 2003). The fluxes and magnitudes were derived from a photometric aperture of 3×3 pixels (1 pixel = 17.504 arcsec), slightly circularized,

² <http://sdc.laeff.inta.es/omc/>

Table 2. Spectral fit results for IBIS/ISGRI data.

Name	ISGRI 18–60 keV [σ]	N_{H} [10^{22} cm $^{-2}$]	f_{20-40} keV [10^{-11} erg cm $^{-2}$ s $^{-1}$]	f_{40-100} keV [10^{-11} erg cm $^{-2}$ s $^{-1}$]	Γ_{ISGRI}^+	$\log L_{20-100}$ keV [erg s $^{-1}$]
IGR J00254+6822	7.5	40 ^c	0.6	0.8	2.1 ± 0.5	42.67
IGR J00335+6126	5.9	0.5 ^s	0.3	0.9	1.1 ± 0.2	44.50
IES 0033+59.5	12.6	0.36 ^a	0.8	0.3	3.6 ^{+0.4} _{-0.3}	44.36
Mrk 348	14.6	30 ^b	4.2	6.6	C	43.74
NGC 526A	4.3	1.6 ^b	2.2	2.9	2	43.62
ESO 297-18	5.2	42 ⁱ	3.1	6.8	1.5 ± 0.3	44.10
IGR J01528-0326	8.5	14 ^c	0.9	2.3	1.2 ^{+0.2} _{-0.5}	43.30
NGC 788	23.4	<0.02 ^a	2.5	3.9	1.8 ± 0.1	43.42
Mrk 590	4.5	0.03	0.5	0.6	2	43.23
IGR J02097+5222	7.7	0.03 ⁱ	1.2	2.0	1.7 ^{+0.3} _{-0.2}	44.25
SWIFT J0216.3+5128	5.1	1.27 ^f	0.8	0.8	2.3 ^{+0.2} _{-1.0}	43.48
Mrk 1040	3.4	0.067 ^b	2.3	3.0	2	43.52
IGR J02343+3229	3.5	2.2 ^d	1.4	1.8	2	43.27
NGC 985	5.8	0.6 ^b	0.9	1.3	2.0 ^{+0.4} _{-0.3}	43.99
NGC 1052	5.6	0.041 ^b	0.8	1.5	1.6 ^{+0.8} _{-0.4}	42.11
RBS 345	5.0	–	0.9	1.9	1.3 ^{+0.6} _{-0.4}	44.49
NGC 1068	7.3	>150 ^a	1.2	1.3	2.3 ^{+0.4} _{-0.3}	43.68
QSO B0241+62	16.3	1.5 ^a	2.0	3.0	1.8 ± 0.1	44.37
IGR J02466–4222	3.3	1	1.0	1.4	2	44.45
IGR J02501+5440	5.1	–	0.6	1.5	1.2 ± 0.3	43.03
MCG-02-08-014	6.3	–	1.3	0.9	2.7 ^{+0.6} _{-0.5}	43.15
NGC 1142	16.2	45 ^b	2.7	4.2	1.8 ± 0.1	44.11
QSO B0309+411	4.0	<0.1 ^s	3.0	3.9	2	45.53
NGC 1275	15.7	3.75 ^a	2.2	0.4	3.7 ^{+0.3} _{-0.2}	43.18
1H 0323+342	5.1	0.1 ^b	0.7	2.4	1.0 ^{+0.4} _{-0.7}	44.43
IGR J03334+3718	6.9	–	1.0	1.5	1.9 ± 0.3	44.25
NGC 1365	5.1	44 ^b	1.5	2.2	1.8 ± 0.6	42.38
IGR J03532-6829	7.3	0.05 ^s	1.4	0.6	3.5 ^{+0.7} _{-0.6}	44.63
3C 111	13.7	0.63 ^a	5.3	6.9	2.0 ± 0.2	44.83
3C 120	22.0	0.2 ⁱ	3.0	4.4	1.8 ± 0.1	44.27
UGC 3142	17.3	1.4 ^x	2.8	3.7	2.0 ± 0.1	44.84
LEDA 168563	5.4	<0.22 ^j	2.2	3.1	1.9 ^{+0.5} _{-0.4}	44.00
ESO 33-2	15.5	0.1 ^b	1.3	2.0	1.8 ± 0.2	43.38
4U 0517+17	24.5	0.1 ^b	3.0	3.6	2.13 ^{+0.09} _{-0.08}	43.68
Ark 120	15.6	<0.1 ^s	2.7	3.4	2.1 ± 0.1	44.18
NGC 2110	4.9	4.3 ^s	7.0	9.3	2	43.34
MCG+08-11-011	7.8	0.183 ^b	5.2	6.7	2.0 ± 0.4	44.05
IRAS 05589+2828	15.4	<0.04 ⁱ	1.4	2.8	1.5 ^{+0.2} _{-0.1}	44.02
SWIFT J0601.9-8636	6.5	5.6 ⁱ	1.3	1.0	2.6 ^{+0.1} _{-0.6}	42.32
IGR J06117-6625	17.8	0.048 ^b	1.9	2.6	1.96 ± 0.16	45.85
Mrk 3	26.7	110 ^a	3.7	6.4	1.73 ± 0.07	43.61
IGR J06239-6052	3.6	20 ^b	0.5	0.7	2	43.65
PKS 0637-752	5.4	0.035 ^b	0.7	1.1	1.7 ± 0.6	46.45
Mrk 6	15.1	10 ^a	1.9	2.3	2.1 ± 0.2	43.53
QSO B0716+714	4.6	<0.01 ^a	0.3	0.3	2	45.24
LEDA 96373	5.3	–	1.4	2.6	1.5 ^{+0.7} _{-0.5}	43.89
IGR J07437-5137	3.5	–	0.4	0.5	2	43.13
IGR J07565-4139	6.2	1.1 ^b	0.7	0.6	2.7 ^{+0.6} _{-0.4}	43.12
IGR J07597-3842	14.2	0.05 ^b	1.8	1.9	2.3 ± 0.2	44.14
ESO 209-12	12.2	0.1 ^b	0.9	1.4	1.8 ^{+0.1} _{-0.2}	43.93
PG 0804+761	6.3	0.023 ^b	1.1	1.5	2.0 ± 0.5	44.81
Fairall 1146	9.9	0.1 ^b	0.9	1.4	1.8 ^{+0.3} _{-0.2}	43.73
QSO B0836+710	15.4	0.11 ^a	2.1	4.1	1.5 ^{+0.2} _{-0.1}	47.93
IGR J09026-4812	17.8	0.9 ^w	0.9	1.4	1.9 ± 0.1	43.91
SWIFT J0917.2-6221	5.8	0.5 ^f	0.8	1.1	1.9 ^{+0.5} _{-0.6}	44.18
IGR J09253+6929	7.0	8 ^d	1.8	2.6	1.9 ± 0.4	44.19
Mrk 110	3.6	0.019 ^b	2.2	3.0	2	44.18
IGR J09446-2636	3.2	0.1 ^b	1.3	1.7	2	45.60

Table 2. continued.

Name	ISGRI 18–60 keV [σ]	N_{H} [10^{22} cm $^{-2}$]	f_{20-40} keV [10^{-11} erg cm $^{-2}$ s $^{-1}$]	f_{40-100} keV [10^{-11} erg cm $^{-2}$ s $^{-1}$]	Γ_{ISGRI}^+	$\log L_{20-100}$ keV [erg s $^{-1}$]
NGC 2992	15.8	0.1 ^l	2.8	4.1	1.9 ± 0.1	42.95
MCG-05-23-016	14.6	1.6 ^a	5.6	8.1	1.9 ± 0.1	43.34
IGR J09523-6231	5.3	8 ^d	0.6	0.7	2.2 ^{+0.6} _{-0.5}	45.41
NGC 3081	9.7	66 ^m	2.6	4.1	1.8 ± 0.2	42.97
SWIFT J1009.3-4250	6.9	30 ^f	1.5	2.0	2.0 ± 0.4	43.95
IGR J10147-6354	3.0	2 ^d	0.5	0.7	2	45.18
NGC 3227	16.6	6.8 ^b	5.6	7.1	2.0 ± 0.1	42.63
NGC 3281	7.5	151 ^b	1.8	2.7	1.9 ± 0.3	43.06
SWIFT J1038.8-4942	5.3	0.6 ^f	0.6	1.4	1.3 ± 0.4	44.21
IGR J10404-4625	6.9	3 ^f	1.2	1.4	2.2 ^{+0.4} _{-0.3}	43.54
Mrk 421	173.8	0.08 ⁱ	22.4	20.6	2.45 ^{0.03} _{-0.02}	44.92
IGR J11366-6002	7.6	0.35 ^o	0.6	0.7	2.2 ^{+0.5} _{-0.4}	42.73
NGC 3783	6.1	0.08 [*]	6.0	8.4	1.9 ± 0.4	43.48
IGR J12026-5349	14.8	2.2 ^a	1.6	2.2	2.0 ± 0.1	43.84
NGC 4051	11.7	<0.02 [*]	1.8	1.5	2.1 ± 0.2	41.58
NGC 4138	9.0	8 ^b	1.2	1.9	1.8 ± 0.3	41.79
NGC 4151	205.7	6.9 ^a	24.0	32.3	C	43.13
NGC 4180	9.4	–	0.9	1.8	1.6 ^{+0.3} _{-0.2}	42.46
Was 49	3.8	10 ^b	0.6	0.8	2	44.12
Mrk 766	6.9	0.8 ^a	1.0	1.5	1.8 ± 0.3	42.95
NGC 4258	6.6	8.7 ^b	1.1	1.1	2.3 ± 0.4	41.04
4C 04.42	7.7	0.1 ^b	0.7	1.8	1.2 ± 0.2	46.83
Mrk 50	6.2	0.018 ^b	0.5	0.4	2.6 ^{+0.7} _{-0.6}	43.09
NGC 4388	78.1	27 ^a	9.8	15.2	C	43.59
NGC 4395	8.8	0.15 ^a	1.5	1.6	2.3 ^{+0.4} _{-0.3}	40.85
3C 273	78.0	0.5 ^a	7.5	10.6	1.92 ± 0.03	46.09
NGC 4507	30.9	29 ^a	6.3	10.0	C	43.70
SWIFT J1238.9-2720	6.3	60 ^f	2.7	5.3	1.6 ^{+0.4} _{-0.3}	44.06
IGR J12391-1612	9.9	3 ^f	1.7	2.2	2.0 ± 0.2	44.08
NGC 4593	33.0	0.02 ^a	3.2	4.1	C	43.08
IGR J12415-5750	6.7	<0.11 ^b	0.8	1.4	1.7 ^{+0.2} _{-0.3}	43.45
PKS 1241-399	3.5	–	0.7	0.9	2	45.23
ESO 323-32	5.6	7 ^f	0.8	1.5	1.6 ^{+0.4} _{-0.3}	43.13
3C 279	8.6	≤0.13 ^a	0.9	1.7	1.6 ± 0.2	46.40
Mrk 783	4.7	0.046 ^b	0.9	1.2	2	44.36
IGR J13038+5348	4.5	<0.03 [*]	1.0	1.3	2	43.67
NGC 4945	78.7	400 ^a	9.9	18.4	C	42.35
IGR J13057+2036	3.1	–	0.4	0.6	2	
ESO 323-77	9.0	55 ^a	1.1	2.1	1.5 ^{+0.3} _{-0.2}	43.21
IGR J13091+1137	7.5	90 ^a	1.6	2.5	2.1 ± 0.3	43.76
IGR J13109-5552	8.7	<0.1 ^p	0.9	1.2	2.0 ^{+0.3} _{-0.2}	44.78
NGC 5033	4.2	0.03 ^b	0.6	0.8	2	41.43
IGR J13149+4422	4.7	5 ^d	0.8	1.1	2	43.77
Cen A	247.2	12.5 ^a	28.1	43.4	1.82 ± 0.01	42.71
ESO 383-18	6.5	17 ^s	0.9	1.2	1.9 ^{+0.4} _{-0.3}	42.86
MCG-06-30-015	21.1	0.03 ^b	2.3	1.7	2.4 ± 0.1	42.74
NGC 5252	3.0	0.68 ^b	2.0	2.7	2	43.76
Mrk 268	5.7	–	0.9	0.7	2.5 ± 0.6	43.78
4U 1344-60	35.2	5 ^a	3.5	4.6	C	43.48
IC 4329A	58.5	0.42 ^a	8.8	12.3	C	44.09
Circinus Galaxy	120.0	360 ^a	10.9	10.1	C	41.96
NGC 5506	27.8	3.4 ^a	7.0	6.2	2.1 ± 0.1	43.16
IGR J14175-4641	8.0	–	0.8	1.3	1.8 ± 0.3	44.48
NGC 5548	3.1	0.51 ^a	1.0	1.3	2	43.19
RHS 39	7.7	<0.05 ^a	1.6	2.2	2.0 ± 0.3	43.63
H 1426+428	4.6	<0.02 [*]	0.6	0.8	2	44.80
IGR J14471-6414	7.2	<0.1 [*]	0.5	0.8	1.8 ± 0.3	43.95
IGR J14471-6319	6.4	2 ^f	0.6	0.8	2.0 ^{+0.5} _{-0.6}	43.67
IGR J14492-5535	8.6	12 ^a	0.9	1.4	1.7 ± 0.3	

Table 2. continued.

Name	ISGRI 18–60 keV [σ]	N_{H} [10^{22} cm $^{-2}$]	f_{20-40} keV [10^{-11} erg cm $^{-2}$ s $^{-1}$]	f_{40-100} keV [10^{-11} erg cm $^{-2}$ s $^{-1}$]	Γ_{ISGRI}^+	$\log L_{20-100}$ keV [erg s $^{-1}$]
IGR J14515-5542	9.4	0.4 ^f	0.8	1.4	1.6 ± 0.2	43.19
IGR J14552-5133	8.5	0.1 ^b	0.6	1.1	1.6 ^{+0.4} _{-0.3}	42.98
IGR J14561-3738	9.4	>100 ^g	0.6	1.2	1.7 ^{+0.2} _{-0.4}	43.37
IGR J14579-4308	15.4	20 ^d	1.1	1.4	2.0 ± 0.2	43.16
Mrk 841	3.2	0.21	1.0	1.4	2	43.87
ESO 328-36	5.7	–	0.4	0.4	2.5 ± 0.6	43.00
IGR J15161-3827	12.3	–	1.0	1.7	1.7 ± 0.2	43.90
NGC 5995	16.4	0.7 ^a	2.2	1.5	2.8 ± 0.2	43.74
IGR J15539-6142	4.6	18 ^f	0.5	0.7	2	42.78
IGR J16024-6107	3.7	<0.1 ^o	0.3	0.4	2	42.46
IGR J16056-6110	3.8	<1 ^c	0.3	0.5	2	43.72
IGR J16119-6036	9.3	0.1 ^b	0.9	1.4	1.8 ^{+0.3} _{-0.2}	43.11
IGR J16185-5928	6.1	<0.1 ^e	0.5	0.9	1.6 ± 0.3	43.57
IGR J16351-5806	10.2	<0.1 ^s	0.8	1.6	1.5 ± 0.2	42.64
IGR J16385-2057	7.2	0.21 ^d	0.8	0.5	3.1 ± 0.4	43.35
IGR J16426+6536	4.4	–	2.6	3.4	2	46.32
IGR J16482-3036	27.5	0.13 ^f	2.5	3.1	2.1 ± 0.1	44.10
ESO 138-1	3.7	150 ^b	0.4	0.6	2	42.26
NGC 6221	4.7	1 ^a	0.5	1.0	2	41.93
NGC 6240	12.1	2 ^b	2.1	3.6	1.7 ± 0.2	43.89
Mrk 501	12.4	0.013 ^b	2.5	1.7	2.8 ± 0.3	44.05
IGR J16558-5203	16.5	0.011 ^b	1.1	1.5	2.0 ± 0.1	44.25
IGR J16562-3301	7.0	0.2 ^f	1.0	2.3	1.32 ^{+0.16} _{-0.07}	43.30
NGC 6300	10.1	22 ^a	3.1	3.6	2.2 ± 0.2	42.30
IGR J17204-3554	6.4	12 ^b	0.3	0.4	2.2 ± 0.5	43.96
GRS 1734-292	106.4	3.7 ^a	4.3	4.4	C	43.96
IGR J17418-1212	6.6	0.1 ^b	0.8	1.5	1.5 ± 0.2	43.85
IGR J17488-3253	27.5	0.7 ^a	1.1	1.6	C	43.39
IGR J17513-2011	16.0	0.6 ^e	0.8	1.1	1.95 ± 0.12	44.00
IGR J18027-1455	15.2	19.0 ^a	1.2	1.7	1.9 ± 0.1	41.86
IGR J18244-5622	3.0	14 ^f	1.3	1.7	2	43.28
IGR J18249-3243	7.5	<0.1 ⁿ	0.5	0.7	1.9 ± 0.4	45.72
IGR J18259-0706	7.8	0.6 ^f	0.6	0.8	2.1 ± 0.3	43.28
PKS 1830-211	25.2	≤0.7 ^a	1.9	3.7	1.49 ^{+0.05} _{-0.07}	48.19
3C 382	3.0	0.88 ^b	3.8	5.0	2	44.85
ESO 103-35	4.9	19 ^a	3.0	4.0	2	43.44
3C 390.3	14.3	<0.1 ^a	2.3	3.9	1.7 ± 0.1	44.67
ESO 140-43	14.0	1.8 ^s	1.7	2.6	1.7 ± 0.2	43.40
IGR J18559+1535	12.0	0.7 ^d	0.9	1.3	2.0 ± 0.2	44.59
ESO 141-55	19.0	0.004 ^t	1.9	2.8	1.9 ± 0.4	44.30
1RXS J192450.8-29143	4.6	0.088 ^b	0.5	0.7	2	45.70
1H 1934-063	9.2	0.1 ^b	1.3	0.7	3.1 ^{+0.4} _{-0.3}	42.71
IGR J19405-3016	11.8	<0.1 ^o	1.3	1.9	1.8 ± 0.2	44.30
NGC 6814	16.2	<0.05 ^a	3.0	4.6	1.8 ± 0.1	42.65
IGR J19473+4452	7.1	11 ^a	1.1	2.0	1.3 ± 0.3	44.33
3C 403	4.5	45 ^b	0.9	1.2	2	44.23
QSO B1957+405	42.6	20 ^a	3.7	5.0	1.97 ± 0.05	44.81
ESO 399-20	4.3	0.048 ^b	0.6	0.9	2	43.33
IGR J20187+4041	12.2	6.1 ^b	0.9	1.3	1.9 ^{+0.1} _{-0.2}	42.99
IGR J20286+2544	10.4	42 ^f	1.8	3.3	1.6 ± 0.2	43.28
Mrk 509	11.2	<0.01 ^a	3.8	4.1	2.3 ± 0.3	44.34
S5 2116+81	4.4	<0.1 ^a	1.3	1.8	2	44.76
IGR J21178+5139	7.7	2 ^f	0.8	1.5	1.5 ± 0.2	44.04
IGR J21247+5058	47.3	0.6 ^k	4.7	7.3	C	44.04
IGR J21277+5656	13.6	0.1 ^b	1.6	1.8	2.2 ± 0.2	43.20
RX J2135.9+4728	9.2	0.4 ⁱ	0.9	1.6	1.7 ± 0.2	43.55
PKS 2149-306	4.6	0.03	0.9	1.2	2	47.98
NGC 7172	19.4	9.0 ^a	3.6	4.7	2.0 ± 0.1	43.13
BL Lac	5.5	0.3 ^b	0.7	1.2	1.8 ^{+0.4} _{-0.3}	44.34

Table 2. continued.

Name	ISGRI 18–60 keV [σ]	N_{H} [10^{22} cm $^{-2}$]	f_{20-40} keV [10^{-11} erg cm $^{-2}$ s $^{-1}$]	f_{40-100} keV [10^{-11} erg cm $^{-2}$ s $^{-1}$]	Γ_{ISGRI}^+	$\log L_{20-100}$ keV [erg s $^{-1}$]
IGR J22292+6647	5.7	0.2 [*]	0.5	0.6	2.3 ± 0.5	44.57
NGC 7314	12.9	0.122 ^b	2.1	2.5	2.2 ± 0.3	42.37
Mrk 915	4.5	<0.1 [*]	0.6	0.8	2	43.28
IGR J22517+2217	6.6	3 ^v	1.6	3.4	1.4 ± 0.4	48.43
3C 454.3	30.8	0.5 ^b	7.1	13.2	1.58 ± 0.06	47.76
1H 2251-179	22.9	<0.19 ^a	3.3	3.8	2.2 ± 0.1	44.85
NGC 7469	6.1	0.061 ^b	1.8	2.3	2.1 ± 0.4	44.39
MCG-02-58-022	15.0	<0.08 ^a	2.0	1.4	2.8 ± 0.2	44.26
IGR J23206+6431	7.7	0.6 [*]	0.4	0.7	1.5 ^{+0.5} _{-0.3}	44.15
IGR J23308+7120	3.7	6 ^o	0.3	0.4	2	43.39
IGR J23524+5842	6.7	6 ^d	0.4	0.5	2.0 ± 0.5	44.79

⁺ “C” indicates that a more complex model is required to fit the data (see Table 3); ^{*} this work; ^a Beckmann et al. (2006), and references therein; ^b Bodaghee et al. (2007), and ref. therein; ^c Landi et al. (2007b); ^d Rodriguez et al. (2008); ^e Malizia et al. (2008); ^f Malizia et al. (2007); ^g Beckmann et al. (2007b); ^h Revnivtsev et al. (2007); ⁱ Winter et al. (2008); ^k Ricci et al. (2009a); ^l Beckmann et al. (2007a); ^m Bassani et al. (1999); ⁿ Landi et al. (2008); ^o Landi et al. (2007c); ^p Molina et al. (2008); ^q Sazonov et al. (2008); ^r Landi et al. (2007a); ^t Gondoin et al. (2003); ^u Landi et al. (2007d); ^v Bassani et al. (2007); ^w Tomsick et al. (2008); ^x Ricci et al. (2009b).

Table 3. Spectral fit of a cut-off power-law model for AGN with more complex IBIS/ISGRI spectra.

Name	N_{H} [10^{22} cm $^{-2}$]	Γ_{ISGRI}	E_{c} [keV]	χ^2_{ν} (d.o.f.)
Mrk 348	30	0.9 ^{+0.4} _{-0.6}	55 ⁺⁵⁶ ₋₂₅	0.91 (8)
NGC 4151	6.9	1.60 ^{+0.06} _{-0.07}	118 ⁺²¹ ₋₁₃	1.10 (9)
NGC 4388	27	1.3 ± 0.1	95 ⁺²⁶ ₋₁₇	0.34 (7)
NGC 4507	29	1.15 ^{+0.28} _{-0.13}	72 ⁺⁵³ ₋₂₂	0.54 (8)
NGC 4593	0.02	1.1 ^{+0.4} _{-0.2}	48 ⁺¹¹⁴ ₋₉	0.87 (7)
NGC 4945	400	1.43 ^{+0.16} _{-0.11}	127 ⁺⁵⁶ ₋₂₆	0.75 (8)
4U 1344-60	5	1.11 ^{+0.29} _{-0.09}	51 ⁺²⁷ ₋₁₂	0.76 (7)
IC 4329A	0.42	1.37 ± 0.17	80 ⁺¹² ₋₁₉	1.50 (9)
Circinus Galaxy	360	1.29 ^{+0.18} _{-0.13}	33 ⁺⁶ ₋₃	1.03 (7)
GRS 1734-292	3.7	1.50 ± 0.10	54 ⁺⁸ ₋₇	0.88 (8)
IGR J17488-3253	0.2	0.74 ^{+0.33} _{-0.12}	40 ⁺⁸ ₋₃	0.98 (7)
IGR J21247+5058	0.6	1.19 ^{+0.13} _{-0.19}	74 ⁺³⁸ ₋₂₈	0.75 (8)

i.e. removing $\frac{1}{4}$ pixel from each corner (standard output from OSA). Therefore the computed values include the contributions by any other source inside the photometric aperture. We flagged in Table 5 those sources that might be affected by a nearby star (at less than 1'), with a potential contamination below 0.2 mag in any case. Other 8 AGN containing a brighter contaminating source within the extraction aperture were not included in this compilation. In addition, for some extended AGN, this 3 × 3 aperture does not cover the full galaxy size, but just their central region.

To only include high-quality data, some selection criteria were applied to individual photometric points. Shots were checked against saturation, rejecting those with long exposures for the brightest sources, if necessary. For faint sources, a minimum signal-to-noise ratio of 3 was required for the longest integration shots. The shortest shots were only used if the signal-to-noise ratio was greater than 10. Because these sources can show extended structure in the OMC images, anomalous PSF, as well as problems in the centroid determination, were allowed. Finally, to avoid contamination by cosmic rays, we excluded those points whose fluxes deviate more than 5 times the standard

deviation from the median value of their surrounding points, applying three iterations of this filter.

We list in Table 5 the median V magnitude of each AGN, the average of error estimates (1σ level) of each photometric point given by OSA 7, $\langle\sigma_V\rangle$, the luminosity in the Johnson V filter (centred on 5500 Å, effective width 890 Å), the α_{OX} value, the number of photometric points used in the analysis and a flag indicating the potential contamination of the photometric value by a nearby star. The value of α_{OX} is measured as the slope of a power law between the two energy ranges

$$\alpha_{\text{OX}} = -\frac{\log(f_0/f_X)}{\log(\nu_0/\nu_X)}. \quad (1)$$

Here, f_0 and f_X are the monochromatic fluxes at the frequencies ν_0 (at 5500 Å) and ν_X (at 20 keV).

No K correction has been applied to the V luminosities, since the redshifts are relatively low and the optical slope of these objects is not well known. Moreover, depending on the redshift, the V band might be contaminated to different degrees by the OIII and H β emission lines. We did not correct for this effect, either.

2.3.1. Optical variability

Among the 57 AGN for which OMC data are available, 3 show strong variability in the photometric V -band data, with an amplitude larger than 0.5 mag: QSO B0716+714, NGC 4151, and 3C 279.

The BL Lac QSO B0716+714 appears as a point source in a low background field and was monitored by OMC during 2 periods, at IJD³ around 1415 (November 2003) and 1555 (April 2004). This source brightened by a factor ~ 4 during this period, as shown in Fig. 2, ranging from $V = 14.60$ mag to 13.05 mag. Moreover, this blazar also shows a day-scale variability pattern within the two monitoring periods, with an amplitude around 0.3 mag.

NGC 4151 is an extended source, classified as Seyfert 1.5, much larger than the OMC aperture. We detected a clear weakening of its central, dominating region by around 0.5 mag (60% in flux) from 11.15 mag to 11.65 mag between May 2003

³ The INTEGRAL Julian Date is defined as IJD = MJD – 51 544.0. The origin of IJD is 2000 January 1 expressed in Terrestrial Time.

Table 4. Spectral fit results for combined JEM-X and IBIS/ISGR1 data.

Name	JEM-X [σ]	N_{H}^b [10^{22} cm^{-2}]	f_{3-20}^c keV	f_{20-100}^c keV	Γ	E_{C} [keV]	$\log L_{3-100}$ keV [erg s^{-1}]	χ^2_{ν} (d.o.f.)
IES 0033+59.5	10.1	0.36	6.0	1.4	$2.75^{+0.18}_{-0.16}$	–	45.16	0.51 (8)
NGC 1275 ^a	38.6	3.75	22.8	3.0	–	–	43.58	>5 ^a
3C 120	5.5	0.2	5.8	7.5	1.76 ± 0.06	–	44.52	0.67 (15)
Mrk 421	155.7	0.08	61.6	32.5	$2.12^{+0.05}_{-0.04}$	133^{+32}_{-21}	45.29	1.43 (14)
NGC 4151 ^a	91.5	6.9	33.2	40.4	$1.75^{+0.04}_{-0.04}$	170^{+30}_{-32}	43.25	1.36 (14)
NGC 4388 ^a	14.3	27	10.3	26.0	$1.26^{+0.09}_{-0.13}$	78^{+33}_{-20}	43.68	0.41 (15)
NGC 4593 ^a	7.0	0.02	4.4	7.7	$1.46^{+0.07}_{-0.15}$	193^{+12}_{-93}	43.34	1.01 (15)
Cen A ^a	57.2	12.5	28.1	43.4	1.85 ± 0.01	–	42.94	1.49 (17)
MCG-06-30-015	11.2	0.03	7.0	5.0	2.10 ± 0.05	–	42.93	0.79 (10)
4U 1344-60 ^a	8.3	5	5.6	21.0	$1.47^{+0.11}_{-0.16}$	86^{+31}_{-18}	43.70	0.76 (15)
IC 4329A ^a	11.3	0.42	14.5	21.1	1.41 ± 0.08	86^{+18}_{-13}	44.31	1.29 (15)
Circinus Galaxy ^a	5.3	360	3.9	21.0	1.2 ± 0.2	30 ± 3	42.03	1.52 (11)
NGC 5506	16.8	3.4	12.1	8.0	2.20 ± 0.08	–	43.27	0.66 (12)
H 1426+428	7.5	< 0.02	6.1	1.2	$2.83^{+0.25}_{-0.21}$	–	44.90	0.67 (9)
Mrk 501	7.9	0.013	10.2	4.8	2.3 ± 0.1	–	44.60	0.73 (15)
GRS 1734-292 ^a	10.5	3.7	6.7	8.0	$1.25^{+0.10}_{-0.16}$	39^{+5}_{-6}	44.02	1.28 (12)
IGR J17488-3253 ^a	21.8	0.72	1.7	2.9	1.63 ± 0.03	–	43.11	1.10 (119)
QSO B1957+405 ^a	10.5	20	16.2	8.3	$1.9^{+0.1}_{-0.2}$	–	45.26	0.76 (9)
Mrk 509	7.2	<0.01	7.5	9.3	1.8 ± 0.1	–	44.66	0.69 (8)
IGR J21178+5139	17.1	2	1.5	2.2	1.7 ± 0.1	–	–	1.61 (13)
IGR J21247+5058 ^a	54.1	0.6	9.5	11.1	1.4 ± 0.1	61^{+22}_{-11}	44.27	1.41 (11)
3C 454.3	6.4	0.5	10.7	20.3	1.54 ± 0.05	–	47.93	0.58 (16)
1H 2251-179	10.7	<0.19	5.7	7.2	1.8 ± 0.1	–	45.10	1.20 (13)

^a see Appendix A; ^b N_{H} values have been fixed during the fit; ^c fluxes are given in [$10^{-11} \text{ erg cm}^{-2} \text{ s}^{-1}$]

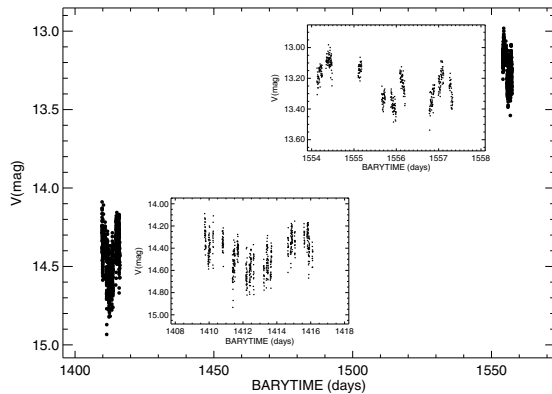


Fig. 2. OMC lightcurve of QSO B0716+714. The insets show a zoom on the lightcurves during the 2 periods when this object was monitored by OMC. The optical luminosity increased by a factor of 4. The photometric accuracy of individual photometric points is $\sigma \sim 0.09$ mag. Barycentric time is given in *INTEGRAL* Julian Date (IJD).

and January 2007. Since the optical photometry is contaminated to some extent by bulge stellar light, the variation in the optical emission from the nucleus itself might have been significantly larger.

The AGN 3C 279 was barely detectable around June 2003, with a 2σ OMC detection at $V = 17.0$. The catalogued value for it in the low state is $V = 17.8$ mag (O’Dell et al. 1978). After May 2005, this blazar was clearly detected with a brightness in the range $V = 14.8$ – 15.8 mag, indicating that it brightened by up to a factor close to 10 (Fig. 3). This is a very active source, with

optical photometry reported in the range $B = 18.3$ to $B = 11.3$ (O’Dell et al. 1978).

Other AGN monitored by OMC also show some hints of variability, such as 3C 273 and 3C 390.3, but at smaller amplitudes (just a few percent over the period considered).

3. Properties of INTEGRAL detected AGN

The catalogue of *INTEGRAL*-detected extragalactic objects presented here comprises 187 sources in total. Out of this sample, 162 objects have been identified as Seyfert galaxies (161 with redshift information), 18 blazars (all of them with redshift), and 7 objects have been claimed to be AGN without further specification of the AGN type. Within the Seyfert group, we found 67 Seyfert 1 to 1.2 objects, 29 intermediate Seyfert 1.5, and 66 Seyfert type 1.9 and type 2.

The redshift distribution of the Seyfert type AGN in this sample is shown in Fig. 4. The average redshift is $z = 0.03$. Figure 5 shows the parameter space filled by *INTEGRAL*-detected AGN in redshift and X-ray luminosity, ranging from low-luminous low-redshift Seyfert as close as $z = 0.001$ up to the high-redshift blazar domain.

To investigate the spectra of AGN subtypes, we derived averaged spectral properties and stacked spectra of the Seyfert 1 and 2 types, as well as for the intermediate Seyferts and the blazars, and according to the intrinsic absorption. The nine brightest sources, two blazars and seven Seyfert, with $>50\sigma$ (Cen A, NGC 4151, GRS 1734-292, NGC 4945, NGC 4388, IC 4329A, Circinus Galaxy, 3C 273, and Mrk 421) have been excluded from the statistical spectral analyses because their high signal-to-noise ratio would dominate the averaged spectra, and also all sources with $<5\sigma$ were ignored. In addition, we excluded the

Table 5. Median V magnitude, the average of error estimates ($\langle\sigma_V\rangle$), luminosity in the Johnson V filter, α_{OX} , the number of photometric points and contamination flag (“Y” indicates potential contamination by a nearby star up to 0.2 mag; see text for details).

Name	V [mag]	$\langle\sigma_V\rangle$ [mag]	$\log L_V$ [erg s $^{-1}$]	α_{OX}	N	Cont. flag
Mrk 348	13.76	0.05	42.71	1.01	81	Y
NGC 788	12.60	0.04	43.09	1.14	1342	
NGC 985	13.73	0.05	43.66	1.13	644	
NGC 1052	11.38	0.03	42.70	1.31	1004	
NGC 1068	9.99	0.02	44.80	1.38	693	
NGC 1275	12.51	0.04	43.27	1.21	856	
NGC 1365	11.51	0.05	42.72	1.27	35	
3C 120	14.00	0.05	43.31	1.02	216	
UGC 3142	15.12	0.22	43.49	0.93	259	
ESO 33-2	13.99	0.09	42.78	1.09	40	
Mrk 3	12.88	0.04	42.95	1.08	425	Y
Mrk 6	13.68	0.06	42.94	1.07	657	
QSO B0716+714	14.27	0.09	45.26	1.19	1116	
ESO 209-12	14.60	0.21	43.24	1.07	387	
PG 0804+761	14.07	0.08	44.28	1.09	299	
4U 0937-12	12.66	0.03	42.56	1.12	443	
MCG-05-23-016	13.12	0.05	42.47	1.03	1514	
NGC 3227	12.06	0.04	42.21	1.11	12	
NGC 3281	12.67	0.04	42.85	1.16	316	
Mrk 421	13.05	0.06	43.58	0.91	3112	
NGC 4051	12.26	0.04	41.67	1.20	76	
NGC 4138	11.87	0.04	42.06	1.26	585	
NGC 4151	11.52	0.04	42.28	1.03	7461	
Mrk 50	14.47	0.09	42.86	1.11	774	Y
NGC 4388	12.26	0.06	42.80	1.05	509	
NGC 4395	14.09	0.11	40.23	1.05	7	
3C 273	12.58	0.04	45.31	1.05	2010	Y
IGR J12391-1612	14.15	0.06	43.34	1.05	104	
NGC 4593	12.24	0.04	42.83	1.14	1204	
ESO 323-32	13.11	0.07	43.03	1.20	158	Y
3C 279	15.52	0.11	45.29	1.01	294	
Mrk 783	15.39	0.16	43.39	1.01	37	
NGC 4945	12.44	0.17	41.43	1.04	327	
IGR J13091+1137	13.70	0.05	43.18	1.07	15	
NGC 5033	11.57	0.03	42.16	1.33	55	
ESO 383-18	14.33	0.08	42.32	1.09	673	Y
MCG-06-30-015	13.23	0.07	42.36	1.09	1268	Y
Mrk 268	14.30	0.06	43.37	1.08	7	
IC 4329A	13.20	0.05	43.00	0.98	501	
NGC 5506	12.93	0.05	42.38	1.03	701	
NGC 5548	13.14	0.05	43.08	1.17	256	
H 1426+428	16.11	0.25	43.72	0.98	619	
NGC 5995	13.47	0.07	43.29	1.05	118	Y
ESO 138-1	13.59	0.11	42.34	1.20	12	Y
NGC 6221	11.91	0.07	42.49	1.33	16	
Mrk 501	13.21	0.04	43.65	1.07	567	
NGC 6300	11.52	0.05	42.38	1.19	31	
3C 390.3	14.61	0.13	43.54	1.00	482	Y
1H 1934-063	13.35	0.05	42.59	1.10	12	
NGC 6814	12.42	0.04	42.31	1.14	134	
ESO 399-20	13.96	0.08	43.07	1.18	84	
Mrk 509	13.38	0.05	43.60	1.03	400	
NGC 7172	12.66	0.04	42.66	1.10	508	
Mrk 915	14.10	0.09	42.75	1.09	40	
1H 2251-179	14.20	0.09	43.83	0.98	1570	Y
NGC 7469	12.70	0.04	44.21	1.15	22	
MCG-02-58-022	14.13	0.06	43.59	1.01	93	

5 Compton thick objects, i.e. NGC 1068, NGC 3281, NGC 4945, Circinus Galaxy, ESO 138-1.

The average Seyfert 1 (including type 1.2) spectral property was constructed using the mean weighted by the errors on the photon indices of 55 ISGRI power-law fit results, the

Seyfert 2 composite spectrum includes 44 sources, and 20 objects form the intermediate Seyfert 1.5 group where spectral fitting allowed constraining the spectral shape (Table 2). In addition, 11 blazars allowed spectral extraction. When computing the weighted average of the various subclasses, the 11 blazars

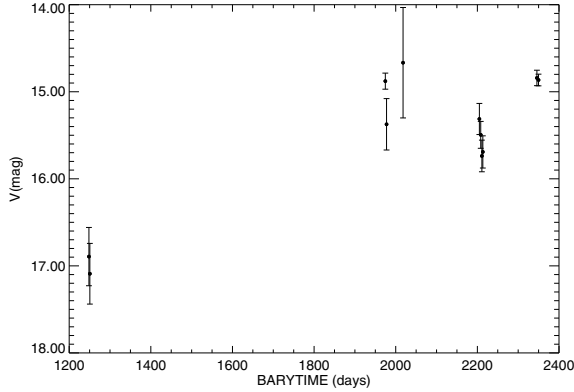


Fig. 3. OMC lightcurve of 3C 279. Barycentric time is given in IJD. Photometric data have been re-binned to obtain one value per revolution (3 days).

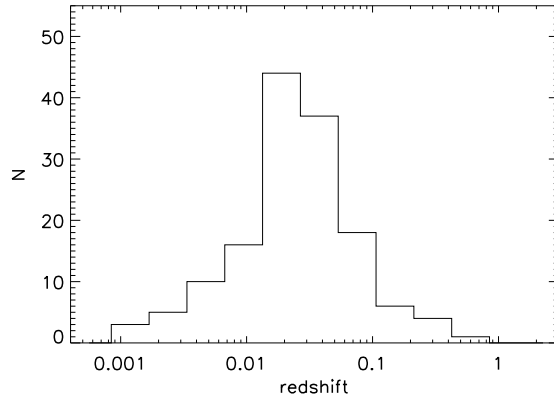


Fig. 4. Redshift distribution of the Seyfert content of 144 *INTEGRAL* detected AGN with detection significance $\geq 4\sigma$. The average redshift is $z = 0.03$.

had a hard X-ray spectrum with $\Gamma = 1.55 \pm 0.04$ when compared to the 119 Seyfert galaxies with $\Gamma = 1.93 \pm 0.01$. The Seyfert 1 ($\Gamma = 1.92 \pm 0.02$) and Seyfert 1.5 ($\Gamma = 2.02 \pm 0.03$) only show slightly steeper hard X-ray spectra than the Seyfert 2 objects ($\Gamma = 1.88 \pm 0.02$). Table 6 gives the properties of the different Seyfert types. All quantities, except for the photon indices, have been averaged in logarithmic space. For 12 objects, a cut-off power law model gave a better representation of the ISGRI spectra (Table 3). The average photon index is in these cases $\langle \Gamma \rangle = 1.3 \pm 0.4$ with a cut-off energy of $\langle E_C \rangle = 86 \pm 25$ keV.

We get a similar result when stacking the IBIS/ISGRI spectra together. Again, only sources above 5σ are considered here. The spectra were renormalised on the 18–30 keV energy bin before stacking them, re-adjusting the errors on the flux so that the significance is taken into account. The significances for the stacked spectra are consistent with what would be expected based on the single spectra significances, i.e. the 18–60 keV significances are 98σ for the Seyfert 1, 61σ (Seyfert 1.5), 94σ (Seyfert 2), and 148σ for all Seyfert spectra stacked together. The results of spectral model fitting to these spectra are summarized in Table 7. A simple power law model gives a photon index of $\Gamma = 1.97 \pm 0.02$ for all Seyfert objects, $\Gamma = 1.96^{+0.03}_{-0.02}$ for the Seyfert 1,

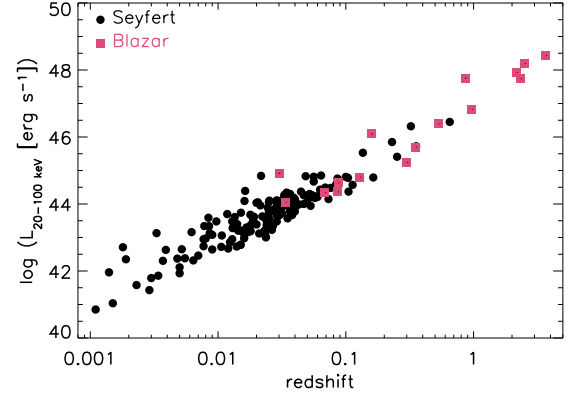


Fig. 5. X-ray luminosity versus redshift of 161 *INTEGRAL* detected AGN with significance $\geq 4\sigma$.

Table 6. Average properties of the *INTEGRAL* AGN. In parentheses, the number of objects used for the given average value is indicated.

	Seyfert 1	Seyfert 1.5	Seyfert 2
$\langle z \rangle$	0.03 (63)	0.014 (24)	0.02 (57)
$\langle \Gamma \rangle^a$	1.92 ± 0.02 (55)	2.02 ± 0.03 (20)	1.88 ± 0.02 (44)
$\langle \log N_H \rangle^b$	21.2 (61)	21.7 (23)	22.9 (51)
$\langle \log L_{20-100 \text{ keV}} \rangle^c$	44.0 (63)	43.3 (24)	43.4 (57)
$\langle \log M_{\text{BH}} \rangle$	7.8 (30)	7.2 (14)	7.7 (27)
$\langle \lambda \rangle^d$	0.064 (30)	0.015 (14)	0.02 (27)
	Unabs	Absorbed	all Sey
$\langle z \rangle$	0.03 (74)	0.014 (60)	0.02 (144)
$\langle \Gamma \rangle^a$	1.94 ± 0.02 (66)	1.91 ± 0.02 (44)	1.93 ± 0.01 (119)
$\langle \log N_H \rangle^b$	21.0 (75)	23.1 (60)	21.9 (135)
$\langle \log L_{20-100 \text{ keV}} \rangle^c$	43.8 (74)	43.4 (60)	43.6 (144)
$\langle \log M_{\text{BH}} \rangle$	7.6 (37)	7.7 (34)	7.6 (71)
$\langle \lambda \rangle^d$	0.06 (37)	0.015 (34)	0.03 (71)

^a Γ is the average photon index derived from the weighted mean on the power law model fits to the single IBIS/ISGRI spectra; ^b absorption is given in $[\text{cm}^{-2}]$; ^c luminosities in $[\text{erg s}^{-1}]$; ^d $\lambda = L_{\text{Bol}}/L_{\text{Edd}}$ is the Eddington ratio.

$\Gamma = 2.02 \pm 0.04$ for Seyfert 1.5, and $\Gamma = 1.89^{+0.04}_{-0.02}$ for the Seyfert 2 class. In all cases, a cut-off power law improves the fit result significantly according to an F-test (Table 7). The resulting model is $\Gamma = 1.4 \pm 0.1$ with cut-off at $E_C = 86^{+16}_{-17}$ keV for all Seyfert galaxies, fully consistent with the average from the 12 cut-off power law model fits. For Seyfert 1 we derive $\Gamma = 1.4 \pm 0.1$ and $E_C = 86^{+21}_{-14}$ keV, and $\Gamma = 1.4 \pm 0.2$ with $E_C = 63^{+20}_{-12}$ keV for intermediate Seyfert 1.5, and $\Gamma = 1.65 \pm 0.05$ with $E_C = 184^{+16}_{-52}$ keV Seyfert 2 galaxies. It should be considered that the latter fit still has a poor quality with $\chi^2_\nu = 2.6$.

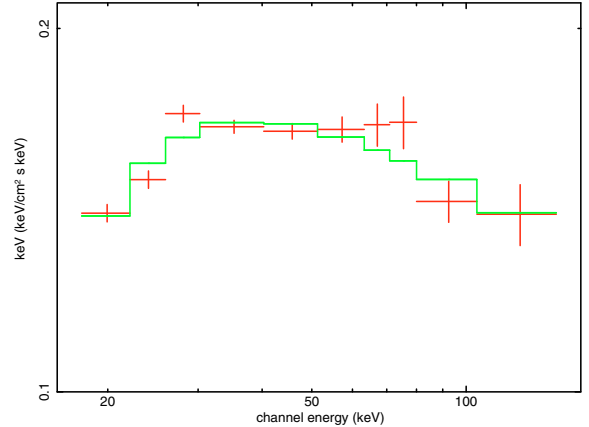
A model that adds a reflection component from cold material to the underlying continuum (the so-called PEXRAV model; Magdziarz & Zdziarski 1995) gives again a better fit in most cases. The underlying continuum shows a similar gradient in the different source classes when not allowing for a high-energy cut-off in the PEXRAV model, so this fit has the same degree of freedom as the one using the cut-off power law. The difference shows up, however, in the inclination angle i and strength R of the reflection component. Here R is defined as the relative amount of reflection compared to the directly viewed primary spectrum.

Table 7. Results from spectral fitting of the stacked IBIS/ISGRI spectra of INTEGRAL AGN

Sample	Γ	E_C [keV]	R	χ^2_ν
Sey 1 ($\geq 5\sigma$)	$1.96^{+0.03}_{-0.02}$	–	–	5.66
	1.44 ± 0.10	86^{+21}_{-14}	–	1.10
($i = 30^\circ$)	1.96 ± 0.02	–	$1.2^{+0.6}_{-0.3}$	1.15
Sey 1.5 ($\geq 5\sigma$)	2.02 ± 0.04	–	–	3.54
	1.36 ± 0.15	63^{+20}_{-12}	–	0.57
($i = 45^\circ$)	2.04 ± 0.04	–	$3.1^{+4.7}_{-1.3}$	0.29
Sey 2 ($\geq 5\sigma$)	$1.89^{+0.04}_{-0.02}$	–	–	3.13
	1.65 ± 0.05	184^{+16}_{-52}	–	2.58
($i = 60^\circ$)	$1.91^{+0.02}_{-0.03}$	–	$1.1^{+0.7}_{-0.4}$	1.67
all Sey ($\geq 5\sigma$)	1.97 ± 0.02	–	–	6.18
	$1.44^{+0.08}_{-0.13}$	86^{+16}_{-17}	–	1.96
($i = 45^\circ$)	1.95 ± 0.02	–	$1.3^{+0.7}_{-0.4}$	1.53
all Sey ($\geq 10\sigma$)	1.98 ± 0.02	–	–	6.04
	$1.41^{+0.10}_{-0.11}$	80^{+17}_{-13}	–	1.23
($i = 45^\circ$)	1.95 ± 0.02	–	$1.3^{+0.7}_{-0.4}$	1.23
Unabs. ($\geq 5\sigma$)	$1.97^{+0.03}_{-0.01}$	–	–	5.64
	$1.53^{+0.09}_{-0.08}$	100^{+25}_{-15}	–	1.82
($i = 45^\circ$)	1.98 ± 0.02	–	$1.3^{+0.6}_{-0.4}$	0.95
Abs. ($\geq 5\sigma$)	$1.91^{+0.04}_{-0.03}$	–	–	1.2
	$1.43^{+0.13}_{-0.08}$	94^{+32}_{-13}	–	1.59
($i = 45^\circ$)	$1.91^{+0.02}_{-0.03}$	–	$1.5^{+1.5}_{-1.4}$	1.03

The value of R depends on the inclination angle i between the normal of the accretion disc and the line of sight. The smaller the inclination angle, the larger the resulting reflection component. As the data are not sufficient to fit R and i simultaneously, the inclination angle was set to $i = 30^\circ$ for Seyfert 1, $i = 45^\circ$ for Seyfert 1.5, and $i = 60^\circ$ for Seyfert 2. It is worth noting that the quality of the fit did not depend on the choice of i . The results are included in Table 7. Using this model, Seyfert 1 and Seyfert 2 show only slightly different underlying continua and a reflection component of the same strength $R \approx 1$ within the statistical errors. Seyfert 1.5 objects appear to have slightly steeper spectra ($\Gamma = 2.0$) and stronger reflection ($R = 3^{+5}_{-1}$). Applying a higher significance level (e.g. $\geq 10\sigma$) for the source selection does not change the results significantly, as shown for all Seyfert galaxies in Table 7. This confirms that the stacked spectra are dominated by the most significant sources. The result of the fit to the whole Seyfert sample with the PEXRAV model is shown in Fig. 6.

The classification according to the Seyfert type of the objects is based on optical observations. An approach to classifying sources due to their properties in the X-rays can be done by separating the sources with high intrinsic absorption ($N_H > 10^{22} \text{ cm}^{-2}$) from those objects that do not show significant absorption in the soft X-rays. Not all objects that show high intrinsic absorption in the X-rays are classified as Seyfert 2 galaxies in the optical, and the same applies to the other AGN sub-types. Nevertheless a similar trend in the spectral slopes can be seen: the 44 absorbed AGN show a hard X-ray spectrum ($\langle \Gamma \rangle = 1.91 \pm 0.02$) consistent with that of the 66 unabsorbed sources ($\langle \Gamma \rangle = 1.94 \pm 0.02$). Using the stacked spectra, the absorbed sources show a slightly flatter continuum with $\Gamma = 1.91^{+0.04}_{-0.03}$ than unabsorbed Seyfert galaxies, with $\Gamma = 1.97^{+0.03}_{-0.01}$. Also here, a cut-off power law has been tested, but comparing it to the simple power law model improves the fit only for the

**Fig. 6.** Stacked IBIS/ISGRI spectrum for Seyfert objects (excluding Compton thick sources) in EF_E versus energy. The spectrum has been fit by a PEXRAV model with $\Gamma = 1.95$ and reflection $R = 1.3$.

unabsorbed sources. For these sources we derive $\Gamma = 1.5 \pm 0.1$ and $E_C = 100^{+25}_{-15}$ keV, and for the absorbed ones $\Gamma = 1.4 \pm 0.1$ with $E_C = 94^{+32}_{-13}$ keV. Thus, for the different absorption classes we get consistent cut-off values and spectral slopes, although the stacked unabsorbed spectrum is represented better by the simple power-law model with no cut-off. Applying the PEXRAV model shows that the spectra can be represented by reflection models. The fit improves significantly when adding a reflection component with $R \approx 1.5$, while the underlying continuum slope is the same as for the simple power law.

A difference between type 1 and type 2 objects is seen in the average luminosity of these subclasses. For 60 absorbed Seyfert galaxies, the average luminosity is $\langle L_{20-100 \text{ keV}} \rangle = 2.5 \times 10^{43} \text{ erg s}^{-1}$, more than a factor of 2 lower than for the 74 unabsorbed Seyfert with redshift information ($\langle L_{20-100 \text{ keV}} \rangle = 6.3 \times 10^{43} \text{ erg s}^{-1}$). The differences in luminosities are exactly the same when excluding the 5 Compton thick objects. The 16 blazars again appear brighter when assuming an isotropic emission, with $\langle L_{20-100 \text{ keV}} \rangle = 10^{46} \text{ erg s}^{-1}$. The latter value has to be used with caution: because the blazar emission is beamed towards the observer, not isotropic but collimated in a jet, blazars are highly variable and *INTEGRAL* detects them mainly in phases of outbursts.

4. Discussion

4.1. The sample in comparison with previous studies

For the whole population of sources seen by *INTEGRAL* we observe an increase in the fraction of unabsorbed objects compared to the first *INTEGRAL* AGN catalogue. Whereas $\frac{2}{3}$ of the Seyfert population in the first sample showed $N_H > 10^{22} \text{ cm}^{-2}$, there are now more unabsorbed than absorbed sources, i.e. only 44% appear to be absorbed. A similar trend has also been observed in the *Swift*/BAT survey (Tueller et al. 2008), where the fraction is $\frac{1}{2}$. This trend is expected because with ongoing observations, IBIS/ISGRI and BAT perform deeper studies, which is also reflected in the increase in the average redshift and luminosity of the objects that are detectable. Sazonov et al. (2004, 2007) have shown that there is an anticorrelation of the fraction of absorbed sources with the X-ray luminosity. In a sample of 95 AGN detected by *RXTE*, they observed that the fraction

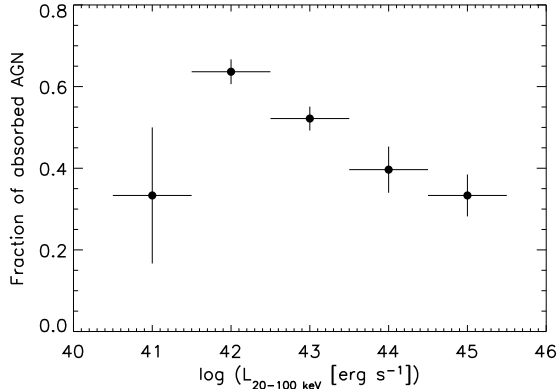


Fig. 7. Fraction of absorbed ($N_{\text{H}} > 10^{22} \text{ cm}^{-2}$) Seyfert galaxies as a function of hard X-ray luminosity for *INTEGRAL* detected AGN ($\geq 4\sigma$). The lowest luminosity bin includes only 3 sources.

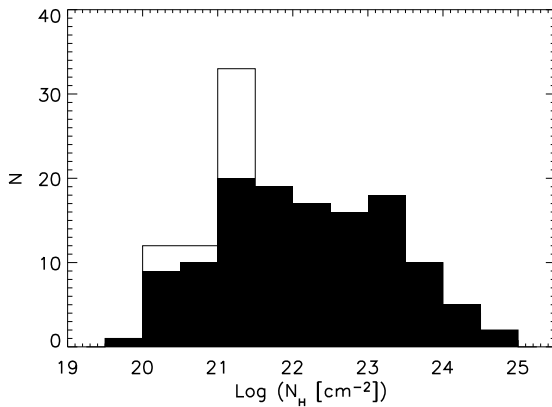


Fig. 8. Distribution of intrinsic absorption of the Seyfert content of *INTEGRAL* detected AGN ($\geq 4\sigma$). The unshaded area indicates objects where the N_{H} value is an upper limit.

of absorbed sources is $\sim 70\%$ for $L_{3-20 \text{ keV}} < 10^{43.5} \text{ erg s}^{-1}$ but only $\sim 20\%$ for objects with $L_X > 10^{43.5} \text{ erg s}^{-1}$. This trend can also be seen in the sample presented here. Determining the fraction of absorbed Seyfert galaxies in logarithmic bins of X-ray luminosity, we see the trend toward a decreasing fraction with luminosity in the range $L_{20-100 \text{ keV}} > 3 \times 10^{41} \text{ erg s}^{-1}$ (Fig. 7). The fraction appears low though in the lowest luminosity bin ($L_{20-100 \text{ keV}} < 3 \times 10^{41} \text{ erg s}^{-1}$), but it has to be considered that this luminosity bin contains only 3 AGN, the Seyfert 1.5 galaxies NGC 4258, NGC 4395, and NGC 5033.

The fraction of Compton thick objects in the sample presented here is only 4% (5 objects out of the 135 Seyfert galaxies with measured intrinsic absorption). Although this sample is not a complete one, this indicates further that the fraction of Compton thick AGN is indeed $\ll 10\%$ as already reported in e.g. Beckmann et al. (2006b) and Bassani et al. (2007). In addition, a recent study based on combined *INTEGRAL* and *Swift*/*BAT* data puts an upper limit of $\lesssim 9\%$ on the fraction of Compton thick AGN (Treister et al. 2009), and one can thus consider most of the Seyfert population detected by *INTEGRAL* and *Swift* to be Compton thin. The distribution of intrinsic absorption (Fig. 8) shows that the Seyfert galaxies in the *INTEGRAL* sample are evenly distributed between 10^{21} cm^{-2} and $3 \times 10^{23} \text{ cm}^{-2}$, as

Table 8. Correlation matrix for *INTEGRAL* AGN.

	M_{BH}	Γ	L_X	Edd. ratio	L_V
	λ				
N_{H}	no	no	no	no	no
M_{BH}	–	no	$>99.99\%$	intrinsic	$>99.99\%$
Γ		–	no	no	no
L_X			–	intrinsic	$>99.99\%$
λ				–	no

already seen in the first *INTEGRAL* AGN catalogue (Beckmann et al. 2006c) and in the *Swift*/*BAT* AGN survey (Tueller et al. 2008). A significant amount of sources have reported N_{H} values of $N_{\text{H}} < 10^{21} \text{ cm}^{-2}$. We assigned $N_{\text{H}} = 10^{21} \text{ cm}^{-2}$ to these objects, which causes the peak in the distribution. The claim of two distinct groups resulting in two peaks in the N_{H} distribution as reported by Paltani et al. (2008) appears therefore caused by low number statistics. Although a clear dependency is seen on the intrinsic absorption when dividing the sample in two groups, there is no significant linear correlation with any of the parameters we tested. We summarize the analysis of the correlations in Table 8. Here the correlation probability is given if larger than 90%. The correlations between Eddington ratio and L_X and M_{BH} are intrinsic, i.e. caused by the dependence of λ on these two parameters.

For synthesis studies of the cosmic X-ray background one will have to take into account that both, the fraction of Compton thick and of absorbed sources, appears to be lower than assumed in most models published so far (e.g. Treister & Urry 2005; Gilli et al. 2007). Although the average redshift in the *INTEGRAL* sample has increased significantly since the first catalogue from $\langle z \rangle = 0.01$ to now $\langle z \rangle = 0.03$, *INTEGRAL* will not be able to probe evolutionary effects. The only possibility of measuring evolutionary effects would be the combination of *Swift*/*BAT* data with a deep ($\sim 10 \text{ Ms}$) *INTEGRAL* IBIS/ISGRI field (Paltani et al. 2008).

A systematic analysis of all *BeppoSAX* observations of AGN has been presented by Dadina (2007). Thirty-nine objects from this work are in common with the *INTEGRAL* sample. Four sources show strong differences in flux by more than a factor of 2 between the measurements, i.e. the Seyfert 2 galaxies NGC 4388, NGC 2110, NGC 7172, and the type 1 radio galaxy 3C 111. All these objects are known to be variable at hardest X-rays (e.g. Beckmann et al. 2007). In addition, the average flux in the 20–100 keV band appears to be higher in the *INTEGRAL* data than in the *BeppoSAX* one. This can be caused by the different time coverage: while *BeppoSAX* observations are mostly snapshots of the sources with duration of $\Delta t \ll 100 \text{ ks}$, the *INTEGRAL* observations of the AGN have the average exposure of 1200 ks. Thus the data presented here can include some short-term bright states, which would have been missed in most cases by *BeppoSAX*. In addition, the fluxes presented here are model fluxes, and because more complex modelling is necessary for the *BeppoSAX* spectra, applying a cut-off and a reflection component in most cases, this leads to lower broad-band model fluxes compared to the simple power law model applied here (see also Sect. 4.2). In addition, there is a systematic difference in the calibration of the ISGRI and PDS detectors, with steeper and higher-normalization Crab spectra extracted for ISGRI (Kirsch et al. 2005). This explains also larger spectral slope values fitted to the ISGRI spectra, when compared with the values quoted by Dadina (2007), although the primary reason for the these differences is the simpler spectral model applied to the *INTEGRAL* data.

Table 9. OSSE detected AGN not seen by *INTEGRAL*.

Name	Type	Exposure ^a [ks]
CTA 102	blazar	180
H 1517+656	BL Lac	19
III Zw2	Sy1/2	15
Mrk 279	Sy1.5	11
M82	Starburst	127
NGC 253	Starburst	1
NGC 7213	Sy1.5	31
NGC 7582	Sy2	–
PKS 2155-304	BL Lac	347
QSO 1028+313	Sy1.5	556

^a ISGRI exposure time.

CGRO/OSSE (Johnson et al. 1993) covered the energy range of approximately 50–10³ keV. It therefore primarily detected AGN with hard and bright X-ray spectra, which we also expect to be detectable by *INTEGRAL*. While the first *INTEGRAL* AGN catalogue listed 24 OSSE-detected AGN not seen by *INTEGRAL*, this number has now decreased to 10. We list those sources and the IBIS/ISGRI exposure time on the particular AGN in Table 9. It can be expected that the persistent sources in this list, i.e. the Seyfert and starburst galaxies, will be detected once a significant amount of exposure time is available for these objects.

As expected, only a few objects are jointly detected by *INTEGRAL* IBIS/ISGRI and *Fermi*/LAT, according to the bright source list based on three months of LAT data (Abdo et al. 2009). These 13 objects are blazars, except for the two radio galaxies Cen A and NGC 1275. The common blazars between ISGRI and LAT are 1ES 0033+595, PKS 0528+134, QSO B0716+714, Mrk 421, 3C 273, 3C 279, Mrk 501, PKS 1830-211, 1ES 1959+650, BL Lac, and 3C 454.3. The group of sources jointly detected by *Fermi*/LAT and ISGRI is expected to increase significantly through *INTEGRAL* target-of-opportunity (ToO) observations of blazars that show a flare in the LAT data.

4.2. The intrinsic hard X-ray spectrum

The effect that Seyfert 1 and low-absorbed objects appear to have steeper X-ray spectra than the Seyfert 2 and highly absorbed AGN was first noticed by Zdziarski et al. (1995), based on *Ginga* and *CGRO/OSSE* data and later confirmed e.g. by Gondek et al. (1996) using combined *EXOSAT*, *Ginga*, *HEAO-1*, and *CGRO/OSSE* spectra. A study of *BeppoSAX* PDS spectra of 45 Seyfert galaxies came to a similar conclusion, although the spectra of Seyfert 2 appeared steeper when considering a possible cut-off in the spectra of Seyfert 1 galaxies (Deluit & Courvoisier 2003). The difference in the hard X-ray spectral slope between Seyfert 1 and 2 has been a point of discussion ever since its discovery. Zdziarski et al. (2000) considered the anisotropy of Compton scattering in planar geometry and effects of reflection, but came to the conclusion that this cannot be the sole explanation. Beckmann et al. (2006) argued that the difference might be a selection effect, as objects have to have a harder X-ray spectrum to be detectable when strong intrinsic absorption is present. With the growing sample of AGN, this argument does not seem to hold, as the absorption in the energy band >20 keV is negligible for Compton thin objects, and also the ongoing identification effort of newly detected hard X-ray sources did not

reveal a different population than already presented in Beckmann et al. (2006).

A solution might be provided when considering the effects of Compton reflection on the hard X-ray spectrum, as shown in the previous section. Recent analysis of a sample of 105 Seyfert galaxies using the spectra collected with *BeppoSAX* in the 2–200 keV band (Dadina 2008) provided no evidence of any spectral slope difference when applying more complex model fitting including a reflection component (PEXRAV). The mean photon index values found for Seyfert 1 and Seyfert 2 samples were $\Gamma = 1.89 \pm 0.03$ and $\Gamma = 1.80 \pm 0.05$. The difference between types 1 and 2 is seen in this model in the different strength of the reflection component, with $R = 1.2 \pm 0.1$ and $R = 0.9 \pm 0.1$, and different cut-off energies of $E_C = 230 \pm 22$ keV and $E_C = 376 \pm 42$ keV, for Seyfert 1 and Seyfert 2, respectively. It has to be pointed out that spectral slope, reflection strength, and cut-off energy are closely linked. The IBIS/ISGRI data have a disadvantage over broad-band data when studying the spectral shape of the hard X-ray continuum, as we lack information about the spectrum below 18 keV. But on the positive side, using data from only one instrument, the spectra do not suffer from the problem of intercalibration factors, which is apparent in all studies using different instruments, and especially when using data from different epochs. In those cases, where spectra are taken by more than one instrument at different times, the flux variability can mimic a stronger or weaker reflection component or cut-off energy (e.g. Panessa et al. 2008).

The *INTEGRAL* data show consistent slopes for the spectra of unabsorbed/type 1 and absorbed/type 2 objects already when a simple power-law model is used. When applying the model used by Dadina (2007) to the stacked *INTEGRAL* spectrum of Seyfert galaxies, we get similar results: the underlying power-law appears to have consistent (within 2σ) spectral slope for type 1 ($\Gamma = 1.96$) and type 2 ($\Gamma = 1.91$) objects and the same reflection strength $R \approx 1.1$. The data do not allow to determine the cut-off energy or inclination angle when fitting the reflection component (Fig. 6). When fitting a simple cut-off power law, the *INTEGRAL* data show the same trend as the *BeppoSAX* sample, i.e. a lower cut-off energy for Seyfert 1 ($E_C = 86$ keV) than for Seyfert 2 ($E_C = 184$ keV). It has to be taken into account, though, that the fit to the Seyfert 2 data is bad quality, and that fixing the cut-off here to the same value as derived for the Seyfert 1, also leads to the same spectral slope. When fitting a reflection model to the stacked data, one gets a consistent photon index of $\Gamma \approx 1.95$ and reflection strength $R \approx 1.3$ for both absorbed and unabsorbed AGN. These values of Γ and R agree with the correlation $R = (4.54 \pm 1.15) \times \Gamma - (7.41 \pm 4.51)$ Dadina (2008) found for the *BeppoSAX* AGN sample, which, for the *INTEGRAL* sample with $\Gamma = 1.95$, would lead to $R = 1.4$. This $R(\Gamma)$ correlation was first noted based on *Ginga* data for extragalactic and Galactic black holes, leading to $R = (1.4 \pm 1.2) \times 10^{-4} \Gamma^{(12.4 \pm 1.2)}$ (Zdziarski et al. 1999), which in our case would result in a smaller expected reflection component with $R = 0.6$ but within 1σ of the value detected here. Absorbed and unabsorbed show a consistent turnover at about $E_C = 100$ keV when a cut-off power law model is applied.

The observed dichotomy of different spectral slopes for type 1 and type 2 objects might therefore be caused by data with too low significance, which do not allow to fit the reflection component, or in general by a strong dependence of the spectral slope on the choice of the fitted model. One aspect that has to be kept in mind is the dependence of the reflection strength R on the model applied and on the geometry assumed. Murphy & Yaqoob (2009) showed recently that their model of a reflection

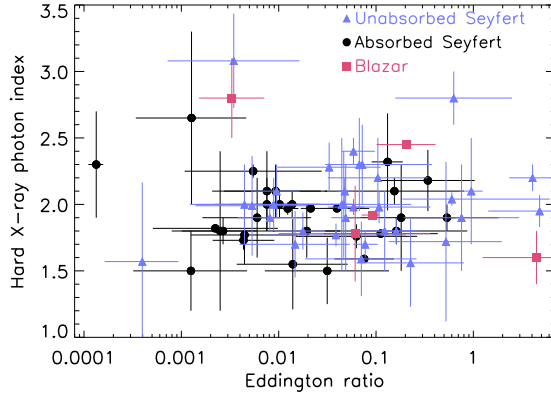


Fig. 9. Photon index of a simple power-law fit to the IBIS/ISGRI data versus Eddington ratio λ .

spectrum from a Compton-thick face-on torus that subtends a solid angle of 2π at the X-ray source is a factor of ~ 6 weaker than that expected from a Compton-thick, face-on disc as modelled in PEXRAV. Therefore, applying a torus model to the data presented here would result in much less reflection strength.

4.3. Eddington ratios and accretion rates in Seyfert galaxies

A different approach to search for differences or similarities in Seyfert galaxies is to study the accretion rates. Middleton et al. (2008) suggest that different accretion states lead to differences in the hardness of hard X-ray ($E > 10$ keV) spectra between types 1 and 2 AGN (type 1 spectra being systematically softer). Using data from *CGRO/OSSE*, *BeppoSAX*, and *INTEGRAL*, they found that the 24 Seyfert 2 galaxies in their sample of hard X-ray selected AGN show an accretion rate (parameterized with the Eddington ratio) in average smaller than that of their 23 Seyfert 1. This effect has also been seen when studying AGN detected by *Swift/BAT* (Winter et al. 2009). This would be consistent with all accreting black holes in general showing harder spectra at low accretion rates (Laor 2000; Remillard & McClintock 2006).

The 20–100 keV luminosities as derived from the IBIS/ISGRI data were used to approximate the bolometric luminosity. Assuming a canonical photon index of 2.0 for a single power law, the total X-ray luminosity is about $L_{(1-200 \text{ keV})} = 3 \times L_{(20-100 \text{ keV})}$. Assuming that the first peak of the spectral energy distribution is as strong as the X-ray luminosity, we derive $L_{\text{Bol}} = 6 \times L_{(20-100 \text{ keV})}$. The Eddington luminosity considering pure hydrogen is given by $L_{\text{Edd}} = 1.26 \times 10^{38} \frac{M}{M_{\odot}} \text{ erg s}^{-1}$, and thus the Eddington ratio is $\lambda = L_{\text{Bol}}/L_{\text{Edd}} = 4.8 \times 10^{-38} L_{(20-100 \text{ keV})} \frac{M_{\odot}}{M} \text{ erg}^{-1} \text{ s}$. The Eddington ratio can be computed for 71 Seyfert objects of the sample presented here. The photon index as determined from IBIS/ISGRI data and the Eddington ratio are compared in Fig. 9. The four AGN on the top left of this figure, with steep spectra and low Eddington ratio ($\lambda < 0.005$), are the Seyfert 1 1H 1934-063, the Seyfert 2 objects SWIFT J0601.9-8636 and NGC 4258, and the blazar Mrk 501. There is no significant correlation detectable, even when excluding these outliers. As observed by Steffen et al. (2003) in *Chandra* data of AGN, it appears that the 2–8 keV luminosity function is dominated by type 1 AGN at high X-ray luminosities and by type 2 at low luminosities. The same effect is seen

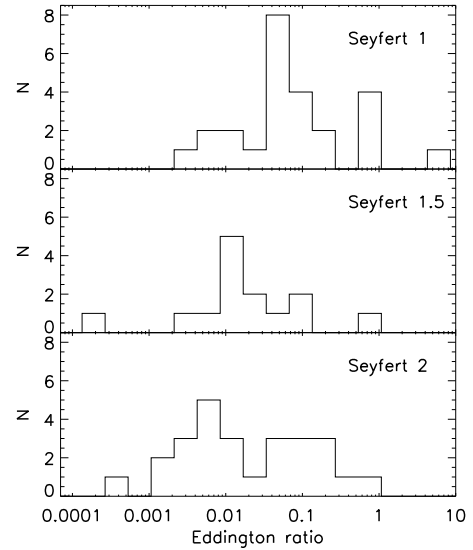


Fig. 10. Distribution of Eddington ratios for Seyfert 1, 1.5, and type 2 AGN in the sample.

also in the *INTEGRAL* luminosity function (Beckmann et al. 2006b). Connected to this, we observe not only that the absorbed sources are less luminous than the unabsorbed ones, but also that absorbed sources have smaller accretion rates as seen in lower Eddington ratios (Fig. 10). In agreement with Middleton et al. (2008) results, we find that the average values of Eddington ratio for Seyfert 1 ($\langle \lambda_{\text{Sy}1} \rangle = 0.064$) are higher than those found for intermediate Seyfert type ($\langle \lambda_{\text{Sy}1.5} \rangle = 0.015$) and Seyfert 2 with ($\langle \lambda_{\text{Sy}2} \rangle = 0.02$) (Fig. 10), although we do not observe the differences in the underlying spectra, as seen in their study. The same applies for the separation into unabsorbed ($\langle \lambda_{(N_{\text{H}} < 10^{22} \text{ cm}^{-2})} \rangle = 0.06$) and absorbed sources ($\langle \lambda_{(N_{\text{H}} > 10^{22} \text{ cm}^{-2})} \rangle = 0.015$). To calculate the probability that the Eddington ratios of Sey1/unabsorbed objects and Sey2/absorbed AGN are drawn from the same population, we applied a Kolmogorov-Smirnov test. We can reject the null hypothesis (same population), with a probability of false rejection of 0.1% and 3% for the Seyfert 1 – Seyfert 2 and unabsorbed – absorbed objects, respectively. On the other hand, since we do not find a significant correlation between the hard X-ray photon index and the Eddington ratio, we cannot back up the scenario by Middleton et al. (2008) as a way to explain the different spectral hardness of type 1 and type 2 AGN.

When studying the effect of radiation pressure on dusty absorbing gas around AGN, Fabian et al. (2008) trace a region in the N_{H} -Eddington ratio plane that is forbidden to long-lived clouds in AGN. In fact, even when the AGN is in the sub-Eddington regime for the ionized gas, it can appear to be super-Eddington for the dusty gas, hence ejecting the surrounding absorbing clouds. Objects in this region of the N_{H} -Eddington ratio plane could present outflows or show transient or variable absorption. Fabian et al. (2009) tested the predictions of this model using the *Swift/BAT* AGN sample of Winter et al. (2008) and find a good agreement, with only 1 object lying in the forbidden area, the Seyfert 1.9 object MCG-05-23-016. This object has been shown to exhibit high accretion rates at the Eddington limit (Beckmann et al. 2008). In Fig. 11 we show the regions defined by Fabian et al. (2009) in the N_{H} -Eddington ratio plane and our AGN sample. The forbidden region is on the

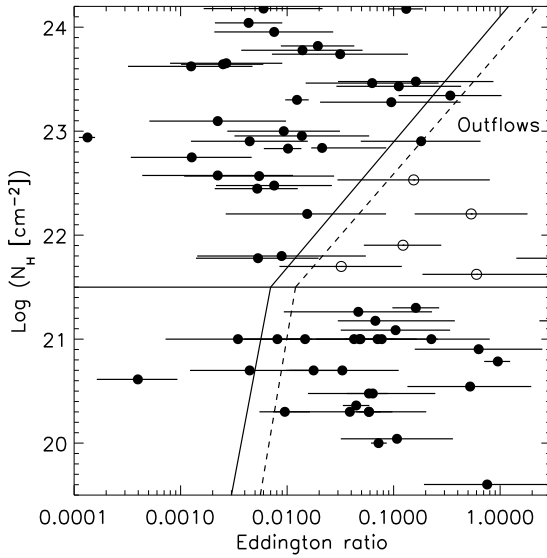


Fig. 11. Intrinsic absorption versus Eddington ratio for the Seyfert galaxies in the *INTEGRAL* sample. The “forbidden zone” described by Fabian et al. (2009) is occupied by 5 *INTEGRAL* AGN (empty circles).

upper-righthand side of the plot and bordered by an upper limit to N_{H} (for absorption due to dust lanes at few kpc from the AGN centre) and the Eddington limit for the dusty gas when only the black hole mass is considered to be gravitationally important (continuous line) or if also as much mass from intervening stars is included (dashed line). It is important to keep in mind that the bolometric luminosity is a critical parameter in defining the limits of the forbidden area, as different estimates of it can be used. Therefore, using a bolometric correction by a factor of few larger than what we applied here would shift the data points towards higher Eddington ratios, occupying the forbidden region completely. Nevertheless, with the bolometric luminosity we estimate ($L_{\text{Bol}} = 6 \times L_{(20-100 \text{ keV})}$), and find 5 objects with a detection significance $>4\sigma$ in this area: IGR J00335+6126, MCG–05–23–016, Mrk 766, IC 4329A, and NGC 5506. Out of these, only MCG–05–23–016 occupies the forbidden region also in Fabian et al. (2009), whereas IGR J00335+6126 was not included and Mrk 766 lacked absorption information in their study, IC 4329A is located close to the border of the forbidden zone, and NGC 5506 is not within this area. This raises the question of whether this region indeed cannot be occupied persistently by Seyfert type AGN, although the 5 objects do display some peculiarities, as described in the following. IC 4329A and IGR J00335+6126 are just above the upper limit N_{H} and MCG–05–23–016 has a complex spectrum with warm absorbers, not necessarily related to dusty gas (Fabian et al. 2009). The Seyfert 1.9 NGC 5506 has been identified as an obscured narrow-line Seyfert 1 (Nagar et al. 2002), which might explain the high accretion rate in this object. And the Seyfert 1.5 Mrk 766 with a black hole mass of only $3.5 \times 10^6 M_{\odot}$ (Uttley & McHardy 2005) might be a similar case to the highly efficient Seyfert MCG–05–23–016 (Beckmann et al. 2008). But the small number of objects and the fact that the uncertainty on the Eddington ratio is still rather large do not allow us to conclusively state that strongly absorbed Seyfert galaxies cannot exhibit high accretion rates over a long phase of their lifetimes.

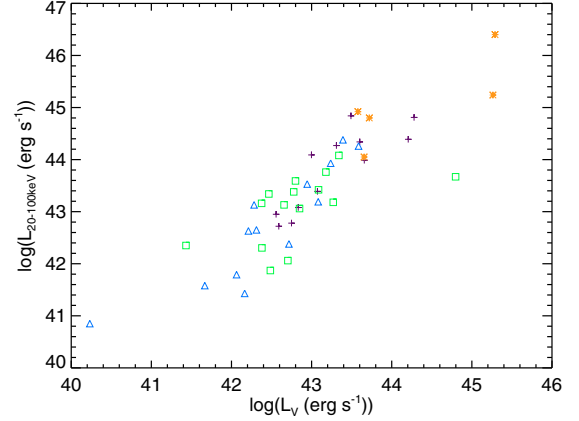


Fig. 12. X-ray luminosity L_X versus V-band luminosity L_V . AGN of different types are located along the same dispersion line, over more than 5 decades in luminosity. Symbols: crosses – Seyfert 1-1.2; triangles – Seyfert 1.5; squares – Seyfert 1.8-2; asterisks – BL Lacs.

4.4. Correlations with optical data and α_{OX}

We show in Fig. 12 the dispersion diagram of L_X vs. L_V , with different symbols for the different classes of objects considered. While the apparent correlation between both luminosities is certainly driven by the distance effect evident in Fig. 5, it is remarkable that the different classes of objects, from Seyfert 2 to blazars, are located on the same correlation line, over more than 5 decades in luminosity. Subtracting the common dependence on redshift through a partial correlation analysis, the correlation between the luminosities is still statistically significant, with a correlation coefficient of 0.74 and the probability of a chance occurrence is $\ll 0.01\%$. To test this correlation further, we made simulations using a bootstrap method (Simpson et al. 1986): to each couple of X-ray flux and redshift we randomly assigned an optical flux, drawn from the real values found for our sample and without excluding multiple choices of the same value (see also Bianchi et al. 2009, for a similar procedure). We then computed the X-ray and optical luminosities and calculated the Spearman and the partial correlation coefficients for the $L_X - L_V$ relation and the Spearman coefficient for the $F_X - F_V$ relation. Repeating this procedure 100 000 times, we were able to build histograms of the correlation coefficients of the simulated samples and found that only 0.001% of the simulated samples have a (Spearman or partial) correlation coefficient greater than measured in the real sample for the $L_X - L_V$ relation. For the $F_X - F_V$ correlation, the probability of chance occurrence is higher but still not significant, $\sim 2\%$. This indicates that the X-ray and optical emissions are indeed correlated, beyond the bias introduced by the common dependence on distance.

To further investigate this relation, we computed the histograms of the α_{OX} values for the different subtypes. We show in Fig. 13 that the peaks of the distributions coincide for the four subsamples, with mean values close to each other (Seyfert 2: 1.14, Seyfert 1.5: 1.13, Seyfert 1-1.2: 1.08, and BL Lac: 1.03). Seyfert 2 and 1.5 nevertheless show an extended wing towards higher α_{OX} ratios. NGC 1068, the prototypical Seyfert 2 galaxy, shows the highest α_{OX} value, 1.38. Because it is a Compton-thick object, this high α_{OX} value can be understood clearly. Other Compton-thick Seyfert galaxies, such as NGC 3165 and ESO138–1, also show α_{OX} values above 1.20. But other objects with high α_{OX} values, such as NGC 1052 and NGC 5033,

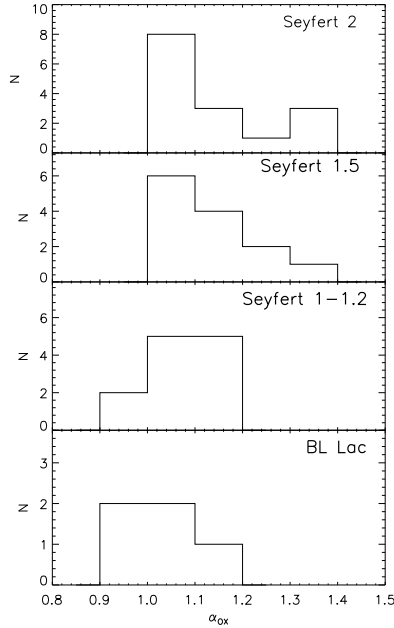


Fig. 13. α_{OX} histograms for 4 subtypes of AGN.

have low hydrogen column densities; in contrast several objects with high neutral columns, like NGC 3281, NGC 4945, and ESO 383–18, show relatively low α_{OX} values.

As discussed in Sect. 2.3.1, only 3 objects in the sample have shown significant optical variability over the period being monitored ($\Delta V > 0.5$ mag). For the blazars QSO B0716+714 and 3C 279, both their L_V and L_X values have to be dominated by the central AGN, with only a minor contribution by stars in V . This is indeed expected for this type of high-luminosity blazars while accretion processes and bulge stars dominate the V band in less active Seyfert galaxies.

That most Seyfert galaxies in the sample look similar when analysed from the point of view of their α_{OX} value indicates that the true nature of these objects is indeed very similar, thus supporting the unified scenario of AGN. The central black hole behaves very similarly with respect to the host galaxy, independent of the type of object. The classification as type 1 or type 2 AGN would mainly derive from observations of parameters dependent on geometrical effects, such as the profile of the emission lines or of the X-ray emission, but would not be tracing systematic differences in the intrinsic nature of these objects.

4.5. A fundamental plane of AGN activity

In the view of unification of different AGN types, it has been pointed out that AGN, spanning black hole masses in the range of $10^5 M_\odot \lesssim M_{BH} \lesssim 10^9 M_\odot$ and even accreting black holes in X-ray binaries with $M_{BH} \sim 10 M_\odot$, show similarities in radiative efficiency and jet power versus accretion rate (e.g. Fender et al. 2007). This connection gave rise to the “fundamental plane” of black hole activity. It has been found that indeed there is a close connection between the radio and X-ray luminosity of Galactic and super massive black holes of the form $L_{radio} \propto L_X^{0.7}$ (Corbel et al. 2000, 2003), linking the jet activity to the total output of the central engine. Later on, a connection of these two

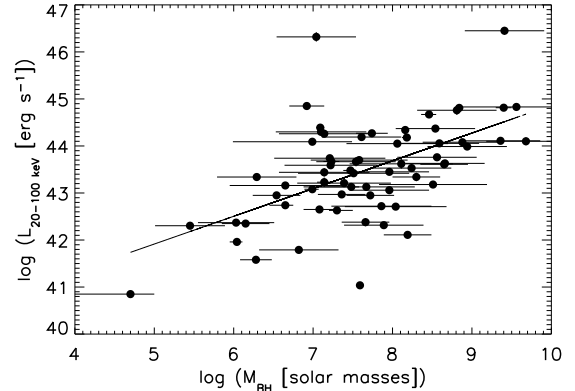


Fig. 14. Hard X-ray luminosity versus black hole masses for Seyfert galaxies. Errors on L_X are smaller than the symbols. More massive AGN appear to be brighter in the hard X-rays with $L_X \sim M_{BH}^{0.7 \pm 0.1}$. The correlation coefficient is 0.52 with a probability of non-correlation $< 2 \times 10^{-6}$.

parameters with the black hole mass itself was found, establishing the fundamental plane of AGN and Galactic black hole activity in the form of $L_{radio} \propto L_X^{0.6} M_{BH}^{0.8}$ (e.g. Merloni et al. 2003).

The correlation between X-ray luminosity and black hole mass is also common to all objects in our sample, showing indeed that more massive AGN are more luminous ($L_X \sim M_{BH}^{0.7 \pm 0.1}$, as shown in Fig. 14). A similar relation has lately been reported for various X-ray selected AGN samples (e.g. Bianchi et al. 2009; Wang et al. 2009), and also in these cases the slope is lower than 1. This could indicate that more massive black holes either have lower accretion rates than less massive objects, or a smaller fraction of their total power is converted into X-ray luminosity (assuming that the bolometric luminosity scales linearly with black hole mass). As reported in Table 8, a significant correlation is also detected between the black hole mass and the optical luminosity. Only for 8 out of 41 objects might the correlation of L_V versus M_{BH} be induced by the method used to estimate the mass, i.e. when deriving the mass from the K-band magnitudes (assumed to represent the bulge luminosity) or from continuum optical luminosity. However, caution should be used in general when considering a correlation between luminosity and black hole mass, because possible selection effects or different biases could contribute to the observed correlation in non complete samples. Woo & Urry (2002) argue that, when correlating bolometric luminosity with black hole mass, the Eddington luminosity sets a (soft) upper limit to the luminosities and therefore determines the empty region of the diagram in the upper left corner. On the other hand, the lower-right corner should be populated by low-luminosity, massive black holes that are not included or are rare in the high-energy AGN samples, such as normal or radio galaxies.

As discussed in detail in the previous section, there is also a significant correlation between optical and X-ray luminosity. Therefore, as summarised in Table 8, we found three significant correlations in our sample between the luminosities L_X and L_V , and the mass of the central black hole M_{BH} . This leads to the assumption that also these parameters, similar to L_X , L_R , and M_{BH} , form a fundamental plane for AGN. By applying an analysis following Merloni et al. (2003), we fit the data with the function

$$\log L_V = \zeta_{VX} \log L_X + \zeta_{VM} \log M_{BH} + b_V. \quad (2)$$

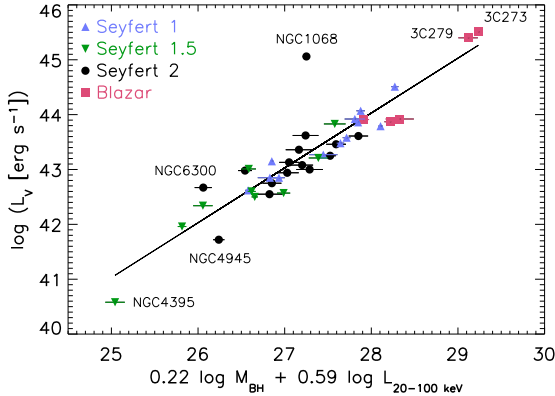


Fig. 15. Fundamental plane of optical luminosity L_V , X-ray luminosity L_X , and mass of the central black hole M_{BH} . Errors on luminosity are smaller than the symbols.

We obtain $\zeta_{VX} = 0.59 \pm 0.07$, $\zeta_{VM} = 0.22 \pm 0.08$, and $b_V = 16.0$, leading to

$$\log L_V = 0.59 \log L_X + 0.22 \log M_{\text{BH}} + 16.0; \quad (3)$$

i.e., $L_V \propto L_X^{0.6} M_{\text{BH}}^{0.2}$. We show this relation in Fig. 15. As already pointed out and discussed here and in Sect. 4.4, we carefully investigated that the effects of distance and selection effect are not causing the correlation observed here.

While the fundamental plane including the radio and X-ray luminosity can be understood as a connection of the jet activity, as visible in the radio, and the accretion flow, as dominating the X-rays, the correlation found here shows a different connection. The optical luminosity is commonly thought to be dominated by the AGN accretion disc (e.g. Siemiginowska et al. 1995) and therefore by the accretion processes onto the supermassive black hole, but there is also a possible contribution by the jet (Soldi et al. 2008) and emission of the bulge, and therefore of the stars in the host galaxy contributing to it. The latter is especially important as the resolution of *INTEGRAL*'s OMC camera does not allow a deconvolution of the core and the bulge. Nevertheless it shows that there is a significant bulge- M_{BH} correlation and that accretion processes are closely linked to the mass of the central black hole. The finding that this fundamental plane holds for all Seyfert types indicates further that these AGN are indeed intrinsically the same.

5. Conclusions

We have presented the second *INTEGRAL* AGN catalogue, including 187 extragalactic objects. The AGN population detected by *INTEGRAL* is dominated by Seyfert galaxies in the local ($z = 0.03$) universe, with moderate X-ray luminosity ($\langle L_{20-100 \text{ keV}} \rangle = 4 \times 10^{43} \text{ erg s}^{-1}$). Seyfert 1 galaxies appear to have higher luminosities ($\langle L_{20-100 \text{ keV}} \rangle = 10^{44} \text{ erg s}^{-1}$) and Eddington ratio ($\langle \lambda_{\text{Sy1}} \rangle = 0.064$) than the Seyfert 2 galaxies ($\langle L_{20-100 \text{ keV}} \rangle = 2.5 \times 10^{43} \text{ erg s}^{-1}$, $\langle \lambda_{\text{Sy2}} \rangle = 0.02$). Although IBIS/ISGRI spectra alone lack the information about the iron line complex and the continuum shape below 18 keV, they can be used to study the average Seyfert spectra in a statistical way. The underlying continuum of the hard X-ray spectrum appears to be consistent between different Seyfert types, both when a simple power-law model is applied and when considering the effects of Compton reflection. Applying the PEXRAV reflection

model with no high energy cut-off, the Seyfert 1 and 2 galaxies show the same underlying power law with $\Gamma \approx 1.95$ and a reflection component of $R \approx 1.1$, when applying different inclination angles of $i \approx 30^\circ$ and $i \approx 60^\circ$, respectively. Although, when applying a cut-off power law model to the stacked spectra, the Seyfert 1 show lower cut-off energies ($E_C = 86^{+21}_{-14} \text{ keV}$) than the Seyfert 2 objects ($E_C = 184^{+16}_{-52} \text{ keV}$), the bad quality of the fit in the latter case and that fixing the cut-off to the value of the Seyfert 1 leads to a similar spectral slope might indicate that the spectra are intrinsically indeed the same.

The same differences as for different Seyfert classes are observable when considering the intrinsic absorption: the unabsorbed sources also have higher luminosities ($\langle L_{20-100 \text{ keV}} \rangle = 6.3 \times 10^{43} \text{ erg s}^{-1}$) and Eddington ratio ($\langle \lambda \rangle = 0.06$) than the absorbed AGN ($\langle L_{20-100 \text{ keV}} \rangle = 2.5 \times 10^{43} \text{ erg s}^{-1}$, $\langle \lambda \rangle = 0.015$). Also separating the objects into absorption classes, the underlying continuum appears similar when considering the effects of Compton reflection. The mass of the central black hole is on average the same among the different Seyfert types and absorption classes, with $\langle M_{\text{BH}} \rangle = 4 \times 10^7 M_\odot$. Also comparing optical to hard X-ray emission, the different Seyfert classes show the same ratio ($\alpha_{\text{OX}} = 1.1$). On average, the hard X-ray spectra of Seyfert 1.5 objects are closer to those of the Seyfert 1 class than to Seyfert 2.

The optical data provided by *INTEGRAL*/OMC can be used to monitor variability. Strong variability ($\Delta V \gtrsim 0.5 \text{ mag}$) is only seen in three objects within the optical sample of 57 AGN, i.e. in the blazars QSO B0716+714 and 3C 279, and in NGC 4151.

The overall picture can be interpreted within the scenario of a unified model. The whole hard X-ray detected Seyfert population fills the parameter space of spectral shape, luminosity, and accretion rate smoothly, and only an overall tendency is seen in which more massive objects are more luminous, less absorbed, and accreting at higher Eddington ratio. An explanation for why the absorbed sources have been claimed to show flatter spectra in the hard X-ray domain when fit by a simple power law can be that the slope of the continuum strongly depends on the fitted model and that Compton reflection processes play a major role here. Considering these effects, it appears that the different Seyfert types are indeed intrinsically the same.

More evidence for the unified scheme is that a fundamental plane can be found between the mass of the central object and optical and X-ray luminosity. The correlation takes the form $L_V \propto L_X^{0.6} M_{\text{BH}}^{0.2}$, similar to what is found in previous studies between L_R , L_X , and M_{BH} . This links the accretion mechanism with the bulge of the host galaxy and with the mass of the central engine in the same way in all types of Seyfert galaxies. The connection is also apparent through the same optical-to-hard X-ray ratio measured in all Seyfert classes.

Evolutionary effects are likely to be beyond the AGN population accessible by *INTEGRAL* and *Swift*. Deep hard X-ray surveys by future missions like *NuSTAR*, *Astro-H*, and *EXIST* will be able to answer this question through deep observations of small portions of the sky.

Acknowledgements. *INTEGRAL* is an ESA project funded by ESA member states (especially the PI countries: Denmark, France, Germany, Italy, Spain, Switzerland), Czech Republic, Poland, and with the participation of Russia and the USA. We thank the anonymous referee for the comments that helped to improve the paper. This research has made use of data obtained through the High Energy Astrophysics Science Archive Research Center Online Service, provided by the NASA/Goddard Space Flight Center. We acknowledge the use of public data from the *Swift* data archive and from the *INTEGRAL* data archive provided by the ISDC. S.S. acknowledges the support by the Centre National d'Etudes Spatiales (CNES). P.L. and A.A.Z. have been supported in part by the Polish MNiSW grants NN203065933 and 362/1/N-INTEGRAL/2008/09/0, and

the Polish Astroparticle Network 621/E-78/BWSN-0068/2008. J.M.M.H., A.D. and J.A. are supported by the Spanish MICINN grant ESP2008-03467.

Appendix A: Notes on individual sources

We include here all Seyfert galaxies above 30σ IBIS/ISGRI detection significance, all sources showing a complex ISGRI spectrum (Table 3), and those for which the results found here differ from previous works.

Mrk 348: the X-ray spectrum of this Seyfert 2 was studied by *RXTE*, showing the same spectral shape as reported here ($\Gamma = 1.8$) and evidence for a reflection component with $R \lesssim 1$ (Smith et al. 2001). Instead of a cut-off power law with $\Gamma = 0.9$ and $E_C = 55$ keV as given in Table 3, the *INTEGRAL* data can be equally well represented by a Compton reflection model (PEXRAV) with $R = 1$ and photon index $\Gamma = 1.8$ and no high-energy cut-off.

NGC 1275 presents a very complex spectrum in *INTEGRAL* data as it includes several components of different physical origin. While the hard X-ray spectrum visible in the IBIS/ISGRI data is dominated by the narrow-line radio galaxy NGC 1275 and its spectrum above 20 keV can be represented by a simple power law model, we observe in JEM-X the Perseus galaxy cluster. An extensive discussion of the *INTEGRAL* spectrum has been presented in Eckert & Paltani (2009).

NGC 4051: this Seyfert 1.5 shows a strong reflection component when fit together with soft X-rays, e.g. $R \simeq 7$ for *Suzaku* (Terashima et al. 2009), and $R \simeq 6$ for combined *Swift*/XRT and IBIS/ISGRI data (Beckmann et al. 2009), while the data presented here allow only to fit a single power law model with $\Gamma = 2.1 \pm 0.2$. When fitting the *Suzaku* data with a simple power law model, Terashima et al. (2009) derive a photon index of $\Gamma = 1.5^{+0.3}_{-0.2}$ for a low flux state, indicating strong flux and spectral variability.

NGC 4151: this bright AGN allows complex modelling beyond the scope of this paper, and we refer to an early *INTEGRAL* analysis by Beckmann et al. (2005), to an analysis of *BeppoSAX* data by de Rosa et al. (2007), and to a study of the different spectral states by Lubiński et al. (2009).

NGC 4388: the hard X-ray data of this Seyfert 2 galaxy have been studied by Beckmann et al. (2004). Their analysis of *INTEGRAL*, *XMM-Newton*, *BeppoSAX*, *CGRO*, and *SIGMA* data showed that the hard X-rays spectrum is well described by an absorbed power law with $\Gamma = 1.65 \pm 0.04$ and $N_H = 2.7 \times 10^{23} \text{ cm}^{-2}$, with no indication of a cut-off or reflection component. The data presented here now show evidence for a cut-off at 80 keV and $\Gamma = 1.3$. Recently, a turn over at $E_C = 30 \pm 13$ keV with $\Gamma = 0.9 \pm 0.3$ was also reported in *Suzaku* data of NGC 4388 (Shirai et al. 2008), detecting also significant spectral variability.

NGC 4507: this Seyfert 2 shows a reflection component of the order of $R = 0.5 - 1$ in *BeppoSAX* observations and a photon index of $\Gamma = 1.3 - 1.9$, while the cut-off energy was not constrained (Dadina 2007). The IBIS/ISGRI data do not require the presence of reflection, and a simple cut-off power law ($\Gamma = 1.1 \pm 0.2$, $E_C = 65^{+27}_{-12}$ keV) is sufficient ($\chi^2 = 3.5$ for 7 d.o.f.). Applying the PEXRAV model without cut-off, we obtained a chi-squared of $\chi^2 = 6.2$ for 7 d.o.f. The value of the photon index and the reflection obtained are $\Gamma = 1.7 \pm 0.1$ and $R = 0.6^{+1.5}_{-0.5}$, respectively, consistent with the *BeppoSAX* observations.

NGC 4593: *BeppoSAX* data of this Seyfert 1 showed a reflection component with $R = 1.1^{+2.6}_{-0.5}$ and $\Gamma = 1.9 \pm 0.1$ but no evidence for a cut-off (Dadina 2007). From IBIS/ISGRI and JEM-X data we found that a power law with a cut-off gives a

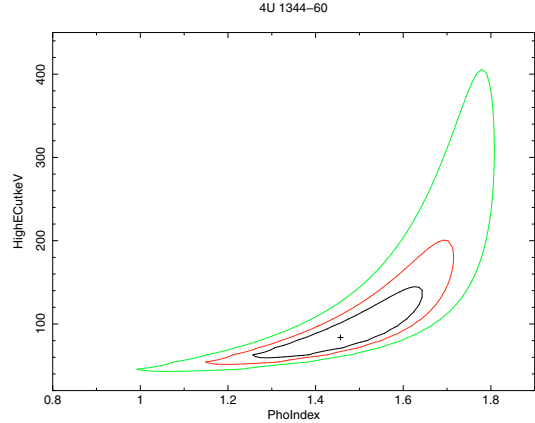


Fig. A.1. Contour plot of the 1–3 sigma confidence levels of cut-off energy [keV] versus photon index Γ . A steeper spectral fit requires a higher cut-off energy.

good fit to the data ($\Gamma = 1.5 \pm 0.1$, $E_C = 193^{+12}_{-93}$ keV, $\chi^2 = 15$ for 15 d.o.f.). The value of the absorption has been fixed to $N_H = 2 \times 10^{20} \text{ cm}^{-2}$. Applying a PEXRAV model with no cut-off also provides a good representation of the data with $\chi^2 = 10.7$ for 15 d.o.f. and gives a photon index of $\Gamma = 1.9 \pm 0.1$ and a reflection component of $R = 1.7^{+1.6}_{-0.8}$, both parameters consistent with the results by Dadina et al. (2007).

NGC 4945: the IBIS/ISGRI spectrum of the Seyfert 2 galaxy NGC 4945 (with an exposure of 276 ks) is amongst the six analyzed by Soldi et al. (2005). In their work the best model to the data is a simple power law ($\Gamma = 1.9^{+0.1}_{-0.1}$), and they give a lower limit to the possible high energy cut-off, $E_C \gg 130$ keV. Using the new IBIS/ISGRI and JEM-X data we found that a simple absorbed power law does not provide a good fit ($\chi^2 = 30$ for 12 d.o.f.) and a cutoff at high energy is necessary. This component improves significantly the goodness of the fit ($\chi^2 = 3.3$ for 11 d.o.f.) and gives a photon index of $\Gamma = 1.4^{+0.2}_{-0.2}$ and a cutoff at $E_C = 121^{+63}_{-34}$ keV. The absorption has been fixed to $N_H = 400 \times 10^{22} \text{ cm}^{-2}$. These values are also consistent with those obtained by Guainazzi et al. (2000), using *BeppoSAX* data.

Cen A is the only extragalactic object also seen by IBIS/PICsIT. Combined IBIS/ISGRI, SPI, and PICsIT data analysis gave a spectral slope of $\Gamma = 1.80 \pm 0.01$ (Lubiński 2009), close to the results presented here. It has been also detected by *Fermi*/LAT (Abdo et al. 2009) and at very high energy gamma-rays by HESS (Aharonian et al. 2009).

4U 1344-60: in Beckmann et al. (2006) the analysis of combined *XMM-Newton* and *INTEGRAL* data showed a good representation of the broad-band data with an absorbed power-law ($\Gamma = 1.65$) plus a Gaussian component. Applying the same simple model to the IBIS/ISGRI data used here, leads to a steep hard X-ray power law ($\Gamma = 1.9 \pm 0.1$) but gives a bad fit result ($\chi^2_\nu > 2$). Using the simultaneous JEM-X and ISGRI data and adding a cut-off, flattens the spectrum: the lower the cut-off energy, the flatter the resulting photon index ($\Gamma = 1.5^{+0.1}_{-0.2}$, $E_C = 86^{+31}_{-22}$), as can be seen in Fig. A.1. Panessa et al. (2008) analysed again non-simultaneous *XMM-Newton* and *INTEGRAL* data, finding a cut-off power law with photon index $\Gamma = 1.75^{+0.18}_{-0.14}$ and $E_C > 78$ keV. Fixing the spectral slope for the combined JEM-X and IBIS/ISGRI spectrum to $\Gamma = 1.75$, we also get a higher cut-off energy of $E_C = 214^{+73}_{-44}$ keV.

IC 4329A: the *BeppoSAX* spectrum of this Seyfert 1 analysed by Dadina (2007) by applying a PEXRAV model showed in several observations a cut-off at energies $E_C > 120$ keV, with a reflection component of $R = 0.5$ – 1.5 and a photon index of $\Gamma = 1.9$ – 2.0 . Using the same model for the combined JEM-X and ISGRI data, we get a flatter spectrum, with $\Gamma = 1.6 \pm 0.3$, $E_C = 124_{-48}^{+243}$ keV and $R = 0.3_{-0.3}^{+0.8}$, and thus a spectrum which is consistent with no reflection component. We therefore applied the simpler cut-off power law model which leads to $\Gamma = 1.4 \pm 0.1$ and $E_C = 86_{-13}^{+18}$ keV.

Circinus Galaxy: the combined IBIS/ISGRI and SPI spectrum of the Circinus galaxy has been studied by Soldi et al. (2005) based on 589 ks exposure time, finding as the best model to the data an absorbed power law ($\Gamma = 1.8_{-0.5}^{+0.4}$) with $N_H = 400 \times 10^{22}$ cm $^{-2}$ and a high-energy cutoff at $E_C = 50_{-18}^{+51}$ keV, values consistent with the ones obtained by previous *BeppoSAX* observations. Using the same model and fixing the hydrogen column density to the one used by Soldi et al. (2005), we found the best fit to the data ($\chi^2 = 16$ for 11 d.o.f.), with parameters consistent with the values listed above ($\Gamma = 1.2 \pm 0.2$, $E_C = 30 \pm 3$ keV). Dadina (2007) analysed two *BeppoSAX* observations applying reflection models with $\Gamma_1 = 1.7 \pm 0.1$, $R_1 = 0.29_{-0.04}^{+0.05}$ and $\Gamma_2 = 1.3 \pm 0.2$, $R_2 = 0.35_{-0.09}^{+0.39}$, both with cut-off at $E_C \lesssim 50$ keV. Adding a reflection component to the data presented here improves significantly the fit ($\chi^2 = 6.1$ for 9 d.o.f.) but the parameter are not well constrained: $\Gamma = 1.8_{-0.6}^{+0.4}$, $E_C = 76_{-30}^{+180}$ keV and $R = 1.6_{-1.1}^{+8.0}$.

PG 1416-129: the Seyfert 1 galaxy had been included in the first *INTEGRAL* AGN catalogue (Beckmann et al. 2006a). Subsequent analysis of the data with improved software showed that the detection of this source was indeed spurious, and we now do not consider this source to be an *INTEGRAL* detected object.

IGR J16351-5806: this Seyfert 2 galaxy has recently been claimed to be a Compton thick AGN with $N_H > 1.5 \times 10^{24}$ cm $^{-2}$ (Malizia et al. 2009). This is based on the observation that the hard X-ray spectrum is rather flat, as also shown here with $\Gamma = 1.5$, and that a strong iron $K\alpha$ line with $EW > 1$ keV is an indicator for a significant reflection component. Malizia et al. fit the spectrum therefore as a pure reflection spectrum. As the ISGRI data alone do not allow fitting the complex model, we assumed the simple model of an unabsorbed power law, as also observed in *Swift*/XRT data (Landi et al. 2007a).

IGR J16426+6536: this narrow-line Seyfert 1 ($z = 0.323 \pm 0.001$, Parisi et al. 2008; Butler et al. 2009) shows a rather high luminosity of $L_{(20-100 \text{ keV})} = 2 \times 10^{46}$ erg s $^{-1}$ but moderate mass of the central black hole ($M = 1.1 \times 10^7 M_\odot$). This leads to a large Eddington ratio of about $\lambda \simeq 90$ (defined in Sect. 4.2). It has to be pointed out though, that the soft X-ray counterpart as detected by *XMM-Newton* exhibits only a flux of 1.1×10^{-12} erg cm $^{-2}$ s $^{-1}$ (Ibarra et al. 2008), about 10 times below what would be expected from the *INTEGRAL* detection with $f_{(20-40 \text{ keV})} = 2.6 \times 10^{-11}$ erg cm $^{-2}$ s $^{-1}$. This might indicate that this source is strongly absorbed, highly variable, or that the optical counterpart is a misidentification, leading to the high super-Eddington accretion rate.

GRS 1734-292: the IBIS/ISGRI data of GRS 1734-292 (for a total exposure of 4040 ks) have been analyzed by Molina et al. (2006), along with *ASCA*/GIS data, who found that the best fit is obtained using an absorbed cut-off power law. Using the new IBIS/ISGRI and JEM-X data we found that the best model ($\chi^2 = 12.1$ for 11 d.o.f.) is an absorbed power-law with a cut-off and a reflection component with the following parameters: $N_H = 3.7 \times 10^{22}$ cm $^{-2}$, $E_C = 220_{-150}^{+200}$ keV, $\Gamma = 2.0_{-0.4}^{+0.3}$ and

$R = 2.7_{-1.8}^{+3.1}$. The black hole mass of GRS 1734-292 has been provided by I. Papadakis (private communication) based on the empirical relation found by Tremaine et al. (2002) between the black hole mass and the stellar velocity dispersion σ_* , estimating σ_* from the width of the [O III] line reported by Marti et al. (1998).

IGR J17488-3253: for this Seyfert 1 galaxy ($z = 0.02$) a fit of simultaneous JEM-X and IBIS/ISGRI data by a cut-off power law model results in $\chi^2_\nu = 5.8$ for 11 degrees of freedom. As the source is located in a dense area, it is possible that the JEM-X data are contaminated by sources within the field of view, especially as the JEM-X data are well represented by a black body model with a temperature of 0.7 keV. We therefore analysed *Swift*/XRT data of the source. A combined fit of XRT and ISGRI data results in $\chi^2_\nu = 1.1$ for 119 degrees of freedom, showing an absorbed power law model with $N_H = 0.72 \pm 0.04$ and $\Gamma = 1.63 \pm 0.03$, representing the data well over the 0.3 keV to 100 keV energy range.

QSO B1957+405 (Cyg A): the IBIS/ISGRI (together with *BeppoSAX*/MECS and PDS) spectrum of Cygnus A has been analyzed by Molina et al. (2006), using data for a total exposure of 426 ks. In their work they fitted the high-energy spectrum with a complex model in order to take into account also the gas emission of the galaxy cluster to which the AGN belongs. For doing so they used an absorbed power law plus a bremsstrahlung component. Following their work we fitted the IBIS/ISGRI and JEM-X spectrum using the same model (plus a cross-calibration constant) and we found that it provides the best fit ($\chi^2 = 6$ for 9 d.o.f.) and that the parameters obtained ($\Gamma = 1.9_{-0.2}^{+0.1}$ and $kT = 4.5_{-2.7}^{+3.7}$ keV) are in good agreement with those they obtained. The value of the absorption has been fixed to $N_H = 2 \times 10^{23}$ cm $^{-2}$.

IGR J21247+5058: the high-energy broad-band spectrum of this radio galaxy was obtained by Molina et al. (2007) by combining *XMM-Newton* and *Swift*/XRT observation with IBIS/ISGRI data. The 0.4–100 keV spectrum is well described by a power law, with slope $\Gamma = 1.5$, characterized by complex absorption due to two layers of material partially covering the source and a high-energy cut-off around 70–80 keV, consistent with our findings ($\Gamma = 1.4 \pm 0.1$, $E_C = 61_{-11}^{+22}$ keV) using JEM-X and ISGRI data. As Molina et al. point out, features such as a narrow iron line and a Compton reflection component, if present, are weak, suggesting that reprocessing of the power-law photons in the accretion disc plays a negligible role in the source.

References

- Abdo, A. A., Ackermann, M., Ajello, M., et al. 2009, *ApJ*, 700, 597
 Abramowicz, M. A., Chen, X.-M., Granath, M., & Lasota, J.-P. 1996, *ApJ*, 471, 762
 Aharonian, F., Akhperjanian, A. G., Anton, G., et al. 2009, *ApJ*, 695, L40
 Antonucci, R. 1993, *ARA&A*, 31, 473
 Arnaud, K. A. 1996, in *Astronomical Data Analysis Software and Systems V*, ed. G. Jacoby, & J. Barnes, ASP Conf. Ser., 101, 17
 Awaki, H., Koyama, K., Inoue, H., & Halpern, J. P. 1991, *PASJ*, 43, 195
 Awaki, H., Murakami, H., Leighly, K. M., et al. 2005, *ApJ*, 632, 793
 Barthelmy, S. D., Barbier, L. M., Cummings, J. R., et al. 2005, *SSRv*, 120, 143
 Bassani, L., Dadina, M., & Maiolino, R. 1999, *ApJS*, 121, 473
 Bassani, L., Molina, M., Malizia, A., et al. 2006, *ApJ*, 636, L65
 Bassani, L., Landi, R., & Malizia, A. 2007, *ApJ*, 669, L1
 Beckmann, V., Gehrels, N., Shrader, C. R., & Soldi, S. 2006a, *ApJ*, 638, 642
 Beckmann, V., Soldi, S., Shrader, C. R., Gehrels, N., & Produit, N. 2006b, *ApJ*, 652, 126
 Beckmann, V., Soldi, S., Shrader, C. R., & Gehrels, N. 2006c, *The X-ray Universe 2005*, 604, 777
 Beckmann, V., Gehrels, N., & Tueller, J. 2007a, *ApJ*, 666, 122

- Beckmann, V., Petry, D., & Weidenspointner, G. 2007b, *ATel*, 1264
- Beckmann, V., Ishibashi, W., Bottacini, E., Ajello, M., & Greiner, J. 2007c, *ATel*, 1317
- Beckmann, V., Courvoisier, T. J.-L., Gehrels, N., et al. 2008, *A&A*, 492, 93
- Beckmann, V., Courvoisier, T. J.-L., Gehrels, N., et al. 2009, *AIP Conf. Ser.*, 1126, 141
- Bian, W., & Gu, Q. 2007, *ApJ*, 657, 159
- Bianchi, S., Bonilla, N. F., Guainazzi, M., et al. 2009, *A&A*, 501, 915
- Bodaghee, A., Courvoisier, T. J.-L., Rodriguez, J., et al. 2007, *A&A*, 467, 585
- Butler, S. C., Tomsick, J. A., Chaty, S., et al. 2009, *ApJ*, 698, 502
- Corbel, S., Fender, R. P., Tzioumis, A. K., et al. 2000, *A&A*, 359, 251
- Corbel, S., Nowak, M. A., Fender, R. P., et al. 2003, *A&A*, 400, 1007
- Courvoisier, T. J.-L., & Türler, M. 2005, *A&A*, 444, 417
- Courvoisier, T. J.-L., Walter, R., Beckmann, V., et al. 2003, *A&A*, 411, L53
- Dadina, M. 2007, *A&A*, 461, 1209
- Dadina, M. 2008, *A&A*, 485, 417
- Deluit, S., & Courvoisier, T. J.-L. 2003, *A&A*, 399, 77
- de Rosa, A., Piro, L., Perola, G. C., et al. 2007, *A&A*, 463, 903
- Domingo, A., Caballero, M. D., Figueras, F., et al. 2003, *A&A*, 411, L281
- Ebisawa, K., Bourban, G., Bodaghee, A., Mowlavi, N., & Courvoisier, T. J.-L. 2003, *A&A*, 411, L59
- Eckert, D., & Paltani, S. 2009, *A&A*, 495, 415
- Fabian, A. C., Vasudevan, R. V., & Gandhi, P. 2008, *MNRAS*, 385, L43
- Fabian, A. C., Vasudevan, R. V., Mushotzky, R. F., Winter, L. M., & Reynolds, L. M. W. C. S. 2009, *MNRAS*, 349, L89
- Fender, R., Körding, E., Belloni, T., et al. 2007, *Proc. of Science*, 6th Microquasar Workshop [arXiv:0706.3838]
- Ferrarese, L., & Merritt, D. 2000, *ApJ*, 539, L9
- Gehrels, N., Chincarini, G., Giommi, P., et al. 2004, *ApJ*, 611, 1005
- Gierliński, M., Nikolajuk, M., & Czerny, B. 2008, *MNRAS*, 383, 741
- Gilli, R., Comastri, A., & Hasinger, G. 2007, *A&A*, 463, 79
- Goncalves, T. S., Martin, D. C., Halpern, J. P., Eracleous, M., & Pavlov, G. G. 2009, *ATel*, 1623
- Gondoin, P., Orr, A., & Lumb, D. 2003, *A&A*, 398, 967
- Gondek, D., Zdziarski, A. A., Johnson, W. N., et al. 1996, *MNRAS*, 282, 646
- Graham, A. W. 2008, *PASA*, 25, 167
- Greene, J. E. & Ho, L. C. 2005, *ApJ*, 627, 721
- Greenhill, L. J. 1997, *ASPC*, 113, 394
- Guainazzi, M., Matt, G., Brandt, W. N., et al. 2000, *A&A*, 356, 463
- Guilbert, P. W., & Rees, M.-J. 1988, *MNRAS*, 233, 475
- Hicks, E. K. S., & Malkan, M. A. 2008, *ApJS*, 174, 31
- Ibarra, A., Kuulkers, E., & Saxton, R. 2008, *ATel*, 1397
- Johnson, W. N., Kinzer, R. L., Kurfess, J. D., et al. 1993, *ApJS*, 86, 693
- Kaspi, S., Smith, P. S., Netzer, H., et al. 2000, *ApJ*, 533, 631
- Kirsch, M. G., Briel, U. G., Burrows, D., et al. 2005, *SPIE*, 5898, 22
- Landi, R., Masetti, N., Gehrels, N., et al. 2007a, *ATel*, 990
- Landi, R., Malizia, A., Masetti, N., et al. 2007b, *ATel*, 1274
- Landi, R., Masetti, N., Stephen, J. B., et al. 2007c, *ATel*, 1288
- Landi, R., Masetti, N., Sguera, V., et al. 2007d, *ATel*, 1322
- Landi, R., Stephen, J. B., Masetti, N., et al. 2009, *A&A*, 493, 893
- Laor, A. 2000, *New Astron. Rev.*, 44, 503
- Lawrence, A., & Elvis, M. 1982, *ApJ*, 256, 410
- Lebrun, F., Leray, J. P., Lavocat, P., et al. 2003, *A&A*, 411, L141
- Lubiński, P. 2009, *A&A*, 496, 557
- Lubiński, P., Walter, R., Beckmann, V., et al. 2009, in prep.
- Lund, N., Budtz-Jørgensen, C., Westergaard, N. J., et al. 2003, *A&A*, 411, L231
- Magdziarz, P., & Zdziarski, A. A. 1995, *MNRAS*, 273, 837
- Malizia, A., Bassani, L., Stephen, J. B., et al. 2003, *ApJ*, 589, L17
- Malizia, A., Landi, R., Bassani, L., et al. 2007, *ApJ*, 668, 81
- Malizia, A., Bassani, L., Bird, A. J., et al. 2008, *MNRAS*, 389, 1360
- Malizia, A., Bassani, L., Panessa, F., de Rosa, A., & Bird, A. J. 2009, *MNRAS*, 349, L121
- Martí, J., Mirabel, I. F., Chaty, S., & Rodríguez, L. F. 1998, *A&A*, 330, 72
- Masetti, N., Morelli, L., Palazzi, E., et al. 2006, *A&A*, 459, 21
- Masetti, N., Parisi, P., Palazzi, E., et al. 2009, *A&A*, 495, 121
- Mas-Hesse, J. M., Giménez, A., Culhane, J. L., et al. 2003, *A&A*, 411, L261
- Merloni, A., Heinz, S., & Di Matteo, T. 2003, *MNRAS*, 345, 1057
- Middleton, M., Done, C., & Schurch, N. 2008, *MNRAS*, 383, 1501
- Molina, M., Malizia, A., Bassani, L., et al. 2006, *MNRAS*, 371, 821
- Molina, M., Bassani, L., Malizia, A., et al. 2008, *MNRAS*, 390, 1217
- Morales, R., & Fabian, A. C. 2002, *MNRAS*, 329, 209
- Murphy, K. D., & Yaqoob, T. 2009, *MNRAS*, 397, 1549
- Nagar, N. M., Oliva, E., Marconi, A., & Maiolino, R. 2002, *A&A*, 391, L21
- Novak, G. S., Faber, S. M., & Dekel, A. 2006, *ApJ*, 637, 96
- O'Dell, S. L., Puschell, J. J., Stein, W. A., & Warner, J. W. 1978, *ApJS*, 38, 267
- O'Dowd, M., Urry, C. M., & Scarpa, R. 2002, *ApJ*, 580, 96
- Paltani, S., & Türler, M. 2005, *A&A*, 435, 811
- Paltani, S., Walter, R., McHardy, I. M., et al. 2008, *A&A*, 485, 707
- Panessa, F., Bassani, L., de Rosa, A., et al. 2008, *A&A*, 467, 519
- Pappa, A., Georgantopoulos, I., Stewart, G. C., & Zezas, A. L. 2001, *MNRAS*, 326, 995
- Parisi, P., Masetti, N., Malizia, A., et al. 2008, *ATel*, 1800
- Peterson, B. M., Ferrarese, L., Gilbert, K. M., et al. 2004, *ApJ*, 613, 682
- Remillard, R. A., & McClintock, J. E. 2006, *ARA&A*, 44, 49
- Revnivtsev, M., Sunyaev, R., Lutovinov, A., & Sazonov, S. 2007, *ATel*, 1253
- Ricci, C., Beckmann, V., Courvoisier, T. J.-L., et al. 2009a, in prep.
- Ricci, C., Beckmann, V., Audard, M., & Courvoisier, T. J.-L. 2009b, *A&A*, submitted
- Rodríguez, J., Tomsick, J. A., & Chaty, S. 2008, *A&A*, 482, 731
- Sazonov, S., & Revnivtsev, M. 2004, *A&A*, 423, 469
- Sazonov, S., Krivonos, R., Revnivtsev, M., Churazov, E., & Sunyaev, R. 2007, *A&A*, 462, 57
- Sazonov, S., Revnivtsev, M., Burenin, R., et al. 2008, *A&A*, 487, 509
- Siemiginowska, A., Kuhn, O., Elvis, M., et al. 1995, *ApJ*, 454, 77
- Shirai, H., Fukazawa, Y., Sasada, M., et al. 2008, *PASJ*, 60, 263
- Simpson, G., & Mayer-Hasselwander, H. 1986, *A&A*, 162, 340
- Smith, D. A., Georgantopoulos, I., & Warwick, R. S. 2001, *ApJ*, 550, 635
- Soldi, S., Beckmann, V., Bassani, L., et al. 2005, *A&A*, 444, 431
- Soldi, S., Türler, M., Paltani, S., et al. 2008, *A&A*, 486, 411
- Steffen, A. T., Barger, A. J., Cowie, L. L., Mushotzky, R. F., & Yang, Y. 2003, *ApJ*, 596, L23
- Terashima, Y., Gallo, L. C., Inoue, H., et al. 2009, *PASJ*, 61, 299
- Tomsick, J. A., Chaty, S., Rodríguez, J., Walter, R., & Kaaret, P. 2008, *ApJ*, 685, 1143
- Treister, E., & Urry, C. M. 2005, *ApJ*, 630, 115
- Treister, E., Urry, C. M., & Virani, S. 2009, *ApJ*, 696, 110
- Tremaine, S., Gebhardt, K., Bender, R., et al. 2002, *ApJ*, 574, 740
- Tueller, J., Mushotzky, R. F., Barthelmy, S. D., et al. 2008, *ApJ*, 681, 113
- Uttley, P., & McHardy, I. M. 2005, *MNRAS*, 363, 586
- Vestergaard, M. 2004, *ASPC*, 311, 69
- Wandel, A. 2002, *ApJ*, 565, 762
- Wang, J., Mao, Y. F., & Wei, J. Y. 2009, *AJ*, 137, 3388
- Winkler, C., Courvoisier, T. J.-L., Di Cocco, G., et al. 2003, *A&A*, 411, L1
- Winter, L. M., Mushotzky, R. F., Tueller, J., & Markwardt, C. 2008, *ApJ*, 674, 686
- Winter, L. M., Mushotzky, R. F., Reynolds, C. S., & Tueller, J. 2009, *ApJ*, 690, 1322
- Woo, J.-H., & Urry, M. 2002, *ApJ*, 579, 530
- Wu, X. B., Wang, R., Kong, M. Z., et al. 2004, *A&A*, 424, 793
- Zdziarski, A. A., Johnson, W. N., Done, C., Smith, D., & McNaron-Brown, K. 1995, *ApJ*, 438, L63
- Zdziarski, A. A., Lubiński, P., & Smith, D. A. 1999, *MNRAS*, 303, L11
- Zdziarski, A. A., Poutanen, J., & Johnson, W. N. 2000, *ApJ*, 542, 703
- Zurita Heras, J. A., Chaty, S., & Tomsick, J. A. 2009, *A&A*, 502, 787

Bibliography

- Abdo, A. A., Ackermann, M., Ajello, M., et al. 2010a, *ApJ*, 715, 429
- Abdo, A. A., Ackermann, M., Ajello, M., et al. 2009, *ApJ*, 700, 597
- Abdo, A. A., Ackermann, M., Ajello, M., et al. 2010b, *ApJ*, 710, 1271
- Ajello, M., Costamante, L., Sambruna, R. M., et al. 2009, *ApJ*, 699, 603
- Ajello, M., Greiner, J., Sato, G., et al. 2008, *ApJ*, 689, 666
- Alexander, D. M., Chary, R., Pope, A., et al. 2008, *ApJ*, 687, 835
- Almaini, O., Lawrence, A., Shanks, T., et al. 2000, *MNRAS*, 315, 325
- Antonelli, L. A., Matt, G., & Piro, L. 1997, *A&A*, 317, 686
- Antonucci, R. 1993, *ARA&A*, 31, 473
- Arago, F. & Barral, J. A. 1854, *Astronomie populaire*, ed. Arago, F. & Barral, J. A.
- Arp, H. 1977, *ApJ*, 218, 70
- Attié, D., Cordier, B., Gros, M., et al. 2003, *A&A*, 411, L71
- Atwood, W. B., Abdo, A. A., Ackermann, M., et al. 2009, *ApJ*, 697, 1071
- Avni, Y. & Bahcall, J. N. 1980, *ApJ*, 235, 694
- Bade, N., Engels, D., Voges, W., et al. 1998, *A&AS*, 127, 145
- Baldovin, C., Savchenko, V., Beckmann, V., et al. 2009, *The Astronomer's Telegram*, 1908, 1
- Barr, P., White, N. E., Sanford, P. W., & Ives, J. C. 1977, *MNRAS*, 181, 43P
- Barr, P. & Mushotzky, R. F. 1986, *Nature*, 320, 421
- Barthel, P. D. 1989, *ApJ*, 336, 606
- Barthelmy, S. D., Barbier, L. M., Cummings, J. R., et al. 2005, *Space Science Reviews*, 120, 143
- Bassani, L., Molina, M., Malizia, A., et al. 2006, *ApJL*, 636, L65
- Bauer, F. E., Vignali, C., Alexander, D. M., et al. 2004, *Advances in Space Research*, 34, 2555
- Bearden, J. A. 1967, *Rev. Mod. Phys.*, 39, 78

- Beckmann, V. 1999, in *Astronomical Society of the Pacific Conference Series*, Vol. 159, BL Lac Phenomenon, ed. L. O. Takalo & A. Sillanpää, 493
- Beckmann, V., Bade, N., & Wucknitz, O. 1999, *A&A*, 352, 395
- Beckmann, V. 2000a, *Blazar Data*, 2, 3
- Beckmann, V. 2000b, PhD thesis, Hamburger Sternwarte, Universität Hamburg (Germany)
- Beckmann, V. & Wolter, A. 2001, *X-ray Astronomy: Stellar Endpoints, AGN, and the Diffuse X-ray Background*, 599, 502
- Beckmann, V. 2002a, in “The Gamma-Ray Universe”, *proc. of the 37th Rencontres de Moriond*, ed. A. Goldwurm, D. N. Neumann, J. Trân Thanh Vân, 417–421
- Beckmann, V. 2002b, in “The Gamma-Ray Universe”, *proc. of the 37th Rencontres de Moriond*, ed. A. Goldwurm, D. N. Neumann, J. Trân Thanh Vân, 179–184
- Beckmann, V., Wolter, A., Celotti, A., et al. 2002, *A&A*, 383, 410
- Beckmann, V. 2003, in *Astronomical Society of the Pacific Conference Series*, Vol. 299, High Energy Blazar Astronomy, ed. L. O. Takalo & E. Valtaoja, 47
- Beckmann, V., Borkowski, J., Courvoisier, T., et al. 2003a, *A&A*, 411, L327
- Beckmann, V., Engels, D., Bade, N., & Wucknitz, O. 2003b, *A&A*, 401, 927
- Beckmann, V., Borkowski, J., Courvoisier, T., et al. 2004a, *Nuclear Physics B Proceedings Supplements*, 132, 301
- Beckmann, V., Favre, P., Tavecchio, F., et al. 2004b, *ApJ*, 608, 692
- Beckmann, V., Gehrels, N., Favre, P., et al. 2004c, in *ESA Special Publication*, Vol. 552, 5th INTEGRAL Workshop on the INTEGRAL Universe, ed. V. Schönfelder, G. Lichti, & C. Winkler, 535
- Beckmann, V., Gehrels, N., Favre, P., et al. 2004d, *ApJ*, 614, 641
- Beckmann, V., Kennea, J. A., Markwardt, C., et al. 2005a, *ApJ*, 631, 506
- Beckmann, V., Shrader, C. R., Gehrels, N., et al. 2005b, *ApJ*, 634, 939
- Beckmann, V., Gehrels, N., Shrader, C. R., & Soldi, S. 2006a, *ApJ*, 638, 642
- Beckmann, V., Kennea, J. A., Markwardt, C., et al. 2006b, in *ESA Special Publication*, Vol. 604, The X-ray Universe 2005, ed. A. Wilson, 241
- Beckmann, V., Soldi, S., Shrader, C. R., & Gehrels, N. 2006c, in *ESA Special Publication*, Vol. 604, The X-ray Universe 2005, ed. A. Wilson, 777
- Beckmann, V., Soldi, S., Shrader, C. R., Gehrels, N., & Produit, N. 2006d, *ApJ*, 652, 126
- Beckmann, V., Barthelmy, S. D., Courvoisier, T., et al. 2007a, *A&A*, 475, 827
- Beckmann, V., Gehrels, N., & Tueller, J. 2007b, *ApJ*, 666, 122

- Beckmann, V., Shrader, C. R., Gehrels, N., Soldi, S., & Produit, N. 2007c, in ESA Special Publication, Vol. 622, ESA Special Publication, 173
- Beckmann, V. 2008, in proc. of the 10th ICATPP Conference On Astroparticle, Particle, Space Physics, Detectors And Medical Physics Applications, eds. Barone et al., World Scientific, 650
- Beckmann, V., Courvoisier, T., Gehrels, N., et al. 2008a, *A&A*, 492, 93
- Beckmann, V., Mereghetti, S., von Kienlin, A., et al. 2008b, GRB Coordinates Network, 7450
- Beckmann, V., Courvoisier, T., Gehrels, N., et al. 2009b, in American Institute of Physics Conference Series, Vol. 1126, American Institute of Physics Conference Series, ed. J. Rodriguez & P. Ferrando, 141–144
- Beckmann, V., Beck, M., Ferrigno, C., et al. 2009a, GRB Coordinates Network, 8968
- Beckmann, V., Soldi, S., Courvoisier, T. J.-L., et al. 2009c, in proceedings of the 7th INTEGRAL Workshop, September 8-11, 2008, Copenhagen, Denmark
- Beckmann, V., Soldi, S., Ricci, C., et al. 2009d, *A&A*, 505, 417
- Beckmann, V., Beck, M., Ferrigno, C., et al. 2010a, GRB Coordinates Network, 10898
- Beckmann, V., Ricci, C., & Soldi, S. 2010b, in proceedings of the Fermi Symposium, Washington D.C., November 2009, arXiv:0912.2254
- Beckmann, V., Ricci, C., Soldi, S., et al. 2010c, in proceedings of 'The Extreme sky: Sampling the Universe above 10 keV', Otranto, October 2009, arXiv:1001.4362
- Beckmann, V., Soldi, S., Ricci, C., et al. 2010d, in proceedings for 'X-ray Astronomy 2009', Bologna, September 2009
- Beckmann, V. & Do Cao, O. 2011, in proceedings of the 8th INTEGRAL Workshop, September 27-30, 2010, Dublin, Ireland
- Berghea, C. T., Weaver, K. A., Colbert, E. J. M., & Roberts, T. P. 2008, *ApJ*, 687, 471
- Bird, A. J., Bazzano, A., Bassani, L., et al. 2010, *ApJS*, 186, 1
- Blain, A. W., Jameson, A., Smail, I., et al. 1999, *MNRAS*, 309, 715
- Blandford, R. D. & Znajek, R. L. 1977, *MNRAS*, 179, 433
- Blandford, R. D. & Rees, M. J. 1978, in BL Lac Objects, ed. A. M. Wolfe, 328–341
- Blandford, R. D. & Levinson, A. 1995, *ApJ*, 441, 79
- Bloom, S. D. & Marscher, A. P. 1996, *ApJ*, 461, 657
- Bodaghee, A., Courvoisier, T., Rodriguez, J., et al. 2007, *A&A*, 467, 585
- Böttcher, M. & Dermer, C. D. 2002, *ApJ*, 564, 86
- Bouchet, L., Jourdain, E., Roques, J., et al. 2008, *ApJ*, 679, 1315

- Bowyer, C. S., Lampton, M., Mack, J., & de Mendonca, F. 1970, *ApJL*, 161, L1
- Brandt, S., Budtz-Jørgensen, C., Lund, N., et al. 2003, *A&A*, 411, L243
- Bregman, J. N., Glassgold, A. E., Huggins, P. J., et al. 1990, *ApJ*, 352, 574
- Bromley, B. C., Miller, W. A., & Pariev, V. I. 1998, *Nature*, 391, 54
- Burrows, D. N., Hill, J. E., Nousek, J. A., et al. 2005, *Space Science Reviews*, 120, 165
- Byram, E. T., Chubb, T. A., & Friedman, H. 1966, *Science*, 152, 66
- Caccianiga, A., Maccacaro, T., Wolter, A., della Ceca, R., & Gioia, I. M. 1999, *ApJ*, 513, 51
- Caccianiga, A., Maccacaro, T., Wolter, A., Della Ceca, R., & Gioia, I. M. 2002, *ApJ*, 566, 181
- Camero Arranz, A., Reig, P., Connell, P., et al. 2004, in *ESA Special Publication*, Vol. 552, 5th INTEGRAL Workshop on the INTEGRAL Universe, ed. V. Schönfelder, G. Lichti, & C. Winkler, 279
- Camero Arranz, A., Wilson, C. A., Connell, P., et al. 2005, *A&A*, 441, 261
- Camero Arranz, A., Wilson, C. A., Connell, P., et al. 2007, in *Astronomical Society of the Pacific Conference Series*, Vol. 361, *Active OB-Stars: Laboratories for Stellar and Circumstellar Physics*, ed. A. T. Okazaki, S. P. Owocki, & S. Stefl, 402
- Cameron, A. G. W. 1967, *Nature*, 215, 464
- Cappelluti, N., Brusa, M., Hasinger, G., et al. 2009, *A&A*, 497, 635
- Caroli, E., Stephen, J. B., di Cocco, G., Natalucci, L., & Spizzichino, A. 1987, *Space Science Reviews*, 45, 349
- Carroll, B. W. & Ostlie, D. A. 1996, *An Introduction to Modern Astrophysics*, ed. Carroll, B. W. & Ostlie, D. A.
- Chen, Y., Wang, J., Yan, C., Hu, C., & Zhang, S. 2009, *ApJL*, 695, L130
- Cheng, F., Danese, L., Franceschini, A., & de Zotti, G. 1985, *MNRAS*, 212, 857
- Chernyakova, M., Neronov, A., Courvoisier, T., et al. 2007, *A&A*, 465, 147
- Chitnis, V. R., Pendharkar, J. K., Bose, D., et al. 2009, *ApJ*, 698, 1207
- Chubb, T. A., Friedman, H., Kreplin, R. W., & Kupperian, J. E. 1957, *Nature*, 179, 861
- Churazov, E., Sunyaev, R., Revnivtsev, M., et al. 2007, *A&A*, 467, 529
- Churazov, E., Sazonov, S., Sunyaev, R., & Revnivtsev, M. 2008, *MNRAS*, 385, 719
- Colbert, E. J. M. & Mushotzky, R. F. 1999, *ApJ*, 519, 89
- Colbert, E. J. M., Strickland, D. K., Veilleux, S., & Weaver, K. A. 2005, *ApJ*, 628, 113
- Comastri, A. 2004, in *Astrophysics and Space Science Library*, Vol. 308, *Supermassive Black Holes in the Distant Universe*, ed. A. J. Barger, 245

- Comastri, A., Iwasawa, K., Gilli, R., Vignali, C., & Ranalli, P. 2009, in proceedings of 'The Energetic Cosmos: from Suzaku to Astro-H', July 2009, Otaru, Hokkaido, Japan, arXiv:0910.1025
- Condon, J. J., Cotton, W. D., Greisen, E. W., et al. 1998, *AJ*, 115, 1693
- Courvoisier, T. 1998, *A&A Rev.*, 9, 1
- Courvoisier, T., Beckmann, V., Bourban, G., et al. 2003a, *A&A*, 411, L343
- Courvoisier, T., Walter, R., Beckmann, V., et al. 2003b, *A&A*, 411, L53
- Courvoisier, T. & Türler, M. 2005, *A&A*, 444, 417
- Crummy, J., Fabian, A. C., Gallo, L., & Ross, R. R. 2006, *MNRAS*, 365, 1067
- Curtis, H. D. 1920, *JRASC*, 14, 317
- Cusumano, G., La Parola, V., Segreto, A., et al. 2010, *A&A*, 510, A48+
- Czerny, B., Róžańska, A., Dovčiak, M., Karas, V., & Dumont, A. 2004, *A&A*, 420, 1
- Dadina, M. 2007, *A&A*, 461, 1209
- Dadina, M. 2008, *A&A*, 485, 417
- Daly, R. A. 2009, *ApJL*, 691, L72
- de Loore, C. & de Greve, J. P. 1975, *Ap&SS*, 35, 241
- de Vries, W. H., Becker, R. H., White, R. L., & Loomis, C. 2005, *AJ*, 129, 615
- Dermer, C. D. & Schlickeiser, R. 1993, *ApJ*, 416, 458
- Dewangan, G. C., Griffiths, R. E., Dasgupta, S., & Rao, A. R. 2007, *ApJ*, 671, 1284
- Di Matteo, T., Springel, V., & Hernquist, L. 2005, *Nature*, 433, 604
- Diehl, R., Baby, N., Beckmann, V., et al. 2003, *A&A*, 411, L117
- Donato, D., Ghisellini, G., Tagliaferri, G., & Fossati, G. 2001, *A&A*, 375, 739
- Done, C., Madejski, G. M., & Smith, D. A. 1996, *ApJL*, 463, L63
- Done, C. & Gierliński, M. 2006, *MNRAS*, 367, 659
- Done, C. 2007, *Progress of Theoretical Physics Supplement*, 169, 248
- Down, E. J., Rawlings, S., Sivia, D. S., & Baker, J. C. 2010, *MNRAS*, 401, 633
- Ebisawa, K., Bourban, G., Bodaghee, A., Mowlavi, N., & Courvoisier, T. 2003, *A&A*, 411, L59
- Edelson, R. & Nandra, K. 1999, *ApJ*, 514, 682
- Einstein, A. 1916, *Annalen der Physik*, 354, 769
- Elvis, M., Maccacaro, T., Wilson, A. S., et al. 1978, *MNRAS*, 183, 129

- Elvis, M. 2000, *ApJ*, 545, 63
- Emmanoulopoulos, D., McHardy, I. M., & Uttley, P. 2010, *MNRAS*, 246
- Engels, D., Hagen, H., Cordis, L., et al. 1998, *A&AS*, 128, 507
- Esin, A. A., McClintock, J. E., Drake, J. J., et al. 2001, *ApJ*, 555, 483
- Esposito, J. A., Bertsch, D. L., Chen, A. W., et al. 1999, *ApJS*, 123, 203
- Fabian, A. C., Rees, M. J., Stella, L., & White, N. E. 1989, *MNRAS*, 238, 729
- Fabian, A. C., Iwasawa, K., Reynolds, C. S., & Young, A. J. 2000, *PASP*, 112, 1145
- Fabian, A. & Miniutti, G. 2009, in "Kerr Spacetime: Rotating Black Holes in General Relativity", ed. D. J. Wiltshire, M. Visser, S. M. Scott, Cambridge Univ. Press, 236–280
- Fanaroff, B. L. & Riley, J. M. 1974, *MNRAS*, 167, 31P
- Favre, P., Courvoisier, T., & Paltani, S. 2005, *A&A*, 443, 451
- Fiore, F., Puccetti, S., Brusa, M., et al. 2009, *ApJ*, 693, 447
- Forman, W., Jones, C., Cominsky, L., et al. 1978, *ApJS*, 38, 357
- Fossati, G., Maraschi, L., Celotti, A., Comastri, A., & Ghisellini, G. 1998, *MNRAS*, 299, 433
- Friedman, H., Lichtman, S. W., & Byram, E. T. 1951, *Physical Review*, 83, 1025
- Galeev, A. A., Rosner, R., & Vaiana, G. S. 1979, *ApJ*, 229, 318
- Garofalo, D. 2009, *ApJ*, 699, 400
- Garofalo, D., Evans, D. A., & Sambruna, R. M. 2010, *MNRAS* accepted, arXiv:1004.1166
- Gehrels, N., Chincarini, G., Giommi, P., et al. 2004, *ApJ*, 611, 1005
- Georgakakis, A., Rowan-Robinson, M., Nandra, K., et al. 2010, *MNRAS*, 406, 420
- George, I. M. & Fabian, A. C. 1991, *MNRAS*, 249, 352
- Ghisellini, G., Padovani, P., Celotti, A., & Maraschi, L. 1993, *ApJ*, 407, 65
- Ghisellini, G., Haardt, F., & Matt, G. 1994, *MNRAS*, 267, 743
- Ghisellini, G. & Madau, P. 1996, *MNRAS*, 280, 67
- Ghisellini, G., Celotti, A., Fossati, G., Maraschi, L., & Comastri, A. 1998, *MNRAS*, 301, 451
- Ghisellini, G., Maraschi, L., & Tavecchio, F. 2009, *MNRAS*, 396, L105
- Ghisellini, G., Tavecchio, F., Foschini, L., et al. 2010, *MNRAS*, 402, 497
- Giacconi, R. & Rossi, B. 1960, *J. Geophys. Res.*, 65, 773
- Giacconi, R., Gursky, H., Paolini, F. R., & Rossi, B. B. 1962, *Physical Review Letters*, 9, 439

- Giacconi, R., Kellogg, E., Gorenstein, P., Gursky, H., & Tananbaum, H. 1971, *ApJL*, 165, L27
- Giacconi, R., Murray, S., Gursky, H., et al. 1972, *ApJ*, 178, 281
- Giacconi, R., Branduardi, G., Briel, U., et al. 1979, *ApJ*, 230, 540
- Gierliński, M. & Done, C. 2004, *MNRAS*, 349, L7
- Gierliński, M., Middleton, M., Ward, M., & Done, C. 2008, *Nature*, 455, 369
- Gilli, R., Maiolino, R., Marconi, A., et al. 2000, *A&A*, 355, 485
- Gioia, I. M., Maccacaro, T., Schild, R. E., et al. 1990, *ApJS*, 72, 567
- Goldwurm, A., David, P., Foschini, L., et al. 2003, *A&A*, 411, L223
- Gondek, D., Zdziarski, A. A., Johnson, W. N., et al. 1996, *MNRAS*, 282, 646
- Gregg, M. D., Becker, R. H., White, R. L., et al. 1996, *AJ*, 112, 407
- Gruber, D. E., Matteson, J. L., Peterson, L. E., & Jung, G. V. 1999, *ApJ*, 520, 124
- Grupe, D., Thomas, H., & Beuermann, K. 2001, *A&A*, 367, 470
- Gursky, H., Kellogg, E. M., Leong, C., Tananbaum, H., & Giacconi, R. 1971, *ApJL*, 165, L43
- Haardt, F. & Maraschi, L. 1991, *ApJL*, 380, L51
- Haardt, F. & Maraschi, L. 1993, *ApJ*, 413, 507
- Hagen, H., Engels, D., & Reimers, D. 1999, *A&AS*, 134, 483
- Hagen, H., Groote, D., Engels, D., Haug, U., & Reimers, D. 1986, *Mitteilungen der Astronomischen Gesellschaft Hamburg*, 67, 184
- Hagen, H., Groote, D., Engels, D., & Reimers, D. 1995, *A&AS*, 111, 195
- Halpern, J. P. 1984, *ApJ*, 281, 90
- Hannikainen, D. C., Rodriguez, J., Vilhu, O., et al. 2005, *A&A*, 435, 995
- Hartman, R. C., Bertsch, D. L., Bloom, S. D., et al. 1999, *ApJS*, 123, 79
- Hayes, M. J. C., Culhane, J. L., Blissett, R. J., Barr, P., & Burnell, S. J. B. 1980, *MNRAS*, 193, 15P
- Heiles, C. 1964, *ApJ*, 140, 470
- Herschel, W. 1786, *Royal Society of London Philosophical Transactions Series I*, 76, 457
- Herschel, W. 1789, *Royal Society of London Philosophical Transactions Series I*, 79, 212
- Herschel, W. 1800a, *Royal Society of London Proceedings Series I*, 1, 98
- Herschel, W. 1800b, *Royal Society of London Philosophical Transactions Series I*, 90, 284
- Herschel, W. 1802, *Royal Society of London Philosophical Transactions Series I*, 92, 477

- Hjalmarsson, L., Zdziarski, A. A., Paizis, A., Beckmann, V., & Vilhu, O. 2004, in ESA Special Publication, Vol. 552, 5th INTEGRAL Workshop on the INTEGRAL Universe, ed. V. Schönfelder, G. Lichti, & C. Winkler, 223
- Hjalmarsson, L., Zdziarski, A. A., Larsson, S., et al. 2008, MNRAS, 384, 278
- Ho, L. C. 1999, ApJ, 516, 672
- Holt, S. S., Boldt, E. A., & Serlemitsos, P. J. 1968, ApJL, 154, L137
- Holt, S. S., Boldt, E. A., & Serlemitsos, P. J. 1969, ApJL, 158, L155
- Hoyle, F. & Fowler, W. A. 1963, MNRAS, 125, 169
- Hoyle, F., Narlikar, J. V., & Wheeler, J. A. 1964, Nature, 203, 914
- Hubble, E. P. 1925, The Observatory, 48, 139
- Hubble, E. P. 1926, ApJ, 64, 321
- Hubble, E. P. 1929a, Proceedings of the National Academy of Science, 15, 168
- Hubble, E. P. 1929b, ApJ, 69, 103
- Hughes, P. A., Aller, H. D., & Aller, M. F. 1992, ApJ, 396, 469
- Iwasawa, K., Fabian, A. C., Ueno, S., et al. 1997, MNRAS, 285, 683
- Iwasawa, K., Wilson, A. S., Fabian, A. C., & Young, A. J. 2003, MNRAS, 345, 369
- Jahnke, K. & Wisotzki, L. 2003, MNRAS, 346, 304
- Jansky, K. G. 1933, Nature, 132, 66
- Johnson, W. N., Grove, J. E., Kinzer, R. L., et al. 1994, in American Institute of Physics Conference Series, Vol. 304, American Institute of Physics Conference Series, ed. C. E. Fichtel, N. Gehrels, & J. P. Norris, 515–524
- Kaastra, J. S. 1992, internal SRON-Leiden report, version 2.0
- Kajava, J. J. E. & Poutanen, J. 2009, MNRAS, 398, 1450
- Kanbach, G., Bertsch, D. L., Fichtel, C. E., et al. 1988, Space Science Reviews, 49, 69
- Kant, I. 1755, Allgemeine Naturgeschichte und Theorie des Himmels, ed. Kant, I.
- Kneiske, T. M., Bretz, T., Mannheim, K., & Hartmann, D. H. 2004, A&A, 413, 807
- Koglin, J. E., An, H., Blaedel, K. L., et al. 2009, in Presented at the Society of Photo-Optical Instrumentation Engineers (SPIE) Conference, Vol. 7437, Society of Photo-Optical Instrumentation Engineers (SPIE) Conference Series
- Köhler, T. 1996, PhD thesis, Doctoral Thesis, Universität Hamburg, (1996)
- Köhler, T., Groote, D., Reimers, D., & Wisotzki, L. 1997, A&A, 325, 502

- Koss, M., Mushotzky, R., Veilleux, S., & Winter, L. 2010, submitted to *ApJ Letters*
- Kraemer, S. B., George, I. M., Crenshaw, D. M., et al. 2005, *ApJ*, 633, 693
- Kriss, G. A., Canizares, C. R., & Ricker, G. R. 1980, *ApJ*, 242, 492
- Kristian, J. 1973, *ApJL*, 179, L61
- Krolik, J. H. & Kallman, T. R. 1987, *ApJL*, 320, L5
- Kubota, A. & Done, C. 2004, *MNRAS*, 353, 980
- La Franca, F., Fiore, F., Comastri, A., et al. 2005, *ApJ*, 635, 864
- Labanti, C., Di Cocco, G., Ferro, G., et al. 2003, *A&A*, 411, L149
- Lacki, B. C., Thompson, T. A., Quataert, E., Loeb, A., & Waxman, E. 2010, submitted to *ApJ*, arXiv:1003.3257
- Lähteenmäki, A. & Valtaoja, E. 1999, *ApJ*, 521, 493
- Laor, A. 1991, *ApJ*, 376, 90
- Laplace, P.-S. 1796, *Exposition du système du Monde*, ed. Laplace, P.-S.
- Lawrence, A. & Elvis, M. 1982, *ApJ*, 256, 410
- Lawrence, A. 1991, *MNRAS*, 252, 586
- Lawrence, A. & Papadakis, I. 1993, *ApJL*, 414, L85
- Lebrun, F., Ballet, J., Paul, J., et al. 1992, *A&A*, 264, 22
- Lebrun, F., Leray, J. P., Lavocat, P., et al. 2003, *A&A*, 411, L141
- Ledden, J. E. & Odell, S. L. 1985, *ApJ*, 298, 630
- Letawe, G. & Magain, P. 2010, *A&A* in press, arXiv:1003.3746
- Letawe, Y., Letawe, G., & Magain, P. 2010, *MNRAS*, 217
- Liu, X., Greene, J. E., Shen, Y., & Strauss, M. A. 2010, submitted to *ApJL*, arXiv:1003.3467
- Lubiński, P. 2009, *A&A*, 496, 557
- Lubiński, P., Zdziarski, A. A., Walter, R., et al. 2010, *MNRAS*, 408, 1851
- Lund, N., Budtz-Jørgensen, C., Westergaard, N. J., et al. 2003, *A&A*, 411, L231
- Lynden-Bell, D. 1969, *Nature*, 223, 690
- Lynden-Bell, D. & Rees, M. J. 1971, *MNRAS*, 152, 461
- Maccacaro, T., della Ceca, R., Gioia, I. M., et al. 1991, *ApJ*, 374, 117
- Magdziarz, P. & Zdziarski, A. A. 1995, *MNRAS*, 273, 837

- Maiolino, R., Alonso-Herrero, A., Anders, S., et al. 2000, *ApJ*, 531, 219
- Malaguti, G., Bazzano, A., Beckmann, V., et al. 2003, *A&A*, 411, L307
- Malizia, A., Bassani, L., Stephen, J. B., et al. 2003, *ApJL*, 589, L17
- Malizia, A., Stephen, J. B., Bassani, L., et al. 2009, *MNRAS*, 399, 944
- Malizia, A., Stephen, J. B., Bassani, L., et al. 2010, *ArXiv e-prints*, 1002.4712
- Malzac, J. 2001, *MNRAS*, 325, 1625
- Malzac, J., Beloborodov, A. M., & Poutanen, J. 2001, *MNRAS*, 326, 417
- Malzac, J. & Petrucci, P. 2002, *MNRAS*, 336, 1209
- Mannheim, K. 1993, *A&A*, 269, 67
- Maraschi, L., Ghisellini, G., Tanzi, E. G., & Treves, A. 1986, *ApJ*, 310, 325
- Maraschi, L., Ghisellini, G., & Celotti, A. 1992, *ApJL*, 397, L5
- Maraschi, L. & Rovetti, F. 1994, *ApJ*, 436, 79
- Maraschi, L. & Tavecchio, F. 2003, *ApJ*, 593, 667
- Markowitz, A. & Edelson, R. 2001, *ApJ*, 547, 684
- Markwardt, C. B., Tueller, J., Skinner, G. K., et al. 2005, *ApJL*, 633, L77
- Marquardt, D. 1963, *SIAM Journal on Applied Mathematics*, 11, 431
- Marshall, F. E., Boldt, E. A., Holt, S. S., et al. 1980, *ApJ*, 235, 4
- Marshall, N., Warwick, R. S., & Pounds, K. A. 1981, *MNRAS*, 194, 987
- Marshall, H. L. 1985, *ApJ*, 299, 109
- Martocchia, A., Karas, V., & Matt, G. 2000, *MNRAS*, 312, 817
- Mas-Hesse, J. M., Giménez, A., Culhane, J. L., et al. 2003, *A&A*, 411, L261
- Masetti, N., Foschini, L., Palazzi, E., et al. 2004, *A&A*, 423, 651
- Mateos, S., Barcons, X., Carrera, F. J., et al. 2007, *A&A*, 473, 105
- Matt, G., Perola, G. C., & Piro, L. 1991, *A&A*, 247, 25
- Matt, G., Piro, L., Antonelli, L. A., et al. 1994, *A&A*, 292, L13
- Matt, G., Guainazzi, M., Frontera, F., et al. 1997, *A&A*, 325, L13
- McClintock, J. E., Remillard, R. A., Canizares, C. R., Veron, P., & van Paradijs, J. 1979, *ApJ*, 233, 809
- McClintock, J. E., Haswell, C. A., Garcia, M. R., et al. 2001, *ApJ*, 555, 477

- McHardy, I. M., Lawrence, A., Pye, J. P., & Pounds, K. A. 1981, *MNRAS*, 197, 893
- McHardy, I. & Czerny, B. 1987, *Nature*, 325, 696
- McHardy, I. M., Koerding, E., Knigge, C., Uttley, P., & Fender, R. P. 2006, *Nature*, 444, 730
- Mereghetti, S., Götz, D., Beckmann, V., et al. 2003a, *A&A*, 411, L311
- Mereghetti, S., Götz, D., Tiengo, A., et al. 2003b, *ApJL*, 590, L73
- Mereghetti, S., Götz, D., von Kienlin, A., et al. 2009, *GRB Coordinates Network*, 8841, 1
- Merloni, A., Heinz, S., & di Matteo, T. 2003, *MNRAS*, 345, 1057
- Mewe, R., Heise, J., Gronenschild, E. H. B. M., et al. 1975, *ApJL*, 202, L67
- Mewe, R., Gronenschild, E. H. B. M., & van den Oord, G. H. J. 1985, *A&AS*, 62, 197
- Middleton, M., Done, C., & Schurch, N. 2008, *MNRAS*, 383, 1501
- Middleton, M. & Done, C. 2010, *MNRAS* in press, arXiv:0908.0224
- Miller, L., Turner, T. J., & Reeves, J. N. 2008, *A&A*, 483, 437
- Miller, L., Turner, T. J., & Reeves, J. N. 2009, *MNRAS*, 399, L69
- Miniutti, G. & Fabian, A. C. 2004, *MNRAS*, 349, 1435
- Mitchell, J. 1784, *Phil. Trans. R. Soc. (London)*, 74, 35
- Miyakawa, T., Ebisawa, K., Terashima, Y., et al. 2009, *PASJ*, 61, 1355
- Molina, M., Bassani, L., Malizia, A., et al. 2009, *MNRAS*, 399, 1293
- Morton, D. C. 1964, *ApJ*, 140, 460
- Murphy, K. D., Yaqoob, T., & Terashima, Y. 2007, *ApJ*, 666, 96
- Mushotzky, R. F., Serlemitsos, P. J., Boldt, E. A., Holt, S. S., & Becker, R. H. 1978, *ApJ*, 220, 790
- Mushotzky, R. F., Done, C., & Pounds, K. A. 1993, *ARA&A*, 31, 717
- Nandra, K., Fabian, A. C., George, I. M., et al. 1993, *MNRAS*, 260, 504
- Nandra, K., George, I. M., Mushotzky, R. F., Turner, T. J., & Yaqoob, T. 1997, *ApJ*, 477, 602
- Nolan, P. L., Tompkins, W. F., Grenier, I. A., & Michelson, P. F. 2003, *ApJ*, 597, 615
- Oda, M. 1964, *Nature*, 202, 1321
- Oepik, E. 1922, *ApJ*, 55, 406
- Oppenheimer, J. R. & Volkoff, G. M. 1939, *Physical Review*, 55, 374
- Orr, M. J. L. & Browne, I. W. A. 1982, *MNRAS*, 200, 1067
- Padovani, P. & Giommi, P. 1995, *ApJ*, 444, 567

- Padovani, P., Giommi, P., Landt, H., & Perlman, E. S. 2007, *ApJ*, 662, 182
- Paizis, A., Beckmann, V., Courvoisier, T., et al. 2003, *A&A*, 411, L363
- Paizis, A., Courvoisier, T., Vilhu, O., et al. 2004, in *ESA Special Publication*, Vol. 552, 5th INTEGRAL Workshop on the INTEGRAL Universe, ed. V. Schönfelder, G. Lichti, & C. Winkler, 229
- Paizis, A., Farinelli, R., Titarchuk, L., et al. 2006, *A&A*, 459, 187
- Paltani, S. & Courvoisier, T. 1994, *A&A*, 291, 74
- Paltani, S. 1999, in *Astronomical Society of the Pacific Conference Series*, Vol. 159, BL Lac Phenomenon, ed. L. O. Takalo & A. Sillanpää, 293
- Paltani, S., Walter, R., McHardy, I. M., et al. 2008, *A&A*, 485, 707
- Papadakis, I. E. 2004, *MNRAS*, 348, 207
- Pariev, V. I. & Bromley, B. C. 1998, *ApJ*, 508, 590
- Penston, M. V., Penston, M. J., Selmes, R. A., Becklin, E. E., & Neugebauer, G. 1974, *MNRAS*, 169, 357
- Perlman, E. S., Padovani, P., Giommi, P., et al. 1998, *AJ*, 115, 1253
- Perola, G. C., Matt, G., Cappi, M., et al. 2002, *A&A*, 389, 802
- Petrucci, P. O., Haardt, F., Maraschi, L., et al. 2001, *ApJ*, 556, 716
- Petry, D., Beckmann, V., Halloin, H., & Strong, A. 2009, *A&A*, 507, 549
- Piccinotti, G., Mushotzky, R. F., Boldt, E. A., et al. 1982, *ApJ*, 253, 485
- Piconcelli, E., Jimenez-Bailón, E., Guainazzi, M., et al. 2005, *A&A*, 432, 15
- Piro, L., Yamauchi, M., & Matsuoka, M. 1990, *ApJL*, 360, L35
- Piro, L., de Rosa, A., Dadina, M., et al. 2000, *Advances in Space Research*, 25, 453
- Polletta, M. d. C., Wilkes, B. J., Siana, B., et al. 2006, *ApJ*, 642, 673
- Pottschmidt, K., Wilms, J., Chernyakova, M., et al. 2003, *A&A*, 411, L383
- Pounds, K. A., Nandra, K., Fink, H. H., & Makino, F. 1994, *MNRAS*, 267, 193
- Poutanen, J. & Svensson, R. 1996, *ApJ*, 470, 249
- Poutanen, J. & Fabian, A. C. 1999, *MNRAS*, 306, L31
- Pozdnyakov, L. A., Sobol, I. M., & Syunyaev, R. A. 1983, *Astrophysics and Space Physics Reviews*, 2, 189
- Predehl, P., Andritschke, R., Bornemann, W., et al. 2007, in *Society of Photo-Optical Instrumentation Engineers (SPIE) Conference Series*, Vol. 6686

- Predehl, P., Boehringer, H., Brunner, H., et al. 2010, in proceedings for 'X-ray Astronomy 2009', Bologna, September 2009, arXiv:1001.2502
- Predehl, P. & Schmitt, J. H. M. M. 1995, *A&A*, 293, 889
- Prieto, M. A., Reunanen, J., Tristram, K. R. W., et al. 2010, *MNRAS*, 402, 724
- Raymond, J. C. & Smith, B. W. 1977, *ApJS*, 35, 419
- Reber, G. 1940, *ApJ*, 91, 621
- Rector, T. A. & Stocke, J. T. 2001, *AJ*, 122, 565
- Reimers, D. 1990, *The Messenger*, 60, 13
- Reimers, D., Köhler, T., & Wisotzki, L. 1996, *A&AS*, 115, 235
- Remillard, R. A. & McClintock, J. E. 2006, *ARA&A*, 44, 49
- Reynolds, C. S. 1996, PhD thesis, Cambridge University
- Reynolds, C. S. 1997, *MNRAS*, 286, 513
- Reynolds, C. S., Fabian, A. C., Brenneman, L. W., et al. 2009, *MNRAS*, 397, L21
- Risaliti, G., Maiolino, R., & Salvati, M. 1999, *ApJ*, 522, 157
- Risaliti, G. 2002, *A&A*, 386, 379
- Roberts, T. P. 2007, *Ap&SS*, 311, 203
- Rodriguez, J., Cabanac, C., Hannikainen, D. C., et al. 2005, *A&A*, 432, 235
- Roming, P. W. A., Kennedy, T. E., Mason, K. O., et al. 2005, *Space Science Reviews*, 120, 95
- Roques, J. P., Schanne, S., von Kienlin, A., et al. 2003, *A&A*, 411, L91
- Rowan-Robinson, M. 1977, *ApJ*, 213, 635
- Ruiz, A., Miniutti, G., Panessa, F., & Carrera, F. J. 2010, *A&A* in press, arXiv:1003.0800
- Ryden, B. 2003, *Introduction to cosmology*, ed. Ryden, B.
- Salpeter, E. E. 1964, *ApJ*, 140, 796
- Sambruna, R. M., Maraschi, L., & Urry, C. M. 1996, *ApJ*, 463, 444
- Sarajedini, V. L., Green, R. F., Griffiths, R. E., & Ratnatunga, K. 1999, *ApJ*, 514, 746
- Savchenko, V., Beckmann, V., Neronov, A., et al. 2009, *GRB Coordinates Network*, 8837, 1
- Savchenko, V., Neronov, A., Beckmann, V., Produit, N., & Walter, R. 2010, *A&A*, 510, 77
- Saxton, R. D., Turner, M. J. L., Williams, O. R., et al. 1993, *MNRAS*, 262, 63
- Sazonov, S. Y. & Revnivtsev, M. G. 2004, *A&A*, 423, 469

- Sazonov, S., Revnivtsev, M., Krivonos, R., Churazov, E., & Sunyaev, R. 2007, *A&A*, 462, 57
- Scheuer, P. A. G. & Readhead, A. C. S. 1979, *Nature*, 277, 182
- Schlegel, D. J., Finkbeiner, D. P., & Davis, M. 1998, *ApJ*, 500, 525
- Schmidt, M. 1968, *ApJ*, 151, 393
- Schmidt, M. & Green, R. F. 1983, *ApJ*, 269, 352
- Schmidt, M. & Green, R. F. 1986, *ApJ*, 305, 68
- Schödel, R., Ott, T., Genzel, R., et al. 2003, *ApJ*, 596, 1015
- Schreier, E., Levinson, R., Gursky, H., et al. 1972, *ApJL*, 172, L79
- Schreier, E. J., Feigelson, E., Delvaille, J., et al. 1979, *ApJL*, 234, L39
- Schreier, E. J., Gorenstein, P., & Feigelson, E. D. 1982, *ApJ*, 261, 42
- Schurch, N. J. & Warwick, R. S. 2002, *MNRAS*, 334, 811
- Schurch, N. J., Warwick, R. S., Griffiths, R. E., & Sembay, S. 2003, *MNRAS*, 345, 423
- Schwarzschild, K. 1916, *Abh. Konigl. Preuss. Akad. Wissenschaften Jahre 1906,92*, Berlin, 1907, 189
- Serlemitsos, P. J., Boldt, E. A., Holt, S. S., Ramaty, R., & Briskin, A. F. 1973, *ApJL*, 184, L1
- Seyfert, C. K. 1943, *ApJ*, 97, 28
- Shaposhnikov, N., Swank, J., Shrader, C. R., et al. 2007, *ApJ*, 655, 434
- Shinozaki, K., Miyaji, T., Ishisaki, Y., Ueda, Y., & Ogasaka, Y. 2006, *AJ*, 131, 2843
- Shirai, H., Fukazawa, Y., Sasada, M., et al. 2008, *PASJ*, 60, 263
- Shklovsky, I. S. 1967, *ApJL*, 148, L1
- Shu, X. W., Yaqoob, T., Murphy, K. D., et al. 2010, *ApJ* in press, arXiv:1003.1789
- Siemiginowska, A., Kuhn, O., Elvis, M., et al. 1995, *ApJ*, 454, 77
- Sikora, M., Begelman, M. C., & Rees, M. J. 1994, *ApJ*, 421, 153
- Simonetti, J. H., Cordes, J. M., & Heeschen, D. S. 1985, *ApJ*, 296, 46
- Skinner, G. K. 2003, in “The Gamma-Ray Universe”, *proc. of the 37th Rencontres de Moriond*, ed. A. Goldwurm, D. N. Neumann, J. Trân Thanh Vân, 423–428
- Skinner, G. K. & Connell, P. 2003, *A&A*, 411, L123
- Slipher, V. M. 1913, *Lowell Observatory Bulletin*, 2, 56
- Soldi, S., Beckmann, V., Bassani, L., et al. 2005, *A&A*, 444, 431
- Soldi, S., Türler, M., Paltani, S., et al. 2008, *A&A*, 486, 411

- Soldi, S., Beckmann, V., & Türler, M. 2010a, in proceedings of the Fermi Symposium, Washington D.C., November 2009, arXiv:0912.2254
- Soldi, S., Ponti, G., Beckmann, V., & Lubiński, P. 2010b, in proceedings of 'The Extreme sky: Sampling the Universe above 10 keV', Otranto, October 2009, arXiv:1001.4348
- Soria, R., Baldi, A., Risaliti, G., et al. 2007, MNRAS, 379, 1313
- Sowards-Emmerd, D., Romani, R. W., & Michelson, P. F. 2003, ApJ, 590, 109
- Steffen, A. T., Barger, A. J., Cowie, L. L., Mushotzky, R. F., & Yang, Y. 2003, ApJL, 596, L23
- Steinle, H., Bonnell, J., Kinzer, R. L., et al. 1999, Advances in Space Research, 23, 911
- Stevens, J. A., Jarvis, M. J., Coppin, K. E. K., et al. 2010, ArXiv e-prints
- Stickel, M., Padovani, P., Urry, C. M., Fried, J. W., & Kuehr, H. 1991, ApJ, 374, 431
- Stoche, J. T., Liebert, J., Schmidt, G., et al. 1985, ApJ, 298, 619
- Stoche, J. T., Morris, S. L., Gioia, I. M., et al. 1991, ApJS, 76, 813
- Sturmer, S. J., Beckmann, V., Bykov, A., Lebrun, F., & Terrier, R. 2004, in ESA Special Publication, Vol. 552, 5th INTEGRAL Workshop on the INTEGRAL Universe, ed. V. Schönfelder, G. Lichti, & C. Winkler, 497
- Tanaka, Y., Nandra, K., Fabian, A. C., et al. 1995, Nature, 375, 659
- Tananbaum, H., Gursky, H., Kellogg, E. M., et al. 1972, ApJL, 174, L143
- Tananbaum, H., Peters, G., Forman, W., et al. 1978, ApJ, 223, 74
- Tavecchio, F., Maraschi, L., & Ghisellini, G. 1998, ApJ, 509, 608
- Tavecchio, F., Maraschi, L., Pian, E., et al. 2001, ApJ, 554, 725
- Treister, E., Cardamone, C. N., Schawinski, K., et al. 2009a, ApJ, 706, 535
- Treister, E., Urry, C. M., & Virani, S. 2009b, ApJ, 696, 110
- Treister, E., Natarajan, P., Sanders, D. B., et al. 2010, Science, 328, 600
- Tueller, J., Mushotzky, R. F., Barthelmy, S., et al. 2008, ApJ, 681, 113
- Türler, M., Chernyakova, M., Courvoisier, T., et al. 2010, A&A in press, arXiv:1001.2110
- Turner, T. J., Nandra, K., George, I. M., Fabian, A. C., & Pounds, K. A. 1993, ApJ, 419, 127
- Turner, T. J., George, I. M., Nandra, K., & Turcan, D. 1999, ApJ, 524, 667
- Ubertini, P., Lebrun, F., Di Cocco, G., et al. 2003, A&A, 411, L131
- Ueda, Y., Akiyama, M., Ohta, K., & Miyaji, T. 2003, ApJ, 598, 886
- Ulrich, M. 2000, A&A Rev., 10, 135

- Ulvestad, J. S. & Wilson, A. S. 1984, *ApJ*, 285, 439
- Urry, C. M. & Shafer, R. A. 1984, *ApJ*, 280, 569
- Urry, C. M., Padovani, P., & Stickel, M. 1991, *ApJ*, 382, 501
- Urry, C. M. & Padovani, P. 1995, *PASP*, 107, 803
- Uttley, P., McHardy, I. M., & Papadakis, I. E. 2002, *MNRAS*, 332, 231
- Uttley, P. & McHardy, I. M. 2004, *Progress of Theoretical Physics Supplement*, 155, 170
- Vagnetti, F., Cavaliere, A., & Giallongo, E. 1991, *ApJ*, 368, 366
- Vaiana, G. S., Davis, J. M., Giacconi, R., et al. 1973, *ApJL*, 185, L47
- van den Heuvel, E. P. J. 1975, *ApJL*, 198, L109
- Vaughan, S., Edelson, R., Warwick, R. S., & Uttley, P. 2003, *MNRAS*, 345, 1271
- Vedrenne, G., Roques, J., Schönfelder, V., et al. 2003, *A&A*, 411, L63
- Veron-Cetty, M. & Veron, P. 1998, *A Catalogue of quasars and active nuclei*, ed. Veron-Cetty, M.-P. & Veron, P.
- Vignati, P., Molendi, S., Matt, G., et al. 1999, *A&A*, 349, L57
- Vilhu, O., Hjalmarsdotter, L., Zdziarski, A. A., et al. 2003, *A&A*, 411, L405
- Vilhu, O., Paizis, A., Hannikainen, D., Schultz, J., & Beckmann, V. 2007, in *ESA Special Publication*, Vol. 622, *ESA Special Publication*, 421
- Voges, W., Aschenbach, B., Boller, T., et al. 1999, *A&A*, 349, 389
- von Kienlin, A., Beckmann, V., Covino, S., et al. 2003a, *A&A*, 411, L321
- von Kienlin, A., Beckmann, V., Rau, A., et al. 2003b, *A&A*, 411, L299
- von Kienlin, A., Rau, A., Beckmann, V., & Deluit, S. 2004, in *American Institute of Physics Conference Series*, Vol. 727, *Gamma-Ray Bursts: 30 Years of Discovery*, ed. E. Fenimore & M. Galassi, 622–625
- Walsh, E. J., Sokolowski, T. I., Miller, G. M., et al. 1974, in *Society of Photo-Optical Instrumentation Engineers (SPIE) Conference Series*, ed. D. H. Menzel, L. Larmore, & D. Crawford, Vol. 44, 175–184
- Walter, R., Lubiński, P., Paltani, S., et al. 2007, *A&A*, 461, L17
- Wang, J. & Zhang, E. 2007, *ApJ*, 660, 1072
- Wang, J., Chen, Y., Yan, C., & Hu, C. 2008, *ApJL*, 673, L9
- Ward, M. J., Wilson, A. S., Penston, M. V., et al. 1978, *ApJ*, 223, 788
- Warwick, R. S., Marshall, N., Fraser, G. W., et al. 1981, *MNRAS*, 197, 865

- Weaver, K. A., Yaqoob, T., Holt, S. S., et al. 1994, *ApJL*, 436, L27
- Weaver, K. A., Nousek, J., Yaqoob, T., et al. 1996, *ApJ*, 458, 160
- Weedman, D. W. 1973, *ApJ*, 183, 29
- Whitrow, G. J. 1971, *Journal for the History of Astronomy*, 2, 208
- Wild, V., Kauffmann, G., Heckman, T., et al. 2007, *MNRAS*, 381, 543
- Willott, C. J., Delorme, P., Omont, A., et al. 2007, *AJ*, 134, 2435
- Wilms, J., Pottschmidt, K., Nowak, M. A., et al. 2004, in *American Institute of Physics Conference Series*, Vol. 714, *X-ray Timing 2003: Rossi and Beyond*, ed. P. Kaaret, F. K. Lamb, & J. H. Swank, 116–119
- Winkler, C., Courvoisier, T., Di Cocco, G., et al. 2003a, *A&A*, 411, L1
- Winkler, C., Gehrels, N., Schönfelder, V., et al. 2003b, *A&A*, 411, L349
- Wisotzki, L., Köhler, T., Groote, D., & Reimers, D. 1996, *A&AS*, 115, 227
- Wisotzki, L., Christlieb, N., Bade, N., et al. 2000, *A&A*, 358, 77
- Wolter, A., Caccianiga, A., della Ceca, R., & Maccacaro, T. 1994, *ApJ*, 433, 29
- Wolter, H. 1952, *Annalen der Physik*, 445, 94
- Woltjer, L. 1959, *ApJ*, 130, 38
- Woo, J. & Urry, C. M. 2002, *ApJ*, 579, 530
- Worsley, M. A., Fabian, A. C., Bauer, F. E., et al. 2005, *MNRAS*, 357, 1281
- Wright, T. 1750, *An Original Theory or New Hypothesis of the Universe*, London, Printed for the author by H. Chapelle
- Yaqoob, T., Murphy, K. D., Griffiths, R. E., et al. 2007, *PASJ*, 59, 283
- Yaqoob, T., Murphy, K. D., Miller, L., & Turner, T. J. 2010, *MNRAS*, 401, 411
- Zdziarski, A. A., Ghisellini, G., George, I. M., et al. 1990, *ApJL*, 363, L1
- Zdziarski, A. A., Fabian, A. C., Nandra, K., et al. 1994, *MNRAS*, 269, L55
- Zdziarski, A. A., Johnson, W. N., Done, C., Smith, D., & McNaron-Brown, K. 1995, *ApJL*, 438, L63
- Zdziarski, A. A., Johnson, W. N., & Magdziarz, P. 1996, *MNRAS*, 283, 193
- Zdziarski, A. A., Leighly, K. M., Matsuoka, M., Cappi, M., & Mihara, T. 2002, *ApJ*, 573, 505
- Zdziarski, A. A., Gierliński, M., Mikołajewska, J., et al. 2004, *MNRAS*, 351, 791
- Zel'Dovich, Y. B. & Novikov, I. D. 1964, *Sov. Phys. Dokl.*, 158, 811
- Zhang, Y. H., Celotti, A., Treves, A., et al. 1999, *ApJ*, 527, 719

Acknowledgments

I would like to thank Pierre Binétruy and François Lebrun for the opportunity to work at the APC for the François Arago Centre and for their support in doing this HDR. A special thank goes to Chris Done, Catherine Boisson, and Peter von Ballmoos, the referees of this thesis, who worked their way through this document and were willing to come to APC to attend the Soutenance. Thanks also to Jérôme Rodriguez and Etienne Parizot for being part of the jury!

Through the years I was given the opportunity to work in several astrophysical institutes, and I would like to thank those who gave me the opportunity to learn and thrive in these places: Dieter Reimers (Hamburger Sternwarte), Laura Maraschi (OAB Milano), Thierry J.-L. Courvoisier (ISDC Geneva), Neil Gehrels (NASA/GSFC), and Ian George (UMBC).

Many colleagues helped me throughout these years, both in scientific and in personal ways, too many to mention them all here in person.

A special thank goes to Simona Soldi: for everything we shared and everything still to come!